Physics of the Solid State, Vol. 42, No. 1, 2000, pp. 1–3. Translated from Fizika Tverdogo Tela, Vol. 42, No. 1, 2000, pp. 3–5.

METALS AND SUPERCONDUCTORS

Movement in an Axial Symmetric Wave Propagating in the Solid State Plasma in External Fields

E. D. Éĭdel'man

St. Petersburg State Chemical-Pharmaceutical Academy, St. Petersburg, 197376 Russia

Received December 28, 1998; in final form, May 20, 1999

Abstract—It is shown that an analog of Thomson waves, existing in an ideal fluid, is possible in metals and semiconductors. Possibility of observation of such waves is discussed. © *2000 MAIK "Nauka/Interperiodica".*

1. INTRODUCTION

Charge carriers with mobility μ when exposed to mutually perpendicular electric **E** and magnetic **B** fields move in a circular motion around an axis oriented in the field **B** direction. In a first approximation, the carrier velocity is perpendicular to **E** and has an order of magnitude of $a\mu^2 EB$, where a is a factor of order unity. Such movement can be obviously considered as rotation.

Then, an analogy can be drawn between movement in an axial symmetric wave (a Thomson wave) propagating along the axis, about which the ideal fluid spins as a whole [1], and the movement in an axial symmetric wave propagating along the magnetic field in a solid state plasma. The analogy embraces not only the symmetry of the movements mentioned but also the possibility to neglect viscosity in both the case of plasmas [2] and the case of an ideal fluid. To the author's knowledge, up to now, nobody has considered analogs of the Thomson wave in metals and semiconductors.

2. STATEMENT OF THE PROBLEM. SOLUTION TO THE PROBLEM UNDER THE ASSUMPTION OF INCOMPRESSIBILITY

Let us consider a long hollow thin cylinder of a conductive material. The length of the cylinder L is much larger than its inner (R_i) and outer (R_e) radii. The cylinder thickness $\Delta R = R_e - R_i$, in turn, is significantly less than either of the radii and so

$$\Delta R \ll \{R_i; R_e\} \ll L. \tag{1}$$

We introduce the cylindrical coordinates r, φ, and z along the cylinder axis. Then, let the external magnetic field **B** be along z and a potential difference U be applied between the cylinder axis and its outer surface. Now we can consider the carriers in the cylindrical layer as rotating as a whole with the angular velocity

$$\Omega = a\mu^2 B\frac{U}{R^2}. \tag{2}$$

Here, R is either of the radii R_i and R_e.

It is enough for qualitative analysis to regard Ω as a constant. Quantitative calculations, taking into account the dependence of the angular velocity on the radial variable r, confirm this assumption.

Let us suppose a wave of a small amplitude travels along the cylinder and has the time and spatial coordinate dependence given by the factor

$$\exp\{i(k_\varphi\varphi + k_z z - \omega t)\}. \tag{3}$$

In a wave of axial symmetry $k_\varphi = 0$, while in the cylinder of infinite length, due to translational symmetry, it would be $k_z = \pi q/\lambda$, where λ is the wavelength and $q = 1, 2, 3, \ldots$. Evidently, it is always possible to find an integer number q_0 for which $k_z = \pi q_0/L$. Let us find the dependence of the velocity in the wave $\mathbf{v} = (v_r; v_\varphi; v_z)$ on the radial variable. To do this, we write the Euler equation taking into account the Coulomb force

$$\frac{\partial \mathbf{v}}{\partial t} + 2\Omega \times \mathbf{v} = \frac{e}{m}\nabla\varphi. \tag{4}$$

Here, $E_1 = -\nabla\varphi$ is the variable component of the electric field in plasma, which also includes the pressure, and e and m are the electric charge and mass of a carrier, respectively. We can solve it simultaneously with the continuity equation. In the case of an incompressible fluid, taking the radial dependence of the velocity v_r in the wave of axial symmetry in the form

$$v_r = v_r(r)\exp\{i(\omega t - k_z z)\}, \tag{5}$$

we find that, just as in the Thomson wave [1], $v_r(r)$ satisfies the equation

$$\frac{d^2 v_r(r)}{dr^2} + \frac{1}{r}\frac{d v_r(r)}{dr} + \left[\left(\frac{4\Omega^2}{\omega^2} - 1\right)k_z^2 - \frac{1}{r_2}\right]v_r(r) = 0, \tag{6}$$

1063-7834/00/4201-0001$20.00

which, in turn, reduces to a harmonic equation when condition (1) is satisfied. The solution of the last equation is given by

$$v_r(r) = \text{const} \times \sin\left[k_z(r - R_i)\left(\frac{4\Omega^2}{\omega^2} - 1\right)^{1/2}\right], \quad (7)$$

vanishing at the inner side of the cylinder (at $r = R_i$). The entire picture of the motion in the wave splits into domains between coaxial cylinders of radii r_p which can be obtained from the relationships

$$k_z(r_p - R_i)\left(\frac{4\Omega^2}{\omega^2} - 1\right)^{1/2} = p\pi, \quad p = 0, 1, 2, \ldots, (8)$$

$v_r = 0$ at these surfaces and, hence, they are never crossed by the plasma.

The solution (7) is also zero at the outer surface of the cylinder, i.e., at $r = R_e$, which leads to the equation

$$k_z\Delta r\left(\frac{4\Omega^2}{\omega^2} - 1\right)^{1/2} = p\pi, \quad (9)$$

relating ω to k_z for waves with a given value of the parameter p, which is the number of the coaxial domains.

The following conclusions can be drawn from this simple model of an incompressible plasma.

First, it follows from (9) that the wave is not attenuated and propagates with an angular velocity

$$\omega = \omega_0 = b\mu^2 B\frac{U}{R^2}k_z\Delta r/[(k_z\Delta r)^2 + \pi^2 p^2]^{1/2}, \quad (10)$$

where b is a factor of order unity.

Second, as seen from the relationships (3)–(7), for a hollow thin cylinder and a wave of a small amplitude it is possible to assume the coordinate and time dependences to be given by the factor

$$\exp\{i[k_r(r - R_i) + k_\varphi\varphi + k_z z - \omega t]\}, \quad (11)$$

where $k_r = p\pi/\Delta r$.

The argument of the exponential function in (11) is the same for a solution which does not satisfy condition (1). In that case, the harmonic functions are replaced by the Bessel functions, whose roots take the place of the numbers $p\pi$.

As a concluding remark to the section it should be mentioned that in the same way as the pressure induced by the Thomson wave is found in an ideal incompressible fluid in [1], a small disturbance of the electric field E_1 produced by the analog of this wave in a plasma can be derived. When the disturbance of the electric field is known, from the Poisson equation

$$\nabla^2\varphi = -en_1\varepsilon \quad (12)$$

(here ε is the permittivity) it is easy to find the perturbation induced by the wave in the concentration of charge carriers n.

3. SINGLE-COMPONENT SOLID-STATE PLASMA OF A METAL

A wave propagating through the electron gas in a metal produces perturbations of the electric current which can be described by

$$\mathbf{j}_1/e = n_1\mathbf{V} + n\mathbf{v} - \mu n\nabla\varphi + \mu n_1\mathbf{E} - D\nabla n_1. \quad (13)$$

This equation takes into account conduction (the conductivity is given by $\sigma = \mu ne$), diffusion (D is the diffusion constant), and a charge carrier transport with the flow of fluid ($\mathbf{V}$ is the flow velocity).

Electron gas cannot be regarded as incompressible. Its compression in the course of wave propagation contributes to the kinetic equation. It suffices to consider this equation in the relaxation time τ approximation [3],

$$\frac{\partial n_1}{\partial t} + \frac{n_1}{\tau} - D\nabla^2 n_1 - \mu n\nabla^2\varphi + \mu(\mathbf{E}\nabla)n_1 + (\mathbf{V}\nabla)n_1 + n\,\mathrm{div}\,\mathbf{v} = 0. \quad (14)$$

Making use of solution (11), from the Euler (4), Poisson (12), and Boltzmann (14) equations, we find a dispersion law for the waves of axial symmetry under no-flow conditions

$$(\omega^2 - 4\Omega^2)\left[1 - \left(1 + \frac{k_r^2}{k_z^2}\right)\frac{\omega(\omega + i\Gamma)}{\omega_p^2}\right] + \frac{k_r^2}{k_z^2}\omega^2 = 0. \quad (15)$$

Here, $\omega_p^2 = ne^2/(m\varepsilon)$ is the square of the plasma frequency, $\Gamma = a_1/\tau + a_2 D/(\Delta r)^2 + a_3\sigma/\varepsilon$ is the decrement, and a_1, a_2, a_3 are parameters of about unity indicating relative contributions of different relaxation processes into absorption of the wave.

The plasma frequency ω_p is always higher than the rotation speed Ω and so the dispersion equation (15) can be rearranged as

$$\omega^4 + i\Gamma\omega^3 + \omega_p^2(\omega^2 - \omega_0^2) = 0. \quad (16)$$

It is obvious that at a low frequency $\omega \ll \omega_p$, from (16) we obtain relationship (10). As shown in [3], in a low-frequency approximation, the electron gas can be assumed to be incompressible, while at a high frequency $\omega \gg \omega_p$, equation (16) results in $\omega = -i\Gamma$, which corresponds to absorption of high-frequency waves [3]. In the general case, we have $\omega = \omega_0 - i\Gamma$. A condition for weak extinction, i.e., $\Gamma \ll \omega_0$ can be expressed as

$$\frac{\mu^2 UB}{R}/v_T \gg \frac{LRl}{(\Delta r)^3}. \quad (17)$$

To derive the last estimation, it was taken into account that the diffusion term $D/(\Delta r)^2$ is the main contribution to the decrement Γ and the diffusion coefficient is of the same order of magnitude as the product of the mean velocity of thermal carrier motion v_T and of the mean free path l, i.e., $D \simeq v_T l$. The inequality (17)

is well satisfied under the condition of a weak magnetic field ($\mu B \simeq 1$) in virtue of the smallness of the mean free path of electrons in typical metals.

In the case of axially asymmetric waves, we have $k_\varphi = 1, 2, 3, \ldots$ and the quantity ω_0, given by (10), is easily shown to be replaced by a multiple of it, $(1 + k_\varphi)\omega_0$.

Taking the flows in the plasma into account would result in replacing the parameter $i\Gamma$ in (15) and (16) by $i\Gamma - \mathbf{kV}$, where $\mathbf{k}$ is obviously given by components (k_r; k_φ; k_z). If the only kind of flow is present, i.e., the flow caused by the fields, and, therefore, its velocity is about ΩR, then the result $\omega \simeq \omega_0 - i\Gamma$ will be true even in the high frequency range.

Both complications mentioned do not change the results qualitatively. Therefore, the only difference between the Thomson waves in an ideal incompressible fluid and the (charge) waves in metals is the weak extinction of the charge waves. At the same time, the waves in the electron gas of a metal and the Thomson waves in the ideal fluid are similar in that both kinds of waves are, in general, the waves of velocity. It is easy to show that the ratio of the velocity amplitude v to the velocity $\omega_0 R$ (a characteristic velocity of the stationary plasma in metals) significantly exceeds (as much as $(L/\Delta r)^2$ times) the ratios φ/U and n_1/n.

4. BICOMPONENT SOLID-STATE PLASMA OF A SEMICONDUCTOR

The wave propagating in the gas of electrons and holes of a semiconductor produces perturbations of both components of the electric current, $\mathbf{j}^\pm$. These perturbations can be written in the form of (13) but separately for the electrons and holes.

In this case, the system of equations of the problem includes the Euler equations (4), written separately for the velocities of charge carriers of two kinds. The angular velocity of the plasma moving as a whole, given by (2), also differs for electrons and holes, which is due to the difference in the carrier mobility $\mu^\pm$. Deviation from neutrality is introduced into the Poisson equation (12) for the semiconductor plasma through the difference of the carrier concentrations $n_1^+ - n_1^-$. At last, in the kinetic equations with the same form as (14) but written separately for electrons and holes, the compressibility of both electrons and holes should be taken into account.

Both charged and quasi-neutral waves are possible in the semiconductor plasma. An analysis of cumbersome equations describing the wave propagating through this bicomponent semiconductor plasma has shown that the results earlier obtained for the electron gas in a metal are valid for semiconductors. It is only necessary in the corresponding equations to take into account the difference in the characteristics of the two plasma components, for example, to take into account two components of diffusion characterized by the diffusivity of electrons D^- and holes D^+.

All the conclusions made in Section 3 for the waves in the plasma of metals can be extended to the case of semiconductors.

To sum up the results obtained, we note that in the first approximation, the frequency of an axial symmetric wave can be obtained from relationship (10), disregarding the type and number of current carriers and without regard to the resulting electric charge or quasi-neutrality of the wave. In the case of an axially a symmetric wave, in addition to the wave given by (10), a drift wave appears with a frequency being a multiple of Ω. A characteristic of the latter wave is an extinction associated either with the limited free-carrier lifetime or with conductivity (for electrically charged waves in the plasma of metal) or, possibly, with diffusion (for quasi-neutral waves in the plasma of a semiconductor). In the drift waves, the sense of inequality (17) is reversed. In the case where no voltage is applied but the radial temperature difference $T_e - T_i$ exists, an analog of the Thomson wave caused by thermoelectric effect is also possible.

Owing to the inequality $\Delta r \ll L$, expanding the frequency in (10) into a series yields $\omega = d_1 k + d_2 k^3$ (d_1 and d_2 are constants here). This demonstrates a possibility for the waves described to form a soliton of the Korteweg–de Vries type [2].

Excitation and observation of the Thomson-type wave in solids is possible by applying a probe field $B' \ll B$ near one of the cylinder end faces, which will cause a frequency deviation $\Omega' \sim B'$. An excitation with such a frequency will propagate along the cylinder axis at a speed of $\Omega'\Delta r/(p\pi)$, so that after a time delay of $(L/\Delta r)/(p\pi/\Omega')$ at the other face of the cylinder it will be possible to detect an additional magnetic field. Such a delay takes place when condition (17) is satisfied. To observe the soliton, a Π-shaped pulse of the magnetic field is necessary. In a weak field $B \simeq 1/\mu$ and at an electrical field level below the heating level, the frequency of the waves analogous to the Thomson waves will be of 10^6–10^7 Hz.

REFERENCES

1. L. D. Landau and E. M. Lifshitz, *Hydrodynamics* (Nauka, Moscow, 1988).

2. E. M. Lifshitz and L. P. Pitaevskiĭ, *Physical Kinetics* (Nauka, Moscow, 1979).

3. M. Steele and B. Vural, *Wave Interaction in Solid State Plasmas* (McGraw-Hill, New York, 1969; Atomizdat, Moscow, 1973).

Translated by S. Klimentov

Physics of the Solid State, Vol. 42, No. 1, 2000, pp. 103–111. Translated from Fizika Tverdogo Tela, Vol. 42, No. 1, 2000, pp. 100–108.

MAGNETISM AND FERROELECTRICITY

Thermodynamics of ^{3}He Solid Monolayers in the Heisenberg Model

T. N. Antsygina and K. A. Chishko

Physicotechnical Institute of Low Temperatures, National Academy of Sciences of Ukraine, Kharkov, 310164 Ukraine
e-mail: chishko@ilt.kharkov.ua

Received May 21, 1999

Abstract—The two-dimensional Heisenberg model is applied to the interpretation of the experimental data on the thermodynamic and magnetic properties of ^{3}He monoatomic films in the millikelvin temperature range, i.e., under conditions when these properties are completely governed by the dynamics of the nuclear spin subsystem. The theoretical results obtained make it possible to describe the internal energy E, the heat capacity C_s, and the magnetic susceptibility χ of the two-dimensional spin-1/2 Heisenberg ferromagnets and antiferromagnets on a triangular lattice within the unified approach over the entire range of temperatures. The data available in the literature on the heat capacity and magnetic susceptibility of ^{3}He films are interpreted in the framework of the advanced theory. Most attention is concentrated on the layers characterized by the ferromagnetic exchange. Comparative analysis of theoretical and experimental data is carried out with the use of two fitting parameters: the exchange interaction constant J and the number of "active" spins n_2 in the layer that is determined from the entropy of the system in the limit $T \longrightarrow \infty$. It is demonstrated that, for the ferromagnetic layers, the theoretical results obtained within the Heisenberg model are in very good agreement with the experimental data reported by different authors. *© 2000 MAIK "Nauka/Interperiodica".*

In recent years, considerable interest has been expressed in studies of ^{3}He films deposited on exfoliated graphite substrates [1–9]. The ^{3}He monolayers provide an excellent example of two-dimensional quantum systems whose physical properties in the millikelvin temperature range are completely governed by the dynamics of a nuclear spin subsystem.

The ^{3}He films investigated experimentally consist of several monoatomic layers [3]. The first monolayer deposited directly on a graphite substrate turns out to be solid and paramagnetic, because the interaction with substrate atoms dominates over the interatomic interaction in the layer. The second ^{3}He layer applied on top of the first layer rather weakly interacts with a substrate, and its properties are determined by the appreciable (of the order of several millikelvins) exchange interaction between atoms within the layer. In its nature, this layer is virtually the ideal two-dimensional spin-1/2 magnet on the triangular lattice. In this layer, the exchange interaction constant J depends on the coverage ρ (the total number of atoms per unit area of a substrate). At small ρ, the second layer exhibits antiferromagnetic properties. As the coverage increases, the J constant changes sign, and the exchange interaction becomes ferromagnetic. Typically, the exchange interaction constant $|J|$ is equal to ~1–3 mK.

A large amount of experimental data on the heat capacity and the magnetic susceptibility of ^{3}He monolayers on graphite has been amassed to date [1–9]. However, it can be stated that there is no general agreement in the literature regarding the choice of an adequate physical model describing the effects observed. In a number of works [1, 3, 4], the Heisenberg model was used for the interpretation of experimental data. At present, the concept advanced by Bäuerle *et al.* [7–9] is more widely accepted. According to this concept, the Heisenberg model is of limited utility for describing the behavior of ^{3}He films in the ferromagnetic state at sufficiently high coverages and, in essence, is inapplicable to the interpretation of their properties in the antiferromagnetic state. The reason is that the processing of the experimental temperature dependences of the spin heat capacity C_s and the magnetic susceptibility χ in the framework of the Heisenberg model leads to different values of the exchange interaction constants J_c and J_χ. As an alternative to the Heisenberg model, the authors of [2, 5, 7–9] proposed the multiple-spin exchange model [10, 11], which involves several exchange interaction constants J_n corresponding to the ring exchange in groups composed of n atoms (n = 2, 3, …, 6). In this model, the J_c and J_χ constants are expressed by different combinations of the J_n constants, and their variation as fitting parameters makes it possible to achieve a reasonable agreement between experimental and theoretical data. However, it should be emphasized that the number of fitting parameters J_n in the multiple-spin

exchange model is more than two, whereas only two constants J_c and J_χ can be obtained experimentally. Therefore, the uncertainty arises in the choice of the J_n constants, and, hence, the advantages in the processing of experimental data that are seemingly offered by the multiple-spin exchange model appear to be sufficiently controversial. It should be also kept in mind that, in virtually all the above works, treatment within the Heisenberg and multiple-spin exchange models is commonly restricted to high-temperature series expansions [12, 13], which, in principle, give no way of describing, for example, such an important feature in the behavior of two-dimensional magnets as the peak in the temperature dependence of the spin heat capacity in the temperature range $T \sim |J|$. De Mello *et al.* [14, 15] attempted to interpret the thermodynamic characteristics of two-dimensional ferromagnets at $T \leq J$ in terms of the Heisenberg model on the basis of the renormalization group approach. However, the authors themselves noted that their theory satisfactorily describes the experimental data only at $T \geq J$ [14, 15].

Therefore, the interpretation of the thermodynamic behavior of ^{3}He two-dimensional films in the low-temperature range $T \leq J$ is an urgent problem. In particular, the question about the boundaries of the applicability of the Heisenberg model to the description of these systems for different exchange types remains open. Recently, one of the authors of this work, within the unified approach, analytically described the thermodynamics of two-dimensional Heisenberg ferromagnets and antiferromagnets on the triangular lattice at arbitrary temperatures [16]. The aim of the present work was to interpret the temperature dependences of the spin heat capacity and the magnetic susceptibility for the ^{3}He solid monolayers at coverages corresponding to the ferromagnetic exchange interaction [1–9] in the framework of the theory developed in [16].

In Section 1 of the paper, we briefly describe new theoretical results obtained in [16] for the thermodynamics of Heisenberg systems on the triangular lattice. Section 2 is dedicated to detailed comparison of the theoretical results with the experimental data of different authors [1–9]. As will be shown below, the correct choice of only two fitting parameters of the theory—the exchange interaction constant J in the Heisenberg model and the number of "active" spins n_2 in the second layer [17, 18]—allows us, within the unified approach, to achieve a very good accord with the experimental data on the heat capacity [1–5] and the susceptibility [7–9] of ^{3}He solid monolayers in the ferromagnetic state and to corroborate the applicability of this model for the above systems. At the end of Section 2, the theoretical results are compared with the experimental data obtained by Siqueira *et al.* [2] on the heat capacity of ^{3}He layers in the antiferromagnetic state. In this case, too, the theoretical and experimental data correlate well.

1. HEAT CAPACITY AND SUSCEPTIBILITY OF TWO-DIMENSIONAL HEISENBERG MAGNETS ON THE TRIANGULAR LATTICE

Let us consider the isotropic Heisenberg system with the spin $S = 1/2$. Hamiltonian of the system can be represented as

$$H = -J\sum_{\mathbf{f}\delta}\mathbf{S}_\mathbf{t}\mathbf{S}_{\mathbf{f}+\delta}, \quad (1)$$

where J is the exchange interaction constant ($J > 0$ for a ferromagnet, and $J < 0$ for an antiferromagnet), $\mathbf{S_f}$ is the spin operator on the site $\mathbf{f}$, and δ is the vector specifying the coordinates of the nearest neighbors on the triangular lattice. The computational technique used in this work is based on the two-time Green function formalism [19]. The uncoupling of functions of greater order was carried out according to the procedure that was proposed by Kondo and Yamaji [20] for the description of the thermodynamics of one-dimensional Heisenberg system and was extended in [21, 22] to two-dimensional magnets on the square lattices. The advantage of this procedure resides in the fact that, without assumption regarding the existence of a long-range order in a system, the problem is reduced to the calculation of correlation functions adequately taking into account the details of a short-range order. Therefore, the technique used explicitly reflects the specific feature of low-temperature Heisenberg magnets, in which, as is known, the long-range order is absent at any finite temperatures; i.e., the thermodynamic mean $\langle S^z\rangle$ is equal to 0 (the Mermin–Wagner theorem [23]).

In [16], the thermodynamics of spin-1/2 Heisenberg ferromagnets and antiferromagnets on the triangular lattice was analyzed in the framework of the above approach. Below, we will briefly describe such results of this work that are necessary for the subsequent comparison of the theoretical and experimental data.[1] The uncoupling of the Green functions of greater order leads to the correlation functions ($\nu = x, y,$ and z)

$$c_1 = 4\langle S^\nu_\mathbf{f} S^\nu_{\mathbf{f}+\delta}\rangle, \quad (2)$$

$$c_2 = 4\langle S^\nu_\mathbf{f} S^\nu_{\mathbf{f}+\delta+\delta'}\rangle, \quad \delta \neq -\delta', \quad \delta + \delta' \neq \delta''. \quad (3)$$

Ultimately, all the thermodynamic characteristics of a system are expressed by these functions.

As follows from definition (2), the c_1 function accounts for the correlations of spin in the site $\mathbf{f}$ with neighbors located in the first coordination sphere. The second correlation function c_2 describes the correlations between spins being two steps apart along the translation vectors $\boldsymbol{\delta}$. Note that, in addition to the trivial

[1] We call attention to the fact that the exchange interaction constant J in formula (1) is two times less than the corresponding constant in [16]. The choice of the Hamiltonian in the form of (1) in the present paper is connected only with convenience of comparison between the theoretical results and numerical experimental data taken from [1–9].

condition $\boldsymbol{\delta} \neq -\boldsymbol{\delta}'$, the definition of c_2 on the triangular lattice requires the fulfillment of the second nonequality in (3). This excludes the two-step paths that can lead to the spin in the first coordination sphere, which corresponds to the correlations between the nearest neighbors that is already included in the function c_1. In addition to correlators (2) and (3), the theory involves the additional parameter α [16, 20], which is chosen so that the following kinematic relationship is met:

$$\langle \mathbf{S}^2 \rangle = S(S+1) = 3/4. \tag{4}$$

It is interesting to note that this uncoupling procedure turns out to be more efficient than the universally adopted method, in which $\alpha \equiv 1$. Specifically, the fulfillment of condition (4) automatically leads to the temperature dependence of the correlation functions, which follows from the direct high-temperature series expansion (see [20, 21]).

After the uncoupling of all the Green functions of greater order and going to the Fourier transform in terms of coordinates, for the function

$$G(\omega, \mathbf{k}) = \sum_{\mathbf{f}} \langle\langle S_{\mathbf{f}}^{\nu} | S_{\mathbf{f}'}^{\nu} \rangle\rangle_{\omega} \exp(i\mathbf{k}\mathbf{f}),$$

we have

$$G(\omega, \mathbf{k}) = \frac{3Jc_1}{\pi} \frac{1-\gamma_{\mathbf{k}}}{\omega^2 - \omega_{\mathbf{k}}^2}. \tag{5}$$

Here, we introduced the following designations:

$$\omega_{\mathbf{k}}^2 = 12J^2(1-\gamma_{\mathbf{k}})[\Delta + 6\tilde{c}_1(1-\gamma_k)], \tag{6}$$

$$\gamma_{\mathbf{k}} = \frac{1}{6}\sum_{\delta} \exp(i\mathbf{k}\boldsymbol{\delta}), \quad \Delta = 1 - 5\tilde{c}_1 + 3\tilde{c}_2, \tag{7}$$

and $\tilde{c}_i = \alpha c_i$ ($i = 1, 2$).

By using the spectral relationships for the Green functions [19], we can obtain the self-consistent set of equations for the determination of α, $\tilde{c}_1$, and $\tilde{c}_2$:

$$\alpha = \frac{12J\tilde{c}_1}{N}\sum_{\mathbf{k}} g(\mathbf{k}), \tag{8}$$

$$1 = \frac{12J}{N}\sum_{\mathbf{k}} \gamma_{\mathbf{k}} g(\mathbf{k}), \tag{9}$$

$$\tilde{c}_2 = \frac{4J\tilde{c}_1}{N}\sum_{\mathbf{k}} (6\gamma_{\mathbf{k}}^2 - 2\gamma_{\mathbf{k}} - 1) g(\mathbf{k}), \tag{10}$$

where N is the total number of sites, and

$$g(\mathbf{k}) = \frac{1-\gamma_{\mathbf{k}}}{\omega_{\mathbf{k}}} \coth\frac{\omega_k}{2T}. \tag{11}$$

Hereafter, we assume that the Boltzmann constant k_B is equal to unity. Note that system (8)–(10) has the form that is formally identical for ferromagnets and antiferromagnets, because it was derived without any special assumptions regarding the sign of the exchange integral [16]. The fundamental difference between ferromagnets and antiferromagnets becomes essential only in specific analysis of system (8)–(10) at $J > 0$ and $J < 0$.

The thermodynamic characteristics of interest are expressed in terms of the $\tilde{c}_1$, $\tilde{c}_2$, and α functions. The internal energy E is equal to the mean value of Hamiltonian (1)

$$\frac{E}{N} = -\frac{9}{4}Jc_1. \tag{12}$$

The heat capacity C_s of the spin subsystem is given by

$$\frac{C_s}{N} = \frac{\partial E}{\partial T}, \tag{13}$$

and the magnetic susceptibility normalized to Curie's constant takes the form

$$\frac{\chi}{C} = \frac{4}{T}\lim_{\mathbf{k}\to 0}\langle S_{\mathbf{k}}^z S_{-\mathbf{k}}^z \rangle = \frac{2c_1}{J\Delta}, \tag{14}$$

where Δ is defined according to (7).

At arbitrary temperatures, the system of equations (8)–(10) can be solved only using numerical techniques. The analytic asymptotics can be found in the limit of high and low temperatures. Before proceeding to the discussion of the results obtained by numerical computations, let us write the asymptotic expressions for the internal energy, heat capacity, and susceptibility of two-dimensional Heisenberg magnets. In the high-temperature limit, at $|\theta| \gg 1$ ($\theta = T/J$), system (8)–(10) can be solved by the expansion in terms of inverse powers of the θ parameter. In this case, for ferromagnets and antiferromagnets, the asymptotic expressions for thermodynamic quantities (12)–(14) formally have the same form and differ only in the sign of the θ parameter. Retaining terms of the order of θ^{-2}, one obtains

$$\frac{E}{JN} \simeq -\frac{9}{4\theta}\left(1 + \frac{1}{2\theta}\right), \tag{15}$$

$$\frac{C_s}{N} \simeq \frac{9}{4\theta^2}\left(1 + \frac{1}{\theta}\right), \tag{16}$$

$$\frac{\chi}{C} \simeq \frac{1}{T(1-3\theta)}. \tag{17}$$

It should be noted that relationships (15)–(17) coincide with the corresponding formulas obtained by the direct high-temperature series expansion (see, for example, [12, 24]).

Compared to the high-temperature limit, the calculation of asymptotics in the low-temperature limit is much more complicated and has the specific features

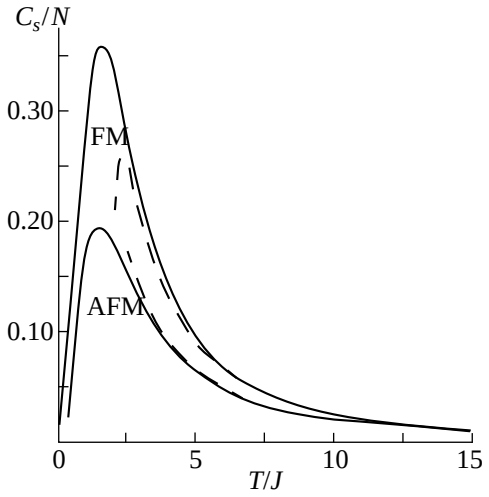

Fig. 1. Spin heat capacities of two-dimensional ferromagnet and antiferromagnet on the triangular lattice as functions of the dimensionless temperature. For comparison, the high-temperature asymptotics taken from [12] are shown by dashed lines.

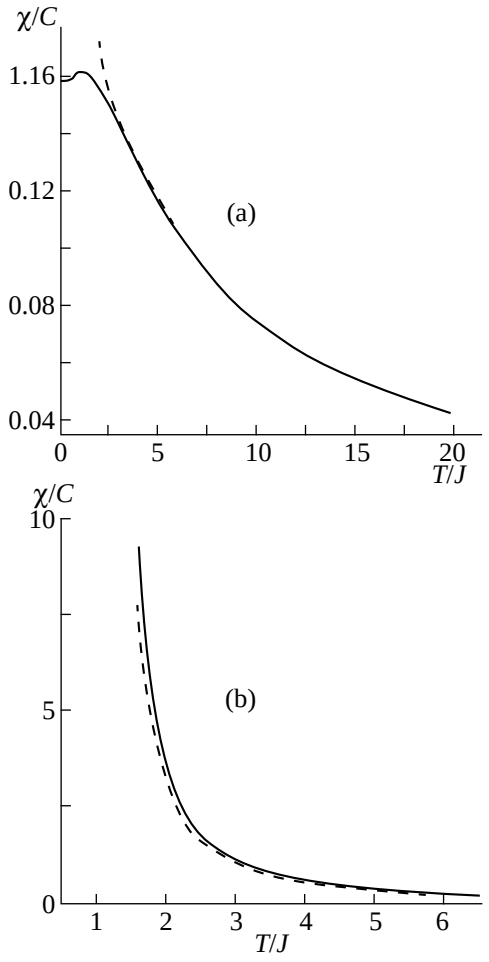

Fig. 2. Magnetic susceptibilities of two-dimensional (a) antiferromagnet and (b) ferromagnet on the triangular lattice as functions of the dimensionless temperature. For comparison, the high-temperature asymptotics taken from [12] are shown by dashed lines.

for the ferromagnetic and antiferromagnetic systems. Specific analysis of the system of equations (8)–(10) essentially depends on the sign of the exchange integral; in particular, the sign of the $\tilde{c}_1$ correlation function is determined by the sign of J. For this reason, either of these two cases should be considered individually [16]. For ferromagnets at low temperatures, we have

$$\frac{E}{JN} \simeq -\frac{3}{2}\left[1 - \frac{\pi}{2\pi\sqrt{3}}\theta^2\right], \tag{18}$$

$$\frac{C_s}{N} \simeq \frac{\pi}{8\sqrt{3}}\theta, \tag{19}$$

$$\frac{\chi}{C} \simeq \frac{4}{3T}\exp\left(\frac{\pi\sqrt{3}}{\theta}\right). \tag{20}$$

Note that relation (19) agrees with similar formula given in [25].

The low-temperature asymptotics for the antiferromagnet on the triangular lattice are such that the coefficients of expansions in power series of temperature can be determined only by the numerical solution of some system of transcendental equations [16]. As a result, the expressions are written as

$$\frac{E}{N|J|} \simeq -0.964 + 0.00725|\theta|^3, \tag{21}$$

$$\frac{C_s}{N} \simeq 0.0218\theta^2, \tag{22}$$

$$\frac{\chi|J|}{C} \simeq 0.159 - 0.013|\theta|^3. \tag{23}$$

As is seen from formulas (19) and (22), the heat capacity of ferromagnets at $T \longrightarrow 0$ is the linear function of the temperature, which is consistent with the theory of spin waves.

In order to obtain the thermodynamic functions in the intermediate temperature range, it is necessary to numerically solve the system of transcendental equations (8)–(10) and to determine the α, $\tilde{c}_1$, and $\tilde{c}_2$ quantities as functions of the temperature. Then, the internal energy, heat capacity, and susceptibility of the magnet are calculated by relationships (12)–(14). The results of numerical calculations are depicted in Figs. 1 and 2. The calculated temperature dependences of the spin heat capacity for the ferromagnet and antiferromagnet on the triangular lattice are displayed in Fig. 1. Figures 2a and 2b demonstrate the temperature dependences of the magnetic susceptibility for the antiferromagnet and ferromagnet, respectively. It can be seen from Fig. 1 that, for the triangular lattice, the heat capacity of the ferromagnet is larger than that of the antiferromagnet over the entire range of temperatures (it is worth noting that, by contrast, for the square lattice, the heat capacity of the antiferromagnet is higher than that of the ferromag-

net [16, 18]). The maximum values of the calculated heat capacities of ferromagnet and antiferromagnet differ two times. It is interesting that the same ratio between the heat capacities at a maximum was experimentally observed by Siqueira *et al.* [2] in the investigation on the ^{3}He films in the ferromagnetic and antiferromagnetic states.

For comparison, the graphs of the high-temperature series expansions determined to within the $\sim|\theta|^{-13}$ terms in [21] are shown by dashed the lines in Figs. 1 and 2. It is easy to see that our results very well agree with the data taken from [21] up to temperatures at which the series expansions in actual fact become inapplicable.

There is one more evident criterion that enables us to assess the efficiency of the proposed approach for analysis of the Heisenberg model. This criterion lies in the fact that the entropy of the spin subsystem

$$S(T) = \int_0^T dT \frac{C_s(T)}{T} \tag{24}$$

at high temperatures should tend to the limit

$$S(\infty) = N\ln 2. \tag{25}$$

Figure 3 depicts the dependence $S(T)$ calculated from formula (24) for the ferromagnet on the triangular lattice. It is seen that, for the ferromagnet, condition (25) is met with a high accuracy. This fact, and also the excellent agreement between the calculated heat capacity and the high-temperature series expansions, suggest that, for the ferromagnet, the proposed method adequately describes the thermodynamics of the spin system over the entire temperature range.

For the antiferromagnet, Fig. 1 demonstrates that our calculated data and the results of the high-temperature series expansions also correlate very well; however, condition (25) is fulfilled notably worse. This fact was mentioned and discussed in detail by Kondo and Yamaji [20] in consideration of the one-dimensional Heisenberg model. In [20], it was shown that the used method correctly predicts the temperature dependence of the heat capacity at low temperatures $C_s \sim aT$, but the a coefficient becomes underestimated. It seems likely that similar situation takes place in our antiferromagnet on the triangular lattice; i.e., the coefficient of the θ^2 term in expression (22) is underestimated. Note also that the applicability range of low-temperature asymptotics (21)–(23), as in the one-dimensional case [20], is extremely narrow. Therefore, all the foregoing permits us to argue that the advanced theory is applicable for describing the thermodynamics of antiferromagnetic system over the entire temperature range with the exception of a narrow range in the vicinity of absolute zero.

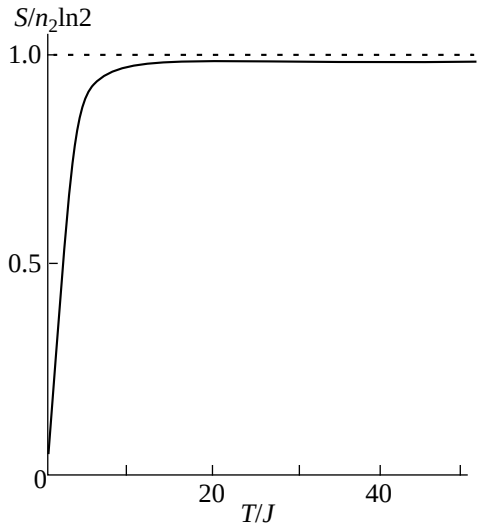

Fig. 3. Entropy of two-dimensional ferromagnet on the triangular lattice.

2. COMPARISON WITH EXPERIMENTAL DATA

The heat capacity and the magnetic susceptibility of the second layer in the ^{3}He films have been measured over wide ranges of the coverages ρ and temperatures (for example, Ishida *et al.* [5] measured C_s down to 90 μK). As to the interpretation of experimental data, the question regarding the applicability of the Heisenberg model for describing the observed properties of ^{3}He films is actively discussed in the literature [2, 4, 5, 8, 9]. The majority of authors believe that the Heisenberg model is appropriate solely for the ferromagnetic layers (moreover, only at the high coverages $\rho \geq 0.26$ Å^{-2}) and is not applicable to antiferromagnetic layers, in which the effects of multiple-spin exchange play an essential part [7, 9]. However, it should be pointed out that this conclusion was made solely on the basis of results obtained with the high-temperature series expansions for both the Heisenberg and multiple-spin exchange models. At the same time, the high-temperature series expansions do not reflect such an important feature in the $C_s(T)$ dependence as the maximum at $T \sim |J|$. Therefore, the fitting of theoretical results to experimental data with the use of these series expansions appears ambiguous and the question as to the applicability range of the Heisenberg model for the systems under consideration remains open.

In this section, we will compare the aforementioned experimental data with the results of our theory, which describes the thermodynamics of the Heisenberg magnets on the triangular lattice over the entire range of temperatures.

In this respect note that, for antiferromagnetic layers, there is a considerable scatter in the data reported by different authors. For example, in [3, 5, 26, 27], it was found that, at high temperatures, the heat capacity

Fitting parameters for comparison of theoretical and experimental data

Experiment	[4, 5]	[9]	[9]	[9]	[2]	[3]	[5]	[3]
ρ, Å^{-2}	0.23	0.2303	0.236	0.2383	0.24	0.24	0.26	0.26
ρ_2, Å$^{-2} \times 10^2$	8.084	8.086	8.115	8.125	8.131	8.131	8.176	8.176
σ	0.77	–	–	–	0.86	0.86	0.97	–
J, mK	2.2	2.18*	1.85*	1.7*	1.6	1.6	0.83	0.83

Note: Constants J marked by asterisk are obtained by fitting to the data on magnetic susceptibility, and the remaining values are found by fitting to the heat capacity.

of ^{3}He films decreases more slowly than $1/T^2$ (in some cases, $C_s \sim 1/T$). On the other hand, the usual behavior $C_s \sim 1/T^2$ at $T \gg |J|$ was observed in [1, 2]. Furthermore, in these works, it was demonstrated that the same universal dependence of the heat capacity on the dimensionless temperature $\theta = T/|J|$ takes place for the films with the coverages ρ in the range 0.178–0.202 Å^{-2} (see Fig. 3 in [2]). This serves as an indirect indication that the Heisenberg model is applicable to the antiferromagnetic systems. At present, it is difficult to draw definite conclusions of whether the above effects are associated with some features of particular experimental techniques or their presence reflects the physical nature of these systems.

The experimental data obtained in different works for ferromagnetic layers are in good agreement, and, consequently, it can be believed that the behavior of the ferromagnetic system is revealed reliably. Therefore, in what follows, we will predominantly compare the theoretical and experimental data concerning the ferromagnetic system.

In the Heisenberg model, the heat capacity per one spin is the universal function of the dimensionless temperature $\theta = T/|J|$. Therefore, for convenience of comparison, the experimental data were processed in the following way. The experimental heat capacity should be normalized to the number of spins involved in the exchange interaction and be represented as a function of the dimensionless variable θ. The total number of atoms N_2 in the second layer is known from independent structural investigations [3, 9]. However, as was first mentioned in [17, 18] and, then, was confirmed in other works [1–3, 7–9], there are strong grounds to believe that spins in the second layer of the ^{3}He multilayer system do not all contribute to the thermodynamic properties of two-dimensional crystal. To put it differently, the number of active spins n_2 in the second layer is always less than the number of atoms N_2 forming this layer. The n_2 number can be evaluated from criterion (25). The entropy of the system was calculated by formula (24) from the experimental temperature dependence of the total spin heat capacity $C_s(T)$ for the layer. Then, we determined the limiting value of the entropy at $T \longrightarrow \infty$, which should be equal to $n_2 \ln 2$ for both the ferromagnetic and antiferromagnetic layers. This limiting entropy allowed us to calculate n_2 and, thus, the heat capacity per one active spin. The ratios

$$\sigma = \frac{n_2}{N_2}$$

determined from the experimental data usually fall in the range 0.75–0.95 [1–9]. Note that, at least, in the ferromagnetic state (0.21 Å$^{-2} < \rho <$ 0.26 Å^{-2}), the value of σ monotonically increases with an increase in ρ; i.e., the larger the coverage, the higher the value of σ. Therefore, an increase in the total coverage ρ leads to an increase in the second layer coverage ρ_2 and also in the fraction of spins involved in the exchange interaction in the second layer ($n_2 \longrightarrow N_2$). Likely, this fact explains the inference made by Roger *et al.* [9] that the Heisenberg model is applicable to layers with the coverage $\rho \geq 0.26$ Å^{-2}. Nowadays, there is no universally accepted physical interpretation of this effect; however, it is quite clear that the effect stems from the structural transformation of the second layer as the next layers are built up. Since the relationship (25) does not depend on the exchange interaction constant J, the number of active spins n_2 in the second layer can serve as an independent fitting parameter used in comparison of the theoretical and experimental data.

The exchange interaction constant J is the second fitting parameter. In all, without any exception, experimental works [1–9], this quantity was evaluated in one way or another from the high-temperature asymptotics of the heat capacity or magnetic susceptibility. In our case, we can fit the J constant in such a way as to obtain the best agreement between the experimental and theoretical dependences over the entire temperature range, including the temperatures corresponding to the maximum of the heat capacity ($T \sim J$) and the low-temperature branch.

The fitting parameters determined by the above-described procedures for different experimental data corresponding to the ferromagnetic state are summarized in the table. The experimental data for the ferromagnetic exchange and the results of theoretical calculations described in Section 2 are compared in Figs. 4–7 (solid lines correspond to the theoretical curves shown in Figs. 1 and 2, and points are the experimental data taken from different works). Since the representation of

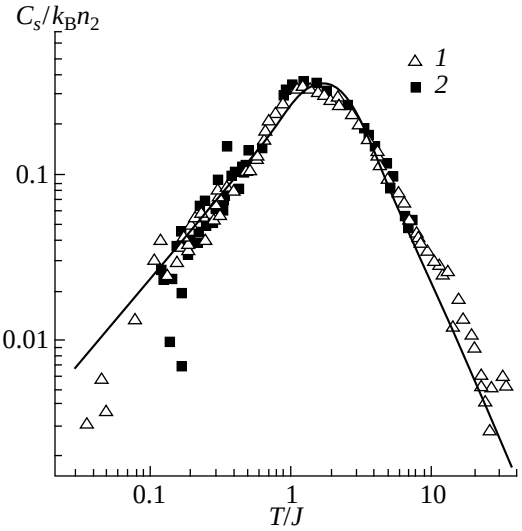

Fig. 4. Dependence of the normalized heat capacity on the dimensionless temperature for the second layer at the coverage $\rho = 0.23$ Å^{-2}. Points are the experimental data taken from (*1*) [4] and (*2*) [5]. Solid line represents the theoretical dependence (see Fig. 1).

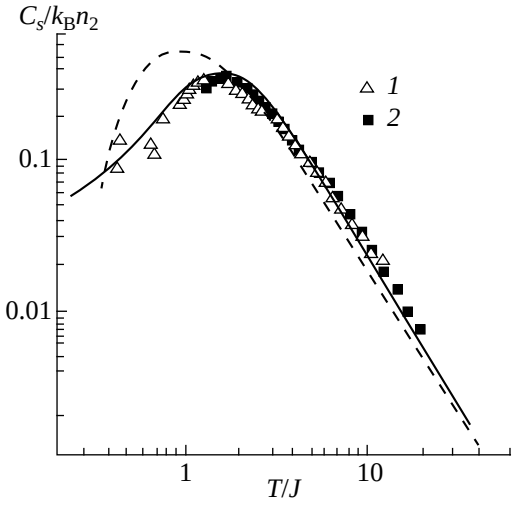

Fig. 5. Dependence of the normalized heat capacity on the dimensionless temperature for the second layer at the coverage $\rho = 0.24$ Å^{-2}. Points are the experimental data taken from (*1*) [2] and (*2*) [3]. Solid line represents the theoretical dependence. Dashed line indicates the dependence obtained by the renormalization group method [15].

all the experimental data in the same figure would be too difficult to grasp, the data for different coverages are demonstrated in different figures.

Figure 4 displays the spin heat capacity of the second layer at the total coverage $\rho = 0.23$ Å^{-2}. As is easy to see, two groups of experimental points taken from [4, 5] agree closely with the theoretical results [16] (the solid line in Fig. 4) at all temperatures. It is of interest that the dependence $C_s(T)$ obtained by Ishida *et al.* [5] more recently and, likely, with a higher accuracy, better fits the correct asymptotic curve described by formula (19) in the low-temperature range.

The theoretical results and the experimental data taken from [2, 3] at the coverage $\rho = 0.24$ Å^{-2} are compared in Fig. 5. In this case, too, there is a very good conformity with our theoretical data (solid line) over the entire range of temperatures. The theoretical dependence of the heat capacity that was calculated by de Mello *et al.* [14, 15] with the use of the renormalization group method at $J = 1.69$ is depicted by the dashed line in Fig. 5. It is clear that this dependence only qualitatively correlates with the experimental data.

Figure 6 illustrates the agreement between our theoretical results and the experimental data taken from [3, 5] for layers with $\rho = 0.26$ Å^{-2}.

The experimental [9] and theoretical dependences of $T \cdot \chi(T)/C$ (where C is Curie's constant) on the dimensionless temperature θ are demonstrated in Fig. 7. The experimental data in [9] were obtained for layers with $\rho = 0.2303$, 0.236, and 0.2383 Å^{-2}. As can be seen from the figure, here, again, our theory describes well the experimental data. The corresponding values of the σ and J fitting parameters are listed in the table. Note that, for the layer with $\rho = 0.23$ Å^{-2}, the exchange interaction constants J determined from the heat capacity and the magnetic susceptibility are coincident, as it should be the case of the Heisenberg model. Unfortunately, except for this case, other examples when the heat capacity and the susceptibility were measured for layers with the identical coverage ρ are not available. Therefore, in order to illustrate the applicability of the Heisenberg model to the interpretation of physical properties of the ferromagnetic second layer,

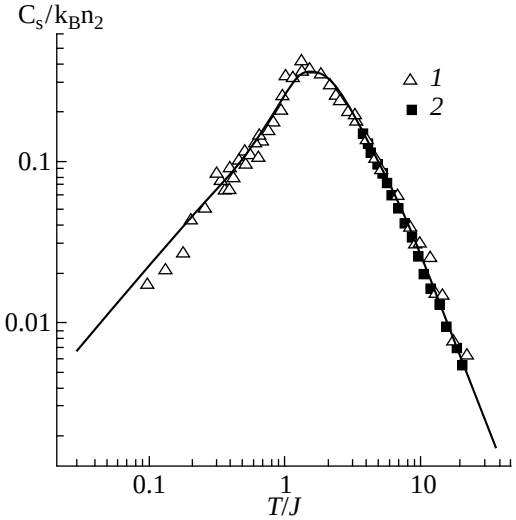

Fig. 6. Dependence of the normalized heat capacity on the dimensionless temperature for the second layer with the coverage $\rho = 0.26$ Å^{-2}. Points are the experimental data taken from (*1*) [4] and (*2*) [5]. Solid line represents the theoretical dependence.

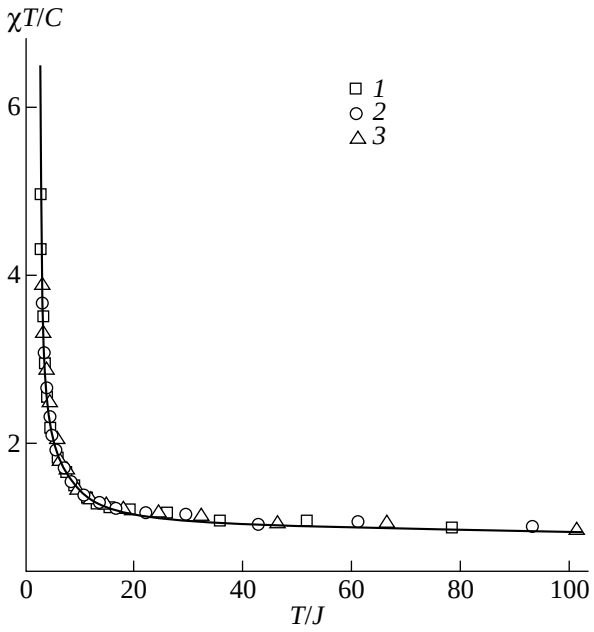

Fig. 7. Dependence of the magnetic susceptibility on the dimensionless temperature for the ferromagnetic layers at ρ = (*1*) 0.2303, (*2*) 0.236, and (*3*) 0.2383 Å^{-2}. Points are the experimental data taken from [9].

the graph of the exchange interaction constants J obtained from the data on the heat capacity and the susceptibility is constructed as a function of the second layer coverage ρ_2 (the values of ρ_2 were calculated from the values of the total coverage ρ by using the Greywall approximation formula [5]) in Fig. 8. It is seen that all the $J(\rho_2)$ values fall on the same smooth curve, which monotonically slopes down with an increase in ρ_2. Consequently, it is evident that the Heisenberg model adequately describes the experimental properties of the ^{3}He monolayer in the ferromagnetic state at the coverages $\rho \geq 0.23$ Å^{-2}.

Now, we briefly dwell on comparison between the theoretical and experimental data for the antiferromagnetic layers. Let us use the data from [2], in which the dependences of the heat capacity normalized to one spin were obtained as a function of the dimensionless temperature $T/|J|$ for several antiferromagnetic layers with the coverages 0.178 Å^{-2} < ρ < 0.202 Å^{-2} (see Fig. 3 in [2]). In this case, the experimental data can be directly used for comparison. Since the corresponding figure from [2] contains a very large number of experimental points, the smoothed experimental dependence is represented in Fig. 9. One can see that the theoretical and experimental data reasonably agree over the entire temperature range. The heat capacities at a maximum are coincident, even though the maximum in the theoretical curve is somewhat shifted toward the right of the maximum in the experimental dependence (the shift $\Delta\theta$ is equal to approximately 0.1).

In summary of analysis carried out in the present work, it can be concluded that the Heisenberg model on the triangular lattice makes it possible to adequately describe the observed physical properties of the ^{3}He ferromagnetic solid monolayers over the entire range of temperatures. This inference is based on the following findings. First, the proposed theory in the case of ferromagnetic layers provides the rigorous quantitative description at arbitrary temperatures. Second, there is the excellent agreement between the experimental and theoretical data on the heat capacity and the magnetic

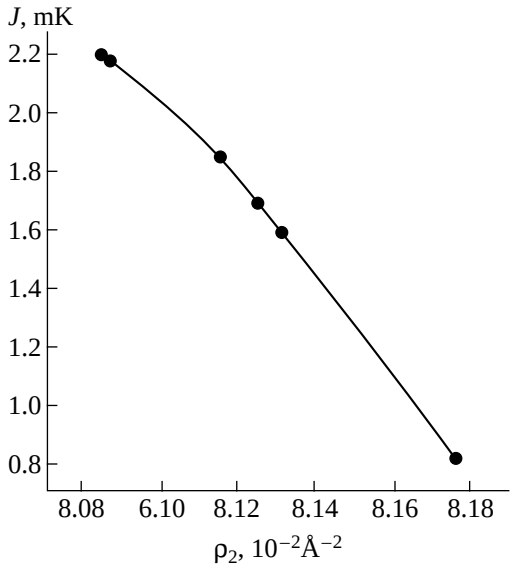

Fig. 8. Dependence of the exchange interaction constant J on the second layer coverage ρ_2 for the ferromagnetic layer.

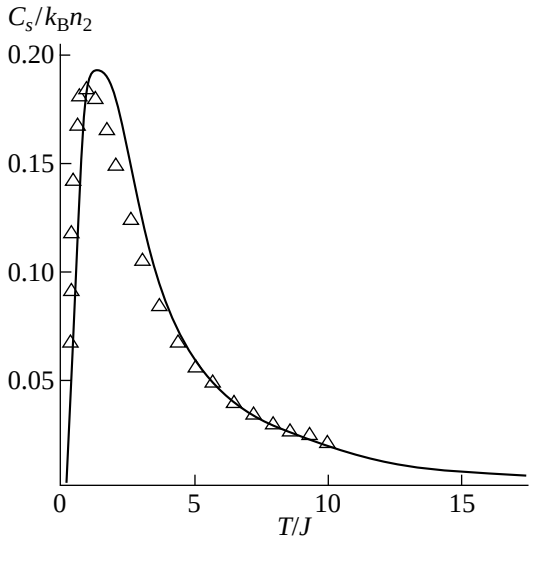

Fig. 9. Experimental (points) [2] and theoretical (solid line) dependences of the normalized heat capacity on the dimensionless temperature for the antiferromagnetic layers at 0.178 < ρ < 0.202 Å^{-2}.

susceptibility, which is achieved by the unique choice of only two independent fitting parameters—the exchange interaction constant J and the number of active spins n_2 in the second layer. Finally, the J constants evaluated from the data on both the heat capacity and the magnetic susceptibility exhibit the same universal dependence on the second layer coverage ρ_2, as should be the case of the Heisenberg model, within which the thermal and magnetic properties are determined by the same exchange interaction constant.

As regards the ^{3}He antiferromagnetic films, the experimental data available in the literature are rather contradictory and, in some cases, do not allow one to make unambiguous conclusions on the properties of the system. In particular, the behavior of the heat capacity of antiferromagnetic layers at high temperatures is still not understood, and the $C_s(T)$ dependences in the low-temperature range are not studied in sufficient detail. The results obtained in the present work indicate that the Heisenberg model furnishes an opportunity to describe the heat capacity of the ^{3}He antiferromagnetic layers; however, the ultimate answer to the question regarding the boundaries of the applicability of this model to the system under consideration calls for further experimental and theoretical investigations.

REFERENCES

1. M. Siqueira, J. Niéki, B. Cowan, *et al.*, Phys. Rev. Lett. **76,** 1884 (1996).
2. M. Siqueira, J. Niéki, B. Cowan, *et al.*, Phys. Rev. Lett. **78,** 2600 (1997).
3. D. S. Greywall, Phys. Rev. B: Condens. Matter **41,** 1842 (1990).
4. M. Morishita, K. Ishida, K. Yawata, *et al.*, Czech. J. Phys., Suppl. S1 **46,** 409 (1991).
5. K. Ishida, M. Morishita, K. Yawata, *et al.*, Phys. Rev. Lett. **79,** 3451 (1997).
6. O. E. Vilches, R. S. Ramos, Jr., and D. A. Ritter, Czech. J. Phys., Suppl. S1 **46,** 397 (1991).
7. C. Bäuerle, Yu. M. Bunkov, S. N. Fisher, *et al.*, Czech. J. Phys. **46** (Suppl.), S1399 (1991).
8. C. Bäuerle, J. Bossy, Yu. M. Bunkov, *et al.*, J. Low Temp. Phys. **110,** 345 (1998).
9. M. Roger, C. Bäuerle, Yu. M. Bunkov, *et al.*, Phys. Rev. Lett. **80,** 1308 (1998).
10. A. Abragam and M. Goldman, *Nuclear Magnetism: Order and Disorder* (Clarendon, Oxford, 1982; Mir, Moscow, 1984).
11. M. C. Cross and D. S. Fisher, Rev. Mod. Phys. **57,** 881 (1985).
12. N. Eltner, R. Singh, and A. P. Yang, Phys. Rev. Lett. **71,** 1629 (1993).
13. M. Roger, Phys. Rev. B: Condens. Matter **56,** R2928 (1997).
14. E. V. L. de Mello and M. A. Continentino, J. Phys.: Condens. Matter **2,** 4161 (1990).
15. E. V. L. de Mello and H. Gogfrin, J. Low Temp. Phys. **108,** 407 (1997).
16. T. N. Antsygina, Fiz. Nizk. Temp. (Kiev) **25,** 533 (1999).
17. V. Elser, Phys. Rev. Lett. **62,** 2405 (1989).
18. P. Schiffer, M. T. O'Keefe, D. D. Osheroff, *et al.*, J. Low Temp. Phys. **94,** 498 (1994).
19. D. N. Zubarev, *Nonequilibrium Statistical Thermodynamics* (Nauka, Moscow, 1971).
20. J. Kondo and K. Yamaji, Prog. Theor. Phys. **47,** 807 (1972).
21. T. N. Antsygina and V. A. Slyusarev, Fiz. Nizk. Temp. (Kiev) **19,** 67 (1993).
22. T. N. Antsygina and V. A. Slyusarev, Fiz. Nizk. Temp. (Kiev) **21,** 127 (1995).
23. H. Mermin and N. D. Wagner, Phys. Rev. Lett. **17,** 1133 (1966).
24. G. S. Rushbrooke, G. A. Baker, Jr., and P. J. Wood, in *Phase Transitions and Critical Phenomena*, Ed. by C. Domb and M. S. Green (Academic, London, 1974), Vol. 3, Chap. 5.
25. K. Yamaji and J. Kondo, Phys. Lett. **45,** 317 (1973).
26. D. S. Greywall and P. A. Busch, Phys. Rev. Lett. **65,** 2788 (1990).
27. M. Morishita, H. Nagani, and H. Fukuyama, J. Low Temp. Phys. **113,** 271 (1998).

Translated by O. Borovik-Romanova

Physics of the Solid State, Vol. 42, No. 1, 2000, pp. 11–14. Translated from Fizika Tverdogo Tela, Vol. 42, No. 1, 2000, pp. 12–15.

METALS AND SUPERCONDUCTORS

Superconductivity in the Zr–D System under Pressure

I. O. Bashkin, M. V. Nefedova, and V. G. Tissen

Institute of Solid State Physics, Russian Academy of Sciences, Chernogolovka, Moscow oblast, 142432 Russia
e-mail: bashkin@issp.ac.ru

Received May 13, 1999

Abstract—The superconducting transition temperature T_c of the $ZrD_{0.48}$ alloy is measured in the pressure range up to 41.5 GPa. The measurements are carried out in a high-pressure chamber with diamond anvils by the inductometric method. It is found that $T_c(P)$ increases to 3.1 K at a pressure below 30 GPa, exhibits a sharp increase up to 8 K near 30 GPa, and then smoothly decreases to ~6.5 K at 41.5 GPa. A similar dependence $T_c(P)$ is obtained for pure Zr. The similarity of the $T_c(P)$ curves suggests that the dependence $T_c(P)$ observed for $ZrD_{0.48}$ is due to the presence of ω-phase in this alloy at pressures $P < 30$ GPa and the ω–β transition at $P \approx 30$ GPa, which leads to the establishment of new ratios between the phases in the Zr–D system. In the pressure range studied, no indications are observed for new superconducting phases similar to the phases of intermediate composition in the Ti–H(D) system, which are formed by the hydrogen transfer from tetrahedral to octahedral interstitials. © *2000 MAIK "Nauka/Interperiodica".*

In the phase *T*–*c* diagram of the Zr–H system at atmospheric pressure, four phases are believed to be equilibrium [1]: the solid solution of hydrogen in hexagonal close-packed (hcp) α-Zr, the hydrogen solid solution based on the body-centered cubic (bcc) high-temperature phase β-Zr, the nonstoichiometric dihydride δ-ZrH_{2-y} with the face-centered cubic (fcc) sublattice of Zr, and the ε-ZrH_{2-y} dihydride with the homogeneity region extending up to the stoichiometric composition $x = H/Zr = 2$. The ε-phase is formed from the δ-phase due to its tetragonal distortion accompanied by an increase in the hydrogen content. The high-temperature phase β-ZrH_x is in an eutectoid equilibrium with α-Zr(H) and δ-ZrH_{2-y} at a point with the coordinates $T = 550$°C and $x = 0.5$ Recent studies [2–5] indicate that one more phase, namely, γ-ZrH with the face-centered orthorhombic sublattice of Zr, also has the stability region at temperatures below ~235°C and slowly arises in the two-phase alloys (α + δ)-ZrH_x even at room temperature.

In all these phases, the hydrogen atoms occupy the tetrahedral interstitials (tetrapores) of the Zr sublattice. The problem of hydrogen transfer from tetrapores to octapores in Zr hydrides under pressure has already been discussed in the literature [5, 6]. In the Ti–H system, which is an analog of the Zr–H system at atmospheric pressure [7–10], such a transfer occurs under a pressure of 2.05 GPa [11, 12]. In the composition range close to the eutectoid composition ($x = 0.7$–0.9), the hydrogen transfer gives rise to a new phase, which, after the quenching under pressure in liquid nitrogen, remains metastable up to atmospheric pressure. In the metastable state, the new phase is characterized by the superconducting transition temperature $T_c = 4.3$ K and also by the reverse isotropic effect ($T_c = 5.0$ K in the Ti–D system) [13, 14]. Empirical estimates of the pressure of the tetra–octa transition for hydrogen in the Zr–H system gave values from 45 [6] to 58 GPa [5]. However, these estimates disregarded the electronic transition in pure Zr under a pressure of 30 GPa [15–18], which is attended by an increase in the metallic radius. The existence of electronic transition in pure Zr decreases the reliability of the estimates obtained in [5, 6] and stimulates interest in the direct experimental measurements. The structural measurements were performed with zirconium dihydride under pressures up to 18 GPa [6, 19], which showed the absence of phase transformations.

The aim of the present work was to carry out the measurements of the superconducting properties of alloys in the zirconium–hydrogen system in the pressure range extended through the use of chambers with diamond anvils and also to verify experimentally whether the new phases, whose existence can be connected with the tetra–octa transfer of hydrogen, are formed in this system under pressures up to ~40 GPa. As the temperature T_c in the Ti–H(Ti–D) system exhibits a reverse isotope effect, we studied the deuteride alloy $ZrD_{0.48}$, which is close in composition to the eutectoid alloy in the Zr–H(D) system ($x = 0.5$ [1]).

1. EXPERIMENTAL TECHNIQUE

The initial alloy of chemical composition $D/Zr = 0.48 \pm 0.01$ was prepared by the saturation of high-purity (~99.96 at. %) zirconium with a gaseous deuterium obtained by heating of a TiD_2 sample (for more detail, see [5]). The deuterium content was determined by the weighing method.

1063-7834/00/4201-0011$20.00

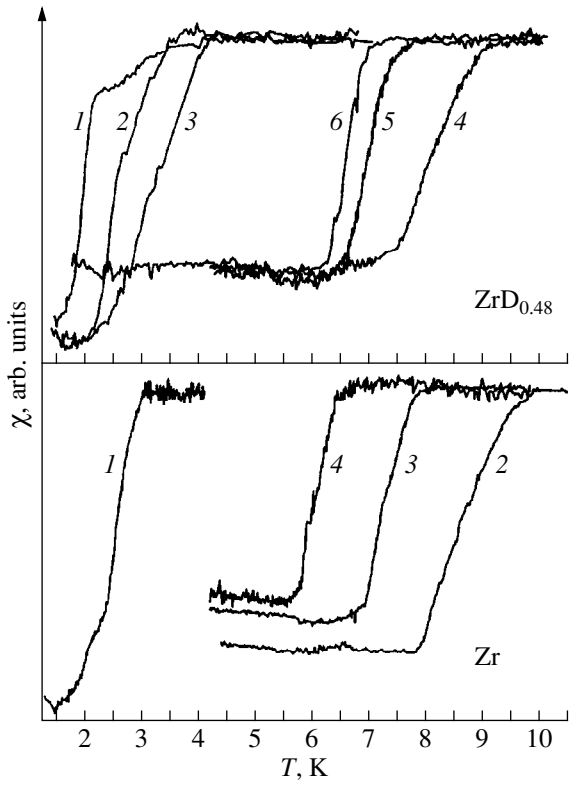

Fig. 1. Experimental temperature dependences of the magnetic susceptibility upon heating of the $ZrD_{0.48}$ sample at pressures of (*1*) 17.9, (*2*) 23.5, (*3*) 28.9, (*4*) 30.1, (*5*) 36.5, and (*6*) 41.5 GPa and the pure Zr sample at pressures of (*1*) 21.7, (*2*) 29.7, (*3*) 36.7, and (*4*) 43 GPa.

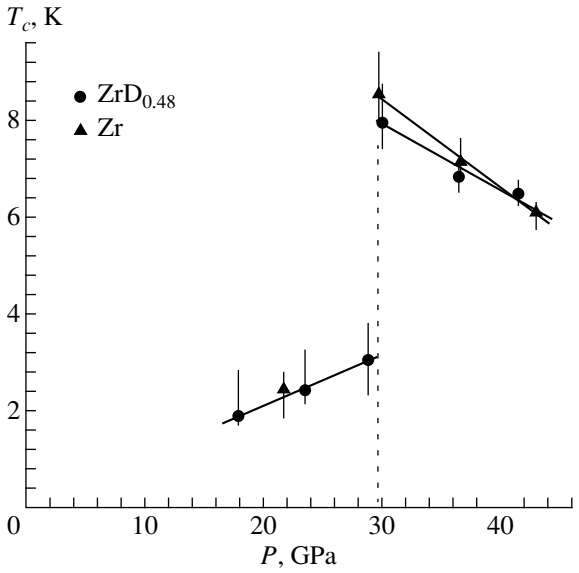

Fig. 2. Pressure dependence of the superconducting transition temperature for $ZrD_{0.48}$ and pure Zr. Short lines indicate the transition temperature ranges. The dotted line corresponds to the ω–β transition in Zr.

High pressures were produced using an apparatus with diamond anvils, which was fabricated from the nonmagnetic materials [20]. A sample and crystals of ruby reference specimen were mounted in the orifice of a metallic gasket with diameter of 0.15 mm. The methanol–ethanol mixture in the ratio 4 : 1 serves as a medium transferring the pressure. The change in pressure and its measurement were performed at room temperature. The pressure was determined from the shift of the ruby *R*-line with an accuracy of ±0.05 GPa. The superconducting transition was determined from the ac measurements of the magnetic susceptibility $\chi(T)$ [21]. The amplitude of the alternating magnetic field with a frequency of 5.2 kHz was equal to 0.3 Oe. The high-pressure apparatus was entirely cooled in a cryostat down to 1.5 K, and the recording of the $\chi(T)$ curve was performed upon heating. The (Cu–Fe)–Cu thermocouple was used to measure the temperature with an accuracy of ±0.2 K. Since the apparatus required the preliminary warming-up for a pressure change and its determination, the measuring cycle for each pressure took a day.

2. RESULTS

The temperature dependences of the magnetic susceptibility $\chi(T)$ for the $ZrD_{0.48}$ alloy in the range $17.9 \le P \le 41.5$ GPa are shown in Fig. 1. Abrupt changes in $\chi(T)$ caused by the superconducting transitions in $ZrD_{0.48}$ are clearly seen in the curves. In the data processing, the superconducting transition point T_c was determined as a temperature at which the $\chi(T)$ jump reached its half-height. The temperatures between which the jump magnitude changed from 10 to 90% were taken as the temperature boundaries of the transition region. Thus determined temperatures and temperature ranges of the superconducting transitions as functions of pressure are given in Fig. 2. It is seen from the figure that T_c monotonically increases with pressure in the range up to ~29 GPa. A jumpwise increase in T_c by about 5 K is observed at a pressure of 30.1 GPa, and then the dependence $T_c(P)$ becomes a decreasing function.

A similar dependence $T_c(P)$ was obtained earlier for pure Zr with the help of electrical resistance measurements [18]. The resistivity data usually somewhat differ from the results obtained with the help of magnetic susceptibility measurements; hence, we repeated our measurements for the initial Zr material, from which the deuteride was prepared. The experimental curves $\chi(T)$ for pure Zr are given in the lower part of Fig. 1, and the results of the curves processing are presented in Fig. 2 together with the data for $ZrD_{0.48}$. It is seen from Fig. 2 that the $T_c(P)$ curves for pure Zr and $ZrD_{0.48}$ coincide to within the spread of experimental points. A certain correlation between our data and the results obtained in the earlier studies on the *T*–*P* diagram of the Zr–H(D) system under a pressure up to 7 GPa [5] and the phase transitions in pure Zr in the pressure range up to 70 GPa

[15–18, 22–24] allows us to make a number of suggestions about the phase transformations in the Zr–H(D) system in the pressure range $P \le 41.5$ GPa.

3. DISCUSSION

Under pressure, pure zirconium undergoes a number of phase transitions [22]. In the *T*–*P* phase diagram of Zr in the ranges $P \le 6.5$ GPa and $T \le 900$°C, the α–β phase boundary has a negative slope up to the triple point with the coordinates $P = 5.5$ GPa and $T = 700$°C, at which α-Zr, β-Zr, and the high-pressure hexagonal phase ω-Zr are in an equilibrium [23]. In the compression experiments with shear [24], the equilibrium pressure of the α–ω transition at room temperature was determined as $P = 2.2$ GPa. However, under quasihydrostatic pressure, the α ⟶ ω transition occurs at 4–7 GPa owing to the hysteresis [18, 23]. Near $P = 30$ GPa, ω-Zr at room temperature transforms into the bcc phase [15–17], and then experiences an isomorphic transition near 56 GPa [17]. The ω–β transition at $P = 30$ GPa is followed by the jumpwise increase in T_c [18]. According to [15–18], the structural transformations and the T_c jump under ultrahigh pressure are due to the *s*–*d* electronic transition, as a result of which the electronic configuration of Zr becomes similar to the configurations of the bcc Group V metals.

In the *T*–*P* phase diagram of the Zr–H (Zr–D) system studied in the ranges $P \le 7$ GPa and $T \le 700$°C, a curve of the phase equilibrium new for this system, the temperature of which increases with pressure, has been found at pressures above 4 GPa [5]. The X-ray powder diffraction analysis of the samples quenched up to 80 K under a pressure of 5–6 GPa showed that this curve is the boundary for the new (second) eutectoid equilibrium involving the ω-, δ-, and ε-phases. Its appearance is explained by the fact that, under pressure, the region of existence of the fcc δ-$ZrH(D)_{2-y}$ dihydride narrows to zero, and the temperature of intersection of the δ-phase homogeneity boundaries at the second eutectoid point increases with pressure [5].

Therefore, in the $ZrD_{0.48}$ alloy close in composition to the eutectoid, the ω-phase with a low hydrogen content and the ε-ZrD_{2-y} dihydride should coexist at pressures above 7 GPa and at room temperature. The close values of $T_c(P)$ for $ZrD_{0.48}$ and pure Zr (Fig. 2) suggest that, in the range up to 30 GPa, the superconductivity of $ZrD_{0.48}$ is due to the presence of the ω-phase, whereas the hydrogen-rich phase, most likely, the ε phase, remains nonsuperconducting. From this fact, it can be concluded with confidence that new superconducting phases, whose appearance can be related to the hydrogen transition from tetrapores into octapores, are not formed in the Zr–D system at pressures up to 30 GPa.

The superconducting transition temperature jump near 30 GPa in $ZrD_{0.48}$ is likely caused by the transformation of the ω-phase in the alloy into the bcc phase. Two most probable variants can be considered for the distribution of hydrogen in the alloy above this transition. In the first case, the β-phase in the Zr–D system at low temperatures and pressures above 30 GPa is depleted in hydrogen and coexists with the nonsuperconducting hydride, ε-ZrD_{y-2}, in which virtually all hydrogen is concentrated. Such an impurity distribution explains in a simple way the similarity in the behavior of $T_c(P)$ for $ZrD_{0.48}$ and pure Zr. However, it seems rather strange, since hydrogen dissolves in both β-Zr and the bcc Group V metals over a wide range of concentrations. The numerous ordered phases are formed in solid solutions of hydrogen in the bcc Group V metals at low temperatures [25]. It can be assumed that, in the Zr–D system, a hydrogen solid solution based on the bcc β-Zr phase is formed above 30 GPa and undergoes ordering at low temperatures. In this case, the coincidence of superconducting transition temperatures in pure metal and its alloy with hydrogen seems to be unusual. In both cases, the superconducting properties of $ZrD_{0.48}$ above 30 GPa can be explained without invoking the tetra–octa transition of hydrogen. However, the question on the presence of this transition in the Zr–H(D) system can be solved unambiguously only with the help of compression structural studies.

Thus, it is shown that pressure dependences of superconducting transition temperatures in the alloy of eutectoid composition $ZrD_{0.48}$ and in pure Zr in the range up to 41.5 GPa virtually coincide. This evidences for the presence of the two-phase ω-Zr(D) + ε-Zr(D) ~ 2 state in $ZrD_{0.48}$ at $P < 30$ GPa. The jumpwise increase in T_c near $P = 30$ GPa is likely connected with the ω–β transition resulting in the appearance of new phase ratios in the Zr–D system. The experimental dependence $T_c(P)$ gives no evidence of the existence of hydrogen transfer from tetrapores to octapores in the Zr–D system under a pressure up to 41.5 GPa.

ACKNOWLEDGMENTS

We are grateful to V.G. Glebovskiĭ and his collaborators (Institute of Solid State Physics, Russian Academy of Sciences) for the preparation of high-purity Zr and E.G. Ponyatovskiĭ (Institute of Solid State Physics, Russian Academy of Sciences) for his unflagging interest in this work and helpful discussions of the results.

This work was supported by the Russian Foundation for Basic Research, project nos. 97-02-17614 and 96-15-96806.

REFERENCES

1. E. Zuzek, J. P. Abriata, A. San-Martin, *et al.*, Bull. Alloy Phase Diagrams **11**, 385 (1990).
2. I. O. Bashkin, V. Yu. Malyshev, and M. M. Myshlyaev, Fiz. Tverd. Tela (Leningrad) **34** (7), 2213 (1992).
3. A. L. Kolesnikov, A. M. Balagurov, I. O. Bashkin, *et al.*, J. Phys.: Condens. Matter **6**, 8977 (1994).

4. A. I. Kolesnikov, I. O. Bashkin, A. V. Belushkin, *et al.*, J. Phys.: Condens. Matter **6**, 8989 (1994).
5. I. O. Bashkin, A. I. Latynin, and V. Yu. Malyshev, Fiz. Tverd. Tela (St. Petersburg) **37** (7), 2108 (1995).
6. V. P. Glazkov, A. V. Irodova, V. A. Somenkov, *et al.*, J. Less-Common Met. **129**, 165 (1987).
7. A. San-Martin and F. D. Manchester, Bull. Alloy Phase Diagrams **8**, 30 (1987).
8. I. O. Bashkin, A. F. Gurov, V. Yu. Malyshev, *et al.*, Fiz. Tverd. Tela (Leningrad) **34** (4), 1276 (1992).
9. I. O. Bashkin, A. F. Gurov, V. Yu. Malyshev, *et al.*, Fiz. Tverd. Tela (Leningrad) **34** (8), 2584 (1992).
10. I. O. Bashkin, A. I. Kolesnikov, and E. G. Ponyatovskiĭ, High-Pressure Res. **14**, 91 (1995).
11. E. G. Ponyatovskiĭ, I. O. Bashkin, V. F. Degtyareva, *et al.*, J. Less-Common Met. **129**, 93 (1987).
12. I. O. Bashkin, T. I. Dyuzheva, L. M. Lityagina, *et al.*, Fiz. Tverd. Tela (St. Petersburg) **35** (11), 3104 (1993).
13. E. G. Ponyatovskiĭ, I. O. Bashkin, V. F. Degtyareva, *et al.*, Fiz. Tverd. Tela (Leningrad) **27** (11), 3446 (1985).
14. I. O. Bashkin, V. Yu. Malyshev, V. I. Rashchupkin, *et al.*, Fiz. Tverd. Tela (Leningrad) **30** (7), 2003 (1988).
15. H. Xia, S. J. Duclos, A. L. Ruoff, *et al.*, Phys. Rev. Lett. **64** (2), 204 (1990).
16. H. Xia, A. L. Ruoff, and Y. K. Vohra, Phys. Rev. B: Condens. Matter **44** (18), 10374 (1991).
17. Y. Akahama, M. Kobayashi, and H. Kawamura, J. Phys. Soc. Jpn. **60** (10), 3211 (1991).
18. Y. Akahama, M. Kobayashi, and H. Kawamura, J. Phys. Soc. Jpn. **59** (11), 3843 (1990).
19. L. M. Lityagina and T. I. Dyuzheva, J. Alloys Compd. **179**, 73 (1992).
20. N. N. Kolesnikov, M. P. Kulakov, M. V. Nefedova, *et al.*, Sverkhprovodimost: Fiz., Khim., Tekh. **6** (2), 281 (1993).
21. V. G. Tissen, E. G. Ponyatovsky, M. V. Nefedova, *et al.*, J. Phys.: Condens. Matter **8**, 3069 (1996).
22. E. Yu. Tonkov, *High Pressure Phase Transformations* (Gordon & Breach, Philadelphia, 1992), Vol. 2, p. 691.
23. A. Jayaraman, W. Klement, Jr., and G. C. Kennedy, Phys. Rev. **131** (2), 644 (1963).
24. V. A. Zil'bershteĭn, N. P. Chistotina, A. A. Zharov, *et al.*, Fiz. Met. Metalloved. **39** (2), 445 (1975).
25. T. Schober and H. Wenzl, in *Hydrogen in Metals*, Ed. by G. Alefeld and J. Völkl (Springer-Verlag, Heidelberg, 1978; Mir, Moscow, 1981), Vol. 2, pp. 17–90.

Translated by T. Galkina

Physics of the Solid State, Vol. 42, No. 1, 2000, pp. 112–113. Translated from Fizika Tverdogo Tela, Vol. 42, No. 1, 2000, pp. 109–110.

MAGNETISM AND FERROELECTRICITY

On the Thermal Expansion of Nanoparticles

V. I. Nikolaev* and A. M. Shipilin**

**Moscow State University, Vorob'evy gory, Moscow, 119899 Russia*
***Yaroslavl State Technical University, Moskovskiĭ pr. 88, Yaroslavl, 150023 Russia*
e-mail: shipilin.phys@staff.ystu.yar.ru
Final version received June 3, 1999

Abstract—Magnetite nanoparticles with an average particle size of 7.5 nm were studied by Mössbauer spectroscopy in the 100–300 K temperature range. Using experimental data on the temperature variation of isomer shifts in the partial spectra of ^{57}Fe nuclei in the *A* and *B* crystal sublattices, the linear thermal expansion coefficient of the ultradisperse magnetite particles in the temperature range studied was estimated within the framework of the molecular orbital formalism: $\alpha = (1.2 \pm 0.2) \times 10^{-4}$ K^{-1}. © *2000 MAIK "Nauka/Interperiodica".*

By nanoparticles, we usually imply the species with linear dimensions below 40 nm. According to the experimental data available (see, e.g., [1–4]), the physical properties of these particles (magnetic characteristics, heat capacity, hardness, etc.) can markedly differ from the properties of their "massive" counterparts. The main factor responsible for this difference is a considerable fraction of the surface layer in the total particle volume.

Below, we present the results of our attempt to use the data of Mössbauer spectroscopy for investigation of the thermal expansion of nanoparticles. The idea of the method used for evaluation of the linear thermal expansion coefficient of nanoparticles is based on determination of the partial isomer shifts in the spectra of ^{57}Fe nuclei in a regular structure as functions of the interatomic distances calculated using the method of molecular orbitals (MO).

Experiments were performed with an ultradisperse powder of magnetite Fe_3O_4 prepared by the standard method of chemical condensation. According to the electron microscopy data, the average particle size in the sample studied was $d \approx (7.5 \pm 0.5)$ nm. The Mössbauer spectra were recorded in the absorption mode using samples with an effective thickness of about 0.15 mg ^{57}Fe/cm^2, which corresponded to the case of "thin" samples [5]. The γ-radiation source was a ^{57}Co isotope in the Cr matrix.

From the standpoint of processing and interpretation of the Mössbauer spectra, it is important to note that small magnetite particles ($d \leq 9$ nm) have the Vervey temperature value above room temperature [6]. This is confirmed by some characteristic details in the room-temperature Mössbauer spectrum of our samples (Fig. 1). In connection with this, the model interpretation of the experimental spectrum was performed assuming the presence of three Zeeman sextets, one corresponding to Fe^{3+} ions in positions *A* of the spinel structure and two others, to Fe^{2+} and Fe^{3+} ions in positions *B* of this structure.

From the standpoint of the purpose of our study, of most importance were the data concerning the temperature variation of the isomer shifts δ^A and δ^B in the partial spectra corresponding to Fe^{3+} ions in the positions *A* and *B* (Fig. 2). This is related to the fact that the wavefunctions of Fe^{3+} ions are studied in sufficient detail and the MO formalism allows a quantitative relationship to be established between the isomer shift δ_I and the interatomic distance [5, 7] through the electron charge density on the Mössbauer nucleus. Moreover, using the differential shift $\delta_I^B - \delta_I^A$, we may determine a free parameter of the spinel structure, the so-called oxygen parameter *u* [5]. This is an important circumstance because the thermal expansion (and the related change in the lattice parameter *a*) in ferrite spinels may be

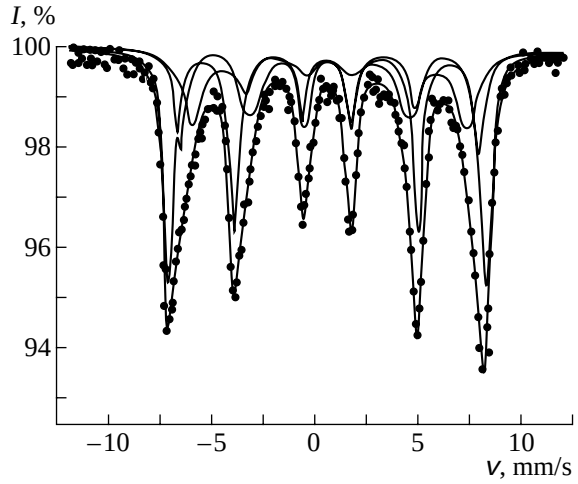

Fig. 1. The room-temperature Mössbauer spectrum of magnetite nanoparticles.

1063-7834/00/4201-0112$20.00

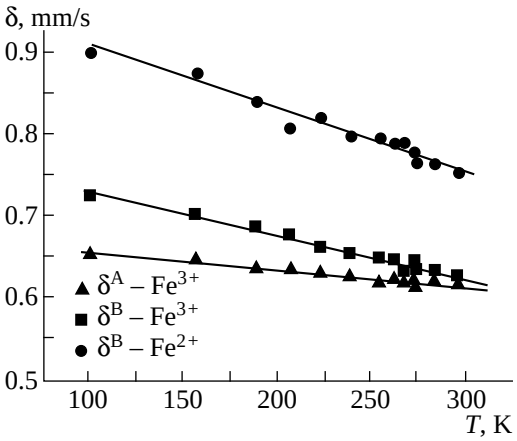

Fig. 2. The temperature dependence of the partial isomer shifts in magnetite nanoparticles.

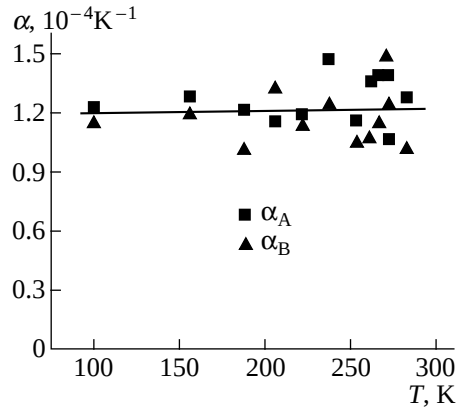

Fig. 3. Plot of the linear thermal expansion coefficient determined from the partial isomer shifts in magnetite nanoparticles versus temperature.

accompanied by variation of the oxygen parameter u and, hence, by additional changes in δ_I^B and δ_I^A [8]. Note that the spinel structure rearrangement related to variations of the oxygen parameter leads to different signs of changes in the cation–ligand distance r for the cations in positions A and B, as reflected by the well-known formulas

$$r^A = \sqrt{3}a(u - 1/4),$$

$$r^B = a\sqrt{(5/8 - u)^2 + 2(3/8 - u)^2}.$$

In particular, as the oxygen parameter u grows at a = const, the r^A distance increases and the r^B value decreases.

In order to calculate the coefficient of linear thermal expansion $\alpha = (1/a)(\partial a/\partial T)_p$, we made two corrections in the initial data on $\delta^A(T)$ and $\delta^B(T)$, so as to take into account the temperature dependence of $u(T)$ and the temperature-induced shift of lines $\delta_I(T)$ in the Mössbauer spectra.[1]

The temperature-induced shift was calculated in a single-parameter approximation, with the effective Debye temperature assumed to be the same for cations in both A and B positions, ϑ_D = 300 (± 30) K, in accordance with data on the temperature variation of the area under the spectral curve $S(T)$. As for the temperature variation of the oxygen parameter u, it was found that this quantity actually depends on the temperature and decreases from 0.384 at room temperature to 0.382 at 100 K.

Figure 3 shows the results of evaluation of the linear thermal expansion coefficient for magnetite particles using data on the temperature-induced shift of the partial Mössbauer spectra corresponding to Fe^{3+} ions in positions A and B. As seen from this figure, the linear thermal expansion coefficient is virtually constant in the temperature interval studied. The results are consistent for the α values determined separately from data on the partial shifts δ^A and δ^B. This agreement could hardly be observed if there were no correction for the temperature-dependent variation of the oxygen parameter u. Note an unusually high absolute value of the linear thermal expansion coefficient: $\alpha = (1.2 \pm 0.2) \times 10^{-4}$ K^{-1}.

In concluding, it should be noted that the above method of determination of the linear thermal expansion coefficient in nanoparticles from data on the ^{57}Fe isomer shift can be readily generalized to allow evaluation of the compressibility factor K_T of these particles. Then, the initial experimental data must refer to dependence of the isomer shift in the partial Mössbauer spectra on the pressure P, and the compressibility coefficient K_T can be determined by analogy with linear thermal expansion coefficient α.

[1] Because changes in the isomer shift δ_I related to the temperature-induced variations of the parameters a and u are relatively small, these contributions can be considered as independent.

REFERENCES

1. E. Tronc, Nuovo Cimento D **18** (2–3), 163 (1996).
2. E. Murad, Phys. Chem. Mineral. **23** (4–5), 248 (1996).
3. A. I. Gusev, Usp. Fiz. Nauk **168** (1), 34 (1998).
4. G. A. Sawatzky and F. van de Woude, J. Colliq. **35**, 47 (1974).
5. V. I. Nikolaev and V. S. Rusakov, *Mössbauer Investigations of Ferrites* (Izdat. MGU, Moscow, 1985).
6. V. I. Nikolaev, V. S. Rusakov, and A. M. Shipilin, Vestn. Mosk. Gos. Univ., Ser. 3, Fiz. Astron. **27** (6), 65 (1986).
7. V. I. Nikolaev, N. N. Oleĭnikov, V. S. Rusakov, *et al.*, Kristallografiya **33** (2), 215 (1988).
8. Yu. F. Krupyanskiĭ and I. P. Suzdalev, Zh. Éksp. Teor. Fiz. **67** (2), 736 (1974).

Translated by P. Pozdeev

Physics of the Solid State, Vol. 42, No. 1, 2000, pp. 114–119. Translated from Fizika Tverdogo Tela, Vol. 42, No. 1, 2000, pp. 111–115.

MAGNETISM AND FERROELECTRICITY

Heat Capacity of $La_{1-x}Sr_xMnO_3$ Single Crystals in Different Magnetic States

M. N. Khlopkin*, G. Kh. Panova*, A. A. Shikov*, V. F. Sinyavskiĭ*, and D. A. Shulyatev**

** Russian Research Center Kurchatov Institute, pl. Kurchatova 1, Moscow, 123182 Russia*
*** Moscow Institute of Steel and Alloys, Leninskiĭ pr. 4, Moscow, 117936 Russia*
e-mail: khlopkin@ismain.isssph.kiae.ru

Received March 23, 1999; in final form, July 1, 1999

Abstract—The heat capacity of three single-crystal samples of $La_{1-x}Sr_xMnO_3$ ($x = 0$, 0.2, and 0.3) is measured in the temperature range 4–400 K. It is found that the heat capacity undergoes abrupt changes due to the transitions from the antiferromagnetic phase to the paramagnetic phase ($x = 0$) and from the ferromagnetic phase to the paramagnetic phase ($x = 0.2$ and 0.3). The phonon contribution to the heat capacity and the Debye characteristic temperatures for the $La_{0.7}Sr_{0.3}MnO_3$ sample are determined over a wide range of temperatures. The electronic density of states at the Fermi level is evaluated. It is demonstrated that an increase in the strontium concentration x brings about an increase in the electronic density of states at the Fermi level. The contributions of spin waves to the heat capacity and the entropy are estimated under the assumption that the phonon spectrum remains unchanged upon doping with Sr. © *2000 MAIK "Nauka/Interperiodica".*

The giant magnetoresistance observed in oxides with the $La_{1-x}Sr_xMnO_3$ perovskite-type structure has attracted considerable attention to research into structural, magnetic, and electronic properties of these materials [1–3].

The stoichiometric compound $LaMnO_3$ is a layered antiferromagnetic dielectric. Its magnetic structure exhibits an antiferromagnetic ordering along the *c*-axis and a ferromagnetic ordering in the crystallographic *ab* planes (MnO layers) separated by the nonmagnetic LaO layers. A weak planar ferromagnetism observed is treated either as an intrinsic property or as an effect associated with the superstoichiometric oxygen. The antiferromagnetic ordering in $LaMnO_3$ at low temperatures is revealed by the neutron diffraction analysis [4]. According to [4], the Néel temperature T_N is equal to 141 K.

Upon doping with strontium, $LaMnO_3$ transforms from the antiferromagnetic insulating state to the metallic ferromagnetic state with the maximum Curie temperature T_c (about 400 K). The doping with divalent strontium that replaces La^{3+} brings about the formation of holes and the appearance of spontaneous magnetization in the $La_{1-x}Sr_xMnO_3$ crystals. In the $La_{1-x}Sr_xMnO_3$ system, the ferromagnetic state is unsaturated at small values of x and reaches a saturation only at $x = 0.3$. For the x values, at which the complete ferromagnetic ordering is not achieved, the neutron scattering spectra at 4.2 K are superpositions of the spectra corresponding to the ferromagnetic and antiferromagnetic orderings.

According to the earlier investigations into the $La_{1-x}Sr_xMnO_3$ system by the photoelectron spectroscopic [5] and optical conductivity [6, 7] methods, the electronic density of state in this system is rather unusual: it is very low and depends on temperature.

In the present work, we experimentally investigated the heat capacity of the $La_{1-x}Sr_xMnO_3$ single-crystal samples at different strontium concentrations ($x = 0$, 0.2, and 0.3) over a wide range of temperatures (0.4–400 K). This made it possible to determine the integral characteristics of the magnon, electron, and phonon excitation spectra (the electronic density of states at the Fermi level, the Debye characteristic temperature over a wide range of temperatures, and the contribution of spin waves to the heat capacity) and also to reveal the change in the magnetic contribution to the heat capacity with an increase in the strontium concentration.

EXPERIMENTAL

Samples of $La_{1-x}Sr_xMnO_3$ single crystals were obtained by the crucibleless zone melting with radiation heating on a URN2-3M apparatus. Preforms in the form of ceramic rods were prepared from the initial materials La_2O_3, $SrCO_3$, and Mn_3O_4 with a purity of no less than 99.99%. Prior to the melting, La_2O_3 was dehydrated by the calcination at a temperature of 900°C for 10 h. In order to compensate for a loss of manganese due to the evaporation from the melted zone, the Mn_3O_4 concentration was increased by 1–2 at. %. The initial materials were mixed in the required proportions and pressed into pellets under a pressure of $(0.6–0.8) \times 10^3$ kg/cm^2. Then, the pellets were crushed and ground in an agate mortar. The batch obtained was pressed into preforms under a pressure of 10^3 kg/cm^2. After the pressing, the preforms were sintered at 1300°C for 24 h in air. The X-

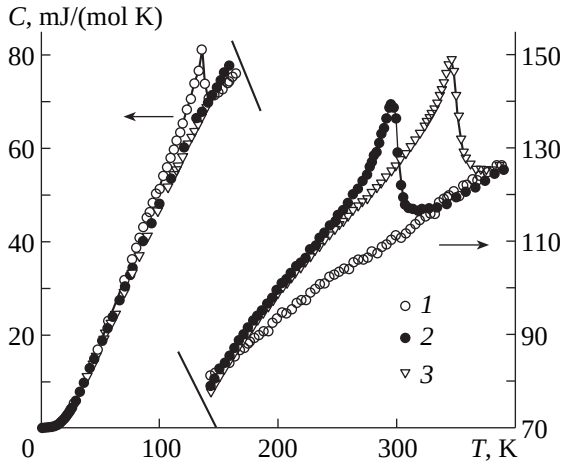

Fig. 1. Temperature dependences of the heat capacity for (*1*) $LaMnO_3$, (*2*) $La_{0.8}Sr_{0.2}MnO_3$, and (*3*) $La_{0.7}Sr_{0.3}MnO_3$ single-crystal samples in the range 4–400 K. Not all experimental points are shown.

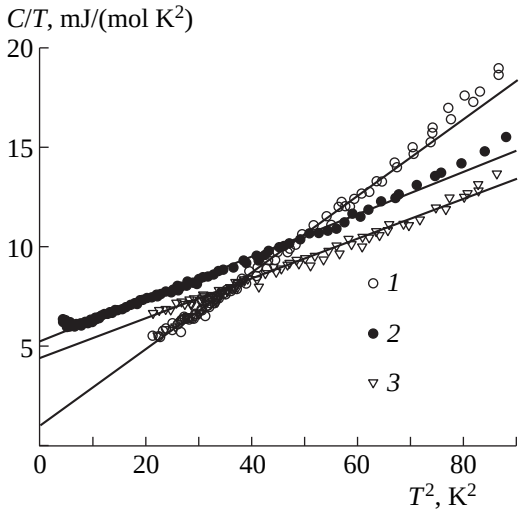

Fig. 2. Temperature dependences of the heat capacity on the C/T–T^2 coordinates in the range 4–9 K for (*1*) $LaMnO_3$, (*2*) $La_{0.8}Sr_{0.2}MnO_3$, and (*3*) $La_{0.7}Sr_{0.3}MnO_3$ single-crystal samples. Solid lines correspond to the equation $C = \gamma T + \beta T^3$.

ray powder diffraction analysis of the preforms obtained was carried out on a DRON-3 X-ray diffractometer. All the preforms were found to be single-phase within the accuracy of the method. The initial preforms destined for the zone melting were cylinders 4–7 mm in diameter and 40 mm in length.

Single crystals of $LaMnO_3$ were grown in air, whereas the $La_{0.8}Sr_{0.2}MnO_3$ and $La_{0.7}Sr_{0.3}MnO_3$ single crystals were grown in an argon atmosphere at a pressure of 3–4 atm; the liquid zone velocity was equal to 5–10 mm/h. According to the data of X-ray diffraction microscopy, the grown single crystals consist of two or three single blocks disoriented relative to each other by 0.5°–1°. The halfwidth of the rocking curve for each block was equal to 5′–10′. The deviation of the crystallographic direction [110] from the axis of single crystal growth was usually equal to 10°–15°. The annealing of a growing crystal at a temperature about 1300°C during the preparation made it possible to avoid the cracking of the grown crystal.

The crystal structure of single-crystal samples was studied by the X-ray diffraction and neutron diffraction analyses. The symmetry and unit cell parameters of the studied samples are presented in the table and agree well with the data available in the literature [8].

The heat capacity in the temperature range 2–150 K was determined by the adiabatic technique with the pulsed heat input [9]. The experimental error was equal to 1% in the range 4–10 K and 0.2–0.5% in the range 10–150 K. At temperatures of 130–400 K, the heat capacity was measured by the differential calorimetric technique [10]; the error of measurements was 2%.

RESULTS

The main experimental results obtained in the study on the heat capacity of $La_{1-x}Sr_xMnO_3$ single-crystal samples are shown in Figs. 1–4 and listed in the table.

Figure 1 displays the temperature dependences of the heat capacity for three single-crystal samples: $LaMnO_3$, $La_{0.8}Sr_{0.2}MnO_3$, and $La_{0.7}Sr_{0.3}MnO_3$. From comparison of these curves, it follows that, upon introduction of Sr atoms, the heat capacity decreases in the temperature range 6–150 K and increases in the range below 6 K.

An abrupt change is observed in the temperature dependence of the heat capacity for $LaMnO_3$ at a temperature of 136 K, which is associated with the phase transition from the antiferromagnetic state to the paramagnetic state at the Néel temperature. The temperature dependences $C(T)$ for the doped samples exhibit more pronounced features of the λ-peak type (at 296 K for $La_{0.8}Sr_{0.2}MnO_3$ and at 345 K for $La_{0.7}Sr_{0.3}MnO_3$), which are caused by the phase transition from the ferromagnetic state to the paramagnetic state. At temperatures just higher than those of the heat-capacity jumps (145–150 K and above 350 K), the heat capacities of all three samples under study are rather close to each other: the difference in heat capacities of the samples does not exceed 3%. The phase transition temperatures determined from the heat capacity maxima are in close agreement with the literature data [11].

The heat capacities measured at temperatures below 10 K are represented on the C/T–T^2 coordinates in Fig. 2. Our experimental data on the heat capacity in the temperature range 4–8 K are adequately (accurate to within 3%) described by the equation $C = \gamma T + \beta T^3$, which cor-

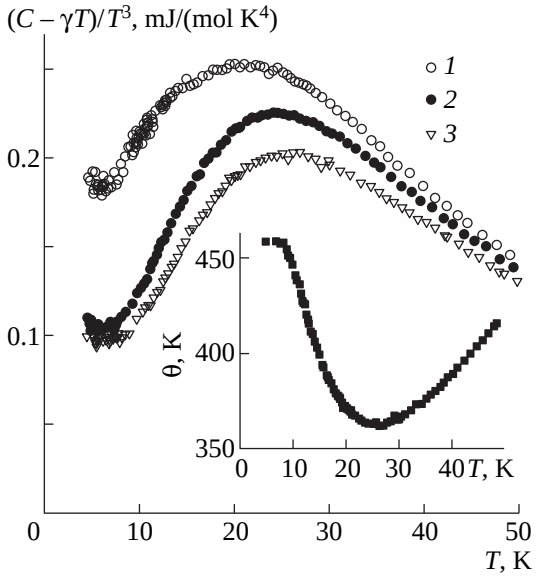

Fig. 3. Temperature dependences of the heat capacity minus the term linear in temperature in the range 4–50 K on the $(C - \gamma T)/T^3$–T coordinates for (*1*) $LaMnO_3$, (*2*) $La_{0.8}Sr_{0.2}MnO_3$, and (*3*) $La_{0.7}Sr_{0.3}MnO_3$ single-crystal samples. Temperature dependence of the Debye characteristic parameter Θ is shown in the inset.

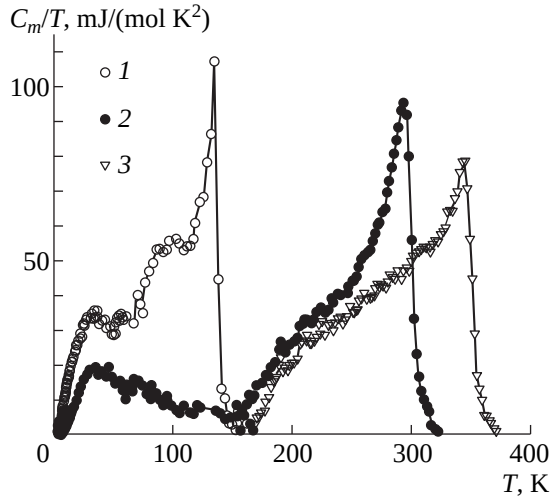

Fig. 4. Temperature dependences of the contribution from spin waves to the heat capacity for (*1*) $LaMnO_3$, (*2*) $La_{0.8}Sr_{0.2}MnO_3$, and (*3*) $La_{0.7}Sr_{0.3}MnO_3$ single-crystal samples.

responds to a straight line on the C/T–T^2 coordinates. The heat capacity of the $La_{0.8}Sr_{0.2}MnO_3$ sample was measured in a broader range of temperatures starting with 2 K. It is seen that the character of the temperature dependence does not change with a decrease in the temperature.

A systematic deviation from this dependence with a tendency toward the positive curvature (concavity downward) is observed at temperatures above 8 K. A comparison of our data with the results obtained by Woodfield *et al.* [12] demonstrates reasonable agreement for the samples with $x = 0.2$ and 0.3. However, for the undoped sample with $x = 0$, our results considerably differ in both magnitude and character of the temperature dependence from the data reported in [12]. In our opinion, this difference can be connected with a high sensitivity of the properties of samples with $x = 0$ to small deviations from the stoichiometry.

The parameters γ, β, and the low-temperature value of the Debye characteristic temperature Θ_{LT} that is related to the β parameter by the relationship $\beta = 12\pi^4 R/(5n\Theta_{LT}^3)$ (where, R is the gas constant, and n is the number of atoms in the formula unit) were determined by the approximation of the experimental data in the temperature range 4–8 K with the least-squares technique and are given in the table.

DISCUSSION

It is common practice to separate the low-temperature heat capacity of a magnetic metal into the electronic contribution proportional to the temperature, the phonon contribution proportional to the temperature cubed, and the contribution of spin waves. The separation of these contributions is usually based on their different temperature dependences. In the simplest theoretical models of antiferromagnets [13], the magnetic contribution to the heat capacity is proportional to T^3 in the three-dimensional case and T^2 in the two-dimensional case. For three-dimensional ferromagnets, the heat capacity of spin waves is proportional to $T^{3/2}$ [13]. As can be seen from Fig. 2, no negative curvature (convexity upward) is observed in the dependence of C/T on T^2, which indicates that, within the limits of experimental error, the contributions proportional to T^2 and $T^{3/2}$ to the heat capacity are absent. This fact is in good agreement with the inferences drawn by Hamilton *et al.* [14], who studied the low-temperature heat capacity of the ferromagnetic compounds $La_{0.77}Ba_{0.23}MnO_3$ and $La_{0.8}Sr_{0.2}MnO_3$ and also did not observe the contributions following these temperature dependences.

Since indications of the antiferromagnetism are absent in the compound with the strontium concentration $x = 0.3$, it can be assumed that the term cubic with respect to the temperature is completely determined by the phonon contribution to the heat capacity. For the $LaMnO_3$ and $La_{0.8}Sr_{0.2}MnO_3$ samples, the term cubic in temperature is contributed by both phonons and antiferromagnetic spin waves.

The term linear in temperature corresponds to the electronic contribution to the heat capacity. For the $La_{0.7}Sr_{0.3}MnO_3$, $La_{0.8}Sr_{0.2}MnO_3$, and $LaMnO_3$ samples, the γ coefficients of the linear term of the heat capacity are equal to 4.4, 5.2, and 1.1 mJ/(mol K^2), respectively. For the dielectric $LaMnO_3$ sample, the nonzero γ coef-

ficient of the term linear in temperature is likely connected with the contribution from small amounts of an impurity phase to the heat capacity. Note that the γ coefficient has about the same nonzero value in both dielectric and superconducting samples in the $La_{2-x}Sr_xCuO_4$ system [15, 16]. Under the assumption that the impurity contribution remains unchanged upon doping $LaMnO_3$ by strontium, an increase in the γ coefficient for the compounds with $x = 0.2$ and 0.3 by a value of 3.3 and 4.1 mJ/(mol K^2), respectively, can be attributed to the appearance of the electronic density of states at the Fermi level $N(E_F)$. These data enable us to evaluate the electronic density of states at the Fermi level from the relationship $\gamma = \pi^2 k^2 N(E_F)$. The found electronic densities of states are given in the table and agree closely with the experimental data reported in [11, 14] and also with the results of calculations for similar system $La_{0.67}Ca_{0.33}MnO$, for which $N(E_F) = 1.4 \times 10^{22}$ state/(eV cm^3) [17]. These findings permit us to draw the conclusion that the electronic density of states at the Fermi level increases upon doping $LaMnO_3$ by strontium.

Figure 3 depicts the temperature dependences of the heat capacity of the studied samples minus the contribution linear in temperature in the range 4–60 K. We suppose that, in the case of $La_{0.7}Sr_{0.3}MnO_3$, the quantity $(C - \gamma T)$ at low temperatures describes the phonon contribution to the heat capacity, because the antiferromagnetism is completely suppressed, and the contribution of ferromagnetic spin waves (proportional to $T^{3/2}$) is not found experimentally and, apparently, is negligibly small in the low-temperature range. For the samples at the strontium concentration $x = 0$ and 0.2, one can expect the presence of the contribution from the antiferromagnetic spin waves to the heat capacity. This contribution is proportional to the temperature cubed and cannot be separated from the phonon contribution reasoning from the character of the temperature dependence.

The temperature dependence of the phonon contribution to the heat capacity provides information regarding the energy density of phonon states and can be conveniently represented in the graphic form as the temperature dependence of the Debye characteristic parameter Θ. Figure 3 demonstrates this dependence obtained by the conversion of the phonon contribution to the heat capacity of the $La_{0.7}Sr_{0.3}MnO_3$ sample. As the temperature increases, the Debye parameter Θ passes through a minimum at a temperature of 25 K, and the ratio between the phonon heat capacity and the temperature cubed reaches a maximum at this temperature. The presence of a minimum in the temperature dependence of the Debye parameter Θ is a typical phenomenon and can be explained by the deviation of the energy dependence of the density of phonon states from the dependence predicted by the simple Debye model due to either the dispersion of acoustic modes or the occurrence of low-lying optical modes.

Parameters characterizing the $LaMnO_3$, $La_{0.8}Sr_{0.2}MnO_3$, and $La_{0.7}Sr_{0.3}MnO_3$ single-crystal samples: symmetry; unit cell parameters *a*, *b*, *c*, and α; Curie paramagnetic temperature T_C; Néel temperature T_N; coefficients γ and β in the equation $C_p = \gamma T + \beta T^3$ describing the heat capacity in the temperature range 4–8 K; low-temperature value of the Debye characteristic temperature Θ_{LT}; and magnetic entropy S_m at high temperatures

Parameter	Sample		
Symmetry	$LaMnO_3$	$La_{0.8}Sr_{0.2}MnO_3$	$La_{0.7}Sr_{0.3}MnO_3$
	Pnma	*R3c*	*R3c*
a, Å	5.7419 ± 0.002	5.4822	5.4714
b, Å	7.6945 ± 0.002	–	–
c, Å	5.5359 ± 0.002	–	–
α, °	–	60.59	60.43
T_c, K	–	296	345
T_N, K	136	–	–
γ, mJ/(mol K^2)	1.1	5.2	4.4
β, mJ/(mol K^4)	0.192	0.108	0.101
Θ_{LT}, K	–	–	458
$N(E_F)$, state/(eV cm^3)	0	2.9×10^{22}	2.4×10^{22}
S_m, J/mol K	6.0	7.5	7.2

As mentioned above, the phonon and magnon contributions to the heat capacity of antiferromagnets are proportional to the temperature cubed, which makes impossible their separation reasoning only from different character of the temperature dependences. However, under the assumption that the phonon contribution to the heat capacity insignificantly varies upon doping $LaMnO_3$ by strontium, the magnon contribution to the heat capacity can be separated relying on the fact that the magnon contributions to the heat capacity of the antiferromagnetic $LaMnO_3$ sample and the ferromagnetic $La_{0.7}Sr_{0.3}MnO_3$ sample are observed in different nonoverlapping temperature ranges. The suggestion was made that the magnon contribution to the heat capacity of the $LaMnO_3$ sample manifests itself in the low-temperature range, that is, below the Néel temperature, whereas, for the $La_{0.7}Sr_{0.3}MnO_3$ sample, the magnon contribution at these temperatures is negligibly small. This assumption can be supported by the fact that the difference between heat capacities of the studied samples at a temperature of about 140 K is absent. In order to separate the contribution of spin waves, the term linear in temperature (and specific for each sample) and the phonon contribution (identical for all the samples) were subtracted from the total heat capacity.

The γ coefficient of the linear term was calculated from the low-temperature asymptotics, and the phonon contribution was determined as the difference between the total heat capacity of a "reference sample" and the relevant term linear in temperature.

The ferromagnetic $La_{0.7}Sr_{0.3}MnO_3$ sample was used as a reference sample at temperatures below 140 K, and the $LaMnO_3$ sample, already being in the paramagnetic state, served as a reference sample at temperatures above 140 K. Thus obtained contribution of spin waves C_m to the heat capacity of the studied samples is shown in Fig. 4. A comparison between the magnetic and phonon heat capacities demonstrates that, at low temperatures, the heat capacity of spin waves in antiferromagnetic $LaMnO_3$ is almost equal to the phonon heat capacity; however, the relative fraction of the magnetic heat capacity rapidly decreases with an increase in the temperature.

The temperature dependences of the magnetic heat capacity of the $LaMnO_3$ and $La_{0.7}Sr_{0.3}MnO_3$ samples show a maximum at the temperatures of the phase transition to the paramagnetic state. The magnetic heat capacity of the $La_{0.8}Sr_{0.2}MnO_3$ sample exhibits two maxima at temperatures of about 30 and 296 K. Since the heat capacity is uniquely related to the entropy, which, in turn, is related to the ordering, the large value of magnetic heat capacity in a certain temperature range indicates an intensive disordering of the system in this range. The presence of two maxima in the temperature dependence of the magnetic heat capacity of the $La_{0.8}Sr_{0.2}MnO_3$ sample suggests that, in this case, the magnetic ordering is disturbed in two different temperature ranges, possibly, due to the separation of the sample into two phases: the phase with a well-defined phase transition at 296 K and another phase characterized by a more gradual transition to the disordered state in the temperature range below 140 K.

The experimental data obtained made it possible to calculate the entropy that corresponds to the disordering of the magnetic system upon transition to the paramagnetic state. The magnetic entropy $S_m = \int (C_m/T)\,dT$ was calculated as the integral of the heat capacity of spin waves C_m over the temperature range from 4 to 400 K. The calculated data are listed in the table. The entropies of the magnetic system at 400 K were found to be close to $R\ln 2 = 5.74$ J/(mol K), where R is the gas constant. It should be remarked that the value of $S = R\ln 2$ is characteristic of a system in which each formula unit involves a localized multiplet. At low temperatures, only the highest-lying level of a multiplet is unoccupied, and all the low-lying levels are completely occupied. As the temperature increases, the populations of only the two highest-lying levels of a multiplet are equalized. The fact that the experimental entropy of the phase transition is close to $R\ln 2$ suggests that the phase transition from the magnetically ordered low-temperature states to the paramagnetic high-temperature state is predominantly determined by the change in the population of the upper doublet.

The experimental results obtained for the temperature dependence of the heat capacity of the $La_{1-x}Sr_xMnO_3$ single-crystal samples can be summarized as follows.

In the temperature range 250–350 K, the heat capacity undergoes abrupt changes due to the transition from the ferromagnetic phase to the paramagnetic phase. The temperatures of transition from the ferromagnetic state to the paramagnetic state and the entropies of this transition are determined.

The electronic density of states at the Fermi level is calculated for the $La_{1-x}Sr_xMnO_3$ samples. The results obtained indicate a change in the electronic spectrum upon doping $LaMnO_3$ by strontium, namely, an increase in the electronic density of states at the Fermi level.

The phonon components of the heat capacity and the Debye characteristic temperatures Θ are calculated over a broad range of temperatures (4–400 K).

The contribution of spin waves to the heat capacity of the $La_{1-x}Sr_xMnO_3$ samples is determined. It is revealed that this contribution changes with an increase in the strontium concentration, which provides support for the coexistence of the ferromagnetic and antiferromagnetic ordering in the samples at the strontium content $x = 0.2$. A comparison of the magnon and lattice heat capacities demonstrates that, at low temperatures, the magnon heat capacity in the antiferromagnetic phase is comparable in magnitude to the lattice heat capacity.

ACKNOWLEDGMENTS

We would like to thank N.A. Chernoplekov and Ya.M. Mukovskiĭ for fruitful discussions.

This work was supported by the Russian Foundation for Basic Research (project no. 17847) and, in part, by the International Scientific Technical Center (project no. 636).

REFERENCES

1. C. N. R. Rao, A. K. Cheetham, and R. Mahesh, Chem. Mater. **8**, 2421 (1996).
2. A. P. Ramirez, J. Phys.: Condens. Matter **9**, 8171 (1997).
3. É. L. Nagaev, Usp. Fiz. Nauk **166** (8), 833 (1996).
4. A. S. Borovik-Romanov and I. N. Kalinkina, Zh. Éksp. Teor. Fiz. **41**, 1694 (1961).
5. E. O. Wollan and W. C. Koehler, Phys. Rev. **100**, 545 (1955).
6. T. Saitoh, A. E. Bocquet, T. Mizokawa, *et al.*, Phys. Rev. B: Condens. Matter **51**, 13 942 (1995).
7. Y. Okimoto, T. Katsufuji, T. Ishikawa, *et al.*, Phys. Rev. Lett. **75**, 109 (1995).
8. E. Granado, N. O. Morello, A. García, *et al.*, Phys. Rev. B **58** (17), 11435 (1998).

9. M. N. Khlopkin, N. A. Chernoplekov, and P. A. Cheremnykh, Preprint No. 3549/10, IAÉ (Kurchatov Inst. of Atomic Energy, 1982).
10. G. Kh. Panova, A. A. Shikov, and T. Kemen', Preprint No. 3246/10, IAÉ (Kurchatov Inst. of Atomic Energy, 1980).
11. A. Urishibara, Y. Morimoto, T. Arima, *et al.*, Phys. Rev. B: Condens. Matter **51** (20), 14 103 (1995).
12. B. F. Woodfield, M. L. Wilson, and J. M. Byers, Phys. Rev. Lett. **78**, 3201 (1997).
13. A. I. Akhiezer, V. G. Bar'yakhtar, and S. V. Peletminskiĭ, *Spin Waves* (Nauka, Moscow, 1967).
14. J. J. Hamilton, E. L. Keathley, H. L. Ju, *et al.*, Phys. Rev. B: Condens. Matter **54**, 14 926 (1996).
15. A. M. Balbashev, D. A. Shulyatev, G. Kh. Panova, *et al.*, Physica C (Amsterdam) **256** (3–4), 371 (1996).
16. P. P. Parshin, M. G. Zemlyanov, G. Kh. Panova, *et al.*, Sverkhprovodimost: Fiz., Khim., Tekh. **1** (2), 34 (1988).
17. W. E. Pickett and D. J. Singh, Phys. Rev. B: Condens. Matter **53**, 1146 (1996).

Translated by O. Borovik-Romanova

Physics of the Solid State, Vol. 42, No. 1, 2000, pp. 120–125. Translated from Fizika Tverdogo Tela, Vol. 42, No. 1, 2000, pp. 116–120.

MAGNETISM AND FERROELECTRICITY

Features of Magnetization Reversal in Trilayer Nanostructures

K. A. Zvezdin

Institute of General Physics, Russian Academy of Sciences, ul. Vavilova 38, Moscow, 117942 Russia
e-mail: zvezdin@hotmail.com

Received February 1, 1999; in final form, June 10, 1999

Abstract—The process of magnetization reversal in an ultrathin magnetic trilayer is analyzed. It is shown that the shape of magnetization hysteresis loops and the giant magnetoresistance essentially depend on the relative magnitudes of magnetic parameters of the top and bottom layers. Hysteresis loops are found for characteristic relative magnitudes of the parameters. Analysis is performed of the dependence of the shape of hysteresis loops on the magnitude of interlayer exchange. A phase diagram is constructed, which determines the regions of existence of characteristic hysteresis loops for different relative magnitudes of the uniaxial anisotropy constant and exchange constant J_1. *© 2000 MAIK "Nauka/Interperiodica".*

1. INTRODUCTION

Magnetic properties of the surfaces of thin films and multilayers attract considerable interest. In recent years, a large variety of unexpected and nontrivial effects have been discovered that are associated with the properties of magnetic surfaces and interfaces: giant magnetoresistance, strong surface anisotropy, a difference in magnitude between magnetic moments in the surface and in the bulk, the oscillatory behavior of the exchange interaction between adjacent magnetic layers, and strong biquadratic exchange in multilayer structures [1–3]. Being of fundamental importance, studies of the properties of these systems are also of significant practical importance to the development of magnetic memory devices, sensors, etc. [4, 5]. When studying the process of magnetization reversal in such systems, it was found that the models proposed for describing this process are too much simplified to be adequate. A better description can be given using computer simulation techniques [6, 7]. In this paper, we investigate magnetization reversal in a trilayer nanostructure (Fig. 1) for different relative magnitudes of the parameters of the top and bottom magnetic layers. These parameters are shown to significantly affect the nature of magnetization reversal and, hence, the shape of magnetization hysteresis curves and magnetoresistance. The nanostructure under study is often referred to as a spin valve.

2. A THEORETICAL MODEL OF A TRILAYER AND BASIC EQUATIONS

A typical trilayer is depicted in Fig. 1. The thickness of magnetic layers is assumed to be small in comparison with their length and width and, hence, the variation of the magnetization through the thickness may be neglected. Therefore, the magnetization distribution depends only on the coordinates x and y. The z axis is normal to the plane of the structure. The thickness of the nonmagnetic spacer is assumed to be small (1–5 nm) and, therefore, the exchange interaction between the magnetic layers should be taken into account. The magnetization is found by solving the Landau–Lifshitz equation

$$\dot{\mathbf{M}} = \gamma[\mathbf{M}\times\mathbf{H}^{\text{eff}}] - \frac{\alpha\gamma}{M_s}[\mathbf{M}\times[\mathbf{M}\times\mathbf{H}^{\text{eff}}]], \qquad (1)$$

where γ is the gyromagnetic ratio, $\mathbf{M}$ is the magnetization, α is the damping constant, and $\mathbf{H}^{\text{eff}}$ is the effective field given by

$$\mathbf{H}^{\text{eff}}(\mathbf{r}) = -\frac{\delta F(\mathbf{r})}{\delta \mathbf{M}} = \mathbf{H}_0 + \mathbf{H}_M(\mathbf{r}) + \mathbf{H}_A(\mathbf{r}) + \mathbf{H}_{in\text{–}exch}(\mathbf{r}) + \mathbf{H}_{inter\text{–}exch}(\mathbf{r}),$$

where F is the free energy, $\mathbf{H}_0$ is the external magnetic field, $\mathbf{H}_A$ is the anisotropy field, and $\mathbf{H}_{in\text{-}exch}$ and

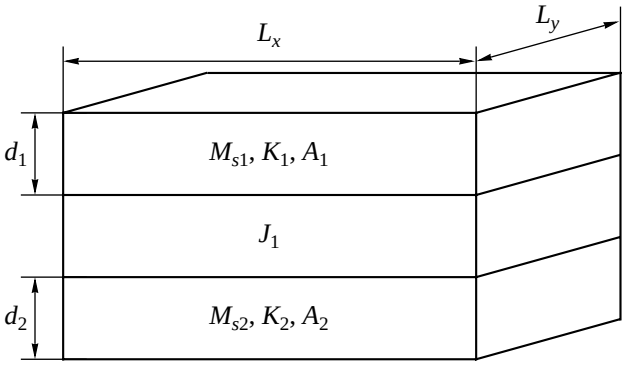

Fig. 1. Trilayer spin-valve structure (schematic).

1063-7834/00/4201-0120$20.00

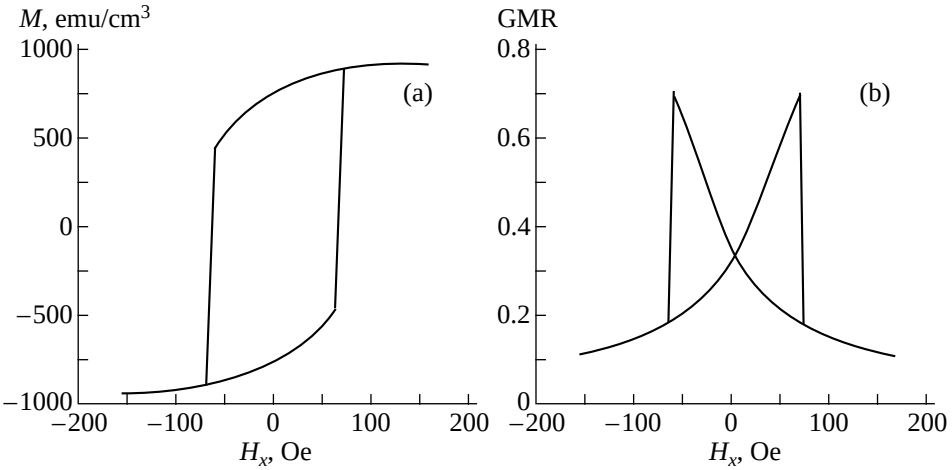

Fig. 2. (a) Magnetization curve of the symmetric structure (average magnetization of the structure vs. magnetic field) and (b) giant magnetoresistance (GMR) vs. magnetic field.

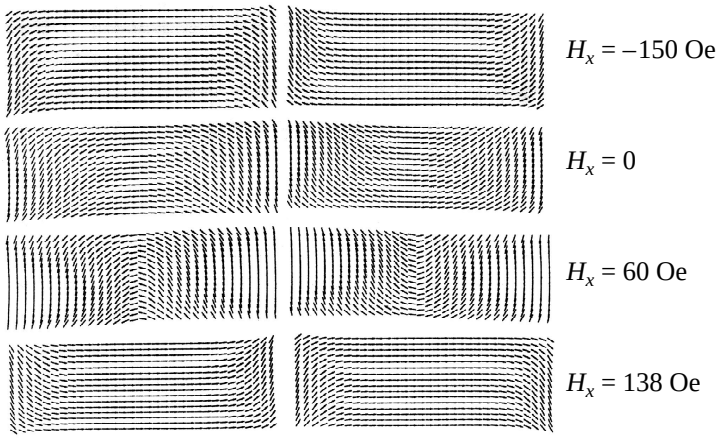

Fig. 3. Magnetization distributions for characteristic points of the hysteresis curve.

$\mathbf{H}_{inter\text{-}exch}$ are the intralayer and interlayer exchange fields, respectively.

In computer simulation, difficulties emerge when we calculate the magnetostatic interaction

$$\mathbf{H}_m(\mathbf{r}) = \sum_l \int_V \mathrm{div}\mathbf{M}_l(\mathbf{r}_l)\frac{\mathbf{r}-\mathbf{r}'}{|\mathbf{r}-\mathbf{r}'|^3}d\mathbf{r}_l,$$

where $\mathbf{r}$ and $\mathbf{r}'$ are the position vectors of the elements between which the interaction is calculated; the summation is performed over all l layers. It should be noted here that the magnetostatic field is a function of all three spatial coordinates (x, y, z). Therefore, this interaction should be calculated everywhere in the volume V [8], which is a very labor-intensive computational problem. For this reason, it is of importance to develop efficient numerical micromagnetic techniques [6, 7, 9]. As mentioned above, we assume that the magnetization distribution $\mathbf{M}(x, y, z)$ is uniform over the thickness of each layer, but the vector $\mathbf{M}$ has a z component. Therefore, this model is quasi-three-dimensional.

3. SYMMETRIC SPIN-VALVE STRUCTURE

Let us first consider a symmetric spin-valve structure consisting of two identical magnetic layers separated by a nonmagnetic spacer. Computer simulation is performed for the following values of parameters: Figure 2 shows a calculated curve (Fig. 2a) and the effect of magnetic switching (Fig. 2b). Figure 3 shows the magnetization distribution calculated for characteristic values of the external field. It is seen from these figures that the magnetization reversal occurs synchronously in the top and bottom magnetic layers; they are switched simultaneously, at the same value of the external magnetic field. The switching mechanism is similar to that

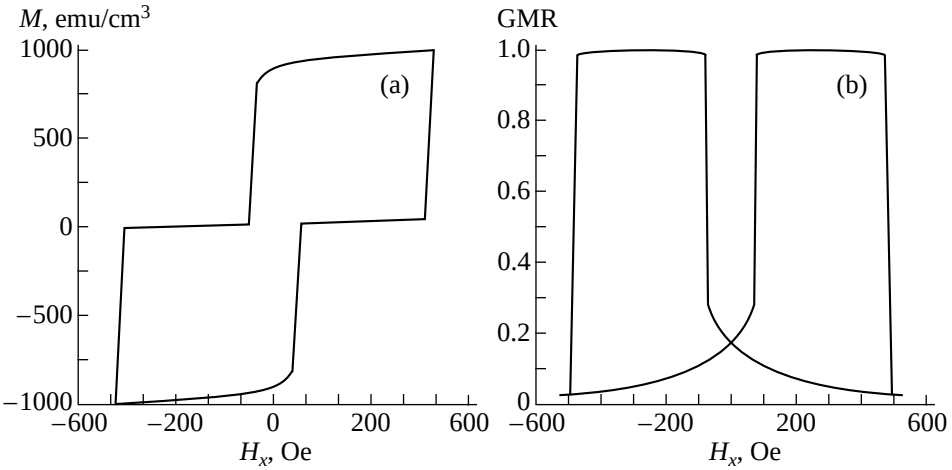

Fig. 4. (a) Magnetization curve and (b) giant magnetoresistance (GMR) of the nonsymmetric structure for the case of $M_{s1}d_1 = M_{s2}d_2$, $K_1 > K_2$.

of a single magnetic plate [9]: Reversed domains are nucleated at the edge of the layers and grow deep into them as the external field increases, so that a 180° domain wall is formed. When the external field reaches a critical value, the "breakdown" occurs and the central regions of the layers are switched.

4. NONSYMMETRIC SPIN-VALVE STRUCTURES

Now, let us consider more complex, nonsymmetric spin-valve structures, consisting of layers with different magnetic and geometrical parameters. As we will see later, the shape of hysteresis curves and the nature of magnetization reversal essentially depend on the relative magnitudes of the parameters of the top and bottom layers. We will consider three cases: (1) $M_{s1}d_1 = M_{s2}d_2$, $K_1 > K_2$; (2) $M_{s1}d_1 > M_{s2}d_2$, $K_1 > K_2$; and (3) $M_{s1}d_1 > M_{s2}d_2$, $K_1 < K_2$, where K_1 and K_2 are the uniaxial anisotropy constants of the top and bottom magnetic layers, respectively. The anisotropy axis is parallel to the x axis.

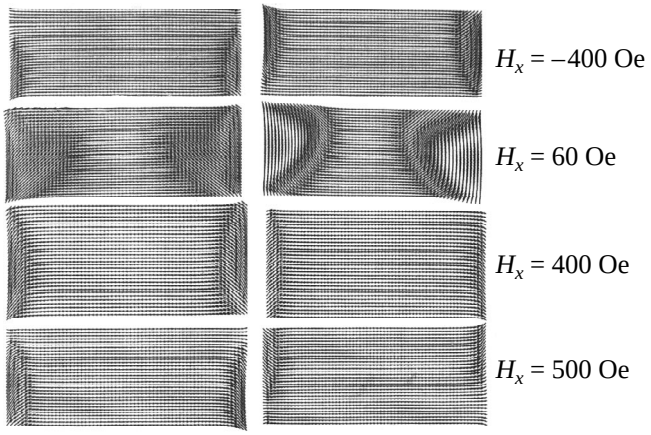

Fig. 5. Magnetization distributions for characteristic points of the hysteresis curve.

4.1. The Case of $M_{s1}d_1 = M_{s2}d_2$, $K_1 > K_2$

Figure 4 shows a magnetic hysteresis curve and the effect of magnetic switching. The magnetization distributions calculated for characteristic values of the external field are presented in Fig. 5. The magnetic hysteresis curve is seen to have two steps, corresponding to the switching of the soft and hard magnetic layers, respectively (Fig. 4a). From the magnetic switching curve (Fig. 4b), it is obvious that a stable antiferromagnetic (AFM) distribution of magnetization takes place in a certain range of the external magnetic field. The calculation is carried out for the following values of magnetic parameters: $K_1 = 1000$ erg/cm^3, $K_2 = 30000$ erg/cm^3, $M_s = 1000$ emu/cm^3, and $d_1 = d_2 = 40$ Å.

From the magnetization distributions (Fig. 5) it is seen that the switching process proceeds more uniformly in the hard magnetic layer than in the soft one. In the former case, the magnetization undergoes a discontinuous change, with its distribution being relatively uniform before the switching. In contrast, the soft magnetic layer is switched very nonuniformly; nonuniformities expand gradually, moving from the edges of the layer to its center. This distinction manifests itself in the fact that on the magnetization curve, the first step is smooth, whereas the second is sharp.

4.2. The Case of $M_{s1}d_1 > M_{s2}d_2$, $K_1 > K_2$

Figure 6 shows a magnetization curve (Fig. 6a) and the effect of magnetic switching (Fig. 6b). In this case, the switching process proceeds highly nonuniformly in

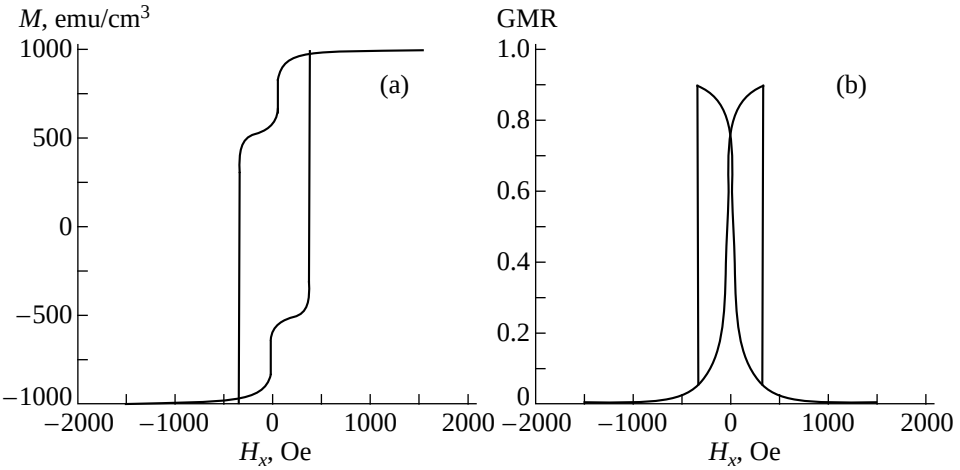

Fig. 6. (a) Magnetization curve and (b) giant magnetoresistance of the nonsymmetric structure for the case of $M_{s1}d_1 > M_{s2}d_2$, $K_1 > K_2$.

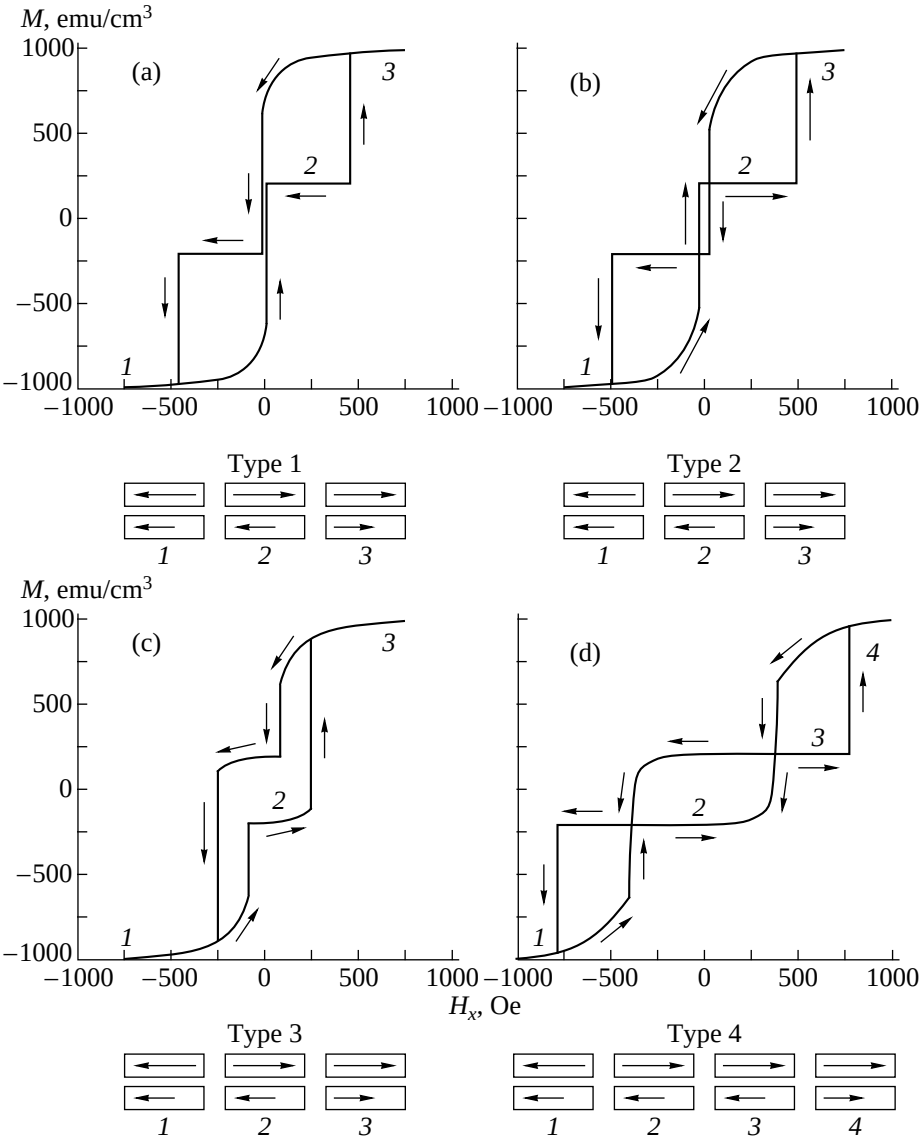

Fig. 7. Four characteristic magnetization curves for the case of $M_{s1}d_1 > M_{s2}d_2$, $K_1 < K_2$ for different values of the antiferromagnetic exchange constant J_1. The order of the layer switching is indicated by arrows below each panel.

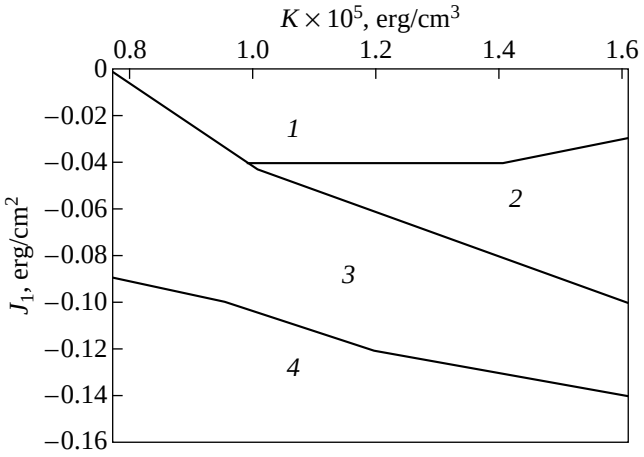

Fig. 8. Diagram determining the ranges of the anisotropy constant K and the interlayer exchange constant in which the characteristic hysteresis curves take place.

both the soft and the hard magnetic layers. Both steps are seen as being very smooth. From the curve of the magnetic switching effect (Fig. 6b), it is obvious that no stable AFM distribution occurs in this case. For a trilayer of this type, magnetic hysteresis curves were observed experimentally in [10].

In this case, calculations are carried out for the following values of magnetic parameters: K_1 = 1000 erg/cm^3, K_2 = 30000 erg/cm^3, M_{s1} = 1200 emu/cm^3, M_{s2} = 800 emu/cm^3, and $d_1 = d_2$ = 40 Å.

4.3. The Case of $M_{s1}d_1 > M_{s2}d_2$, $K_1 < K_2$

In this case, we investigate the dependence on the relative magnitudes of the uniaxial anisotropy constant of the hard magnetic layer and the interlayer AFM exchange constant J_1. Four typical hysteresis curves are obtained (Fig. 7), characterizing four different types of magnetization reversal. Calculations are performed for the following values of magnetic parameters: M_{s1} = 1200 emu/cm^3, M_{s2} = 800 emu/cm^3, and $d_1 = d_2$ = 40 Å.

We also calculate a diagram (Fig. 8) determining the regions of occurrence of these types of magnetization reversal depending on the relative magnitudes of the uniaxial anisotropy and interlayer exchange.

Let us discuss each of the four types of a hysteresis curve.

(1) When the AFM exchange is weak, the shape of a hysteresis curve is similar to that shown in Fig. 7a. At a certain positive value of the external field, the soft magnetic layer is switched with a large remanent magnetization. As the external field is further increased, the hard magnetic layer switched with a less remanent magnetization.

(2) As the interlayer exchange is increased, the hysteresis curve becomes three-looped (Fig. 7b). A special feature of this case is that the magnetization of the system can be opposed to the external field. This takes place when the transition occurs from the state with negative magnetization to that with positive magnetization, whereas the external field remains negative. This effect may be explained by the fact that the exchange field produced by the magnetic layer exceeds the external magnetic field and the anisotropy field hindering the magnetization reversal. This phenomenon was observed experimentally in [11] (see also [3]).

(3) When the interlayer AFM exchange increases further, the order of the layer switching is reversed; first the layer with the larger anisotropy constant and then the soft magnetic layer are switched (Fig. 7c). This may be due to the exchange field produced by the layer with higher magnetization (and weak anisotropy) far exceeding the exchange field produced by the layer with low magnetization (and strong anisotropy). At a certain value of J_1, the former field becomes higher than the external field and the anisotropy field, which hinder the layer switching. At the same time, the exchange field in the soft magnetic layer is lower than the fields hindering the switching process, because this field is produced by the layer with low magnetization.

(4) And, finally, when J_1 increases still further, we have a hysteresis curve shown in Fig. 7d. This curve is similar to that in the second case, but the switching process proceeds much differently. The hard magnetic layer is reversed first. Then, as the external field increases, the soft magnetic layer is also reversed, but the hard magnetic layer is reversed once again. Then, finally, the hard magnetic layer is reversed for the third time, so that both layers become switched. In this case, the AFM exchange is so strong that the switching of the layer with higher magnetization is accompanied by the switching of the other layer.

5. CONCLUSION

Thus, we performed a computer simulation and constructed magnetic hysteresis curves for characteristic relative values of parameters of the magnetic layers. The process of magnetization reversal was investigated as a function of the strength of the interlayer exchange and the relative values of the anisotropy constants of the magnetic layers. A phase diagram was constructed determining the regions of existence of characteristic hysteresis loops, depending on the interlayer exchange and the relative magnitudes of the anisotropy constants.

REFERENCES

1. P. Gründberg, R. Shreiber, Y. Pang, *et al.*, Phys. Rev. Lett. **57**, 2442 (1986).
2. J. C. Slonczewski, J. Appl. Phys. **73**, 5957 (1993).

3. V. V. Dobrovitskiĭ, A. K. Zvezdin, and A. F. Popkov, Usp. Fiz. Nauk **166** (4), 439 (1996) [Phys.–Usp. **166** (1996)].
4. D. D. Tang, P. K. Wang, V. S. Speriosu, *et al.*, IEEE Trans. Magn. **31**, 3206 (1995).
5. L. V. Golubev, D. V. Kirin, A. Yu. Polozov, *et al.*, Proc. ITP **13** (2), 9 (1997).
6. S. G. Osipov, Doctoral Dissertation in Mathematical Physics (Moscow, 1993).
7. L. Greenhard and V. A. Rokhlin, J. Comput. Phys. **73**, 325 (1987).
8. W. F. Brown, Jr., *Micromagnetics* (Wiley, New York, 1963).
9. K. A. Zvezdin, Degree Work (Moscow State Univ., Moscow, 1997).
10. T. Zhu, J. Shi, K. Nordquist, *et al.*, IEEE Trans. Magn. **33**, 3601 (1997).
11. K. Takanashi, H. Kurokawa, and H. Fujimori, Appl. Phys. Lett. **63**, 1585 (1993).

Translated by Yu. Epifanov

Physics of the Solid State, Vol. 42, No. 1, 2000, pp. 126–131. Translated from Fizika Tverdogo Tela, Vol. 42, No. 1, 2000, pp. 121–125.

MAGNETISM AND FERROELECTRICITY

Magnetic Ordering in Granular System

Yu. I. Gorobets*, Yu. I. Dzhezherya, and A. F. Kravets***

** Institute of Magnetism, National Academy of Sciences of Ukraine, Kiev, 252680 Ukraine*

*** Kiev Polytechnical Institute, pr. Peremogi 37, Kiev, 252056 Ukraine*

e-mail: kravets@imag.kiev.ua

Received in final form, June 21, 1999

Abstract—The conditions of the formation of different magnetic structures with ferromagnetic (FM) and antiferromagnetic (AFM) ordering in granular materials containing a subsystem of ferromagnetic granules are considered within the phenomenological approach. It is supposed that the magnetostatic field and the exchange interaction between conduction electrons and magnetic ions are responsible for the formation of magnetic structure. © *2000 MAIK "Nauka/Interperiodica".*

The discovery of the giant magnetoresistance effect in multilayer films with sequentially alternating layers of magnetic and nonmagnetic metals [1], as well as in granular films with ferromagnetic inclusions (granules) dispersed in a nonmagnetic matrix [2, 3], has offered considerable scope for the development of a new class of micromagnetic electronic devices and lent impetus to complex investigations into the physical properties of these structures.

The degree of ordering in the arrangement of granules, their shape, concentration, and sizes substantially affect magnetic characteristics of granular films such as the static and dynamic susceptibility, giant magnetoresistance, temperature phase transitions, etc. It has been found that the upper boundary of saturation fields for different effects in these structures is governed, in particular, by the sizes of granules and their shape. The maximum susceptibility is observed in samples with large-sized spherical granules and also in the samples involving thin granules of disk form, which rather easily reverse magnetization in their plane provided that the magnetocrystalline anisotropy of a ferrogranule material is sufficiently weak [4]. As a rule, magnetic inclusions are irregularly arranged in granular films produced by the conventional method. However, there is evidence for the existence of regular two-dimensional magnetic lattices obtained by the lithographic techniques [5, 6].

The purpose of this work was to consider the conditions for the formation of different structures with ferromagnetic (FM), antiferromagnetic (AFM), and paramagnetic (PM) ordering of the magnetic moments of granules in granular films. In order to describe the exchange interaction, we advanced the phenomenological theory that provided a basis for determining the conditions of the existence of ferromagnetic, antiferromagnetic, and paramagnetic states in granular and quasi-granular films (the latter film was produced by the annealing of a multilayer magnetic film). Moreover, the temperature phase diagram was constructed for these systems.

As is known, multilayer magnetic films during annealing transform into quasi-granular structures with magnetic inclusions in the form of disks whose planes are parallel to the film plane [7, 8]. Let us consider the magnetic properties of these systems under the assumption that ferromagnetic inclusions have the form of disks with thickness L and cross-section d ($L \ll d$). We assume that the plane of circular ferrogranules (hereafter, granules) is parallel to the $Y0X$ plane.

It is evident that, at nanoscale sizes, the granules are in a single-domain state. Owing to the form anisotropy, the magnetostatic self-energy of thin-disk granules is $E_i^a = 2\pi M_i^2 / v_i$, (where $\mathbf{M}_i$ and $v_i = \pi d_i^2 L_i/4$ are the magnetic moment and the volume of the ith granule, respectively). Consequently, their magnetization is orthogonal to the $0Z$ axis and lies in the film plane.

As follows from the calculations performed with allowance for the magnetostatic interaction, the formation of magnetic threads is energetically favorable for the lattices consisting of thin cylindrical granules with a rectangular cell. In these threads, the magnetic moments line up in the form of chains so that the magnetizations of adjacent chains are oppositely directed relative to each other (Fig. 1). The chains of magnetic

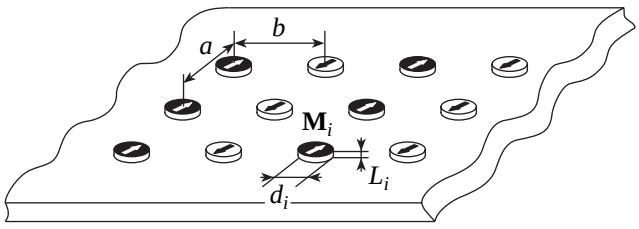

Fig. 1. Magnetic ordering in the two-dimensional lattice of cylindrical magnetic granules.

1063-7834/00/4201-0126$20.00 © 2000 MAIK "Nauka/Interperiodica"

granules shown in Fig. 1 resemble ferromagnetic domains. This structure exhibits zero net magnetic moment and two subsystems magnetized in the opposite directions. Hence, in what follows, this system will be treated as antiferromagnetically ordered. Analysis shows that the magnetostatic energy of the system in this state is less than that in the ferromagnetic state.

If the interaction between granules was magnetostatic only, the granule arrangement depicted in Fig. 1 would be reasonable for the system. However, as was shown in [9, 10], the exchange interaction arises between granules in the case of their close packing even in a nonconducting matrix (for example, Co–Al–O). The exchange interaction gives rise to the magnetic ordering and the giant magnetoresistance effect owing to the spin-dependent tunneling of conduction electrons.

In the study on the magnetic properties of the system, the magnetization of granules $\mathbf{M}_i/v_i$ is conventionally taken to mean the contribution of magnetic ions due to the inner shell electrons, which are strongly localized in magnetic atoms. Note that these electrons insignificantly contribute to the transport processes. The matrix represents a subsystem of conduction electrons that occupies the whole of the interionic space in the system under consideration. The matrix magnetization $\mathbf{m}(\mathbf{r})$ is determined by the polarization of conduction electrons of a material.

The magnetic energy of a matrix can be described within the phenomenological approach based on the use of the spin density function as an order parameter [11]:

$$\psi(\mathbf{r}) = \begin{pmatrix} \psi_1(\mathbf{r}) \\ \psi_2(\mathbf{r}) \end{pmatrix}. \quad (1)$$

The matrix magnetization is expressed in terms of the $\psi(\mathbf{r})$ functions via the known relationships

$$m_\alpha(\mathbf{r}) = \mu_B \psi^+ \hat{\boldsymbol{\sigma}}_\alpha \psi, \quad (2)$$

where $\hat{\boldsymbol{\sigma}}_\alpha$ denotes the Pauli matrices, and μ_B is the Bohr magneton.

The magnetic energy of a film involving ellipsoidal granules can be written as the sum

$$E = E_M + E_\psi + E_{M\psi}. \quad (3)$$

Here, the magnetostatic energy of granules is given by

$$E_M = -\frac{1}{2}\sum_{i\neq j} J^{\alpha\beta}(\mathbf{R}_{ij}) M_i^\alpha M_j^\beta + 2\pi \sum_i (N_\alpha M_i^{\alpha^2}/v_i), \quad (4)$$

where

$$J^{\alpha\beta}(\mathbf{R}_{ij}) = \frac{1}{v_i v_j} \times \int_{v_i} d\mathbf{r} \int_{v_j} d\mathbf{r}' \left(\frac{3(x_\alpha - x'_\alpha)(x_\beta - x'_\beta) - (\mathbf{r}-\mathbf{r}')\delta_{\alpha\beta}}{|\mathbf{r}-\mathbf{r}'|^5} \right),$$

i and j are the indices of granules; N_α denotes the demagnetization coefficients of granules; α and β are x, y, and z; $\mathbf{R}_{ij}$ is the vector connecting the centers of granules (hereafter, the summation is conducted over the doubly repeated indices α and β); and $\mathbf{M}_i$ is the magnetic moment of a granule whose components in the spherical coordinate system with the polar axis $0Z$ take the form

$$\mathbf{M}_i = M_i(\cos\varphi_i \sin\theta_i, \cos\varphi_i \sin\theta_i, \cos\theta_i).$$

The first and second terms in equation (4) describe the exchange energy and magnetodipole self-energy of the ferromagnetic granule system, respectively.

In relationship (3), the third term is the energy of exchange interaction between the magnetization of conduction electrons and the magnetic moment of granules

$$E_{M\psi} = -J\mu_B \int d\mathbf{r} (\psi^+ \hat{\sigma}_\alpha \psi) \sum_i \Theta_i(\mathbf{r})(M_i^\alpha/v_i), \quad (5)$$

where J is the exchange interaction constant. The function $\Theta_i(\mathbf{r})$ introduced in relationship (5) is defined as follows:

$$\Theta_i(\mathbf{r}) = \begin{cases} 1, & \mathbf{r} \in v_i, \\ 0, & \mathbf{r} \notin v_i. \end{cases}$$

The E_ψ quantity that corresponds to the magnetic energy of a matrix can be represented as

$$E_\psi = \int d\mathbf{r} \{ A \nabla\psi^+ \nabla\psi + (I/2)\mu_B^2 (\psi^+ \hat{\boldsymbol{\sigma}} \psi)^2 \}, \quad (6)$$

where A and I are some phenomenological parameters.

The second term in relationship (6) accounts for an increase in the energy of a nonmagnetic matrix upon polarization of conduction electrons. In the phenomenological theory, the first term traditionally described a variation in the energy upon spatial modulations of the order parameter.

For simplicity, the terms describing the contributions of conduction electrons to the magnetostatic energy of the system can be omitted from consideration because of the small magnetizations.

Assume that the concentration of magnetic inclusions in the system is small. Then, on average, the volume per one magnetic granule $a^3 = V/N \gg v_i$ (where V is the volume of the system, and N is the number of granules). Therefore, the quantity a can be considered

a characteristic scale of inhomogeneity in the arrangement of granules.

By varying the energy of the system [equation (1) with respect to ψ^+, we obtain the equation for the spin density function

$$-\left(\frac{1}{a}\right)^2\nabla^{*2}\psi = \frac{1}{m_0}\left(\sum_i \Theta_i(\mathbf{r})\frac{\mathbf{M}_i}{v_i} - \frac{I}{J}\mu_B(\psi^+\hat{\boldsymbol{\sigma}}\psi)\right)\hat{\boldsymbol{\sigma}}\psi, \quad (7)$$

where $\nabla^{*2} = a^2\nabla^2$ is the Laplacian operator in terms of dimensionless variables, $l = \sqrt{A/J\mu_B m_0}$ is the characteristic length of magnetic interaction, and $m_0 = M_i/v_i$ is the magnetization of a granule material (in this work, it is constant).

Now, we consider the case when the characteristic length l is considerably larger than the mean intergranule distance, so that the following relation is met:

$$l \gg a. \quad (8)$$

The right-hand side of equation (7) can be treated as a perturbation, and its solution is written as

$$\psi(\boldsymbol{\rho}) = \psi_0 + (a/l)^2\psi_1(\boldsymbol{\rho}) + \ldots, \quad (9)$$

where $\boldsymbol{\rho} = \mathbf{r}/a$, and ψ_0 is constant. The latter quantity is determined from the solvability condition of the equation for the correction $\psi_1(\boldsymbol{\rho})$.

This condition has the form

$$\int dV\left\{\sum_i \Theta_i(\mathbf{r})\frac{\mathbf{M}_i}{v_i} - \frac{I}{J}\mu_B(\psi_0^+\hat{\boldsymbol{\sigma}}\psi_0)\right\} = 0. \quad (10)$$

The integration in equation (10) is performed over the entire volume of the system.

The solution of equation (10) within the above approximations leads to the following expression for the magnetization of conduction electrons:

$$\mu_B(\psi_0^+\hat{\boldsymbol{\sigma}}\psi_0) = \frac{J}{I}\frac{1}{V}\sum_i \mathbf{M}_i. \quad (11)$$

Therefore, with condition (8), the result obtained is similar to that derived in the theory of paramagnetism for a system of Fermi particles, provided that conduction electrons travel in the effective magnetic field $\mathbf{H} = (J/I)\sum_i \mathbf{M}_i$. The I^{-1} quantity has the role of the paramagnetic susceptibility of conduction electrons, and, hence, it can be evaluated from the relationship $I^{-1} \approx \chi = \nu(\varepsilon_F)\mu_B^2$, where $\nu(\varepsilon_F)$ is the density of electron conduction states at the Fermi level.

As a result, the magnetic energy (1) of a granular film is determined by the state of the subsystems of magnetic granules and, with allowance for approximation (8) and relationships (5), (6) and (11), takes the form

$$E = E_M - \frac{1}{2}\frac{J^2 I^{-1}}{V}\sum_{i,j}\mathbf{M}_i\mathbf{M}_j. \quad (12)$$

A complete analysis of the magnetic configuration of the system can be carried out only with the regular lattices consisting of granules identical in their shape and sizes. The techniques for producing films with these characteristics are currently under development [5, 6, 12]. For example, a regular tetragonal lattice of magnetic disks (2×10^{-4} cm in diameter) with a period of 4×10^{-4} cm was obtained in the [FeNi / Ag] multilayer films by the standard microphotolithographic technique [5]. This two-dimensional ordered system covered with a thin conducting nonmagnetic film shows a giant magnetoresistance effect. Moreover, the magnetoresistance of this system is saturated in response to weak magnetic fields, which indicates an insignificant antiferromagnetic ordering of the magnetic moments of granules. Similar regular two-dimensional structures can also be obtained by the laser-focused atomic deposition of ferromagnetic films [13].

The employment of granular films with random parameters of granules, which are produced by evaporation, has received wide current acceptance. It should be mentioned that the investigation into the magnetic structure of the granular film surface indicates the domain structure in the form of magnetic granule chains [14], which, in turn, confirms the ordering of the magnetic moments of granules.

By using expression (12), we determine the conditions of realizing the ferromagnetic and antiferromagnetic ordering in granular films in the case when at least the short-range order between granule groups can be distinguished. Note that the existence of short-range order in the orientation of the moments of individual granules stems from the properties of the magnetostatic field, which is induced by the magnetic moments of these granules and is potential in nature. As is known, the force lines of potential fields do not intersect. Hence, in a certain fragment of the granular film, there is a preferred direction corresponding to the averaged orientation of the force lines. The magnetic moments of granules are aligned parallel to the force lines of the field, and, therefore, the ordering should also be traced in their orientation.

It is easy to verify that $J^{\alpha\beta}(\mathbf{R}_{ij})$ is a homogeneous function with the degree of homogeneity $k = -3$. Consequently, for the dimensionless variables $\boldsymbol{\rho}_{ij} = \mathbf{R}_{ij}/a$, the following relationship is fulfilled:

$$J^{\alpha\beta}(\mathbf{R}_{ij}) = a^{-3}J^{\alpha\beta}(\boldsymbol{\rho}_{ij}). \quad (13)$$

For a granule in the form of a flat disk lying in the *Y*0*X* plane, the demagnetization coefficients meet the relationships $n_z \approx 1$ and $n_x = n_y \ll n_z$. By using relation-

ships (12) and (13), and taking into consideration that the integral of motion $\mathbf{M}_i^2$ is constant, the effective field affecting the magnetic moment of a granule can be represented as

$$\mathbf{H}_i^{ef} = -4\pi m_0 \cos\theta_i \mathbf{e}_z + \varepsilon_i \mathbf{H}_i^m, \tag{14}$$

where

$$\varepsilon_i = \frac{v_i}{a^3} \ll 1,$$

$$\mathbf{H}_i^m = v_i^{-1} \sum_j \mathbf{e}_\alpha J^{\alpha\beta}(\boldsymbol{\rho}_{ij}) M_j^\beta + V^{-1} \sum_j J^2 \chi \mathbf{M}_j.$$

Since the net moment of granules is rather large, the state of their magnetization can be determined with the Langevin statistical averaging. According to formula (14), the mean value of the magnetization components of the ith granule is represented in the form

$$\langle \mathbf{m}_i \rangle = Z^{-1} \int d\Omega_i \mathbf{m}_i \exp(-D_i \cos^2\theta_i + \varepsilon D_i \mathbf{h}_i^m \mathbf{m}_i),$$

$$Z = \int d\Omega_i \exp(-D_i \cos^2\theta_i + \varepsilon D_i \mathbf{h}_i^m \mathbf{m}_i), \tag{15}$$

where

$$D_i = \frac{2\pi m_0^2 v_i}{(k_B T)}, \quad \mathbf{h}_i^m = \mathbf{H}_i^m / 2\pi m_0, \quad d\Omega_i = -d\cos\theta_i d\varphi_i,$$

$\mathbf{m}_i = \mathbf{M}_i / M_i$ and k_B is Boltzmann's constant.

For granules with $m_0 = 10^3$ G, diameter $d \approx 6$ nm, and thickness $L_z \approx 2$ nm, at $T \approx 300$ K, we obtain $D \approx 6 \gg 1$. Consequently, in relationship (15), the integration over $\cos\theta_i$ can be carried out by the Laplace asymptotic method with a high accuracy. As a result, we have

$$\langle m^z \rangle = 0,$$

$$\begin{Bmatrix} \langle m_i^z \rangle \\ \langle m_i^y \rangle \end{Bmatrix} = \frac{\int_0^{2\pi} d\varphi_i \begin{pmatrix} \cos\varphi_i \\ \sin\varphi_i \end{pmatrix} \exp\{D_i \varepsilon (h_i^x \cos\varphi_i + h_i^y \sin\varphi_i)\}}{\int_0^{2\pi} d\varphi_i \exp\{D_i \varepsilon (h_i^x \cos\varphi_i + h_i^y \sin\varphi_i)\}}. \tag{16}$$

In order to simplify further calculations, the parameters of magnetic inclusions are replaced by their mean values. Then, $M_i = M$ and $\nu_i = \nu$.

Suppose that a certain fragment of the film involves two subsystems of magnetic granules, so that their mean moments $\langle \mathbf{M}_1 \rangle$ and $\langle \mathbf{M}_2 \rangle$ are oriented along the $0X$ axis.

By writing h_i^y and h_i^x in equation (16), we replace M_j^α with the mean values. Then,

$$h_i^x = \langle m_1^x \rangle (2\pi)^{-1} \sum_j^{N_1} J^{xx}(\boldsymbol{\rho}_{ij}) + \langle m_2^x \rangle (2\pi)^{-1} \sum_j^{N_2} J^{xx}(\boldsymbol{\rho}_{ij}),$$

$$h_i^y = \langle m_1^x \rangle (2\pi)^{-1} \sum_j^{N_1} J^{yx}(\boldsymbol{\rho}_{ij}) + \langle m_2^x \rangle (2\pi)^{-1} \sum_j^{N_2} J^{yx}(\boldsymbol{\rho}_{ij}), \tag{17}$$

where $\langle m_1^x \rangle = \langle M_1^x \rangle / M$, $\langle m_2^x \rangle = \langle M_2^x \rangle / M$, and $N_1 = N_2 = N/2$ are the numbers of particles in the subsystems.

Taking into consideration the properties of the $J^{\alpha\beta}(\boldsymbol{\rho}_{ij})$ functions, it can easily be shown that, for regular lattices of granules, $h_i^y = 0$. In the general case, $h_i^y \neq 0$, but the alternating character of $J^{yx}(\boldsymbol{\rho}_{ij})$ implies the fulfillment of the condition $\left| \sum_j^{N_{1,2}} J^{yx}(\boldsymbol{\rho}_{ij}) \right| \ll \left| \sum_j^{N_{1,2}} J^{xx}(\boldsymbol{\rho}_{ij}) \right|$, and, hence, the h_i^y value is negligibly small and can be eliminated from further consideration.

On this basis, equations (16) after the integration take the form

$$\langle m_1^x \rangle = I_1\{X_1\}/I_0\{X_1\}, \quad \langle m_2^x \rangle = I_1\{X_2\}/I_0\{X_2\}, \tag{18}$$

where

$$\begin{pmatrix} X_1 \\ X_2 \end{pmatrix} = \frac{T_c}{T} \frac{2}{\gamma_1 + \gamma_2} \left\{ \frac{1}{2} J^2 I^{-1} (\langle m_1^x \rangle + \langle m_2^x \rangle) + \gamma_1 \begin{pmatrix} \langle m_1^x \rangle \\ \langle m_2^x \rangle \end{pmatrix} - \gamma_2 \begin{pmatrix} \langle m_2^x \rangle \\ \langle m_1^x \rangle \end{pmatrix} \right\},$$

$$T_c = \frac{M^2(\gamma_1 + \gamma_2)}{2a^3 k_B}.$$

In equations (18), we introduced the mean parameters

$$\gamma_1 = \frac{1}{N_1} \sum_i^{N_1} \sum_j^{N_1} J^{xx}(\boldsymbol{\rho}_{ij}) = \frac{1}{N_2} \sum_i^{N_2} \sum_j^{N_2} J^{xx}(\boldsymbol{\rho}_{ij}),$$

$$\gamma_2 = -\frac{1}{N_1} \sum_i^{N_1} \sum_j^{N_2} J^{xx}(\boldsymbol{\rho}_{ij}) = -\frac{1}{N_2} \sum_i^{N_2} \sum_j^{N_1} J^{xx}(\boldsymbol{\rho}_{ij}), \tag{19}$$

where $I_0(x)$ and $I_1(x)$ are the Bessel functions of imaginary argument. The differences from the Langevin the-

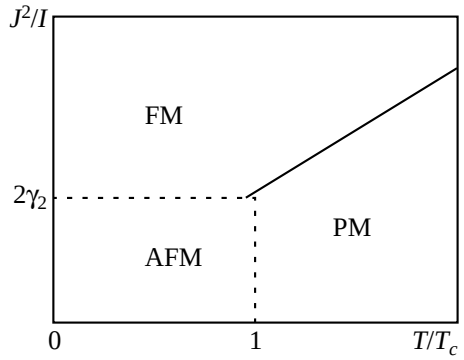

Fig. 2. Phase diagram of a granular system in the magnetic state.

ory reside in the "freezing" of the degree of freedom of magnetic moments along the $0Z$ direction.

A set of transcendental equations (18) can possess the following qualitatively different types of solutions:

$\langle m_1^x \rangle = \langle m_2^x \rangle = 0$ for the paramagnetic state,

$\langle m_1^x \rangle = \langle m_2^x \rangle = \langle m \rangle$ for the ferromagnetic ordering,

$\langle m_1^x \rangle = -\langle m_2^x \rangle = \langle m \rangle$ for the antiferromagnetic ordering.

Let us consider in more detain the conditions of realizing a particular state.

For the ferromagnetic ordering, $\langle m_1^x \rangle = \langle m_2^x \rangle = \langle m \rangle$ and

$$X_1 = X_2 = 2\langle m \rangle \frac{T_c}{T} \frac{JI^{-1} + \gamma_1 - \gamma_2}{\gamma_1 + \gamma_2}. \quad (20)$$

Analysis of the set of equations (18) reveals that they possess nontrivial solutions at the condition

$$\frac{T}{T_c} < \left(\frac{\gamma_1 - \gamma_2 + J^2 I^{-1}}{\gamma_1 + \gamma_2} \right). \quad (21)$$

For the antiferromagnetic ordering, $\langle m_1^x \rangle = -\langle m_2^x \rangle = \langle m \rangle$ and

$$X_1 = -X_2 = \langle m \rangle \times 2\frac{T_c}{T}. \quad (22)$$

In this case, the condition for a nontrivial solution to the set equations (18) has the form

$$T < T_c. \quad (23)$$

The found regions of the ferromagnetic and antiferromagnetic phases share a common region. Analysis of the system in the antiferromagnetic phase for the resistance to small ferromagnetic perturbations along the $0Y$ direction was performed with the use of equation (11) and yielded the criterion for the transition from the antiferromagnetic state to the ferromagnetic state

$$2J^2 I^{-1} \geq \gamma_2. \quad (24)$$

This condition is rather reasonable because, for the equality sign in relationship (24), the energies of the ferromagnetic and antiferromagnetic states are equal to each other.

Figure 2 displays the phase diagram for granular films, which was constructed in the J^2I^{-1}–T/T_c coordinates with allowance for conditions (21)–(24) specifying the phase boundaries.

The well-defined phase boundaries shown in Fig. 2 can be observed in materials with a perfect lattice. In the general case, the boundaries separate the regions with the predominance of the relevant phases.

The numerical parameters γ_1 and γ_2 are of the order of unity. For example, the calculations performed in the limit of low granule concentrations $v/a^3 \ll 1$ for lattices of granules lead to the following results: (a) $\gamma_1 = 4.8$ and $\gamma_2 = 0.3$ for a two-dimensional lattice with a tetragonal cell and (b) $\gamma_1 = 3.7$ and $\gamma_2 = 1.7$ for a three-dimensional lattice with a cubic cell.

The critical temperature T_c for a granular film with the granule parameters $m_0 \approx 10^3$ G and $v^{1/3} \approx 6 \times 10^{-7}$ cm at the volume concentration of magnetic material $v/a^3 \approx 5\%$ was estimated at about 200 K. At higher ferromagnet concentrations, the γ_1 and γ_2 parameters depend on the granule size.

Note that the proposed approach, as applied to the system of spherical granules (the case of normal granular films) leads to the appearance of the Langevin function in equations (18) rather than the Bessel functions. A comparison of the results obtained for these two cases shows that the critical temperature T_c for the system of disk granules is higher by a factor of 3/2 than that for the system of spherical granules. This is likely due to the freezing of the degree of freedom in the $0Z$ direction for flat granules.

Now, we write the relationship for T_c in the form

$$T_c = (\gamma_1 + \gamma_2) \frac{m_0^2 v}{2k_B a^3} v. \quad (25)$$

It should be noted that, at a constant concentration of magnetic material v/a^3, the critical temperature linearly increases with an increase in the granule volume. This effect is caused by the change in the role of the magnetostatic interaction with an increase in the granule size.

Finally, with the results obtained, let us derive the relationship that determines the gain in energy of the magnetostatic interaction in the antiferromagnetic phase as compared to that of the ferromagnetic phase. In the relative units, it can be written as

$$\sigma = \frac{|E_{AFM}| - |E_{FM}|}{|E_{AFM}|} \underset{J=0}{=} \frac{2\gamma_2}{\gamma_1 + \gamma_2}. \quad (26)$$

The value of σ is equal to approximately 10% for a two-dimensional lattice (Fig. 1) and about 60% for a three-dimensional lattice with a cubic cell.

These estimates indicate that the ferromagnetic ordering in granular films at a low granule concentration can be achieved only as a result of the indirect exchange interaction between granules through conduction electrons, provided that condition (21) is fulfilled.

REFERENCES

1. M. N. Baibich, J. M. Broto, A. Fert, *et al.*, Phys. Rev. Lett. **61** (21), 2472 (1988).
2. J. Q. Xiao, J. S. Jiang, and C. L. Chien, Phys. Rev. Lett. **68** (25), 3749 (1992).
3. A. E. Berkowitz, J. R. Mitchell, M. J. Carey, *et al.*, Phys. Rev. Lett. **68** (25), 3745 (1992).
4. T. L. Hylton, Appl. Phys. Lett. **62** (19), 2431 (1993).
5. T. L. Hylton, M. A. Parker, K. R. Coffey, *et al.*, Appl. Phys. Lett. **67** (8), 1154 (1995).
6. S. A. Gusev, L. A. Mazo, Yu. N. Nozdrin, M. V. Sapozhnikov, L. V. Sukhodeev, and A. A. Fraerman, in *Abstracts of Papers of the Sixteenth International School–Workshop NMMM* (Moscow, Russia, 1998), p. 494.
7. T. L. Hylton, K. R. Coffey, M. A. Parker, and J. K. Howard, Science (Washington, D.C., 1883–) **261**, 1021 (1993).
8. J. C. Sionczewski, J. Magn. Magn. Mater. **129** (2–3), LI23 (1994).
9. H. Fujimori, S. Mitani, and S. Ohnuma, Mater. Sci. Eng., B **31**, 219 (1995).
10. A. F. Kravets, C. S. Kim, A. Y. Vovk, A. N. Pohorilyi, and O. V. Shypil, in *Book of Abstracts of the Seventh European Magnetic Materials and Application Conference* (Zaragoza, Spain, 1998), p. 28.
11. V. G. Bar'yakhtar and Yu. I. Gorobets, *Cylindrical Magnetic Domains and Their Lattices* (Naukova Dumka, Kiev, 1988).
12. S. V. Gaponov, S. A. Gusev, L. A. Mazo, Yu. N. Nozdrin, M. V. Sapozhnikov, L. V. Sukhodeev, and A. A. Fraerman, in *Abstracts of Papers of the Sixteenth International School–Workshop NMMM* (Moscow, Russia, 1998), p. 42.
13. R. J. Celotta, R. Gupta, R. E. Sholten, *et al.*, J. Appl. Phys. **79** (8), 6079 (1996).
14. Y. J. Chen, W. Y. Cheung, I. H. Wilson, *et al.*, Appl. Phys. Lett. **72** (19), 2472 (1998).

Translated by O. Borovik-Romanova

Physics of the Solid State, Vol. 42, No. 1, 2000, pp. 132–138. Translated from Fizika Tverdogo Tela, Vol. 42, No. 1, 2000, pp. 126–132.

MAGNETISM AND FERROELECTRICITY

"Nonmagnetic" (Antiferromagnetic) Magnetic Polaron[1]

I. A. Merkulov

Ioffe Physicotechnical Institute, Russian Academy of Sciences, Politekhnicheskaya ul. 26, St. Petersburg, 194021 Russia

Received August 5, 1999

Abstract—It is shown that, within deep narrow quantum potential wells in systems based on semimagnetic semiconductors containing Mn^{2+} ions, both magnitude and sign of the exchange interaction between electrons in the conduction band and in the *d*-shell of a magnetic ion depend significantly on the spatial position of this ion. This situation allows magnetic polarons with zero magnetic moment to appear, for which the localized-electron-induced spatial distribution of polarization of the surrounding magnetic ions exhibits an antiferromagnetic character. The possibility of experimental detection of these "nonmagnetic" magnetic polarons is considered. © *2000 MAIK "Nauka/Interperiodica".*

1. INTRODUCTION

By definition, magnetic polaron is a complex formed by a localized charge carrier and surrounding magnetic ions with their spins correlated by the exchange interaction [1–3]. In semimagnetic semiconductors of the $Cd_xMn_{1-x}Te$ type, these complexes may possess rather large magnetic moments reaching about one hundred of Bohr magnetons (see, e.g., [4, 5]). This is explained by a comparatively large field created by a localized carrier on the neighboring magnetic ions ($B_p \cong 1T$) and by a large number of these ions ($\sim 10^3$).

However, this estimate implicitly assumes that the exchange interaction field $\mathbf{B}_p(\mathbf{r})$ created by the charge carrier has approximately the same direction in the entire localization region. In fact, this assumption was valid for the previously studied magnetic polarons formed by localized electrons or holes.[2]

Below, we will demonstrate that, within a deep narrow quantum well with high potential barriers in the above semimagnetic semiconductor systems, both magnitude and sign of the exchange interaction between an electron in the conduction band and electrons in the *d*-shell of a Mn^{2+} ion depend significantly on the spatial position of the magnetic ion. This may lead to a situation where the spin correlation between the electron in the conduction band and the surrounding ions would markedly decrease the energy of the charge carrier,

$$E_p = -\int (\mathbf{M}(\mathbf{r})\mathbf{B}_p(\mathbf{r}))d^3r \approx -\frac{dM}{dB}\int B_p^2 = (\mathbf{r})d^3r > k_B T, \quad (1)$$

at a virtually zero total spin of this complex:

$$\mathbf{M}_p = \frac{dM}{dB}\int \mathbf{B}_p(\mathbf{r})d^3r \approx 0. \quad (2)$$

Here, $\mathbf{M}(\mathbf{r})$ is the density of the magnetic moment of Mn^{2+} ions in the electron localization region, dM/dB is the magnetic susceptibility of the magnetic ion system, k_B is the Boltzmann constant, and T is the absolute temperature.

In Section 2, we will present qualitative considerations showing the principal possibility of a situation where both magnitude and sign of the exchange interaction between a localized two- dimensional (2D) electron and the *d*-shell electrons of a Mn^{2+} ion would depend on the position of this ion in a nanometer-size heterostructure. Section 3 gives mathematical relationships describing spatial variation of the exchange interaction parameters for a quantum potential well with rectangular walls. On this basis, formulas are derived describing dependence of the magnetic moment and energy of a magnetic polaron on the quantum potential well width and depth. Section 4 presents calculations for semimagnetic semiconductor heterostructures of the $Cd_{1-x}Mn_xTe$ type, in which magnetic polarons can be reliably detected by optical methods [7]. In section 5 we will discuss the possibility of experimental observation of the magnetic polaron with zero magnetic moment.

2. QUALITATIVE MODEL ANALYSIS

As demonstrated in [8] for semimagnetic semiconductor heterostructures, a decrease in the characteristic

[1] This work was partly supported by the DFG Foundation (grant no. SFB410) and by the Russian Foundation for Basis Research (project no. 96-15-96392).

[2] Berkovskaya *et al.* [6] considered a magnetic polaron formed by a hole localized at an acceptor and by the surrounding magnetic ions occurring within a narrow spherical layer at a distance slightly above the Bohr radius. It was found that the lowest energy state of this system corresponds to a nontrivial distribution of the magnetic polarization, which differs from zero at any particular point of this sphere but gives zero values of the exchange interaction field and the magnetic polarization on averaging over the whole sphere.

size of the system (and, hence, an increase in the dimensional quantization energy) is accompanied by dramatic variations in the parameter of exchange interaction between a localized electron and surrounding magnetic ions. This behavior is related to an admixture of wavefunctions of the valence band top to the Bloch electron wavefunction amplitude. This admixture increases with the distance from the Brillouin zone center and, as a result, a new channel of exchange interaction–the kinetic exchange–is opened, which is forbidden with respect to symmetry at the point Γ of the conduction band [9]. In $Cd_{1-x}Mn_xTe$ solid solutions, a parameter characterizing the magnitude of the exchange interaction has the opposite sign and a markedly greater value (by a factor exceeding 5) as compared to the corresponding quantity for the potential exchange interaction at the point Γ [8–10]. Thus, as the admixture of the valence band states to the conduction band states increases, the exchange interaction parameter decreases and even changes in sign.

A calculation of this parameter was performed in our previous work [8] within the framework of the Kane band model. We have analyzed the splitting of the electron spin levels in the exchange field created by a spatially homogeneous polarization of magnetic ions induced by the applied magnetic field. Theoretical description of this situation required knowledge of the exchange interaction parameter averaged over the system volume, and the corresponding theory was developed in [8].

At the same time, the exchange interaction constant exhibits a rather unusual spatial variation in the state described by superposition of the *s* and *p* functions. The reason is the phase difference between the *s* and *p* parts of the standing planar wave being equal to π/2. As a result, the envelope of the *s* component in a standing wave describing bottom states of the lowest 2D band in the quantum potential well has the shape of cos*qz* (not changing sign upon mirror reflection from the potential well center $z = 0$), while the *p* function envelope has the shape of sin*qz* (odd with respect to the mirror reflection operation). Here, q denotes the electron wavevector component normal to the potential well plane. For a potential well with infinite walls, this value can be expressed through the well width L by a well-known formula $q = \pi/L$ [11, 12].[3] Thus, the *s* component of the wavefunction is large at the wall and is zero at the center of the well. Accordingly, the potential exchange interaction plays a major role at the center, while the kinetic exchange interaction is maximum at the wall. As a result, both magnitude and sign of the parameter of exchange interaction between the spins of electron and Mn^{2+} ion depend on the magnetic ion position in the quantum structure.

3. THEORETICAL MODEL CALCULATIONS

In order to calculate spatial variation of the parameter of exchange interaction between a 2D electron and Mn^{2+} ions, let us consider an equation for the electron wavefunction at the bottom of the first band of dimensional quantization. Inside the potential well ($-L/2 < z < L/2$)

$$\begin{aligned}\Psi_{\pm 1/2} &= C_W\{E(q)(E(q)+\Delta)\cos qz|S|\pm 1/2\rangle \\ &\quad - i\sin qz(P\hbar q/3m_0)[\Delta(X \pm iY)|\mp 1/2\rangle \\ &\quad - (3E(q)+2\Delta)Z|\pm 1/2\rangle]\}/[(E(q)(E(q)+\Delta))^2 \\ &\quad + |P\hbar q/3m_0|^2(2\Delta^2 + (3E(q)+2\Delta)^2)]^{1/2},\end{aligned} \tag{3}$$

where $E(q)$ is the energy of an electron with the wavevector q measured from the top of the valence band. This energy is related to the wavevector by the following relationship:

$$\begin{aligned}&\left|\frac{\hbar\langle s|p_z|Z\rangle}{m}\right|^2 q^2 \\ &= \frac{(E(q)-E_g)E(q)(E(q)+\Delta)}{\left(E(q)+\frac{2}{3}\Delta\right)},\end{aligned} \tag{4}$$

where m_0 is the mass of the free electron, $\langle s|p_z|Z\rangle$ is the element of the momentum matrix calculated between functions of the conduction band bottom and the valence band top, E_g is the bandgap width, and Δ is the distance between tops of the valence band and the subband split as a result of the spin–orbit interaction. As seen, a maximum of the *s* wave correspond to a node of the *p* wave and vice versa.

Under the barriers ($|z| > L/2$), all components of the electron wavefunction exhibit the same spatial variation described by the "tunneling" exponent

$$\begin{aligned}\Psi_{\pm 1/2} &= C_B\{\tilde{E}(Q)(\tilde{E}(Q)+\tilde{\Delta})S|\pm 1/2\rangle \\ &\quad \mp i(P\hbar Q/3m_0)[\tilde{\Delta}(X \pm iY)|\mp 1/2\rangle \\ &\quad - (3\tilde{E}(Q)+2\tilde{\Delta})Z|\pm 1/2\rangle]\}/[(\tilde{E}(Q)(\tilde{E}(Q)+\tilde{\Delta}))^2 \\ &\quad + |P\hbar Q/3m_0|^2(2\tilde{\Delta}^2 + (3\tilde{E}(Q)+2\tilde{\Delta})^2)]^{1/2} \\ &\quad \times \exp\left\{Q\left(\frac{L}{2} \mp z\right)\right\},\end{aligned} \tag{5}$$

$$\left|\frac{\hbar P}{m_0}\right|^2 Q^2 = \frac{(\tilde{E}_g - \tilde{E}(Q))\tilde{E}(Q)(\tilde{E}(Q)+\tilde{\Delta})}{(\tilde{E}(Q)+2/3\tilde{\Delta})}, \tag{6}$$

[3] This estimate for q follows immediately from the condition that the wavefunction has a zero value at the infinitely high wall. However, the *s* and *p* components of a 2D electron wavefunction cannot simultaneously acquire zero values. According to [12], $q = \pi/L$ if the barrier height V increases simultaneously with the well width. In the limiting case of $V \longrightarrow \infty$, we have $V/E_{B,g} \longrightarrow 0$; otherwise, the first level of dimensional quantization corresponds to $qL < \pi$.

where quantities with the "tilda" symbol refer to the band structure parameters inside the barrier material. Taking into account that, as demonstrated in [11, 12], envelopes of the *s* wave and the *p*-wave *z* component normal to the wall are continuous on the wall, we obtain

$$C_B = C_W\{E(q)(E(q)+\Delta)[(\tilde{E}(Q)(\tilde{E}(Q)+\tilde{\Delta}))^2 + |P\hbar Q/3m_0|^2(2\tilde{\Delta}^2 + (3\tilde{E}(Q)+2\tilde{\Delta})^2)]^{1/2}\}/\{\tilde{E}(Q) \times(\tilde{E}(Q)+\tilde{\Delta})[(E(q)(E(q)+\Delta))^2 + |P\hbar q/3m_0|^2(2\Delta^2 + (3E(q)+2\Delta)^2)]^{1/2}\}\cos(qL/2). \quad (7)$$

The position of levels inside the quantum potential well is determined by the following equation:

$$\frac{q}{Q}\tan\left(q\frac{L}{2}\right) = \frac{E(q)(E(q)+\Delta)(3\tilde{E}(Q)+2\tilde{\Delta})}{\tilde{E}(Q)(\tilde{E}(Q)+\tilde{\Delta})(3E(q)+2\Delta)}, \quad (8)$$

which has to be solved consistently with equations (4) and (6) taking into account that $\tilde{E}(Q) = E(q) + V_B$ and V_B is the barrier hight for a hole. Combined with the normalization condition

$$\frac{|C_W|^2}{2}\left[L + [(E(q)(E(q)+\Delta))^2 - |P\hbar q/3m_0|^2(2\Delta^2 + (3E(q)+2\Delta)^2)]/[(E(q)(E(q)+\Delta))^2 + |P\hbar q/3m_0|^2(2\Delta^2 + (3E(q)+2\Delta)^2)]\frac{\sin qL}{q}\right] + \frac{|C_B|^2}{Q} = 1, \quad (9)$$

equations (7) and (8) determine the values of coefficients entering into general expressions (3) and (5) for the 2D electron wavefunction. Using equations (3) and (5), the Hamiltonian of the exchange interaction between a 2D electron and an ion occurring at a point with the coordinates (*z*, *R*) can be written as

$$\hat{H}_{ex} = \left(\sum_\eta s_\eta \alpha_{\eta\eta}(z) J_\eta\right)\delta(\boldsymbol{\rho} - \mathbf{R}), \quad (10)$$

where $\boldsymbol{\rho}$ is the 2D radius-vector describing the position of the electron in the plane of the potential well. Note that the exchange interaction parameter in equation (10), in contrast to the analogous parameter for a bulk semiconductor with a cubic structure, is a second-rank tensor and has a different dimensionality. The two principal axes of this tensor are equivalent and occur in the plane of the quantum potential well, the third axis is normal to this plane, and the eigenvalues depend on the magnetic ion position. For ions inside the well ($|z| < L/2$), we have

$$\alpha_{ii}(z, E) = \alpha_{ii}^{(f)}(E) + \alpha_{ii}^{(af)}(E)\cos(2qz). \quad (11)$$

Here, amplitudes of the constant and variable components of the *sp–d* exchange are given by the formulas

$$\alpha_{ii}^{(f)}(E) = \alpha'_C(E) + \beta'_{ii,C}(E); \quad \alpha_{ii}^{(af)}(E) = \alpha'_C(E) - \beta'_{ii,C}(E), \quad (12)$$

where

$$\alpha'_C(E) = \frac{\alpha_C(E(q)(E(q)+\Delta))^2|C_W|^2}{2\left[(E(q)(E(q)+\Delta))^2 + \left(\frac{p\hbar k}{3m_0}\right)^2[(3E(q)+2\Delta)^2 + 2\Delta^2]\right]}, \quad (13)$$

$$\beta'_{ZZ,C}(E) = \frac{[\beta_{pot} + \beta_{kin}\gamma(E_e)]\left(\frac{p\hbar q}{3m_0}\right)^2[(3E(q)+2\Delta)^2 - 2\Delta^2]C_W|^2}{2\left[(E(q)(E(q)+\Delta))^2 + \left(\frac{p\hbar k}{3m_0}\right)^2[(3E(q)+2\Delta)^2 + 2\Delta^2]\right]}, \quad (14)$$

$$\beta'_{XX,C}(E) = \beta'_{YY,C}(E) = \frac{[\beta_{pot} + \beta_{kin}\gamma(E_e)]\left(\frac{p\hbar q}{3m_0}\right)^2(3E(q)+2\Delta)^2|C_W|^2}{2\left[(E(q)(E(q)+\Delta))^2 + \left(\frac{p\hbar k}{3m_0}\right)^2[(3E(q)+2\Delta)^2 + 2\Delta^2]\right]}, \quad (15)$$

are the electron-energy-dependent contributions to the exchange constant, which are related to an exchange via the states at the conduction band bottom $\alpha'(E)$ and the valence band top $\beta'_C(E)$; α_C is the parameter of the exchange interaction between electron and magnetic ion at the conduction band bottom; β_{pot} and β_{kin} are the potential and kinetic components of the exchange constant of a hole at the valence band top, respec-

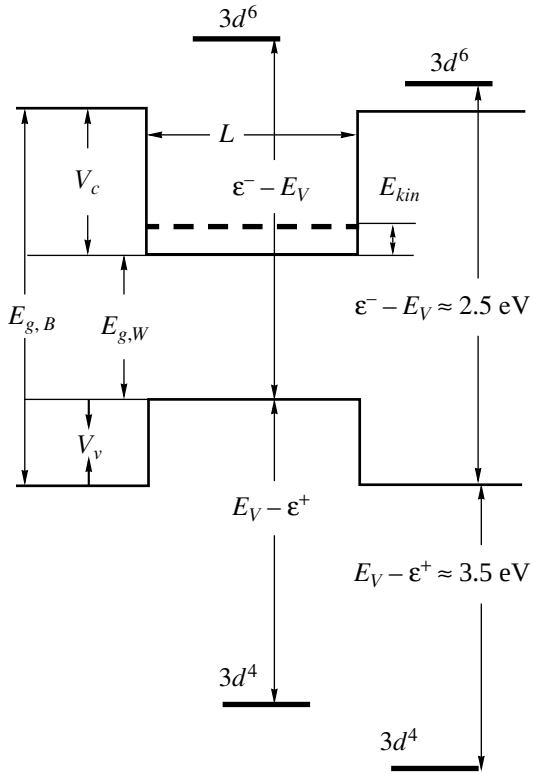

Fig. 1. Schematic diagram showing spatial distribution of the potential energy of charge carriers, positions of the acceptor and donor levels on the *d* shell of manganese ions in the a quantum potential well and under the barriers. Dashed line shows the dimensional quantization level for an electron with the energy E; ε^+ and ε^- are the energies of the donor ($3d^4$) and acceptor ($3d^6$) levels of manganese (distances from these levels to the valence band top taken from [8, 10, 13]). A virtual capture of electrons on the *d* levels is responsible for the kinetic component of the exchange interaction between a conduction electron and the *d*-shell electrons of manganese.

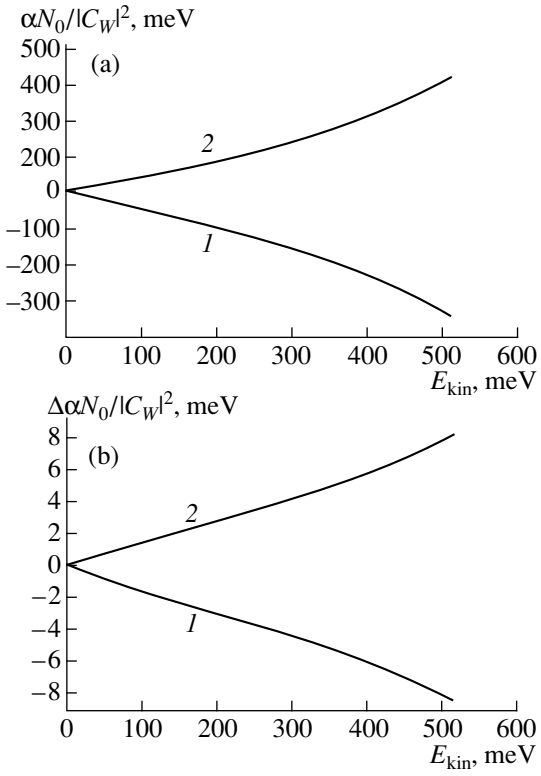

Fig. 2. Plots of (a) the constant (ferromagnetic) and variable (antiferromagnetic) components of the exchange interaction of a 2D electron with *d*-shell electrons of manganese and (b) the anisotropy of these components in a state described by the standing wave (3) versus the dimensional quantization energy. (a): (*1*) $\alpha^f_{ZZ}(E)N_0/|C_W|^2$; (*2*) $\alpha^{af}_{ZZ}(E)N_0/|C_W|^2$; (b): (1) $(\alpha^f_{ZZ}(E) - \alpha^f_{XX}(E))N_0/|C_W|^2$; (2) $(\alpha^{af}_{ZZ}(E) - \alpha^{af}_{XX}(E))N_0/|C_W|^2$. The calculation was performed for a $Cd_xMn_{1-x}Te$ solid solution with the parameters corresponding to the limit of small magnetic ion concentration ($x \longrightarrow 0$); N_0 is the concentration of positions occupied by magnetic ions in the crystal lattice studied.

tively; and

$$\gamma(E) = \frac{(E_v - \varepsilon^+)(\varepsilon^- - E_v)}{[(E_v + E_g + E) - \varepsilon^+][\varepsilon^- - (E_v + E_g + E)]} \quad (16)$$

is a factor describing the resonance dependence of the kinetic exchange on the distance to the acceptor (ε^-) and donor (ε^+) levels of the magnetic ion [8], that is, on the electron energy difference between the conduction band and the *d* levels of manganese ion with six or four electrons (see Fig. 1).

Figure 2 shows the plots of the constant (ferromagnetic) and variable (antiferromagnetic) components of the exchange interaction parameter versus the dimensional quantization energy of the electron $E_{\text{kin}} = E(q) - E_g$. The calculation was performed for semimagnetic CdMnTe solid solutions. As seen, the ferromagnetic component of the exchange interaction monotonically decreases, and the antiferromagnetic component– increases with decreasing E_{kin}.

Under the barrier ($|z| > L/2$), we have

$$\tilde{\alpha}_{ii}(\tilde{E}) = 2(\tilde{\alpha}'_C(\tilde{E}(Q)) + \tilde{\beta}'_{ii,C}(\tilde{E}(Q))), \quad (17)$$

where $\tilde{\alpha}'$ ad $\tilde{\beta}'$ are given by expressions (13)–(15) with the material parameters and the amplitude C_W in the quantum well replaced by the corresponding values for the barrier.

Note that, because the ratio of the spin–orbit energy splitting in the valence band to the bandgap width is small ($\Delta/E_g \le 0.5$), the anisotropy of exchange interaction in CdMnTe is insignificant. For this reason, in what follows we will assume $\Delta/E_g \approx 0$. The relative error of this approximation is $\Delta/(3E_g) < 0.2$.

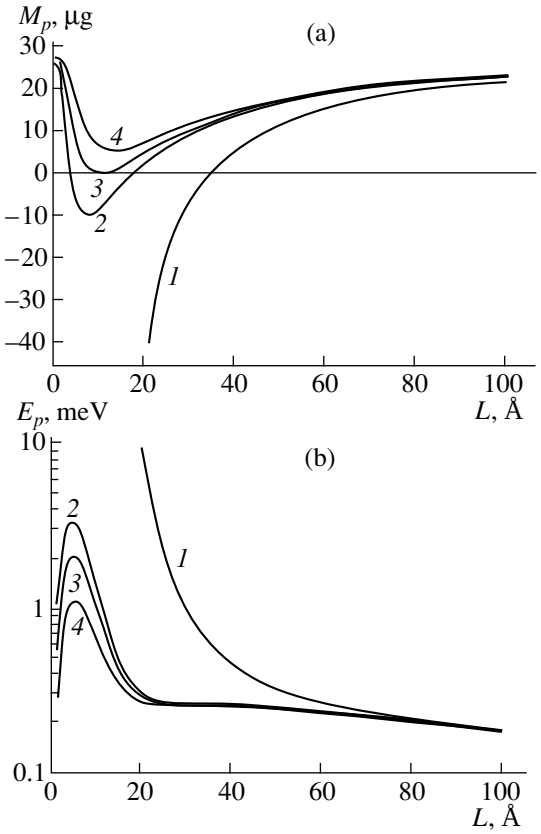

Fig. 3. Plots of (a) the magnetic moment and (b) the energy of a magnetic polaron versus the quantum potential well width for a semimagnetic semiconductor with the same Mn ion concentration ($x = 0.1$) in the quantum potential well and under the barrier (other parameters as indicated in the text) for the barrier height $V_C = \infty$ (*1*); 600 meV (*2*); 555 meV (*3*); 500 meV (*4*).

4. NONMAGNETIC POLARONS IN CDMNTE HETEROSTRUCTURES

Using equations (10)–(17), we may write an explicit expression for the exchange magnetic field created at the surrounding magnetic ions by a localized 2D electron:

$$\mathbf{B}_p(z,\boldsymbol{\rho}) = \begin{cases} \tilde{\alpha}(E)\dfrac{|\psi(\boldsymbol{\rho})|^2}{\mu g_{\mathrm{Mn}}} \\ \quad \times \exp\left\{-2Q\left(z-\dfrac{L}{2}\right)\right\}\langle \mathbf{s}\rangle, \quad \dfrac{L}{2} < z, \\ [\alpha^{(f)}(E) + \alpha^{(af)}(E)\cos(2qz)] \\ \quad \times \dfrac{|\psi(\boldsymbol{\rho})|^2}{\mu g_{\mathrm{Mn}}}\langle \mathbf{s}\rangle, \quad -\dfrac{L}{2} < z < \dfrac{L}{2}, \\ \tilde{\alpha}(E)\dfrac{|\psi(\boldsymbol{\rho})|^2}{\mu g_{\mathrm{Mn}}} \\ \quad \times \exp\left\{-2Q\left(z+\dfrac{L}{2}\right)\right\}\langle \mathbf{s}\rangle, \quad z < -\dfrac{L}{2}, \end{cases} \tag{18}$$

where $\langle \mathbf{s}\rangle$ is the average spin of the localized electron and $\psi(\boldsymbol{\rho})$ is the wave function describing the charge carrier localization in the potential well plane. Substituting (18) into (1) and (2), we eventually obtain the formulas describing the magnetic moment and energy of the polaron:

$$\mathbf{M}_p = \frac{dM}{dB} \times \frac{[\alpha^{(f)}(E)L + \alpha^{(af)}(E)\sin(qL)/q] + \tilde{\alpha}(\tilde{E})/Q}{\mu g_{\mathrm{Mn}}}\langle \mathbf{s}\rangle, \tag{19}$$

$$E_p = \frac{(dM/dB)}{8(\mu g_{\mathrm{Mn}})^2\Omega}[L[2\alpha^{(f)2}(E) + \alpha^{(af)2}(E)] + \tilde{\alpha}(\tilde{E})/Q + \alpha^{(af)}(E)\sin(qL)(\alpha^{(f)}(E) + \alpha^{(af)}(E)\cos(qL))/q], \tag{20}$$

where $\Omega = \left(\int |\psi(\boldsymbol{\rho})|^4 d^2\rho\right)^{-1}$ is the area of electron localization in the quantum potential well. Below, we will use an estimate $\Omega = 10^{-12}$ cm^2, which corresponds to the area of a circle with a radius equal to the Bohr radius of a Coulomb's donor. The magnetic susceptibility is expressed by an empirical formula [14]

$$\frac{dM}{dB} = \frac{7J_0 x N_0(\mu_{\mathrm{B}} g_{\mathrm{Mn}})^2}{6k_{\mathrm{B}}(T+T_0)}. \tag{21}$$

The calculation is performed for a $Cd_{0.9}Mn_{0.1}Te$ solid solution with the following set of parameters:

$$\begin{gathered} \beta_{\mathrm{pot}}N_0 = 0, \quad \alpha_C(0)N_0 = 220 \text{ meV}, \\ N_0 \approx 7\times 10^{22} \text{ cm}^{-3}, \quad \beta_{\mathrm{kin}}N_0 = -880 \text{ meV}, \\ E_g = (1.606 + 1.592x) \text{ eV} = 1.765 \text{ eV}, \\ P^2/m_0 = 21 \text{ eV}, \quad T = 2 \text{ K}, \\ T_0 = 4.2 \text{ K}, \quad J_0 = 1.04. \end{gathered} \tag{22}$$

It was assumed that the barrier heights in the conduction (V_C) and valence (V_V) bands are related as $3V_C = 7V_V$ [15, 16].

Figure 3 shows the magnetic moment and energy of a polaron formed by the localized 2D electron plotted as a function if the quantum potential well width. In the calculation, the magnetic ion concentrations in the well was taken equal to that under the barrier ($x = 0.1$). The plots are constructed for four values of the barrier height, including three finite values V_C = 500, 550, 600 meV and the infinite barrier. As is seen, the E_p value in a quantum potential well with infinitely high walls monotonically increases with decreasing L, while the polaron energy in finite wells in exhibit a change

from growth to decrease at a sufficiently small width. Qualitatively, both increase in the polaron energy and the decrease in E_p for very narrow wells are naturally related to changes in the size of the electron localization region. In the quantum potential wells of large width, a decrease in L leads to a decrease in the localization region volume and an increase in $E_p(L) \propto 1/L$. In very narrow wells, the electron wavefunction penetrates to increasing depth of the barrier and, as the L value decreases, the volume of the localization region increases and the polaron energy drops.

The magnetic moment M_p of a magnetic polaron also significantly depends on the width and depth of the quantum potential well. For a not too narrow potential well (Fig. 3a) with the ferromagnetic exchange component depending on the kinetic energy of electron as depicted in Fig. 2, a decrease in the well width leads to decreasing M_p. If the well width is small and the major role belongs to the exchange interaction with magnetic ions occurring in the barrier, the character of variation of the magnetic moment with the well width changes to the opposite: a decrease in L leads to an increase in M_p.

As the barrier height increases, a minimum value of the magnetic moment of the polaron decreases and (for $V_C > 550$ meV) becomes negative. Strictly speaking, it is a spin correlator between electron and surrounding magnetic ions that changes the sign. There are two values of the well width at which the polaron magnetic moment is zero. A large value increases from 11 Å for $V_C \approx 550$ meV to 34 Å for the well with infinite walls. Detailed description of the polaron magnetic moment in this region of L requires special analysis, because large V_C values may give rise to resonances between the electron energy level and the acceptor 6*d* level of manganese ions occurring within the barrier or (at still greater V_C) inside the well.

Figure 4 shows a distribution of the magnetic moment density of a polaron with $M_p = 0$ over the well width for $V_C \approx 550$ meV and for the well with infinite walls. In the first case (Fig. 4a), the sign of the magnetic ion polarization changes to opposite on the passage from barrier into well. Note that a change in the sign of the exchange component in the barrier takes place before that in the well, because a distance between the 6*d* level of manganese and the valence band top is approximately constant for various materials [10]. Thus, for a fixed electron energy, a decrease in the valence band top energy is accompanied by decreasing resonance denominator in the formula (16) for the kinetic exchange parameter.

In the case of infinitely high barrier, the electron wavefunction does penetrate into the barrier and the "nonmagnetic" (ferromagnetic) magnetic polaron appears when the average exchange constant is zero.

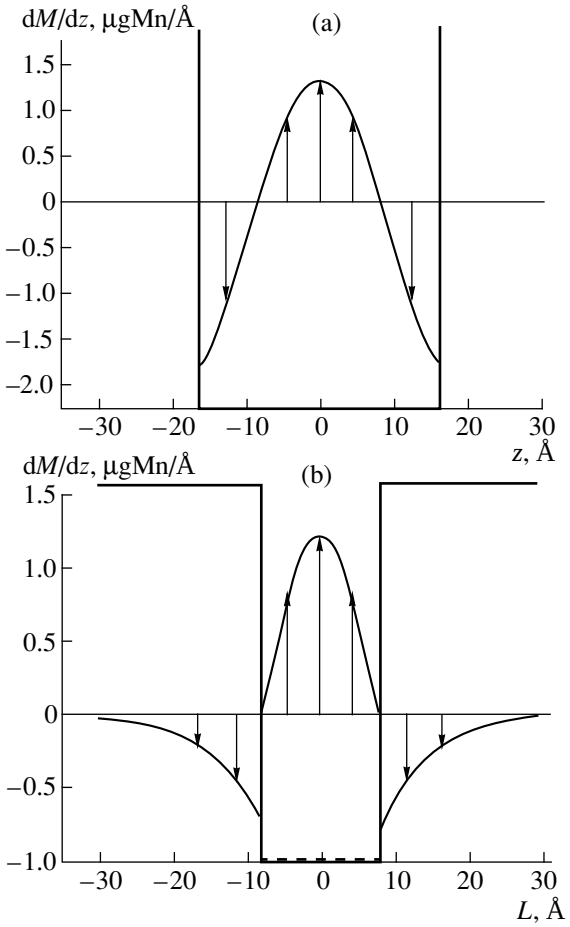

Fig. 4. Spatial distribution of the magnetic moment density for a "nonmagnetic" magnetic polaron with (a) relatively small (555 meV) and (b) infinite barrier height. For V_C = 555 meV, the magnetic moments of Mn ions in the well and under the barrier are oriented in opposite directions and mutually compensate each other. For the infinite barrier, the probability to detect an electron under the barrier is zero– and in this case, the "nonmagnetic" magnetic polaron is manifested by antiferromagnetic ordering of the spins of magnetic ions in the well.

5. EXPERIMENTAL OBSERVATION OF A POLARON WITH ZERO MAGNETIC MOMENT

A combination of decreasing ferromagnetic component and increasing antiferromagnetic component of the exchange interaction, together with a resonance dependence of the kinetic exchange on the difference between energies of the 2D electron and the 6*d* electron of manganese, leads to a rather involved character of variation of the polaron energy with the quantum potential well width (Fig 3a, curves *1–3*). However, no specific features take place for $M_p = 0$. Therefore, measurements of the magnetic polaron energy cannot be used for detecting the magnetic polaron possessing zero magnetic moment.

This unusual "nonmagnetic" magnetic polaron can be detected, for example, in experiments on the Raman light scattering with the electron spin reversal [8, 17].

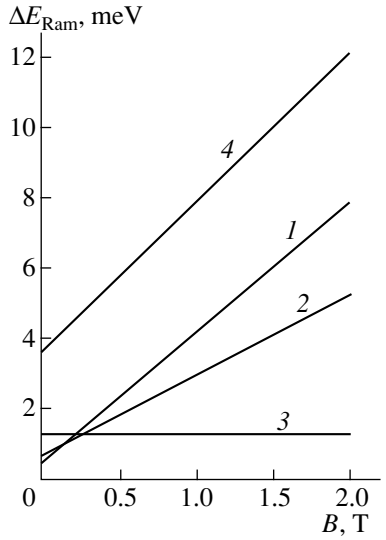

Fig. 5. Plots of the Stokes shift versus applied magnetic field strength for the Raman scattering with the electron spin reversal in a magnetic-polaron state. The calculation was performed for a quantum potential well with infinite walls and the widths L = 60 (*1*), 45 (*2*), 34 (*3*), and 25 Å (*4*), the other parameters being the same as in Fig. 3.

As can be readily demonstrated for a sample placed in a not too strong magnetic field **B** (i.e., with the field strength significantly below the saturation level), the Raman scattering with the electron spin reversal in a magnetic-polaron state is accompanied by the Stokes shift:

$$\hbar\Delta(B) \approx 2(E_p + M_p B). \qquad (23)$$

Thus, by measuring the Stokes shift in a zero field, we obtain the double magnetic polaron energy, and by determining the slope of the $\hbar\Delta(B)$ curve, the double magnetic polaron moment. For a usual magnetic polaron, the energy ($E_p \propto M_p^2$) rapidly decreases with the slope of the $\hbar\Delta(B)$ curve. In contrast, the Stokes shift for a "nonmagnetic" (antiferromagnetic) polaron has a finite value at $\hbar\Delta(B) = 0$, which is independent of the applied magnetic field.

Figure 5 shows an example of theoretical curves calculated for the Stokes shift in the spectra of Raman scattering with spin reversal of a 2D electron in a magnetic polaron. The calculation was performed for four values of the quantum potential well width L = 60, 45, 34, and 25 Å. As the well width decreases, the slope of the $\hbar\Delta(B)$ plot decrease to zero (corresponding to M_p = 0) and then increases again. At the same time, the Stokes shift in a zero field would monotonically increase with decreasing L.

6. CONCLUSION

We have demonstrated that reconstruction of the internal structure of the electron Bloch wavefunction amplitude in semimagnetic dimensionally-quantized nanometer heterostructures leads to a strong spatial variation of the parameter of exchange interaction between an electron in the conduction band and surrounding magnetic ions. As a result, a potential exchange component characterized by a positive value of the exchange interaction parameter is significant at some points of the structure, and the kinetic exchange component with a negative value of the parameter plays a determining role at the other points. The alternating sign of the exchange interaction provides conditions for the appearance of a magnetic polaron with zero magnetic moment, in which the spins of magnetic ions exhibit antiferromagnetic ordering.

7. ACKNOWLEDGMENTS

The author is grateful to D.R. Yakovlev, K.V. Kavokin, B.P. Zakharchee, V.I. Perel', W. Ossau, and G. Landwehr for fruitful discussions.

REFERENCES

1. P. G. de Gennes, Phys. Rev. **118** (1), 141 (1960).
2. E. L. Nagaev, J. Magn. Magn. Mater. **110** (1), 39 (1992).
3. P. A. Wolf, in *Semiconductors and Semimetals*, Ed. by J. F. Furdyna and J. Kossut (Academic Press, London, 1988), Vol. 25, p. 413.
4. I. A. Merkulov, D. R. Yakovlev, K. V. Kavokin, *et al.*, Pis'ma Zh. Éksp. Teor. Fiz. **62** (4), 313 (1995).
5. I. A. Merkulov, D. R. Yakovlev, K. V. Kavokin, *et al.*, Fiz. Tverd. Tela **39** (11), 2079 (1997).
6. Yu. F. Berkovskaya, E. M. Vakhabova, B. L. Gel'mont, *et al.*, Zh. Éksp. Teor. Fiz. **94** (4), 183 (1988).
7. D. R. Yakovlev and K. V. Kavokin, Comm. Condens. Matter Phys. **18** (2), 51 (1996).
8. I. A. Merkulov, D. R. Yakovlev, A. Keller, *et al.*, Phys. Rev. Lett. **83**, 1431 (1999).
9. A. K. Bhattacharjee, G. Fishman, and B. Coqblin, Physica **117**, 118, 449 (1983).
10. B. E. Larson, K. C. Hass, E. Ehrenreich, *et al.*, Phys. Rev. B: Condens. Matter **37** (8), 4137 (1988).
11. E. L. Ivchenko and G. E. Pikus, *Superatties and Other Heterostructures* (Springer-Verlag, Berlin, 1995).
12. R. A. Suris, Fiz. Tekh. Poluprovodn. (Leningrad), **20** (11), 1258 (1986).
13. T. Dietl, in *Handbook of Semiconductors, Diluted Magnetic Semiconductors*, Ed. by S. Mahajan (North-Holland, Amsterdam, 1994), Vol. 3b, p. 1252.
14. J. A. Gay, R. Planel, and G. Fishman, Solid State Commun. **29** (5), 435 (1979).
15. A. Wasiela, Y. Merled'Aubigne, J. E. Nicholls, *et al.*, Semicond. Sci. Technol. **7** (4), 571 (1992).
16. B. Kuhn-Heinrich, W. Ossau, T. Litz, *et al.*, J. Appl. Phys. **75** (12), 8046 (1994).
17. A. K. Ramdas and S. Rodrigues, in *Semiconductors and Semimetals*, Ed. by J. F. Furdyna and J. Kossut (Academic Press, London, 1988), Vol. 25, p. 345.

Translated by P. Pozdeev

Physics of the Solid State, Vol. 42, No. 1, 2000, pp. 139–141. Translated from Fizika Tverdogo Tela, Vol. 42, No. 1, 2000, pp. 133–135.

MAGNETISM AND FERROELECTRICITY

Ferroelastoelectric Phenomena in a Uniaxial Ferroelectric TGS Crystal

E. F. Dudnik, V. M. Duda, and A. I. Kushnerev

Dnepropetrovsk State University, pr. Gagarina 72, Dnepropetrovsk, 320625 Ukraine

e-mail: elf@ff.dsu.ua

Received April 26, 1999

Abstract—Possibility of the ferroelastoelectric behavior manifestations in a uniaxial ferroelectric TGS crystal was investigated. Analysis of the spontaneous piezoelectric moduli tensors for each of the 180°-domains formed as a result of the phase transition in TGS revealed possible directions for simultaneous application of the electric field and mechanical stresses to induce the switching effect in TGS. Influence of the uniaxial mechanical stresses σ_{11}, σ_{22}, σ_{33} on the parameters of saturated and unsaturated dielectric hysteresis loops in TGS is considered. It was found that a nontraditional $E_3\sigma_{12}$ combination of fields may lead to the domain switching in TGS crystals. © *2000 MAIK "Nauka/Interperiodica".*

According to the classification of Aizu [1], crystals containing domains (oriented states) with different components of the piezoelectric constants belong to the high-order ferroics and are called ferroelastoelectrics. Switching of these crystals from one to another state can be induced only by simultaneous application of the electric field and mechanical stresses. The class of ferroelastoelectrics includes, for example, quartz crystals at temperatures below that of the phase transition from α to β modification (T_c = 573.5°C) [2].

The symmetry analysis indicates that all ferroelectrics are potential ferroelastoelectrics. From the standpoint of investigation into the ferroelastoelectric properties, especially favorable conditions are offered by the "purely" uniaxial ferroelectrics, in which the effect of mechanical stresses is not masked by the ferroelastic behavior.

An example of typical "purely" uniaxial ferroelectric crystals is offered by triglycine sulfate (TGS), exhibiting a phase transition of the $2m \longleftrightarrow 2$ type at 49.2°C to give rise to two oriented states (domains) S_1 and S_2. The tensor of spontaneous piezoelectric moduli for one of these 180°-domains (S_1) has the following form [3]:

$$d_{ijk}^{S1} = \begin{pmatrix} 0 & 0 & 0 & 2d_{123} & 0 & 2d_{112} \\ d_{211} & d_{222} & d_{233} & 0 & 2d_{213} & 0 \\ 0 & 0 & 0 & 2d_{323} & 0 & 2d_{312} \end{pmatrix}. \quad (1)$$

The tensor of spontaneous piezoelectric moduli for another 180°-domain (S_2) can be obtained by multiplying tensor (1) by –1.

Analysis of the form of the spontaneous piezoelectric moduli tensor (1) allows the directions to be determined in which the electric field and mechanical stresses must be simultaneously applied in order to produce the switching effect in TGS crystals, provided that the material possesses ferroelastoelectric properties. The corresponding combinations are as follows:

$$E_1\sigma_{23};\ E_1\sigma_{12};\ E_2\sigma_{11};\ E_2\sigma_{22};$$
$$E_2\sigma_{33};\ E_2\sigma_{13};\ E_3\sigma_{23};\ E_3\sigma_{12}. \quad (2)$$

Below, we present the results of investigation of the TGS crystal switching upon the combined action of electric field and mechanical stresses in these directions.

1. EXPERIMENTAL METHODS

The crystallophysical system of coordinates, in which the necessary TGS crystal cuts (*X*, *Y*, *Z*) were prepared, was analogous to that adopted in [4]. Experiments on the TGS crystal switching by application of various combinations of the electric field and mechanical stresses were performed using a special sample crystal holder. This device allowed the electric field and mechanical stresses to be simultaneously applied to a sample either in the mutually perpendicular directions or in the same direction.

The sample surfaces perpendicular to the polar axis were coated with platinum (by vacuum deposition) or graphite (by rubbing) to obtain electrodes for the field application. Uniaxial mechanical stresses were applied along the axes *X* (σ_{11}), *Y* (σ_{22}), and *X* (σ_{33}) and the effect of these stresses upon the parameters of the dielectric hysteresis loop (DHL) measured according to a modified Sawyer–Tower scheme was studied in the temperature range 20–50°C.

In order to study the possibility of crystal switching by the field combinations $E_1\sigma_{23}$ and $E_3\sigma_{12}$, the electrodes were applied onto the sample surfaces perpen-

1063-7834/00/4201-0139$20.00

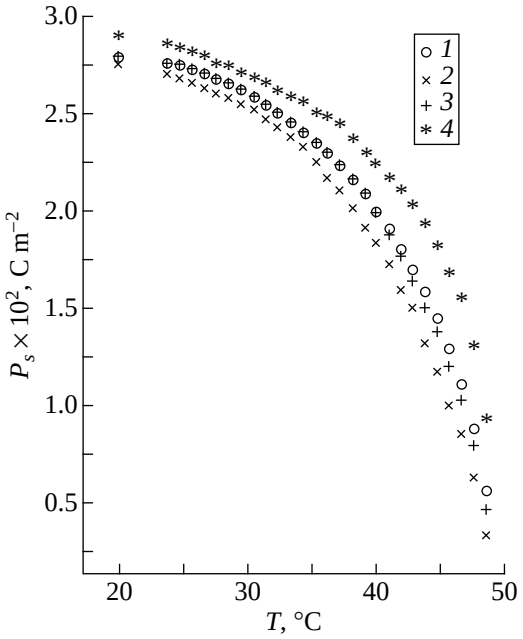

Fig. 1. Temperature dependence of the spontaneous polarization P_s in TGS crystals: (*1*) unstressed; (*2*) stressed at 40 MPa along the *X*-axis; (*3*) stressed at 3.6 MPa along the *Y*-axis; (*4*) stressed at 40 MPa along the *Z*-axis.

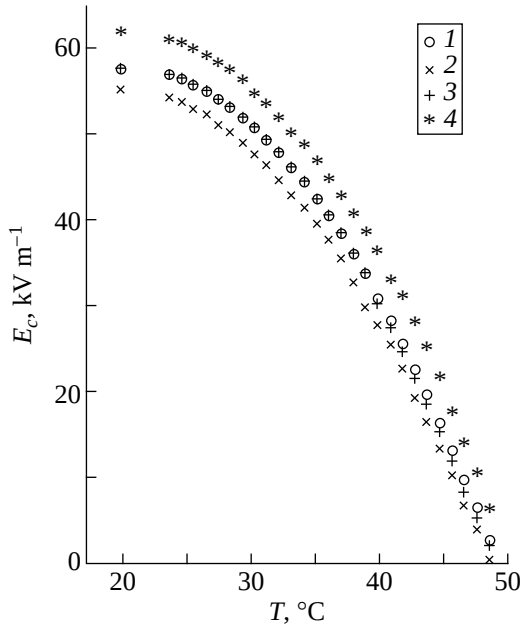

Fig. 2. Temperature dependence of the coercive field E_c in TGS crystals: (*1*) unstressed; (*2*) stressed at 40 MPa along the *X*-axis; (*3*) stressed at 3.6 MPa along the *Y*-axis; (*4*) stressed at 40 MPa along the *Z*-axis.

dicular to the axes *X, Y* and *Z, Y,* respectively. Note that the piezoelectric coefficients with like indices have the same absolute values and opposite signs for the domains in TGS crystals with opposing orientations of the spontaneous polarization vector. Therefore, measurements of the piezoelectric response on the crystal faces perpendicular to the polar axis *Y* under the action of compressive stresses σ_{22} allows the direction and degree of polarization of a TGS crystal sample to be determined.

2. TGS CRYSTAL SWITCHING BY THE $E_2\sigma_{11}$, $E_2\sigma_{22}$, AND $E_2\sigma_{33}$ FIELD COMBINATIONS

Field combinations of the $E_2\sigma_{11}$, $E_2\sigma_{22}$, and $E_2\sigma_{33}$ types are quite readily realized in experiment by applying compressive stresses σ_{11}, σ_{22}, σ_{33} in the course of DHL measurements.

Figures 1 and 2 show the results of DHL measurements on saturated samples (corresponding to virtually complete switching of the TGS crystal), performed at various temperatures upon the application of mechanical compressive stresses σ_{11}, σ_{22}, and σ_{33}. As seen from this figure, the σ_{11} and σ_{22} stresses lead to a decrease, and the σ_{33} stresses–to an increase in the spontaneous polarization P_s in the entire temperature range studied. We believe that this behavior is caused by the direct piezoeffect and corresponds to different signs of the piezoelectric coefficients ($\mathrm{sgn}\, d_{21} = \mathrm{sgn}\, d_{22} = -\mathrm{sgn}\, d_{23}$).

It is interesting to consider effects of the corresponding mechanical stresses upon magnitude of the coercive field E_c (Fig. 2). As seen from the curves depicted in Fig. 2, the mechanical stresses σ_{11} and σ_{22} lead to a decrease, and the σ_{33} stresses, to an increase in the E_c value, thus favoring or retarding the re- polarization process in TGS, respectively.

At the same time, the DHL study in the unsaturated regime (corresponding to incomplete re-polarization processes) showed that application of the electric field with a strength below certain "critical" level (approximately equal to the E_c value for saturated DHL curves) leads to an increase in the measured polarization value (proportional to the re-polarized crystal domain volume) in the presence of σ_{11} and σ_{22} stresses, and to a decrease in the polarization in the presence of σ_{33} stresses. These trends are opposite to the behavior observed for the same mechanical stresses acting upon the system with saturated DHL. These data indicate that the σ_{11} and σ_{22} stresses favor the motion of domains while the σ_{33} stresses retard this mobility. It must be noted that the "critical" field strength is virtually not affected by the application of mechanical stresses and the observed phenomena exhibit a reversible character.

The above results can be explained taking into account that TGS crystals are not only ferroelectrics, but possess the ferroelastoelectric properties as well. As is known [1], simultaneous application of the electric field and mechanical stresses in definite crystallo-

graphic directions to a ferroelastoelectric sample leads to the crystal transition into a monodomain state, that is, to establishing one of the several possible oriented states. A change in the sign of one of the external factors (i.e., the change from compressive to tensile stresses or alteration of the electric field direction) leads to switching from one to another oriented state by means of the domain wall motion, similar to that observed in ferroelectrics. However, since the ferroelastoelectric crystals are ferroics of a higher order than are simple ferroelectrics, the corresponding electric and mechanical coercive field strengths prove to be sufficiently high at low temperatures (far from the temperature of the structural phase transition). For example, the motion of ferroelastoelectric domains upon combined application of the electric field and mechanical stresses in quartz crystals is observed only at a temperature 3 K below the $\alpha \longrightarrow \beta$ transition temperature [2].

The TGS crystals, in contrast to quartz, are not "purely" ferroelastoelectric systems and are mostly known as "purely" ferroelectric compounds. Since the ferroelectric 180°-domains in TGS possess the ferroelastoelectric properties as well, this system is subject to the action of two driving forces. The low Curie temperature of TGS crystals suggests that the ferroelastoelectric behavior can be observed at room temperature.

The alternating electric field E_2 is a re-polarizing field in the ferroelectric state and, in combination with mechanical stresses, gives rise to an additional driving force related to the ferroelastoelectric properties. The two driving forces may act either in the same or in the opposite directions, depending on the signs of the piezoelectric coefficients. Taking this circumstance into account and analyzing the signs of piezoelectric coefficients in the system studied ($-d_{21}, -d_{22}, +d_{23}$), we may conclude that the field combinations $E_2\sigma_{11}$ and $E_2\sigma_{22}$ would favor the motion of domain walls, while the $E_2\sigma_{23}$ combination will hinder this mobility.

Evidently, by changing the sign of mechanical stresses (compressive versus tensile) we may alter the behavior of both DHL-saturated and unsaturated crystals and observe the trends opposite to those described above.

3. TGS CRYSTAL SWITCHING BY THE $E_1\sigma_{23}$ AND $E_3\sigma_{12}$ FIELD COMBINATIONS

Since TGS is a uniaxial ferroelectric, in which the re-polarization is produced by applying the electric field along the *Y* axis, the crystal state switching by one of the combinations $E_1\sigma_{12}$, $E_1\sigma_{23}$, $E_3\sigma_{12}$, or $E_3\sigma_{23}$ (whereby the electric field is perpendicular to P_s) would be a direct evidence of the ferroelastoelectric properties of the system. We have undertaken an experimental verification of this possibility.

First, the TGS samples were converted into a monodomain state by exposure to an electric field with the strength 300 kV/m applied along the polar axis *Y*, after which the piezoelectric modulus d_{22} was measured and its sign (i.e., the crystal polarization direction) was determined. Then a combination of the fields ($E_3\sigma_{12}$ or $E_1\sigma_{23}$) was applied to the sample, with an electric field strength of 400 kV/m and a mechanical stress of 15 MPa. The experiments were performed at room temperature. A comparison of the values and signs of the piezoelectric response before and after the combined action indicated the degree of sample switching.

The $E_1\sigma_{23}$ combination weakly affected the piezoelectric response even upon prolonged action. At the same time, exposure to the $E_3\sigma_{12}$ combination for 30–90 min led to a change in the sign of the piezoeffect in several samples. Separate application of the electric field and mechanical stresses of the same magnitude to the same samples led to no changes in the piezoelectric response. This result indicates that the $E_3\sigma_{12}$ combination produces switching P_s in the TGS crystal, which allows TGS crystals to be classified as both ferroelectrics and ferroelastoelectrics.

It should be noted that the above results have a preliminary character and are currently verified in independent experiments.

REFERENCES

1. K. Aizu, J. Phys. Soc. Jpn. **34** (1), 121 (1973).
2. J. W. Laughner, V. K. Wadhawan, and R. E. Newnham, Ferroelectrics **36**, 439 (1981).
3. E. F. Dudnik, V. M. Duda, and A. I. Kushnerev, Ukr. Fiz. Zh. **43** (2), 243 (1998).
4. V. P. Konstantinova, I. M. Sil'vestrova, and K. S. Aleksandrov, in *Physics of Dielectrics* (Izdat. Akad. Nauk SSSR, Moscow, 1960), p. 351.

Translated by P. Pozdeev

Physics of the Solid State, Vol. 42, No. 1, 2000, pp. 142–145. Translated from Fizika Tverdogo Tela, Vol. 42, No. 1, 2000, pp. 136–140.

MAGNETISM AND FERROELECTRICITY

Effect of Electric Field on the Percolation Phase Transition in Lead Scandotantalate Single Crystals

L. S. Kamzina and N. N. Kraĭnik

Ioffe Physicotechnical Institute, Russian Academy of Sciences, Politekhnicheskaya ul. 26, St. Petersburg, 194021 Russia
e-mail: kamzina@kas.ioffe.rssi.ru

Received June 10, 1999

Abstract—The effect of a dc electric field on the phase transition process in lead scandotantalate single crystals differing in the degree of ion ordering has been studied by small-angle light scattering (SAS). The spontaneous phase transition occurring in these crystals is shown to be accompanied by a sharp SAS intensity peak indicating the percolation nature of this transition. A phase diagram in the field–temperature coordinates has been constructed for all the PST crystals studied in the work. The electric field and the temperature variation rate have been found to affect the SAS intensity. *© 2000 MAIK "Nauka/Interperiodica".*

$AB'B''O_3$ perovskite-type ferroelectrics, to which the lead scandotantalate $PbSc_{1/2}Ta_{1/2}O_3$ (PST) belongs, represent a broad class of substances, where chemical disorder in the arrangement of the B' and B" ions gives rise to relaxor behavior. The degree of diffuseness of the phase transition between the ferroelectric and the paraelectric phase depends on the extent of ordering of the Sc^{3+} and Ta^{5+} ions (s) at the octahedral lattice sites. In crystals with a long-range order ($s \sim 1$ corresponds to practically ordered compounds), one observes a clearly pronounced first-order ferroelectric phase transition with no intermediate relaxor phase between the ferroelectric and the paraelectric phase [1,2]. By properly varying the temperature regime of single-crystal growth [3] or sample heat-treatment conditions [4], one can affect the degree of ion ordering and, thus, modify the relaxor properties.

The possibility of realizing phase transitions of different characters in the same material accounts for the scientific interest in these compounds and makes PST crystals a particularly convenient subject for the investigation of relaxor behavior in various substances. Besides, some relaxors, among which are the PST and PSN crystals, possess another unique property. They exhibit, in addition to typical relaxor behavior, a spontaneous transition between the ferroelectric and relaxor phases at temperatures below that corresponding to the maximum in the dielectric permittivity in a zero electric field [1,5]. Such transitions in ceramic PLZT samples with 17/30/70 and 12/40/60 compositions were reported in [6,7], and in the ordered and disordered PST ceramic, in [1]. This phenomenon appears particularly interesting and significant, because only in this case can one observe the ferroelectric relaxor together with conventional ferroelectric behavior in the same compound without applying any external field. This pattern of behavior distinguishes them from other relaxors, which exhibit such transitions only in an electric field. The existence of a spontaneous transition was confirmed by a sharp drop of the dielectric permittivity [1] at a certain temperature (T_d) in a sample cooled below the temperature of the maximum in ε, by the absence of a frequency dependence in the temperature interval between T_d and $T_{\max \varepsilon}$, an anomaly in the transition heat, and by double dielectric hysteresis loops observed above the spontaneous transition temperature [8].

Particularly many studies have appeared recently on the effect of a dc electric field on the character of the spontaneous phase transition from the normal ferroelectric to the relaxor state in ordered and disordered PST ceramics. This may be attributed to the fact that the electric field acts differently on the relaxor properties and the character of the spontaneous phase transition in these compounds. The application of an electric field can increase the uniformity and stability of the ferroelectric state and its effect on the relaxor properties, which could help in studying the nature of the relaxor behavior. All these studies dealt only with the changes in the dielectric properties of the PST and PSN ceramics induced by an electric field. Unfortunately, the anomaly in the ε curve corresponding to the spontaneous transition in these compounds is not pronounced clearly enough (one observed only a sharp drop in ε under cooling, whereas when heated, the anomaly in the ε of the sample was practically not seen at all), and the temperature of the anomaly itself is very close to that of the maximum in ε ($\Delta T \sim 1$–5 K, depending on the degree of the phase-transition diffuseness). Therefore, in order to obtain a revealing pattern of the effect of an electric field on the shape of the dielectric anomaly, it would be required, on the one hand, to have a sufficiently sensitive setup, and on the other, to perform measurements within a broad electric-field range.

1063-7834/00/4201-0142$20.00

Optical methods, including small-angle light scattering (SAS), are more sensitive in studying the effect of an external field on the variation of spatial nonuniformities in polarization. Our previous investigations of the diffuse phase transition in PST single crystals made by the SAS method [8,9] established the existence of a sharp peak in the temperature dependence of SAS intensity, which argues for the percolation nature of the transition between the relaxor and ferroelectric phases. The temperature at which this peak was observed lies below that of the maximum in ε. The difference between these temperatures is the larger, the less ordered the ions are. One can confidently state that the temperature of the anomalous SAS peak can be associated with a spontaneous phase transition from the ferroelectric to the relaxor phase.

Thus, the objectives of this work were twofold: investigation of the effect of a dc bias field on the spontaneous phase transition in PST single crystals, and on the character of the percolation processes accompanying this transition. Besides, it appeared of interest to follow the influence of the rate of the sample temperature variation during the experiment on the spontaneous phase transition itself.

1. EXPERIMENTAL TECHNIQUE AND THE SAMPLES

We studied SAS measured in the transmission geometry [10] on a series of PST ferroelectrics differing in the degree of ordering of the Sc^{3+} and Ta^{5+} ions. The crystals were synthesized in different growth temperature regimes [11] and had the following characteristics: PST I—$T_{\max\varepsilon}$ = 297 K, $T_{\text{an. peak}}$ = 287 K, s = 0.65; PST II—$T_{\max\varepsilon}$ = 301 K, $T_{\text{an. peak}}$ = 294 K, s = 0.7; PST III—$T_{\max\varepsilon}$ = 309 K, $T_{\text{an. peak}}$ = 304 K, s = 0.95; and PST IV—$T_{\max\varepsilon}$ = 316 K, $T_{\text{an. peak}}$ = 313 K, s = 0.98. The degree of ordering s was measured by x-ray diffraction. The electric field was applied along the [001] direction at 273 K, and the light was propagated along [100]. The dielectric measurements were carried out at a frequency of 50 kHz. All the measurements were performed under heating. The sample temperature variation rate was 3 K/min, unless otherwise specified. After the electric-field application, the samples were thermally depolarized before each measurement.

2. EXPERIMENTAL RESULTS AND DISCUSSION

Figs. 1 and 2 display the temperature dependences of the SAS intensity and of the dielectric permittivity for the PST IV and PST I crystals obtained under heating in the absence of an electric field. In both figures one can clearly see SAS peaks at the T_d temperature, which supports the existence of a percolation-type spontaneous ferroelectric transition and the onset in this transition of a large-scale nonuniform structure. As seen from the curves in Fig. 1 taken in the heating and cooling runs, the difference between the peak positions is ~11 K. This temperature hysteresis is one of the principal features of a first-order phase transition. The difference between the temperatures of the anomalous peak and of the maximum in ε for the PST IV crystal is only ~2–3 K. The temperature where a sharp increase of the dielectric permittivity sets in (curve *2* in Fig. 2) corresponds to the temperature of the anomalous peak (T_d) in the ε curve. As is obvious from curve *2*, the ε anomaly obtained in a heating run is not clearly manifest, whereas the SAS peak is distinct. Application of a dc electric field shifts the temperature of the spontane-

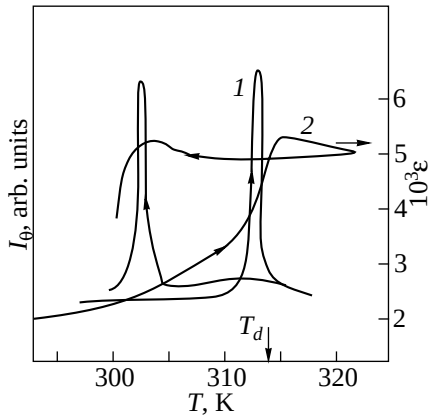

Fig. 1. Temperature dependences of small-angle light scattering intensity (curve *1*) and dielectric permittivity (curve *2*) for the PST IV crystal. Scattering angle 30 arcmin.

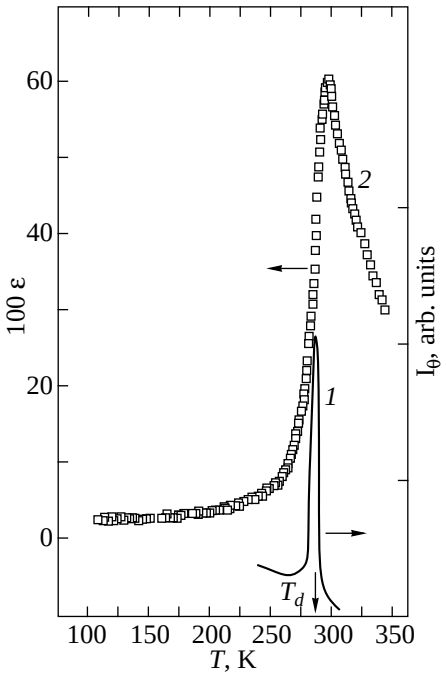

Fig. 2. Temperature dependences of small-angle light scattering intensity (curve *1*) and dielectric permittivity (curve *2*) for the PST I crystal. Scattering angle 20 arcmin.

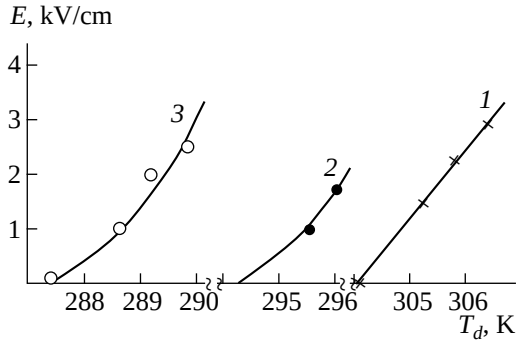

Fig. 3. Temperature of the spontaneous ferroelectric transition (T_d) *vs* the bias electric field for PST III, PST II, and PST I crystals (curves *1*, *2*, and *3*, respectively).

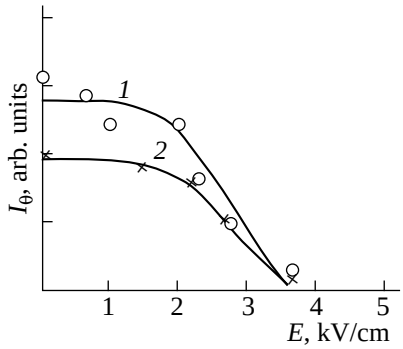

Fig. 4. Electric field dependence of small-angle light scattering intensity for the PST II and PST III crystals (curves *1* and *2*, respectively). Scattering angle 20 arcmin.

ous ferroelectric transition toward higher temperatures, as is the case with PST ceramic samples [2]. That the temperature of the anomalous SAS peak measured at zero frequency in the absence of an electric bias corresponds to that of the spontaneous transition in the temperature dependence of the dielectric permittivity obtained at 50 kHz, is another argument in favor of the nonrelaxation character of this transition.

The SAS intensity measurements carried out under the application of a dc electric field on the PST I, PST II, and PST III crystals were used to construct an electric-field dependence of the temperature of the spontaneous transition (Fig. 3). The transition temperature T_d in the practically ordered PST III crystal depends linearly on an electric field, which is typical of a first-order phase transition from the ferroelectric to the paraelectric state (curve *1* in Fig. 3). The PST III crystal is a practically ordered sample, in which only 5% of the sample volume remained disordered. For the more disordered crystals PST I (curve *3*) and PST II (curve *2*) the dependence of T_d on an electric field differs somewhat from a linear course, although the presence of the SAS peak and the results published in [8] indicate that the phase transition from the ferroelectric to the relaxor state in a disordered crystal is of the first order. This deviation from the linear dependence in the PST I and PST II crystals, in which 35 and 30% of the volume is disordered, respectively, can be ascribed to the existence of the relaxor state within a sufficiently broad temperature region and to the presence of polarization in local regions of the crystal at temperatures above T_d. These findings agree with the results of the study [2] carried out on the PST ceramic, where it was shown that local polarization vanishes only at ~170°C, when the compound transforms into a paraelectric state.

The second part of the work deals with an investigation of percolation-type processes in PST crystals performed in various electric fields and at various crystal-temperature variation rates. As follows from our measurements and from [2], an increase of the electric field up to 10 kV/cm reduces the magnitude of ε at the maximum for disordered samples by nearly a factor of three and practically does not affect that for ordered ones. There is no information in the literature on the effect of an electric field on the percolation phase transition.

Figure 4 plots the dependence of SAS intensity *vs* the electric field for the PST II and PST III crystals (curves *1* and *2*, respectively). Despite the different degree of ion ordering in these crystals, the behavior of the SAS intensity is practically the same in them and differs from the behavior of the maximum value of ε. One readily sees that in fields $E > 2$ kV/cm the SAS intensity drops dramatically, with the peak vanishing at ~4 kV/cm. Our analysis [12] of the polarization characteristics of SAS intensity in disordered PST crystals revealed that the surface fractal structure forming in this transition has a heterophase, rather than domain origin. The external electric field applied to a sample changes the profile of spatial fields and, therefore, affects the positions of the interfaces, their structure and thickness, and initiates coalescence of the neighboring polar regions, which results in a decrease of the total area of the interfaces separating them. Hence, an increase of the electric field should reduce the SAS intensity. Our experimental data are in accordance with the theoretical conclusions [13] that the SAS intensity near a phase transition in a disordered system placed in an electric field is inversely proportional to the latter.

We conclude by presenting some comparative data on the effect of the temperature variation rate (sample heating rate) on the SAS intensity in a PST crystal (in the absence of an electric field) and in the classical relaxor PMN (in an electric field of 3 kV/cm). In relaxor ferroelectrics, the temperature at which the macrodomain state sets in an electric field, as well as the amplitude of the dielectric anomaly observed at this temperature, depends not only on the electric field strength, but also on the temperature variation rate (the FHaZEC regime) [14,15]. Indeed, the phase transition from a micro- to macrodomain state correlates with the kinetics of microdomain reorientations. The stronger the electric field applied to a sample, the faster the mac-

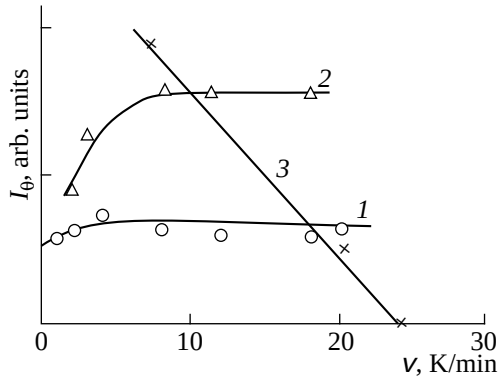

Fig. 5. Effect of the sample heating rate on small-angle light scattering intensity in PST II (curve *1*) and PST I (curve *2*) with no electric field applied, and in the classical relaxor PMN (curve *3*) measured in an electric field of 3 kV/cm. Scattering angle 20 arcmin.

rodomain state sets in, and the weaker the field, the longer the time needed for this. The field applied to a sample may induce a phase transition to the macrodomain state only if the rate of this process is fast enough for this state to set in during the experiment [16]. Hence, in order to observe dielectric and optic anomalies at the temperature of the transition to the macrodomain state, one should choose an appropriate experiment time (sample heating rate) and the electric field strength. Obviously, the effect of the heating rate on the magnitude of the anomalies should become manifest particularly strongly in the relaxor ferroelectrics, in which the orientation of the polar regions and the motion of their interfaces, as well as of the domain walls in polar clusters, play an important role. In PST crystals, most of the sample volume is ordered, with only a very small fraction of it remaining disordered, and therefore the effect of the rate on, say, the SAS intensity should be less pronounced. This is seen clearly from Fig. 5. At the temperature variation rate ~20–25 K/min, the anomalous peak in the PMN crystal disappears (curve *3*), whereas in the PST crystals (curves *1* and *2*) its amplitude remains practically constant.

Thus, our study has shown that the spontaneous phase transition observed in PST single crystals with different degrees of ion ordering is of the first order, has a percolation nature, and is accompanied by the occurrence of an anomalously narrow SAS intensity peak. The dependence of the spontaneous transition temperature on the applied electric field has been found, with a linear dependence characteristic of a first-order transition observed only in an ordered PST sample. Increasing the electric field above 2 kV/cm results in a sharp decrease of the SAS intensity and a disappearance of the peak at ~4 kV/cm, which is apparently associated with the decrease of the interface area. A study has been made of the effect of the sample temperature variation rate on the SAS intensity. The amplitude of the SAS intensity peak remains practically constant, with the rate increasing up to 20 K/min, which distinguishes the PST crystals from the classical relaxor PMN.

REFERENCES

1. F. Chu, N. Setter, and A. K. Tagantsev, J. Appl. Phys. **74**, 5129 (1993).
2. F. Chu, G. R. Fox, and N. Setter, J. Am. Ceram. Soc. **81**, 1577 (1998).
3. O. I. Prokopalo, I. P. Raevskiĭ, M. A. Malitskaya, *et al.*, Ferroelectrics **45,** 89 (1982).
4. N. Setter and L. E. Cross, J. Appl. Phys. **51**, 4356 (1980).
5. F. Chu, I. M. Reaney, and N. Setter, J. Appl. Phys. **77**, 1671 (1995).
6. C. G. F. Stenger and A. J. Burggraaf, J. Phys. Chem. Solids **41** (1980).
7. X. Dai, Z. Xu, and D. Viehland, J. Appl. Phys. **79**, 1021 (1996).
8. F. Chu, I. M. Reaney, and N. Setter, J. Am. Ceram. Soc. **78**, 1947 (1995).
9. L. S. Kamzina and A. L. Korzhenevskiĭ, Pis'ma Zh. Éksp. Teor. Fiz. **50**, 146 (1989).
10. L. S. Kamzina, A. L. Korzhenevskiĭ, and O. Yu. Korshunov, Fiz. Tverd. Tela **36**, 479 (1994).
11. L. S. Kamzina, A. L. Korzhenevskiĭ, O. Yu. Korshunov, *et al*., Izv. Akad. Nauk SSSR, Ser. Fiz. **54**, 613 (1990).
12. A. L. Korzhenevskiĭ and L. S. Kamzina, Fiz. Tverd. Tela **40**, 1537 (1998).
13. A. L. Korzhenevskiĭ, Ferroelectrics **100**, 39 (1989).
14. L. S. Kamzina, N. N. Kraĭnik, and O. Yu. Korshunov, Fiz. Tverd. Tela **37**, 2765 (1995).
15. Yao Xi, Chen Zhili, and L. E. Cross, J. Appl. Phys. **54**, 3399 (1983).
16. V. A. Isupov, Phys. Status Solidi B **213**, 211 (1999).

Translated by G. Skrebtsov

Physics of the Solid State, Vol. 42, No. 1, 2000, pp. 146–152. Translated from Fizika Tverdogo Tela, Vol. 42, No. 1, 2000, pp. 141–146.

MAGNETISM AND FERROELECTRICITY

The Dynamics of 180° Domains in a Ferroelectric in the Process of Polarization Reversal and Electron Emission

V. V. Kolesnikov, A. T. Kozakov, and A. V. Nikol'skiĭ

Research Institute of Physics, Rostov State University, pr. Stachki 194, Rostov-on-Don, 344104 Russia

e-mail: kozakov@iphis.rnd.runnet.ru

Received December 30, 1998; in final form, June 17, 1999

Abstract—A model is proposed to describe the evolution of 180° domains in a ferroelectric. Closed analytic expressions are obtained for the velocity of sideways motion of a 180° domain wall in an electric field and numerical calculations are performed. The connection between polarization reversal and electron emission is discussed. © *2000 MAIK "Nauka/Interperiodica".*

1. INTRODUCTION

Recently, considerable attention has been focused on the processes of polarization reversal and domain-wall motion in connection with the development of pulsed ferroelectric-based cathodes with current densities up to 100 A/cm^2 [1–5]. The physical nature of intense electron emission observed in this case is associated with the process of polarization reversal in the ferroelectric caused by nanosecond high-voltage pulses. The electron emission was first observed during motion of a 180° domain wall in $BaTiO_3$ [6]; more recently, an analogous investigation was made in [7]. An unusual effect, also associated with inhomogeneous polarization distribution in surface layers and named anomalous electron emission, was exhibited by some ferroelectric electrets when irradiated by soft X-rays [8, 9].

To adequately describe the physical mechanisms of the polarization reversal in these new phenomena, a more consistent theoretical approach to polarization reversal is needed than the classical theory of nucleation commonly used for solving problems of this kind [10, 11]. Specifically, account must be taken of the processes occurring on the electrodes.

An appropriate method based on the concepts of the kinetics of phase transitions [12–14] was used in [15, 16] to investigate the dynamics of head-to-head domains. However, some assumptions made in these papers do not permit the method to be applied to 180° domain walls with whose motion the electron emission is associated [1–4, 6, 7]. A theoretical analysis of the latter phenomenon is given in this paper.

This analysis is based on the general ideas [14–16] of the mechanisms of stratification of a spatially uniform system during phase transitions. Mathematically, the formation of domain walls is due to an N-shaped singularity in the equation of state of the ferroelectric, that is, in the dependence of the electric field $E_s(P)$ on the polarization P. The manner in which the stratification occurs depends on the conductivity of the material and carrier concentration n_0. The nucleation and forward growth of wedge-shaped domains (of a new phase) with a small wedge angle is observed at low n_0 [10, 11, 16], when the Debye screening length l_D exceeds the dimensions of the sample. As n_0 increases, so does the wedge angle, and at a certain value of n_0 the bulk new "phase" appears with the opposite polarization direction. This phase increases in volume through the motion (along the polar axis) of the plane front of a kink-like nonlinear wave of a large amplitude resulting in polarization reversal. In [15, 16], this model was used to theoretically analyze the motion of head-to-head domains.

In high-resistivity materials (with small n_0), the polarization reversal can also be described in terms of a kink-like wave propagating perpendicular to the polar axis and to the electric field E_0 (see Fig. 1). This process corresponds to the sideways motion of the 180° domain wall. In the general case, the velocity of domain walls is a function of two time parameters: the relaxation time τ_s of polarization and the dielectric relaxation time τ_d dependent on the conductivity of the material. The time τ_s can be estimated from experimental data on the frequency dispersion of the dielectric permittivity and is obtained to be $\tau_s \approx 10^{-8}$–10^{-11} s [10, 11]. The ratio τ_s/τ_d may vary over wide limits depending on the conductivity and the mechanism of the ferroelectric phase transition. At the same time, in studying the dynamics of head-to-head domains, it was implicitly assumed in [15, 16] that $\tau_s = 0$. This assumption is not well founded physically, especially in the case of sideways motion of a 180° domain wall, where there are no bound charges on the wall and, hence, its motion is not limited by dielectric relaxation and is characterized by a single relaxation time, τ_s. For this reason, the system of equations used in [15, 16] must be supplemented by the kinetic equation describing the relaxation of polarization. This will be done in the following section, where we present the theoretical model used in this paper.

1063-7834/00/4201-0146$20.00

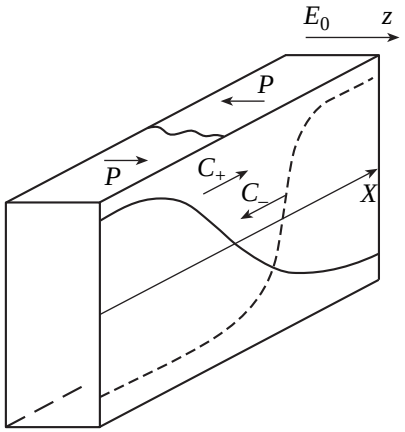

Fig. 1. Geometry of the theoretical model of sideways motion of a 180° domain wall (schematic); profiles of nonlinear kink-like waves C_+ and C_- are shown by solid and dashed line, respectively.

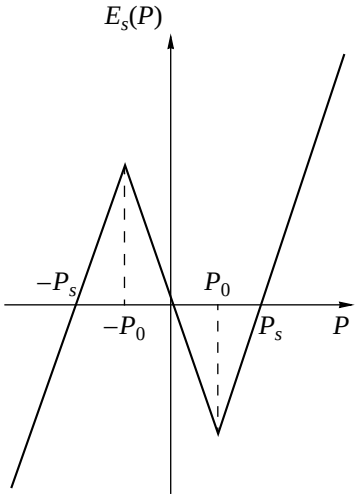

Fig. 2. Model $E_s(P)$ dependence (equation of state) of a ferroelectric (schematic).

2. A THEORETICAL MODEL

The model geometry of sideways motion of the 180° domain wall is shown in Fig. 1. We assume that only the x components of the electric field E_0 and polarization P are nonzero. The polarization is a function of only one spatial variable, x, while the field E_0 is uniform over the sample. Strictly speaking, the latter assumption is valid only if there is no gap between the ferroelectric and electrodes; the effect of a gap on the switching process will be discussed later. In what follows, differentiation with respect to time t and space coordinate x is indicated by the corresponding subscript. The rate of polarization relaxation P_t is proportional to the derivative of the thermodynamic potential $\tilde{F}(P, E_0)$ with respect to P taken at the field E_0 kept fixed [12]. Therefore, we have $P_t \sim \delta\tilde{F}/\delta P = E_s(P) - E_0$. With the potential $\tilde{F}$ including gradient corrections, the above relation leads to the following nonlinear equation [17–19] governing the relaxation of polarization P:

$$\eta P_t = E_0 - E_s(P) + l^2 P_{xx}, \tag{1}$$

where l is the correlation length [14] and η is a characteristic time constant. In the general case of a nonuniform field, equation (1) should be solved in combination with Poisson's equation and the continuity equation, which gives the distributions of the polarization $P(t, x)$ and electric field. For a stationary nonlinear wave propagating with a velocity c, the polarization P is a function only of the difference $(x - ct)$. Hence, introducing the notation $Y = \eta P$ and $D = l^2/\eta$, we may write (1) in the form

$$DY_{xx} + cY_x + E_0 - E_s(Y) = 0. \tag{2}$$

In this paper, we solve this equation under the assumption that $E_s(P)$ has the following model form (see Fig. 2):

$$E_s(Y) - E_0 = \begin{cases} K(Y + Y_-) & Y + \Delta_0 < 0, \\ -K_0(Y + \Delta_-) & |Y| < \Delta_0, \\ K(Y - Y_+) & Y - \Delta_0 > 0, \end{cases} \tag{3}$$

where

$$Y_\mp = Y_0\left(1 \mp \frac{\varepsilon}{\varepsilon_s}\bar{E}_0\right), \quad Y_0 = \eta P_s,$$

$$\Delta_- = \frac{\delta_0}{\varepsilon}\bar{E}_0 Y_0, \quad K = 4\pi/\varepsilon\eta, \quad K_0 = 4\pi/\delta_0\eta,$$

$$\Delta_0 = \eta P_0, \quad \varepsilon_s = \varepsilon + \delta_0, \quad \bar{E} = E_0/E_c; \tag{3a}$$

ε is the permittivity of the ferroelectric; δ_0 is a parameter defining the slope of the $E_s(P)$ curve in the instability region (ε; $\delta_0 > 0$); and $E_c = 4\pi P_s/\varepsilon_s$ is the coercive field. Sideways motion of the 180° domain wall is described by a kink-like solution for which $Y(\pm\infty) \longrightarrow \pm Y_\pm$ and in the region $0 < x < x_0$ we have $|P| < P_0$, i.e., $|Y| < \Delta_0$. This solution has the form

$$Y + Y_- = a_- e^{\lambda_- x} \quad x > x_0,$$

$$Y + \Delta_- = b_+ e^{\alpha_+ x} + b_- e^{\alpha_- x} \quad 0 < x < x_0, \tag{4}$$

$$Y - Y_+ = a_+ e^{\lambda_+ x} \quad x < 0,$$

where

$$\lambda_\pm = -\alpha \pm \kappa_s, \quad \kappa_s = \frac{1}{2D}\sqrt{c^2 + 4KD},$$

$$\alpha_\pm = -\alpha \pm \kappa, \quad \kappa = \frac{1}{2D}\sqrt{4K_0 D - c^2},$$

$$\alpha = c/2D. \tag{4a}$$

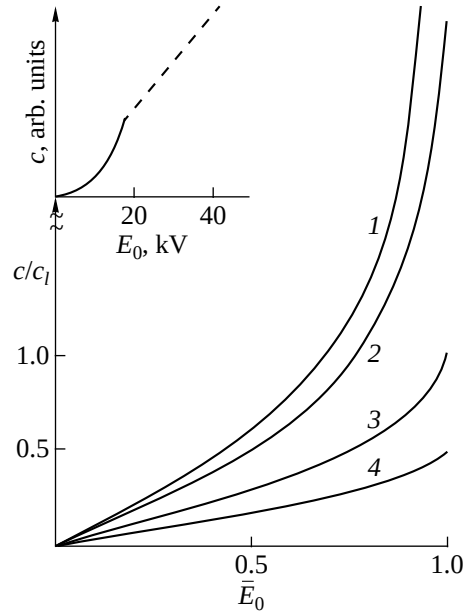

Fig. 3. Velocity of a 180° domain wall c as a function of electric field $\bar{E}_0$ for $\varepsilon/\delta_0 = 0$; 0.1; 1.0; and 4.0 (curves *1* to *4*, respectively). The inset shows an experimental curve for TGS [10].

Matching together the expressions for the function Y and its derivative on each side of the points $x = 0$ and x_0 and using the conditions $Y(0) = \Delta_0$ and $Y(x_0) = -\Delta_0$, we obtain a system of two equations, one of which gives the position of the point x_0,

$$\tan(\kappa x_0) = 2\frac{\delta_0}{\varepsilon}\frac{(\varepsilon/\delta_0 - s^2)^{1/2}(1+s^2)}{1-\delta_0/\varepsilon - 2\delta_0 s^2/\varepsilon}, \qquad (5)$$

while the other determines the dimensionless velocity $s = c/c_l$ (with $c_l = \sqrt{4KD}$),

$$\frac{1+\bar{E}_0}{1-\bar{E}_0} = g_0^2(s), \qquad (6)$$

where $g_0(s) = \exp(sx_0/2L)(s + \sqrt{1+s^2})$ and $L = 2D/c_l$.

In the limit of $\delta_0 \longrightarrow 0$ and $x_0 \longrightarrow 0$, we have $g_0(s) \approx s + \sqrt{1+s^2}$ and a simple analytic expression is obtained for $s(\bar{E}_0)$ from (6),

$$s = \frac{\bar{E}_0}{\sqrt{1-\bar{E}_0^2}}. \qquad (7)$$

It follows from the above expressions that in the ranges of parameters where stationary kink-like solutions of (1) exist, the velocity of the wave reaches its maximum value $s_0 = (\varepsilon/\delta_0)^{1/2}$ when $E_0 = E_c$ (i.e., $\bar{E}_0 = 1$). If $E_0 > E_c$, there are no stationary solutions and the mechanism of polarization reversal becomes different. Near the coercive field, $E_0 \lesssim E_c$, the function $s(\bar{E}_0)$ has a singularity

$$\sqrt{s_0 - s} \approx -\pi\sqrt{s_0/2}/\ln 2s_0^2(1-\bar{E}_0). \qquad (8)$$

Figure 3 shows $s(\bar{E}_0)$ curves calculated numerically from (5) and (6) for several values of the parameters and an experimental curve for triglycine sulfate [10]. It is seen that in the region where the field becomes strong, the experimental curve has a discontinuity in slope, which may be associated with the above-mentioned singularity located near the coercive field. It follows from the results presented, that in the vicinity of the coercive field, the shape of the $c(E_0)$ curve is sensitive to the specific form of the equation of state of the ferroelectric $E_s(P)$ in the region of instability. Hence, for the model to be more adequate in this region, the approximation to $E_s(P)$, given by (3), should be refined.

Let us evaluate the quantity $c_l = (4KD)^{1/2}$ characterizing the velocity of the domain wall. Note that the linearized equation (1) describes the Debye relaxation of polarization with relaxation time $\tau_s \equiv 1/K = \varepsilon\eta/4\pi$. Hence, $c_l = 2\sqrt{\varepsilon}\, l/\tau_s$. From experimental data on frequency dispersion of ε it follows that $\tau_s \sim 10^{-8}$–10^{-11} s [10, 11]. Putting $\varepsilon \sim 10^4$ and $l \sim 5$ Å [14–16], we obtain $c_l \sim 10^3$–10^6 cm/s. In many experiments with metallic electrodes [10, 11], the velocity of domain walls was observed to be of the same order, commonly being higher than the velocity of sound.

3. PERIODIC SOLUTIONS

In addition to kink-like solutions, there are periodic solutions of (2). Using a common method [17, 19], it can be shown that $c = 0$ for the periodic solutions and that closed trajectories in the Y_x–Y phase plane are determined by the equation

$$DY_x^2 = \tilde{F}(Y) - \tilde{F}_0, \qquad (9)$$

where the thermodynamic potential may be written as $\tilde{F} = \int_0^Y dY(E_s(Y) - E_0)$.

The amplitude and period of the wave are specified by the value of the constant $\tilde{F}_0$. As $\tilde{F}_0$ approaches the minimum of the thermodynamic potential $\tilde{F}$, the wave disintegrates and becomes a system of isolated nuclei of the new phase. Considering an individual nucleus in the limit as $\delta_0 \longrightarrow 0$ in (3), simple expressions can be obtained for the dimension $2x_0$ of a planar nucleus and the activation energy for its formation $\Delta\tilde{\tilde{F}}_{\text{act}}$, which is defined as the change in the total thermodynamic potential $\tilde{\tilde{F}}$ (volume integral of $\tilde{F}$ including the gradient terms) required for the nucleus to be created from the spatially uniform state. Matching together the solu-

tions of (2) on each side of the nucleus boundary $x = x_0$ [13] and using the conditions $Y(\pm\infty) = -Y_-$ yields

$$\exp(-d) = \bar{E}_0 \equiv E_0/E_c. \quad (10)$$

Here, $d = 2kx_0$ and $k = (K/D)^{1/2}$.

The activation energy per unit area of the side surface of a nucleus is

$$\Delta\tilde{\tilde{F}}_{\text{act}} = \frac{P_s E_c}{k}(1 - \bar{E}_0 + \bar{E}_0 \ln \bar{E}_0). \quad (11)$$

The quantity $\Delta\tilde{\tilde{F}}_{\text{act}}$ is finite at $\bar{E}_0 = 0$, falls off steeply with increasing $\bar{E}_0$, and tends towards zero as $E_0 \longrightarrow E_c$. Evaluations from (11) show that the formation of nuclei in the bulk is likely only if $E_0 \sim E_c$. For example, for a disk-shaped nucleus of diameter about 10^{-4} cm at $\varepsilon \sim 10^4$ and $P_s \sim 10$ μC, we have $\Delta\tilde{\tilde{F}}_{\text{act}} \sim 10^2$ eV if $E_0 \sim 0$, whereas at $\Delta E_0/E_c \sim 0.1$, i.e., near the coercive field, we have $\Delta\tilde{\tilde{F}}_{\text{act}} \sim 0.5$ eV. Note that the classical theory of nucleation (which applies, strictly speaking, only when $\bar{E}_0$ is small) predicts that, formally, $\Delta\tilde{\tilde{F}}_{\text{act}}$ is finite for any $\bar{E}_0$ [11, 12]. The specific form of the $\Delta\tilde{\tilde{F}}_{\text{act}}(E_0)$ function is dictated by the shape of the nucleus.

4. NUCLEUS GROWTH

The periodic solutions and those corresponding to a nucleus are both unstable [17, 19]. If the polarization distribution in a nucleus deviates by δY from a stationary distribution $Y_0(x)$, the nucleus either collapses or increases infinitely in size. The latter process is not stationary and at the later stages (as $t \longrightarrow \infty$), the polarization distribution corresponds to two kink-like waves propagating in opposite directions with velocity c found above. The equation determining the kinetics of nucleus growth in the initial stage is obtained by varying (1) about $Y_0(x)$,

$$\delta Y_t = \left(D\frac{d^2}{dx^2} - \nu(x)\right)\delta(Y). \quad (12)$$

Here, the "potential" $\nu(x)$ is

$$\nu(x) = \left.\frac{\delta E_s}{\delta Y}\right|_{Y = Y_0(x)}. \quad (12a)$$

In the limit as $\delta_0 \longrightarrow 0$ in (3), this potential reduces to a sum of δ potentials

$$\nu(x) = K - \frac{K\Delta Y}{|Y_0'(x_0)|}(\delta_+ + \delta_-), \quad (12b)$$

where $\delta_\pm = \delta(x \pm x_0)$ and $\Delta Y = \eta P_s$.

Assuming $\delta Y \sim \exp(-\lambda t)Y_\lambda(x)$, we seek a solution to (12) by expanding it in terms of eigenfunctions $Y_\lambda(x)$ that satisfy a Schrödinger-like equation

$$\left(-D\frac{d^2}{dx^2} + \nu\right)Y_\lambda = \lambda Y_\lambda. \quad (13)$$

Unstable solutions correspond to bound states for which $\lambda < 0$. Putting $\lambda = K - \kappa^2 D$ and joining the solutions corresponding to the δ potentials by a conventional technique [13], we arrive at a dispersion relation

$$1 - \kappa(1 - \exp(-d)) = \pm\exp(-\kappa d). \quad (14)$$

Here, κ is a dimensionless "momentum" of the nucleus [in units of $k = (K/D)^{1/2}$ and d is its dimensional width. Equation (14) has two roots: $\kappa = 1$, $\lambda = 0$ for the upper (plus) sign and $\kappa > 1$, $\lambda < 0$ for the lower sign. Physically, the first root corresponds to a displacement of the nucleus as a unit; the nucleus is indifferent to such perturbations ($\lambda = 0$). The second solution (with $\lambda < 0$) describes spontaneous growth of the nucleus. Simultaneous solution of (10) and (14) gives the root λ as a function of the field $\bar{E}_0$.

The solution δY describing the nucleus growth in the region $x > x_0$ can be represented as

$$\delta Y \sim \exp(-\kappa(x - c_s t)), \quad (15)$$

where $c_s = |\lambda|/\kappa$ is a parameter characterizing the initial growth rate.

Let us evaluate c_s for a low field E_0. Using (10) and (14), it can be shown in this case that $c_s \sim 2c_l\bar{E}_0$, where $c_l = (4KD)^{1/2}$. A comparison between this result and (7) shows that the initial growth rate c_s is twice as high as the steady-state velocity of an isolated kink-like wave. Observations of a higher nucleus growth rate in experiments on polarization reversal were repeatedly reported [10, 11]. The typical value of the increment λ determining the relaxation rate of both the nucleus and periodic waves is of the order of $1/\tau_s \equiv K$ and, according to our evaluation $\tau_s \sim 10^{-8}$–10^{-11} s made above, it falls in the frequency range of pulsed cathodes [1–5].

5. DISCUSSION

In experiments on electron emission, the dynamics of 180° domains considered above has peculiar features. We will discuss one aspect concerning the influence of a gap d between the electrodes and ferroelectric. In the case of a plate of thickness L having no charges that can screen the polarization, the equation of state of the system is given by the known relation [14]

$$E(P) = \beta P + E_s(P), \quad (16)$$

where $E_s(P) = -\alpha P + \gamma P^3$ and $\beta = 4\pi d/L$.

The process of polarization reversal has a number of special features in this case. If the gap is so large that $\beta > \beta_c \equiv \alpha$, then the $E_s(P)$ curve has no N-shaped portion and there are no solutions corresponding to an iso-

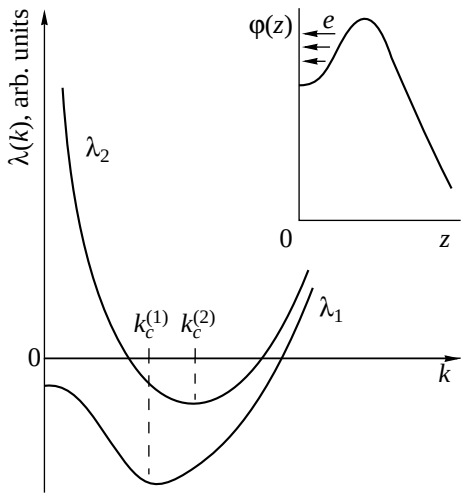

Fig. 4. Schematic dependence of the decrement $\lambda(k)$ on the wave vector k lying in the plane of the sample for the surface layer of a ferroelectric electret; the inset shows the distribution of the potential $\varphi(z)$ in the layer according to [8].

lated 180° wall (kink), because these solutions may appear only when there are asymptotic states with opposite directions of polarization. In fact, the switching effect is also absent; when the field is removed, the system will relax to its initial state and its behavior will be quasi-linear. However, the situation is different in the case where there is electron emission and the electrodes and ferroelectric can exchange electrical charges. Physically, it is clear that if this process is fast, the behavior of the system will be similar to that in the case where the gap is absent. The periodic distribution of polarization taking place for $\beta > \beta_c$ [14] will be unstable (see Section 3) and evolve to a uniform state (dictated by the applied field) through the growth of 180° domains. The kink-like waves will also be made possible. The polarization reversal will be accompanied by a change in the charge state of the surface layer of the ferroelectric. The kink-like solutions may also appear in the case where electron emission is absent, but the gap is narrow and $\beta < \beta_s$. Rigorous analysis [14] shows that the critical value β_s is less than β_c obtained from (16). However, the asymptotic uniform states of the kink are stable only if $\beta < \beta_c$. The parameter β_s is a function of temperature and the plate thickness L.

Under the time-varying electric field, when the pulsed cathode is operated, the above-mentioned coupling between the processes of switching and emission will give rise to stationary nonlinear oscillations of the charge distribution in the ferroelectric surface layer and of the polarization distribution. For this coupling to be efficient, the characteristic time of electron emission must be comparable with the relaxation time of 180° domains $\tau_s \sim 10^{-8}$–10^{-10} s. To obtain some amount of information about the charge state of the surface layer, we may use data on the effect of anomalous electron emission (AEE) from ferroelectric electrets during their irradiation with X rays [8, 9]. In this case, the intensity of electron emission is more than two orders of magnitude higher than from the neutral surface. According to the theoretical model proposed in [8], this effect is due to the fact that in the ferroelectric surface layer there occurs an electron flow towards vacuum [see the inset of Fig. 4, showing the potential $\varphi(z)$] produced by the inhomogeneous polarization distribution in the electret [8]; in particular, $P \ll P_s$ in the surface layer. Such a state of the surface layer, uniform over the plane of the sample, may become unstable and the transition to an inhomogeneous state will occur in which the potential φ will be modulated over the surface. This transition may explain a broadening of the electron emission spectrum observed in experiment [8, 9]. Let us assume that the charge of the electret is localized and separated from the surface by a distance Δ. Following [18], we also assume that there are surface states (or adsorbate states) whose charge may be changed. Then, our problem reduces to the problem of the stability of a ferroelectric plate of thickness Δ lying on an anisotropic dielectric with dielectric permittivities ε_x and ε_z. Using (1), we arrive at an equation for the decrement λ as a function of the wave vector k in the plane of the sample

$$\tan(sk\Delta) = \varepsilon_+ s\{\varepsilon_z s_0 + (1 + 2/k\Lambda)\tanh(s_0 kL)\}/\{\varepsilon_z\varepsilon_0(1 + 1/k\Lambda) - [(\varepsilon_+ s)^2 - (1 + 1/k\Lambda)/k\Lambda]\tanh(s_0 kL)\}. \quad (17)$$

Here, $s_0 = (\varepsilon_x/\varepsilon_z)^{1/2}$; $\delta(\varepsilon_x/\varepsilon_+)^{1/2}$; $\varepsilon_+^{-1} = \alpha + \lambda - k^2 l^2$, L is the thickness of the sample, and Λ is a parameter inversely proportional to the density of surface states [18]. Equation (17) determines an infinite number of branches of the function $\lambda(k)$. Two of them, corresponding to states with the lowest energy, are plotted in Fig. 4 for the case of $L \longrightarrow \infty$. It is seen that, there are ranges of k in which $\lambda(k) < 0$ and, therefore, the transition of the surface layer of the ferroelectric electret to an inhomogeneous state may occur with the formation of a periodic 180° domain structure. In this case, in the surface layer there will be regions of different potential and electric field and, according to [8], of different emission activity. Experimentally, the relative size of these regions will be different depending on the specific picture of the stratification of the ferroelectric. For example, irradiation with X-rays will cause the free-electron density to increase and the parameter Λ to decrease, which may lead to the formation of new dissipative (polarization) structures characteristic of open nonlinear systems [20–22]. When Λ is small enough, the system will become unstable with respect to homogeneous fluctuations, with $k = 0$, for which $\lambda(0) < 0$ (see Fig. 4).

Experimental observations show [9] that for a single crystal of lead magnesium niobate and single crystals of

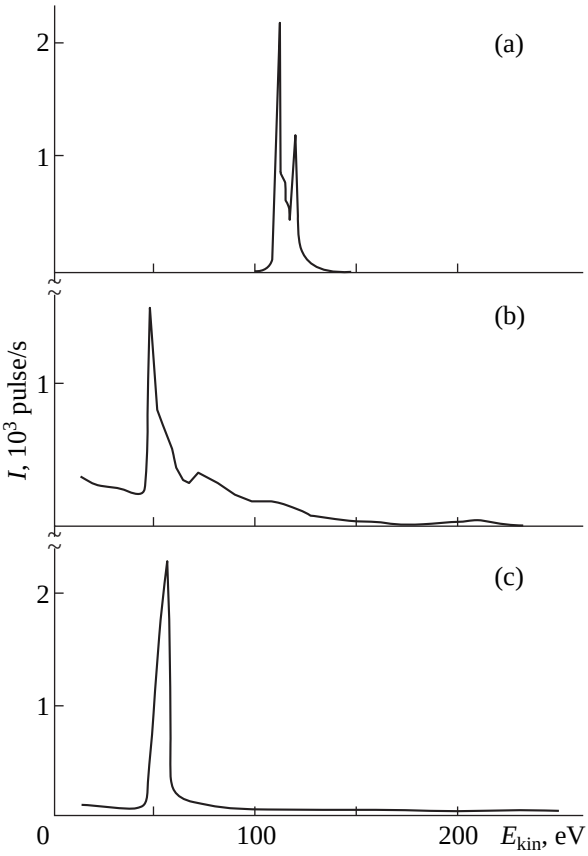

Fig. 5. Experimental spectra of anomalous electron emission from (a) a narrow strip (0.2 × 10 mm) of ceramics PKR-70; (b) a strip (10 × 10 mm) of ceramics PLZT-8 at the surface potential about 40–50 V; and (c) a conventional pulsed emitter.

lithium niobate and lithium tantalate, the full width at half-maximum of emission spectra is frequently above 100 eV. Such high values may be due to the inhomogeneous state of the surface layer of ferroelectric electrets. Under irradiation, the characteristics of the inhomogeneous state are varied and the spectrum width also changes. When the surface potential is low (30–50 V), the spectra become narrow (down to 3 eV).

The AEE spectra exhibit a finite-size effect, which is also consistent with the features of the stratification process; the instability corresponding to $\lambda(k) < 0$ occurs only in a finite range of k. This explains the fact that in the case of electron emission from strips (1–5 mm wide) of polarized ceramics PKR-70 ($PbTiO_3$-based material) and PLZT ($PbTiO_3$- and $PbZrO_3$-based material doped with La), an increase in the spectrum width (from 3 to 18 eV) was observed with an increase in the width of the strips. Figure 5 shows AEE spectra obtained from a narrow strip of PKR-70 (Fig. 5a), a wide strip of PLZT at a low surface potential (Fig. 5b), and a conventional pulsed emitter (Fig. 5c). In the last case, the emitting surface of the emitter was a system of narrow strips of width ~200 μm, each separated by metallic electrodes. In accordance with predictions of the model described above, the AEE spectra in these three cases were observed to be qualitatively similar to each other and to the electron emission spectrum from a cold ferroelectric cathode excited with voltage pulses [23].

CONCLUSION

Thus, the above discussion of the mechanisms of anomalous electron emission shows that when a pulsed cathode is operated, the charge state and electrophysical properties of its surface layer are similar to those of a ferroelectric electret [8, 9].

At present, we are performing a detailed study of the features of AEE spectra indicated above.

ACKNOWLEDGMENTS

The authors are grateful to V.P. Sakhnenko for helpful discussions and encouragement.

REFERENCES

1. A. Sh. Aĭrapetov, I. V. Ivanchik, A. N. Lebedev, *et al.*, Dokl. Akad. Nauk SSSR **311** (3), 594 (1990).
2. A. M. Kostsov, A. S. Sidorkin, V. S. Zal'tsberg, *et al.*, Fiz. Tverd. Tela (Leningrad) **24**, 3446 (1982) [Phys. Solid State **24**, 1952 (1982)].
3. A. S. Sidorkin, P. V. Logvinov, A. M. Savvinov, *et al.*, Fiz. Tverd. Tela (St. Petersburg) **38**, 624 (1996) [Phys. Solid State **38** (1996)].
4. L. Schachter, J. D. Ivers, J. A. Nation, *et al.*, J. Appl. Phys. **73**, 8097 (1993).
5. V. F. Puchkarev and G. A. Mesyats, J. Appl. Phys. **78**, 5633 (1995).
6. R. C. Miller and A. Savage, J. Appl. Phys. **31**, 662 (1960).
7. G. I. Rosenman, V. A. Okhapkin, Yu. L. Chepelev, *et al.*, Pis'ma Zh. Éksp. Teor. Fiz. **39**, 397 (1984) [JETP Lett. **39**, 477 (1984)].
8. A. T. Kozakov, V. V. Kolesnikov, V. P. Sakhnenko, *et al.*, Fiz. Tverd. Tela (St. Petersburg) **38**, 2524 (1996) [Phys. Solid State **38**, 1385 (1996)].
9. A. T. Kozakov, V. V. Kolesnikov, A. V. Nikol'skiĭ, *et al.*, Fiz. Tverd. Tela (St. Petersburg) **39** (4), 679 (1997) [Phys. Solid State **39**, 594 (1997)].
10. G. A. Smolenskiĭ, V. A. Bokov, V. A. Isupov, N. N. Kraĭnik, R. B. Pasynkov, and M. S. Shur, *Ferroelectrics and Antiferroelectrics* (Nauka, Leningrad, 1971).
11. M. E. Lines and A. M. Glass, *Principles and Applications of Ferroelectrics and Related Materials* (Clarendon, Oxford, 1977; Mir, Moscow, 1981).
12. E. M. Lifshitz and L. P. Pitaevskiĭ, *Physical Kinetics* (Nauka, Moscow, 1979).
13. A. G. Khachaturyan, *Theory of Phase Transformations and the Structure of Solid Solutions* (Nauka, Moscow, 1974).
14. E. V. Chenskiĭ and V. V. Tarasenko, Zh. Éksp. Teor. Fiz. **88**, 1089 (1982) [JETP **56**, 618 (1982)].

15. E. V. Chenskiĭ, Fiz. Tverd. Tela (Leningrad) **11**, 666 (1969) [Phys. Solid State **11**, 534 (1969)].
16. M. S. Shur, Fiz. Tverd. Tela (Leningrad) **10**, 2653 (1968) [Phys. Solid State **10**, 2087 (1968)].
17. B. W. Knight and G. A. Peterson, Phys. Rev. **155**, 393 (1967).
18. A. S. Sidorkin, B. M. Darinskiĭ, and A. S. Sigov, Fiz. Tverd. Tela (St. Petersburg) **39**, 922 (1997) [Phys. Solid State **39**, 823 (1997)].
19. A. F. Volkov and Sh. M. Kogan, Usp. Fiz. Nauk **96**, 633 (1968) [Sov. Phys. Usp. **5**, 39 (1970)].
20. P. Glansdorff and I. Prigogine, *Thermodynamic Theory of Structure, Stability and Fluctuations* (Wiley–Interscience, London, 1971; Mir, Moscow, 1973).
21. V. V. Kolesnikov, Fiz. Tverd. Tela (St. Petersburg) **38**, 220 (1996) [Phys. Solid State **38**, 122 (1996)].
22. V. V. Kolesnikov and N. F. Losev, Dokl. Ross. Akad. Nauk **355**, 628 (1997).
23. O. Auciello, M. A. Ray, D. Palmer, *et al.*, Appl. Phys. Lett. **66**, 2183 (1995).

Translated by Yu. Epifanov

Physics of the Solid State, Vol. 42, No. 1, 2000, pp. 15–21. Translated from Fizika Tverdogo Tela, Vol. 42, No. 1, 2000, pp. 16–22.

METALS AND SUPERCONDUCTORS

Nonlocal Josephson Electrodynamics of a Magnetic (Two- or Three-dimensional) Superconductive Thin Film

A. I. Lomtev

Donetsk Physicotechnical Institute, National Academy of Sciences of Ukraine, Donetsk, 340114 Ukraine
e-mail: medvedev@host.dipt.donetsk.ua

Received February 1, 1999; in final form, June 22, 1999

Abstract—For the Josephson junction in a two- or three-dimensional magnetic superconductive thin film, an integro-differential equation of phase-difference dynamics, including time and space nonlocality, is deduced. It is shown that the magnetic subsystem induces the substantial renormalization of the spectrum of small-amplitude electromagnetic excitations and causes them to decay. *© 2000 MAIK "Nauka/Interperiodica".*

INTRODUCTION

By now, the equations of nonlocal Josephson electrodynamics have been obtained and examined for five cases. These are the following: (1) the tunnel junction at the butt of two superconductive ultrathin films whose thicknesses are much smaller than the value of the London length; (2) the tunnel junction between massive superconductors whose thicknesses are considerably greater than the London penetration depth; (3) the tunnel junction between superconductive layers of finite thickness in a direction perpendicular to the magnetic field; (4) the tunnel junction at the butt between superconductive plates of finite thickness along the magnetic field; and (5) the tilted (tapered) Josephson junction between superconductive plates of finite thickness along the magnetic field.

Thus, in [1–8], it has been shown that the nonlocal effects may be essential even in contacts of large thickness d along the magnetic field (in the direction of the vortices) ($d \gg \lambda$, λ is the London penetration depth), i.e., even in the cases that were considered before in a local approximation. Otherwise, in the case of thin films, when $d \ll \lambda$, the effect of nonlocality is very important and grows into the decisive factor. The corresponding equations have been obtained and examined in [9–12]. The Josephson junction between two superconductive layers of finite thickness in the direction perpendicular to the magnetic field in vortices has been studied in [13]. In the recent works [14, 15], the examination of the butt-contact and tilted (tapered) junction, respectively, of finite thickness along the vortex magnetic field has been performed for the arbitrary ratio d/λ.

Nowadays, a wide range of magnetic superconductors is known, exhibiting new unique properties [16–18]. In addition to the ternary compounds [19], superconductivity and magnetism coexistence was established for the HTSC compounds of the REBaCuO and RECuO type, where RE is a rare-earth ion, and others. The strong antiferromagnetic correlation of the spins of copper atoms in the CuO_2 planes in the superconducting state is the most important feature of the HTSC materials [20].

Therefore, nonlocal electrodynamics of the Josephson junction in ultrathin magnetic superconductive films characterized by $d \ll \lambda$ becomes all the more pressing for investigation. In this case, the problem may be reduced to that of an infinitely thin two-dimensional superconductive plane, when the dependence of physical characteristics of a superconductive contact on the coordinate along the normal to the film plane may be neglected, and the current and the magnetic field may be thought of as slowly varying through the plate thickness [21].

The system under consideration—a thin film of magnetic superconductor—may be two- or three-dimensional in magnetic properties, when the magnetic permeability $\hat{\mu}$ would be dependent on two (in the film plane) or three coordinates and on time as well.

The geometry of the problem is as follows: the film plane coincides with the xy-plane, the current propagates along the y-axis, and the line of weak bonding is associated with the x-axis.

BASIC EQUATIONS OF ELECTRODYNAMICS OF A MAGNETIC SUPERCONDUCTIVE THIN FILM

As in [22], we start from Maxwell's equations for the magnetic induction vector $\mathbf{B}(r, t) = \mathrm{rot}\mathbf{A}(r, t)$ ($\mathbf{A}(r, t)$ is the vector potential), given by the sum of the magnetic field $\mathbf{H}(r, t)$, generated by a persistent current $\mathbf{j}(r, t)$, and of the magnetization $\mathbf{M}(r, t)$

$$\mathrm{rot}\mathbf{B}(r, t) = \frac{4\pi}{c}\mathbf{j}(r, t) + 4\pi\mathrm{rot}\mathbf{M}(r, t). \qquad (1)$$

The relation between the current, the potential and the phase of the order parameter $\Theta(r, t)$ (with the Lon-

don gauge of the potential div $\mathbf{A}(r, t) = 0$) is specified by the expression

$$\mathbf{j}(\mathrm{r}, t) = (c/4\pi\lambda^2)[\mathbf{S}(\boldsymbol{\rho}, t) - \mathbf{A}(r, t)], \quad (2)$$

where $r = (x, y, z)$, $\boldsymbol{\rho} = (x, y)$, and the vector $\mathbf{S}(\boldsymbol{\rho}, t)$ is determined by the phase gradient

$$\mathbf{S}(\rho, t) = \frac{\Phi_0}{2\pi}\nabla\Theta(\rho, t). \quad (3)$$

Here, Φ_0 is a quantum of the magnetic flux.

The phase of the order parameter satisfies the condition

$$\mathrm{rot}\mathbf{S}(\rho, t) = -z\frac{\Phi_0}{2\pi}\frac{\partial\varphi(x, t)}{\partial x}\delta(y), \quad (4)$$

where z is the unit vector along the z-axis, $\delta(y)$ is the Dirac delta-function, and $\varphi(x, t)$ is determined by the phase difference of the order parameter in the junction

$$\varphi(x, t) = \Theta(x, +0, t) - \Theta(x, -0, t). \quad (5)$$

The equations (1) and (2) lead to the relation

$$\mathrm{rot}\mathbf{H}(r, t) = \frac{c}{4\pi\lambda^2}[\mathbf{S}(\rho, t) - \mathbf{A}(r, t)], \quad (6)$$

which may be presented for the ultrathin film ($d \ll \lambda$) in the form

$$\mathrm{rot}\mathbf{H}(r, t) = \lambda_{\mathrm{eff}}^{-1}[\mathbf{S}(\rho, t) - \mathbf{A}(r, t)]\delta(z), \quad (7)$$

where $\lambda_{\mathrm{eff}} = \lambda^2/d$ is the Pearl penetration depth.

THE FILM OF A TWO-DIMENSIONAL MAGNETIC SUPERCONDUCTOR

At first, we will assume that the system under consideration is two-dimensional not only in superconductive, but in magnetic properties as well, when the magnetic permeability can be written as

$$\hat{\mu} = \mu(\mathbf{r} - \mathbf{r}', t - t') = \mu(\boldsymbol{\rho} - \boldsymbol{\rho}', t - t')\delta(z - z'). \quad (8)$$

Therefore, in the case of a two-dimensional magnetic superconductor, the magnetic field $\mathbf{H}(r, t)$ is connected with the magnetic induction $\mathbf{B}(r, t)$ through the integral material relation

$$\mathbf{H}(\mathbf{r}, t) = \int_{-\infty}^{t} dt' \int_{-\infty}^{\infty} d\boldsymbol{\rho}'\mu^{-1}(\boldsymbol{\rho} - \boldsymbol{\rho}', t - t')\mathbf{B}(\boldsymbol{\rho}', z, t'), \quad (9)$$

where $\mu(\boldsymbol{\rho} - \boldsymbol{\rho}', t - t')$ is the magnetic permeability of the two-dimensional superconductive film.

From relations (7) and (9), we obtain the equation for the vector potential

$$\mathrm{rot}\left\{\int_{-\infty}^{t} dt' \int_{-\infty}^{\infty} d\rho'\mu^{-1}(\boldsymbol{\rho} - \boldsymbol{\rho}', t - t')\mathrm{rot}\mathbf{A}(\boldsymbol{\rho}', z, t')\right\} = \lambda_{\mathrm{eff}}^{-1}[\mathbf{S}(\boldsymbol{\rho}, t) - \mathbf{A}(\boldsymbol{\rho}, z, t)]\delta(z), \quad (10)$$

which expresses the potential in terms of the source field $\mathbf{S}(\rho, t)$.

From the continuity equation $\mathrm{div}\,\mathbf{j}(r, t) = 0$ and equation (2) it follows that $\mathrm{div}\,\mathbf{S}(\rho, t) = 0$. Consequently, the vector field $\mathbf{S}(\rho, t)$ may be represented as the rotor of a vector field $F(\rho, t)$

$$\mathbf{S}(\rho, t) = \mathrm{rot}\mathbf{F}(\rho, t), \quad (11)$$

where

$$\mathbf{F}(\rho, t) = \hat{z}F(\rho, t). \quad (12)$$

Substituting (12) in relation (4), we obtain the equation for $F(\rho, t)$

$$\Delta F(\rho, t) = \frac{\Phi_0}{2\pi}\frac{\partial\varphi(x, t)}{\partial t}\delta(y). \quad (13)$$

On the one hand, the current density $f_y(x, 0, t)$ through the Josephson junction is the sum of three components: the Josephson supercurrent density, the density of the normal (quasiparticle) current, and of the capacitive displacement current

$$j_y(x, 0, t) = j_c\left[\sin\varphi(x, t) + \frac{\beta}{\omega_J^2}\frac{\partial\varphi(x, t)}{\partial t} + \frac{1}{\omega_J^2}\frac{\partial^2\varphi(x, t)}{\partial t^2}\right]d\delta(z), \quad (14)$$

where β is the damping parameter and j_c and ω_J are the critical current and the Josephson frequency, respectively.

On the other hand, from equation (2) it follows that the current density $j_y(x, 0, t)$ may be represented in the form

$$j_y(x, 0, t) = \frac{c}{4\pi\lambda_{\mathrm{eff}}}[S_y(x, 0, t) - A_y(x, 0, 0, t)]\delta(z). \quad (15)$$

Equating expressions (14) and (15), we see that

$$j_c\left[\sin\varphi(x, t) + \frac{\beta}{\omega_J^2}\frac{\partial\varphi(x, t)}{\partial t} + \frac{1}{\omega_J^2}\frac{\partial^2\varphi(x, t)}{\partial t^2}\right] = \frac{c}{4\pi\lambda^2}[S_y(x, 0, t) - A_y(x, 0, 0, t)]. \quad (16)$$

To obtain a closed equation of dynamics for the phase difference $\varphi(x, t)$, it is necessary to find the functional relation between

$$\Delta_y(x, t) = S_y(x, 0, t) + A_y(x, 0, 0, t) \tag{17}$$

and $\varphi(x, t)$.

To solve equation (10), let us introduce the Fourier-transforms of the vectors $\mathbf{A}(r, t)$, $\mathbf{S}(\rho, t)$ and of the scalar function $\mu^{-1}(\rho, t)$

$$\mathbf{A}(\rho, z, t) = \int \frac{d^2q\,dp\,d\omega}{(2\pi)^4} \exp(iq\rho + ipz - i\omega t) A(q, p, \omega), \tag{18}$$

$$\mathbf{S}(\rho, t) = \int \frac{d^2q\,d\omega}{(2\pi)^3} \exp(iq\rho - i\omega t)\mathbf{S}(q, \omega), \tag{19}$$

$$\mu^{-1}(\rho, t) = \int \frac{d^2q\,d\omega}{(2\pi)^3} \exp(iq\rho - i\omega t)\mu^{-1}(q, \omega). \tag{20}$$

Using (18) and (19), we write $\Delta_y(x, t)$ as the integral

$$\Delta_y(x, t) = \frac{1}{(2\pi)^2} \int_{-\infty}^{\infty} d\omega \int_0^{\infty} q\,dq \int_{-\pi}^{\pi} d\vartheta [S_y(q, \omega) - A_y(q, \omega)] \exp(iqx\cos\vartheta - i\omega t), \tag{21}$$

where $q = (q_x^2 + q_y^2)^{1/2}$, ϑ is the polar angle in the plane (q_x, q_y), and

$$\mathbf{A}(q, \omega) = \int_{-\infty}^{\infty} \frac{dp}{2\pi} \mathbf{A}(q, p, \omega). \tag{22}$$

Thus, the solutions of (10) may be written in the form

$$\mathbf{A}(q, p, \omega) = \lambda_{\text{eff}}^{-1} \mu(q, \omega)(q^2 + p^2)[\mathbf{S}(q, \omega) - \mathbf{A}(q, \omega)]. \tag{23}$$

As it is evident from (22) and (23), the relation between $\mathbf{S}(q, \omega)$ and $\mathbf{A}(q, \omega)$ may be written as

$$\mathbf{A}(q, \omega) = \frac{\mu(q, \omega)}{\mu(q, \omega) + 2q\lambda_{\text{eff}}} \mathbf{S}(q, \omega), \tag{24}$$

and, hence,

$$S_y(q, \omega) - A_y(q, \omega) = \frac{2q\lambda_{\text{eff}}}{\mu(q, \omega) + 2q\lambda_{\text{eff}}} S_y(q, \omega). \tag{25}$$

To obtain $S_y(q, \omega)$, equation (13) should be differentiated with respect to the coordinate x, because, according (11) and (12), $S_y(\rho, t)$ equals $-\partial F(\rho, t)/\partial x$. As a result, we have

$$\Delta S_y(\rho, t) = -\frac{\Phi_0}{2\pi} \frac{\partial^2 \varphi(x, t)}{\partial x^2} \delta(y). \tag{26}$$

From (26) it follows that

$$S_y(q, \omega) = \frac{\Phi_0}{2\pi q^2} \int_{-\infty}^{\infty} dx \int_{-\infty}^{\infty} dt \exp(-iq\cos\vartheta x + i\omega t) \frac{\partial^2 \varphi(x, t)}{\partial x^2}. \tag{27}$$

Combining (27), (25), (21), and (16), we obtain an integro-differential equation of dynamics of the phase difference $\varphi(x, t)$ in the Josephson junction at any type of magnetic ordering in a two-dimensional magnetic superconducting film:

$$\sin\varphi(x, t) + \frac{\beta}{\omega_J^2} \frac{\partial \varphi(x, t)}{\partial t} + \frac{1}{\omega_J^2} \frac{\partial^2 \varphi(x, t)}{\partial t^2} = l_J \int_{-\infty}^{\infty} dx' \int_{-\infty}^{\infty} dt' K\left(\frac{x - x'}{2\lambda_{\text{eff}}}, t - t'\right) \frac{\partial^2 \varphi(x', t')}{\partial x'^2}, \tag{28}$$

where $l_J = \lambda_J^2/\lambda$, λ_J is the Josephson penetration depth, and the kernel $K\left(\frac{x - x'}{2\lambda_{\text{eff}}}, t - t'\right)$, nonlocal with respect to the space and time variables, has the form

$$K\left(\frac{x - x'}{2\lambda_{\text{eff}}}, t - t'\right) = \int_0^{\infty} \frac{dq}{\pi} \int_{-\infty}^{\infty} \frac{d\omega}{2\pi} \frac{2\lambda_{\text{eff}} J_0[q(x - x')] \exp[-i\omega(t - t')]}{\mu(q, \omega) + 2q\lambda_{\text{eff}}}. \tag{29}$$

Here, J_0 is the zero-order Bessel function. Time nonlocality of equation (28) is caused by the frequency dispersion of the magnetic permeability $\mu(q, \omega)$.

Since $\lambda \gg a$ (a is the lattice constant), it is natural to use the hydrodynamical description of the magnetic subsystem. Restricting ourselves to the temperature range of the paramagnetic state, we obtain the expression

$$\mu(q, \omega) = 1 + i4\pi \frac{\chi_0 D_2 q^2}{\omega + iD_2 q^2}, \tag{30}$$

where χ_0 is the static magnetic susceptibility; $D_2 = (1/3)(2\pi)^{1/2} Ja^2[s(s + 1)]^{1/2}$ is the spin diffusion coefficient for two-dimensional Heisenberg-type magnets, J is the intralayer exchange parameter, and s is the spin. In the strict sense, the superconduction current screens the long-wave part of the exchange and electromagnetic interaction thereby renormalizing the parameters of the magnetic subsystem. However, in the paramagnetic interval of temperature, we will not take this into account and will make only order-of-magnitude estimates in what follows.

Let us consider the spectrum of small-amplitude electromagnetic excitations (SAEE) propagating along the Josephson junction with a wave vector Q and a frequency Ω

$$\varphi(x, t) = \varphi_0 \exp[i(Qx - \Omega t)], \quad |\varphi_0| \ll 1. \qquad (31)$$

From (28), combined with (29)–(31), the following dispersion equation $\hat{\Omega} = \hat{\Omega}(\hat{Q})$ is obtained in the absence of dissipation ($\beta = 0$), transport current and external field,

$$\hat{\Omega}^2 = 1 + \frac{2}{\pi} l \hat{Q}^2 I(\hat{Q}, \hat{\Omega}), \qquad (32)$$

where

$$I(\hat{Q}, \hat{\Omega}) = \int_0^\infty \frac{dx}{1 + \hat{Q}\cosh x + \dfrac{4\pi\chi_0 \hat{Q}^2 \cosh^2 x}{b + \hat{Q}^2 \cosh^2 x}}. \qquad (33)$$

Here, dimensionless quantities $\hat{Q} = 2\lambda_{\text{eff}} Q$ and $\hat{\Omega} = \Omega/\omega_J$ have been introduced, and the following designations are used:

$$l = l_J/2\lambda_{\text{eff}}, \quad b = -i\eta\hat{\Omega}, \quad \eta = \omega_J/\Omega_{\text{eff}},$$

$$\Omega_{\text{eff}} = D_2/(2\lambda_{\text{eff}})^2.$$

At $\chi_0 = 0$ (nonmagnetic superconductor), equations (32) and (33) give a well-known spectrum of SAEE in long- and short-wave regions, calculated in [12]. In this case, $\hat{\Omega}$ is a real function of the wave vector $\hat{Q}$, and, in nondissipative limit, the modes do not decay. At $\chi_0 \neq 0$ (magnetic superconductor), the situation is quite different. The typical value of χ_0 for antiferromagnets lies in the interval 10^{-3}–10^{-5}. Numerical analysis showed that at $\chi_0 = 10^{-3}$, which is comparable with the value of magnetic susceptibility of the cuprous subsystem in HTSC-materials, equations (32) and (33) have a complex solution $\hat{\Omega} = \hat{\Omega}(\hat{Q}) = \mathrm{Re}\hat{\Omega}(\hat{Q}) + i\mathrm{Im}\hat{\Omega}(\hat{Q})$ with a small negative imaginary part satisfying the condition

$$|\mathrm{Im}\hat{\Omega}(\hat{Q})| \mathrm{Re}\hat{\Omega}(\hat{Q}) \ll 1. \qquad (34)$$

This points to damping of SAEE caused by the influence of the magnetic subsystem. Therewith, a small share of the energy of electromagnetic waves is transferred to the magnetic subsystem and irreversibly dissipates because of spin-wave diffusion. No increasing solutions were found. In Fig. 1, the electromagnetic wave spectrum renormalized by the magnetic subsystem and the damping decrement in the Josephson junction are shown for the values of the wave vector $0 \leq \hat{Q} \leq 1$ and the following values of parameters: $\chi_0 = 10^{-3}$, $l = 1$, and $\eta = 10^3$. In Fig. 2, at the same values of parameters, the spectrum and the damping decrement of SAEE are shown for the values of the wave vector in the interval $1 \leq \hat{Q} \leq 100$.

A THREE-DIMENSIONAL MAGNETIC SUPERCONDUCTING FILM

Now, let us suppose that the system under consideration is three-dimensional in magnetic properties, which implies the magnetic susceptibility $\hat{\mu}$ of the film to be dependent on three space coordinates and time, $\hat{\mu} = \mu(r - r', t - t')$.

In this case, the magnetic field $\mathbf{H}(r, t)$ is related to the magnetic induction $\mathbf{B}(r, t)$ by the integral material equation

$$\mathbf{H}(r, t) = \int_{-\infty}^{t} dt' \int_{-\infty}^{\infty} dr' \mu^{-1}(r - r', t - t')\mathbf{B}(r', t'). \qquad (35)$$

From (7) and (35), we obtain an equation for the vector potential as a function of the source field $\mathbf{S}(\rho, t)$,

$$\mathrm{rot}\left\{ \int_{-\infty}^{t} dt' \int_{-\infty}^{\infty} dr' \mu^{-1}(r - r', t - t')\mathrm{rot}\mathbf{A}(r', t') \right\} = \lambda_{\text{eff}}^{-1}[\mathbf{S}(\rho, t) - \mathbf{A}(\rho, z, t)]\delta(z). \qquad (36)$$

Let us introduce the Fourier-transforms for $\mathbf{A}(r, t)$, $\mathbf{S}(\rho, t)$ similar to (18) and (19), and represent the function $\mu^{-1}(r, t)$ in the form

$$\mu^{-1}(r, t) = \int \frac{d^2 q\, dp\, d\omega}{(2\pi)^4} \times \exp(iq\rho + ipz - i\omega t)\mu^{-1}(q, p, \omega). \qquad (37)$$

Now the solutions of (36) become

$$\mathbf{A}(q, p, \omega) = \lambda_{\text{eff}}^{-1} \frac{\mu(q, p, \omega)}{p^2 + q^2}[\mathbf{S}(q, \omega) - \mathbf{A}(q, \omega)]. \qquad (38)$$

As follows from (22) and (38), the relations between $\mathbf{S}(q, \omega)$ and $\mathbf{A}(q, \omega)$ may be written as

$$\mathbf{A}(q, \omega) = \left(1 + \frac{\lambda_{\text{eff}}}{R(q, \omega)}\right)^{-1} \mathbf{S}(q, \omega), \qquad (39)$$

where $R(q, \omega)$ is the integral

$$R(q, \omega) = \int_{-\infty}^{\infty} \frac{dp}{2\pi} \frac{\mu(q, p, \omega)}{p^2 + q^2}, \qquad (40)$$

therefore, we have

$$S_y(q, \omega) - A_y(q, \omega) = \frac{\lambda_{\text{eff}}}{R(q, \omega) + \lambda_{\text{eff}}} S_y(q, \omega). \qquad (41)$$

Combining (27), (41), (21), and (16), we obtain the integro-differential equation of dynamics of the phase

difference in the Josephson junction in three-dimensional MSTF for any type of magnetic ordering

$$\sin\varphi(x,t) + \frac{\beta}{\omega_J^2}\frac{\partial\varphi(x,t)}{\partial t} + \frac{1}{\omega_J^2}\frac{\partial^2\varphi(x,t)}{\partial t^2} = l_J\int_{-\infty}^{\infty}dx'\int_{-\infty}^{\infty}dt'K\left(\frac{x-x'}{2\lambda_{\text{eff}}}, t-t'\right)\frac{\partial^2\varphi(x',t')}{\partial x'^2}, \quad (42)$$

where the kernel of the integral, $K\left(\frac{x-x'}{2\lambda_{\text{eff}}}, t-t'\right)$, nonlocal with respect to space and time variables, has the form

$$K\left(\frac{x-x'}{2\lambda_{\text{eff}}}, t-t'\right) = \int_0^{\infty}\frac{dq}{\pi}\int_{-\infty}^{\infty}\frac{d\omega}{2\pi}\frac{\lambda_{\text{eff}}J_0[q(x-x')]\exp[-i\omega(t-t')]}{q[R(q,\omega)+\lambda_{\text{eff}}]}. \quad (43)$$

Nonlocality of (42) in time results from the frequency dispersion of the magnetic susceptibility $\mu(q, p, \omega)$ (through the function $R(q, \omega)$.

As in the previous section, at $\lambda \gg a$, it is natural to use here the hydrodynamical description of the magnetic subsystem. Restricting ourselves to the paramagnetic interval of temperature, we obtain an expression for the magnetic susceptibility

$$\mu(q,p,\omega) = 1 + i4\pi\frac{\chi_0 D_3(q^2+p^2)}{\omega + iD_3(q^2+p^2)}, \quad (44)$$

where D_3 is the spin diffusion coefficient for a three-dimensional Heisenberg-type magnet.

According to (40) and (44), the function $R(q, \omega)$ takes the form

$$R(q,\omega) = \frac{f_0(q,\omega) + i4\pi\chi_0 q}{2q f_0(q,\omega)}, \quad (45)$$

where $f_0(q, \omega)$ is equal to

$$f_0(q,\omega) = [(q^4+\omega^2/D_3^2)^{1/2}/2 - q^2/2]^{1/2} + i[(q^4+\omega^2/D_3^2)^{1/2}/2 + q^2/2]^{1/2}. \quad (46)$$

Let us consider the spectrum of SAEE (31), which propagate along the Josephson junction with a wave vector Q and a frequency Ω.

In the absence of dissipation ($\beta = 0$), transport current, and an external field, we obtain the following dispersion equation $\hat{\Omega} = \hat{\Omega}(\hat{Q})$ from (42), combined with (43), (45), (46), and (31):

$$\hat{\Omega}^2 = 1 + \frac{2}{\pi}l\hat{Q}I(\hat{Q},\hat{\Omega}), \quad (47)$$

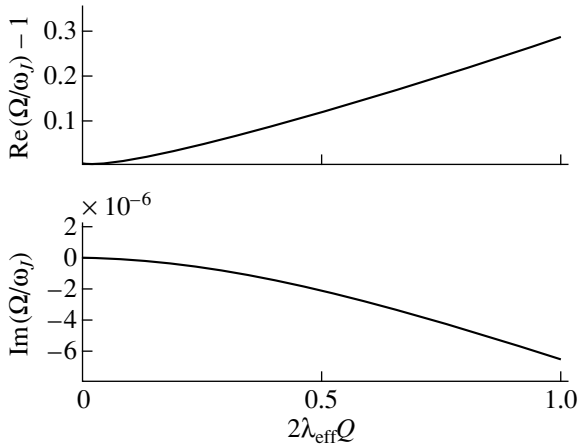

Fig. 1. Spectrum (renormalized by the magnetic subsystem) and damping decrement of SAEE in the Josephson junction in the two-dimensional MSTF for wave vectors in the interval $0 \le \hat{Q} \le 1$.

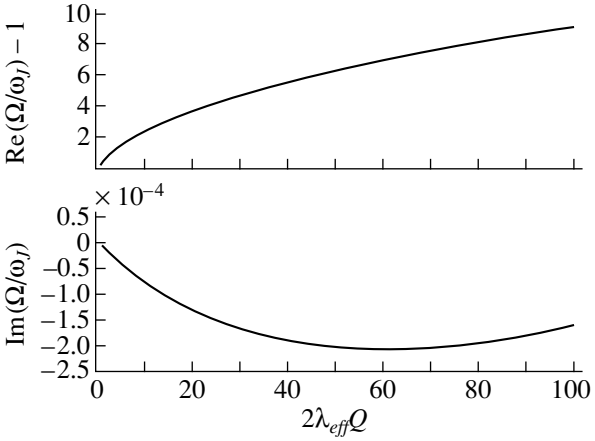

Fig. 2. Spectrum (renormalized by the magnetic subsystem) and damping decrement of SAEE in the Josephson contact in the two-dimensional MSTF for wave vectors in the interval $1 \le \hat{Q} \le 100$.

where

$$I(\hat{Q},\hat{\Omega}) = \int_0^{\infty}\frac{dxF_0(\hat{Q}\cosh x, \hat{\Omega})}{F_0(\hat{Q}\cosh x, \hat{\Omega})(1+\hat{Q}\cosh x) + i4\pi\chi_0\hat{Q}\cosh x}, \quad (48)$$

and

$$F_0(x,y) = [(x^4+\eta^2y^2)^{1/2}/2 - x^2/2]^{1/2} + i[(x^4+\eta^2y^2/2 + x^2/2]^{1/2}, \quad (49)$$

and, as in the foregoing, we introduced the dimensionless quantities

$$\hat{Q} = 2\lambda_{\text{eff}}Q, \quad \hat{\Omega} = \Omega/\omega_J$$

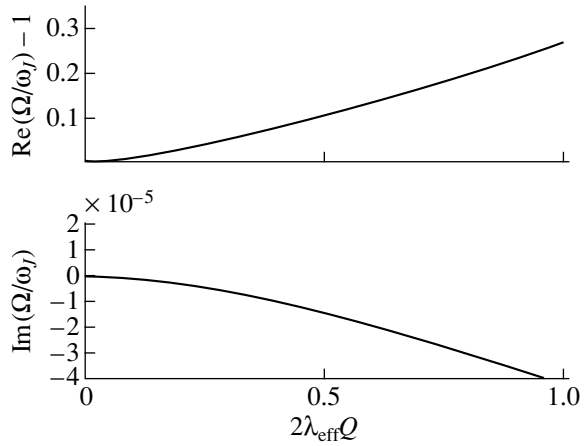

Fig. 3. Spectrum (renormalized by the magnetic subsystem) and damping decrement of SAEE in the Josephson junction in the three-dimensional MSTF for wave vectors in the interval $0 \le \hat{Q} \le 1$.

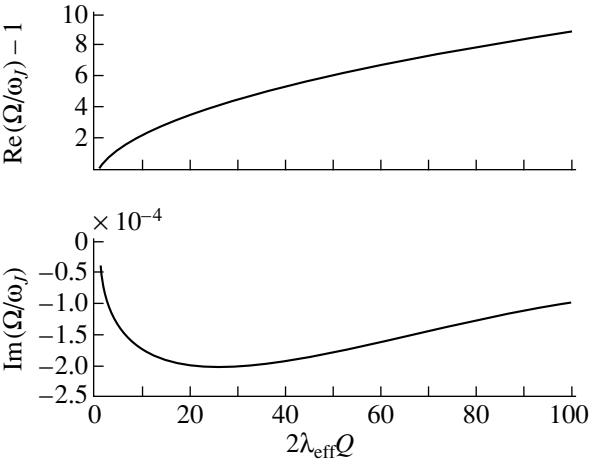

Fig. 4. Spectrum (renormalized by the magnetic subsystem) and damping decrement of linear SAEE in the Josephson contact in the three-dimensional MSTF for wave vectors in the interval $1 \le \hat{Q} \le 100$.

and the designations

$$l = l_J/2\lambda_{\text{eff}}, \quad \eta = \omega_J/\Omega_{\text{eff}}, \quad \Omega_{\text{eff}} = D_3/(2\lambda_{\text{eff}})^2.$$

At $\chi_0 = 0$ (nonmagnetic superconductor), equations (47) and (48) lead to the known spectrum of SAEE calculated for long- and short-wave ranges in [12]. In this case, the frequency $\hat{\Omega}$ is a real function of the wave vector $\hat{Q}$ and the modes do not decay in the nondissipative limit. At $\chi_0 \neq 0$, for the magnetic superconductor, the situation is different. The typical value of χ_0 for antiferromagnets lies in the interval 10^{-3}–10^{-5}. Numerical analysis showed that, at the value $\chi_0 = 10^{-3}$ (comparable with the value of the magnetic susceptibility for the cuprous subsystem of HTSC materials), $l = 1$, and $\eta = 10^{-3}$, equation (47) combined with (48) and (49) has a complex solution $\hat{\Omega} = \hat{\Omega}(\hat{Q}) = \mathrm{Re}\hat{\Omega}(\hat{Q}) + i\,\mathrm{Im}\hat{\Omega}(\hat{Q})$ with a small negative imaginary part satisfying the condition

$$\left|\mathrm{Im}\hat{\Omega}(\hat{Q})\right|/\mathrm{Re}\hat{\Omega}(\hat{Q}) \ll 1. \qquad (50)$$

This points to damping of SAEE caused by the influence of the magnetic subsystem, when a small share of the electromagnetic wave energy dissipates because of spin-wave diffusion. No increasing solutions were found. The spectrum renormalized by the magnetic subsystem and the damping decrement of electromagnetic waves in the Josephson junction are shown in Figs. 3 and 4 for the wave-vector magnitudes $0 \le Q \le 1$ and $1 \le \hat{Q} \le 100$, respectively.

CONCLUSION

From the foregoing, it is clear that nonlocality with respect to the space variables is very significant and becomes a fundamental and decisive factor for Josephson electrodynamics of thin films of both two- and three-dimensional magnetic superconductors.

Time nonlocality of Josephson electrodynamics of MSTF in the cases of two and three dimensions is connected with frequency dispersion of the magnetic susceptibility, which eventually results from delay processes.

According to (30) and (44), damping of electromagnetic excitations in the Josephson junction in MSTF is associated with the complex-valued magnetic susceptibility of media, and the physical mechanism of such damping is the process of spin diffusion with a finite relaxation time, due to which a small share of electromagnetic field energy dissipates irreversibly. The mere absence or presence of damping of linear electromagnetic waves in the Josephson junction (in the nondissipative limit) may be indicative of, respectively, the nonmagnetic or magnetic type of superconductor.

The numerical study showed that the real parts $\mathrm{Re}\hat{\Omega}(\hat{Q})$ of the linear electromagnetic excitation spectra in the Josephson junction of two- and three-dimensional MSTF differ from those in a nonmagnetic superconductor only slightly (in the third decimal place), because the static magnetic susceptibility χ_0 is small.

Numerically, the spectra $\mathrm{Re}\hat{\Omega}(\hat{Q})$ of SAEE propagating along the Josephson junction also differ only slightly (in the fourth decimal place) for two-dimensional (Figs. 1 and 2) and three-dimensional (Figs. 3, 4) magnetic superconductors. The significant distinction of two and three-dimensional superconductors is observed in damping decrements of SAEE $\mathrm{Im}\hat{\Omega}(\hat{Q})$. This fact provides a way to determine the dimension of magnetic ordering in a thin film.

ACKNOWLEDGMENTS

The author is grateful to the participants of the seminar governed by Yu.V. Medvedev for criticism; to A.S. Zel'tser for help with numerical calculations, to V.N. Krivoruchko, Yu.E. Kuzovlev, Yu.G. Pashkevich, and A.É. Filippov for their useful discussions, attention, and encouragement.

REFERENCES

1. Yu. M. Aliev, V. P. Silin, and S.A. Uryupin, Sverkhprovodimost' **5** (2), 228 (1992).
2. A. Gurevich, Phys. Rev. B **46**, 3187 (1992).
3. Yu. M. Aliev, V. P. Silin, and S. A. Uryupin, Pis'ma Zh. Éksp. Teor. Fiz. **57**, 187 (1993) [JETP Lett. **57**, 193 (1993)].
4. Yu. M. Aliev and V. P. Silin, Zh. Éksp. Teor. Fiz. **104**, 2526 (1993) [JETP **77**, 142 (1993)].
5. Yu. M. Aliev and V.P. Silin, Phys. Lett. A **117** (2), 259 (1993).
6. V. P. Silin, Pis'ma Zh. Éksp. Teor. Fiz. **58**, 726 (1993) [JETP Lett. **58**, 701 (1993)].
7. G. L. Alfimov and V. P. Silin, Zh. Éksp. Teor. Fiz. **106**, 671 (1994) [JETP **79**, 369 (1994)].
8. V. P. Silin, Pis'ma Zh. Éksp. Teor. Fiz. **60**, 442 (1994) [JETP Lett. **60** (1994)].
9. Yu. M. Ivanchenko and T. K. Soboleva, Pis'ma Zh. Éksp. Teor. Fiz. **51**, 100 (1990) [JETP Lett. **51**, 114 (1990)].
10. Yu. M. Ivanchenko and T. K. Soboleva, Phys. Lett. A **147**, 65 (1990).
11. Yu. M. Ivanchenko and T. K. Soboleva, Fiz. Tverd. Tela **32**, 2029 (1990) [Phys. Solid State **32**, 1181 (1990)]; R. G. Mints and I. B. Snapiro, Phys. Rev. B **51**, 3054 (1995).
12. I. O. Kulik and I. K. Yanson, Josephson Effect in Superconductive Tunneling Structures [in Russian] (Nauka, Moscow, 1970); Yu. E. Kuzovlev and A. I. Lomtev, Zh. Éksp. Teor. Fiz. **111**, 803 (1997) [JETP **84**, 986 (1997)].
13. A. I. Lomtev, Zh. Éksp. Teor. Fiz. **113**, 2256 (1998) [JETP **86**, 1234 (1998)].
14. A. I. Buzdin, L. N. Bulaevskiĭ, M. L. Kulich, *et al.*, *Usp. Fiz. Nauk* **144**, 597 (1984) [Sov. Phys. Usp. **144** (1984)]; A. I. Buzdin and L. N. Bulaevskiĭ, Usp. Fiz. Nauk **149**, 45 (1986) [Sov. Phys. Usp. **149**, 412 (1986)].
15. Yu. A. Izyumov, N. M. Plakida, and Yu. N. Skryabin, Usp. Fiz. Nauk **159**, 621 (1989) [Sov. Phys. Usp. **159**, 1060 (1989)].
16. *Superconductivity in Ternary Compounds*, Ed. by M. Maple and A. Fischer (Springer, Berlin, 1982; Mir, Moscow, 1985); *Physical Properties of the High-Temperature Superconductors*, Ed. by D. M. Ginsberg (World Science, Singapore, 1989; Mir, Moscow, 1990).
17. A. A. Abrikosov, *Foundations of Metal Theory* (Nauka, Moscow, 1987).
18. E. M. Lifshitz and L. P. Pitaevskiĭ, *Statistical Physics* (Nauka, Moscow, 1978).
19. H. Umezawa, H. Matsumoto, and M. Tachiki, *Thermo-Field Dynamics and Condensed States* (North-Holland, Amsterdam, 1982; Mir, Moscow, 1985).
20. B. I. Halperin and P. C. Hohenberg, Phys. Rev. **188**, 898 (1969).
21. P. M. Richards and M. B. Salamon, Phys. Rev. B**9**, 32 (1974).
22. A. I. Buzdin, Pis'ma Zh. Éksp. Teor. Fiz. **40**, 193 (1984) [JETP Lett. **40**, 956 (1984)].

Translated by N. Ostrovskaya

Physics of the Solid State, Vol. 42, No. 1, 2000, pp. 153–160. Translated from Fizika Tverdogo Tela, Vol. 42, No. 1, 2000, pp. 147–153.

LATTICE DYNAMICS. PHASE TRANSITIONS

X-ray Diffraction Study of Ion Thermal Vibrations in R_2CuO_4 (R = Pr and Gd) Crystals

A. A. Levin*, Yu. I. Smolin*, Yu. F. Shepelev*, E. I. Golovenchits, and V. A. Sanina****

**Grebenshchikov Institute of Silicate Chemistry, Russian Academy of Sciences, ul. Odoevskogo 24/2, St. Petersburg, 199155 Russia*

***Ioffe Physicotechnical Institute, Russian Academy of Sciences, Politekhnicheskaya ul. 26, St. Petersburg, 194021 Russia*

e-mail: E.Golovenchits@shuvpop.ioffe.rssi.ru

Received April 21, 1999

Abstract—An X-ray diffraction study is reported of the symmetry in the spatial distribution of thermal vibrations of Cu^{2+}, Gd^{3+}, and Pr^{3+} ions in Gd_2CuO_4 and Pr_2CuO_4 crystals. An analysis of the pattern of the angular thermal-vibration amplitude distribution obtained experimentally at different temperatures allows a conclusion about the character of the local Jahn–Teller effect for the Cu^{2+} ions, structural phase transitions, and the orbital ground state of the Cu^{2+} ions. © *2000 MAIK "Nauka/Interperiodica".*

This paper reports a high-precision X-ray diffraction investigation of the symmetry of ion displacements in thermal vibrations in R_2CuO_4 crystals (R = Pr and Gd). What one actually studies is the symmetry of the local crystal-field potential, because the spatial distribution of the amplitudes of ion thermal vibrations is determined by this symmetry. An analysis of the experimentally measured local-potential symmetry allows us to elucidate a number of important structural characteristics in crystals, such as the presence and character of local-symmetry distortions and of structural phase transitions. The main objective of this work was to study the Jahn–Teller effect and the orbital ground state of Cu^{2+} ions in R_2CuO_4 crystals with the rare-earth (RE) elements R = Pr and Gd. Information on these crystal characteristics is also contained in data on the symmetry of the effective local potential.

The quasi-2D R_2CuO_4 crystals with RE elements (R = Nd, Pr, Sm, Eu) possess the *T*' tetragonal structure (space group *I*4/*mmm*), which persists at all temperatures [1, 2]. La_2CuO_4 and Gd_2CuO_4 undergo structural phase transitions from the high-temperature tetragonal to the low-temperature orthorhombic phase (see [2] and [3], respectively). La_2CuO_4 and R_2CuO_4 with RE elements also differ in the symmetry of the nearest-neighbor environment of the Cu^{2+} ions, namely, in La_2CuO_4 it is octahedral, and in R_2CuO_4, it forms square lattices in the CuO_2 layers.

It is usually accepted that the Cu^{2+} ions in all R_2CuO_4 crystals (R = La and RE) have a singlet orbital ground state with wave functions $d_{x^2-y^2}$ or d_{z^2}, which originates from the orbital cubic doublet $\Gamma_3(e_g)$ (the notation adopted here is the same as in [4, 5]). This orbital state follows from calculations based on the simplest version of the crystal-field theory, taking into account only the nearest neighbors [4, 5]. However, we managed to explain the results of an experimental investigation [6, 7] of the magnetic and structural properties of the Eu_2CuO_4 crystal within a common scheme by assuming a nonzero orbital angular momentum of the Cu^{2+} ion in the ground state. It was accepted that the orbital ground state of the Cu^{2+} ion is a degenerate tetragonal doublet (with wave functions d_{xz} and d_{yz}) originating from the ground cubic triplet $\Gamma_5(t_{2g})$. Note that the anisotropy in the (001) plane observed experimentally [8] in R_2CuO_4 crystals with RE ions was considered to be due to the orbital ground state being a $d_{x^2-y^2}$ singlet with an admixture of a tetragonal doublet.

The symmetry of ion displacements in thermal vibrations and their anharmonicity were studied earlier in Eu_2CuO_4 and La_2CuO_4 crystals [9]. It was shown that the spatial distribution of Cu^{2+} thermal displacements in La_2CuO_4 corresponds to a two-well local potential created by the Jahn–Teller vibronic effect and to a singlet orbital ground state of the Cu^{2+} ion. The average orbital angular momentum for a singlet is known to be zero. Linear spin-orbit coupling is inefficient here, and the structural state of the crystal is determined by the vibronic Jahn–Teller interaction [4, 5].

In the case of the Eu_2CuO_4 crystal, the symmetry of the Cu^{2+} thermal displacements corresponded to an effective crystal-field local potential characteristic of a cubic nearest-neighbor environment (with a $Z = 8$ coordination) [9]. A degenerate orbital ground state of the Cu^{2+} ions in the form of a tetragonal doublet (or a mixed state with a strong enough admixture of an excited doublet to the ground singlet) should correspond to this effective local potential. In these condi-

1063-7834/00/4201-0153$20.00

tions, the average orbital angular momentum in the ground state is nonzero, and the linear spin-orbit coupling is efficient and suppresses the Jahn–Teller effect [4, 5]. Indeed, the experimentally measured symmetry of Cu^{2+} thermal displacements in Eu_2CuO_4 crystals does not reveal any manifestations of the vibronic Jahn–Teller effect, and the crystal retains a tetragonal symmetry for all temperatures [9].

Thus, experimental investigations of the symmetry of thermal vibrations of copper ions in La_2CuO_4 and Eu_2CuO_4 revealed a radical difference between the situations in these crystals. In this paper, an investigation of thermal vibrations is conducted similarly to those made in [9] for R_2CuO_4 crystals with the RE elements R = Pr and Gd. We were interested in the extent to which the situation for the R_2CuO_4 tetragonal crystals with different RE elements is common, as well as in the specific features of the Gd_2CuO_4 crystal, which has an orthorhombically distorted T' structure at $T < 600$ K and in which the nearest-neighbor environment of copper ions in the lattice is the same as in the purely tetragonal R_2CuO_4 crystals.

1. EXPERIMENTAL RESULTS

We performed a complete X-ray diffraction characterization of Pr_2CuO_4 and Gd_2CuO_4 crystals at four temperatures (145, 175, 295, and 395 K). The measurements were carried out on single crystals grown by spontaneous crystallization by a method similar to the one described in [10], but with a somewhat different crystallization regime. The ratio of the charge to the crucible volume, as well as the temperature regime of crystallization, were chosen so as to favor crystallization in the bulk (rather than on the melt surface) under a minimum temperature gradient. This permitted us to produce single crystals characterized by stoichiometry in oxygen and by a low structural strain density, which distinguishes them substantially from crystals grown in the surface layer of a melt in the presence of a temperature gradient.

The samples chosen for X-ray diffraction measurements were from the same lots from which the crystals for the investigation [11] of the magnetic and structural properties were taken. The samples chosen were rectangular prisms $0.18 \times 0.20 \times 0.11$ (Pr_2CuO_4) and $0.13 \times 0.10 \times 0.10$ (Gd_2CuO_4) mm in size. All the measurements were carried out on the same samples and in the same setup. During the measurements, the samples were cooled by blowing them over with nitrogen vapors of the appropriate temperature.

The measurements of X-ray reflections at all θ angles (up to that for which $\sin\theta/\lambda = 1.075$ Å^{-1}) were carried out on an automated single-crystal diffractometer by ω scanning under a perpendicular beam in the layer-by-layer arrangement by rotating the crystal around the a axis. MoK_α radiation ($\lambda = 0.71069$ Å) with a graphite monochromator was used.

The structural parameters were refined by the least-squares technique in a block-matrix approximation, mainly by the scheme employed in [9]. As in [9], the extinction was taken into account by the Becker–Coppens [12] technique for type-II crystals ($r_{ext} \ll \lambda g$, where r_{ext} is the radius of the spherical mosaic block, and g is a mosaic distribution parameter) with a Lorentzian distribution of the blocks.

The anharmonicity parameters of the thermal factor of Eu_2CuO_4 and La_2CuO_4 crystals were refined [9] by the Edgeworth model [13], which permitted one to obtain the minimum divergence factors (R and R_w). However, in this work both the Edgeworth and the Gram–Charlier models [14] gave practically the same values of the divergence factors. On the other hand, it is known [15] that the application of the Edgeworth model always results in the appearance of regions in which the probability density functions (PDF) are negative. In order to reduce such negative regions, this study made use of the Gram–Charlier model to refine the parameters of the anharmonic temperature factor

$$T(\mathbf{h}) = T_{harm}(\mathbf{h})[1 + (2\pi i)^3/3!\, c_{pqr}\mathbf{h}_p\mathbf{h}_q\mathbf{h}_r + (2\pi i)^4/4!\, d_{pqrs}\mathbf{h}_p\mathbf{h}_q\mathbf{h}_r\mathbf{h}_s].$$

Here, $T_{harm}(\mathbf{h}) = \exp(-\beta_{pq}\mathbf{h}_p\mathbf{h}_q)$ and β_{pq} are anisotropic harmonic temperature parameters, c_{pqr} and d_{pqrs} are anharmonic temperature parameters of the third and fourth order, respectively, and $\mathbf{h}$ is the scattering vector with components $(h_1, h_2, h_3) = (h, k, l)$. The temperature factor parameters thus obtained were used to construct the PDF, which is the Fourier transform of the temperature factor.

A preliminary analysis showed that at all temperatures, the Pr_2CuO_4 crystal has tetragonal symmetry (space group $I4/mmm$). The experimental and main structural parameters for Pr_2CuO_4 are listed in Table 1. The Gd_2CuO_4 crystal exhibited practically the same symmetry for all temperatures. Table 2 presents the experimental and main structural parameters for Gd_2CuO_4. A neutron diffraction study [3] revealed weak orthorhombic distortions caused by displacements of oxygen atoms (O1) in the CuO_2 plane of the Gd_2CuO_4 crystal. We took these distortions into account by splitting the positions of the O1 oxygen atoms into two half-filled, closely lying (~0.3 Å) positions (see Table 2). If one leaves these oxygen atoms in the ideal position (as in Pr_2CuO_4, see Table 1), then a least-squares refinement results in a very large temperature factor due to the anisotropic harmonic component β_{11}. Thus, the Cu^{2+} and Gd^{3+} positions in the model of the Gd_2CuO_4 structure accepted by us are the same as in the tetragonal Pr_2CuO_4 crystal, whereas the O1 ions are displaced from their positions.

Table 1. Details of the experiment and the structural parameters of the Pr_2CuO_4 single crystal (space group *I*4/*mmm*, dimensions $0.13 \times 0.10 \times 0.10$ mm)

Parameter	145 K	175 K	296 K	396 K
a, Å	3.949(1)	3.951(1)	3.953(2)	3.9583(6)
b, Å	*a*	*a*	*a*	*a*
c, Å	12.211(3)	12.215(3)	12.232(3)	12.2484(9)
N_{refl} ($I > 3\sigma(I)$)	288	327	266	266
R, %	2.15	2.78	2.05	2.11
R_w, %	2.25	2.93	2.24	2.28
μ, cm^{-1}	305.5(1)	305.1(1)	304.3(1)	303.12(7)
r_{ext}, Å	2602(15)	2626(16)	3288(15)	3380(16)
Pr(0, 0, *z*/*c*), *p* = 1				
z/*c*	0.35143(2)	0.35136(2)	0.35132(2)	0.35122(2)
B_{eq}, $Å^2$	0.302(2)	0.362(2)	0.522(2)	0.652(2)
U_{11}, Å	0.0676(3)	0.0679(4)	0.0861(3)	0.0934(3)
U_{22}, Å	U_{11}	U_{11}	U_{11}	U_{11}
U_{33}, Å	0.0484(6)	0.0673(6)	0.0707(4)	0.0854(4)
$c_{333} \times 10^8$	1.0(8)	−0.5(10)	−0.7(8)	−3.4(9)
$c_{113} \times 10^8$	−15(8)	−15(12)	−19(10)	−13(11)
$c_{223} \times 10^8$	c_{113}	c_{113}	c_{113}	c_{113}
$d_{1111} \times 10^9$	521(45)	511(53)	786(49)	1077(56)
$d_{2222} \times 10^9$	d_{1111}	d_{1111}	d_{1111}	d_{1111}
$d_{3333} \times 10^9$	2.2(3)	4.2(3)	1.5(3)	4.4(3)
$d_{1122} \times 10^9$	−317(23)	−371(30)	−513(24)	−980(31)
$d_{1133} \times 10^9$	−14(2)	−19(3)	−12(2)	−13(3)
$d_{2233} \times 10^9$	d_{1133}	d_{1133}	d_{1133}	d_{1133}
Cu(0, 0, 0), *p* = 1				
B_{eq}, $Å^2$	0.261(5)	0.304(7)	0.439(6)	0.536(7)
U_{11}, Å	0.060(1)	0.058(1)	0.072(1)	0.076(1)
U_{22}, Å	U_{11}	U_{11}	U_{11}	U_{11}
U_{33}, Å	0.053(2)	0.069(2)	0.079(1)	0.093(1)
$d_{1111} \times 10^9$	271(140)	174(179)	130(148)	144(169)
$d_{2222} \times 10^9$	d_{1111}	d_{1111}	d_{1111}	d_{1111}
$d_{3333} \times 10^9$	0.4(9)	1.0(11)	0.3(10)	1.7(11)
$d_{1122} \times 10^9$	−184(66)	−190(100)	−325(71)	−373(107)
$d_{1133} \times 10^9$	−15(7)	−16(10)	−8(8)	−30(9)
$d_{2233} \times 10^9$	d_{1133}	d_{1133}	d_{1133}	d_{1133}
O1(0, 1/2, 0), *p* = 1				
B_{eq}, $Å^2$	0.61(4)	0.56(5)	0.82(5)	1.06(6)
U_{11}, Å	0.096(6)	0.095(8)	0.105(6)	0.122(7)
U_{22}, Å	0.070(7)	0.051(11)	0.092(6)	0.099(7)
U_{33}, Å	0.096(6)	0.098(6)	0.107(5)	0.125(5)
O2(0, 1/2, 1/4), *p* = 1				
B_{eq}, $Å^2$	0.46(2)	0.56(3)	0.59(3)	0.72(3)
U_{11}, Å	0.081(3)	0.079(6)	0.080(4)	0.088(4)
U_{22}, Å	U_{11}	U_{11}	U_{11}	U_{11}
U_{33}, Å	0.068(6)	0.093(6)	0.099(5)	0.109(5)

Note: *a*, *b*, *c* are unit cell parameters; N_{refl} is the number of chosen independent nonequivalent reflections with $I > 3\sigma(I)$; *R* is the final divergence factor; R_w is the final weight divergence factor, weights calculated by Cruikshank; μ is the absorption coefficient (the error calculated from the errors of unit-cell measurements); r_{ext} is the extinction parameter obtained by least-squares refinement (the radius of the mosaic spherical block); *p* are site occupation coefficients; U_{ii} are rms thermal atom displacements (the harmonic part of the temperature factor); c_{pqr} and d_{pqrs} are the anharmonic temperature parameters of the third and fourth orders, respectively; B_{eq} is equivalent isotropic temperature factor, $B_{eq} = 4/3\Sigma\, \beta_{ii} a_i$, where β_{ii} are the anisotropic temperature parameters.

2. ANALYSIS OF EXPERIMENTAL DATA

It is known that the character of the local Jahn–Teller effect is determined to a considerable extent by the orbital ground state of the ions responsible for this effect [4, 5]. The type of the orbital ground state of the 3*d* ions also affects the principal interactions in magnetic crystals, namely, the exchange and spin-orbit coupling.

As shown in the nearest-neighbor approximation of the crystal-field theory, the orbital ground state of 3*d* ions is determined by the actual type of the ion (d^1–d^9) and by the character of the ion environment, which determines the sign of the crystal-field cubic component [4, 5]. The Cu^{2+} ion (d^9) can exist in the following orbital ground states in a cubic lattice: (*i*) the orbital doublet $\Gamma_3(e_g)$ (the orbital angular momentum $|1\rangle = \pm 2$ and the wave functions $d_{x^2-y^2}$ and d_{z^2}) for an octahedral ($Z = 6$) and a square ($Z = 4$) environment and (*ii*) the orbital triplet $\Gamma_5(t_{2q})$ (orbital angular momenta $|1\rangle = \pm 1$, 0 and the wave functions d_{xz}, d_{yz}, and d_{xy}) for a tetrahedron and a cube ($Z = 4$ and $Z = 8$) [4, 5].

If the local crystal-field potential is indeed created by the nearest-neighbor ion environment, determination of the orbital ground state of a 3*d* ion does not usually raise any problems. However, in the cases where the effective local potential of an ion in the lattice is not solely determined by its nearest-neighbor environment, the orbital ground state may differ from the one corresponding to the nearest-neighbor approximation; it can be quite complex and have an admixture of excited states. These cases require a special experimental investigation.

The experimentally observed local-potential symmetry can be associated with an effective nearest-neighbor ion environment in the cubic lattice, and one can assume that it is this environment that determines the orbital ground state. Because the potential of a cubic crystal field substantially exceeds, as a general rule, those of a tetragonal or an orthorhombic lattice distortion, the effective local potential symmetry obtained experimentally for the crystal under study offers the possibility of gaining information on the orbital ground state of the Cu^{2+} ions.

Gd_2CuO_4

Figures 1 and 2 plot the PDF by lines of equally probable displacements of the Cu^{2+} and Gd^{3+} ions in Gd_2CuO_4 in the (001) and (010) planes obtained at different temperatures.

Note that the PDF distribution of Cu^{2+} ions in Gd_2CuO_4 reproduces basically that for Eu_2CuO_4 (see Fig. 1 in [9]). For all temperatures at which the measurements were made, the Cu^{2+} PDFs in $Gd_2C_4O_4$ were found to be centrosymmetric, i.e. the positions of the maximum values of PDF (taken as 100%) are not displaced from the centers of the figures (which correspond to the ion positions in the cell). Thus, one can infer that in this case, the vibronic Jahn–Teller effect is not observed, because a characteristic feature of the Jahn–Teller effect is the displacement of ions from their central positions [4, 5].

Similar to Eu_2CuO_4, the PDF isolines in the (100) and (010) planes are extended along the [011] and [101] diagonals. The values of the softest effective local potential with a cubic ($Z = 8$) effective nearest-neighbor environment should correspond to these directions. In this case, Cu^{2+} ions in the Gd_2CuO_4 crystal should have a tetragonal doublet (d_{xz} and d_{yz}) as the orbital ground state. However, one cannot exclude here, as in the case of Eu_2CuO_4, a mixed orbital ground state, i.e., a state described by a combination of the wave functions of the orbital singlet and the orbital doublet. As already mentioned, if the orbital ground state is degenerate and represented by a tetragonal doublet, the average orbital angular momentum in the ground state is not completely frozen by the crystal field ($|l_z\rangle \neq 0$, although $|l_z\rangle \ll 1$ due to vibronic reduction [5]). Nevertheless, linear spin-orbit coupling is efficient in this case. The orbital ground state in the form of a doublet can occur only if the spin-orbit coupling exceeds the vibronic Jahn–Teller interaction, and if an orbital state with a nonzero angular momentum is dominant [4, 5]. We believe that this is the situation that occurs for the Cu^{2+} ions in Gd_2CuO_4 and Eu_2CuO_4. As is seen from Fig. 1, as the temperature increases, the relative Cu^{2+} displacements in the (010) and (100) planes along the [100] (or [010]) and [001] directions change. At $T = 145$ K (Fig. 1b), the maximum displacements are observed to occur along [100]; at $T = 175$ K (Fig. 1d), the displacements are the largest along the [001] directions, and at still higher temperatures, displacements along [100] are again dominant. Thus, near $T \approx 175$ K the situation is special in that the local effective potential changes without any change in the general crystal symmetry; i.e., we have an isostructural phase transition. Note that these data correlate with experimental microwave measurements of dielectric permittivity [11], which also indicated the presence of a structural transition in a Gd_2CuO_4 crystal at a similar temperature.

Turning now to the main features of the PDF of Gd^{3+} ions in Gd_2CuO_4 crystals (Fig. 2), we note that here, the PDF distribution symmetry is basically similar to that of Cu^{2+} ions in the same crystals (Fig. 1). We also have here a predominantly cubic coordination of the effective local potential and, likewise, there are no displacements of the PDF peaks from the centers of the figures. As seen from Figs. 1 and 2, in the vicinity of 175 K the temperature dependence of ion displacements in thermal vibrations exhibits a feature that can be associated with an isostructural phase transition.

Note that the nearest-neighbor environment of RE ions in R_2CuO_4 tetragonal crystals with a *T*' structure

Table 2. Details of the experiment and the structural parameters of the Gd_2CuO_4 single crystal (space group $I4/mmm$, dimensions $0.13 \times 0.10 \times 0.10$ mm)

Parameter	145 K	175 K	296 K	396 K
a, Å	3.887(1)	3.888(1)	3.8917(5)	3.895(1)
b, Å	a	a	a	a
c, Å	11.876(1)	11.877(1)	11.8883(5)	11.8952(6)
N_{refl} ($I > 3\sigma(I)$)	253	251	250	257
R, %	2.87	2.69	2.79	2.76
R_w, %	3.17	2.80	2.96	2.95
μ, cm^{-1}	424.8(2)	424.6(2)	423.3(1)	422.4(2)
r_{ext}, Å	2826(36)	2434(33)	2897(35)	3105(34)
Gd(0, 0, z/c), $p = 1$				
z/c	0.34926(3)	0.34926(3)	0.34922(3)	0.34920(3)
B_{eq}, $Å^2$	0.251(3)	0.244(3)	0.478(3)	0.537(2)
U_{11}, Å	0.0607(6)	0.0582(5)	0.0832(4)	0.0850(4)
U_{22}, Å	U_{11}	U_{11}	U_{11}	U_{11}
U_{33}, Å	0.0463(10)	0.0500(9)	0.0655(7)	0.0771(6)
$c_{333} \times 10^8$	–1.8(14)	–0.6(13)	–1.4(14)	–2.4(13)
$c_{113} \times 10^8$	–0.3(16)	–3.9(14)	–25(16)	–10(15)
$c_{223} \times 10^8$	c_{113}	c_{113}	c_{113}	c_{113}
$d_{1111} \times 10^9$	251(78)	191(66)	765(78)	502(63)
$d_{2222} \times 10^9$	d_{1111}	d_{1111}	d_{1111}	d_{1111}
$d_{3333} \times 10^9$	–0.02(54)	–1.0(5)	–3.4(5)	–2.8(5)
$d_{1122} \times 10^9$	–261(39)	–73(31)	–673(36)	–614(36)
$d_{1133} \times 10^9$	3.0(43)	6.0(37)	36(4)	21(4)
$d_{2233} \times 10^9$	d_{1133}	d_{1133}	d_{1133}	d_{1133}
Cu(0, 0, 0), $p = 1$				
B_{eq}, $Å^2$	0.235(10)	0.234(9)	0.447(10)	0.529(9)
U_{11}, Å	0.054(2)	0.052(2)	0.074(1)	0.079(1)
U_{22}, Å	U_{11}	U_{11}	U_{11}	U_{11}
U_{33}, Å	0.055(3)	0.059(3)	0.078(2)	0.088(2)
$d_{1111} \times 10^9$	–33(278)	–10(231)	305(262)	509(236)
$d_{2222} \times 10^9$	d_{1111}	d_{1111}	d_{1111}	d_{1111}
$d_{3333} \times 10^9$	–1.9(19)	–3.6(19)	–7.3(21)	–8.6(20)
$d_{1122} \times 10^9$	–46(144)	–18(123)	–649(132)	–652(129)
$d_{1133} \times 10^9$	12(17)	20(14)	58(16)	41(14)
$d_{2233} \times 10^9$	d_{1133}	d_{1133}	d_{1133}	d_{1133}
O1(x/c, 1/2, 0), $p = 0.5$				
x/c	0.0452(22)	0.0504(22)	0.0491(25)	0.0417(26)
B_{eq}, $Å^2$	0.52(13)	0.56(11)	0.84(13)	0.99(15)
U_{11}, Å	0.070(34)	0.087(22)	0.113(21)	0.130(22)
U_{22}, Å	0.086(14)	0.089(13)	0.099(12)	0.096(11)
U_{33}, Å	0.086(12)	0.076(13)	0.098(12)	0.106(9)
O2(0, 1/2, 1/4), $p = 1$				
B_{eq}, $Å^2$	0.60(5)	0.50(4)	0.56(4)	0.81(15)
U_{11}, Å	0.089(8)	0.078(7)	0.080(6)	0.097(6)
U_{22}, Å	U_{11}	U_{11}	U_{11}	U_{11}
U_{33}, Å	0.083(11)	0.082(10)	0.093(9)	0.110(8)

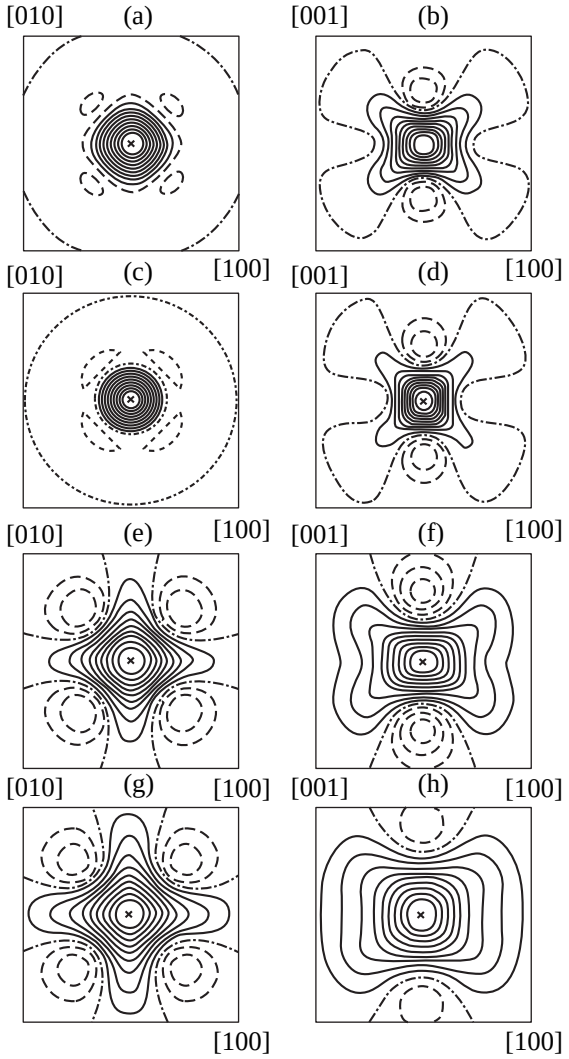

Fig. 1. PDF of Cu^{2+} ions in Gd_2CuO_4 crystals for the planes (a, c, e, g) (001) and (b, d, f, h) (010) obtained at the temperatures (K): (a, b) 145, (c, d) 175, (e, f) 295, and (g, h) 395. The PDFs curves were constructed with a 10% step from the maximum value (100%) specified in the figures by a cross. The dash-dotted lines correspond to PDF zero. The negative values of the PDF are shown by dashed lines. The frame size 0.48×0.48 Å^2.

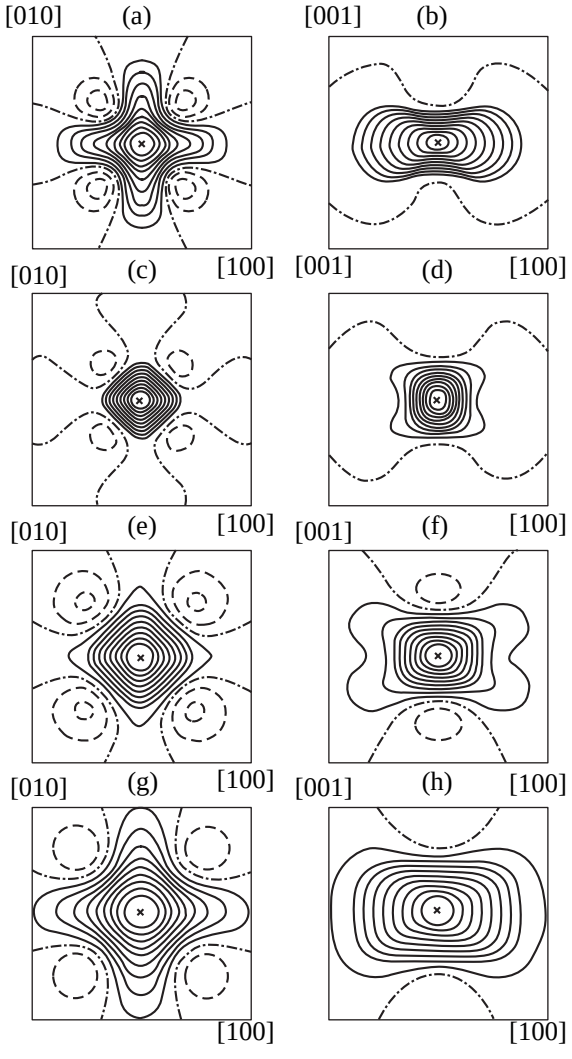

Fig. 2. PDF of Gd^{3+} ions in Gd_2CuO_4 crystals for the planes (a, c, e, g) (001) and (b, d, f, h) (010) obtained at the temperatures (K): (a, b) 145, (c, d) 175, (e, f) 295, and (g, h) 395. The PDF step, line designation, and the frame size are the same as in Fig. 1.

does have cubic oxygen-ion coordination (with $Z = 8$). However, the upper and lower four oxygen ions, which are the nearest neighbors of the RE ions and are their body centers, are not fully equivalent, because one of the four-ion groups lies in the CuO_2 plane (the O1 positions in Tables 1 and 2), and the second group is located in the plane containing only oxygen ions (the O2 positions in Tables 1 and 2). As a result, the pattern of the local RE symmetry distortions can be affected by the states of both the copper and RE ions. In the cases where the RE ions are not of the Jahn–Teller type, and the Cu^{2+} ions do not exhibit the vibronic Jahn–Teller effect, the PDF of RE ions should have cubic symmetry (with $Z = 8$). The Gd^{3+} ion, whose ground state is $^8S_{7/2}$, is a typical example of an RE without the Jahn–Teller effect, and Cu^{2+} ions in Gd_2CuO_4 crystals do not exhibit the vibronic Jahn–Teller effect (see Fig. 1). In this case, the local potential for the Gd^{3+} ions indeed has cubic symmetry. Thus, the similarity between the angular PDF distributions of the Gd^{3+} and Cu^{2+} ions in Gd_2CuO_4 crystals may be considered as an additional argument for the correctness of the above analysis of the PDF symmetry for the Cu^{2+} ions.

Pr_2CuO_4

The PDF of Cu^{2+} ions in the Pr_2CuO_4 crystal is a multiply connected region with six maxima displaced

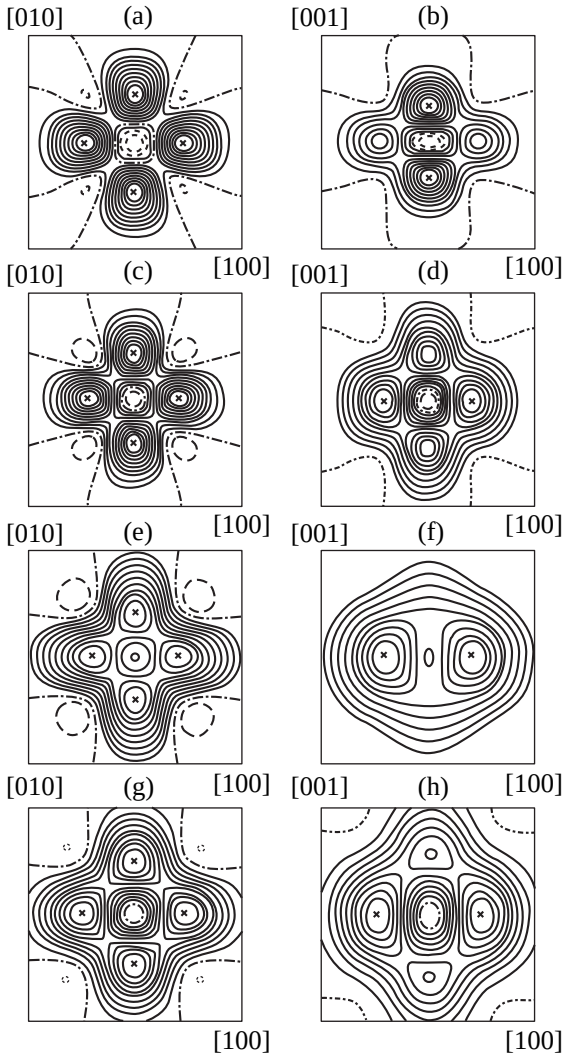

Fig. 3. PDF of Cu^{2+} ions in Pr_2CuO_4 crystals for the planes (a, c, e, g) (001) and (b, d, f, h) (010) obtained at the temperatures (K): (a, b) 145, (c, d) 175, (e, f) 295, and (g, h) 395. The PDF step, line designation, and the frame size are the same as in the preceding figures.

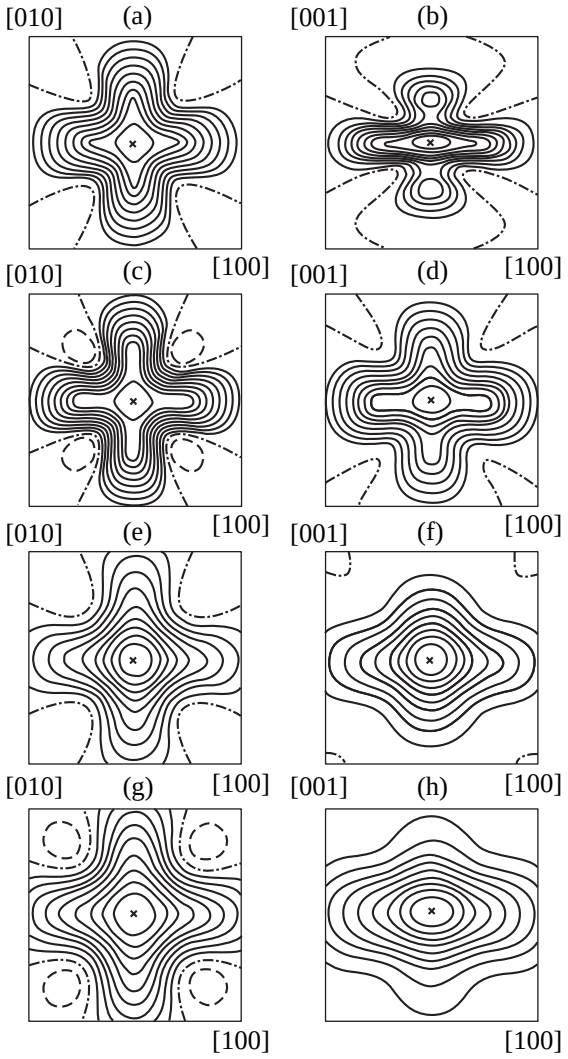

Fig. 4. PDF of Pr^{3+} ions in Pr_2CuO_4 crystals for the planes (a, c, e, g) (001) and (b, d, f, h) (010) obtained at the temperatures (K): (a, b) 145, (c, d) 175, (e, f) 295, and (g, h) 395. The PDF step, line designation, and the frame size are the same as in the preceding figures.

symmetrically from the center (Fig. 3). The equilibrium ion positions (corresponding to the maximum values of the PDF) are displaced from the central position and, hence, the vibronic Jahn–Teller effect can exist. However, in Pr_2CuO_4, in contrast to La_2CuO_4 (see Fig. 2 in [9]), the lowering of the local symmetry induced by the Jahn–Teller effect is substantially weaker, with the corresponding local potential having six wells with the tetragonal symmetry intact. In this case, the vibronic Jahn–Teller interaction is apparently weaker than in La_2CuO_4. Note that each of the off-center regions of the multiply connected PDF has the same symmetry as in the Gd_2CuO_4 and Eu_2CuO_4 crystals, which corresponds to the cubic coordination of the local effective potential for Cu^{2+} ions ($Z = 8$).

The observed angular PDF of the Cu^{2+} ions in Pr_2CuO_4 can be interpreted if one assumes the existence here of a mixed orbital ground state described by wave functions of both the singlet state and the tetragonal doublet. The state of the crystal is determined by both the vibronic Jahn–Teller and the spin-orbit coupling, which are close in magnitude. In these conditions, one observes neither a complete suppression of the vibronic Jahn–Teller effect (as in Gd_2CuO_4 and Eu_2CuO_4) nor total splitting, down to the singlets of the orbital ground state (as in La_2CuO_4).

As in Gd_2CuO_4, in Pr_2CuO_4 the Cu^{2+} displacements in the (010) and (100) planes exhibit a temperature dependence (see Figs. 3b, 3d, 3f, 3h). In the low-temperature region (Fig. 3b, $T = 145$ K), the displacements

along the [001] directions are the largest; at the same time at $T = 175$, 295, and 395 K (Figs. 3d, 3f, 3h), the largest are the [100] (or [010]) displacements. Thus, the maximum displacements of the Cu^{2+} ions in thermal vibrations undergo a change in direction at a temperature within the 145–175 K interval. Studies of the microwave dielectric permittivity in Pr_2CuO_4 crystals revealed a diffuse structural phase transition in the same temperature interval [11]. An analysis of the angular PDF distributions permits the conclusion that in this temperature region, the crystal undergoes an isostructural phase transition, which retains the general symmetry of the crystal while bringing about a change in the direction of the maximum Cu^{2+} ion displacement.

As is evident from Fig. 4, the PDF of Pr^{3+} ions in Pr_2CuO_4, in contrast to Gd^{3+} ions in Gd_2CuO_4, reproduces less accurately that of the copper ions, although it is fairly similar in shape to the Gd^{3+} PDF. This appears only natural, because the local positions of RE elements in all R_2CuO_4 crystals are close. Some differences in the shape of the PDF of Pr^{3+} ions in Pr_2CuO_4 from that of Gd^{3+} ions in Gd_2CuO_4 are apparently due to the fact that Pr^{3+} ($^3H_4$) is a Jahn–Teller ion, and copper ions in Pr_2CuO_4 exhibit the vibronic Jahn–Teller effect (see Fig. 3). It is these two factors that apparently account for some PDF asymmetry along the [001] direction (Figs. 4b, 4d, 4f, 4h). Note that the Jahn–Teller effect with RE elements manifests itself most clearly for Eu^{3+} ions in Eu_2CuO_4 crystals (see Fig. 4 in [9]). In all the crystals that we studied (with the exception of La_2CuO_4), the PDFs of copper and RE ions exhibit extended flat regions, indicating a quite strongly developed anharmonicity of ion thermal vibrations. The same is seen from Tables 1 and 2. Studies of the magnetic and dielectric properties of R_2CuO_4 crystals (R = Eu, Pr, Gd) [6, 7, 11] established the existence in them for $T > 100$ K of diffuse phase transitions and nonuniform structural and magnetic states of the random-field type. It is apparently such states and phase transitions that could account for the observed anharmonicity of ion thermal vibrations in these crystals.

Thus, Cu^{2+} ions in R_2CuO_4 crystals (R = Eu, Pr, Gd) have an orbital ground state with a nonzero orbital angular momentum. As for crystals with RE elements (R = Eu, Gd), the properties of these crystals are determined by the degenerate ground tetragonal doublet and spin-orbit coupling. In La_2CuO_4, the orbital ground state does not have a nonzero orbital angular momentum (orbital singlet), and the main interaction determining the structural properties of the crystal is the vibronic Jahn–Teller coupling. In the Pr_2CuO_4 crystal, we observed a more complex situation, where a mixed orbital ground state (a singlet and a tetragonal doublet) exists, and both types of the interaction are efficient (the spin-orbit and the vibronic Jahn–Teller coupling).

ACKNOWLEDGMENTS

This work was supported by the Russian Foundation for Basic Research, project no. 97-02-18061.

REFERENCES

1. H. Müller-Buschbäumand and W. Wollschlager, Z. Anorg. Allg. Chem. **414**, 76 (1975).
2. L. A. Muradyan, R. A. Tamazyan, A. M. Kevorkov, *et al.*, Kristallografiya **35**, 861 (1990).
3. M. Braden, W. Paulus, A. Cousson, *et al.*, Europhys. Lett. **25**, 625 (1994).
4. K. I. Kugel' and D. I. Khomskiĭ, Usp. Fiz. Nauk **136**, 621 (1982).
5. A. Abragam and B. Bleaney, *Electron Paramagnetic Resonance of Transition Ions* (Clarendon, Oxford, 1970; Mir, Moscow, 1972), Vol. 2, p. 349.
6. A. V. Babinskiĭ, S. L. Ginzburg, E. I. Golovenchits, *et al.*, Pis'ma Zh. Éksp. Teor. Fiz. **57**, 289 (1993).
7. E. I. Golovenchits, V. A. Sanina, and A. V. Babinskiĭ, Zh. Éksp. Teor. Fiz. **110**, 714 (1996).
8. T. Yildrim, A. B. Harris, A. Aharony, *et al.*, Phys. Rev. B: Condens. Matter **56**, 260 (1997).
9. E. I. Golovenchits, V. A. Sanina, A. A. Levin, *et al.*, Fiz. Tverd. Tela (St. Petersburg) **39**, 1600 (1997).
10. A. V. Babinskiĭ, E. I. Golovenchits, N. V. Morozov, *et al.*, Fiz. Tverd. Tela (Leningrad) **34**, 60 (1992).
11. E. I. Golovenchits and V. A. Sanina, Fiz. Tverd. Tela (St. Petersburg) **41**, 1437 (1999).
12. P. J. C. Becker and P. Coppens, Acta Crystallogr. Sect. A: Cryst. Phys., Diffr., Theor. Gen. Crystallogr. **30**, 129 (1974).
13. V. G. Tsirel'son, Kristallokhimiya **27** (1), 268 (1993).
14. *International Tables for X-ray Crystallography* (Kynoch, Birmingham, 1974), Vol. 4.

Translated by G. Skrebtsov

Physics of the Solid State, Vol. 42, No. 1, 2000, pp. 161–164. Translated from Fizika Tverdogo Tela, Vol. 42, No. 1, 2000, pp. 154–157.

LATTICE DYNAMICS. PHASE TRANSITIONS

Spontaneous Phase Transition from Relaxor to Macrodomain Ferroelectric State in Single-Crystal $PbSc_{0.5}Nb_{0.5}O_3$– $BaSc_{0.5}Nb_{0.5}O_3$ Solid Solutions

I. P. Raevskiĭ, V. V. Eremkin, V. G. Smotrakov, E. S. Gagarina, and M. A. Malitskaya

Research Institute of Physics, Rostov State University, Rostov-on-Don, 344090 Russia

e-mail: smotr@iphys.rnd.runnet.ru

Received March 10, 1999

Abstract—The cooling of $Pb_{1-x}Ba_xSc_{0.5}Nb_{0.5}O_3$ solid solutions with $x \le 0.04$ leads to a spontaneous transition from a relaxor to a macrodomain ferroelectric state, accompanied by anomalous variation of the dielectric and optical properties of the material. As the barium content in the system increases, the relaxor state becomes more stable and eventually "freezes" at $x \approx 0.05$. The crystals with $x = 0.06$ exhibited the appearance of a macrodomain ferroelectric phase induced both by an external electric field with a strength of 1.5 kV/cm and by an internal electric field formed in the course of dielectric aging. © *2000 MAIK "Nauka/Interperiodica".*

1. INTRODUCTION

Properties of a compositionally-ordered ferroelectric compound with the formula $PbSc_{0.5}Nb_{0.5}O_3$ (PSN) can be modified within a broad range even without changing the chemical composition, namely, by varying the degree of ordering of the Sc and Nb ions occupying equivalent sites of the crystal lattice [1–3]. In the state of high ordering, the PSN crystals and ceramics exhibit a non-smeared ferroelectric phase transition. In a disordered state of the ferroelectric, the transition smears and PSN exhibits the properties characteristic of the so-called relaxors [2], in which both the maximum dielectric permittivity ε_m and the temperature T_m corresponding to the maximum of $\varepsilon(T)$ are significantly dependent on the temperature.

Later investigations [4] showed that even almost complete disorder of Sc and Nb in the structure of PSN ceramics is insufficient to obtain a stable relaxor state similar to that observed for a model relaxor system $PbMg_{1/3}Nb_{2/3}O_3$: cooling of a PSN sample is accompanied by a spontaneous transition from a relaxor (microdomain) to a macrodomain state reflected by a jump on the $\varepsilon(T)$ curve. In order to obtain a stable relaxor state in PSN, it is necessary to provide for an additional disordering of the crystal lattice. Disappearance of the jump in $\varepsilon(T)$ and enhancement of the frequency dependence of ε in the PSN ceramics, interpreted as "freezing" of the relaxor state [4], was achieved by increasing the concentration of lead vacancies V_{Pb} from 0.2–0.5 at. % (the level inherent in the ceramics as a result of uncontrolled PbO evaporation in the course of annealing) to 1.5–2 at. % [5]. However, the structural investigation [5] showed that even this increase in the V_{Pb} concentration does not eliminate the spontaneous transition from relaxor to macrodomain state, although the transition becomes strongly smeared and takes place at lower temperatures. It should be also noted that the V_{Pb} formation leads to the appearance of approximately the same number of oxygen vacancies, that is, the concentration of induced defects is in fact approximately twice that of V_{Pb}. Moreover, the V_{Pb} vacancies are essentially the charged polar defect, which accounts for their strong interaction with heterophase fluctuations [6] and must favor "freezing" of the relaxor state. Thus, it is still unclear what is the defect concentration actually ensuring the relaxor state "freezing" in PSN and whether this critical defect concentration depends on their nature (polar vs. nonpolar).

It is known that a partial substitution of isovalent barium ions for lead in the PSN ceramics also results in smearing of the $\varepsilon(T)$ maximum and increasing of the relaxor properties [7–9]. However, since the ion radius of Ba^{2+} is greater than that of Pb^{2+}, the defects formed upon the $Pb^{2+} \longrightarrow Ba^{2+}$ substitution must be nonpolar. Moreover, while the concentration and homogeneity of the V_{Pb} distribution in a sample are difficult to control, the partial substitution of barium for lead would simplify this task. We may expect that a gradual increase in the barium content would allow an increase in stability of the relaxor state in PSN up to its complete "freezing."

It is difficult to perform such investigations on ceramic samples because of difficulties in obtaining equilibrium solid solutions of the $Pb_{1-x}Ba_xSc_{0.5}Nb_{0.5}O_3$ (PBSN) system, which are related to a considerable difference in reactivity between the PSN and $BaSc_{0.5}Nb_{0.5}O_3$ (BSN) [8]. This difference leads to a gradient of the component concentrations in the grains of PBSN ceramics, which is reflected by additional anomalies in the $\varepsilon(T)$ curves reported in a number of works [8, 9]. Smearing of the $\varepsilon(T)$ maximum as a result of the formation of macroscopic and/or mesoscopic

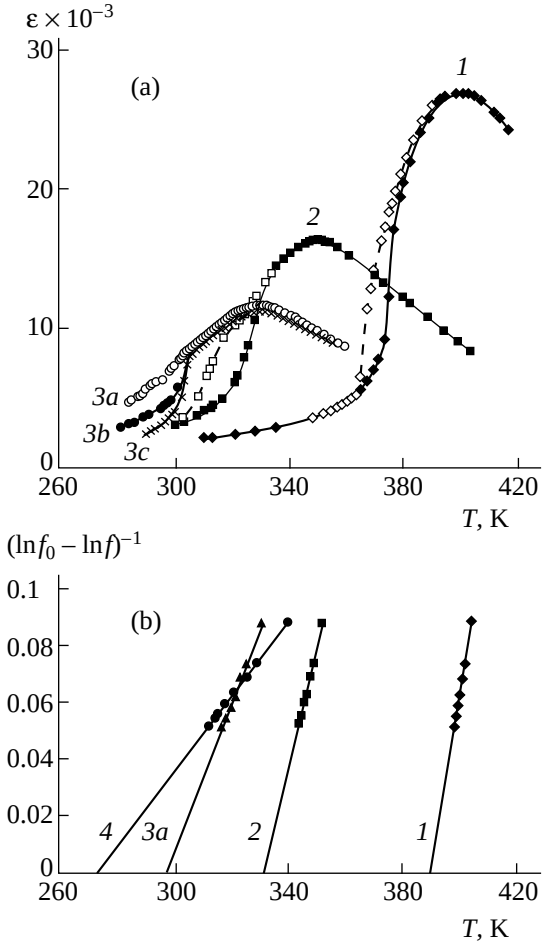

Fig. 1. (a) The ε(*T*) plots for the $Pb_{1-x}Ba_xSc_{0.5}Nb_{0.5}O_3$ solid solution crystals with x = (*1*) 0.2, (*2*) 0.04, and (*3*) 0.06 measured on heating (solid lines) and subsequent cooling (dashed lines); curve *3b* was measured upon holding the crystal for 80 days at room temperature (aged sample); curve *3c* was measured upon cooling the crystal from 100 to 30°C in a constant electric field with the strength 1500 V/cm; (b) the plots of $(\ln f_0 - \ln f)^{-1}$ versus T_m for $Pb_{1-x}Ba_xSc_{0.5}Nb_{0.5}O_3$ with x = (*1*) 0, (*2*) 0.04, (*3a*) 0.06, and (*4*) 0.08 illustrating validity of the Vogel–Fulcher law.

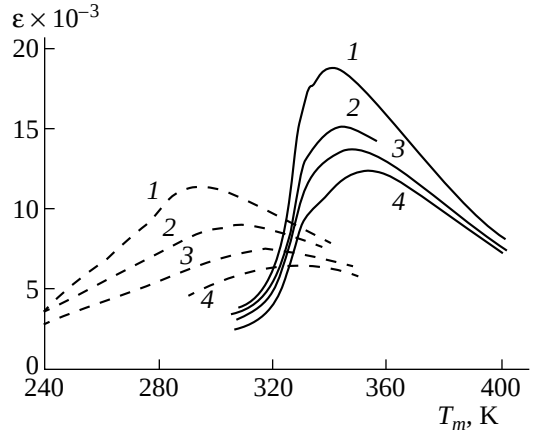

Fig. 2. The ε(*T*) plots for the $Pb_{1-x}Ba_xSc_{0.5}Nb_{0.5}O_3$ solid solution crystals with x = 0.04 (solid lines) and 0.08 (dashed lines) measured on heating at various frequencies of the probing electric field f (Hz): (*1*) 10^3, (*2*) 10^4, (*3*) 10^5, and (*4*) 10^6.

composition inhomogeneities masks the effects developed on the microscopic level, related to the ion substitution in the crystal lattice sites. In order to reach the equilibrium state, it is necessary to increase the temperature and duration of annealing of the samples of PBSN ceramics. However, this would increase the probability of formation of the additional V_{Pb} vacancies favoring, as noted above, the relaxor state "freezing."

The purpose of this work was to obtain single crystals of a PBSN solid solution and study the effect of the isovalent substitution of barium for lead on the spontaneous transition from relaxor to macrodomain ferroelectric state.

2. EXPERIMENTAL RESULTS AND DISCUSSION

Transparent yellow crystals of $Pb_{1-x}Ba_xSc_{0.5}Nb_{0.5}O_3$ with $0 \le x \le 0.58$ (determined from data obtained with a Camebax-Micro electron microscope–analyzer), with predominantly an isometric shape and a size of 1–2 mm, were grown by the bulk crystallization technique. The methods of crystal growth and investigation were analogous to those described elsewhere [10]. The X-ray diffraction analysis showed that the value of the reduced unit cell parameter of a rhombohedrally distorted perovskite crystal lattice increases almost linearly with x. In contrast to the case of ceramics [8], no line broadening was observed in the X-ray diffraction patterns of PBSN as compared to those of PSN, which is indirect evidence of the equilibrium character of the solid solutions studied. Nor did the diffractograms of the PBSN crystals contained any superstructural reflections related to ordering of the Sc and Nb ions. This result agrees with our previous data [3, 10] indicating that PSN crystals grown in the temperature range employed (1170–1060°C) are strongly disordered.

The results of dielectric measurements showed that increasing barium content leads to decrease in the T_m value corresponding to the ε(*T*) maximum for PBSN crystals, increase in the degree of smearing of this maximum, and a decrease in the peak height ε_m (Fig. 1a). All the crystal samples studied exhibited a significant frequency dispersion of ε values and an increase in the T_m value with the frequency f of the probing electric field. The pattern of variation of the ε(*T*) curves with increasing frequency observed in the crystals with $x \ge 0.08$ was typical of the relaxor behavior (Fig. 2). For the crystals with $0 \le x \le 0.04$, the ε(*T*) curves exhibit a jump at a temperature slightly below T_m (Figs. 1a and 2). The position of this feature, in contrast to the T_m value, is virtually independent of the frequency f, but shows a considerable temperature hysteresis increasing with x (Fig. 1a). A similar anomaly of ε(*T*) was previously observed for disordered PSN ceramics and related to a spontaneous transition from relaxor to macrodomain ferroelectric state [4, 5].

Since the latter transition was previously observed only in ceramic samples, it was of interest to study

related changes in the optical properties of PSN and PBSN crystals. Room-temperature measurements in the transmitted polarized light showed that crystals exhibit symmetric quenching (at an angle of 45° relative to the side crystal faces) during the table rotation. This character of quenching corresponds to a rhombohedral structure of the low-temperature crystal phase formed in PSN ad PBSN. Indeed, because of the natural crystal faceting by planes on the {100} type in the perovskite basis and the possibility of the optical axis orientation in directions of the [111] type, the axes of the central cross-section of the optical indicatrix by the plane of the wave front parallel to a developed plane of the plate crystal make an angle of ~45° with the visible plate edges.

On heating, the crystal exhibits a transition to the relaxor state accompanied by a sharp drop in the magnitude of birefringence (to virtually zero in the central part of the sample) followed by the motion of smeared phase fronts toward the outer boundaries. Separate parts of the crystal (in particular, those near the crystal ends) may remain clarified even above the phase transition temperature, still exhibiting quenching in the forward direction. Incomplete quenching of the crystal is probably related to internal mechanical stresses caused by defects, including the near-surface growth layers.

On the subsequent cooling, the spontaneous transition to a macrodomain ferroelectric phase was accompanied by the development of birefringence, typical of the crystals belonging to the rhombohedral system, and by a considerable temperature hysteresis with a width close to that observed for the $\varepsilon(T)$ curve. The aforementioned increase in the T_m value of PBSN with the probing field frequency f is well described by the Vogel–Fulcher formula

$$f = f_0 \exp[-E/k(T_m - T_0)], \qquad (1)$$

where f_0 is the frequency of attempts to surmount the potential barrier E, k is the Boltzmann constant, T_0 ids the Vogel–Fulcher temperature interpreted as a temperature of the "static freezing" of electric dipoles or the transition to a "dipole glass" state [4–6, 11] (Fig. 1b). For PBSN crystals, $f_0 = (0.5–1) \times 10^{11}$ Hz is close to the values reported for some other ferroelectric relaxors [4, 11]. In the crystals with $0 \le x \le 0.04$, the T_0 values are close to the temperature of the jump in $\varepsilon(T)$, which is analogous to what was observed for disordered PSN ceramics [4, 5] (Fig. 1). The activation energies E in the Vogel–Fulcher formula, as well as the differences T between T_m (measured at f = 1 kHz) and T_0, increase with x to reach $\Delta T \approx 50–60$ K and $E = 0.08 \pm 0.01$ eV at $x \approx 0.4$ and then remain approximately constant. It should be noted that nearly the same ΔT and E values were observed for the crystals of a classical ferroelectric relaxor $PbMg_{1/3}Nb_{2/3}O_3$ [4, 11]. Note that the curves of $\Delta T(x)$ and $E(x)$ exhibit breaks at $x \approx 0.05$, that is, in the region of Ba concentrations corresponding to "freezing" of the relaxor state (Fig. 3).

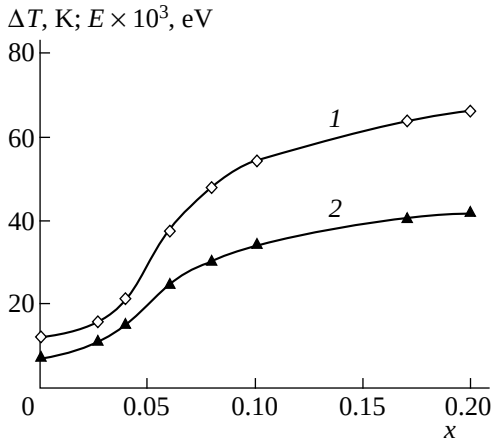

Fig. 3. The plots of (*1*) activation energy E in the Vogel–Fulcher law and (*2*) difference ΔT between the position of maximum dielectric permittivity (measured at 1 kHz) and the Vogel–Fulcher temperature T_0 versus concentration for the $Pb_{1-x}Ba_xSc_{0.5}Nb_{0.5}O_3$ solid solution crystals.

Some of the crystals studied exhibited the phenomenon of so-called dielectric aging, whereby the ε values and the dielectric losses tend to decrease with time. A similar aging was previously observed both in the usual ferroelectrics and in relaxors, and was explained by stabilization (fixation) of the domain structure as a result of the screening of domain boundaries and the formation of internal electric fields [2, 12, 13]. In the crystals with x = 0.06, exhibiting no spontaneous transition from relaxor to macrodomain state during cooling of a paraelectric phase, the room-temperature aging for several weeks resulted in development of the optical birefringence. Subsequent heating made the crystal optically isotropic at a temperature markedly lower than T_m. This temperature also corresponded to a jump on the $\varepsilon(T)$ curve (Fig. 1a, curve *3b*).

Thus, the properties of aged crystals with x = 0.06 are analogous to those of the PBSN crystals with a lower Ba content (in which the heating induces the transition from macrodomain ferroelectric to relaxor state) and of the classical ferroelectric relaxors $PbMg_{1/3}Nb_{2/3}O_3$ and $PbMg_{1/3}Zn_{2/3}O_3$, subjected to the action of a constant electric field with a strength exceeding 2–2.5 and 10–20 kV/cm, respectively [14]. Apparently, the observed changes in properties of the PBSN crystals are related to the appearance of a macrodomain ferroelectric phase under the action of internal electric fields formed in the course of dielectric aging. The magnitude of these fields in a relaxor ceramics of the $PbMg_{1/3}Nb_{2/3}O_3$–$PbTiO_3$ reached a level of several kV/cm [2], being comparable with the external field strength necessary to induce the macrodomain phase formation in $PbMg_{1/3}Nb_{2/3}O_3$.

In order to obtain additional information concerning the effect of the electric field on the properties of PBSN, we have measured the $\varepsilon(T)$ curves of a crystal with x = 0.06 in the regime of heating without applied

field upon cooling the crystal from 100 to 30°C in a constant electric field of various strength. After each measurement, the crystal was heated to 150°C to remove the residual effects. At an external field strength of 0.5 kV/cm, no changes were observed in the shape of the $\varepsilon(T)$ curve as compared to that of the non-aged crystal cooled in the absence of the field. On cooling in a field of 1.5 kV/cm, the $\varepsilon(T)$ curve exhibited a jump similar to that observed for an aged crystal (Fig. 1a, curve *3c*). Heating the crystal to 120–150°C completely eliminated the residual effects, and the $\varepsilon(T)$ curves observed on the subsequent cooling and heating coincided with the initial curve (Fig. 1a, curve *3a*). These results give evidence that the external field, comparable with the internal ones, formed in the course of dielectric aging [2] and induces a macrodomain ferroelectric phase in PBSN crystals with $x = 0.06$. Apparently, a change in the properties of PBSN crystals with $x = 0.06$ in the course of aging is analogous to the behavior reported in some works [15] where a macrodomain ferroelectric state was observed in relaxor systems as a result of the electron beam action during the electron-microscopic investigation. Indeed, the intensification of the dielectric aging process under the action of light or ionizing radiation, increasing the concentration of nonequilibrium charge carriers and facilitating development of the screening effects, was observed in many ferroelectrics [12, 13].

Thus, the relaxor (microdomain) state in disordered PSN crystals is unstable. Cooling of the crystals leads to their spontaneous transition into a macrodomain ferroelectric state, which is accompanied by anomalous variation of the dielectric and optical properties. During partial substitution of barium for lead, which results in additional disordering of the crystal lattice, stability of the relaxor state gradually increases and this state exhibits "freezing" at a critical barium concentration of $x \approx 0.05$. In crystals with a barium content slightly above the critical level, the macrodomain ferroelectric phase can be induced by application of a comparatively small external electric field or by a internal electric field formed in the course of dielectric aging.

Note that the critical barium concentration $x \approx 0.05$ corresponding to "freezing" of the relaxor phase in PSN–BSN crystals is close to the total concentration of vacancies in the lead and oxygen sublattices corresponding to suppression of the spontaneous transition from relaxor to macrodomain ferroelectric state in PSN ceramics. Thus, the concentration of defects responsible for "freezing" of the relaxor phase is apparently independent of whether the defects are polar or nonpolar.

ACKNOWLEDGMENTS

The work was partly supported by the Russian Foundation for Basic Research, project 96-02-17463.

REFERENCES

1. C. G. F. Stenger and A. J. Burggraaf, Phys. Status Solidi A **61**, 653 (1980).
2. L. E. Cross, Ferroelectrics **76** (1–4), 241 (1987).
3. A. A. Bokov and I. P. Rayevsky, Ferroelectrics **90** (1–4), 125 (1989).
4. F. Chu, I. M. Reaney, and N. Setter, Ferroelectrics **151** (1– 4), 343 (1994).
5. F. Chu, I. M. Reaney, and N. Setter, J. Appl. Phys. **77** (4), 1671 (1995).
6. F. Chu, N. Setter, and A. K. Tagantsev, J. Appl. Phys. **74** (8), 5129 (1993).
7. M. Ya. Dambekalne, K. Ya. Borman, A. R. Shternberg, *et al*., Izv. Ross. Akad. Nauk, Ser. Fiz. **57** (3), 78 (1993).
8. I. P. Pronin, T. Ayabaev, N. V. Zaĭtseva, *et al*., Neorg. Mater. **32** (12), 1528 (1996).
9. C. Malibert, B. Dkhil, J.-M. Kiat, *et al*., J. Phys.: Condens. Matter. **9**, 7485 (1997).
10. V. Eremkin, V. Smotrakov, E. Gagarina, *et al*., J. Korean Phys. Soc. **32** (Suppl.), S1597 (1998).
11. D. Viehland, S. Jang, L. E. Cross, *et al*., Phil. Mag. B **64**, 335 (1991).
12. V. M. Fridkin, *Photosegnetoelectrics* (Nauka, Moscow, 1979).
13. I. P. Raevskiĭ, M. A. Malitskaya, P. F. Tarasenko, *et al*., Zh. Tekh. Fiz. **54** (7), 1325 (1984).
14. L. S. Kamzina and N. N. Kraĭnik, Fiz. Tverd. Tela (S.-Peterburg) **40** (3), 527 (1998).
15. L. E. Cross, Ferroelectrics **151** (1–2), 305 (1994).

Translated by P. Pozdeev

Physics of the Solid State, Vol. 42, No. 1, 2000, pp. 165–169. Translated from Fizika Tverdogo Tela, Vol. 42, No. 1, 2000, pp. 158–162.

LATTICE DYNAMICS. PHASE TRANSITIONS

Multicritical Behavior of Disordered Systems with Two Order Parameters

V. V. Prudnikov, P. V. Prudnikov, and A. A. Fedorenko

Omsk State University, pr. Mira 55, Omsk, 644077 Russia
e-mail: prudnikv@univer.omsk.su

Received February 10, 1999; in final form, May 14, 1999

Abstract—A field-theoretic description of phase transitions in disordered systems with two coupled order parameters is given. An analysis of renormalization-group functions is performed directly for three-dimensional systems in a two-loop approximation by using the Pade–Borel summation technique. Fixed points are found corresponding to stable multicritical behavior. The effect of frozen point impurities on the phase diagrams of the system is studied. *© 2000 MAIK "Nauka/Interperiodica".*

1. INTRODUCTION

There is a large class of systems [1, 2] in which a phase transition is observed which cannot be described with a single order parameter transforming according to an irreducible representation. Phase diagrams of such systems have a singular multicritical (bicritical or tetracritical) point. At the bicritical point, two lines of second-order phase transitions and one line of a first-order phase transition meet, whereas four lines of second-order phase transitions meet at the tetracritical point. In the immediate vicinity of a multicritical point, the system exhibits special critical behavior characterized by competition between different types of ordering. In the case of bicritical behavior, one type of ordering of the system suppresses the other, whereas in the case of tetracritical behavior, a mixed phase may occur in which both types of ordering coexist.

A model Hamiltonian of a system with two coupled order parameters ϕ and ψ transforming according to two different irreducible representations of dimensions n and m, respectively, has the form

$$\mathcal{H}_0 = \int d^d x \Big(\frac{1}{2}[r_1\phi^2 + r_2\psi^2 + (\nabla\phi)^2 + (\nabla\psi)^2] + \frac{u_{10}}{4!}(\phi^2)^2 + \frac{u_{20}}{4!}(\psi^2)^2 + \frac{2u_{30}}{4!}\phi^2\psi^2 \Big),$$

$$\phi^2 = \sum_{i=1}^{n} \phi_i^2, \quad \psi^2 = \sum_{i=1}^{m} \psi_i^2,$$

$$(\nabla\phi)^2 = \sum_{i=1}^{n} (\nabla\phi_i)^2, \quad (\nabla\psi)^2 = \sum_{i=1}^{m} (\nabla\psi_i)^2. \qquad (1)$$

The problem of a phase transition in such a system was treated in [3, 4] by the ε-expansion method in a one-loop approximation. Recently, with the aim of refining the dependence of the multicritical behavior on the structure of order parameters, we have performed [5] a direct field-theoretic description of a three-dimensional system in terms of the Hamiltonian (1) in a two-loop approximation, without resorting to ε expansion. Studies of critical phenomena show [6] that this approach allows one to most adequately describe the critical behavior. Very accurate results can be obtained by applying this method in a many-loop approximation in combination with methods for summation of asymptotically convergent series. Using the Pade–Borel summation technique, analysis of renormalization group functions was made in [5] in a two-loop approximation and fixed points were determined which correspond to stable bicritical and tetracritical behavior. The coordinates of the fixed points and the conditions for their stability differ essentially from those found in [3, 4], which leads to noticeable changes in the phase diagrams in the critical region and to other types of symmetry of the system at the multicritical point.

In this paper, we investigate the effect of frozen point impurities on the multicritical behavior of a system with two coupled order parameters. It is known [7] that the disorder caused by frozen impurities in a system may be in the form of random fluctuations of the local critical temperature or in the form of random fields. The statistical properties of disordered systems differ essentially in these two cases, because random fields break down the symmetry of the system to the sign reversal of an order parameter. The systems with disorder of the random critical-temperature type are exemplified by ferro- and antiferromagnets with nonmagnetic impurity atoms in the absence of an external magnetic field, whereas anisotropic antiferromagnets with nonmagnetic impurity atoms in a uniform magnetic field have disorder of the random-field type [8]. In this paper, we investigate the multicritical behavior of systems with disorder of the critical-temperature type. Such behavior may be observed in disordered systems

1063-7834/00/4201-0165$20.00

in which, as in MnAs [9], the sequence of phase transitions can be described in terms of two coupled order parameters of different nature corresponding to a structural and a ferromagnetic phase transition, or in *XY*-type antiferromagnets such as Cr_2TeO_6 and $KCuF_3$ [10], in which a multicritical point appears in the absence of an external magnetic field. In some cases, the description of the multicritical behavior of disordered binary alloys composed of magnetic atoms of two species with mixed exchange interaction may correspond to the assumption of disorder of the random critical-temperature type in a system with two coupled order parameters [11, 12].

Early investigations of the effect of disorder of the random-temperature type on the multicritical behavior of the system were performed in [11–13] by the ε-expansion method in the one-loop approximation. However, it was clearly demonstrated on the example of a homogeneous system [5] that the results obtained in the one-loop approximation are in rather poor agreement with the actual multicritical behavior. One would expect even more essential discrepancies in the case of disordered systems, as may be inferred from the results obtained for disordered systems with a single order parameter [14, 15]. For disordered Ising-type systems, an accidental degeneracy occurs in the set of renormalization group equations for interaction vertex functions in the one-loop approximation [16]. For these reasons, we cannot use this approximation when studying the effect of impurities on the critical behavior of disordered systems. In this paper, we apply a field-theoretic method directly to three-dimensional systems and use the two-loop approximation.

2. RESULTS AND DISCUSSION

The Hamiltonian of a system with two coupled order parameters, in which there are frozen impurities producing disorder of the random-temperature type, can be written in the form

$$\mathcal{H}[\phi, \psi] = \mathcal{H}_0[\phi, \psi] + \mathcal{H}_{\text{imp}}[\phi, \psi], \tag{2}$$

where $\mathcal{H}_0[\phi, \psi]$ is the Hamiltonian (1) for the homogeneous system. The term $\mathcal{H}_{\text{imp}}[\phi, \psi]$ describing the interaction of impurities with fluctuations of the order parameters is written as

$$\mathcal{H}_{\text{imp}}[\phi, \phi] = \frac{1}{2}\int d^d x[V_1(x)\phi^2 + V_2(x)\psi^2]. \tag{3}$$

Here, $V_i(x)$ are the potentials of the random field of impurities characterized by a Gaussian distribution; in the case of point impurities, their correlators are

$$\begin{aligned}\langle\langle V_i(x)\rangle\rangle &= 0, \quad \langle\langle V_1(x)V_1(x')\rangle\rangle = -u_{40}\delta(x-x'),\\ \langle\langle V_2(x)V_2(x')\rangle\rangle &= -u_{50}\delta(x-x'),\\ \langle\langle V_1(x)V_2(x')\rangle\rangle &= -u_{60}\delta(x-x').\end{aligned} \tag{4}$$

Using the method of replicas, we take an average over random configurations of impurities and reduce the problem of statistical description of the weakly disordered system to the problem of statistical description of a homogeneous system with the effective Hamiltonian

$$\begin{aligned}\mathcal{H}_{\text{repl}}[\boldsymbol{\phi}, \boldsymbol{\psi}] &= \sum_{\alpha=1}^{k}\mathcal{H}_0[\phi_\alpha, \psi_\alpha]\\ &+ \frac{1}{2}\sum_{\alpha=1}^{k}\sum_{\beta=1}^{k}[u_{40}\phi_\alpha^2\phi_\beta^2 + u_{50}\psi_\alpha^2\psi_\beta^2 + 2u_{60}\phi_\alpha^2\psi_\beta^2],\end{aligned} \tag{5}$$

which contains k samples ("replicas") of the initial Hamiltonian $\mathcal{H}_0$ of the homogeneous system and a number of extra terms (with impurity vertices u_{40}, u_{50}, and u_{60}) which describe the effective interaction of $(k \times n)$-component and $(k \times m)$-component order parameters through the impurity field. Thermodynamically, this statistical model is equivalent to the initial disordered model in the limit $k \longrightarrow 0$.

In the framework of the field-theoretic approach [17], the asymptotic critical behavior and the structure of phase diagrams in the fluctuation region are determined by the Callan–Symanzik renormalization group equation for the vertex parts of the irreducible Green's functions. To find expressions for the (renormalization group) β functions in terms of the renormalized interaction vertices u_i $(i = 1,\ldots, 6)$ involved in the renormalization group equation, we apply a common method based on the Feynman diagram technique and the renormalization procedure [18]. In the two-loop approximation, we obtain the following expressions for the β functions:

$$\begin{aligned}\beta_1(u) &= -u_1 + \frac{(n+8)}{6}u_1^2 + \frac{m}{6}u_3^2 + 24u_1u_4\\ &- \frac{(41n+190)}{243}u_1^3 - \frac{2m}{27}u_3^3 - \frac{23m}{243}u_1u_3^2\\ &- \frac{184m}{81}u_1u_3u_6 - \frac{16m}{9}u_3^2u_6 - \frac{(400n+2096)}{81}u_1^2u_4\\ &- \frac{5920}{27}u_1u_4^2 - \frac{8m}{9}u_3^2u_4,\end{aligned}$$

$$\begin{aligned}\beta_2(u) &= -u_2 + \frac{(m+8)}{6}u_2^2 + \frac{n}{6}u_3^2 + 24u_2u_5\\ &- \frac{(41m+190)}{243}u_2^3 - \frac{2n}{27}u_3^3 - \frac{23n}{243}u_2u_3^2\\ &- \frac{184n}{81}u_2u_3u_6 - \frac{16n}{9}u_3^2u_6 - \frac{(400m+2096)}{81}u_2^2u_5\\ &- \frac{5920}{27}u_2u_5^2 - \frac{8n}{9}u_3^2u_5,\end{aligned}$$

$$\beta_3(u) = -u_3 + \frac{2}{3}u_3^2 + \frac{(n+2)}{6}u_1u_3 + \frac{(m+2)}{6}u_2u_3$$

$$+ 4u_3u_4 + 4u_3u_5 + 16u_3u_6 - \frac{5(n+m)+72}{486}u_3^3$$
$$- \frac{23(n+2)}{486}u_1^2u_3 - \frac{23(m+2)}{486}u_2^2u_3 - \frac{(n+2)}{9}u_1u_3^2$$
$$- \frac{(m+2)}{9}u_2u_3^2 - \frac{20(n+m)+432}{81}u_3^2u_6$$
$$- \frac{8(n+3)}{9}u_3^2u_4 - \frac{8(m+3)}{9}u_3^2u_5 - \frac{368}{27}u_3u_4^2$$
$$- \frac{368}{27}u_3u_5^2 - \frac{92(n+2)}{81}u_1u_3u_4 - \frac{92(m+2)}{81}u_2u_3u_5$$
$$- \frac{8(n+2)}{3}u_1u_3u_6 - \frac{8(m+2)}{3}u_2u_3u_6 - 64u_3u_6^2$$
$$- 64u_3u_4u_6 - 64u_3u_5u_6, \quad (6)$$

$$\beta_4(u) = -u_4 + 16u_4^2 + \frac{n+2}{3}u_1u_4 + \frac{m}{3}u_3u_6$$
$$- \frac{3040}{27}u_4^3 - \frac{2m}{27}u_3^2u_6 - \frac{8m}{3}u_3u_6^2 - \frac{400(n+2)}{81}u_1u_4^2$$
$$- \frac{23(n+2)}{243}u_1^2u_4 - \frac{5m}{243}u_3^2u_4 - \frac{184m}{81}u_3u_4u_6,$$

$$\beta_5(u) = -u_5 + 16u_5^2 + \frac{m+2}{3}u_2u_5 + \frac{n}{3}u_3u_6$$
$$- \frac{3040}{27}u_5^3 - \frac{2n}{27}u_3^2u_6 - \frac{8n}{3}u_3u_6^2 - \frac{400(m+2)}{81}u_2u_5^2$$
$$- \frac{23(m+2)}{243}u_2^2u_5 - \frac{5n}{243}u_3^2u_5 - \frac{184n}{81}u_3u_5u_6,$$

$$\beta_6(u) = -u_6 + 8u_6^2 + \frac{(n+2)}{6}u_1u_6 + \frac{(m+2)}{6}u_2u_6$$
$$+ \frac{n}{6}u_3u_4 + \frac{m}{6}u_3u_5 + 4u_4u_6 + 4u_5u_6 - \frac{64}{3}u_6^3$$
$$- \frac{4(n+2)}{3}u_1u_6^2 - \frac{4(m+2)}{3}u_2u_6^2 - \frac{23(n+2)}{486}u_1^2u_6$$
$$- \frac{23(m+2)}{486}u_2^2u_6 - \frac{368}{27}u_4^2u_6 - \frac{368}{27}u_5^2u_6 - 32u_4u_6^2$$
$$- 32u_5u_6^2 - \frac{n}{27}u_3^2u_4 - \frac{4n}{9}u_3u_4^2 - \frac{m}{27}u_3^2u_5$$
$$- \frac{4m}{9}u_3u_5^2 - \frac{5(n+m)}{486}u_3^2u_6 - \frac{20(n+m)}{81}u_3u_6^2$$
$$- \frac{92(n+2)}{81}u_1u_4u_6 - \frac{92(m+2)}{81}u_2u_5u_6$$
$$- \frac{16n}{9}u_3u_4u_6 - \frac{16m}{9}u_3u_5u_6.$$

It is well known that the perturbation series are asymptotically convergent in this case and the quantities represented by the interaction vertices of fluctuations of the order parameters are too large for expressions (6) to be used immediately in the fluctuation region $r_1, r_2 \longrightarrow 0$. To extract the desired physical information from these expressions, we apply the generalized Pade–Borel method, which is used to find the sum of an asymptotically convergent series. The direct and inverse Borel transformations generalized to the six-dimensional case have the form

$$f(u_1, \ldots, u_6) = \sum_{i_1, \ldots, i_6} c_{i_1, \ldots, i_6} u_1^{i_1} u_2^{i_2} u_3^{i_3} u_4^{i_4} u_5^{i_5} u_6^{i_6}$$
$$= \int_0^\infty e^{-t} F(u_1 t, \ldots, u_6 t)\, dt,$$

$$F(u_1, \ldots, u_6) = \sum_{i_1, \ldots, i_6} \frac{c_{i_1, \ldots, i_6}}{(i_1 + \ldots + i_6)} u_1^{i_1} u_2^{i_2} u_3^{i_3} u_4^{i_4} u_5^{i_5} u_6^{i_6}. \quad (7)$$

To perform the analytic continuation of the Borel transform, we introduce a power series in an auxiliary variable λ

$$F(u_1, \ldots, u_6\lambda)$$
$$= \sum_{k=0}^{\infty} \lambda^k \sum_{i_1, \ldots, i_6} \frac{c_{i_1, \ldots, i_6}}{k!} u_1^{i_1} u_2^{i_2} u_3^{i_3} u_4^{i_4} u_5^{i_5} u_6^{i_6} \lambda_{i_1 + \ldots + i_6, k} \quad (8)$$

and take the Pade approximant $[L/M]$ at the point $\lambda = 1$. This technique was proposed and applied in [19] for describing the critical behavior of a number of systems characterized by several interaction vertices of fluctuations of order parameters. It was found in [19] that the Pade approximation in the variable λ conserves the symmetry of the system. This property is of importance in multivertex models.

To calculate the β functions in the two-loop approximation, we use approximant [2/1]. The nature of the multicritical behavior depends on the presence of a stable fixed point that is determined from the set of equations

$$\beta_i(u_1^*, u_2^*, u_3^*, u_4^*, u_5^*, u_6^*) = 0 \quad (i = 1, \ldots, 6). \quad (9)$$

This fixed point is stable if the real parts of the eigenvalues b_i of the matrix

$$B_{i,j} = \frac{\partial \beta_i(u_1^*, u_2^*, u_3^*, u_4^*, u_5^*, u_6^*)}{\partial u_j} \quad (10)$$

are positive.

The system of β functions obtained by calculating the sums representing them has a wide variety of fixed points for each value of n and m. The table shows stable fixed points for the physically most interesting values of n and m and also a number of fixed points unstable

Fixed points of the disordered system and the eigenvalues of the stability matrix

n	m	u_1^*	u_2^*	u_3^*	u_4^*	u_5^*	u_6^*	b_i (i = 1, …, 6)
1	1	1.58892	1.58892	0	−0.03448	−0.03448	0	0.4612 ± 0.222i, 0.0362, 0.4612 ± 0.222i, 0.0362
1	2	1.58892	0.93832	0	−0.03448	−0.00026	0	0.4612 ± 0.222i, 0.0183, 0.0183, 0.6671, 0.0017
1	2	1.58892	0.93498	0	−0.03448	0	0	0.4612 ± 0.222i, 0.0172, 0.0172, 0.6673, −0.0017
1	3	1.58892	0.82962	0	−0.03448	0	0	0.4612 ± 0.222i, 0.0834, 0.0834, 0.1315, 0.6814
1	3	1.58892	1.28357	0	−0.03448	−0.07098	0	0.4612 ± 0.222i, 0.3266, 0.3266, 5.9782, −3.1324
2	2	0.93832	0.93832	0	−0.00026	−0.00026	0	0.6671, 0.0017, 0.0017, 0.0005, 0.0005, 0.6671
2	2	0.93498	0.93498	0	0	0	0	0.6673, −0.0017, −0.0017, −0.0017, −0.0017, 0.6673
2	3	0.93832	0.82962	0	−0.00026	0	0	0.6671, 0.0017, 0.0659, 0.0659, 0.1315, 0.6814
2	3	0.93498	0.82962	0	0	0	0	0.6673, −0.0017 0.1315 0.6814, 0.0648, 0.0648
3	3	0.82962	0.82962	0	0	0	0	0.6814, 0.1315, 0.1315, 0.6814, 0.1315, 0.1315

in the two-loop approximation, which will be useful in subsequent analysis. The table also shows the eigenvalues of the stability matrix (10) for the corresponding fixed points.

Analysis of the nature of the fixed points and their stability allows the following conclusions to be made. In the presence of impurities in the system, the order parameters become decoupled in their fluctuations and only the tetracritical behavior with the general symmetry $SO(n) \oplus SO(m)$ of the system is stable. In the case of one-component order parameters ($n = m = 1$), the presence of impurities is crucial and leads to the critical behavior with indices corresponding to the indices of a disordered Ising model [14, 15]. As for the cases of $n = 1$, $m = 2$ and $n = 2$, $m = 2$, calculations predict stability of a fixed point for which the impurity vertices

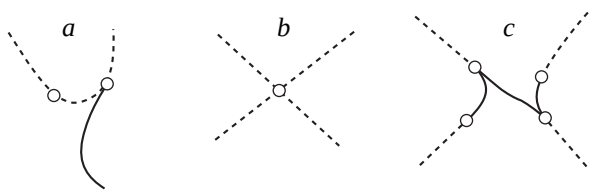

Fig. 1. Possible types of phase diagrams (schematic): solid lines correspond to first-order phase transitions and dashed lines, to second-order phase transitions.

u_4^* and u_5^* are nonzero for both order parameters. However, we are inclined to believe that in higher approximations, the situation will reverse and that fixed point will become stable at which the order parameters are decoupled and the impurity vertices are nonzero only for one-component order parameters. This is indicated by the weak stability of fixed points of the former type and the weak instability of fixed points of the latter type. Furthermore, a similar situation is encountered in a study of the effect of impurities on the critical behavior of a system with a one order parameter in the two-loop approximation [14, 20]. In the case of $n, m \geq 3$, only the homogeneous fixed point is stable that is identical to a critical point of type 3 of a homogeneous system [5] and has a tetracritical character. Thus, when the order parameters of a system have two or more components, the presence of impurities produces no effect on their critical behavior, and the multicritical behavior has a tetracritical character. The presence of impurities in systems with two order parameters severely restricts the number of possible types of stable fixed points and, hence, the number of possible phase diagrams in comparison with homogeneous systems. Of fundamental importance is the restriction that disordered systems cannot have a phase diagram with a bicritical point. In these systems, critical fluctuations and fluctuations of the local critical temperature for interacting fields whose bare vertices satisfy the bicritical-behavior con-

dition $u_{30}^2 \geq u_{10}u_{20}$ [5] make the bicritical behavior unstable and result in a decoupling of the order parameters. As a consequence, phase diagrams with a bicritical character outside the critical region will contain portions of lines of first-order phase transitions in the critical region as shown in Fig. 1*a*. If the bare vertices of the system satisfy the tetracritical-behavior condition $u_{30}^2 < u_{10}u_{20}$, only phase diagrams shown in Figs. 1b and 1c are possible.

CONCLUSION

It is hoped that the differences in the multicritical behavior found here between homogeneous and disordered systems with competing order parameters will be taken into account in experimental studies of the multicritical behavior of the systems in question.

ACKNOWLEDGMENTS

This work was supported by the Russian Foundation for Basic Research, grant no. 97-02-16124.

REFERENCES

1. K. S. Aleksandrov, A. T. Anistratov, B. V. Beznosikov, and N. V. Fedoseeva, *Phase Transitions in Crystals of Halides ABX_3* (Nauka, Novosibirsk, 1981).
2. Y. Shapira, in *Multicritical Phenomena* (Plenum, London, 1984), p. 35.
3. I. F. Lyuksyutov, V. L. Pokrovskiĭ, and D. E. Khmel'nitskiĭ, Zh. Éksp. Teor. Fiz. **69**, 1817 (1975) [JETP **42**, 923 (1975)].
4. J. M. Kosterlitz, D. R. Nelson, and M. E. Fisher, Phys. Rev. B: Solid State **13**, 412 (1976).
5. V. V. Prudnikov, P. V. Prudnikov, and A. A. Fedorenko, Pis'ma Zh. Éksp. Teor. Fiz. **68**, 900 (1998) [JETP Lett. **68**, 950 (1998)].
6. G. A. Baker, B. G. Nickel, M. S. Green, *et al.*, Phys. Rev. Lett. **36** (23), 1351 (1976); J. C. Le Guillou and J. Zinn-Justin, Phys. Rev. Lett. **39**, 95 (1977); G. A. Baker, B. G. Nickel, and D. I. Meiron, Phys. Rev. B: Solid State **17**, 1365 (1978); J. C. Le Guillou and J. Zinn-Justin, Phys. Rev. B: Condens. Matter **21**, 3976 (1980).
7. R. B. Stinchcombe, in *Phase Transitions and Critical Phenomena*, Ed. by C. Domb and J. L. Lebositz (Academic, New York, 1983), Vol. 7, p. 151.
8. S. Fishman and A. Aharony, J. Phys. C **12**, L729 (1979).
9. B. E. Naĭsh, Yu. N. Skryabin, and V. N. Syromyatnikov, Fiz. Met. Metalloved. **52**, 1147 (1981).
10. D. Mukamel, Phys. Rev. B: Solid State **14**, 1303 (1976).
11. Yu. A. Izyumov, Yu. N. Skryabin, and V. M. Laptev, Phys. Status Solidi B **87**, 441 (1978).
12. V. M. Laptev and Yu. N. Skryabin, Fiz. Tverd. Tela (Leningrad) **22**, 2949 (1980).
13. A. A. Lisyanskiĭ and A. É. Filippov, Ukr. Fiz. Zh. **32**, 626 (1987).
14. G. Jug, Phys. Rev. B: Condens. Matter **27**, 609 (1983).
15. I. O. Mayer, A. I. Sokolov, and B. N. Shalayev, Ferroelectrics **95**, 93 (1989); I. O. Mayer, J. Phys. A **22**, 2815 (1989).
16. A. B. Harris and T. C. Lubensky, Phys. Rev. Lett. **33**, 1540 (1974); T. C. Lubensky, Phys. Rev. B: Solid State **11**, 3573 (1975); D. E. Khmel'nitskiĭ, Zh. Éksp. Teor. Fiz. **68**, 1960 (1975) [JETP **41**, 981 (1975)].
17. D. Amit, *Field Theory, the Renormalization Group and Critical Phenomena* (McGraw-Hill, New York, 1976).
18. J. Zinn-Justin, *Quantum Field Theory and Critical Phenomena* (Clarendon, Oxford, 1989).
19. S. A. Antonenko and A. I. Sokolov, Phys. Rev. B: Condens. Matter **49**, 15901 (1994); K. B. Varnashev and A. I. Sokolov, Fiz. Tverd. Tela (St. Petersburg) **38**, 3665 (1996); A. I. Sokolov, K. B. Varnashev, and A. I. Mudrov, Int. J. Mod. Phys. B **12**, 1365 (1998).
20. V. V. Prudnikov and A. N. Vakilov, Zh. Éksp. Teor. Fiz. **101**, 1853 (1992) [JETP **74**, 990 (1992)].

Translated by Yu. Epifanov

Physics of the Solid State, Vol. 42, No. 1, 2000, pp. 170–176. Translated from Fizika Tverdogo Tela, Vol. 42, No. 1, 2000, pp. 163–169.

LATTICE DYNAMICS. PHASE TRANSITIONS

Phase Transformations in Equiatomic Alloy TiZr at Pressure up to 70 kbar

I. O. Bashkin, A. Yu. Pagnuev, A. F. Gurov, V. K. Fedotov, G. E. Abrosimova, and E. G. Ponyatovskiĭ

Institute of Solid State Physics, Russian Academy of Sciences, Chernogolovka, Moscow oblast, 142432 Russia
e-mail: bashkin@issp.ac.ru

Received May 18, 1999

Abstract—The effect of pressure on the $\alpha \rightleftharpoons \beta$ and $\omega \rightleftharpoons \beta$ transformations in the equiatomic alloy TiZr is studied by the differential thermal analysis (DTA) and calorimetric technique. The α–β equilibrium at atmospheric pressure occurs at a temperature of 579°C, and the heat of transition ΔH is 40.9 ± 2.0 J/g. As the pressure increases up to 28 kbar, the temperature of the α–β equilibrium linearly decreases, $dT/dP = -2.2 \pm 0.3$ K/kbar. In the pressure range 28–48 kbar, the β-phase undergoes a transition to the two-phase (α + ω) state upon cooling to room temperature. At pressures above the triple point with the coordinates $P = 49 \pm 3$ kbar and $T = 460 \pm 30$°C, the cooling of the β-phase gives rise to only the hexagonal ω-phase with the unit cell parameters $a = 4.843$ Å, $c = 2.988$ Å, and $c/a = 0.617$ under normal conditions. The slope of the ω–β equilibrium boundary is positive at pressures up to 70 kbar, $dT/dP \approx 0.46$ K/kbar. The $\omega \longrightarrow \alpha$ transformation at atmospheric pressure proceeds in the temperature range $T = 425$–470°C with the enthalpy of transition $\Delta H = 2.8$ J/g. © *2000 MAIK "Nauka/Interperiodica".*

The phase equilibria in pure titanium and zirconium have been investigated in considerable detail in the *T*–*P* regions up to the triple points of the α–β–ω equilibrium [1]. At atmospheric pressure, the low-temperature hexagonal close-packed (hcp) α-phase transforms into the high-temperature body-centered cubic (bcc) β-phase at $T = 882$°C for titanium and at $T = 863$°C for zirconium [1]. An increase in the pressure leads to a decrease in the α–β transition temperatures down to triple points with the coordinates $T = 640$°C and $P = 80$ kbar for titanium [2] and $T = 700$°C and $P = 55$ kbar for zirconium [3]. The equilibrium boundary between the α-phase and the high-pressure hexagonal ω-phase exhibits a positive slope. In the compression experiments with shear [4], it was found that the equilibrium pressures of the α–ω transitions at $T = 20$°C are equal to 20 and 22 kbar for titanium and zirconium, respectively. In quasi-hydrostatic pressure chambers, the complete conversion to the ω-phase due to the hysteresis can be achieved at substantially higher pressures (40–80 kbar at room temperature [1–4]) than the equilibrium pressure. The β–ω equilibrium boundaries above the triple points exhibit a small positive slope [1]. In addition to the aforementioned equilibria, the reversible transition from the ω-phase to the β-phase at room temperature is observed in pure zirconium under a pressure of 350 kbar [5, 6].

The Ti–Zr system is characterized by the complete solubility of components in both the liquid and solid states [7]. Upon the mutual doping, the α–β transition temperature decreases and reaches a minimum for the TiZr equiatomic alloy. The data available in the literature on the minimum temperature differ considerably, from 525°C in the review of early works [7] to 610°C in more recent works [8, 9].

The question of the α–ω transformations in the Ti–Zr alloys remained open until the behavior of these alloys was investigated in the pressure range up to 80–100 kbar [10, 11]. With the electron microscopic method, Dobromyslov *et al.* [10] observed the precipitation of the ω-phase in a series of the Ti_xZr_{1-x} alloys preliminarily compressed to a pressure of 80 kbar at room temperature when the titanium concentration in the alloy was either no more than 32.2 at. % or no less than 97.5 at. %. From these observations, the inference was drawn that the curve describing the pressure of the α–ω transition in the Ti–Zr system shows a maximum [10]. More recently, Aksenenkov *et al.* [11] subjected the Ti–Zr alloys containing from 50 to 74 at. % Ti to shear deformation under a pressure up to 90 kbar at temperatures of 300°C and 77 K (as is known, the shear promotes phase transformations [4, 12]). The subsequent X-ray diffraction study of the samples led these authors to the conclusion that the mutual doping of Ti and Zr results in an increase in the equilibrium pressure of the α–ω transformation, and its value for the TiZr equiatomic alloy is as high as 66 kbar [11]. The calculations of the *T*–*P*–*c* diagrams for the Ti–Zr system within the regular-solution approximation demonstrated that, upon mutual doping of Ti and Zr, the triple point of the α–β–ω equilibrium should shift toward higher pressures and lower temperatures as compared to the pure metals [11]. According to these calculations,

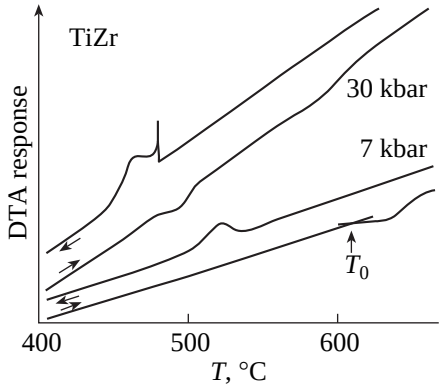

Fig. 1. DTA curves for the $Ti_{49.6}Zr_{50.4}$ alloy in the pressure range 2–30 kbar (a lens-type chamber). Lower and upper pairs of the curves correspond to pressures of 7 and 30 kbar, respectively. Heating and cooling are shown by arrows. Determination of the initial temperature of the α ⟶ β transformation is illustrated in the heating curve at 7 kbar.

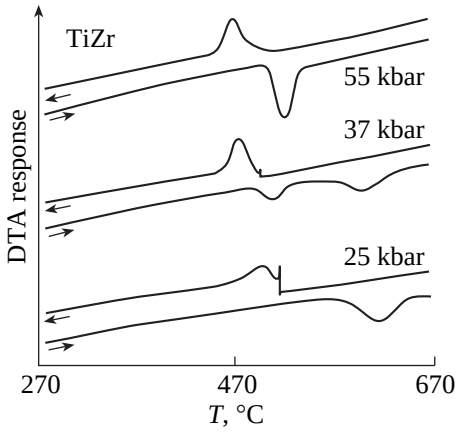

Fig. 2. DTA curves for the $Ti_{49.6}Zr_{50.4}$ alloy in the pressure range 24–70 kbar (a toroid-type chamber). Lower, middle, and upper pairs of the curves correspond to pressures of 25, 37, and 55 kbar, respectively. Heating and cooling are shown by arrows.

the parameters of the triple point for the TiZr equiatomic alloy are equal to 85 kbar and 420°C.

The aim of this work was to investigate the high-temperature region of the *T–P* diagram for the TiZr equiatomic alloy. We measured the pressure dependence of the α–β transition temperature. It was found that, at relatively low pressures, the *T–P* diagram has a triple point. This point was identified as the α–β–ω equilibrium point. The parameters of the triple point were determined from the intersection of the boundaries for the α–β and ω–β transformations. The characteristics of the α–β and ω–β transformations at atmospheric pressure were measured by the calorimetric technique. The unit cell parameters for ω-phase of the TiZr alloy were refined.

1. EXPERIMENTAL

An equiatomic alloy TiZr was prepared from rods of titanium and zirconium (iodide grade) remelted by the vacuum electron-beam zone melting. The purity of Ti and Zr obtained by this technique, as a rule, is higher than 99.95% (including interstitial impurities) [13, 14]. Then, a zirconium rod of calculated weight was coaxially pressed into a titanium tube and repeatedly remelted under vacuum. The chemical composition of the prepared rod was measured at nine points distributed over its length and cross-section by using a JXA-5 electron-probe X-ray microanalyzer. It was found that the alloy is homogeneous and contains 49.6 at. % Ti and 50.4 at. % Zr with an accuracy of ± 0.4 at. %. The unit cell parameters for the hexagonal close-packed phase of the alloy are a = 3.104 Å and c = 4.923 Å. The samples in the form of pellets 5–8 mm in diameter and 1.5–2 mm in height were either cut from the ingot or pressed from chips produced on a lathe.

Compression measurements were performed by the differential thermal analysis (DTA) at temperatures up to 750°C in quasi-hydrostatic pressure chambers calibrated against the phase transitions in Bi and Ti. We used chambers of two types with the operating pressure ranges from 2 to 30 kbar (a lens-type chamber) and from 20 to 70 kbar (a toroid-type chamber). The pressure was determined accurate to within ± 5%. Elements of an experimental assembly were arranged inside a sleeve fabricated from pyrophyllite annealed at 900°C. The sleeve was inserted into a channel of a catlinite container. The studied sample and a reference sample (stainless steel) in pyrophyllite dishes were arranged in an operating channel in a symmetric fashion about the symmetry plane of the container (the experimental assembly was described in more detail in [15]). The heating and cooling rates were equal to about 40 K/min. Signals from differential and absolute thermocouples were fed into an N-306 self-recorder. The temperature, which corresponds to a maximum of the thermal peak in the DTA curve, was taken as the phase transition point. The boundaries of the phase transition range were determined as points of intersection between two tangent lines, of which one tangent line is an extension of the normal portion of the DTA curve and the other line is an inflectional tangent to ascending or descending branches of the peak, respectively.

In the operating channel, there are unpredictable temperature gradients [15], which, at high temperatures, can bring about systematic errors in magnitudes of temperatures, even though these errors are of less importance in determination of the relative changes in the transition temperatures. In order to simplify the determination of the curve location in the *T–P* diagram, the α–β transition temperature in the TiZr alloy at atmospheric pressure was measured by the calorimetric technique. Then, the pressure dependences of the transition temperatures, which were obtained in particular experiments, were located with reference to the temperature found by the calorimetric technique.

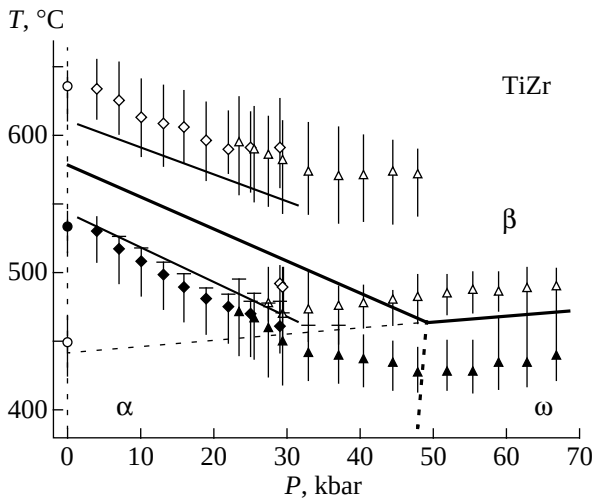

Fig. 3. Curves of the $\alpha \rightleftharpoons \beta$ and $\omega \rightleftharpoons \beta$ transformations in the *T*–*P* phase diagram of the $Ti_{49.6}Zr_{50.4}$ alloy. Symbols indicate the maxima of thermal peaks, vertical segments represent the transformation ranges, and horizontal dashes display sharp peaks of explosion-like heat release in cooling curves. Open and solid symbols correspond to the heating and cooling, respectively. Circles are the calorimetric data at $P = 1$ atm. Rhombuses and triangles represent the results of measurements in two pressure ranges in different chambers. Thin lines are drawn by the least-squares method through the initial points of the $\alpha \rightleftharpoons \beta$ transformation ranges determined in a lens-type chamber, solid heavy lines indicate the schematic boundaries of the α–β and ω–β equilibria, and dotted lines show the extrapolation of the ω–β equilibrium curve to atmospheric pressure. The dashed line corresponds to the α–ω phase boundary.

The calorimetric measurements at atmospheric pressure were carried out on a Perkin–Elmer DSC7 differential scanning calorimeter in the range from room temperature to 700°C in an argon stream at heating and cooling rates of 20 K/min. Prior to each experiment, the calorimeter was calibrated in temperature and sensitivity against In and Zn references samples. The DTA curves were processed with a software package furnished with a calorimeter.

The X-ray diffraction patterns were recorded in reflection geometry under normal conditions on a DRON4.07 automated diffractometer (MoK_α radiation). The patterns were fitted with the DBWS-9411 standard program for multiphase profile analysis.

2. RESULTS AND DISCUSSION

The greater part of the DTA measurements under pressure was performed with bulk samples cut from an ingot of the initial alloy. Figures 1 and 2 demonstrate the evolution of thermal anomalies in the DTA curves. At the lowest pressures, the heating and cooling curves show only one thermal peak at the temperature corresponding to the α–β transformation in the alloy. As the pressure increases, the α–β transition temperature decreases. Beginning with a pressure of about 7 kbar, the thermal effects in the cooling curves exhibit a new feature: the onset of the transformation manifests itself as a sharp peak corresponding to the explosion-like heat release, after which the curve returns to the shape characteristic of thermally activated transformations with normal kinetics. The height of a sharp peak of explosion-like heat release is determined by the fraction of the product that undergoes the $\beta \longrightarrow \alpha$ transition in a jumpwise fashion. The fraction increases in a certain pressure range and, then, decreases to the complete disappearance at pressures above 37 kbar (cf. Figs. 1, 2). This feature suggests two mechanisms of the $\beta \longrightarrow \alpha$ transformation: as the mobility of metal atoms decreases with an increase in the pressure and a decrease in the temperature, the thermally activated character of the $\beta \longrightarrow \alpha$ transformation progressively changes to martensitic explosion-like. The change in the mechanism of the $\beta \longrightarrow \alpha$ transformation is confirmed by the shape of the cooling curves at pressures below 7 kbar: the ascending branches of peaks in these curves are sawtooth rather than smooth, which implies that the initial stage of the transformation in these cases occurs as a sequence of small abrupt changes.

Beginning with a pressure of 27.5 kbar, the heating curves also exhibit a new feature (Figs. 1, 2). At temperatures ~100 K below the thermal peak of the α–β transformation, the second peak appears in the heating curves. Initially, the second peak is small in area, but, with a further increase in the pressure, its area increases, whereas the first peak decreases in area down to the complete disappearance at pressures above 48 kbar (Fig. 2). No splitting of the peaks is observed in the cooling curves. If the sample was cooled from a temperature lying in the range between the completion of the first transformation and the onset of the second transformation upon heating, the area of the peak in the cooling curve was less than that observed upon cooling from a temperature lying above the completion of the second transformation. This suggests that, upon heating, two transformations proceed at different temperatures, whereas, upon cooling, these processes occur within the same temperature range and contribute to the same peak in the DTA curves. The aforementioned features of the DTA curves are summarized in the *T*–*P* diagram of the TiZr alloy (Fig. 3), in which symbols correspond to the maxima of the peaks and vertical segments indicate the ranges of thermal anomalies. A clear-cut change in the slope of the transition curves shown in Fig. 3 and the splitting of thermal anomalies in the heating curves indicate that, at temperatures below the transition lines, there is the transition from the α-phase to the high-pressure phase.

A series of DTA measurements with the chip-pressed isotropic sample under a pressure up to 60 kbar was carried out with the aim to provide support for the existence of the high-pressure phase and also to reveal its structure. The sole difference between the thermal effects in the DTA curves obtained in these experiments and those shown in Figs. 1 and 2 resides in the absence

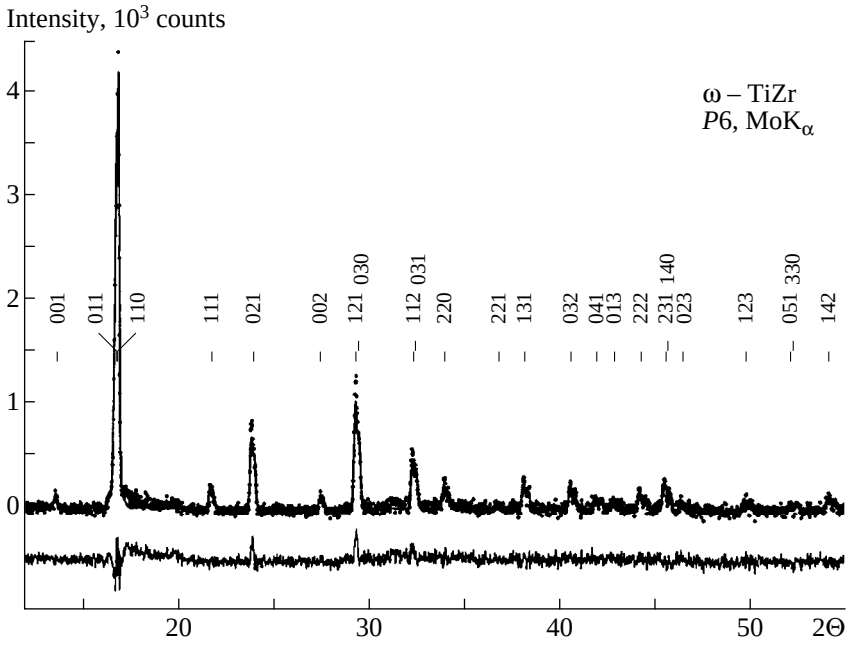

Fig. 4. X-ray diffraction pattern (MoK_α radiation) for the high-pressure phase of the $Ti_{49.6}Zr_{50.4}$ alloy. Points are the experimental data, and the solid line represents the fitting curve. The difference pattern is shown at the bottom. Dashes indicate the calculated positions of reflections (Mo$K_{\alpha 1}$ radiation, four reflections with relative intensities < 0.015 are omitted).

of the peaks corresponding to the explosion-like onset of the β ⟶ α transformation in all the cooling curves. The sample was cooled under a pressure of 60 kbar and, then, was unloaded at room temperature. The X-ray diffraction pattern of this sample is depicted in Fig. 4. This pattern is well identified with the hexagonal ω-phase with the unit cell parameters a = 4.843 Å, c = 2.988 Å, and c/a = 0.617 (space group $P6$). The calculated and theoretical discrepancy factors are R_{calcd} = 5.4% and R_{theor} = 4.0%. The positions of reflections with perceptible intensity (for the Mo$K_{\alpha 1}$ radiation) are indicated by dashes in Fig. 4. The splitting of lines into the $K_{\alpha 1}$ and $K_{\alpha 2}$ doublets illustrates the quality of samples and their single-phase nature. The difference pattern represented below the experimental X-ray diffraction pattern in Fig. 4 demonstrates the quality of the fitting. The unit cell parameters obtained are approximately 0.01 Å larger than the corresponding parameters for the compressed samples [11].

In order to confirm that the presence of two thermal effects in the heating curves at pressures in the range between 27.5 and 48 kbar is brought about by the formation of two phases (namely, the α- and ω-phases) upon cooling, another pressed sample was prepared using the procedure described above, but at a maximum pressure of 35 kbar. As expected, the X-ray diffraction pattern of this sample is a superposition of the diffraction patterns for the α- and ω-phases.

For the T–P diagram to be correctly constructed, the experimental data on the phase transformations in the TiZr alloy at different pressures should be referred to the characteristics of the α–β transition at atmospheric pressure. As mentioned above, there is a large scatter in these characteristics determined by different authors. This is not surprising, since the mechanism and kinetic characteristics of the α–β transformation can depend on factors such as the impurity composition, the presence of new phase nuclei governed by the defect structure of the alloy, and the heating and cooling rates. In this respect, for the purpose of more accurately referring the data obtained at different pressures to those measured at atmospheric pressure, we made special measurements of some characteristics for the α–β transformation in the TiZr alloy by the calorimetric technique.

In order to evaluate how the prehistory and defect structure affect the parameters of the α–β transition, the calorimetric measurements were performed with samples of three types: the bulk samples annealed under a vacuum of 10^{-5} mm Hg at 750°C and cooled together with a furnace, the chip-pressed samples without annealing, and the samples completely transformed into the ω-phase after the compression experiments. The thermal anomalies observed in the first heating–cooling cycles for these three samples are compared in Fig. 5a. To obtain a pictorial representation of the thermal effects of the transformations in Fig. 5, the base lines were subtracted from the experimental calorimetric curves. The base lines were plotted for each curve with a cubic spline from the reference points outside the range of thermal anomaly. In turn, the thermal anomaly range in the calorimetric curve was determined from the deviation of its derivative from values that rather weakly vary outside this range.

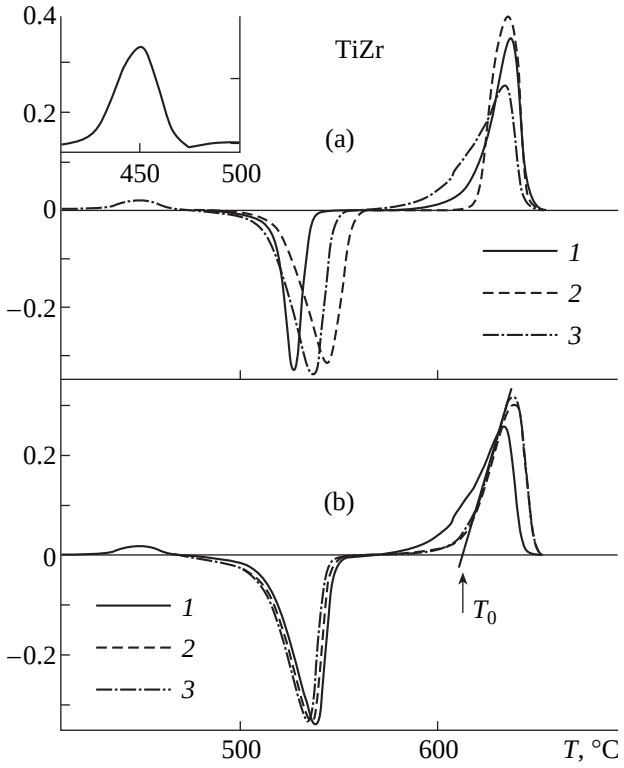

Fig. 5. (a) Calorimetric curves of the $Ti_{49.6}Zr_{50.4}$ alloy in the first heating–cooling cycles for (*1*) bulk sample annealed under vacuum at 750°C, (*2*) chip-pressed sample (without annealing), and (*3*) ω-phase sample after the DTA experiment under pressure. Heating curves are at the top, and cooling curves are at the bottom. Heating and cooling rates $dT/d\tau$ are 20 K/min. The thermal peak associated with the $\omega \longrightarrow \alpha$ transformation in the third sample is shown on an enlarged scale in the inset. (b) Calorimetric curves of the three heating–cooling cycles for the $Ti_{49.6}Zr_{50.4}$ sample after the DTA experiment under pressure (the initial state corresponds to the ω-phase; cycle numbers are given in the legend). Heating curves are at the top, and cooling curves are at the bottom. Heating and cooling rates $dT/d\tau$ are 20 K/min. Graphic determination of the initial temperature T_0 of the $\alpha \longrightarrow \beta$ transformation is illustrated in the heating curve for the third cycle.

All the curves exhibit thermal peaks associated with the α–β transformation. The peaks are approximately identical in areas, but differ considerably in shape. For the strongly deformed pressed sample, the ascending branch of the peak is steepest, and the peak width does not exceed 30 K. Upon heating in a calorimeter, the sample, which has been transformed into the ω-phase under pressure, initially undergoes the irreversible $\omega \longrightarrow \alpha$ transformation in the temperature range 425–470°C (shown on an enlarged scale in the inset in Fig. 5a). For this sample, the peak corresponding to the α–β transition begins at the lowest temperature and rises least steeply. The ascending branch of the peak shows more than one inflection point, which indicates the multistage character of the process. The total width of the peak is almost twice as large as that for the pressed sample. Therefore, the differences in defect structures of the samples differently treated prior to the measurements actually have a pronounced effect on the initial temperature and the character of the transformation in the alloy.

However, the effect of preliminary treatment of the alloy manifests itself so strongly only in the first cycle. Beginning with the second cycle, the thermal peaks for all the samples become identical in shape, and the temperature range of anomalies in different experiments and cycles coincide to within ± 5 K (Fig. 5b). As in the DTA experiments, the onset of the transformation was determined from the intersection of two tangent lines (see Fig. 5). The initial temperature T_0 averaged over all the experiments is equal to 612°C for heating and 546°C for cooling. Usually, it is believed that the temperature of the phase equilibrium is the average of the initial temperatures obtained upon heating and cooling, which results in T_{eq} = 579°C for the α–β transformation in the TiZr alloy. The hysteresis interval associated with this transformation is equal to 66 K. The averaged enthalpy ΔH of the α–β transition is 40.9 ± 2.0 J/g. As can be seen from Fig. 5, the peaks are asymmetric: upon both heating and cooling, the low-temperature portions of the peaks show a tail whose origin is difficult to explain by methodical causes. Most likely, the low-temperature tail stems from the phase strain hardening in the $\beta \longrightarrow \alpha$ transformation, which retards the completion of the transformation upon cooling, and, in the next heating cycle, the transformation is preceded by stress relaxation. An alternative, but less probable, explanation implies strong changes in the α-phase near the phase transition. The elucidation of the nature of this low-temperature tail is beyond the scope of the present work. However, it is clear that, if the tail is brought about by the phase hardening or pretransitional anomaly in the α-phase, the true enthalpy of the α–β transition should be less than our value given above by approximately the area under this section of the calorimetric curve.

A comparison with the available data on the initial temperature of the $\alpha \longrightarrow \beta$ transformation in the TiZr alloy shows good agreement (to within 3 K) between our results and those obtained in [8] (heating rate, 300 K/min). On the other hand, our estimate for the onset of the $\beta \longrightarrow \alpha$ transition considerably differs from the temperature (600°C) reported in [8]. The reasons for this disagreement are not quite clear. In particular, Auffredic *et al.* [8] pointed out the influence of impurities on the temperatures and hysteresis interval of the $\alpha \rightleftharpoons \beta$ transformations and also the possibility of reaction between the TiZr alloy and container material of the measuring cell. The fact that the peak shapes are irreproducible in the sequentially measured thermal curves also suggests that the experimental results obtained in [8] depend on foreign factors such as contamination of the alloy in the course of thermal cycles. Blacktop *et al.* [9] measured only the $\alpha \longrightarrow \beta$ transition temperatures and obtained the values of T_0 = 606°C for the $Ti_{0.6}Zr_{0.4}$ alloy and T_0 = 591°C for the $Ti_{0.4}Zr_{0.6}$

alloy, which are considerably less than the T_0 temperatures obtained in our work and in [8]. In our case, the found enthalpy of the α–β transition lies between the value of ΔH = 35.4–36.7 J/g for the TiZr alloy with the smallest content of the initial impurities [8] and ΔH = 45.8–51.2 J/g for the alloys with 40 and 60 at. % Ti [9]. With due regard for the fact that the origin of the low-temperature tail of thermal peaks in Fig. 5 remains unknown, the true enthalpy of the α–β transition in our TiZr alloy can coincide with the value reported in [8], to within the limits of experimental error. Consequently, except for the β ⟶ α transition temperatures, our calorimetric data and the results obtained in [8] are in a reasonable agreement.

The enthalpy of the ω ⟶ α transformation in the ω-TiZr alloy after the DTA experiment under pressure is equal to 2.8 J/g. Note that a small thermal peak in the vicinity of 450°C was also observed for the sample, which, after the annealing under vacuum, was cooled to room temperature (for this purpose, the external heating furnace was removed from an evacuated sealed silica tube with the sample). This indicates that the ω-phase is formed in the TiZr alloy even at relatively low rates of quenching. The formation of metastable phase under these conditions points to the existence of a high barrier to the β ⟶ α transition and agrees with the large hysteresis interval for the α–β transformation.

The α–β transition parameters, which were measured by the calorimetric technique, served as the references points for the construction of the *T*–*P* diagram in Fig. 3. The α ⟷ β transition curves plotted in the pressure range up to 30 kbar (a lens-type chamber) and the calorimetric data are in complete agreement. The slopes dT/dP of straight lines drawn by the least-squares method through the initial temperatures of transitions are equal to –1.9 and –2.5 K/kbar for heating and cooling, respectively. By passing the α–β equilibrium boundary as the midline between the curves of the direct and reverse transformations, we have dT/dP = –2.2 ± 0.3 K/kbar. This is somewhat lesser in magnitude than the slopes of the α–β equilibrium curves for pure Ti and Zr (approximately –3 K/kbar [1–3]). The hysteresis interval for the α–β transformation in TiZr alloy increases with an increase in the pressure and a decrease in the temperature, which can be accounted for by the fact that a decrease in the temperature hinders the overcoming of potential barriers to the transition.

At pressures up to 30 kbar, the experimental points obtained in the pressure range 24–70 kbar (a toroid-type chamber) fall on an extension of the α ⟷ β transition curves (Fig. 3). In the range from 30 to 50 kbar, the slope of the β ⟶ α transition curve smoothly changes upon cooling, so that the curve goes into the β ⟶ ω transition curve. The points of the ω ⟶ β transitions upon heating fall on the straight line with the slope dT/dP = 0.46 K/kbar. Upon linear extrapolation to atmospheric pressure, the ω ⟶ β transition curve intersects the temperature axis in the range of the ω ⟶ α transformations. The hysteresis interval of the β–ω transformation is small as compared with that of the α–β transformation, which is indicative of a lower potential barrier to the β ⟷ ω transitions.

Now, let us discuss the nature of the two-phase state formed after the DTA cooling cycle at pressures in the intermediate range 28–48 kbar. It is believed that the ω-phase formed in this case is metastable. This assumption is based on the above fact that the β ⟶ α transformation is substantially hindered owing to a decrease in the diffusive mobility of metal components with an increase in the pressure and a decrease in the temperature. At the same time, as the pressure increases, the depth of the local minimum in the thermodynamic potential that corresponds to the ω-phase approaches the depth of the absolute minimum corresponding to the α-phase. Well before the depths of minima turn out to be equal to each other, that is, beginning with a pressure of ~28 kbar, the barrier to the transition from the β-phase to the ω-phase (metastable at these pressures) becomes less than the barrier to the transition to the α-phase. Therefore, in the pressure range 28–48 kbar, the β-phase becomes unstable upon cooling and transforms into both the stable α-phase and the metastable ω-phase, which, in turn, is responsible for two transitions upon the subsequent heating. In the pressure range, where the ω-phase becomes stable, the α ⟶ β transition is not observed in the heating curves.

On the other hand, if the (α + ω) two-phase state was thermodynamically stable under these pressures at low temperatures, this would imply that, in the *T*–*c* sections of the three-dimensional *T*–*P*–*c* diagram, the points of equal concentrations for the α–β and ω–β equilibria should differ in concentration. As a consequence, for the TiZr equiatomic alloy, the β ⟶ ω transformation upon cooling at the pressures $P > 48$ kbar should be accompanied by the intersection of the two-phase (ω + β)-region. The intersection of the (ω + β)-region would lead to the dispersion of concentration in the ω-phase and the smearing of its X-ray diffraction pattern, which, however, is not observed experimentally.

Therefore, with a fair degree of confidence, it can be concluded that the point of the α–β–ω three-phase equilibrium in the TiZr equiatomic alloy is located at $P = 49 \pm 3$ kbar and $T = 460 \pm 30$°C, i.e., at the considerably lower pressure as compared to the value predicted earlier from the calculation by Aksenenkov *et al.* [11].

At atmospheric pressure, the α ⟷ β transformations in the TiZr equiatomic alloy are characterized by a rather large hysteresis interval (up to 66 K) and the heat of transition $\Delta H = 40.9 \pm 2.0$ J/g. The α–β equilibrium temperature determined as the average of the transition points upon heating and cooling is equal to 579 ± 5°C. In the pressure range up to 28 kbar, the α–β equilibrium temperature linearly decreases with the slope of the equilibrium curve in the *T*–*P* diagram dT/dP = –2.2 ± 0.3 K/kbar. At pressures in the range

from 28 to 48 kbar, the β-phase upon cooling transforms into the two-phase mixture of the stable α-phase and the metastable ω-phase, which, upon subsequent heating transforms into the β-phase through two individual phase transitions. At pressures above the triple point with the coordinates $P = 49 \pm 3$ kbar and $T = 460 \pm 30$°C, the ω-phase is the low-temperature stable phase. The hysteresis interval for the $\omega \rightleftharpoons \beta$ transformations is close to zero, and the slope of the ω–β equilibrium boundary is positive, $dT/dP = 0.46$ °C/kbar. Under normal conditions, the unit cell parameters of the ω-phase are as follows: $a = 4.843$ Å, $c = 2.988$ Å, and $c/a = 0.617$. At atmospheric pressure, the ω-phase of the TiZr alloy transforms into the α-phase in the temperature range 425–470°C with the heat of transition $\Delta H = 2.8$ J/g.

ACKNOWLEDGMENTS

This work was supported by the Russian Foundation for Basic Research, project nos. 97-02-17614 and 96-15-96806.

We would like to thank V.G. Glebovskiĭ and his collaborators (Institute of Solid State Physics, Russian Academy of Sciences) for preparing an ingot of the high-purity TiZr alloy.

REFERENCES

1. E. Yu. Tonkov, *High Pressure Phase Transformations* (Gordon & Breach, Philadelphia, 1992), Vol. 2, pp. 682, 691.
2. F. P. Bundy, in *New Materials and Investigation Techniques for Metals and Alloys* (Metallurgiya, Moscow, 1966), p. 230.
3. A. Jayaraman, W. Klement, Jr., and G. C. Kennedy, Phys. Rev. **131** (2), 644 (1963).
4. V. A. Zil'bershteĭn, N. P. Chistotina, A. A. Zharov, *et al.*, Fiz. Met. Metalloved. **39** (2), 445 (1975).
5. H. Xia, A. L. Ruoff, and Y. K. Vohra, Phys. Rev. B: Condens. Matter **44** (18), 10 374 (1991).
6. Y. Akahama, M. Kobayashi, and H. Kawamura, J. Phys. Soc. Jpn. **60** (10), 3211 (1991).
7. M. Hansen and K. Anderko, *Constitution of Binary Alloys* (McGraw-Hill, New York, 1958; Metallurgizdat, Moscow, 1962).
8. J. P. Auffredic, E. Etchessahar, and J. Debuigne, J. Less-Common Met. **84,** 49 (1982).
9. J. Blacktop, J. Crangle, and B. B. Argent, J. Less-Common Met. **109,** 375 (1985).
10. A. V. Dobromyslov, N. I. Taluts, K. M. Demchuk, *et al.*, Fiz. Met. Metalloved. **65** (3), 588 (1988).
11. V. V. Aksenenkov, V. D. Blank, B.A. Kul'nitskiĭ, *et al.*, Fiz. Met. Metalloved. **69** (5), 154 (1990).
12. D. K. Bulychev, I. Ya. Georgieva, O. P. Maksimova, *et al.*, Fiz. Met. Metalloved. **32** (6), 1260 (1971).
13. I. O. Bashkin, A. F. Gurov, V. Yu. Malyshev, *et al.*, Fiz. Tverd. Tela (Leningrad) **34** (4), 1276 (1992).
14. I. O. Bashkin, A. I. Latynin, and V. Yu. Malyshev, Fiz. Tverd. Tela (St. Petersburg) **37** (7), 2108 (1995).
15. T. E. Antonova, I. T. Belash, and S. A. Ivakhnenko, Fiz. Tekh. Vys. Davleniĭ (5), 85 (1981).

Translated by O. Borovik-Romanova

Physics of the Solid State, Vol. 42, No. 1, 2000, pp. 177–178. Translated from Fizika Tverdogo Tela, Vol. 42, No. 1, 2000, pp. 170–171.

LATTICE DYNAMICS. PHASE TRANSITIONS

On the Temperature Dependence of the Heterostructure Period near the Metal–Semiconductor Phase Transition in a Vanadium Dioxide Film

A. L. Semenov and E. N. Solodovnikova

Ul'yanovsk State University, ul. L'va Tolstogo 42, Ul'yanovsk, 432700 Russia

e-mail: semenov@quant.univ.simbirsk.su

Received December 15, 1998; in final form, May 24, 1999

Abstract—The effect of the nonlocality of the metallic-state instability upon the formation of semiconducting domains is considered theoretically in terms of the "strain" theory of the formation of superlattices consisting of alternating metallic and semiconducting phases in a vicinity of the critical point of the thermodynamically equilibrium phase transition metal–semiconductor in single-crystal vanadium oxide films. The above effect is shown to lead to the stabilization of a heterostructure in the region where the dimensions of the semiconducting and metallic domains are approximately equal. The obtained theoretical temperature dependence of the heterostructure period d is compared with the experimental data. © *2000 MAIK "Nauka/Interperiodica".*

1. The experimental investigations [1] of single-crystal vanadium dioxide films of thickness $h = 0.18$ μm on a substrate with the crystal axis c of the film being parallel to the substrate show that with decreasing temperature near the critical point $T_c = 340$ K, there first appear isolated, relatively far separated regions of the semiconductor phase in the form of long stripes of width $a \approx 1.2$ μm located perpendicular to the c axis. As the temperature decreases further, the positions of the semiconductor domains and their dimensions remain unaltered, whereas in the region of the retained metallic phase, new semiconductor regions of a similar shape are formed, so that the general picture looks like a s quasi-one-dimensional heterostructure of alternating metallic and semiconductor phases.

The theory of the superlattice formation that was developed in [2] based on the "strain" mechanism implies that the sufficient condition for the formation of a semiconductor domain is the existence in the metallic phase of at least one point with a Peierls instability against the transition into the semiconductor state [3–5]. The theoretical temperature dependence of the spatial period $d(T)$ of the heterostructure [2] is in qualitative agreement with the experimental data of [1], but the plateau observed in the experimental curve (see figure) has not been explained in [2].

In this work, we take into account, in terms of [2], that for a semiconductor domain of size a to be formed in the metallic phase, a region with the Peierls instability should appear, whose dimensions should be close to that of the arising semiconductor domain (effect of the nonlocality of the metallic-phase instability). This imposes more rigid conditions (as compared to the case of point instability of the metallic phase considered in [2]) on the possibility of the formation of new semiconductor domains and thus stabilizes the heterostructure. This makes it possible to more adequately describe the available experimental data. In particular, this permits us to account for the almost horizontal plateau in the experimental $d(T)$ dependence, which corresponds to almost identical dimensions of the metallic (b) and semiconductor (a) domains ($b \approx a$).

2. Let us consider a VO_2 film in which several isolated semiconductor stripes of width a were formed at a certain temperature T. We introduce the coordinate axis X in such a manner that it is parallel to the c axis (which is parallel to the substrate surface) with the origin located at the center of the metallic phase domain. Upon the transition into the semiconductor phase, VO_2 is known to expand along the c axis [6]; the corresponding expansion coefficient is

$$\alpha = \frac{l_s - l_m}{l_s} \sim 10^{-3}, \tag{1}$$

where l_s and l_m are the lengths of the VO_2 sample along the crystal axis c in the semiconductor and metallic states, respectively. Owing to this expansion, a mechanical stress σ directed along the crystal axis c arises in the metallic region of the film (at $|x| < b/2$), which can be approximately calculated by the following formula [2]:

$$\sigma = \sigma(x) = \frac{4\alpha E}{5}\left[J\left(\frac{4E_0}{5Eh}\left(\frac{b}{2} + x\right)\right) + J\left(\frac{4E_0}{5Eh}\left(\frac{b}{2} - x\right)\right)\right]. \tag{2}$$

Here, E and E_0 are Young's moduli of the film and sub-

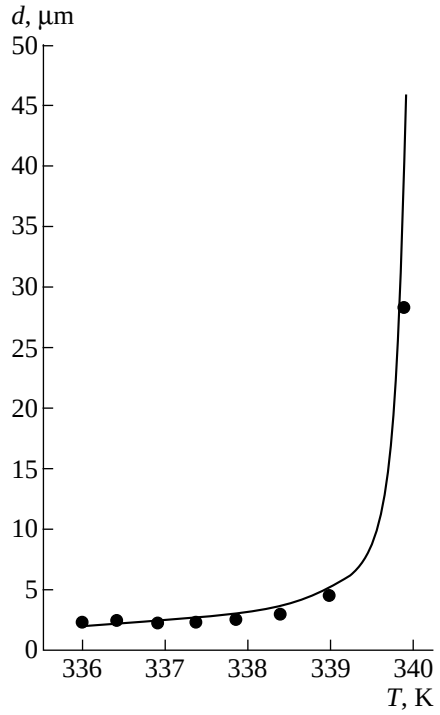

Experimental and calculated dependences of the superlattice period d on temperature T. Solid line corresponds to numerical calculation using formulas (2) and (5); solid circles represents the results obtained from the experimental data on the diffraction of light on a quasi-periodic superlattice formed by different phases that arise in the VO_2 film [1].

strate, respectively; and

$$J(x) = \cos(x)\left[\frac{\pi}{2} - Si(|x|)\right] + \sin(x)Ci(|x|). \quad (3)$$

It can be seen from (2) and (3) that the mechanical stress σ is greatest near the boundaries with the semiconductor domains (at $x = \pm b/2$) and decreases toward the center of the metallic domain ($x = 0$); the characteristic length is $l \approx Eh/E_0 \approx a/2$.

The temperature T_c of the instability of the metallic phase with respect to the transition into the semiconductor state is well described (in a wide range of changing stresses) by the formula [3, 7]

$$T_c = T_0 + \gamma\sigma. \quad (4)$$

where $T_0 = T_c(\sigma = 0) \cong 340$ K is the temperature of the Peierls instability of VO_2 at $\sigma = 0$, and $\gamma = \partial T_c/\partial\sigma \cong -1.2 \times 10^{-9}$ K cm^2/dyne. Therefore, we find the condition for the formation (at a temperature T) of a new semiconductor domain of size a in the center of the metallic domain as follows:

$$T = T_0 + \gamma\sigma\left(\frac{a}{2}\right). \quad (5)$$

The results of a numerical analysis of equations (2), (5), which form a closed set of equations for the determination of the temperature dependence of the average spatial period of the heterostructure $d = a + b$, are shown in the figure.

In the temperature range $336 < T < 339$ K, the theoretical results obtained agree well with the experimental data of [1]. At temperatures of 339–340 K, when $b \gg a$, the mechanical stress σ (2) produced by the semiconductor domains in the region $|x| < (b - a)/2$ is small in comparison with random mechanical stresses in the film that may arise during film preparation (due to cracks, scratches, and other defects). Therefore, the process of the formation of new domains of the semiconductor phase at the initial stage (at $b \gg a$) is primarily determined by the initial spatial fluctuations of strains in the film and cannot be described in terms of the suggested theory.

REFERENCES

1. K. A. Valiev, V. G. Mokerov, V. V. Saraikin, *et al.*, Fiz. Tverd. Tela (Leningrad) **19** (9), 1537 (1977) [Sov. Phys.–Solid State **19** (9), 1487 (1977)].
2. V. I. Emel'yanov and A. L. Semenov, Fiz. Tverd. Tela (Leningrad) **32** (10), 3083 (1990) [Sov. Phys.–Solid State **32** (10), 1790 (1990)].
3. V. I. Emel'yanov, N. L. Levshin, and A. L. Semenov, Vestn. Mosk. Univ., Ser 3: Fiz., Astron. **30** (5), 52 (1989).
4. A. L. Semenov, Fiz. Tverd. Tela (St. Petersburg) **39** (5), 925 (1997) [Russ. Phys.–Solid State **39** (5), 826 (1997)].
5. A. L. Semenov, Zh. Éksper. Teor. Fiz. **111** (4), 1398 (1997) [JETP **84** (4), 774 (1997)].
6. T. Kawakudo and T. Nakagawa, J. Phys. Soc. Jpn. **19** (4), 517 (1964).
7. L. A. Ladd and W. Paul, Solid State Commun. **7** (2), 425 (1969).

Translated by S. Gorin

Physics of the Solid State, Vol. 42, No. 1, 2000, pp. 179–183. Translated from Fizika Tverdogo Tela, Vol. 42, No. 1, 2000, pp. 172–175.

LATTICE DYNAMICS. PHASE TRANSITIONS

Phase Transition Kinetics in Loaded Solids

A. A. Vakulenko and S. A. Kukushkin

Institute of Problems in Machine Science, Russian Academy of Sciences, Vasil'evskiĭ Ostrov, Bol'shoĭ pr. 61, St. Petersburg, 199178 Russia

e-mail: anna@mech.ipme.ru
e-mail: ksa@math.ipme.ru

Received June 2, 1999

Abstract—A study is undertaken into the kinetics of phase transitions in solids under a load at a fixed temperature. The critical size of the micropores forming at a given load in the course of a phase transition in a material is found. The steady-state flux of pores in size space and the time required to reach this state, which depend at a given load on the surface energy of the solid and on an additional parameter characterizing the boundary kinetics of microdefects, are calculated. The parameters found in this work, which describe the onset of the latent stage in the fracture of a solid and the intensity of defect formation in the material in this stage, are new in the mechanics of fracture. This approach allows generalization to load-induced structural and martensitic transitions. © *2000 MAIK "Nauka/Interperiodica".*

This work is a continuation of our investigation [1] on the initial stages in the fracture of strained solids. The model of microcrack formation has been developed in [1]. According to this model, the deformation of a solid initiates fluctuations of the surfaces of the already existing microflaws. When entering the region where the load gradient exceeds a critical level, the fluctuations begin to grow. In these conditions, the surface of a microflaw can lose stability, and the fluctuations will propagate into the bulk of the material. It is these fluctuations that are actually microcracks.

Thus, the fracture starts with the development of microflaws, and it is the kinetics of their nucleation that we are going to study in this work.

The concept of the fracture of strained solids as a multi-stage process is well known and has been reliably supported by the experiments on many materials under diverse testing conditions. Investigations of various stages of the process has stimulated the development of the micromechanics of fracture and become the subject of a number of monographs [2–4]. Identification of the onset of the latent stage preceding the formation of microcracks in a solid is currently an urgent problem, because actually from this moment, microflaws can be studied by methods of the mechanics of deformable continuum. Note that the process of pore formation in solids is usually considered as pore nucleation from a supersaturated vacancy solution [2]. It is assumed that vacancies in a solid are either created by ionizing radiation or are already present at a given temperature. The pores themselves grow through the diffusion of incoming vacancies, and extended diffusion fields appear in the solid. Obviously enough, pore formation in a loaded sample occurs in a somewhat different manner.

1. PHYSICAL ESSENCE OF THE PROBLEM

Loading a deformable solid with defects, without which it cannot exist in a thermodynamic equilibrium, generates heterophase fluctuations of stresses, strains, and material density. After the local stresses have reached a certain level, microflaws start to nucleate in the solid. These microflaws grow not by the vacancy diffusion mechanism, but rather through the creation of vacancies in the immediate vicinity of the pore surface or at the surface itself, and through their transfer from the solid into the pore. Thus, we conceive pore nucleation under loading as a process similar to nucleation of a new phase from a melt [5, 6].

It is well known that the driving force of any first-order phase transition is the difference between the thermodynamic potentials in the new and old phases. In the case of solutions, this potential difference is a consequence of a difference between the concentrations and, correspondingly, the energy states of atoms in the new and the old phase. For pure solutions, this potential difference is a result of different stabilities of the new and old phases to temperature. In the case of pore growth under loading, the driving force of pore formation can be likewise the difference between the thermodynamic potentials of the continuum (the old phase) and the pore (the new phase). This potential difference originates from the difference between the vacancy states in the solid and the pore under loading. Consider now quantitatively the process of micropore nucleation and, in order to obtain the critical size of the micropores, we start with calculating the minimum work required to create a micropore.

1063-7834/00/4201-0179$20.00 © 2000 MAIK "Nauka/Interperiodica"

2. MICROPORES OF CRITICAL SIZE

In accordance with [7], we can write the Gibbs potential in a loaded solid as $\Phi(\sigma) = F(\sigma) - A^e$, where F is the free energy of the solid, and $A^e(\sigma, V) = \int_{(V)} \sigma : \varepsilon dV$ is the elastic potential energy of the region of the solid in volume V, where σ and ε are the stress and strain tensors.[1] When a material is loaded, there arise local metastable regions, in which, before the pore nucleation, the stress is σ_v, and after the pore formation, $\sigma'_{v'}$. We denote the specified macroscopic uniform (mean) stresses in a loaded solid by σ_0.

We assume the micropore nucleus forming in a metastable medium under loading to be spherical. Besides, we assume for the sake of simplicity that the vacancy is an elementary structural element making up the pore.[2] The difference between the thermodynamic potentials before and after the nucleation can be written as $F'(\sigma'_{v'}) - A^e(\sigma_v, V') - (F(\sigma_v) - A^e(\sigma_v, V))$. We express the minimum work done by an external load to produce a nucleus through the difference between the thermodynamic potentials and additional terms in the form of the work done by the elastic stresses A^e and the work required to create the surface

$$A_{\min} = \Phi'(\sigma'_{v'}) - \Phi(\sigma_v) - (A^e(\sigma_v, V') - A^e(\sigma'_{v'}, V')) + 4\pi\gamma r^2, \quad (1)$$

where $4\pi\gamma r^2$ describes the work of formation of the surface for a nucleus of size r. Assuming a small degree of metastability, for the state with a new phase, we have the first-order approximation $\Phi'(\sigma'_{v'}) = \Phi'(\sigma_v) + (A^e(\sigma_v, V') - A^e(\sigma'_{v'}, V'))$. Introducing the chemical potentials for a vacancy in the medium μ and in the pore of radius $R = \infty$, μ' and using this expansion, from (1), we obtain

$$A_{\min} = -\frac{4}{3}\frac{\pi r^3}{\Omega}(\mu(\sigma_v) - \mu'(\sigma_v)) + 4\pi\gamma r^2, \quad (2)$$

where Ω is the vacancy volume. By varying the work (2)

$$\frac{\delta A_{\min}}{\delta r} = \frac{4\pi r^2}{\Omega}\left(-(\mu(\sigma_v) - \mu'(\sigma_v)) + \frac{2\gamma\Omega}{r}\right), \quad (3)$$

one obtains the maximum of the volume for $\frac{\delta A_{\min}}{\delta r} = 0$, which is reached at the critical size r_c of the nucleus. As follows from (3), at $r < r_c$, the nuclei decrease in size, at $r > r_c$, they grow, and for $r = r_c$ the nucleus is at equilibrium, where

$$r_c = \frac{2\gamma\Omega}{\mu(\sigma_v) - \mu'(\sigma_v)}. \quad (4)$$

Here, σ_v is the stress tensor corresponding to the metastable state of the effective region. The chemical potential of a vacancy in the original medium $\mu(\sigma_v)$ can be expressed in a first approximation through the chemical potential in the unstressed state and the work done by the stresses on the strains associated with the stress-induced distortion of the vacancy: $\mu(\sigma_v) = \mu(0) + \Omega\varepsilon_0 : \sigma_v$. The chemical potential of vacancies in the pore nucleus phase is equal to $\mu(0)$, then

$$r_c = \frac{2\gamma}{\varepsilon_0 : \sigma_0}. \quad (5)$$

As follows from (5), nucleation of pores under load is similar to sedimentation of a solid phase from a solution, where the role of supersaturation is played by a specified stress tensor σ_0.

A particular case of this relation for all-sided tensile stresses is discussed in monograph [9] with usual reservations about the impossibility of homogeneous nucleation through mutual diffusion, which would require stresses in excess of the elastic limit of a material. The approach developed in this work makes use of a probabilistic measure of the formation of a nucleus, which assumes, at the physical level, the existence of heterophase stress-field fluctuations under load and the possibility of realization of formula (5).

In the uniaxial case, when the only component s of the σ_0 tensor is close to its extreme value s_f, the critical size should be equal to the size of the starting defect a, of which the pore originates.[3] This brings us to the relation $\varepsilon_f s_f = 2\gamma/a$, which at $a = \frac{4}{\pi}a_0$, coincides with the breaking strength by Orowan [10] and is $\frac{\pi}{2}\frac{\gamma}{a_0}$, where a_0 is the equilibrium interplanar distance (with no load applied), and ε_f is the limiting strain.

3. KINETICS OF MICROPORE FORMATION IN A BRITTLE BODY

We have shown that the process of micropore formation is similar to the nucleation of a new phase in first-order phase transitions. A loaded solid is locally in a metastable state. The transition of a metastable to the stable state occurs through formation in the originally homogeneous body of micropores, i.e., nuclei of voids,

[1] For $\sigma = -PI$, where I is the identity tensor, we have the isobaric–isothermal potential, and the critical size of defects for this case is considered in [8].

[2] In a general case, any point or line defects can act as structural elements.

[3] It should be pointed out that the model of vacancy as a defect with surface tension is a good approximation to estimate the energy of formation of vacancies, bivacancies, and the vacancy migration energy in a material.

by the fluctuation mechanism. As is seen from formula (3), stable nuclei are those of the critical size.

Our description of the micropore formation process will be based on the Fokker–Planck equation, which is used widely in the kinetics of first-order phase transitions [5]. For this purpose, we introduce the distribution function of micropore nuclei in size $f(r, t)$, where r is the micropore radius, and $f(r, t)dr$ is the number of nuclei with sizes in the interval $[r + dr, r)$ at instant of time t in a unit volume of the material. Note that one can use two approaches to derive the equation describing micropore formation. The first of them is due to Zeldovich [11, 12]. In this approach, in deriving the rate equation, one should use the equilibrium distribution function of nuclei in size. By the second approach developed in [13, 6], in order to derive the equation for new phase nucleation, one has to find the relation between the probabilities of emission and absorption of structural elements. In our case, these structural elements are vacancies. When using the latter approach, there is no need to invoke the equilibrium distribution function. In the final count, both approaches yield the same results. Using [11–13], we can obtain the rate equation describing the evolution of the nucleus distribution function in size, that is,

$$\frac{\partial f}{\partial t} = \frac{\partial}{\partial r} D_r \left[\frac{1}{T_0} \frac{\delta A_{\min}}{\delta r} f(r, t) + \frac{\partial f}{\partial r} \right], \quad (6)$$

where D_r is the pore diffusion coefficient in the size space. The expression $-\frac{1}{T_0} D_r A'_{\min}$ is the drift coefficient for equation (6) and determines the average rate of pore radius variation

$$\frac{dr}{dt} = -\frac{1}{T_0} D_r \frac{\delta A_{\min}}{\delta r}. \quad (7)$$

To find the diffusion coefficient in the size space, one has to consider the kinetics of averaged growth in accordance with the boundary kinetics of vacancy transport through the nucleus boundary r, which is given by the equality $\frac{dr}{dt} = -V$, where V is the rate of this process. We accept within a linear approximation that the rate of vacancy transport from the solid into a pore is proportional to the force acting on a vacancy, $V = \beta F$, where, in accordance with Section 2, the thermodynamic force F is determined by the expression $F = -\frac{\mu - \bar{\mu}}{a}$; here a is the size of the structural element, and $\tilde{\mu} = \mu' + \frac{2\gamma\Omega}{r}$. Hence, using (3), one can write the rate of pore nucleus growth in the form

$$\frac{dr}{dt} = -A'_r \frac{\beta\Omega}{4\pi a r^2}. \quad (8)$$

As follows from expressions (3) and (4), at $r < r_c$, we have $A'_r > 0$, and the nuclei decrease in size in accordance with (8), whereas, at $r > r_c$, they continue to grow. A comparison of expressions (7) and (8) yields the following relation for the diffusion coefficient in the size space

$$D_r = \frac{\beta\Omega T_0}{4\pi a r^2}. \quad (9)$$

Relation (9) shows that, as the radius increases, the diffusion coefficient in the size space decreases, which results in a decrease of the probability for a pore to appear as its size increases.

4. CHARACTERISTICS OF THE PORE NUCLEATION PROCESS

By solving the steady-state equation (6) and taking into account (8) and (9) subject to the natural boundary conditions $f(r, t) \longrightarrow N(t)$, where $N(t)$ is the number of atoms per unit volume, at $r \longrightarrow 0$, and $f(r, t) \longrightarrow 0$ at $r \longrightarrow \infty$, in the same way as it is done in [6, 11, 12], we can obtain the characteristics of the kinetic process. The steady-state number of nuclei passing through a unit volume per unit time is estimated from the expression for the steady-state flux I

$$I = D_{r_c} \pi^{-1/2} \sqrt{-\frac{1}{2T_0} \frac{\partial^2 A_{\min}}{\partial r^2}(r_c)} \exp\left[-\frac{A_{\min}(r_c)}{T_0} \right]. \quad (10)$$

In (10), the diffusion coefficient in the size space is given by equation (9). The values of the diffusion coefficient (9), the minimum work (2), and its second derivative for the critical radius are calculated using (5)

$$D_{r_c} = \frac{\beta T_0 \Omega (\varepsilon_f : \sigma_0)^2}{16\pi a \gamma^2}, \quad (11)$$

$$A_{\min}(r_c) = \frac{4\pi}{3} \frac{\gamma^3}{(\varepsilon_0 : \sigma_0)^2}, \quad (12)$$

$$\left. \frac{\partial^2 A_{\min}}{\partial r^2} \right|_{r = r_c} = -8\pi\gamma. \quad (13)$$

From expressions (11) and (13), one finds the steady-state flux

$$I = \frac{\beta \sqrt{T_0}\, \Omega (\varepsilon_0 : \sigma_0)^2}{8\pi a \gamma^{3/2}} \exp\left(-\frac{4\pi\gamma^3}{3T_0 (\varepsilon_0 : \sigma_0)^2} \right). \quad (14)$$

This expression provides a scalar characteristic of the initial stage in the fracture process, which is essentially the stage of nucleation of stable microdefects. If the σ_0 level grows from one sample to another, the flux (14) increases, and the critical size of the pore nuclei decreases. For $\sigma_0 \longrightarrow \sigma_f$, the flux in the size space per

unit time reaches a maximum, so that the material can undergo macrofracture by the ideal brittle mechanism.

The time for a steady-state flux to set in can be written as

$$t \sim \frac{(\delta r_c)^2}{D_{r_c}}, \tag{15}$$

where δr_c is the width of the region near the critical point given by the expression [13]

$$\delta r_c = \left(-\frac{1}{2T_0}\frac{\partial^2 A_{\min}}{\partial r^2}(r_c)\right)^{-1/2}.$$

Thus, using (11) and (13), we can calculate the time of establishment of a steady-state flux for a phase transition under load (15) from the relation

$$t = \frac{4\gamma a}{\beta\Omega(\varepsilon_0 : \sigma_0)^2}. \tag{16}$$

For $\sigma_0 \longrightarrow \sigma_f$, the time t decreases to reach in the limit its minimum $t_{\min}$. Relation (16) can be used to derive the relation connecting the surface energy ($A_\gamma = \gamma a^2$) with the potential energy of the structural element of the medium ($A = \Omega\varepsilon_0 : \sigma_0$), which has the form $\alpha A_\gamma = A$, where $\alpha = \frac{\sqrt[4]{\pi/3}}{t\beta\gamma}$ is a dimensionless parameter less than unity. Ideal brittle fracture occurs at $\alpha = 1$, which yields an estimate for the kinetic parameter $\beta = \frac{\sqrt[4]{\pi/3}}{t_1\gamma}$. In the case of nonideal brittle fracture, the excess of the potential energy of a strained medium $(\alpha - 1)A_\gamma$ is expended to propagate an acoustic wave, whose eigenfrequencies are determined by the size of the critical nucleus, and the amplitude depends also on the excess of potential energy [7]. The elastic potential energy of a material behaving in a plastically elastic manner is expended to create plastic zones near micropores. We believe that (16), as well as relation (14), are characteristics of the latent stage in the brittle fracture of materials.

A similar situation occurs in loaded bodies, in which martensitic or structural transformations take place [14]. Indeed, equations (6), (8), and (9) derived by us to describe the kinetics of micropore formation also adequately reproduce the formation of new-phase nuclei in diffusionless transformations. In deriving these equations, we did not invoke additional assumptions concerning the nature of the new phase, a micropore being nothing else but a negative crystal.

When considering a structural transition, we have to replace the coefficient β in the equation (8) describing the pore growth rate with another coefficient characterizing the rate of atom transfer from one phase to another. All the other equations remain unchanged.

5. DISCUSSION

We have considered here the nucleation of pores within the framework of the kinetics of a first-order phase transition in a loaded material. The critical radius of a stable pore nucleus in a loaded material, which is determined by the surface energy of a body and the potential energy of a strained medium, has been obtained. The kinetics of pore nucleation is described using an additional parameter characterizing the behavior of a material on the microscale.

The kinetics of a phase transition in a loaded body is determined by the flux of nuclei in the size space (14) and the time for this flux to reach a steady-state level (16), similar to the processes involved in sedimentation of a solid phase from a solution. The characteristics of a phase transition under loading determine the onset of the latent stage of fracture and the structural level of microdamage of the material in this stage. Expressions (14) and (16) describe qualitatively the behavior of a material in the initial stage of fracture under loading. In experiments carried out at different levels of a fixed load, the intensity of creation of the nuclei of the elements accounting for the fracture increases noticeably with increasing load, and the time of establishment of the steady-state intensity decreases. The latent stage in the fracture of a material itself consists in a buildup and interaction of the forming nuclei, which result in their coalescence. In the limiting case of extreme loads, the minimum size of the fracture nuclei gives rise to a spontaneous disintegration of the body into parts (its transformation in a void), with no latent stage of fracture practically observed at the macrolevel. In the opposite case, when the loads are small, a large defect can form, the time required for another such defect to appear in the material is long, and, therefore, the latent stage lasts substantially longer.

The characteristics of the nucleation kinetics can be used in nonsteady-state problems of the mechanics of fracture as well. In particular, in the problem of crack propagation, the time required for a steady-state flux of nuclei to set in determines the minimum time of interaction of a crack with the microdefects forming at its tip.

In the case of structural or martensitic transformations, these characteristics play a similar role.

ACKNOWLEDGMENTS

This work was supported by the Russian Foundation for Basic Research (project no. 99-03-32768) and the Integration program (project no. 589).

We are grateful to A.V. Osipov for his participation in discussions of the results and helpful remarks.

REFERENCES

1. A. A. Vakulenko and S. A. Kukushkin, Fiz. Tverd. Tela (St. Petersburg) **40** (3), 75 (1998).

2. P. G. Cheremskoĭ, V. P. Betekhtin, and V. V. Slezov, *Pores in a Solid* (Energoatomizdat, Moscow, 1990).
3. J. Čadek, *Crepp Kovovych materialu* (Academia, Prague, 1984; Mir, Moscow, 1987).
4. S. Suresh, *The Fatigue of Materials* (Cambridge Univ. Press, Cambridge, 1991).
5. S. A. Kukushkin and V. V. Slezov, *Disperse Systems on the Surface of Solids: an Evolutionary Approach* (Nauka, St. Peterburg, 1996).
6. V. V. Slezov and S. A. Kukushkin, Fiz. Tverd. Tela (St. Petersburg) **38** (2), 433 (1996).
7. L. D. Landau and E. M. Lifshits, *The Theory of Elasticity* (Nauka, Moscow, 1965; Pergamon, Oxford, 1980), Vol. 7.
8. L. D. Landau and E. M. Lifshits, *Statistical Physics (*Nauka, Moscow, 1965; Pergamon, Oxford, 1980), vol. 5.
9. Ya. E. Geguzin, *The Diffusion Zone* (Nauka, Moscow, 1979).
10. A. Kelly, *Strong Solids (*Oxford Univ. Press, London, 1971; Mir, Moscow, 1976).
11. S. A. Kukushkin and A. V. Osipov, Usp. Fiz. Nauk **168** (10), 1083 (1998).
12. E. M. Lifshits and L. P. Pitaevskiĭ, *Kinetics in Physics* (Nauka, Moscow, 1979).
13. V. V. Slezov and J. Schmelzer, Fiz. Tverd. Tela (St. Petersburg) **36** (2), 353 (1994).
14. A. L. Roitburd and D. E. Temkin, Dokl. Akad. Nauk **288** (1), 111 (1986).

Translated by G. Skrebtsov

Physics of the Solid State, Vol. 42, No. 1, 2000, pp. 184–188. Translated from Fizika Tverdogo Tela, Vol. 42, No. 1, 2000, pp. 176–179.

LATTICE DYNAMICS. PHASE TRANSITIONS

Symmetry Analysis of the Possible Low-Temperature Phases in $KDy(MoO_4)_2$

N. M. Nesterenko

Physicotechnical Institute of Low-Temperatures, National Academy of Sciences of Ukraine, Kharkov, 310164 Ukraine

Received January 21, 1999; final version received June 21, 1999

Abstract—The possible asymmetric phases in the Jahn–Teller crystal of $KDy(MoO_4)_2$ are analyzed. Phases appearing upon a second-order phase transition from an orthorhombic D_{2h}^{14} group with the unit cell volume doubling are described. It is shown that $KDy(MoO_4)_2$ crystals are capable of featuring the Jahn–Teller pseudoeffect caused by the interaction between the electron states of dysprosium ions and the compressive (tensile) or shear deformations. © *2000 MAIK "Nauka/Interperiodica".*

A second-order phase transition in $KDy(MoO_4)_2$ was originally detected in the absorption spectra [1]. An increase in the energy difference between the ground level and the first excited level in the main multiplet $^6H_{15/2}$ of the Dy^{3+} ion, observed upon decreasing the temperature from $T \sim 15$ K to the liquid-helium temperatures, was explained by ordering of the type of the cooperative Jahn–Teller effect [1, 2]. However, study of the optical birefringence and magnetic properties of $KDy(MoO_4)_2$ [3, 4] showed that the latter effect involves a sequence of phase transitions described by two critical temperatures: $T_1^{cr} \sim 14.5$ K and $T_2^{cr} \sim 11.5$ K. Note that it was assumed that $KDy(MoO_4)_2$ is characterized by an incommensurate crystal structure in the 14.5–11.5 K temperature interval [3, 4].

Unfortunately, no X-ray diffraction data are available at present on the symmetry of low-temperature phases in dysprosium molybdates. A symmetry analysis performed in [5] described a separate second-order phase transition; the analysis was based on the character of anomalies in the transverse sound velocity at 12 K [6].

The purpose of this work was to analyze the possible second-order phase transitions for the point in the Brillouin zone where the phase transitions are accompanied by doubling of the crystal unit cell volume. The results of analysis are compared to experimental EPR data for the initial (space group D_{2h}^{14}, $T = 300$ K [7]) and low-temperature phases and the results of ultrasonic measurements [6].

1. SYMMETRY ANALYSIS

Let us consider the possible variants of decrease in the crystal symmetry within the framework of the Landau theory. The table (second column) presents irreducible representations related to the boundary points of the Brillouin zone of the $G_0 = D_{2h}^{14}$ group, where the unit cell volume exhibits doubling, and to the point with $\mathbf{k} = 0$ [7] (here and below we use the notation of axes adopted in the Kovalev tables [8]). All the active representations admit the second-order phase transitions with a decrease in the symmetry. For vectors $\mathbf{k}_{20}$, $\mathbf{k}_{21}$ and $\mathbf{k}_{22}$, the phase transitions to commensurate phases proceed via intermediate incommensurate phases.

All the two-dimensional representations listed correspond to a single planar group $L = C_{4v}$ [9] and, hence, the thermodynamic potential as a function of (η, ξ) is characterized by the same set of invariants $(\eta^2 + \xi^2)$, $(\eta^4 + \xi^4)$, $\eta^2\xi^2$ and can be written (retaining terms up to the sixth order and neglecting the gradient invariants) in the following form:

$$\Phi(\eta, \xi) = 1/2\alpha(T)(\eta^2 + \xi^2) + 1/4\beta_1(\eta^4 + \xi^2) + 1/2\beta_2(T)\eta^2\xi^2 + 1/6\beta_3(\eta^2 + \xi^2)^3 \ldots \quad (1)$$

Each two-dimensional representation may induce three commensurate asymmetric phases (G_1, G_2, G_3). Stationary solutions of equation (1) are possible for nonzero values of the order parameter $(\eta, 0)$, $(0, \eta)$, and (η, η), that is, for the phases G_1 and G_2 [9, 10].

The results of our symmetry analysis are summarized in the table. The table lists phases capable of featuring the second-order phase transitions from the initial orthorhombic structure and the first-order phase transitions close to the second-order ones. Also indicated are the factor groups G_1/G_1^Γ and G_2/G_2^Γ isomorphous to the point groups of the most symmetric phases G_1 and G_2, where G_1^Γ and G_2^Γ are the subgroups of translations for G_1 and G_2. Symmetry of the G_3 phases with arbitrary values of the order parameter (η, ξ) is

1063-7834/00/4201-0184$20.00

determined in each case as the intersection of groups for the phases characterized by the $(\eta, 0)$ and (η, η) order parameters. The indices of the space groups for the phases induced by the components $\{\eta, 0\}$ and $\{0, \eta\}$ of the order parameter are the same for all representations. The table also indicates the local symmetry of the Jahn–Teller centers in the asymmetric phases. Note that the local symmetry of dysprosium ions in $KDy(MoO_4)_2$ at $T = 4.2$ K is C_1 [11].

2. DISCUSSION

For the comparison with experiment, let us consider mixed invariants including the lowest powers of components of the order parameter and the stress tensor. These quantities differ for the transitions into monoclinic and orthorhombic phases. In the first case, we may construct two types of the mixed invariants using components of the order parameter and the deformation tensor: $(\eta^2 - \xi^2)u_{ij}$ and $\eta\xi u_{ij}$, where $i, j = x, y, z$. In the case of phase transitions to orthorhombic phases, the $(\eta^2 - \xi^2)u_{ij}$ invariants are absent because the combination $(\eta^2 - \xi^2)$ transforms according to odd representations of the orthorhombic group.

For the directions x, y, z selected in the table, the elastic energy of an orthorhombic crystal can be written in the following form:

$$E_{e1} = c_{11}u_{xx}^2 + c_{22}u_{yy}^2 + c_{33}u_{zz}^2 + c_{44}u_{yz}^2 + c_{55}u_{xz}^2 + c_{66}u_{xy}^6. \quad (2)$$

The types of anomalies in the longitudinal sound velocity, corresponding to transitions at the boundary points of the Brillouin zone are known and, in the simplest case of the G_0–G_1 transition, can be written as [10]

$$c_{ii} = c_{ii}^0 - \alpha_i^2/2\beta_1, \quad (3)$$

where $i = 1, 2, 3$; c_{ii}^0 are the elastic moduli at $T > T^{tr}$; α_i^2 is the coefficient at the mixed invariant of the type $(\eta^2 + \xi^2)u_{ii}$; and $\beta_1 = \text{const} > 0$ is the coefficient at the order parameter term of the fourth power. The jump is retained at the tricritical point. At the point of transition to the monoclinic phase, one of the transverse moduli has a jump of the same sign as that of the longitudinal moduli, while the two other moduli exhibit a break point at $T = T^{tr}$ and a linear increase at $T < T^{tr}$. The phase transitions to an orthorhombic phase are accompanied by jumps only in the longitudinal moduli. For the G_0–G_2 chain, the anomalies are observed at different temperatures because $\alpha(T)$ is replaced by $\beta_2(T)$.

Let us turn to the analysis of data for the ultrasound velocity anomalies in $KDy(MoO_4)_2$ in the temperature range 1.5–30 K [6] (see Figs. 1a and 1b). Anomalies observed at $T_2 \sim 12$ K in the velocity of longitudinal c_{33} (1) and transverse c_{44} (3) waves have a similar ν-like shape. Since the ultrasound velocity at a liquid-helium temperature is lower than that at elevated temperatures (above 17 K), the change Δc_{ij} is related to a phase transition at the boundary point of the zone [5]. We may suggest that the axis $C_2 \parallel y$ is retained at temperatures below $T_2 \sim 12$ K. This axis is retained upon a phase transition to the monoclinic phase induced by the representations τ_{78}, τ_{79} of the point $\mathbf{k}_{23}$ in the Brillouin zone of the initial phase (see table). Selection of the centrosymmetric crystal group at low temperatures agrees with the data obtained from the Raman and IR spectra [12, 13].

However, as seen from Figs. 1a and 1b, the elastic moduli exhibit changes in a broad temperature range. Vitebskiĭ *et al.* [6] related the smeared temperature profiles to the effect of fluctuational contributions. Let us consider some features in the behavior of elastic moduli, which are not related to the fluctuations and not discussed in [5].

Active points in the Brillouin zone of the D_{2h}^{14} symmetry group leading to monoclinic ad orthorhombic phases

Brillouin vector	Representation	G_d/G_d^Γ	Symmetry at R^{3+} position
	$\tau_2(A_{1u})$	D_2	C_2
$\mathbf{k}_{19} = 0$	$\tau_3(B_{1g})$	C_{2h}, $2_1 \parallel x$	C_1
$\mathbf{x} \parallel \mathbf{c}$	$\tau_4(B_{1u})$	C_{2v}, $2_1 \parallel x$	C_1
$\mathbf{y} \parallel \mathbf{a}$	$\tau_5(B_{2g})$	C_{2h}, $2 \parallel z$	C_2
$\mathbf{z} \parallel \mathbf{b}$	$\tau_6(B_{2u})$	C_{2v}, $2 \parallel z$	C_2
	$\tau_7(B_{3u})$	C_{2h}, $2_1 \parallel y$	C_1
	$\tau_8(B_{3g})$	C_{2v}, $2_1 \parallel y$	C_1
	$\tau_{69}(\eta, 0)$	C_{2h}, $2_1 \parallel y$	C_1
$\mathbf{k}_{20} = 1/2\mathbf{b}_1$	(η, η)	C_{2h}, $2_1 \parallel y$	C_1
$\mathbf{b}_1 \parallel x$	$\tau_{70}(\eta, 0)$	C_{2h}, $2_1 \parallel y$	C_1
	(η, η)	C_{2h}, $2_1 \parallel y$	C_1
	$\tau_{61}(\eta, 0)$	C_{2v}, $2_1 \parallel x$	C_1
$\mathbf{k}_{21} = 1/2\mathbf{b}_2$	(η, η)	C_{2h}, $2_1 \parallel z$	C_1
$\mathbf{b}_2 \parallel y$	$\tau_{62}(\eta, 0)$	C_{2v}, $2_1 \parallel x$	C_1
	(η, η)	C_{2h}, $2_1 \parallel z$	C_1
	$\tau_{47}(\eta, 0)$	D_2	C_2
$\mathbf{k}_{22} = 1/2\mathbf{b}_3$	(η, η)	C_{2v}, $2 \parallel z$	C_2
$\mathbf{b}_3 \parallel z$	$\tau_{48}(\eta, 0)$	D_2	C_1
	(η, η)	C_{2v}, $2_1 \parallel z$	C_1
	$\tau_{78}(\eta, 0)$	C_{2h}, $2_1 \parallel x$	C_2
$\mathbf{k}_{23} = 1/2(\mathbf{b}_2 + \mathbf{b}_3)$	(η, η)	C_{2h}, $2 \parallel z$	C_2
	$\tau_{79}(\eta, 0)$	C_{2h}, $2_1 \parallel y$	C_1
	(η, η)	C_{2h}, $2 \parallel z$	C_1

Note: Unit cell parameters of the orthorhombic lattice $\mathbf{a} = 5.084$ Å, $\mathbf{b} = 18.18$ Å, $\mathbf{c} = 7.97$ Å; G_d/G_d^Γ is the factor group isomorphous to the point groups $G_d = G_1, G_2$.

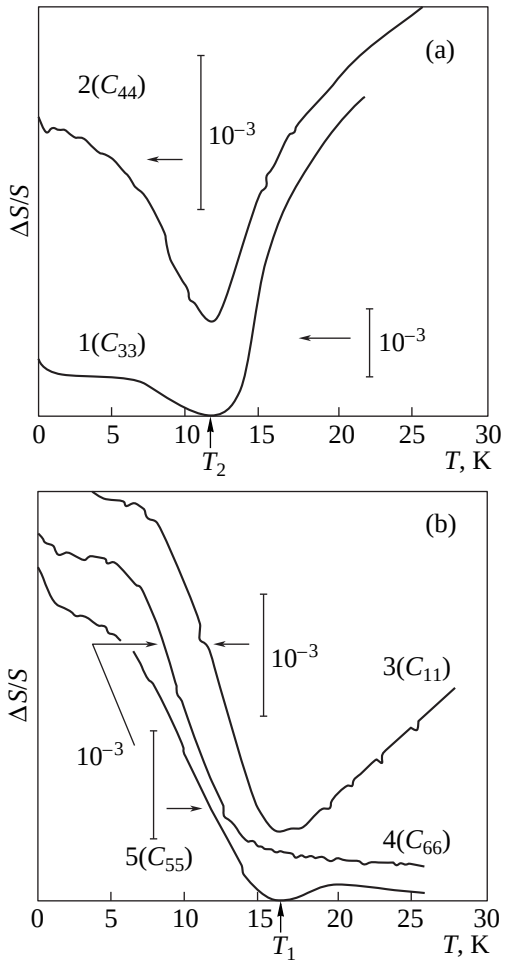

Fig. 1. Temperature variation of relative changes in the longitudinal and transverse sound velocity along the principal axes of an orthorhombic crystal: (*1*) **q** ∥ **b** ∥ **z**; (*2*) **q** ∥ **b** ∥ **z**; **u** ∥ **a** ∥ **y**; (*3*) **q** ∥ **c** ∥ **x**; (*4*) **q** ∥ **a** ∥ **y**; **u** ∥ **c** ∥ **x**; (*5*) **q** ∥ **b** ∥ **z**; **u** ∥ **c** ∥ **x**; [6]. The scales of the c_{66} and c_{55} moduli are the same.

The elastic moduli c_{11} (4) and c_{55} (6) exhibit a break at higher temperatures (17 K) as compared to the temperature of anomalies in c_{33} and c_{44} (12 K). As seen from Figs. 1a and 1b, there are two temperatures ($T_1 \sim$ 17 K; $T_2 \sim$ 12 K) at which the moduli vary in the opposite directions.

Let us assume that a difference in the behavior of elastic moduli at T_1 and T_2 is caused by sequentially occurring phase transitions. If the anomalies at 17 K are induced by a phase transition into phase G_2 (i.e., into the second monoclinic phase, $C_2 \parallel z$), which proceeds with respect to the parameter η and takes place at the same point $\mathbf{k}_{23}$, then the jump should be observed in the transverse sound velocity c_{66}. However, a more pronounced anomaly is observed in the transverse modulus c_{55} at 17 K (Fig. 1a), which is characteristic of the phase transition into a monoclinic phase with the axis $C_2 \parallel y$.

In order to elucidate the reasons of this behavior, let us consider an additional order parameter ξ related to the representations τ_2–τ_8 ($\mathbf{k}_{19} = 0$). Simple considerations show that an allowance of the interaction between the order parameter ξ and deformations cannot explain an increase in the modulus c_{11}, as well in potential (1), near the temperature of the second-order phase transition. For the further analysis, let us consider the interaction of deformation with the electron subsystem related to the Jahn–Teller ions.

The main multiplet ${}^6H_{15/2}$ of the Dy^{3+} ion is characterized by a half-integer total moment $J = 15/2$. In the crystal field, the state degenerate with respect to J splits into eight Kramers levels. Their wavefunctions correspond to double-valued representations $E'_{1/2}$ of the orthorhombic group D_{2h}^{14}, since the direct self-product $E'_{1/2} \cdot E'_{1/2}$ contains the A- and B-representations of the local group C_2, the electron states of the Jahn–Teller ion may interact both the fully symmetric components of the deformation tensor and with the deformations changing the local symmetry of the Jahn–Teller centers. Because it is the c_{11} modulus that exhibits an anomalous break above the T_2^{cr} temperature, we will take into account only the interaction with deformations of the u_{xx} type. A relationship between rare-earth ions and the deformation can be expressed in the following form [14]:

$$E_{str} = -\tau u_{xx}\sigma^x, \qquad (4)$$

where σ^x is the energy of splitting between the Kramers doublets 0 and 1 above T_1. Then the total elastic energy of the crystal can be written as a sum

$$E_{eff} = E_{el} + E_{str},$$

where E_{el} is the elastic energy of the orthorhombic crystal without an allowance for the interaction with the electron subsystem at temperatures above T_2.

Let us consider the elastic energy E_{eff} of the crystal in the temperature range $T > T_2$, that is, assuming that $\langle\eta\rangle = 0$. Taking into account the conditions $E_{eff} > 0$ and $dE_{eff}/du_{ii} = 0$, we obtain a relationship

$$\tau\sigma^x \sim c_{11}u_{xx} + c_{22}u_{yy} + c_{33}u_{zz},$$

which implies that the electron–deformation interaction compensates for a change in the elastic energy in the temperature interval $T > T_2$, thus leading to a temperature-induced energy splitting between levels 0 and 1. We should also take into account that $u_{ii} \sim \delta l_i/l_i$ (l_i is the crystal size along the corresponding direction) and that the effective energy must exhibit a minimum in the vicinity of the phase transition temperature: $dE_{eff}/dT = 0$. Then, the value of splitting $\langle\sigma^x(t)\rangle$ in the electron spectrum, which is related to the cooperative Jahn–Teller effect, depends on the values of moduli and their derivatives and may be also affected by changes in the sam-

ple shape. Note that these factors may account for the difference between the temperatures T_1 and T_2, as well as between T_1^{cr} and T_2^{cr}. The most interesting problem is that determining the symmetry of the low-temperature phase in the intermediate temperature interval. Let us return to Fig. 1b. Since the anomalous increase in the modulus c_{11} begins at a temperature where the longitudinal modulus c_{55} exhibits a break, we may suggest that this behavior is also related to the electron subsystem. However, as noted above, the relationship with deformation cannot be linear because $1/c_{ij} \sim 1/(T - T^{cr})$.

The above considerations show that the phase transformation in $KDy(MoO_4)_2$ is described as a transition of the displacement type, "softening" the low-energy vibrations at the boundary point of the Brillouin zone. Anomalies of the type of the collective Jahn–Teller effect, observed in the absorption spectra, result from sharp changes in the longitudinal moduli in the pretransition region and are apparently determined by the elastic electron–deformation interaction. If the electron–deformation interaction is related only to the A_{1g} component of the deformation, the splitting of levels of the Jahn–Teller centers above T_2 may be not accompanied by a decrease in the local symmetry of the Jahn–Teller ions in $KDy(MoO_4)_2$ [15].

It is also necessary to note some features of the transformation in $KDy(MoO_4)_2$, which are characteristic of the phase transitions of the order–disorder type. If the symmetry of the low-temperature phase is not higher than monoclinic ad the phase transition is accompanied by doubling of the inequivalent Jahn–Teller centers (this number increases to eight), the ratio of the number N of positions occupied by the Jahn–Teller centers in the low-symmetry phase to the group order n is $N/n = 2$. Therefore, one unit cell in the monoclinic phase contains both the orientation-inequivalent centers and the energy-inequivalent Jahn–Teller centers not related by any symmetry elements. In the temperature interval featuring redistribution of the Jahn–Teller centers with respect to the types of inequivalent positions, the properties of the low-temperature phase may be close to those of incommensurate systems.

In addition, the adiabatic potential for each Jahn–Teller center in the orthorhombic phase has several minima caused by the presence of two $\{R^{3+}(MoO_4)_2\}_\infty^-$ layers in the unit cell. This is related to the fact that each ion is involved in two types of the displacement of layers differing by the polarization. If the temperature is sufficiently low, the symmetry axis C_2 at the Jahn–Teller ion position is lost, the minima become inequivalent, and the unit cell exhibits a monoclinic distortion.

In conclusion, it should be noted that the symmetry analysis of possible phases can be used for interpretation of the phase diagram of $KEr(MoO_4)_2$, which is isostructural to $KDy(MoO_4)_2$. The former crystal exhibits no shift of the electron energy levels at low temperatures, although an anomaly in the c_{22} modulus at 11 K, analogous to that described above for c_{11} (see Fig. 1a), was reported in [16]. However, the other moduli do not change to any significant extent and, despite an electron–deformation coupling, no cooperative Jahn–Teller effect was observed in this crystal. The anomalies in the SHF absorption reported for $KEr(MoO_4)_2$ [17] can be related to the structural features of crystals of this type considered above.

Thus, the analysis of possible low-temperature phases, which agrees with the experimental data for $KDy(MoO_4)_2$, allows us to make some general conclusions. The elastic anomalies in $KDy(MoO_4)_2$ cannot be described using a single point $\mathbf{k}_{23}$ of the Brillouin zone. A more realistic approach consists in considering a cascade of phase transitions $\mathbf{k}_{19}$–$\mathbf{k}_{23}$ occurring within a narrow temperature interval. These phase transitions are "linked" in the temperature interval featuring a relatively sharp change in the longitudinal moduli, which accompanies "softening" of the boundary low-frequency vibrations. A combination of the properties of phase transitions of the displacement type and the order–disorder type may lead to more complicated phase diagrams considered in [18].

The above analysis also suggests that the anomalies in $KDy(MoO_4)_2$, which are characteristic of the cooperative Jahn–Teller effect, can be induced by the electron–deformation interaction–quadratic for the shear deformations and linear for the A_{1g} deformations, which allows us to expect a change in the linear dimensions of samples near the critical temperature.

The results of ultrasonic measurements were presented and interpreted in our work with permission of the authors of [6], which confirmed reliability of these data.

ACKNOWLEDGMENTS

I am grateful to the authors of [6] for kindly providing the ultrasonic data and to N.F. Kharchenko, N.A. Sergienko, and Ya.I. Zagvozdina for fruitful discussions and useful consultation.

The work was partly supported by the INTAS Foundation, grant no. 94-935.

REFERENCES

1. A. I. Zvyagin, T. S. Stetsenko, V. G. Yurko, *et al.*, Pis'ma Zh. Teor. Éksp. Fiz. **17** (4), 190 (1973).
2. M. J. M. Leask, O. C. Tropper, and M. L. Wells, J. Phys. C: Solid State Phys. **14** (24), 3481 (1981).
3. Yu. Kharchenko, Low-Temp. Phys. **22** (4), 306 (1996).
4. N. F. Kharchenko, and Yu. N. Kharchenko, Low-Temp. Phys. **24** (9), 689 (1998).
5. I. M. Vitebskiĭ, S. V. Zherlitsyn, A. A. Stepanov, *et al.*, Fiz. Nizk. Temp. **16** (8), 1064 (1990).
6. I. M. Vitebskiĭ, S. V. Zherlitsyn, A. I. Zvyagin, *et al.*, Fiz. Nizk. Temp. **12** (8), 1108 (1986).

7. V. F. Bagulya, A. I. Zvyagin, V. I. Kut'ko, *et al*., Ferroelectrics **110**, 21 (1990).
8. O. V. Kovalev, *Irreducible Representations of Space Groups* (Izdat. Akad. Nauk USSR., Kiev, 1961).
9. Yu. M. Gufan, *Structural Phase Transitions* (Nauka, Moscow, 1980).
10. A. P. Levanyuk and D. G. Sannikov, Fiz. Tverd. Tela **16** (8), 2257 (1974).
11. V. A. Vinokurov and P. V. Klevtsov, Kristallografiya **17**, 21 (1990).
12. D. Mihailovic, J. F. Ryan, and M. C. K. Wiltshire, J. Phys. C: Solid State Phys. **20** (20) 3047 (1987).
13. D. Mihailovic, J. F. Ryan, and M. C. K. Wiltshire, J. Phys. C: Solid State Phys. **20** (20) 3063 (1987).
14. R. J. Elliott, R. T. Hartley, W. Hayes, *et al*., Proc. Roy. Soc. A (London) **328**, 217 (1972).
15. D. R. Taylor, Phys. Rev, B: Condens. Matter. **40** (1), 493 (1989).
16. G. A. Zvyagina, S. V. Zherlitsyn, and V. D. Fil', *Abstracts of Papers. The All-Union School-Seminar on the Physics of Ferroelastics* (Uzhgorod, 1991), p. 93.
17. V. I. Kut'ko and M. I. Kobets, Low-Temp. Phys. **21** (11), 898 (1995).
18. V. S. Vikhnin and O. A. Zaitsev, Fiz. Tverd. Tela **39** (5), 548 (1997).

Translated by P. Pozdeev

Physics of the Solid State, Vol. 42, No. 1, 2000, pp. 189–192. Translated from Fizika Tverdogo Tela, Vol. 42, No. 1, 2000, pp. 180–183.

LOW-DIMENSIONAL SYSTEMS. SURFACE PHYSICS

The Effect of Spatial Quantization of the Electronic Spectrum on the Exchange Interaction in Multilayers

Yu. P. Irkhin

Institute of Metal Physics, Ural Division, Russian Academy of Sciences, ul. S. Kovalevskoĭ 18, Ekaterinburg, 620219 Russia
e-mail: valentin.irkhin@imp.uran.ru

Received June 8, 1999

Abstract—A strong influence of the quantization of the electronic spectrum of nonmagnetic spacers in multilayers is discovered on the dependence of the exchange interaction on the thickness of the spacer. It is shown that the antiferromagnetic dip is observed experimentally in Fe/Cr multilayers, as small thicknesses can be interpreted in terms of the simple RKKY approximation. © *2000 MAIK "Nauka/Interperiodica".*

1. INTRODUCTION

In this paper, we consider the influence of the spatial quantization of the momenta of conduction electrons of nonmagnetic spacers in multilayers on the magnetic susceptibility χ and exchange interaction $I(R)$, where R is the thickness of the spacer.

In the literature, several mechanisms have been suggested to explain the occurrence of an ordered magnetic structure in multilayers. These mechanisms are based on the RKKY interaction, with allowance made for the lattice discreteness and the actual geometry of the Fermi surface.

Although the nature of the experimentally observed magnetic effects has been qualitatively understood, no unambiguous quantitative explanation of these effects has yet been given. In particular, there are no adequate calculations of the periods and amplitudes of oscillations and the thickness dependences, which are the main characteristics of the magnetic structure of multilayers (see, e.g., [1]).

A serious problem is explaining long-period oscillations corresponding to small values of the wave vector $\mathbf{k}$, which cannot be the Fermi momentum $\mathbf{k}_F$ or other characteristic wave vectors of the electronic structure, if one recalls that the amplitude of these oscillations is rather large.

A dramatic example is the so-called antiferromagnetic (AFM) dip observed in Fe/Cr multilayers with small thicknesses of Cr layers [2] (see Fig. 1). This dip may be due to an intense long-period harmonic in the interaction between magnetic layers.

To our knowledge, only one attempt to explain the AFM dip has been made in the literature. In addition to the RKKY interaction in the framework of the Friedel–Anderson *sd* model, a mechanism was proposed in [3] that corresponds to fourth-order perturbation theory in the *sd* interaction. It was shown in [3] that experimental data can be explained by the balance between the two mechanisms just mentioned. However, the fourth-order terms should be assumed to be large in that case. In this paper, we propose an alternative mechanism [3].

2. CALCULATION OF $I(R)$ IN A MULTILAYER

The indirect exchange interaction $I(R)$ between magnetic layers separated by nonmagnetic spacers of a thickness R occurs owing to conduction electrons of spacers and in the RKKY approximation it can be written in the form

$$I(\mathbf{R}) = (V/(2\pi)^3)^2 \iint I(\mathbf{k}, \mathbf{k}') \exp(i(\mathbf{k}-\mathbf{k}')\mathbf{R}) d\mathbf{k} d\mathbf{k}',$$

$$I(\mathbf{k}, \mathbf{k}') = I_{sd}^2 f(\varepsilon_\mathbf{k})(1-\varepsilon_\mathbf{k})/(\varepsilon_\mathbf{k}-\varepsilon_{\mathbf{k}'}). \quad (1)$$

Here, $I_{sd}(\mathbf{k}, \mathbf{k}')$ is the exchange integral of conduction

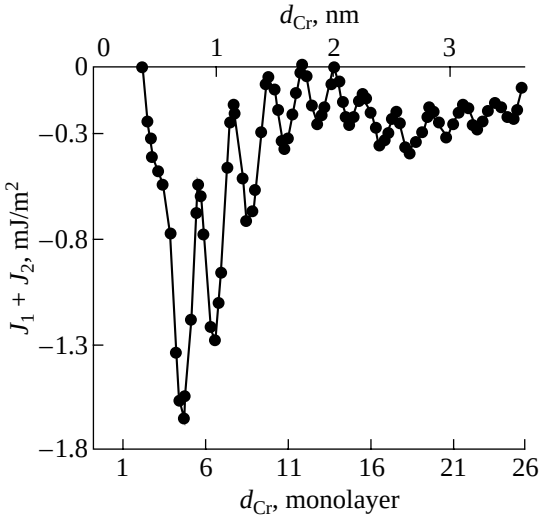

Fig. 1. Exchange interaction energy (per unit area of interface surface) as a function of the thickness of a chromium spacer (after [2]).

electrons (with momenta $\mathbf{k}$ and $\mathbf{k}'$) interacting with the spins of magnetic ions, $f(\varepsilon_{\mathbf{k}})$ is the Fermi function, $\varepsilon(\mathbf{k})$ is the energy of an electron, and V is the normalization volume.

In the free-electron approximation, integration in (1) leads to the following familiar formulas for the inhomogeneous magnetic susceptibility $\chi(\mathbf{q})$ with $\mathbf{q} = \mathbf{k} - \mathbf{k}'$ and for the oscillatory exchange interaction $I(R)$ (N is the number of atoms in the volume V):

$$\chi(q) = (mk_F/8\pi^2 N\hbar^2) \times [1 + ((4k_F^2 - q^2)/4k_F q)\ln|(q + 2k_F)/(q - 2k_F)|], \quad (2)$$

$$I(R) = (9\pi/2)(I_{sd}^2/\varepsilon_F)(\sin x - x\cos x)/x^4, \quad x = 2k_F R. \quad (3)$$

In this paper, we calculate $I(R)$ while taking into account the following two special features of the situation in multilayers.

(i) The possibility of restricting our consideration to the one-dimensional case because only $I(R_z)$ is of interest (the z axis is normal to the plane of the multilayer). Integrating it with respect to the coordinates x and y, we will obtain the interaction $I(R_z)$ between magnetic layers.

(ii) The spatial quantization of the momenta k_z of electrons of a nonmagnetic spacer.

In addition to the isotropic cases (2) and (3), we will also consider the case where there is an inherent direction (the z axis) in the system. Assuming $I_{sd}(\mathbf{k}, \mathbf{k}')$ to be independent of $\mathbf{k}$ and $\mathbf{k}'$, we may take I_{sd}^2 outside the integral in (1) and, going to the variables $\mathbf{k}$ and $\mathbf{q}$, we write the denominator in the form

$$\varepsilon(\mathbf{k} + \mathbf{q}) - \varepsilon(\mathbf{k}) = \frac{\hbar^2}{2m}(2k_\perp q_\perp \cos\varphi + 2k_z q_z + q_z^2 + q_\perp^2), \quad (4)$$

where φ is the angle between $k_\perp$ and $q_\perp$ in the xy plane. In this case, expression (1) can be reduced to a known integral in the two-dimensional case [4] by introducing a new variable

$$q_\perp + 2k_z q_z/q_\perp + q_z^2/q_\perp \longrightarrow q^*. \quad (5)$$

Integrating with respect to $k_\perp$ and φ in (1), we obtain

$$I(q^*, q_z) = \frac{V_2 m}{4\pi\hbar^2 q_\perp} \times \begin{cases} q^* - \sqrt{(q^*)^2 - 4k_{F\perp}^2}, & q^* > 2k_{F\perp}, \\ q^*, & q^* \le 2k_{F\perp}. \end{cases} \quad (6)$$

Here, V_2 is the normalization volume in the 2D case.

Formally, expression (6) is identical to the result obtained in the 2D case in [4], but q^* is dependent on q_z and k_z in (6). With (6), we can evaluate the integral in (1) and find $I(R_\perp, R_z)$ in the anisotropic case.

In this paper, we restrict our consideration to the case where the medium is infinite in the planes perpendicular to the $\perp z$ axis and ignore the discrete atomic structure of magnetic layers in these planes. The thickness of the nonmagnetic layer is assumed to be finite. Under these assumptions, the problem becomes much simpler; $I(\mathbf{R})$ depends only upon R_z, and we can perform the integration with respect to $\{R_x, R_y\} = R_\perp$ in (1), which yields $\delta_{q\perp,0} = \delta_{qx,0}\delta_{qy,0}$ on the right-hand side of (1). As a consequence, the product $q^* q_\perp$ becomes, as seen from (5),

$$q^* q_\perp = q_z(2k_z + q_z). \quad (7)$$

It is worth noting that if the discrete atomic structure (with a lattice parameter $\mathbf{a}_\perp$) in the planes perpendicular to the z axis is accounted for, we will obtain the dependence $I(\mathbf{R}) = \sum_a I(\mathbf{R} + \mathbf{a}_\perp)$, which includes the exchange interaction both between ions lying along a line parallel to the z axis and between neighboring ions lying in the planes perpendicular to the z axis. In that case, $\delta_{\mathbf{q}\perp,0}$ does not appear in the integral in (1) and we obtain a more general expression for $I(q_\perp, q_z)$, for example, in the form of (6). A more detailed treatment shows that the quantitative results will be different in that case, but the overall picture will be the same.

Further, we take into consideration the spatial quantization of the momenta along the z axis,

$$k_z = \pi n/aN_z, \quad n = \pm 1, 2, \ldots, N_z, \quad (8)$$

$$q_z = k_z' - k_z = \frac{\pi\nu}{aN_z}, \quad \nu = \pm 1, 2, \ldots, 2N_z. \quad (9)$$

As a result, from (1) we obtain

$$I(q_z) = I_{sd}^2 \frac{m}{4\hbar^2}\sum_{k_z} \frac{f(\varepsilon_k)(1 - f(\varepsilon_{k+q}))}{q_z(q_z + 2k_z)}, \quad (10)$$

$$I(R_z) = 1/N_z \sum_q I(q_z)\exp(iq_z R_z). \quad (11)$$

At low temperatures, $T \sim 0$, the Fermi functions in (10) determine the limits of summation over k_z and q_z or, equivalently, over n and ν. Introducing the notation $f = n_F$, we have

$$f + 1 - n \le \nu \le N - n,$$
$$f + 1 + n \le \nu \le N + n, \ (\le n \le f). \quad (12)$$

Since the limits (12) of summation over ν depend on n, first we sum over ν and then over n. Taking into account

that in our discrete case, $\exp(iq_zR_z) = \exp(i\pi\nu) = (-1)^\nu$, we thus obtain

$$I(R_z) = \frac{I_{sd}^2 ma^2}{2\pi^2\hbar^2 N_z}\sum_{n=-f}^{f}\left\{\sum_{\nu=-f+1-n}^{N_z-n}\frac{(-1)^\nu}{\nu(\nu+2n)} + \sum_{\nu=-f+1+n}^{N_z+n}\frac{(-1)^\nu}{\nu(\nu-2n)}\right\} = \frac{I_{sd}^2 ma^2}{2\pi^2\hbar^2 N_z}F(N_z, f), \quad (13)$$

where the function $F(N_z, f)$ is an analog of the Ruderman–Kittel function for a continuous spectrum.

In (13), the Fermi level f is assumed to be doubly occupied. In some cases, the occupation of the level f may be incomplete and, hence, the lower limits of summation over ν in (13) will be $\nu = f \pm n$, which, in contrast to (13), may lead to an integrable divergence at $\nu = 2n$. That divergence will be of the same nature as the divergence at the point $q = 2k_F$ of the continuous spectrum in the 1D case.

Calculating (13), we arrive at finite sums

$$S_1(r) = \sum_{p=1}^{r}\frac{1}{2p}, \quad S_2(r) = \sum_{p=1}^{r}\frac{1}{2p+1}, \quad (14)$$

which obey simple recurrence relations and can be approximated by analytic expressions

$$S_1(r) = 1/2(C + \ln r + 1/2r) + O_1(r),$$
$$S_2(r) = 1/2(C + \ln r) + \ln 2 + O_2(r), \quad (15)$$

where $O_1(r)$ and $O_2(r)$ are small quantities except when r is small, $r = 1, 2$. Only the difference of S_1 and S_2 is involved in $\sum$ (13), so that the logarithmic terms ($\ln r$) cancel each other out and the summation over n in (13) can be carried out analytically. For the function $F(R_z)$ in (13) we thus obtain (putting $N_z = N$ in what follows)

$$F(R_z) = F_e(N, f) + F_o(N, f), \quad (16)$$

where the subscripts "e" and "o" indicate the contributions from different n-dependent terms even and odd, respectively, with respect to the layers, and

$$F_e(N, f) = \frac{1}{N}\left[S_1\left(\frac{N-f}{2}+1\right) + S_1\left(\frac{N+f}{2}-1\right) - 2S_1\left(\frac{N}{2}\right) - \frac{1}{N} - \frac{1}{N-2}\right]_{f>2} + \frac{1}{f}\left[S_1(f-2) - \frac{1}{f} - \frac{1}{2}\right]_{f>4} + \frac{2}{f}\left[\Delta\left(\frac{N-f}{2}\right) - \Delta\left(\frac{N+f}{2}\right) + \Delta(f)\right] - \frac{2}{f-2}[\Delta(1) - \Delta(f=1)]_{j>2},$$
$$\Delta(r) = S_1(r) - S_2(r), \quad (17)$$

or, using expansions (15),

$$F_e(N, f) = \frac{1}{N_z}\left[\ln\left(\frac{N^2-f^2}{N^2}\right) + \frac{N}{N^2-(f-1)^2} - \frac{3N-4}{N(N-2)}\right]_{f>2} + \frac{1}{f-2}\left[1 + \frac{1}{2(f-1)} - 2\ln 2\right]_{f>2} + \frac{1}{2f}\left[C - 1 + \ln(f-2) + \frac{1}{2(f-2)} - \frac{2}{f}\right]_{f>4} + \frac{2}{f}\left[\frac{f}{N^2-f^2} + \frac{1}{4f} - \ln 2\right]. \quad (18)$$

Formula (17) is also true for the case of $f = 2$, where only the expression in the third square brackets remains in (17). Further,

$$F_o(N, f) = \frac{1}{N+1}\left[S_1\left(\frac{N-f}{2}\right) - S_1\left(\frac{N+f}{2}\right)\right] - \frac{1}{f+1}[S_1(f-1) - S_1(1)]_{f\geq 4} - \frac{2}{f-1}[-1 - S_1(f-1) + S_2(f)]. \quad (19)$$

With expansions (15), formula (19) becomes

$$F_o(N, f) = \frac{1}{N+1}\left[\frac{1}{2}\ln\frac{N-f}{N+f} + \frac{f}{N^2-f^2}\right] - \frac{1}{2(f+1)}\left(C + \ln f - \frac{1}{2f} - 1\right) + \frac{2}{f-1}\left(1 - \ln 2 - \frac{1}{4f}\right), \quad (f>2,\ N-f>2). \quad (20)$$

Formulas (16)–(20) are true for the case where N and f are even integers. The function $F(N, f)$ for the odd values of N and f and for their combinations with even values of N and f can be found using the following relationships, which can be derived from (13):

$$\Delta F_N^{\pm}(N_o \equiv N_e \pm 1, f_e) = F(N_o, f_e) - F(N_e, f_e) = \begin{cases}\frac{2}{N+1}\left[-\Delta(v) + \Delta(u) + \frac{f}{(N+1)(N+f+1)}\right], \\ \frac{2}{N}\left[\Delta(v) - \Delta(u) - \frac{f}{N(N-f)}\right],\end{cases} \quad (21)$$

$$\Delta F_f^-(N_e, f_e - 1) = F(N_e, f_e - 1) - F(N_e, f_e) = \frac{2}{f}\left[\Delta(u) - \Delta(v) - \frac{3}{2f}\right],$$

$$\Delta F_N^-(N_o = N_e - 1,\ f_o) \equiv F(N_e - 1,\ f_o) - F(N_e,\ f_e)$$
$$= \frac{2}{N}\left[-\Delta(u') - \Delta(v') - \frac{N_e - 1}{N_e(N_e - 2)}\right], \quad (22)$$

$$u = (N_e + f_e)/2, \quad v = (N_e - f_e)/2,$$

$$u' = (N_e + f_o + 1)/2, \quad v' = (N_e - f_o + 1)/2. \quad (23)$$

Expressions (16)–(23) allow one to calculate $F(N, f)$ for any integer values of N and f. These expressions should be combined with the term in (13) corresponding to $n = 0$,

$$F_o(N, f) = \sum_{\nu = f+1}^{N} (-1)^\nu/\nu^2. \quad (24)$$

Analysis of these formulas shows that (i) F decreases slowly with increasing N; (ii) $F(N, f) < 0$ for all N; (iii) $F(N_o, f) < F(N_e, f)$; and, finally, (iv) $F(N, f)$ varies nonmonotonically with both N and f, most noticeably for small N and f ($N, f < 5$) and for odd values of N. This last effect is due to the fact that $F(N, f)$ is larger for odd values of N than for even ones and this accounts for, in particular, a minimum observed at $N \sim 6$.

Figure 2 shows an $I(N)$ curve for $f/N = 1/2$. The last condition corresponds to the case where discrete levels are filled in proportion to the thickness of the nonmagnetic spacer $R_z = Na$. Indeed, the number of doubly occupied levels is equal to $f = N_z/2$, where z is the number of conduction electrons per atom. If $z = 1$, the number of occupied levels is $N/2$ and, hence, $f = 1$ for $N = 2$, $f = 2$ for $N = 4$, and so on. Therefore, of interest is the $I(N)$ dependence $I(N, f)$ for $f/N = \text{const} = z/2$.

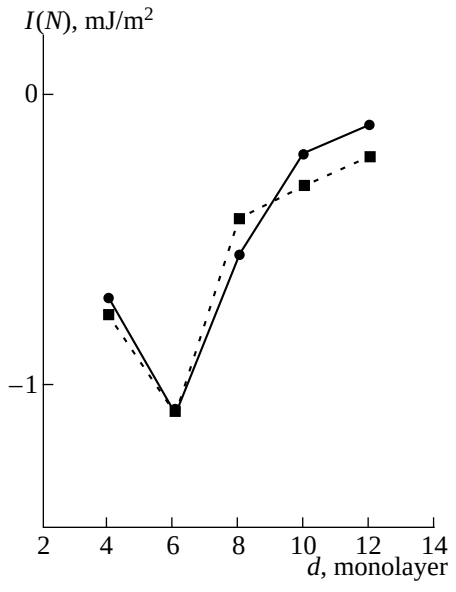

Fig. 2. Theoretical $I(N_z, f)$ dependence calculated from (25) for $f/N_z = 1/2$: circles are experimental data corresponding to Fig. 1 and squares are theoretical values.

3. DISCUSSION AND COMPARISON WITH EXPERIMENT

The $I(N)$ dependence under spatial-quantization conditions differs essentially from that in the case of a continuous spectrum. This suggests that the AFM dip observed experimentally in Fe/Cr multilayers [2, 3] can be interpreted in terms of our model. It is seen from Fig. 2 that there is a pronounced minimum of $I(N)$ for $f/N = 0.5$ (one electron per atom, which is natural in our model), and its position is predicted to be at $N = 6$, which is consistent with the experiment, despite our model being too simple to expect a quantitative agreement.

Let us evaluate the strength of the AFM exchange interaction $I(R_z) = I(N, f)$, which is determined for the most part by the exchange integral I_{sd}. Putting $I_{sd} = 0.1$ eV, from (13) we obtain the minimum value of $I(N)$ which agrees with the experimental value in Fig. 1. The quantity $I(N, f)$ per unit area of the interface surface (in mJ/m^2) is

$$I(N, f = N/2) = 11(1/N)F(N, f), \quad (25)$$

and its graph is presented in Fig. 2. It is seen that the experimental data of Fig. 1 correlates well with the calculated dependence with a single adjustable parameter, I_{sd}. The fitted value of I_{sd} is consistent with data published in the literature, which suggests that spatial quantization may be an important factor determining physical properties of multilayers.

ACKNOWLEDGMENTS

The author is grateful to A.Kh. Nasibullin for making some preliminary calculations and to V.Yu. Irkhin for his critiques.

REFERENCES

1. Yu. P. Irkhin and A. Kh. Nasibullin, in *Proceedings of XV School–Seminar on New Magnetic Materials of Microelectronics* (Mosk. Gos. Univ., Moscow, 1996).
2. J. A. Wolf, O. Leng, R. Schreiber, *et al.*, J. Magn. Magn. Mater. **121** (1–3), 253 (1993).
3. Y. Wang, P. M. Levy, and J. L. Fry, Phys. Rev. Lett. **65**, 2732 (1990).
4. B. Coqblin, *The Electronic Structure of Rare Earth Metals and Alloys* (Academic, London, 1974).

Translated by Yu. Epifanov

Physics of the Solid State, Vol. 42, No. 1, 2000, pp. 193–196. Translated from Fizika Tverdogo Tela, Vol. 42, No. 1, 2000, pp. 184–187.

ATOMIC CLUSTERS. FULLERENES

Acoustic Study of the Melting and Solidification of Gallium Incorporated in an Opal Matrix

J. M. Dereppe*, B. F. Borisov, E. V. Charnaya**, A. V. Shelyapin**, M. M. Nassar**, and Yu. A. Kumzerov*****

**Université de Louvain, D-1348 Louvain La Neuve, Belgium*

***Institute of Physics, St. Petersburg State University, ul. Pervogo Maya 100, Petrodvorets, 198904 Russia*

****Ioffe Physicotechnical Institute, Russian Academy of Sciences, Politekhnicheskaya ul. 26, St. Petersburg, 194021 Russia*

Received April 8, 1999; in final form, May 27, 1999

Abstract—An acoustic study is reported of the crystallization and melting of gallium embedded in an opal-like matrix. The variations of the velocity and absorption of longitudinal ultrasonic waves during phase transitions in the α and β modifications have been found to be hysteretic in nature. It is shown that acoustic methods do not detect gallium melting and crystallization in the tetragonal phase forming in a restricted geometry. Experimental evidence for heterogeneous crystallization of gallium in pores has been obtained. © *2000 MAIK "Nauka/Interperiodica".*

Phase transitions in materials incorporated in porous glass matrices with pores ranging in size from a few to hundreds of nanometers have been stimulating considerable interest in connection with the possibility of studying various size effects and the significance of confined geometry. Recent experimental investigations of such phase transformations in porous glasses covered transitions to the superfluid and the superconducting state, transitions in liquid crystals, separation in binary liquids, the ferroelectric phase transition, structural transformations in solids, transition to the glassy state, gas formation and condensation (see references in [1]), and the melting-crystallization phase transition (see [1–11] and references therein). The latter type of phase transitions was investigated primarily for liquids wetting a glass surface. Studies of the melting and crystallization of nonwetting liquids, done to a considerably lesser extent, were performed on such fusible metals as mercury, indium, and gallium. We are aware of only two papers [12, 13] reporting on the melting and crystallization in opals. The temperature dependences of the liquid gallium concentration in artificial opal were measured by the NMR method [12]. In [13], temperature dependences of X-ray spectra of crystalline gallium and of the electrical resistivity of a sample were obtained for a similar matrix. It is known that acoustic methods can provide valuable information on phase transitions of various natures, including melting and crystallization, and it therefore appeared reasonable to carry out an acoustic investigation of opals in the region of the melting and solidification temperatures of the metals embedded in this material. The present paper reports the results of such a study performed on gallium.

The matrix of an artificial opal represents a piecewise-regular dense packing of SiO_2 spheres about 250 nm in diameter. The opal structure was described in considerable detail, for instance, in [14]. The densely packed spheres enclose octahedral and tetrahedral voids differing in size by about a factor of two (of the order of 100 and 50 nm, respectively). The total volume occupied by these pores adds up to approximately 25% of the sample volume. Gallium was introduced into the opal matrix under a pressure of up to 9 kbar. The pore filling determined by weighing the sample was about 85%.

The acoustic studies were performed by pulse-phase measurements. One obtained temperature dependences (in the 160–320-K range) of the velocity and damping of longitudinal ultrasonic waves relative to their room-temperature values at a frequency of 5 MHz. The error $\Delta v/v$ of the relative velocity measurements did not exceed 10^{-5}, and that of the damping $\Delta\alpha/\alpha$, 5%. The sample was parallelepiped–shaped, with a volume of about 1 cm^3.

Figure 1 presents the temperature dependences of ultrasonic velocity in a sample heated preliminarily to 320 K, which were obtained under cooling of the sample down to 160 K and its subsequent heating to 320 K. The choice of the upper boundary (320 K) of this temperature cycle was motivated by the x-ray diffraction observation [11, 13] that the melting of the gallium embedded in a porous matrix is completed at substantially lower temperatures, about the melting point of the conventional bulk α modification (303 K). A similar dependence for the damping coefficient is displayed in Fig. 2. The plots of Figs. 1 and 2 clearly show the changes in the velocity and damping corresponding to the melting and crystallization of gallium in the pores.

1063-7834/00/4201-0193$20.00

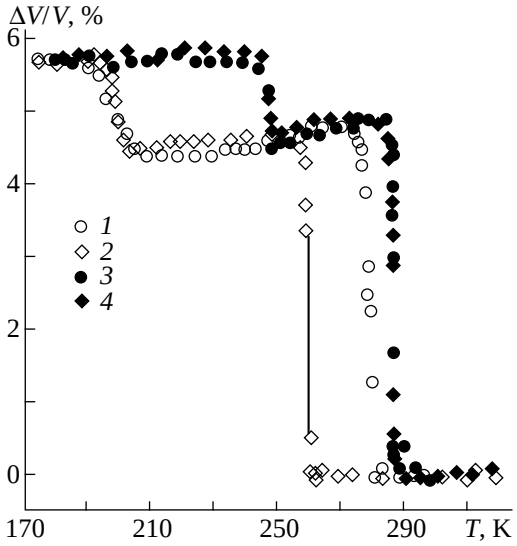

Fig. 1. Temperature dependences of the velocity of longitudinal ultrasonic waves under cooling (*1*, *2*) and under heating (*3*, *4*) obtained in a full cycle (*2*, *4*) and after a preliminary heating to 303 K (*1*, *3*). The line segment connects two successive experimental points.

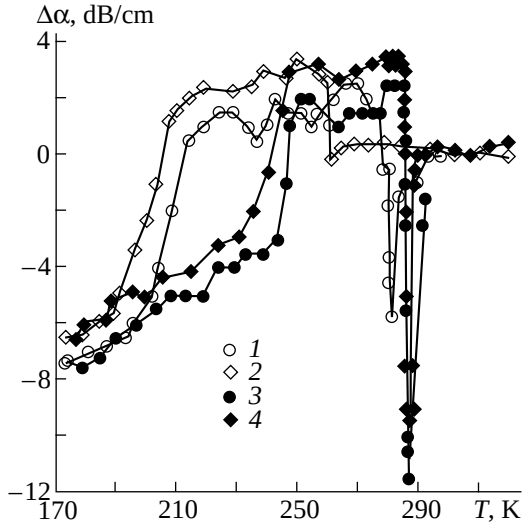

Fig. 2. Temperature dependences of the damping of longitudinal ultrasonic waves under cooling (*1*, *2*) and under heating (*3*, *4*) obtained in a full cycle (*2*, *4*) and after a preliminary heating to 303 K (*1*, *3*). The solid lines connect experimental points.

The acoustic anomalies have a two-stepped nature, with the melting and crystallization being separated by a substantial temperature shift giving rise to a double hysteresis loop. The total change in the ultrasonic velocity on the phase transitions adds up to about 6%, which demonstrates a high enough sensitivity of the acoustic method in studies of the melting and crystallization of metals in pores.

The regions of gallium melting in the pores are shifted noticeably relative to the melting point of the α modification of bulk gallium. In the NMR study [12], where measurements of the amount of liquid gallium performed in the course of sample heating and cooling also demonstrated a double hysteresis loop, the lowering of the melting temperature was assigned to a thermodynamic size effect [15, 16], and the double loop itself, to the existence of voids of two characteristic sizes in the opal matrix. X-ray diffraction showed [13], however, that gallium in the opal matrix is capable of crystallizing in three different modifications, one of which differs from the known bulk-gallium phases and has tetragonal symmetry [17], whereas the other two coincide with the disordered α phase of bulk gallium and the β phase forming usually under strong supercooling of bulk liquid gallium. The phase transitions of these three modifications are shifted in temperature with respect to one another. The first to solidify under cooling (somewhat below 300 K) is the tetragonal modification, which differs from the bulk phases, after which the α modification freezes near 260 K, followed by the onset of β phase solidification below 220 K. When heated, their melting becomes completed near 310, 290, and 240 K, respectively. A comparison of the results of our acoustic measurements with the x-ray diffraction data reveals that the high-temperature hysteresis loop in Figs. 1 and 2 can be associated with the melting-crystallization region of the α modification of gallium, whereas the low-temperature loop can be associated with the phase transitions in the β modification. No acoustic anomalies were observed by us to occur near the onset of solidification of the gallium tetragonal phase in the opal pores and near the end of its melting. This result can be interpreted in two ways: namely, either the tetragonal modification does not form in the sample under study at all, or the ultrasound velocity and damping are not sensitive to its formation. Although the sample studied here is similar to the one investigated in [13], the assumption of the gallium crystalline phases being different in them appears justified, because according to [11, 17, 18], one of two identical porous-glass matrices with pores 4 nm in size exhibited only the tetragonal modification, whereas in the second matrix one observed, besides the tetragonal phase, a successive formation of the two others. Apparently insignificant variations in the pore geometry and filling may produce a strong effect on the structure of solid gallium under the conditions of confined geometry. In order to verify the existence of the tetragonal modification in the sample under study, we performed acoustic studies in a thermal cycling regime in which the sample, after a cooling to 175 K, was then successively heated to temperatures in the 320–290 K interval. These studies revealed that when the sample was cooled after a preliminary heating to $310 < T < 320$ K, the dependences of the ultrasonic velocity and damping reproduced the general pattern of the relations shown graphically in Figs. 1 and 2 for the total cycle (from 320 to 175 K). However, after a preliminary heating to tem-

peratures below 310 K, the solidification of the α modification set in considerably earlier. The case with heating to 303 K is shown for the illustrations in Figs. 1 and 2. The shift of the solidification region should apparently be assigned to an increase of the number of crystallites of the high-temperature tetragonal phase as a result of its incomplete melting when heated below 310 K. Such crystallites can serve as centers of crystallization of the α modification in the opal matrix voids. Incidentally, the independence of the β modification freezing of the temperature to which the preliminary heating was continued is most likely due to the fact that our thermal cycling regime does not affect the number of crystallites of the tetragonal and α phases below 250 K. The above interpretation supports the assumption of the acoustic methods being insensitive to the formation of the gallium tetragonal phase in the opal matrix, which may be caused by various factors, including the closeness between the acoustic impedances of this modification and of molten gallium, or the tetragonal modification being present in small amounts. Note that the electrical resistivity of gallium-filled opal was found to be insensitive to the formation in a porous matrix not only of the tetragonal, but also of the β modification [13].

The present study has not revealed any clear connections between the melting temperature shifts and the existence of two characteristic void sizes in opals. One possible explanation of this observation consists in that the size of the crystallites forming in the pores differs from that of the latter, as this was pointed out for indium and gallium embedded in various porous matrices [10, 11, 13]. This makes a quantitative interpretation of the lowering of the melting points of the α and β modifications within the model of the thermodynamic size effect difficult. A quantitative interpretation for the tetragonal modification is in principle possible only by comparing the melting temperatures of crystallites of different size embedded in various porous matrices, because this modification forms neither in bulk gallium nor in micron-sized drops [19].

In Figs. 1 and 2, one clearly sees a temperature hysteresis between the solidification and melting of gallium in opal. This hysteresis was observed for all liquids in porous glass matrices studied thus far, both wetting and not. The explanations proposed for this shift between the melting and crystallization are contradictory [3, 4, 11, 13, 20]. The suggestion that the hysteresis is the result of the liquid being supercooled appears the most natural. At first glance, this suggestion is contradicted by the high reproducibility of the solidification temperatures stressed in most papers, and by their independence of the cooling rate. These features of the process stimulated development of a model of "geometric freezing" described in detail [3, 20]. By this model, the freezing in pores occurs when the energy of a solid particle, including the surface energy, becomes smaller than that of a liquid particle [3, 20]. To be able to account for the hysteresis, this model requires additional speculation. We believe that the contradiction between the assumption of the supercooling of liquids in pores and the reproducibility of solidification temperatures is removed if one takes into account the strong temperature dependence of nucleation in homogeneous crystallization and of the probability of crystallization at foreign nuclei in heterogeneous nucleation [21]. This factor is known to result in the reproducible freezing of bulk liquids, although it occurs substantially below the melting points [21]. Inhomogeneities on the inner surfaces of porous matrices, oxides, and in the case of gallium—crystallites of other modifications, could serve as centers of heterogeneous crystallization. Thus, our data on the increase of the α modification solidification temperature in a sample subjected to preliminary heating to a lower temperature provide an argument for the heterogeneous crystallization of a supercooled melt. Note that the assumption of heterogeneous crystallization of indium in a porous glass put forward in [10] was based on calorimetric measurements.

We would also like to point out an interesting feature of the acoustic properties of a gallium-filled opal matrix. Namely, when the α modification is freezing or, particularly, when it is melting, one observes a pronounced increase of the sample transmission, which becomes manifest in a strong decrease of the ultrasonic damping coefficient within a narrow temperature interval (Fig. 2). This effect was not observed to occur in acoustic studies of porous glasses filled with gallium or other liquids [1, 3, 5, 7, 22].

ACKNOWLEDGMENTS

Support of the Russian Foundation for Basic Research (grant no. 99-02-16786) is gratefully acknowledged.

REFERENCES

1. B. F. Borisov, E. V. Charnaya, P. G. Plotnikov, *et al.*, Phys. Rev. B **58**, 5329 (1998).
2. J. A. Duffy, N. J. Wilkinson, H. M. Fretwell, *et al.*, J. Phys.: Condens. Matter **7**, L27 (1995).
3. E. Molz, A. P. Y. Wong, M. H. W. Chan, *et al.*, Phys. Rev. B **48**, 5741 (1993).
4. J. H. Strange, M. Rahan, and E. G. Smith, Phys. Rev. Lett. **71**, 3589 (1993).
5. B. F. Borisov, E. V. Charnaya, Yu. A. Kumzerov, *et al.*, Solid State Commun. **92**, 531 (1994).
6. E. Shabanova, E. V. Charnaya, K. Schaumburd, *et al.*, Physica B **229**, 268 (1997).
7. B. F. Borisov, E. V. Charnaya, W.-D. Hoffmann, *et al.*, J. Phys.: Condens. Matter **9**, 3377 (1997).
8. Yu. A. Kumzerov, A. A. Naberezhnov, S. B. Vakhrushev, *et al.*, Phys. Rev. B **52**, 4772 (1995).
9. M. Schindler, A. Dertinger, Y. Kondo, *et al.*, Phys. Rev. B **53**, 11451 (1996).
10. K. M. Unruh, T. E. Huber, and C. A. Huber, Phys. Rev. B **48**, 9021 (1993).

11. E. V. Charnaya, C. Tien, C. S. Wur, *et al.*, Phys. Rev. B **58**, 11089 (1998).
12. E. Shabanova, E. V. Charnaya, K. Schaumburg, *et al.*, J. Magn. Reson. A **122**, 67 (1996).
13. E. V. Charnaya, C. Tien, K. J. Lin, *et al.*, J. Phys.: Condens. Matter **10**, 7273 (1998).
14. V. N. Bogomolov, Yu. A. Kumzerov, S. G. Romanov, *et al.*, Physica C **208**, 371 (1993).
15. P. Pawlow, Z. Phys. Chem. **65**, 545 (1909).
16. É. L. Nagaev, Usp. Fiz. Nauk **162** (9), 49 (1992).
17. I. G. Sorina, C. Tien, E. V. Charnaya, *et al.*, Fiz. Tverd. Tela **40**, 1552 (1998).
18. C. Tien, C. S. Wur, K. J. Lin, *et al.*, Phys. Rev. B **54**, 11880 (1996).
19. A. Di Cicco, Phys. Rev. Lett. **81**, 2942 (1998).
20. D. D. Awschalom and J. Warnock, in *Molecular Dynamics in Restricted Geometries*, Ed. by J. Klafter and J. M. Drake (Wiley, New York, 1989), p. 351.
21. A. R. Ubbelohde, *The Molten State of Matter* (Wiley, New York, 1978).
22. B. F. Borisov, M. R. Gruzman, and E. V. Charnaya, in *Acoustics of Inhomogeneous Media*, Ed. by V. K. Kedrinskiĭ (Novosibirsk, 1997), p. 55.

Translated by G. Skrebtsov

Physics of the Solid State, Vol. 42, No. 1, 2000, pp. 197–198. Translated from Fizika Tverdogo Tela, Vol. 42, No. 1, 2000, pp. 188–189.

ATOMIC CLUSTERS. FULLERENES

On a Change in the Energy Structure of the C_{60} Fullerene Molecular Orbitals Induced by Chemical Bonding

Yu. F. Biryulin, V. S. Vikhnin, and V. N. Zgonnik

Ioffe Physicotechnical Institute, Russian Academy of Sciences, Politekhnicheskaya ul. 26, St. Petersburg, 194021 Russia

e-mail: biryulin@nano.ioffe.rssi.ru

Received April 15, 1999

Abstract—The paper presents experimental data and a simple theoretical model for the change in the energy of radiative transitions in the HOMO-LUMO molecular-orbital system of the C_{60} fullerene induced by a chemical covalent attachment of polymer chains or other ligands to the latter. © *2000 MAIK "Nauka/Interperiodica".*

It has recently been shown [1] in the specific case of star-shaped polymers with a fullerene core that attachment of polymer chains to C_{60} through covalent bonds substantially affects the fullerene electronic structure. A photoluminescence study of radiative transitions in the HOMO-LUMO molecular-orbital system of fullerene with chemically attached polystyrene chains led us to conclude that each newly forming covalent chemical bond causes a change in the HOMO-LUMO structure, which increases the energy gap treated as a forbidden gap of the C_{60}. This increase in the radiative-transition energy may be considered in a first approximation as linear (with the number of the polystyrene chains attached to the fullerene varying from one to six). It obeys approximately a linear empirical relationship $\Delta E = 0.04n$, where ΔE is the energy shift of the photoluminescence spectrum maximum expressed in eV and n is the number of the polystyrene chains attached to the fullerene. This experimental finding is displayed graphically in Fig. 1.

A theoretical consideration of this observation should be started from the mixing of the ligand-fragment wave functions (in our case, these are the C–C and C–H covalent bonds forming in the course of the reaction of lithium polystyryl with fullerene [2]) with the fullerene ground state. In a first approximation, it can be presented in the form $(\psi + \alpha\Psi_1\Psi_2)/(1 + \alpha^2)^{1/2}$, where ψ is the wave function of electrons in the fullerene molecule, Ψ_1 and Ψ_2 are the wave functions of the electrons belonging to the ligand fragments and affecting the electronic structure of the fullerene, as one of its C–C double bonds ruptures to form a C–C bond (with the polystyrene chain) and a C–H bond (as a result of a reaction of lithium polystyryl with fullerene and water and substitution of hydrogen for Li at the other end of the ruptured double bond [2]), and α is the mixing coefficient. In a general case, such wave-function mixing may be considered approximately as a sum of the perturbations introduced by each pair of the newly formed chemical bonds. As a result, the wave function of the system can be written in the form

$$(\psi + \Sigma\alpha_i\Psi_i\Psi_{i+1})/(1 + \Sigma\alpha_i^2)^{1/2}.$$

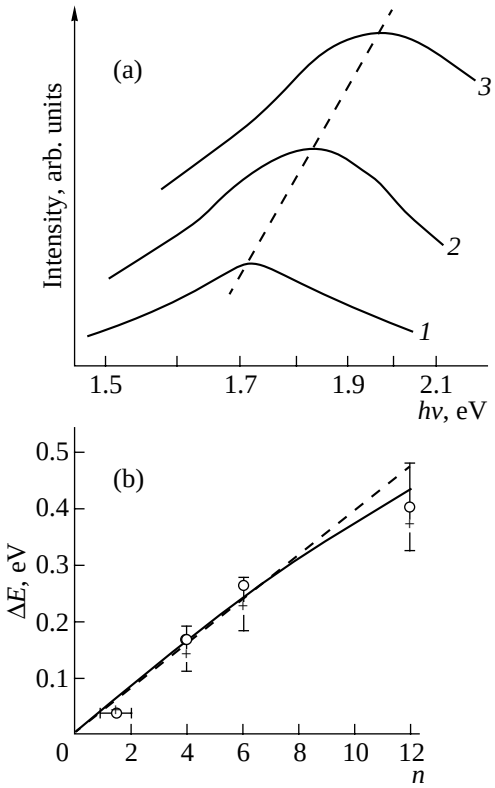

Fig. 1. (a) PL spectra of films of fullerene-containing polystyrenes with different numbers of attached polystyrene (PS) chains: (*1*) 1–2 PS chains, (*2*) 4 PS chains, and (*3*) 6 PS chains at $T = 300$ K; and (b) energy shift of the maximum in a PL spectrum *vs* the number of polystyrene chains attached to the fullerene: experimental points are circles (300 K) and crosses (77 K); the points for $n = 12$ refer to a $C_{60}(C_6H_5)_{12}$ film; the dashed line is linear empirical relation $\Delta E = 0.04n$ and the solid line is calculated using (1).

1063-7834/00/4201-0197$20.00 © 2000 MAIK "Nauka/Interperiodica"

This mechanism yields the following photon energy emitted in the HOMO-LUMO radiative transition:

$$h\nu = [\Delta^2 + n(W_1^2 + W_2^2)]^{1/2},$$

where Δ is the original HOMO-LUMO gap of the unperturbed fullerene, n is the number of pairs of the newly formed chemical bonds (one pair per "ruptured" double bond), and W_1 and W_2 are the matrix elements of the state-mixing Hamiltonian for the cases of the C–C and C–H bond formation, respectively.

The above dependence of the HOMO-LUMO gap on a chemical bond number is weaker than a square-root one. For a bond number large enough, the growth of the effective HOMO-LUMO gap should reach, in accordance with (1), a square-root dependence.

Relation (1) agrees well with the experiment (Fig. 1b) within experimental error.

Despite the assumption of $(W_1^2 + W_2^2)$ being independent of the successively increasing bond number n (which can fail for sufficiently large n), the proposed simple model appears to adequately reproduce the real physical situation and is capable of accounting for the experimentally observed energy shift of the maximum in the photoluminescence spectrum of a fullerene when new chemical bonds appear on its spherical surface. The actual type of the bonds may affect the magnitude of the matrix elements $W_{1,2}$, but the relationship itself, in our opinion, should retain its nature. This also explains why the energy shift is not affected by the ligand chemical structure and why only the type of the bond is significant; indeed, while the structure of the fullerene depends only slightly on the properties of the polymer chain as a whole or of the phenylene rings attached to it, it is greatly affected by the nearest atoms to which the fullerene is covalently bonded.

ACKNOWLEDGMENTS

This work was supported by the State Program "Modern Trends in Physics of Condensed Media" (Subprogram "Fullerenes and Atomic Clusters"), grant no. 98076, Polimer-2.

REFERENCES

1. A. N. Aleshin, Yu. F. Biryulin, N. B. Mironkov, *et al.*, Fullerene Sci. Technol. **6** (3), 545 (1998).
2. V. N. Zgonnik, E. Yu. Melenevskaya, L. S. Litvinova, *et al.*, Vysokomol. Soed., Ser. A **38** (2) 203 (1996).

Translated by G. Skrebtsov

Physics of the Solid State, Vol. 42, No. 1, 2000, pp. 22–23. Translated from Fizika Tverdogo Tela, Vol. 42, No. 1, 2000, pp. 23–24.

SEMICONDUCTORS AND DIELECTRICS

Effect of Temperature and Uniform Compression on Local-Center Luminescence in $TlGaS_2$ Layered Crystals

V. F. Agekyan

Institute of Physics (Petrodvorets Branch), St. Petersburg State University, Petrodvorets, 198904 Russia

Received May 5, 1999

Abstract—Changes in the local-center luminescence spectrum initiated by structural defects in the $TlGaS_2$ crystal are studied in the temperature range from 2 to 77 K and under a hydrostatic pressure up to 35 kbar. The effect of hydrostatic compression can be explained by the relative slipping of the two elementary layers comprising the layer stack, which results in a lowering of the symmetry of the cavities occupied by the thallium atoms. © *2000 MAIK "Nauka/Interperiodica".*

Ternary layered semiconductors of the $TIM^{III}X_2^{VI}$ type (M = In or Ga; X = S, Se, or Te) can crystallize in different polytype structures [1], including mixed polytype systems. The unit cell of the $TlGaS_2$ monoclinic crystal contains seven molecules, which accounts for its very rich vibrational spectrum. The $TlGaS_2$ layered stack is made up of two elementary layers, each layer being a sequence of Ga_4S_{10} pyramidal groups, which, in turn, are built of GaS_4 tetrahedra. The pyramids of the two elementary layers face each other with the vertices, and the thallium atoms lie in the trigonal cavities thus formed.

The luminescence spectra of $TlGaS_2$ crystal samples, which were grown by the Bridgman–Stockbarger method and contained structural defects, exhibit a vibronic system due to the emission of a local center. The system consists of two zero-phonon lines *A* and *B* with energies of 16790 and 16796 cm^{-1} and a large number of vibrational replicas. These vibrational replicas can be divided into two groups. The first group (up to 20 cm^{-1}) contains closely lying lines corresponding to low-frequency interlayer vibrations, and the second group (up to 400 cm^{-1}) includes higher-frequency intralayer vibrations. The assignment of the zero-phonon lines and a number of vibrational lines by the Raman scattering technique, as well as the EPR and Zeeman splitting investigations of the zero-phonon lines caused by this center, were performed in [2]. The paramagnetic properties of the center originate apparently from the unsaturated valence bonds of thallium atoms.

The objective of the present study was to compare the effects of heating and hydrostatic compression on the zero-phonon emission lines of the local center in $TlGaS_2$ and their replicas, which correspond to interlayer vibrations. Upon heating from 2 to 15 K, the phonon luminescence components increase several times as compared to the zero-phonon lines *A* and *B* (Fig. 1). A further heating of the crystal results in a strong broadening of the structure originating from the interlayer vibrations. At 15 K, the *A* and *B* lines become equal in intensity, and this situation persists at higher temperatures.

The hydrostatic pressure *P* was applied at 2 K and measured from the *R*-line shift of a ruby sample (with a low chromium concentration) placed alongside the $TlGaS_2$ sample inside the compressed volume. The maximum pressure *P* was 35 kbar. As the pressure *P* increases, the strongest component E_g of the low-fre-

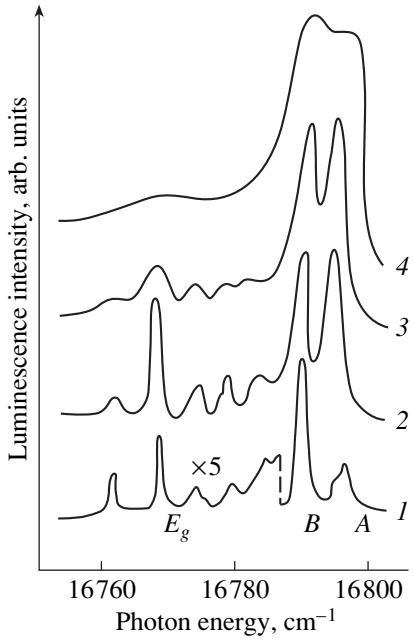

Fig. 1. Emission spectra of a local center in $TlGaS_2$ upon heating. Evolution of the zero-phonon lines *A* and *B* and their replicas corresponding to low-frequency interlayer vibrations. Temperature (K): (*1*) 2, (2) 15, (*3*) 40, and (*4*) 77.

1063-7834/00/4201-0022$20.00 © 2000 MAIK "Nauka/Interperiodica"

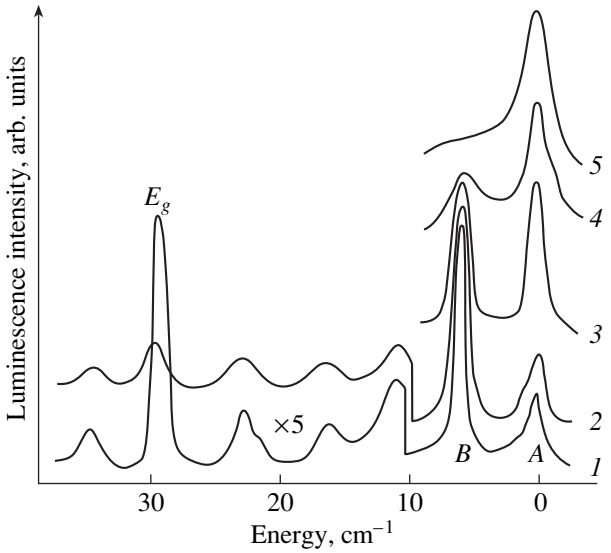

Fig. 2. Emission spectra of a local center in $TlGaS_2$ at hydrostatic pressures (kbar): (*1*) 0, (*2*) 3, (*3*) 7, (*4*) 25, and (*5*) 35. T = 2 K. Spectra *3–5* contain only the zero-phonon lines *A* and *B*.

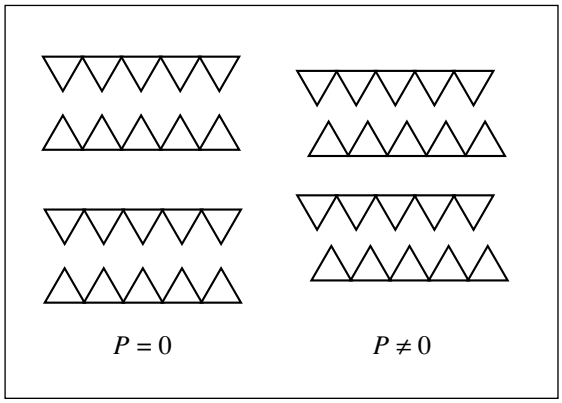

Fig. 3. Schematic representation of variation in the relative position of the two elementary layers making up the layer stack under hydrostatic compression of a $TlGaS_2$ crystal.

quency interlayer vibrations becomes suppressed, the spectrum shifts as a whole toward longer wavelengths at a rate of about 2 cm^{-1}/kbar, and the *A* line increases in intensity as compared to the *B* line, so that the *A* line becomes dominant at $P > 25$ kbar (Fig. 2).

The smooth variation of the intensity ratio for the zero-phonon components indicates that these changes are not due to the polytype phase transitions initiated by heating or hydrostatic compression. The equalization of intensities of the *A* and *B* zero-phonon lines with an increase in temperature is accounted for by the population of the upper component of the excited doublet state of the center. As regards the intensity redistribution between the *A* and *B* lines, as well as among the components of the interlayer vibrational structure, under hydrostatic compression, it can be attributed to a change in the symmetry of the crystal field in which the center is located. Compression of the crystal brings together the elementary layers comprising the layer stack. This results in a relative displacement of the pyramid vertices facing each other in the two layers of the layer stack, as this is shown schematically in Fig. 3. The displacement brings about, in particular, the lowering of the trigonal symmetry of the interlayer cavities containing the thallium regular sites. This symmetry lowering changes the selection rules and, as a consequence, the relative oscillator strengths of the *A* and *B* transitions from the doublet sublevels of the excited state to the ground state of the center. Note that the crystal deformation remains elastic up to at least 35 kbar, and the removal of the pressure completely restores the emission spectrum.

Thus, application of hydrostatic pressure to the $TlGaS_2$ anisotropic layered crystal containing structural defects causes nontrivial changes in the local-center luminescence spectrum, which indicate an elastic relative slipping of the two elementary layers making up the layer stack.

REFERENCES

1. D. Müller and H. Hahn, Z. Anorg. Allg. Chem. **438**, 208 (1978).
2. G. I. Abutalybov, V. F. Agekyan, S. V. Pogarev, *et al.*, Fiz. Tverd. Tela (Leningrad) **29**, 1436 (1987).

Translated by G. Skrebtsov

Physics of the Solid State, Vol. 42, No. 1, 2000, pp. 24–28. Translated from Fizika Tverdogo Tela, Vol. 42, No. 1, 2000, pp. 25–28.

SEMICONDUCTORS AND DIELECTRICS

Wannier–Mott Excitons in Narrow-Gap Semiconductor Heterostructures

A. P. Silin and S. V. Shubenkov

Lebedev Physical Institute, Russian Academy of Sciences, Leninskii pr. 53, Moscow, 117924 Russia

Received April 28, 1999; in final form, May 19, 1999

Abstract—Spectra of excitons in a bulk semiconductor and in a thin semiconducting layer are investigated in the two-band Dirac model. The dependences of the exciton binding energy on the energy gap and, in the two-dimensional case, on the layer width are obtained. The fine structures of exciton spectra are revealed. *© 2000 MAIK "Nauka/Interperiodica".*

Analytical and numerical calculations of the exciton binding energy performed for all kinds of different wide-gap semiconductor structures are well-known [1–3]. However, the dependence of the exciton binding energy on the energy gap of a semiconductor has not yet been investigated. This stems from the fact that, first, the ratio of the exciton binding energy to the energy gap is small, and, second, it is constant. That is why the influence of the energy gap finiteness is masked by other effects, such as the anisotropy of energy bands, dispersion of dielectric function, etc. Nonetheless, the investigation of the exciton ground state splitting caused by the finiteness of the energy gap is very interesting. Recent technological progress makes possible semiconductor structures for which the investigation of the exciton binding energy as a function of the energy gap is fairly actual. This is explained by the fact that the effective energy gap in semiconductor heterostructures can be easily changed since it depends on the dimensions of quantum well, quantum wire, or quantum dot, in which charge careers are localized (see, for example, [4]). It should be also noted that the exciton binding energy in two-dimensional and quasi-one-dimensional structures is substantially larger than it is in the three-dimensional case. The effects under consideration are especially essential for the heterostructures composed of semiconductors in which the ratio of the exciton binding energy to the energy gap can exceeds 1/10 (see, for example, [5]). These semiconductors are considered to be narrow-gap in our case.

In this work, we considered two problems: the formation of three-dimensional and two-dimensional excitons in a narrow-gap semiconductor with isotropic energy bands and constant isotropic permittivity ε. In this case, the free current carriers are described by the Dirac equation [6]

$$i\hbar\frac{\partial}{\partial t}\psi = (\nu\hat{\boldsymbol{\alpha}}\hat{\mathbf{p}} + \hat{\beta}\Delta)\psi. \quad (1)$$

Hereafter, $\hat{\boldsymbol{\alpha}}$ and $\hat{\beta}$ are the Dirac matrices; $\hat{\mathbf{p}}$ is the operator of the three-dimensional momentum; $\Delta = E_g/2$ is the halfwidth of the forbidden gap; ψ is the envelope of the electron wavefunction; ν is the Kane matrix element (quasi-speed of light), $\nu = \sqrt{\Delta/m} \ll c$; c is the velocity of light in vacuum; and m is the electron effective mass, which is equal to the effective mass of the hole in this model. In this case, the dispersion law is

$$E(p) = \pm\sqrt{p^2\nu^2 + \Delta^2}. \quad (2)$$

The three-dimensional exciton in a bulk semiconductor is considered in Section 1. The two-dimensional exciton in a thin semiconducting layer in a superlattice or quantum well is considered in Section 2.

1. EXCITON IN BULK NARROW-GAP SEMICONDUCTOR

The calculation of the exciton binding energy is, in general, analogous to the positronium problem. The difference is in the mode of inclusion of the interaction into the free Dirac equation (1) [7]. In quantum electrodynamics, the term corresponding to the interaction with the electromagnetic field is written as

$$\hat{V} = \frac{e}{c}\int \hat{j}^{\mu}(\mathbf{r})\hat{A}^{\mu}(\mathbf{r})d^3\mathbf{r}. \quad (3)$$

Here, e is the electron charge; $\hat{j}^{\mu} = (\hat{\bar{\psi}}\gamma^{\mu}\hat{\psi})$ is the current density operator, $\hat{\bar{\psi}} = \hat{\psi}^*\gamma^0$; $\hat{A}^{\mu} = (\hat{\Phi}, \hat{\mathbf{A}})$ is the electromagnetic field operator; and $\gamma^{\mu} = (\gamma^0, \boldsymbol{\gamma})$ are the Dirac matrices, convolution on the four-component index μ is implied. Because of the presence of two characteristic constants expressed in units of velocity, the current operator in a narrow-gap semiconductor

contains the coefficient v/c before the vector part (see [7])

$$j^{\mu} = (j^0, j^i) = \left(\hat{\bar{\psi}}\gamma^0\hat{\psi}, \frac{v}{c}\hat{\bar{\psi}}\gamma^i\hat{\psi}\right),$$

and the term representing the interaction with the electromagnetic field has another form

$$\hat{V} = e\int\hat{\psi}^*(\mathbf{r})\hat{\psi}(\mathbf{r})\hat{\Phi}(\mathbf{r})d^3r + \frac{ev}{c}\int\hat{\bar{\psi}}(\mathbf{r})\boldsymbol{\gamma}\hat{\psi}(\mathbf{r})\hat{\mathbf{A}}(\mathbf{r})d^3r. \quad (4)$$

Formula (4) is obtained under gauge invariance requirement. Since the condition $v \ll c$ is always fulfilled in semiconductors, it is clear that only the first term

$$\hat{V} = e\int\hat{\psi}^*(\mathbf{r})\hat{\psi}(\mathbf{r})\hat{\Phi}(\mathbf{r})d^3r \quad (5)$$

should be retained. A comparison of formulas (5) and (3) shows that the exciton fine structure is calculated without regard for the delay of the electron–hole Coulomb interaction and the magnetic interaction between the particles.

In order to obtain the spectrum of the bound state of two particles, we constructed the effective single-particle Hamiltonian taking into account their dynamics and interaction up to α^2 ($\alpha = e^2/\varepsilon\hbar v$). For this purpose, we calculated the electron–hole scattering amplitude in the second approximation of perturbation theory on α and restored the effective Hamiltonian using the scattering amplitude

$$i\hbar\frac{\partial}{\partial t}\psi = \hat{H}\psi,$$

$$\hat{H} = \hat{H}_0 + \hat{V}_1 + \hat{V}_2 + \hat{V}_3 + \hat{V}_4,$$

$$\hat{H}_0 = \frac{\hat{p}^2}{m} - \frac{e^2}{\varepsilon r},$$

$$\hat{V}_1 = -\frac{\hat{p}^4}{4m^3v^2} + 4\pi\mu^2\delta(\mathbf{r}),$$

$$\hat{V}_2 = 4\mu^2\frac{(\hat{\mathbf{S}}, \hat{\mathbf{I}})}{r^3},$$

$$\hat{V}_3 = 0,$$

$$\hat{V}_4 = \frac{4}{3}\pi\mu^2\hat{\mathbf{S}}^2\delta(\mathbf{r}) + 6\frac{\mu^2}{r^3}\left(\frac{(\hat{\mathbf{S}}, \mathbf{r})(\hat{\mathbf{S}}, \mathbf{r})}{r^2} - \frac{1}{3}\hat{\mathbf{S}}^2\right). \quad (6)$$

Here, $\hat{H}_0$ is the effective Hamiltonian representing the electron–hole interaction in the effective mass approximation (the interaction of the conduction and valence band is not taken into account); $\hat{V}_1$ is the correction for orbital effects; $\hat{V}_2$ is the spin–orbit interaction; $\hat{V}_3$ is the spin–spin interaction (in case of the exciton, this term is small with respect to the parameter v/c and is introduced for comparison with the positronium); $\hat{V}_4$ is the exchange (annihilation) interaction; ψ is the three-component wavefunction (it means that the spin of the electron–hole system can be zero or unity); $\hat{\mathbf{S}}$ is the spin operator; $\hat{\mathbf{I}}$ is the orbital momentum operator; and $\mu = e/2\sqrt{\varepsilon}mv$ is the quantity analogous to the effective Bohr magneton in a semiconductor $\mu^* = e\hbar/mc$, which appears in the terms taking into account the interaction with the magnetic field (we did not take the magnetic field into account). A similar procedure was performed for the electron and the positron (see, for example, [8]). For comparison, we present the potential of electron–positron interaction in vacuum to an accuracy of the terms proportional to α_0^2 (the fine structure constant is $\alpha_0 = e^2/\hbar c$), that is,

$$i\hbar\frac{\partial}{\partial t}\psi = \hat{H}\psi,$$

where

$$\hat{H} = \hat{H}_0 + \hat{V}_1 + \hat{V}_2 + \hat{V}_3 + \hat{V}_4,$$

$$\hat{H}_0 = \frac{\hat{p}^2}{m_e} - \frac{e^2}{r},$$

$$\hat{V}_1 = -\frac{\hat{p}^4}{4m_e^3c^2} + 4\pi\mu_0^2\delta(\mathbf{r}) - \frac{e^2}{2m_e^2c^2r}\left(\hat{\mathbf{p}}^2 + \frac{(\hat{\mathbf{p}}, \mathbf{r})(\hat{\mathbf{p}}, \mathbf{r})}{r^2}\right),$$

$$\hat{V}_2 = 6\mu_0^2\frac{(\hat{\mathbf{S}}, \hat{\mathbf{I}})}{r^3},$$

$$\hat{V}_3 = 6\frac{\mu_0^2}{r^3}\left(\frac{(\hat{\mathbf{S}}, \mathbf{r})(\hat{\mathbf{S}}, \mathbf{r})}{r^2} - \frac{1}{3}\hat{\mathbf{S}}^2\right) + 4\pi\mu_0^2\left(\frac{4}{3}\hat{\mathbf{S}}^2 - 2\right)\delta(\mathbf{r}),$$

$$\hat{V}_4 = 4\pi\mu_0^2\hat{S}^2\delta(\mathbf{r}),$$

$$\mu_0 = \frac{e}{2m_ec}. \quad (7)$$

Here, m_e is the free electron mass; and $\hat{H}_0$, $\hat{V}_1$, $\hat{V}_2$, $\hat{V}_3$, and $\hat{V}_4$ have the same meaning as in the case of exciton.

It is not surprising that, in general, the number of terms in the electron–hole interaction potential (6) is less than that in the electron–positron (7) potential, because formula (6) does not contain the terms corresponding to the delay of the interaction and the magnetic interaction between particles. The presence of corrections $\hat{V}_1$, $\hat{V}_2$, $\hat{V}_3$, and $\hat{V}_4$ in Hamiltonian (6) leads to the appearance of the exciton fine structure. To

Table 1. Ortho–para splitting of the exciton ground state for different semiconductors

Crystal	GaSb	GaAs	InSb	InAs	InP	AlSb	ZnTe	ZnSe	ZnS	CdTe	CdSe	CdS
E_g, meV	813	1410	236	425	1416	2320	2301	2670	3912	1606	1842	2583
E_x, meV	1.8	5.1	0.5	1.8	6.5	7.5	13.0	19.0	40.1	10.0	15.7	29.4
ΔE_0, meV	0.011	0.049	0.003	0.020	0.080	0.065	0.20	0.036	1.10	0.17	0.36	0.89

calculate the splitting of energy levels, we averaged the corrections $\hat{V}_1$, $\hat{V}_2$, $\hat{V}_3$, and $\hat{V}_4$ over unperturbed wavefunctions of excitonic states with different values of the energy n, the total momentum j, the orbital momentum l, the spin s, and the projection of the orbital momentum m. Note that, for the states with this set of quantum numbers, the correction terms are diagonal. This fact is essential because the unperturbed states are degenerate. Using the results taken from [8] in the averaging, one can easily obtain the complete expression for the exciton energy

$$E_x^{njls} = -\frac{1}{4n^2} + \alpha^2\frac{3}{64n^2} - \alpha^2\frac{(1-\delta_{l0})}{8n^3(2l+1)} + \alpha^2\frac{\delta_{l0}(1-\delta_{s0})}{12n^3} + \alpha^2\frac{(1-\delta_{l0})(1-\delta_{s0})}{8n^3} \times \begin{cases} -\dfrac{1}{l(l+1)(2l+1)}, & j = l, \\ -\dfrac{4l-1}{l(2l-1)(2l+1)}, & j = l-1, \\ \dfrac{4l+5}{(l+1)(2l+3)(2l+1)}, & j = l+1. \end{cases} \quad (8)$$

Here, the energy is counted off from the bottom of the conduction band. The result is expressed in terms analogous to the atomic units. The unit length and unit energy are defined by the relations $a_x = \varepsilon\hbar^2\nu^2/\Delta e^2$ and $E_x = \Delta e^4/\varepsilon^2\hbar^2\nu^2$, respectively. It is useful to present the value of the ortho–para splitting as an important special case of formula (8)

$$\Delta E_0 = E_x^{1101} - E_x^{1000} = \frac{\alpha^2}{12}. \quad (9)$$

It is convenient to express the energy of the ortho–para splitting in terms of the observable values E_x and E_g

$$\Delta E_0 = \frac{8E_x^2}{3E_g}. \quad (10)$$

The splitting for some semiconductors is listed in Table 1.

2. EXCITON IN THIN LAYER OF NARROW-GAP SEMICONDUCTOR

In order to determine the fine structure of quasi-two-dimensional exciton, we applied the approach analogous to that used in the previous section. To consistently calculate the corrections conditioned by the nonparabolic dispersion of free electrons and holes (2) and also by their nonidentity, we used the following model.

(1) The noninteracting charge carriers are described by the Dirac equation (1).

(2) Both the electrons and holes are localized in the quantum well created along one of the coordinate axes (the z-axis) with the aid of the modulation of the energy gap

$$\Delta = \Delta(z) = \begin{cases} \Delta_1, & |z| < a; \\ \Delta_2, & |z| > a. \end{cases} \quad (11)$$

It is assumed that the barrier height for electrons and holes essentially exceeds the energy of the dimensional quantization and the walls of the well are infinite, that is, $\Delta_2 \gg \Delta_1$.

(3) The width of the well $2a$ is assumed to be considerably less than the radius of the bulk exciton $r_x = 2e\hbar^2\nu^2/\Delta_1 e^2$, $\delta = a/r_x \ll 1$; that is, the separation between the levels of dimensional quantization is much larger than the binding energy of the bulk exciton $E_x = \Delta_1 e^4/4\varepsilon^2\hbar^2\nu^2$. Thus, it is suggested that there is one exciton on each level of dimensional quantization.

(4) The dielectric constant of the medium surrounding the layer of the narrow-gap semiconductor is considered to be equal to the dielectric constant of the layer ε, whose frequency and spatial dispersion is supposed to be negligible. If the nonidentity of interacting particles is not taken into account, the complete two-particle equation has the following form:

$$\hat{E}\Phi(r_-, r_+) = \hat{H}\Phi(r_-, r_+),$$

$$\hat{H} = \nu\hat{\alpha}_-\hat{\mathbf{p}}_- + \nu\hat{\alpha}_+\hat{\mathbf{p}}_+ + \hat{\beta}_-\Delta(z_-) + \hat{\beta}_+\Delta(z_+) - e^2/\varepsilon r. \quad (12)$$

Here, $\hat{\mathbf{p}}_\pm = -i\hbar\partial/\partial\mathbf{r}_\pm$, the index plus (minus) corresponds to the hole (electron), and $r = |\mathbf{r}_- - \mathbf{r}_+|$. The corrections caused by the nonidentity of the electron and the hole (the "annihilation" corrections) will be analyzed below. We considered the exciton on the lowest level of dimensional quantization. The free particle on the lowest level is represented by the wavefunction in the standard gauge of the Dirac equation (the final

Table 2. Exciton binding energy and its splitting for layers of some semiconductors of different width

Crystal	InSb		GaSb		GaAs		InAs		InP		AlSb		ZnTe	
a, Å	20	100	20	100	20	100	20	100	20	100	20	100	20	100
$E_x^{(2)}$, meV	3.8	1.8	9.0	6.3	17	13.6	5.8	3.5	14.0	11.8	28.4	28.4	50.0	45.8
$\tilde{A}_1$	0.015	0.070	0.019	0.010	0.02	0.10	0.009	0.04	0.20	0.11	0.024	0.15	0.03	0.22
$\tilde{A}_2$	0.028	0.070	0.06	0.29	0.01	0.54	0.018	0.11	0.01	0.53	0.01	0.83	0.01	0.80

result does not depend on the gauge; see, for example, [8])

$$Z_0(z) = C\begin{pmatrix} \omega\cos(k_0 z) \\ \hat{\sigma}_z\omega\dfrac{i\hbar\nu k_0\sin(k_0 z)}{E_0+\Delta_1}\end{pmatrix}, \quad |z| < a. \qquad (13)$$

Here, $\omega = \begin{pmatrix} a \\ b\end{pmatrix}$, where a and b are arbitrary complex numbers. The energy E_0 and wavenumber k_0 can be obtained from the dispersion equation

$$\begin{cases} \tan(2k_0 a) = -\dfrac{\hbar k_0\nu}{\Delta_1} \\ E_0^2 = \Delta_1^2 + \nu^2 k_0^2. \end{cases} \qquad (14)$$

To obtain the two-dimensional equation describing the electron–hole interaction, formula (12) should be averaged over z_+ and z_-. In the first approximation on δ and α, as expected, we obtained the Schrödinger equation for two particles of mass $m^* = E_0/\nu$, which interact by Coulomb's law

$$\left(\frac{\hat{\mathbf{q}}_-^2\nu^2}{2E_0} + \frac{\hat{\mathbf{q}}_+^2\nu^2}{2E_0}\right)\phi(\boldsymbol{\eta}_-, \boldsymbol{\eta}_+) - \frac{e^2}{\varepsilon\eta}\phi(\boldsymbol{\eta}_-, \boldsymbol{\eta}_+) = (E-2E_0)\phi(\boldsymbol{\eta}_-, \boldsymbol{\eta}_+). \qquad (15)$$

Here, $E = 2E_0$ is the exciton energy, which is counted off from the lowest level of the dimensional quantization; $\boldsymbol{\eta}_\pm$ are the two-dimensional vectors defining the coordinates of particles in the XY plane; $\boldsymbol{\eta} = \boldsymbol{\eta}_- - \boldsymbol{\eta}_+$; $\eta = |\boldsymbol{\eta}|$; and $\hat{\mathbf{q}}_\pm = -i\hbar\partial/\partial\boldsymbol{\eta}_\pm$ is the two-dimensional momentum. The solution of this equation is well-known (see, for example, [9]). We present only the formula for the binding energy of the two-dimensional exciton

$$E_x^{(2)} = \frac{m^* e^4}{4\varepsilon^2\hbar^2\left(n-\frac{1}{2}\right)^2} = \frac{E_0\alpha^2}{4\left(n-\frac{1}{2}\right)^2}. \qquad (16)$$

This energy is obtained in the first approximation on δ and α. As in the case of the three-dimensional exciton, in order to obtain the corrections linear in δ and α, we considered the electron–hole scattering amplitude. Averaging it over z_+ and z_-, we retained the terms linear in (δ, α). Using these terms, we restored the corrections to the scattering potential of equation (15), which are linear in (δ, α). The annihilation corrections are found to be complex in the general case; the imaginary part diverges at $(2k_0 - E_0\sqrt{\varepsilon}/\hbar c) \longrightarrow 0$. The matter is that, at $2k_0 \approx E_0\sqrt{\varepsilon}/\hbar c$, the one-photon annihilation cross-section

$$\sigma_{1\gamma}^{ann} \propto \left(4k_0 - \frac{E_0^2\varepsilon}{\hbar^2 c^2}\right)^{-2} \qquad (17)$$

is large, and it is incorrect to treat the exciton as the bound state. Hence, in the case of the exciton, we supposed that the width of the well a satisfies the condition

$$4k_0^2 \gg \Delta_1^2\varepsilon/\hbar^2 c^2. \qquad (18)$$

The inverse relation and the restriction accepted in this section are hardly fulfilled simultaneously in real semiconductors. Taking into account these facts, the correction to the Coulomb potential has the form

$$\hat{U} = \hat{U}^{(ann)} + \hat{U}_1. \qquad (19)$$

To estimate the order of terms in equation (19), it is convenient to introduce the dimensionless quantities defining the unit length and unit energy as $\tilde{a} = 2\nu\hbar/E_0\alpha$ and $\tilde{E} = E_0\alpha^2/2$, respectively. Then,

$$\tilde{U}^{(ann)}(\eta) = \pi\tilde{A}_1(\zeta)(\hat{\mathbf{S}}^2 - 2\hat{S}_z^2)\delta(\eta),$$

$$\tilde{A}_1(\zeta) = \alpha\frac{(1+\zeta^2\phi^2)^{1/2}\left(\frac{3}{4}\zeta + \frac{3}{8}\zeta^2 + \frac{1}{4}\zeta\phi^2\right)}{\left(1+\frac{1}{2}\zeta + 2\zeta^2\phi^2\right)^2},$$

$$\tilde{U}_1(\eta) = \pi\tilde{A}_2(\zeta)\delta(\eta),$$

$$\tilde{A}_2(\zeta) = \delta(1+\zeta^2\phi^2)^{1/2}\left(1+\frac{1}{2}\zeta + 2\zeta^2\phi^2\right)^{-2}\left[\frac{4}{3} - \frac{5}{4}\phi^2 + \zeta\left(2-\frac{1}{2}\phi^2\right) + \zeta^2\left(\frac{8}{3}\phi^2 - \frac{3}{4}\right) + \zeta^3\left(2\phi^2+\frac{1}{2}\right) + \frac{4}{3}\zeta^4\phi^4\right]. \qquad (20)$$

Here, $\zeta = \nu\hbar/a\Delta_1 = \alpha/2\delta$ is the dimensionless parameter characterizing the increase in the energy gap at a given width of the layer; $\phi = k_0 a \propto 1$ is determined by the equation $\tan 2\phi = -2\phi\zeta$ (see relation (14)). It is interesting that $\tilde{A}_1(\zeta)$ is the first-order infinitesimal with respect to α, whereas, in the three-dimensional case, all the energy corrections are of an order of α^2 or higher. $\tilde{A}_2(\zeta)$ is the function of the first order in $\max(\alpha, \delta)$. Indeed, if the condition $\zeta \gg 1$ is fulfilled, we have $\tilde{A}_2 \propto \alpha$. If $\zeta \ll 1$, then $\tilde{A}_2 \propto \delta$. The total binding energy expressed in the same units is

$$E_x^n = \frac{1}{2(n-1/2)^2} - \frac{\delta_{m0}}{2(n-1/2)^3}(\tilde{A}_2 - \tilde{A}_1\delta_{s1}\delta_{s_z0}). \quad (21)$$

Here, s, s_z, and m are the quantum numbers: the total spin, its projection onto the z-axis, and the projection of the orbital momentum onto the z-axis, respectively. The exciton binding energy and its splitting for some semiconductors are listed in Table 2 [9].

ACKNOWLEDGMENTS

We are grateful to S.G. Tikhodeev for his participation in discussions of the results.

This work was supported by the Russian Foundation for Basic Research (project nos. 96-02-16701 and 97-02-16346), the Ministry of Science and Technology (project no. 97-1087), and the INTAS (project no. 96-0398).

REFERENCES

1. R. Knox, *Theory of Excitons* (Academic, New York, 1963; Mir, Moscow, 1996).
2. V. M. Agronovich, *Theory of Excitons* (Nauka, Moscow, 1968).
3. E. A. Andryushin and A. P. Silin, Fiz. Tverd. Tela (Leningrad) **35**, 1947 (1993).
4. A. P. Silin, Usp. Fiz. Nauk **147**, 485 (1993).
5. M. V. Valeĭko, I. I. Zaslavskiĭ, A. V. Matvienko, *et al.*, Pis'ma Zh. Éksp. Teor. Fiz. **43**, 140 (1986).
6. B. A. Volkov, B. G. Idlis, and M. Sh. Usmanov, Usp. Fiz. Nauk **165**, 799 (1995).
7. E. A. Andryushin, A. P. Silin, and S. V. Shubenkov, Kratk. Soobshch. Fiz. **7–8**, 22 (1995).
8. A. I. Akhiezer and V.B. Berestetskiĭ, *Quantum Electrodynamics* (Nauka, Moscow, 1989), Chap. 83.
9. A. P. Silin and S. V. Shubenkov, Kratk. Soobshch. Fiz. **7–8**, 9 (1996).

Translated by A. Pushnov

Physics of the Solid State, Vol. 42, No. 1, 2000, pp. 29–36. Translated from Fizika Tverdogo Tela, Vol. 42, No. 1, 2000, pp. 29–36.

SEMICONDUCTORS AND DIELECTRICS

To the Theory of Magnetic-Moment Anisotropy of Shallow Acceptor Centers in Diamond-like Semiconductors

A. V. Malyshev

Ioffe Physicotechnical Institute, Russian Academy of Sciences, Politekhnicheskaya ul. 26, St. Petersburg, 194021 Russia

Received June 3, 1999

Abstract—The spin quartet splitting of the ground state sublevels of shallow acceptor centers in a magnetic field has been calculated for diamond-like semiconductors with a strong spin-orbit coupling, such as Ge and GaAs. The anisotropy of this splitting has been shown to depend strongly on the binding energy and to be very sensitive to small changes in the Luttinger band parameters. These strong dependences permit one to use calculated ground-state g factors to determine the Luttinger magnetic band-structure parameters κ and q. A new method is proposed for determination of these parameters, and their values for Ge and GaAs are calculated. © *2000 MAIK "Nauka/Interperiodica".*

A large number of experimental and theoretical studies deal with the electronic states of shallow acceptor centers in cubic semiconductors. High-resolution spectra were measured by IR absorption [1–7], photoconductivity [8–10], and other [11–14] methods. These results were interpreted qualitatively in terms of group theory [15], and quantitatively using variational [16] and numerical [17–19] calculations of the acceptor-center states in a magnetic field. The g factors calculated by these methods are in good agreement with the experimental data obtained for excited states. Both experimental and theoretical results obtained by different methods for the acceptor ground state differ noticeably, thus making determination of the ground state of the acceptor center an urgent problem. This paper presents the results of a theoretical calculation of the ground-state magnetic moment of shallow acceptors in diamond-like semiconductors with a strong spin-orbit coupling, analyzes the anisotropy of the magnetic splitting of the ground-state spin quartet, discusses the possibility of using ground-state g-factor calculations to determine the band parameters of a material, and proposes a new method for determination of the Luttinger magnetic parameters κ and q.

It is well known that an external magnetic field splits the carrier localized states degenerate in the projection of the angular momentum (the Zeeman effect). In cubic semiconductors with a strong spin-orbit coupling (such as Ge and GaAs), the ground state of a hole localized on a shallow acceptor center is fourfold degenerate in the projection of the total angular momentum ($F_z = \pm 3/2, \pm 1/2$) [20]. It was shown [21, 22] that, in the general case, the spin Hamiltonian describing the linear Zeeman effect for a quartet of levels of symmetry Γ_8 can be written as

$$\hat{H}' = -\mu_B[g_1(F_xH_x + F_yH_y + F_zH_z) + g_2(F_x^3H_x + F_y^3H_y + F_z^3H_z)]. \quad (1)$$

Here, $\mu_B = e\hbar/(2mc)$ is the Bohr magneton and F_α ($\alpha = x, y, z$) are the projections of the total localized-hole angular momentum on the crystallographic axes.[1]

In contrast to the simplest case of the spin doublet, where the Zeeman effect is isotropic and described by a single parameter (the g factor), in the general case the magnetic splitting of a quartet of levels depends on the magnetic-field direction and is determined by two parameters (g_1 and g_2).

In order to calculate these parameters describing the interaction of a hole localized on an acceptor with a magnetic field, one has to know the hole wave function. Until recently, the wave function of an acceptor-bound hole was calculated either by a variational procedure [16, 23–25], within which the form of the wave function is postulated and the accuracy is difficult to assess, or numerically (see, e.g., [19]). The studies quoted above made use of simplified models, which disregard either the valence-band warping or the central-cell corrections to the acceptor potential. As we are going to show here, these factors substantially affect the magnitude and anisotropy of the magnetic moment of an impurity center (the g_1 and g_2 parameters).

A new method for calculation of the ground-state wave function of a spherical Coulomb acceptor based on solving coupled integral equations in momentum representation was proposed in [26]. This method was

[1] In the literature, one frequently uses electronic notation for labeling the hole sublevels, in which case the minus sign on the right-hand side of equality (1) is dropped.

subsequently generalized to the case where account was taken of the cubic lattice symmetry [27] and the difference of the hole attractive potential from the Coulombic form (the chemical shift) [28, 29], which made possible high-accuracy description of acceptors with different binding energies. Within this method, the dependence of the wave function $\Psi(\mathbf{k})$ on the direction of the wave vector $\mathbf{k}$ is obtained analytically (to within 2%), and the wave function is presented in a compact form convenient for subsequent manipulations. The wave functions derived in this way will be used in the present work to calculate the magnetic splitting of the acceptor ground state (the g_1 and g_2 quantities). The calculations will be carried out by perturbation theory in the first order in the magnetic field.

1. ACCEPTOR MAGNETIC-MOMENT OPERATOR

The state of a free hole in a fourfold-degenerate valence band Γ_8 in the presence of an external constant magnetic field is described by the Luttinger Hamiltonian [30]

$$\hat{H}_L(\mathbf{H}) = \frac{1}{m}\left\{\left(\gamma_1 + \frac{5}{2}\gamma_2\right)\frac{\hat{p}^2}{2}\right.$$

$$- \gamma_2(\hat{p}_x^2\hat{J}_x^2 + \hat{p}_y^2\hat{J}_y^2 + \hat{p}_z^2\hat{J}_z^2) - 2\gamma_3(\{\hat{p}_x, \hat{p}_y\}\{\hat{J}_x, \hat{J}_y\} + \{\hat{p}_y, \hat{p}_z\}\{\hat{J}_y, \hat{J}_z\} + \{\hat{p}_z, \hat{p}_x\}\{\hat{J}_z, \hat{J}_x\}) \quad (2)$$

$$\left. - \kappa\frac{|e|\hbar}{c}\hat{\mathbf{J}}\mathbf{H} - q\frac{|e|\hbar}{c}(\hat{J}_x^3 H_x + \hat{J}_y^3 H_y + \hat{J}_z^3 H_z)\right\}.$$

Here, $\hat{\mathbf{p}} = \hbar\mathbf{k} - (|e|/c)\mathbf{A}$ is the hole momentum, $\mathbf{A} = (1/2)[\mathbf{H}\times\mathbf{r}]$ is the vector potential of the magnetic field $\mathbf{H}$, $\hat{J}_\alpha$ ($\alpha = x, y, z$) are the matrix operators of the free-hole spin projection in the valence band, and γ_1, γ_2, γ_3, κ, and q are the Luttinger band parameters.

The Hamiltonian of an acceptor-bound hole contains, besides the kinetic energy operator (2), the potential energy operator, which does not depend on the magnetic field. The attractive potential of an acceptor center can be represented as a superposition of a long-range Coulomb potential and a short-range central-cell potential, whose inclusion permits consideration of acceptors with different binding energies [28, 29].

Thus, the interaction of an acceptor-bound hole with a magnetic field is described by operator (2) and depends, in the general case, on the type of the impurity (the acceptor binding energy). By separating in (2) the perturbation linear in the magnetic field, one can obtain the operator of the "intrinsic" magnetic moment of the acceptor center it possesses in the absence of a magnetic field. In the case where the magnetic field is directed along the z axis, the perturbation operator can be written as

$$\hat{H}' = -\hat{M}_z H_z, \quad (3)$$

where $\hat{M}_z$ is the operator of the z projection of the intrinsic acceptor-center magnetic moment

$$\hat{M}_z = \mu_B\left[\left(\gamma_1 + \frac{5}{2}\gamma_2\right)\hat{L}_z - 2\gamma_2\hat{N}_{2z} - 2\gamma_3\hat{N}_{3z} + 2\kappa\hat{J}_z + 2q\hat{J}_z^3\right],$$

$$\hat{L}_z = [\hat{\mathbf{r}}\times\hat{\mathbf{k}}]_z = \hat{x}\hat{k}_y - \hat{y}\hat{k}_x, \quad \hat{N}_{2z} = \hat{x}\hat{k}_y\hat{J}_y^2 - \hat{y}\hat{k}_x\hat{J}_x^2,$$

$$\hat{N}_{3z} = (\{\hat{x}, \hat{k}_x\} - \{\hat{y}, \hat{k}_y\})\{\hat{J}_x, \hat{J}_y\} + \{\hat{x}, \hat{k}_z\}\{\hat{J}_y, \hat{J}_z\} - \{\hat{y}, \hat{k}_z\}\{\hat{J}_z, \hat{J}_x\}, \quad (4)$$

where $\hat{x}$, $\hat{y}$, and $\hat{k}_\alpha = -i\nabla_\alpha$ ($\alpha = x, y, z$) are the components of the hole position-vector and wave-vector operators.

2. METHODS OF CALCULATION

By comparing the expressions for the matrix elements of operators (1) and (3) for the acceptor states with the z projections of the total angular momentum $F_z = \pm 3/2$ and $F_z = \pm 1/2$ we obtain two coupled linear equations for the g_1 and g_2 parameters

$$\left(\gamma_1 + \frac{5}{2}\gamma_2\right)\left\langle\frac{3}{2}\middle|\hat{J}_z\middle|\frac{3}{2}\right\rangle - 2\gamma_2\left\langle\frac{3}{2}\middle|\hat{N}_{2z}\middle|\frac{3}{2}\right\rangle - 2\gamma_3\left\langle\frac{3}{2}\middle|\hat{N}_{3z}\middle|\frac{3}{2}\right\rangle + 2\kappa\left\langle\frac{3}{2}\middle|\hat{J}_z\middle|\frac{3}{2}\right\rangle + 2q\left\langle\frac{3}{2}\middle|\hat{J}_z^3\middle|\frac{3}{2}\right\rangle = g_1\frac{3}{2} + g_2\left(\frac{3}{2}\right)^3,$$

$$\left(\gamma_1 + \frac{5}{2}\gamma_2\right)\left\langle\frac{1}{2}\middle|\hat{L}_z\middle|\frac{1}{2}\right\rangle - 2\gamma_2\left\langle\frac{1}{2}\middle|\hat{N}_{2z}\middle|\frac{1}{2}\right\rangle - 2\gamma_3\left\langle\frac{1}{2}\middle|\hat{N}_{3z}\middle|\frac{1}{2}\right\rangle + 2\kappa\left\langle\frac{1}{2}\middle|\hat{J}_z\middle|\frac{1}{2}\right\rangle + 2q\left\langle\frac{1}{2}\middle|\hat{J}_z^3\middle|\frac{1}{2}\right\rangle = g_1\frac{1}{2} + g_2\left(\frac{1}{2}\right)^3. \quad (5)$$

The angular brackets denote here the integration over the whole $\mathbf{k}$ space. Knowing the $\Psi_{F_z}(\mathbf{k})$ wave functions, one can readily calculate the matrix elements on the right-hand sides of the equalities, after which, if the Luttinger parameters are known, (5) becomes an inhomogeneous system of two linear equations with respect to g_1 and g_2. The angular dependence of the wave functions $\Psi_{F_z}(\mathbf{k})$ used in the calculations was obtained in a very compact analytical form [28, 29]. This permitted us to integrate the matrix elements over the angles analytically and to reduce the original three-dimensional integrals to one-dimensional ones, which

considerably simplified the subsequent calculations and expressions for the g_1 and g_2 parameters

$$g_1 = \left(\gamma_1 + \frac{5}{2}\gamma_2\right)\bar{L}_1 - 2\gamma_3\bar{N}_1 + 2\kappa\bar{J}_1 + 2q\bar{J}_1^3,$$
$$g_2 = \left(\gamma_1 + \frac{5}{2}\gamma_2\right)\bar{L}_2 - 2\gamma_3\bar{N}_2 + 2\kappa\bar{J}_2 + 2q\bar{J}_2^3. \quad (6)$$

Here,

$$\bar{L}_1 = \left\langle \frac{(13-7\Delta)\Delta g_{20}(k)^2}{30} + \frac{\Delta(13+28\Delta)g_{20}(k)g_{24}(k)}{30\sqrt{21}} + \frac{(1976-749\Delta)\Delta g_{24}(k)^2}{4290}\right\rangle,$$

$$\bar{N}_1 = \left\langle \frac{(37+17\Delta)\Delta g_{20}(k)^2}{120} + \frac{(1781-1169\Delta)g_{14}(k)g_{24}(k)}{2860} + \frac{(59+64\Delta)g_{20}(k)g_{24}(k)}{40\sqrt{21}} + \frac{(6884+4159\Delta)g_{24}(k)^2}{17\,160} - \frac{(13+28\Delta)(7g_{14}(k)g_{20}(k)-3g_{10}(k)g_{24}(k))}{120\sqrt{21}} + (-13+7\Delta) \times \frac{-3g_{10}(k)g_{20}(k)+kg_{20}(k)g'_{10}(k)-kg_{10}(k)g'_{20}(k)}{60} - \frac{k(13+28\Delta)(g_{20}(k)g'_{14}(k)-g_{14}(k)g'_{20}(k))}{120\sqrt{21}} - \frac{k(13+28\Delta)(g_{24}(k)g'_{10}(k)-g_{10}(k)g'_{24}(k))}{120\sqrt{21}} + \frac{k(-1976+749\Delta)(g_{24}(k)g'_{14}(k)-g_{14}(k)g'_{24}(k))}{8580}\right\rangle,$$

$$\bar{J}_1 = \left\langle \frac{g_{10}(k)^2+g_{14}(k)^2}{4} + \frac{(-7+10\Delta^2)g_{20}(k)^2}{60} - \frac{(21+20\Delta^2)g_{20}(k)g_{24}(k)}{30\sqrt{21}} + \frac{(-1379+1070\Delta^2)g_{24}(k)^2}{8580}\right\rangle,$$

$$\bar{J}_1^3 = \left\langle \frac{91(-1+\Delta^2)g_{20}(k)^2}{240} - \frac{13\sqrt{7/3}(3+2\Delta^2)g_{20}(k)g_{24}(k)}{120} + \frac{7(-197+107\Delta^2)g_{24}(k)^2}{2640}\right\rangle,$$

$$\bar{L}_2 = \left\langle \frac{2(-1+\Delta)\Delta g_{20}(k)^2}{15} - \frac{2\Delta(1+4\Delta)g_{20}(k)g_{24}(k)}{15\sqrt{21}} + \frac{2\Delta(-152+107\Delta)g_{24}(k)^2}{2145}\right\rangle,$$

$$\bar{N}_2 = \left\langle \frac{(\Delta-1)(6g_{10}(k)g_{20}(k)+g_{20}(k)^2)}{30} + \frac{(-137+167\Delta)g_{14}(k)g_{24}(k)}{715} - \frac{(7+8\Delta)g_{20}(k)g_{24}(k)}{10\sqrt{21}} - \frac{(332+73\Delta)g_{24}(k)^2}{4290} - \frac{(1+4\Delta)(-7g_{14}(k)g_{20}(k)+3g_{10}(k)g_{24}(k))}{30\sqrt{21}} - \frac{k(-1+\Delta)(g_{20}(k)g'_{10}(k)-g_{10}(k)g'_{20}(k))}{15} - \frac{k(1+4\Delta)(g_{10}(k)g'_{24}(k)-g_{24}(k)g'_{10}(k))}{30\sqrt{21}} - \frac{k(1+4\Delta)(g_{14}(k)g'_{20}(k)-g_{20}(k)g'_{14}(k))}{30\sqrt{21}} - \frac{k(-152+107\Delta)(g_{24}(k)g'_{14}(k)-g_{14}(k)g'_{24}(k))}{2145}\right\rangle,$$

$$\bar{J}_2^3 = \left\langle \frac{g_{10}(k)^2+g_{14}(k)^2}{4} - \frac{(-13+10\Delta^2)g_{20}(k)^2}{60} + \frac{(39+20\Delta^2)g_{20}(k)g_{24}(k)}{30\sqrt{21}} - \frac{(-2561+1070\Delta^2)g_{24}(k)^2}{8580}\right\rangle, \quad (7)$$

$$\bar{J}_2 = \left\langle \frac{(1-\Delta^2)g_{20}(k)^2}{15} + \frac{2(3+2\Delta^2)g_{20}(k)g_{24}(k)}{15\sqrt{21}} - \frac{(-197+107\Delta^2)g_{24}(k)^2}{2145}\right\rangle,$$

where $\Delta = \gamma_3/\gamma_2$, and the angular brackets denote integration over the modulus of the wave vector: $\langle f(k)\rangle = \int_0^\infty f(k)k^2dk$. The functions $g_{10}(k)$, $g_{14}(k)$, $g_{20}(k)$, and $g_{24}(k)$ determine the dependence of the acceptor ground-state wave function $\Psi_{F_z}(\mathbf{k})$ on the modulus of the wave vector. In the general case, these functions are calculated numerically by the technique described in [28, 29]. The prime on the $g_{ij}(k)$ functions refers to differentiation with respect to the modulus of the wave vector.

In the case where the experimental values of the g_1 and g_2 quantities are known for one or several different acceptor centers (differing in the ground-state binding energy), expressions (6) become equations for the band parameters, which permits one to solve the inverse problem, i.e., to determine the band parameters from known g factors. For each type of the impurity (differing in the binding energy), one can calculate the wave functions and matrix elements (7) entering the system (6), which is a system of two linear equations for the magnetic parameters κ and q. Thus, the knowledge of the g_1 and g_2 quantities for an acceptor center permits one to calculate the magnetic band constants.

If the g factors are known for several different centers, the Luttinger magnetic parameters can be obtained by minimizing the rms deviation of the theoretical from experimental values as a function of the band parameters. This approach was used, for instance, to determine the complete set of the Luttinger parameters for GaAs by comparing the calculated splittings of the magnetic sublevels of the ground and first excited acceptor states [19] with experimental data [3] obtained within a broad magnetic-field range. The above calculations [19], however, did not take into account the corrections due to the central cell to the impurity potential and did not include the contribution of the operator $2\mu_B q\hat{J}^3_\alpha$ cubic in the hole spin to the acceptor magnetic moment: besides, the magnetic constant κ, rather than being considered an independent parameter, was calculated using an approximate expression. As shown below, this could change the ground-state g factors by a few times.

In the present work, we are going to use experimental values of the γ parameters determining the hole effective masses in the valence subbands. These parameters are known from cyclotron-resonance experiments with a high accuracy (see, e.g., [31]). There are several sets of values of the magnetic constants κ and q [19, 32] which differ noticeably from one another. As will be shown below, small changes of these parameters can result in a change of the g_1 and g_2 quantities by a few times. For this reason the magnetic constants κ and q will be determined here by comparison of the calculated and experimental g factors.

3. RESULTS OF THE CALCULATIONS

The ground-state wave functions of various acceptor centers found in [28, 29] were used to derive the dependence of the g_1 and g_2 quantities on acceptor binding energy for a number of semiconductors. The results of such calculations for Ge and GaAs are presented by solid lines in the figure. The triangles are experimental values of the g factors for Ge : B [5], Ge : Ga [5] and GaAs : C [3], GaAs : Be [4]. The dashed lines are calculated within the zero-range potential model, which permits us to derive wave functions in an analytic form [33]. The band parameter sets used

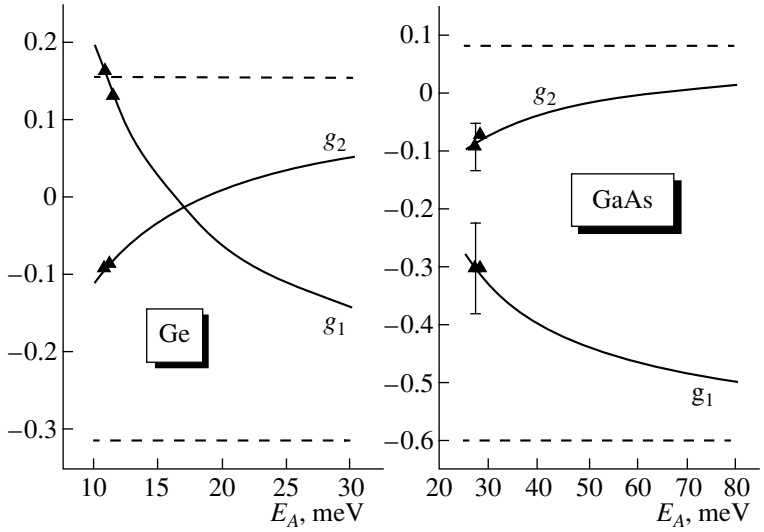

Acceptor ground-state g factors (g_1 and g_2) vs. binding energy for Ge and GaAs.

Table 1. Comparison of the values of g_1 and g_2 calculated in this work with available experimental data (The signs of the g_1 and g_2 parameters taken from [3–6] are reversed, which corresponds to crossing over from the electronic notation of the acceptor sublevels used in those publications to the hole one.)

Acceptor center	E_A (meV)	γ_1	γ_2	γ_3	κ	q	g_1	g_2
GaAs : Be	28	6.85	2.1	2.9	1.30	0.017	−0.31	−0.08
GaAs : Be	28	6.65	1.95	2.63	1.1	0.017	−0.22	−0.085
GaAs : Be [4]	28						−0.30	−0.07
GaAs : C [3]	27						−0.30(8)	−0.09(5)
Ge : B	10.82	13.38	4.24	5.69	3.134(4)	0.086(3)	0.158	−0.093
Ge : B [5]	10.82						0.164(1)	−0.091(1)
Ge : Ga	11.32	13.38	4.24	5.69	3.134(4)	0.086(3)	0.137	−0.083
Ge : Ga [5]	11.32						0.132(2)	−0.084(2)
Ge : Ga [11]	11.32						−0.16(8)	0.08(4)
Ge : Zn^-	87	13.38	4.24	5.69	3.134(4)	0.086(3)	−0.079	0.023
Ge : Zn^- [6]	87						−0.53(1)	−0.002(7)

Note: The magnetic band parameters κ and q were calculated by the method described in Section 2.

in the calculations are as follows: $\gamma_1 = 13.38$, $\gamma_2 = 4.24$, $\gamma_3 = 5.69$ [31,32], $\kappa = 3.134$, and $q = 0.0861$ for Ge, and $\gamma_1 = 6.85$, $\gamma_2 = 2.1$, $\gamma_3 = 2.9$ [32, 34], $\kappa = 1.30$, and $q = 0.017$ [35] for GaAs. The κ parameter for Ge and GaAs and the parameter q for Ge were derived from a comparison with the experimental data quoted in [4, 5] by the technique described in Section 2.

The plots in the figure reveal a strong dependence of the g_1 and g_2 quantities on binding energy, i.e., on the type of the impurity (the chemical shift). The calculations show that the dependence of the g_1 parameter on the binding energy E_A is dominated by the matrix element $\bar{N}_1$, which is negative and whose magnitude decreases monotonically with increasing E_A. For Ge, the g_1 parameter is positive for low energies, $E_A \leq 0.9E_B$ (here and henceforth E_B is the Bohr energy of the heavy hole; for GaAs, E_B = 51.3 meV, and for Ge, E_B = 18.25 meV), and also falls off monotonically with increasing binding energy. At $E_A \approx 0.9E_B$, g_1 vanishes. In the case of GaAs, the g_1 parameter behaves qualitatively in the same way, but, in contrast to Ge, the sign reversal occurs at very low binding energies, where there are no real impurity centers. Here, the binding energy is noticeably lower than the Coulomb energy, which corresponds to the repulsive potential of the central cell (to a negative chemical shift).

The behavior of the g_2 parameter with binding energy is determined primarily by the matrix element $\bar{L}_2$, which is positive and grows monotonically with E_A. The g_2 quantity is negative for low binding energies, $E_A \leq E_B$, both for Ge and GaAs, and grows monotonically with increasing energy. At $E_A \approx E_B$ the g_2 parameter passes through zero and reverses sign. Thus, the anisotropy of the magnetic splitting of the acceptor ground state, which is determined by the g_2 parameter, varies qualitatively with increasing binding energy; namely, at $E_A \approx E_B$ the g_2 quantity becomes zero, the acceptor ground-state magnetic moment becomes isotropic, and the splitting no longer depends on the magnetic-field direction.

In the general case ($g_1 \neq 0$, $g_2 \neq 0$), the splittings of the acceptor-center magnetic sublevels are given by the expressions

$$\Delta E^{[001]}_{\pm 3/2} = \mp \mu_B \frac{3}{2} H \left(g_1 + \frac{9}{4} g_2 \right),$$

$$\Delta E^{[001]}_{\pm 1/2} = \mp \mu_B \frac{1}{2} H \left(g_1 + \frac{1}{4} g_2 \right) \tag{8}$$

for the magnetic field **H** directed along the [001] axis and

$$\Delta E^{[111]}_{\pm 3/2} = \mp \mu_B \frac{3}{2} H \sqrt{\frac{2}{3}\left(g_1 + \frac{9}{4} g_2 \right)^2 + \frac{1}{3}\left(g_1 + \frac{5}{4} g_2 \right)^2},$$

$$\Delta E^{[111]}_{\pm 1/2} = \mp \mu_B \frac{1}{2} H \left(g_1 + \frac{13}{4} g_2 \right) \tag{9}$$

for the **H** field aligned with the [111] axis.

In the case where the g_1 parameter becomes zero (for Ge, at $E_A \approx 0.9E_B$), the splitting is completely determined by the g_2 parameter. For the [001] direction, the splitting of the states with $F_z = \pm 3/2$ is 27 times as large as that of the $F_z = \pm 1/2$ states, the magnetic-moment anisotropy for the $F_z = \pm 3/2$ states is small ($\Delta E^{(3/2)}_{111} / \Delta E^{(3/2)}_{001} = \sqrt{187/243} \approx 0.88$), and the magnetic

Table 2. Comparison of the values of g_1 and g_2 calculated in this work for different Luttinger band-parameter sets with theoretical data in [19] (The signs of the g_1 and g_2 parameters taken from [19] are reversed, which corresponds to crossing over from the electronic notation of the acceptor sublevels used in that publication to the hole one.)

Acceptor center	E_A (meV)	γ_1	γ_2	γ_3	κ	q	g_1	g_2
GaAs : C	27	6.65	1.95	2.63	1.1	0.017	−0.214	−0.089
GaAs : A_{Coul}	25.70	6.65	1.95	2.63	1.1	0.017	−0.202	−0.095
GaAs : A_{Coul}	25.70	6.65	1.95	2.63	1.1	0	−0.210	−0.118
GaAs : A_{Coul} [19]	25.59	6.65	1.95	2.63	1.1	0	−0.208	−0.115
Ge : Ga	11.32	13.35	4.24	5.69	3.41	0.07	0.595	−0.131
Ge : A_{Coul}	10.35	13.35	4.24	5.69	3.41	0.07	0.639	−0.151
Ge : A_{Coul}	10.35	13.35	4.24	5.69	3.41	0	0.595	−0.236
Ge : A_{Coul} [19]		13.35	4.24	5.69	3.41	0	0.590	−0.226

moment of states with $F_z = \pm 1/2$ is strongly anisotropic ($\Delta E_{111}^{(1/2)}/\Delta E_{001}^{(1/2)} = 13$).

For deeper impurity centers, whose binding energy exceeds the heavy-hole Bohr energy ($E_A > E_B$), the g_1 and g_2 quantities have opposite signs, and the anisotropy of the magnetic-sublevel splitting with $F_z = \pm 3/2$ is larger than that for the $F_z = \pm 1/2$ states.

Some of the above qualitative features in the behavior of the acceptor-center magnetic moment are observed experimentally. For instance, the sign reversal of the g_1 parameter with increasing binding energy was found to occur for acceptors in Ge. Table 1 lists experimental and calculated values of the g factors for various acceptor centers in Ge. One readily sees that, for shallow impurity centers (B and Ga [5]), the g_1 parameter is positive, whereas for the deeper Zn^- acceptor [6] this parameter is negative. Table 1 demonstrates good quantitative agreement between the theoretical and experimental data for shallow acceptor centers.

Isotropic magnetic splitting of the ground state was experimentally observed in Ge doped with Zn, which is a doubly charged acceptor in this material. Experiment [6] gave a very small value of g_2 for the ground state of the singly charged Zn^- center (see Table 1). The theoretical results listed in Table 1 for Ge : Zn^- agree only qualitatively with the experiment; indeed, as in the experiment, the absolute magnitude of g_2 is small, and the sign of g_1 for the deep Zn^- center is opposite to that for the shallow centers. The poor quantitative agreement with experimental data is possibly due to the fact that Zn^- is a fairly deep acceptor in Ge and the binding energy of its ground state ($E_A = 87$ meV [32]) is more than four times as large as the heavy-hole Bohr energy E_B. Because of the high binding energy, the contribution of the spin-split valence band to the wave function of the center and to the magnetic moment is not small. This contribution should be taken into account when attempting a quantitative interpretation of experimental results obtained with deep acceptors, which is outside the scope of the model considered here.

The g factor of the acceptor center was calculated in a spherical approximation [36–38]. The results quoted in these publications can be obtained from those presented in this work in the corresponding limit ($\gamma_3 = \gamma_2 = \gamma$). It was shown [37, 38] that the ground-state g factor calculated in a spherical approximation depends only weakly on the binding energy and can be approximated well both in the zero-range potential model and in the other widely used limiting model of a Coulomb center within which the central-cell corrections are neglected completely. As seen from the figure, in contrast to the case of a spherical acceptor [37, 38] the limiting model of zero-range potential (the dashed lines) is at odds with the experimental data and more accurate calculations (the solid lines). This model yields only asymptotic values of g_1 and g_2 for high binding energies ($E_A \gg E_B$). The zero-range potential model used in the spherical approximation [36, 37] reproduces well the splitting of the $F_z = \pm 3/2$ sublevels in a magnetic field directed along the [001] axis ($g_F \approx g_{3/2}^{[001]} = g_1 + (9/4)g_2$).

Let us note a significant point associated with calculations of the acceptor magnetic moment, taking into account the cubic symmetry of the lattice. In theoretical calculations of g_1 and g_2, the contribution of the $2\mu_B q \hat{J}_\alpha^3$ operator to the acceptor-center magnetic moment (4) is, as a rule, neglected [16, 19]; i.e., one sets $q = 0$. The reason for this lies in that the q constant is of the relativistic nature and must be small [20, 30]; indeed, for Ge and GaAs the magnitude of q is typically two orders of magnitude smaller than that of the γ_i and κ parameters. This approach is justified when considering highly excited acceptor states, for which the g factors are large in absolute magnitude, and the $\hat{J}_\alpha^3$ operator does indeed contribute little. In the ground state the g_1 and g_2 quantities are, as a rule, small, so that the contribution of the $2q\hat{J}_\alpha^3/F_z$ operator may be comparable to these quantities. For example, as seen from Table 2,

neglecting the q parameter results in a change of the g_2 parameter by a factor of 1.5 for the same binding energy of the unperturbed acceptor in Ge (the κ and q parameters do not affect the binding energy in a zero-order approximation). Thus, neglecting the q constant for acceptor states with small values of the magnetic moment (comparable to the contribution due to the $2\mu_B q\hat{J}_\alpha^3$ operator) can bring about a change of the result by a few times. Among such states is, as a rule, the ground state ($1S_{3/2}$) and, possibly, the first excited state ($2P_{3/2}$) of the acceptor center.

The splittings of the magnetic sublevels of the ground and first excited acceptor states in Ge and GaAs were numerically calculated [19] within a broad magnetic-field range, taking into account the cubic symmetry of the crystal. A fitting to experimental data [3] yielded a new set of the band parameters γ_1, γ_2, γ_3, and κ for GaAs and demonstrated good agreement of the theoretical values of g_1 and g_2 with experimental data obtained for excited states. The value of g_1 calculated for the acceptor ground state in GaAs differed by more than 30% from the measurement, a discrepancy that, until present, remained unaccounted for.

Table 2 presents the calculated [19] values of g_1 and g_2 for GaAs and Ge (rows 4 and 8), as well as the results of our calculations carried out for the band parameters obtained in [19] and using the simplifying assumptions made in the quoted work, i.e., assuming a Coulomb acceptor and $q = 0$ (rows 3 and 7). The results obtained in these two independent calculations are in very good agreement with one another. However, as is evident from Table 2, the g_1 and g_2 parameters change strongly when one introduces the corrections due to the central cell and the finiteness of the q parameter; indeed, for $q = 0.017$ [35] for GaAs and $q = 0.07$ [32] for Ge the value of g_2 changes by about a factor of 1.5 (rows 6 and 2), and taking into account the non-Coulomb nature of the potential (rows 1 and 5) changes the result for g_1 and g_2 by 10–20% (with the binding energy changing by 5–10%). Besides, in [19] the κ constant was not varied when fitting the band parameters for GaAs. It was assumed that it satisfies the relation $\gamma_1 - 2\gamma_2 - 3\gamma_3 + 3\kappa + 2 = 0$ [39], which is valid only in an approximate way. It will be shown, however, that small variations in the κ parameter may bring about large changes in the magnitude and anisotropy of the magnetic-sublevel splitting. Thus it is using the Coulomb acceptor model and an approximate relation for κ and neglecting the term $2\mu_B q\hat{J}_\alpha^3$ in the magnetic moment that accounts for the large errors in the calculation of the acceptor ground-state g factors quoted in [19].

Another important result of the calculations is the strong dependence of the g_1 and g_2 quantities on the Luttinger band parameters. For instance, a decrease of the magnetic constant κ for Ge by 10% (from 3.41 to 3.1) results in a sign reversal of g_1 (for the same unperturbed acceptor binding energy). Note that the absolute value of g_1 changes here by a factor of about three.

The strong dependence of the g_1 and g_2 quantities on the magnetic band parameters makes possible the determination of these constants to a high accuracy. Table 1 lists experimental data for g_1 and g_2 obtained for GaAs [3, 4] and Ge [5, 6, 11], as well as the calculated values of these quantities and of the band parameters κ and q. The determination of the κ constant for GaAs was based on the experimental data from [4], because a better spectral resolution was attained here. For the same reason the data for Ge were taken from [5]. The κ and q constants were derived by solving the coupled equations (6). As seen from Table 1, the calculated values of g_1 and g_2 are in very good agreement with the experimental data obtained on shallow acceptors.

The good agreement of our present calculations with the available theoretical and experimental data suggests that the model proposed for the acceptor ground-state magnetic moment can give an accurate quantitative description of the Zeeman effect in shallow acceptor centers. This is due, in a large measure, to the fact that the comprehensive model of the acceptor ground state developed in [28, 29] permits one to obtain the wave function of a center with a high accuracy. This factor, as well as the strong dependences of the g_1 and g_2 quantities on the magnetic constants κ and q, raises hope that the latter are determined with a good accuracy within the method proposed in the present work.

The main results of this work can be summed up as follows.

(1) Expressions have been derived for the g_1 and g_2 quantities for the ground state of a shallow acceptor center in cubic semiconductors with strong spin-orbit coupling.

(2) It has been shown that the g_1 and g_2 parameters describing the splitting of the acceptor sublevel quartet in a magnetic field depend strongly on the ground-state binding energy. These dependences have been calculated for GaAs and Ge, and they are shown to be in good quantitative agreement with experimental data.

(3) It has also been shown that the $2\mu_B q\hat{J}_\alpha^3$ operator, which is frequently neglected in calculations, contributes significantly to the magnetic moment of the ground and, possibly, of the first excited state of the acceptor.

(4) The paper proposes the reasons for the noticeable discrepancies between the previous theoretical g-factor calculations and experimental data for the acceptor ground state.

(5) The g_1 and g_2 quantities have been demonstrated to be very sensitive to small changes in the Luttinger magnetic band constants κ and q.

(6) A new method is proposed for determination of the magnetic parameters κ and q, which makes use of

the strong dependences of the g_1 and g_2 quantities on these parameters and the acceptor binding energy. This method has been employed to calculate the magnetic constants for Ge and GaAs.

It should be noted, in conclusion, that the model proposed in this work is valid for fairly shallow acceptor centers whose binding energy is small compared to the valence-band spin-orbit splitting.

ACKNOWLEDGMENTS

The author is grateful to I.A. Merkulov and A.V. Rodina for fruitful discussions and to B.P. Zakharchenya for continual interest in these studies.

Support of the Russian Foundation for Basic Research (Grant 96-15-96392) is gratefully acknowledged.

REFERENCES

1. H. P. Soepangkat and P. Fisher, Phys. Rev. B **8**, 870 (1973).
2. J. Schubert, M. Dahl, and E. Bangert, in *High Magnetic Fields in Semiconductor Physics II*, Ed. by G. Landwehr (Springer, Berlin, 1989).
3. R. Atzmüller *et al.*, J. Phys.: Condens. Matter **3**, 6775 (1991).
4. R. A. Lewis and M. Henini, Phys. Status Solidi B **210**, 821 (1998).
5. P. Fisher *et al.*, Phys. Rev. B **47**, 12999 (1993).
6. P. Fisher, C. A. Freeth, and R. E. M. Vickers, Phys. Status Solidi B **210**, 827 (1998).
7. R. E. M. Vickers, P. Fisher, and C. A. Freeth, Phys. Status Solidi B **210**, 839 (1998).
8. R. F. Kirkman, R. A. Stradling, and P. Lin-Chung, J. Phys. C **11**, 419 (1978).
9. J. Broeckx *et al.*, J. Phys. C **12**, 4061 (1979).
10. Y. Kamiura *et al.*, Solid State Commun. **38**, 883 (1981).
11. H. Tokumoto and T. Ishiguro, Phys. Rev. B **15**, 2099 (1977).
12. R. I. Dzhioev, B. P. Zakharchenya, and V. G. Fleĭsher, Pis'ma Zh. Éksp. Teor. Fiz. **17**, 224 (1973).
13. D. Bimberg, K. Cho, and W. Kottler, in *Proc. Int. Colloque on Physics in High Magnetic Fields* (Grenoble, 1974), Colloques Internationaux CNRS, No. 242 (Paris, 1975).
14. D. Bimberg, Phys. Rev. B **18**, 1794 (1978).
15. A. K. Bhattacharjee and S. Rodriguez, Phys. Rev. B **6**, 3836 (1972).
16. P. Lin-Chung and R. F. Wallis, J. Phys. Chem. Sol. **30**, 1453 (1969).
17. N. O. Lipari and M. Altarelli, Solid State Commun. **33**, 47 (1980).
18. J. Broeckx and P. Claus, Solid State Commun. **28**, 355 (1978).
19. Schmitt *et al.*, J. Phys.: Condens. Matter **3**, 6789 (1991).
20. G. L. Bir and G. E. Pikus, *Symmetry and Strain-Induced Effects in Semiconductors* (Nauka, Moscow, 1972; New York, 1974).
21. B. Bleaney, Proc. Phys. Soc. **73**, 937 (1959).
22. B. Bleaney, Proc. Phys. Soc. **73**, 939 (1959).
23. W. Kohn and D. Schechter, Phys. Rev. B **99**, 1903 (1955).
24. K. S. Mendelson and H. M. James, J. Phys. Chem. Solids **25**, 729 (1964).
25. A. Baldereschi and N. O. Lipari, Phys. Rev. B **8**, 2697 (1973).
26. B. L. Gel'mont and A. V. Rodina, Fiz. Tekh. Poluprovodn. **25**, 2189 (1991).
27. I. A. Merkulov and A. V. Rodina, Fiz. Tekh. Poluprovodn. **28**, 321 (1994).
28. A. V. Malyshev, I. A. Merkulov, and A. V. Rodina, Fiz. Tekh. Poluprovodn. **30**, 159 (1996).
29. A. V. Malyshev, I. A. Merkulov, and A. V. Rodina, Phys. Rev. B **55**, 4388 (1997).
30. J. M. Luttinger, Phys. Rev. **102**, 1030 (1956).
31. J. C. Hensel and K. Suzuki, Phys. Rev. B **9**, 4219 (1974).
32. Landolt-Borstein, *Numerical Data and Functional Relationships in Science and Technology*, Vol. 17, subvol. A (Springer, 1982).
33. V. I. Perel' and I. N. Yasievich, Zh. Éksp. Teor. Fiz. **82**, 237 (1982).
34. K. Hess *et al.*, *Proc. 13th Int. Conf. on Physics of Semiconductors* (Rome), Ed. by F. G. Fumi (North-Holland, Amsterdam, 1976), p. 142.
35. X. Marie, T. Amand, P. Le Jeune, *et al.* (Submitted to Phys. Rev. B).
36. B. L. Gel'mont and M. I. D'yakonov, Fiz. Tekh. Poluprovodn. **7**, 2013 (1973).
37. A. V. Malyshev and I. A. Merkulov, Fiz. Tverd. Tela **39**, 58 (1997).
38. A. V. Malyshev, I. A. Merkulov and A. V. Rodina, Phys. Status Solidi B **210**, 865 (1998).
39. H.-R. Trebin, U. Rössler, and R. Ranvaud, Phys. Rev. B **20**, 686 (1979).

Translated by G. Skrebtsov

Physics of the Solid State, Vol. 42, No. 1, 2000, pp. 37–40. Translated from Fizika Tverdogo Tela, Vol. 42, No. 1, 2000, pp. 37–39.

SEMICONDUCTORS AND DIELECTRICS

Electron Characteristic Loss Spectra of Molybdenum Dichalcogenides

A. N. Timoshkin, V. Val. Sobolev, and V. V. Sobolev

Udmurt State University, Krasnoarmeiskaya ul. 71, Izhevsk, 426034 Russia
e-mail: sobolev@uni.udm.ru

Received March 16, 1999; in final form, June 28, 1999

Abstract—The complete sets of the fundamental optical functions of molybdenum dichalcogenides have been considered for the first time. The energies of their bulk and surface plasmons of two types are determined. It is found that the energies of long-wavelength plasmons correlate with the energies of the deep minima in the reflectivity and $\varepsilon_2 E^2$ spectra and the maxima in the reflectivity phase spectra. © *2000 MAIK "Nauka/Interperiodica".*

The electronic structure of solids over a wide range of energies is studied experimentally by using the spectra of reflection, transmission, photoemission, etc. [1]. The light is traditionally used as a source of excitation, which permits one to obtain the spectrum of transverse transition components. The longitudinal components of a transition spectrum can be measured with the use of fast charged particles. By the perturbation theory, the intensity of the energy transfer from a particle is determined by the energy loss function $W(\nu, E, q)$, which is expressed through a double integral of the function of the velocity ν, momentum q, and energy E of the particles. Using certain approximations and normalizations, from the measured function W, one derives a function $-\mathrm{Im}(\varepsilon^{-1})$, which is called the function of bulk characteristic losses, unlike the surface loss function $-\mathrm{Im}(1 + \varepsilon)^{-1}$.

Within the range of comparatively high energies and very small values of $\varepsilon_1(E)$ and $\varepsilon_2(E)$, the energy loss function spectra contain very broad intense bands caused by excitation of all valence electrons. They are universally assigned to bulk and surface plasmons with the band maxima located at E_{PV} and E_{PS}, respectively. One can also observe substantially weaker and very narrow maxima associated with excitation of the longitudinal components of interband or excitonic transitions. The presence of the latter transitions causes a decrease in E_{PV} and E_{PS} compared to the free-electron plasmon energy E_P.

The experimental techniques used to measure the losses W are far from being simple, and the error of E_{PV} determination reaches $\Delta E \approx 0.5$ eV. In this respect, the methods used to calculate the loss spectra from the experimental optical reflectivity spectra are of particular importance. The objective of this work was to establish the bulk and surface characteristic-loss spectra for the MoS_2, $MoSe_2$, and $MoTe_2$ crystals and to reveal the specific features in the correlation between the spectral structures of $-\mathrm{Im}(\varepsilon^{-1})$, $-\mathrm{Im}(1 + \varepsilon)^{-1}$, and other optical fundamental functions.

Dichalcogenides of the MoX_2 group are semiconductors with E_g in the vicinity of 1 eV. These compounds have a pronounced layered structure. They have been investigated for many years following theoretical predictions of their anomalous properties, specifically of the high-temperature superconductivity [2, 3].

1. CALCULATION TECHNIQUE

The complete set contains 15 optical fundamental functions [4], namely, the reflectivity R and absorptivity μ; the indices of refraction n and absorption k; the real (ε_1) and imaginary (ε_2) parts of the dielectric permittivity; the $\varepsilon_2 E^2$ function proportional to the joint density of states at a constant oscillator strength; the effective number of the valence electrons $n_{\mathrm{eff}}(E)$ participating in transitions to a given energy E and the effective permittivity $\varepsilon_{\mathrm{eff}}$; the characteristic losses of the bulk ($-\mathrm{Im}\varepsilon^{-1}$) and surface $-\mathrm{Im}(1 + \varepsilon)^{-1}$ plasmons; the phase of the reflected wave Θ; and the electro-optic differential functions α, β, and $R^{-1}dR/dE$. Usually, the complete set of functions is calculated from one experimental spectrum $R(E)$, but over a very wide range of energy, by means of the Kramers–Kronig integral relations and analytical functions. The calculational method is described in considerable detail and has been employed before [4, 5].

2. RESULTS AND DISCUSSION

The reflectivity spectra of MoS_2, $MoSe_2$, and $MoTe_2$ single crystals were measured experimentally at 300 K in the $E \perp C$ polarization in the energy ranges 1–12.5 eV [6] and 1–30 eV [7]. The $R(E)$ spectra obtained in [7] were used by us to derive the complete sets of the optical fundamental functions for these three compounds.

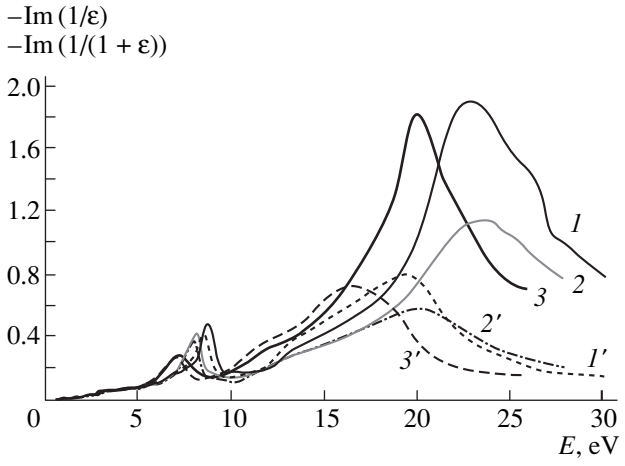

Fig. 1. Spectra of (*1*, *2*, *3*) $-\mathrm{Im}\varepsilon^{-1}$ and (*1'*, *2'*, *3'*) $-\mathrm{Im}(1+\varepsilon)^{-1}$ for (*1*, *1'*) MoS_2, (*2*, *2'*) $MoSe_2$, and (*3*, *3'*) $MoTe_2$ crystals in the range 0–25 eV.

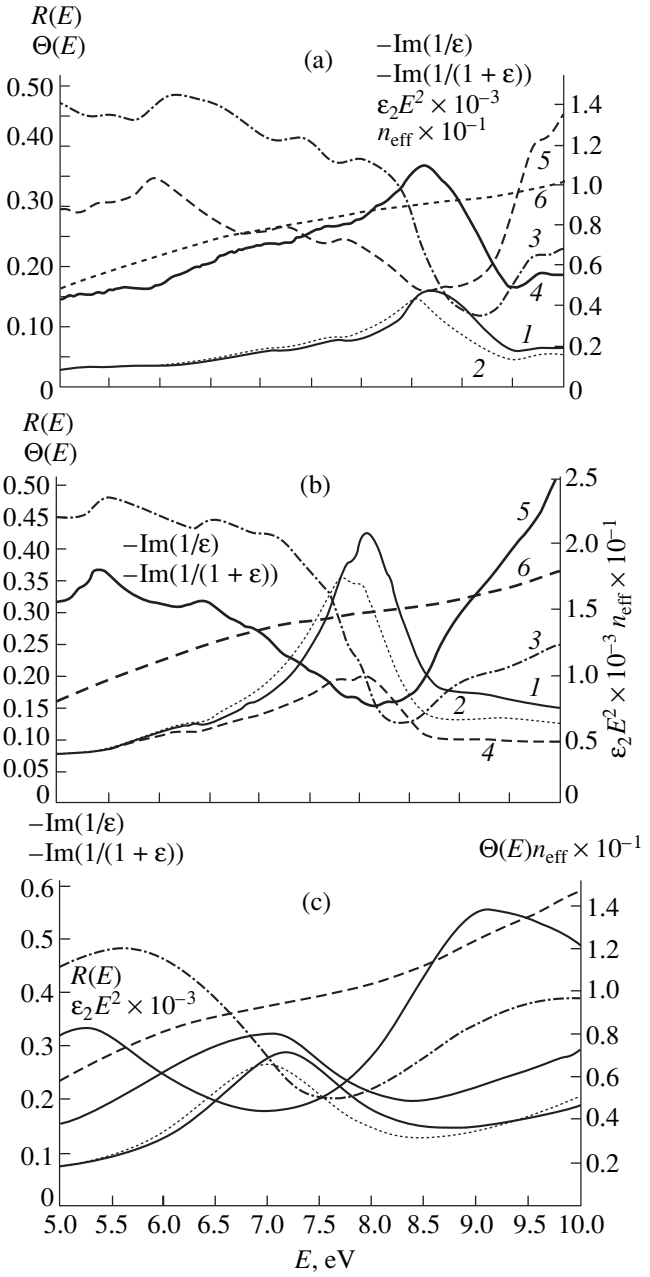

Fig. 2. Spectra of (*1*) $-\mathrm{Im}\varepsilon^{-1}$, (*2*) $-\mathrm{Im}(1+\varepsilon)^{-1}$, (*3*) *R*, (*4*) Θ, (*5*) $\varepsilon_2 E^2$, and (*6*) n_{eff} for (a) MoS_2, (b) $MoSe_2$, and (c) $MoTe_2$ crystals in the range 5–10 eV.

The present paper briefly considers only the loss spectra (Figs. 1, 2, and table).

According to our calculations, the energies of the bulk (E_{PVO}) and surface (E_{PVS}) plasmons vary in the MoS_2–$MoSe_2$–$MoTe_2$ series from 22.90 to 19.95 eV and from 19.35 to 16.30 eV, respectively. The experimental data on E_{PVE} are available only for bulk plasmons in MoS_2 and $MoTe_2$; they are equal to approximately 22.3 and 22.2 eV, respectively [2]. Estimates for the plasmon energies obtained for MoX_2 in the free-electron approximation range from 27.3 to 22.5 eV. In some cases, the E_{PVO} energies are estimated directly from the ε_1 spectrum at $\varepsilon_1 \approx 0$. For MoX_2, such an evaluation substantially underestimates E_{PVO}, namely, by 0.75 eV (MoS_2), 1.7 eV ($MoSe_2$), and 0.5 eV ($MoTe_2$). An analysis of our calculated data for E_{PVO} permits one to readily predict the expected E_{PVE} energy for $MoTe_2$, i.e., ~20 eV (it is given in parentheses in the table). No experimental study has been made of surface plasmons in MoX_2. According to our calculations, their energies are less than those of the bulk plasmons by ~3.55 eV (MoS_2, $MoTe_2$) and by ~5.0 eV ($MoSe_2$). As expected from the general theory of plasmons [1], E_P is noticeably larger than E_{PVO}. In the case of MoX_2, $\Delta E = E_P - E_{PVO}$ = 4.4 eV (MoS_2), 2.8 eV ($MoSe_2$), and 2.5 eV ($MoTe_2$).

Apart from the above strongest, broad band, the spectrum of the bulk and surface characteristic losses exhibits one more band at lower energies, $E \approx 7$–9 eV, which is narrow and substantially weaker. It should be pointed out that this band, like the main plasmon band, does not have a counterpart in the reflectivity and absorption spectra, i.e., in the spectra of *R*, ε_2, *k*, and $\varepsilon_2 E^2$. As follows from an analysis of the spectra of the optical fundamental functions of MoX_2 crystals, the maximum of this additional band in the bulk and surface loss spectra coincides with a high accuracy with the energy of the deep minimum in the $\varepsilon_2 E^2$ function, the energy of a pronounced narrow maximum of the reflected-wave phase Θ(*E*), and the intersection point of the $\varepsilon_1(E)$ curve with the energy axis $\varepsilon_1(E) \approx 0$. It lies ~0.3–0.4 eV below the very deep reflectivity minimum. These features of the additional loss maxima, besides the main band, permit the conclusion that they are also due to the purely plasma effects. The energies of the long-wavelength bulk and surface plasmons (type I) differ by only 0.2–0.3 eV, i.e., ten times less than those in the case of the main plasmons (type II). The energies

Energies (eV) of the calculated plasmons E_P, E_{PVO}, and E_{PSO}; experimental E_{PVE}; extrema in ε_1, R, $\varepsilon_2 E^2$, and phase Θ; and the effective number of valence electrons for the MoX_2 crystals and graphite

Parameter	$MoTe_2$		$MoSe_2$		MoS_2		Graphite	
	I	II	I	II	I	II	I	II
E_P	–	22.50	–	25.30	–	27.30	12.50	23.0
E_{PVO}	7.20	19.95	8.10	22.45	8.75	22.90	7.10	26.3
E_{PSO}	7.00	16.30	7.80	17.40	8.55	19.35	6.50	20.10
E_{PVE}	(~7.1)	(~20.0)	8.00	22.20	8.70	23.30	6.3–7.5	25–28
$E(\varepsilon_1 = 0)$	7.05	19.45	8.05	20.75	8.65	22.15	6.95	25.6
$E(\min R)$	7.55	–	8.40	–	9.15	–	8.3	–
$E(\min \varepsilon_2 E^2)$	7.05	–	8.05	–	8.75	–	9.9	–
$E(\max \Theta)$	7.0	–	8.1	–	8.75	–	7.29	–
N_{eff}	10	24	12	28	9	21	1.4	6

of the type-I plasmons were estimated approximately from the experimental loss spectra of MoS_2 (~8.7 eV) and $MoSe_2$ (~8 eV) [2]. By our estimates for $MoTe_2$, the type-I plasmon band should lie in the $-\mathrm{Im}\varepsilon^{-1}$ spectra in the vicinity of 7.1 eV (this value is given in the table in parentheses).

Plasmons of two types differing strongly in energy and intensity in the loss spectra are well known to exist in graphite [8]. They are accounted for by the strongly pronounced layered crystal structure of graphite and the separation of the valence electrons into two groups (the π and σ electrons). The compounds of the MoX_2 group have also a layered structure. It is not accidental that the optical axes of MoX_2 and graphite are perpendicular to the basal plane of the samples. The crystal structure and the character of interatomic interactions in the MoX_2 dichalcogenides are considerably more complex than those in graphite. Therefore, in MoX_2, one could expect a more complex model of bonding-orbital orientation and participation of *d* electrons in both intra- and interlayer interatomic coupling. In this connection, it is of interest to compare the parameters of the MoX_2 and graphite plasmons.

We calculated the complete set of the optical fundamental functions for graphite from the reflectivity spectrum in the range 0–40 eV [8] in the same way as it was done for MoX_2. The table lists our data, except for E_P and E_{PVE} [9, 10]. An analysis of the data in the table reveals a noticeable similarity of the features of two plasmon types in two different groups of layered crystals, namely, MoX_2 and graphite. Therefore, one can argue that all types of layered crystals should have plasmons of two different types. The extent of separation of the valence electrons into two different groups depends on the actual anisotropy of a crystal lattice. One of the most sensitive methods of revealing these two groups of valence electrons consists in measuring the characteristic losses, specifically the method based on the calculations of the reflectivity spectra.

The positions of the type-I and type-II maxima in the $-\mathrm{Im}\varepsilon^{-1}$ and $-\mathrm{Im}(1+\varepsilon)^{-1}$ spectra of MoX_2 crystals differ by ~3.5–5 eV (II) and 0.2 eV (I). In the energy range $E < 7$ eV, the loss spectra contain many very weak narrow peaks, whose positions in the surface and bulk loss spectra coincide to within 0.01 eV. These peaks are due to direct interband and excitonic transitions. A comparison of the loss and ε_2 spectra for MoX_2 shows that the loss peaks are located higher in energy than the ε_2 peaks by ~0.5–1 eV for $E > 2.5$ eV and virtually coincide for lower energies. As follows from an analysis of these data, the energy of the longitudinal–transverse transition splitting is very small, $\Delta E < 0.05$ eV for $E < 2.5$ eV, and increases with an increase in the energy by about an order of magnitude for higher energies.

Thus, we have established for the first time the existence of two types of surface and bulk plasmons in the MoS_2, $MoSe_2$, and $MoTe_2$ crystals, the closeness in energies of the long-wavelength plasmons, the minimum in $\varepsilon_2 E^2$, the maximum in $\Theta(E)$, $E(\varepsilon_1 = 0)$, and the sharp minimum in $R(E)$, and close analogies of these compounds with graphite. Therefore, the distinct separation of the valence electrons and atomic interactions into two different groups in graphite has been proven to extend to the considerably more complex layered crystal structures of the MoX_2 group as well. The model of two different valence-electron groups is apparently characteristic of layered and strongly anisotropic crystals. The probability of realization of this model in a particular crystal can be found from the intensity of the long-wavelength plasmon. A detailed analysis of the $n_{\text{eff}}(E)$ spectrum will permit quantitative separation of the valence electrons into two different groups participating in transitions to a given energy *E*.

ACKNOWLEDGMENTS

This work was supported by the Basic Natural Sciences Center at St. Petersburg State University.

REFERENCES

1. D. Pines, *Elementary Excitations in Solids* (Benjamin, New York, 1963; Mir, Moscow, 1965).
2. A. D. Yoffe, Festkörperprobleme **13**, 1 (1973).
3. V. V. Sobolev and V. V. Nemoshkalenko, *Calculational Methods in the Theory of Solids: The Electronic Structure of Rare-Metal Dichalcogenides* (Naukova Dumka, Kiev, 1990).
4. V. V. Sobolev and V. V. Nemoshkalenko, *Calculational Methods in the Theory of Solids: The Electronic Structure of Semiconductors* (Naukova Dumka, Kiev, 1988).
5. V. V. Sobolev and V. Val. Sobolev, Fiz. Tverd. Tela (St. Petersburg) **36** (9), 2560 (1994).
6. V. V. Sobolev, V. I. Donetskikh, A. A. Opalovskiĭ, *et al.*, Fiz. Tekh. Poluprovodn. (Leningrad) **5** (6), 1025 (1971).
7. A. R. Beal and H. P. Hughes, J. Phys. C: Solid State Phys. **12** (5), 881 (1979).
8. E. A. Taft and H. R. Philipp, Phys. Rev. A **138** (1), 197 (1965).
9. J. G. Carter, R. H. Huebner, R. N. Hamm, *et al.*, Phys. Rev. A **137** (2), 639 (1965).
10. F. R. McFeely, S. P. Kowalczyk, L. Ley, *et al.*, Phys. Rev. B: Solid State **9** (12), 5268 (1974).

Translated by G. Skrebtsov

Physics of the Solid State, Vol. 42, No. 1, 2000, pp. 4–10. Translated from Fizika Tverdogo Tela, Vol. 42, No. 1, 2000, pp. 6–11.

METALS AND SUPERCONDUCTORS

Reflectivity Spectra of New Organic Metal $(BEDO\text{-}TTF)_5[CsHg(SCN)_4]_2$

R. M. Vlasova*, N. V. Drichko*, V. N. Semkin*, E. I. Zhilyaeva, O. A. Bogdanova**, R. N. Lyubovskaya**, and A. Graja*****

** Ioffe Physicotechnical Institute, Russian Academy of Sciences, Politekhnicheskaya ul. 26, St. Petersburg, 194021 Russia*
*** Institute for Problems of Chemical Physics, Russian Academy of Sciences, Chernogolovka, Moscow oblast, 142432 Russia*
**** Institute of Molecular Physics, Poland Academy of Sciences, 60-179 Poznan, Poland*
e-mail: rema.vlasova@shuvpop.ioffe.rssi.ru

Received June 8, 1999

Abstract—The polarized reflectivity and optical conductivity spectra of microcrystals of the new organic conductor $(BEDO\text{-}TTF)_5[CsHg(SCN)_4]_2$ based on the donor molecule bis(ethylenedioxy)tetrathiafulvalene (BEDO-TTF) have been studied in the spectral ranges 600–6500 and 9000–40000 cm^{-1} at 300 K for three principal lattice directions. The optical evidence for the quasi-two-dimensional character of the conducting electronic system is obtained. The conclusion is made that the studied crystal is the quasi-two-dimensional semimetal with overlapping electron energy bands. The basic parameters of the electronic system of the crystal are determined in the framework of the Drude model. It is found that the allowed electron energy bands of the crystal are somewhat narrower than those of the previously studied structurally allied superconductor based on the same molecule. The features of vibrational structure are identified in the $\sigma(\omega)$ spectra for the specified three polarizations. © *2000 MAIK "Nauka/Interperiodica".*

A large number of high-conductivity radical cation salts based on the bis(ethylenedithio)tetrathiafulvalene (BEDT-TTF) molecule have been synthesized in recent years [1–3]. The properties of these compounds vary over a broad range (from semiconductors to quasi-two-dimensional metals and superconductors) depending on the structure of the BEDT-TTF conducting radical cation layers and the chemical nature of anions. Among the twenty superconductors produced on the basis of the BEDT-TTF molecule, there is a group of *k*-$(BEDT\text{-}TTF)_2Cu[N(CN)_2]X$ salts with the highest superconducting transition temperatures T_c observed in organic compounds: T_c = 12.3 K at 0.3 kbar (X = Cl), 11.6 K (X = Br) [1], and 11.3 K ($X = Cl_{0.5}Br_{0.5}$) [4].

In the search for new organic superconductors, Suzuki *et al.* [5] synthesized the new donor heterocyclic molecule—an analog of the BEDT–TTF molecule, in which four sulfur atoms in the six-membered rings are replaced by the oxygen atoms—bis(ethylenedioxy)tetrathiafulvalene (BEDO-TTF) (Fig. 1). In the case of the conventional phonon (Bardeen–Cooper–Schrieffer) mechanism of superconductivity, Wudl *et al.* [6] assumed that the replacement of four sulfur atoms with lighter oxygen atoms can lead to an increase in the T_c temperature due to a decrease in the overall mass of the molecule and the higher density of states at the Fermi level in salts based on BEDO-TTF. On the other hand, according to Yamaji [7], the superconducting transition temperature can increase in the BEDO-TTF salts as a result of an increase in the frequency of intramolecular vibrations interacting with the electronic system. By now, two superconductors were synthesized on the basis of this molecule: $(BEDO\text{-}TTF)_5Cu_2(NCS)_3$ with T_c = 1.1 K [1] and $(BEDO\text{-}TTF)_2ReO_4(H_2O)$ with T_c = 2.5 K [8, 9]. The polarized reflectivity spectra of the later superconductor were studied by Sommer *et al.* [10] and also by Swietlik and Kushch [11].

Recently, we synthesized a new family of organic metals based on the BEDO-TTF molecule, namely, $(BEDO\text{-}TTF)_m[MHg(SCN)_4]_2$ (where M = Cs, Rb, K, NH_4, and Li), and investigated the structure and the electrical conductivity of some compounds [12, 13].

In the present work, we studied the polarized reflectivity spectra of the $(BEDO\text{-}TTF)_5[CsHg(SCN)_4]_2$ compound—a new organic metal belonging to the above family of salts, which undergoes a transition (at 85 K) to the dielectric state with a decrease in the temperature. The measurements were carried out over a wide spectral range (600–6500 and 9000–40000 cm^{-1}) at a temperature of 300 K. The spectra obtained were compared with the corresponding spectra of the $(BEDO\text{-}TTF)_2ReO_4(H_2O)$ superconductor [10].

1. EXPERIMENTAL

Crystals of $(BEDO\text{-}TTF)_5[CsHg(SCN)_4]_2$ are black, well-faceted parallelepipeds 2 × 0.5 × 0.2 mm in size with smooth specular surfaces.

The main crystal data are as follows: triclinic crystal system, space group $P1$, Z = 1, a = 10.436 Å,

b = 10.709 Å, c = 19.973 Å, α = 89.59°, β = 81.88°, γ = 72.76°, and V = 2109 Å^3 [13]. The crystals have a layered structure: the BEDO-TTF$^{+0.4e}$ radical cation layers alternate with the anion layers along the c-axis aligned parallel to the (ab) plane. (The oxidation state of the BEDO-TTF molecules is +0.4e.) In the conducting layer, the BEDO-TTF$^{+0.4e}$ radical cations form stacks and ribbons. The stacks are oriented along the b–2a direction (i.e., along [$\bar{2}$**10**]) with the shortest contacts (3.55–3.67 Å) between the S atoms of the adjacent molecules. In the stacks, almost planar molecules BEDO-TTF are packed in a face-to-face manner. The planar ribbons are aligned along the 3b–a direction. In the ribbons, the contacts between the adjacent molecules are shortest (3.36–3.47 Å), and the molecules are arranged side-by-side. In the anionic layers, the Hg atom is coordinated with four SCN groups to produce a tetrahedron. The $[Hg(SCN)_4]^{2-}$ anions linked by the Cs^+ ions give rise to the chains along the a-axis. The cation and anion layers are linked by the shortest contacts.

The external faceting of the crystal is formed by the ab (001) and bc (100) faces. The b–2a direction of stacks, which we designated as **I**, coincides with the direction of the long crystal edge.

The polarized reflectivity spectra $R(\omega)$ at normal light incidence to the more developed (001) and side (100) crystal faces in the range 600–6500 cm^{-1} were recorded on a Perkin–Elmer 1725X Fourier spectrometer equipped with a microscope with a nitrogen-cooled MCT detector (light beam diameter, 100 μm; resolution, 4 cm^{-1}; "golden wire" as a polarizer). In the range 9000–40000 cm^{-1}, the spectra were taken on a double-beam microspectroreflectometer devised at the State Optical Institute (beam diameter, 25 μm; resolution, 60 cm^{-1}; Glan–Thompson prism as a polarizer). The quality and position of the analyzed surface with respect to the microscope axis and the orientation of the crystal in the light wave field were inspected through an exit pupil of instruments. When measuring the reflection from each face, different microregions on the surface of several crystals were examined to choose the region with the highest reflectivity for each face. The absolute reflectivities were determined with respect to an aluminum mirror and SiC.

The reflectivity spectra of the developed crystal face (001) were measured in the polarizations corresponding to the largest anisotropy of the spectra in the range 600–6500 cm^{-1}. These are the polarizations in which the electric vector of light wave is parallel and perpendicular to the direction of the BEDO-TTF stacks, i.e., **E** ∥ **I** and **E** ⊥ **I**. The spectra of the side crystal face (100) were measured at **E** ∥ **I** and **E** ⊥ (ab); i.e., **E** is almost parallel to **c**. The crystal was oriented in the light wave field with an accuracy of 7°–10°.

The optical conductivity spectra $\sigma(\omega)$ were obtained from the $R(\omega)$ spectra by the Kramers–Kronig method.

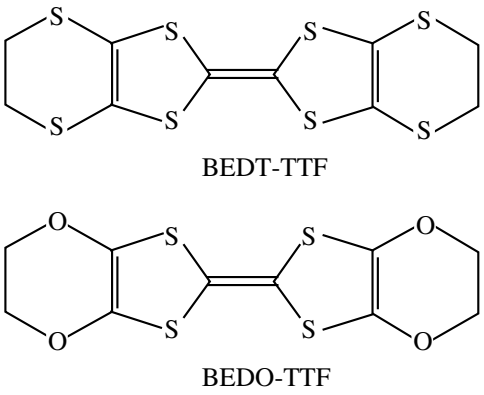

Fig. 1. Structural formulas of the bis(ethylenedithio)tetrathiafulvalene (BEDT-TTF) and bis(ethylenedioxy)tetrathiafulvalene (BEDO-TTF) molecules.

In the low-frequency range, the extrapolation was performed in the Hagen–Rubens approximation $R(\omega) = 1 - \alpha\omega^{1/2}$. In the high-frequency range, we employed the standard extrapolation in the form $R(\omega) \sim (\omega_0/\omega)^{\alpha}$. In the spectral range 6500–9000 cm^{-1} (not measured in the present work), the reflectivity spectra were extrapolated using the spectra obtained earlier in this range for crystals of the BEDT-TTF salts [14].

2. RESULTS

Figures 2a and 2b demonstrate the reflectivity spectra obtained for faces (001) and (100) in the $(BEDO\text{-}TTF)_5[CsHg(SCN)_4]_2$ crystals in the range 600–40000 cm^{-1}.

As can be seen from Fig. 2a, the maximum reflectivity is achieved in polarization **E** ⊥ **I**, and the minimum reflectivity is observed at **E** ∥ **I**. For both polarizations, the reflectivity at low frequencies is rather high: up to 0.75 at **E** ⊥ **I** and up to 0.60 at **E** ∥ **I**. **E** ⊥ **I**, as the frequency increases, the reflectivity first smoothly decreases, then rapidly declines, and exhibits a well-defined plasma edge in the range 2500–6000 cm^{-1} and a deep minimum (down to 0.05) at about 6000 cm^{-1}. For **E** ∥ **I**, an increase in the frequency results in a smoother decrease in the reflectivity. In this case, the plasma edge is less pronounced and observed in the narrower range 3700–5500 cm^{-1} with a minimum at 5500 cm^{-1}. It is seen that, for both polarizations, the spectra obtained are qualitatively similar to the spectra of metals and have the shape close to the reflectivity spectra of the $(BEDO\text{-}TTF)_2ReO_4(H_2O)$ superconductor [10]. The anisotropy observed in the spectra of the (001) face is insignificant.

In the frequency range below 2000 cm^{-1}, the spectra at **E** ⊥ **I** show features in the form of shallow minima at 860, 1188, 1199, 1440, and 1612 cm^{-1}. In our opinion, these features are brought about by the interaction between the electronic system and intramolecular

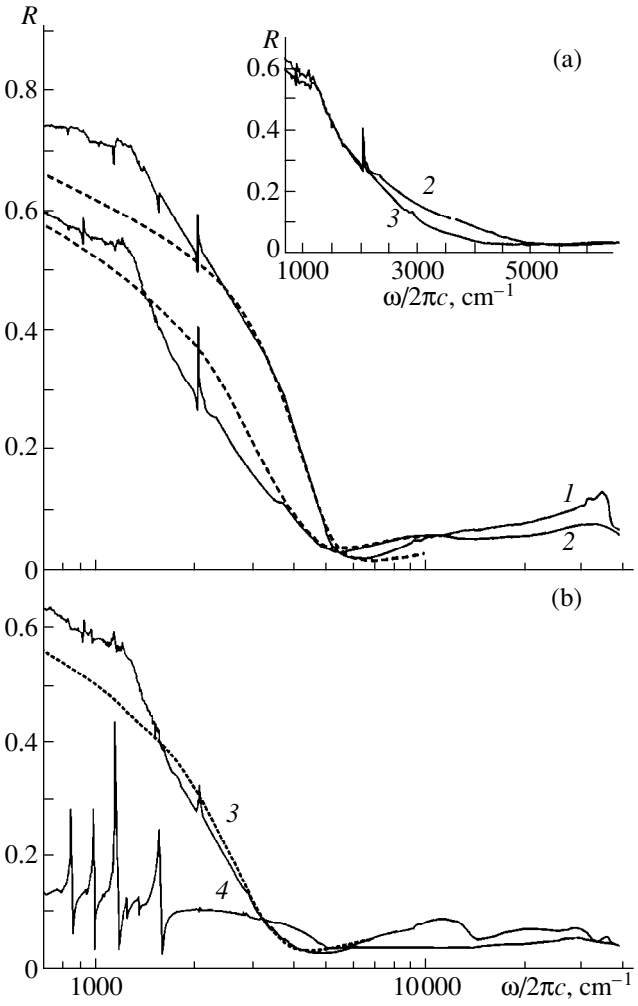

Fig. 2. Polarized reflectivity spectra of the $(BEDO\text{-}TTF)_5[CsHg(SCN)_4]_2$ crystal: (a) the (001) face at (*1*) **E** ⊥ **I** and (*2*) **E** ‖ **I** and (b) the (100) face at (*3*) **E** ‖ **I** and (*4*) **E** ⊥ (*ab*) plane. Solid lines correspond to the experimental data, and dashed lines represent the results of calculations within the Drude model. Inset: (*2*) the (001) face and (*3*) the (100) face at **E** ‖ **I**.

vibrations of the BEDO-TTF molecule, which is typical of organic conductors. At **E** ‖ **I**, there are only two vibrational features: a rather strong band in the form of a "minimum–maximum" at 956 cm^{-1} and a very shallow minimum at 1188 cm^{-1}. For both polarizations, a narrow intense doublet attributed to the characteristic stretching vibrations of the CN groups in the anion is observed at 2100 cm^{-1}.

The reflectivity spectra of the side crystal face (100) at **E** ‖ **I** and **E** ⊥ (*ab*) plane are displayed in Fig. 2b. A strong anisotropy of the reflectivity for this plane qualitatively differs from a weak anisotropy of the reflectivity in the (001) plane. The reflectivity spectrum at **E** ‖ **I** shows metallic behavior and is close in shape to the reflectivity spectrum of the (001) face in this polarization (**E** ‖ **I**). The difference between these spectra resides in the fact that, as is seen from the inset in Fig. 2a, the plasma edge in the reflectivity spectrum of the (100) face occurs at a lower frequency with a minimum at about 4500 cm^{-1}. The spectrum measured in the other polarization, i.e., at **E** ⊥ (*ab*) plane (when the **E** vector is virtually perpendicular to the conducting layers) exhibits a qualitatively different behavior. In the entire IR range, one can observe a low reflectivity (from 0.13 to 0.06), typical of dielectrics. In the range below 2000 cm^{-1}, against this low background, there appear narrow intense vibrational features at frequencies of 864, 1010, 1188, 1201, 1270, 1378, and 1609 cm^{-1}, which are associated with the optically active vibrations of the BEDO-TTF molecule. A very weak band attributed to the vibrations of the CN groups in the anion is also observed at about 2100 cm^{-1}.

In the range 9000–40000 cm^{-1} lying above the plasma frequency, the reflectivity spectra contain very broad weak bands. The reflectivity spectrum of the (001) face at **E** ⊥ **I** involves the band (R_{max} = 0.13) with a maximum at 32400 cm^{-1}. A similar, but weaker band (R_{max} = 0.08) is observed in the spectra of both (001) and (100) faces at **E** ‖ **I**. For the polarization when the **E** vector is perpendicular to the conducting layers [face (100), **E** ⊥ (*ab*) plane], there is a band at about 13000 cm^{-1}. We believe that these bands are associated with the intramolecular electron transitions in the BEDO-TTF molecule. The structural analysis [13] and the band intensities suggest that the band at 32400 cm^{-1} is predominantly polarized along the short molecular axis, whereas the band at 13000 cm^{-1} is polarized along the long molecular axis.

The optical conductivity spectra σ(ω) in the range 700–6000 cm^{-1} are depicted in Fig. 3. It is seen that, for the polarizations when the **E** vector lies in the plane of conducting layers, i.e., **E** ⊥ **I** and **E** ‖ **I** for the (001) face and **E** ‖ **I** for the (100) face, the shape of three spectra is qualitatively identical. In the range 700–1500 cm^{-1}, the conductivity decreases rather sharply. At frequencies above 1500 cm^{-1}, the metallic conductivity smoothly decreases with an increase in the frequency. For the (001) face at **E** ‖ **I**, one can see a small inflection near 4000 cm^{-1} against the background of a smooth decrease in the conductivity. It is worth noting that, over the entire frequency range studied, the optical conductivity for the (001) face at **E** ‖ **I** is larger than that for the (100) face in the same polarization because of the difference in the reflectivity spectra. In the range below 2000 cm^{-1}, the σ(ω) spectra under consideration exhibit weak vibrational features in the form of narrow bands or bands with a "minimum–maximum" shape, which is characteristic of the features brought about by the resonance interaction between the intramolecular vibrations and conduction electrons.

As is seen from Fig. 3, unlike the metallic character of the σ(ω) spectra for the polarizations with the **E** vector lying in the plane of conducting layers, the σ(ω)

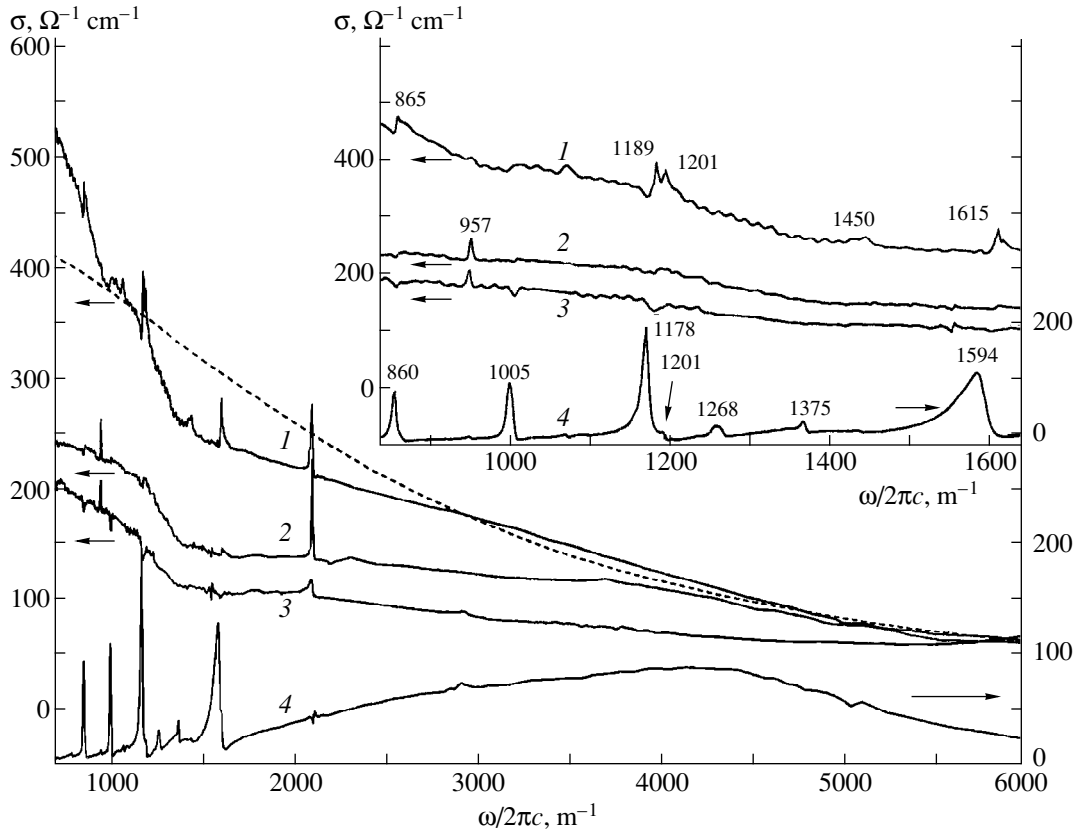

Fig. 3. Optical conductivity spectra of the $(BEDO\text{-}TTF)_5[CsHg(SCN)_4]_2$ crystal for the (001) face at (*1*) **E** ⊥ **I** and (*2*) **E** || **I** and for the (100) face at (*3*) **E** || **I** and (*4*) **E** ⊥ (*ab*) plane. Solid lines correspond to the experimental data, and dashed line represent the results of calculations within the Drude model. Inset: the same spectra in the range 700–1600 cm^{-1} on an enlarged scale.

spectrum does not show the metallic behavior when the **E** vector is perpendicular to this plane [face (100), **E** ⊥ (*ab*) plane]. A very broad (2000–6000 cm^{-1}) electron-type band with a maximum near 4000 cm^{-1} is clearly observed in the σ(ω) spectrum. In the range below 2000 cm^{-1}, the spectrum contains intense narrow bands associated with the optically active intramolecular vibrations of the BEDO-TTF molecule. The assignment of all the vibrational features observed in the $R(\omega)$ and σ(ω) spectra will be given below in the discussion of experimental data.

3. DISCUSSION

3.1. Electronic Phenomena

The $R(\omega)$ and σ(ω) spectra of the $(BEDO\text{-}TTF)_5[CsHg(SCN)_4]_2$ crystals (Figs. 2, 3) indicate that the metallic behavior of the reflectivity and optical conductivity in the IR range is observed only in the case when the **E** vector is parallel to the plane of the BEDO-TTF layers and does not occur when the **E** vector is perpendicular to this plane. The found anisotropy suggests the quasi-two-dimensional character of the conducting electronic system in the crystals. A similar result was obtained in our earlier work [14] for a number of conductors and superconductors based on the BEDT-TTF molecule. The quasi-two-dimensional character of the electronic system can also manifest itself in a broad maximum in the σ(ω) spectrum at about 4000 cm^{-1} in the case when the **E** vector is perpendicular to the plane of conducting layers in the crystal [face (100), **E** ⊥ (*ab*) plane]. Owing to the large focal aperture of an objective lens in an IR microscope, the light incident on the crystal involves oblique rays. As was demonstrated by Bulaevskiĭ and Kukharenko [15], in a quasi-two-dimensional crystal, the oblique incidence of light on a crystal face perpendicular to conducting planes should bring about the direct excitation of plasmons when the **E** vector lies in the incidence plane. Actually, as is seen from Fig. 3, the broad maximum in the σ(ω) spectrum is located near the plasma minimum (4500 cm^{-1}) observed for this face at **E** || **I**. A similar maximum for the corresponding polarization was previously observed for the $(BEDO\text{-}TTF)_2Cu[N(CN)_2]Cl_{0.5}Br_{0.5}$ crystals in our earlier work [16], in which other possible causes of its appearance in the spectra were also discussed.

As the $R(\omega)$ and σ(ω) spectra of the studied crystal exhibit a behavior close to metallic, their quantitative analysis was performed by the fitting of the calculated

Table 1. Parameters of the electronic structure of the $(BEDO\text{-}TTF)_5[CsHg(SCN)_4]_2$ crystal

Polarization	ω_p, cm^{-1}	γ, cm^{-1}	ε_∞	Ω_p, cm^{-1}	m^*
E ⊥ **I**, (001)	8000	2400	2.5	7200	1.0
E ∥ **I**, (001)	7400	3100	3.2	5700	1.6
E ∥ **I**, (100)	6000	2300	3.2	5300	2.4

spectra to the experimental data with the use of the Drude expression for the frequency dependence of the dielectric constant

$$\varepsilon(\omega) = \varepsilon_\infty - \omega_p^2/\omega(\omega + i\gamma),$$

where ω_p is the plasma frequency, ε_∞ is the dielectric constant of the lattice at high frequencies, and γ is the damping constant for charge carriers. It should be emphasized that the precise fitting of the reflectivity spectra can be obtained only in a narrow range covering the plasma edge and the plasma minimum: 3000–6500 cm^{-1} at **E** ⊥ **I** and 3750–6500 cm^{-1} at **E** ∥ **I** for the (001) face and 3000–6000 cm^{-1} at **E** ∥ **I** for the (100) face. In the range of smooth decrease in σ (2500–6500 cm^{-1}), the $\sigma(\omega)$ spectrum is sufficiently well described by the Drude frequency dependence. Table 1 presents the found parameters ω_p, ε_∞, γ and the effective masses of charge carriers m^*, which were calculated from the relationship $\omega_p^2 = 4\pi ne^2/m^*$ (where $n = 0.95 \times 10^{21}$ cm^{-3} is the charge carrier concentration obtained from the X-ray diffraction analysis [13]). The values of ω_p found from the sum rule $\Omega_p^2 = 8\int\sigma(\omega)d\omega$ are also listed in Table 1. At lower frequencies, the experimental spectra deviate from the simple Drude dependence described by the parameters given in Table 1.

Note that the ω_p values obtained for the $(BEDO\text{-}TTF)_5[CsHg(SCN)_4]_2$ crystal are somewhat less than those for the $(BEDO\text{-}TTF)_2ReO_4(H_2O)$ superconductor (ω_p = 9900 and 7850 cm^{-1} for two polarizations). This indicates that the allowed electron energy bands in the studied BEDO-TTF-based organic crystal with the metal–dielectric transition are somewhat narrower than those in the superconductor based on the same molecule.

As shown above, the $R(\omega)$ and $\sigma(\omega)$ spectra of the crystals under consideration deviate from the simple Drude dependence. We believe that one of the reasons for this deviation can be the presence of several types of charge carriers, as is the case for the $(BEDO\text{-}TTF)_2ReO_4(H_2O)$ compound [10]. The band structure calculations performed by Kahlich *et al.* [17] demonstrate that the aforementioned compound is the semimetal with overlapping valence and conduction bands, and the valence band overlaps with two more bands. Therefore, the electronic properties of this compound

Table 2. Location and assignment of the features of vibrational structure in the $\sigma(\omega)$ spectra of the $(BEDO\text{-}TTF)_5[CsHg(SCN)_4]_2$ crystal

Band frequencies in the $\sigma(\omega)$ spectra, cm^{-1}			Frequencies (cm^{-1}), symmetry, and mode of vibrations in BEDO-TTF (D_{2h} symmetry) [18]			
E ∥ **I**, (001)	**E** ⊥ **I**, (001)	**E** ⊥ (*ab*)	frequency (cm^{-1})		symmetry	vibrational mode
			observed	calculated		
	1615		1657	1654	$a_g(2)$	C=C bond stretching in fulvalene rings
		1594	1647	1647	$b_{1u}(2)$	"
	1450		1445	1454	$a_g(4)$	CH_2 bending
		1375	1374	1393	$b_{2u}(45)$	
		1268	1270	1279	$b_{1u}(29)$	Bending of ethylene fragment
	1189					
			1196	1203	$a_g(6)$	C–O–C vibrations
	1201					
		1178	1170	1169	$a_u(14)$	Bending of ethylene fragment
		1200	1199	1203	$b_{1u}(30)$	C–O–C vibrations
954		1005	1015	1014	$b_{1u}(31)$	
	865		865	860	$a_g(8)$	Mixed vibrations of six-membered rings in BEDO-TTF
		860	864	861	$b_{1u}(32)$	

are affected by all four bands. It can be supposed that similar overlapping of bands also takes place in the $(BEDO\text{-}TTF)_5[CsHg(SCN)_4]_2$ crystals. In our opinion, the vibronic and electron–electron interactions can also contribute to the above deviation.

It follows from Table 1 that the ω_p and γ parameters at $\mathbf{E} \parallel \mathbf{I}$ are different for the (001) and (100) faces. This difference likely implies that the parameters and the relevant spectra $R(\omega)$ (inset in Fig. 2a) depend on the direction of the wavevector $\mathbf{k}$ in the quasi-two-dimensional crystals under consideration.

3.2. Vibrational Features

The locations of vibrational features in the $\sigma(\omega)$ spectra for three polarizations of the incident light are given in Table 2. The assignment of these features was performed by comparison of their locations in the spectrum with the frequencies of normal vibrations in the neutral BEDO-TTF molecule, which were found in [18] by the calculation and measurements of the Raman and IR spectra for BEDO-TTF crystals. It is seen from Table 2 that the locations of the features observed at $\mathbf{E} \perp \mathbf{I}$ (except for the band at 1615 cm^{-1}) correspond to the frequencies of the totally symmetric (a_g) intramolecular vibrations. This corroborates the above conclusion that the vibrational features are brought about by the interaction of the electronic system with these vibrations. The location of the band at 1615 cm^{-1} differs from the frequency of the $a_g(2)$ intramolecular vibrations by about 40 cm^{-1}. This is likely explained by the fact that the frequency of the $a_g(2)$ intramolecular vibrations (the C=C bond stretching in fulvalene rings) in the $BEDO\text{-}TTF^{+0.4e}$ cation in the salt crystals is less than the frequency in the neutral molecule due to a stronger interaction of these vibrations with the electronic system, as evidenced by the broadening of this band. The doublet character of the feature at 1189–1201 cm^{-1} can be associated with the presence of crystallographically nonequivalent BEDO-TTF cations in the crystals [13]. It is worth nothing that the vibrational features brought about by the interaction of the electronic system with the a_g intramolecular vibrations are observed for the $\mathbf{E} \perp \mathbf{I}$ polarization. This polarization corresponds to the charge transfer in the direction perpendicular to stacks; i.e., when the molecules are arranged in a side-by-side fashion, and the charge transfer can lead to a change in the molecular symmetry [19]. It can be assumed that some change in the symmetry reduces the vibronic interaction in this compound, and, hence, the vibronic features observed in the spectra are of low-intensity. At $\mathbf{E} \parallel \mathbf{I}$, the spectrum contains only one band at 954 cm^{-1}, which is attributed to the optically active vibrations $b_{1u}(31)$. As can be seen from Fig. 3 and Table 2, for polarization $\mathbf{E} \perp (ab)$, the band at 1594 cm^{-1}, which is assigned to the $b_{1u}(27)$ vibrations, differs from the other bands in this spectrum: it is shifted by 51 cm^{-1} with respect to the relevant band for BEDO-TTF and is considerably broadened. These features are caused by the same factors that have been considered above for the $a_g(2)$ vibrations, which also correspond to the stretching of the C=C bonds in the fulvalene rings.

Thus, the polarized spectra of reflectivity $R(\omega)$ and optical conductivity $\sigma(\omega)$ of the new organic conductor $(BEDO\text{-}TTF)_5[CsHg(SCN)_4]_2$ based on the bis(ethylenedioxy)tetrathiafulvalene molecule are studied. Comparison of these spectra with the spectra of the $(BEDO\text{-}TTF)_2ReO_4(H_2O)$ superconductor indicates that the conductor studied in this work has the electronic structure of quasi-two-dimensional semimetal with overlapping electron energy bands. The main parameters of quasi-two-dimensional electronic system ω_p, ε_∞, γ, m^*, and their anisotropy are determined within the Drude model. It is found that the allowed electron energy bands in the studied conductor are somewhat narrower than those in the superconductor based on the same molecule. The vibrational features arising from the interaction of the two-dimensional electronic system with the totally symmetric intramolecular vibrations a_g and also the bands of the optically active vibrations b_{1u} and b_{2u} of the BEDO-TTF molecule are identified in the spectra.

ACKNOWLEDGMENTS

We would like to thank N.F. Kartenko and A.S. Kolosova for their assistance in the crystal orientation.

This work was supported by the Russian Foundation for Basic Research (project nos. 98-02-18303 and 97-03-33686a) and, in part, by the Poland Academy of Sciences (grant no. 7T08A 003 12).

REFERENCES

1. J. M. Williams, J. R. Ferraro, R. J. Thorn, K. D. Carlson, U. Geiser, H. H. Wang, A. M. Kini, and M.-H. Whangbo, *Organic Superconductors (Including Fullerenes): Synthesis, Structure, Properties, and Theory* (Prentice Hall, Englewood Cliffs, 1992).
2. R. B. Lyubovskii, R. N. Lyubovskaya, and O. A. Dyachenko, J. Phys. I **6**, 1609 (1996).
3. A. Graja, Condens. Matter News **3**, 14 (1994).
4. N. D. Kushch, L. I. Buravov, A. G. Khomenko, *et al.*, Synth. Met. **53**, 155 (1993).
5. T. Suzuki, H. Yamochi, G. Srdanov, *et al.*, J. Am. Chem. Soc. **111**, 3108 (1989).
6. F. Wudl, H. Yamochi, T. Suzuki, *et al.*, J. Am. Chem. Soc. **112**, 2461 (1990).
7. K. Yamaji, Solid State Commun. **61** (7), 413 (1987).
8. S. Kahlich, D. Schweitzer, I. Heinen, *et al.*, Solid State Commun. **80**, 191 (1991).
9. L. I. Buravov, A. G. Khomenko, N. D. Kushch, *et al.*, J. Phys. I **2**, 529 (1992).

10. W. Sommer, J. Moldenhauer, D. Schweitzer, *et al.*, Synth. Met. **68**, 133 (1995).
11. R. Swietlik and N. D. Kushch, Phys. Status Solidi A **142**, 515 (1994).
12. R. N. Lyubovskaya, E. I. Zhilyaeva, S. A. Torunova, *et al.*, Synth. Met. **85**, 1581 (1997).
13. E. I. Zhilyaeva, O. A. Bogdanova, R. N. Lyubovskaya, *et al.*, Synth. Met. **99**, 169 (1999).
14. R. M. Vlasova, O. O. Drozdova, V. N. Semkin, *et al.*, Fiz. Tverd. Tela (St. Petersburg) **41** (1999).
15. L. N. Bulaevskiĭ and Yu. A. Kukharenko, Fiz. Tverd. Tela (Leningrad) **14** (8), 2401 (1972).
16. R. M. Vlasova, O. O. Drozdova, V. N. Semkin, *et al.*, Fiz. Tverd. Tela (St. Petersburg) **35** (3), 795 (1993).
17. S. Kahlich, D. Schweitzer, C. Rovira, *et al.*, Z. Phys. B: Condens. Matter **94**, 39 (1994).
18. K. I. Pokhodnia, M. E. Kozlov, V. G. Onischenko, *et al.*, Synth. Met. **55–57**, 2364 (1993).
19. M. G. Kaplunov and R. N. Lyubovskaya, J. Phys. I **2**, 1811 (1992).

Translated by O. Borovik-Romanova

Physics of the Solid State, Vol. 42, No. 1, 2000, pp. 41–50. Translated from Fizika Tverdogo Tela, Vol. 42, No. 1, 2000, pp. 40–48.

SEMICONDUCTORS AND DIELECTRICS

Optical Phonon Spectra of PbF_2 Single Crystals

A. V. Bazhenov, I. S. Smirnova, T. N. Fursova, M. Yu. Maksimuk, A. B. Kulakov, and I. K. Bdikin

Institute of Solid State Physics, Russian Academy of Sciences, Chernogolovka, Moscow oblast, 142432 Russia

Received in final form, July 7, 1999

Abstract—The spectra of dipole-active optical phonons are measured for the cubic and orthorhombic phases of PbF_2 single crystals. The frequencies and eigenvectors of normal modes in the *Pnma* orthorhombic phase are calculated. It is found that the spectrum of the cubic phase exhibits excess vibrational modes of the PbF_2 orthorhombic phase. © *2000 MAIK "Nauka/Interperiodica".*

Single-crystal lead fluoride is a promising material for the development of ionizing radiation detectors [1]. In this respect, the investigations into the optical properties and the lattice dynamics of PbF_2 crystals are of considerable interest from the experimental and theoretical viewpoints. Two modifications of PbF_2 are known: the orthorhombic modification, whose symmetry is described by the space group *Pnma* D_{2h}^{16} (62), and the cubic modification with crystal symmetry represented by the space group $Fm\bar{3}m$ O_h^5 (225). The spectra of dipole-active optical phonons in the orthorhombic phase have hitherto not been studied, whereas the spectra of dipole-active phonons in the PbF_2 cubic phase were investigated, for example, in [2, 3]. Except for a phonon feature that should be observed in the cubic phase, the spectra of this phase contain additional bands, for example, at about 140 cm^{-1}; however, their nature has remained unknown. In the present work, we measured the spectra of dipole-active optical phonons in the cubic and orthorhombic phases of PbF_2 single crystals and theoretically analyzed the eigenvectors and natural frequencies of optical phonons in the *Pnma* phases. It was revealed that the spectrum of the cubic phase contains several excess bands, which become more pronounced with a decrease in the temperature of the crystal from 300 to 5 K. Moreover, it was demonstrated that the excess vibrational modes correspond to the PbF_2 orthorhombic phase.

1. EXPERIMENT

1.1. Experimental Technique

Single crystals of the PbF_2 cubic phase were grown by the Czochralski method. The studied samples of cubic PbF_2 single crystals had the unit cell parameter $a = 5.92$ Å.

It is known that orthorhombic PbF_2 can be produced from aqueous solutions [4]. However, small sizes of the resulting single crystals (as small as 20 μm) make the investigation of their vibrational spectra impossible. In this work, single crystals of the orthorhombic phase were grown with the use of a saturated solution of PbF_2 in a mixture of perchloric acid with distilled water. Cooling of the solution at a rate of 1–2 K/h resulted in transparent faceted crystal plates up to $3 \times 3 \times 0.15$ mm in size [5]. According to the X-ray diffraction analysis, the crystals obtained are orthorhombic, and the unit cell parameters are as follows: $a = 6.42 \pm 0.02$ Å, $b = 3.89 \pm 0.02$ Å, $c = 7.63 \pm 0.02$ Å, space group *Pnma*. The developed surface of plates is characterized by the (001) orientation. Since the crystal plates were very thin, the reflectivity spectra were measured only for two orientations: **E** || **a** and **E** || **b** (the light wavevector **q** || **c**).

The infrared (IR) reflectivity spectra of PbF_2 single crystals were recorded on a Fourier-transform spectrometer in a geometry close to that of the normal light incidence on the single-crystal surface. In order to elucidate the temperature evolution of the reflectivity spectra in the range 5–300 K, the samples were fastened on a cold conductor in a vacuum cavity of a helium-flow cryostat.

1.2. Experimental Results

The reflectivity spectra of the cubic and orthorhombic single crystals at $T = 300$ K are displayed in Figs. 1 and 2, respectively. In both cases, the one-phonon excitations are observed in the frequency range $\nu < 400$ cm^{-1}. At these frequencies, the spectrum of the cubic crystal exhibits a broad band. The spectrum of the orthorhombic phase is more complex: it was measured in two polarizations **E** || **b** and **E** || **a** (Figs. 2a and 2b, respectively).

The dependences $\sigma(\nu)$ and $\mathrm{Im}[-1/\varepsilon(\nu)]$ (where ε is the dielectric function) that have been derived from the Kramers–Kronig transformation are also depicted in these figures. The locations of maxima in these dependences allow one to determine the frequencies of transverse optical (TO) and longitudinal optical (LO) phonons at the Γ point of the Brillouin zone. Because

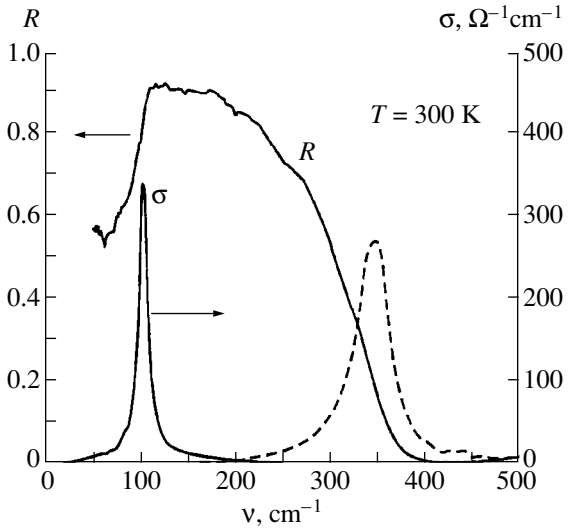

Fig. 1. Reflectivity (R), optical conductivity (σ), and Im($-1/\varepsilon$) (dashed line, arbitrary units) of the cubic PbF_2 single crystal at T = 300 K.

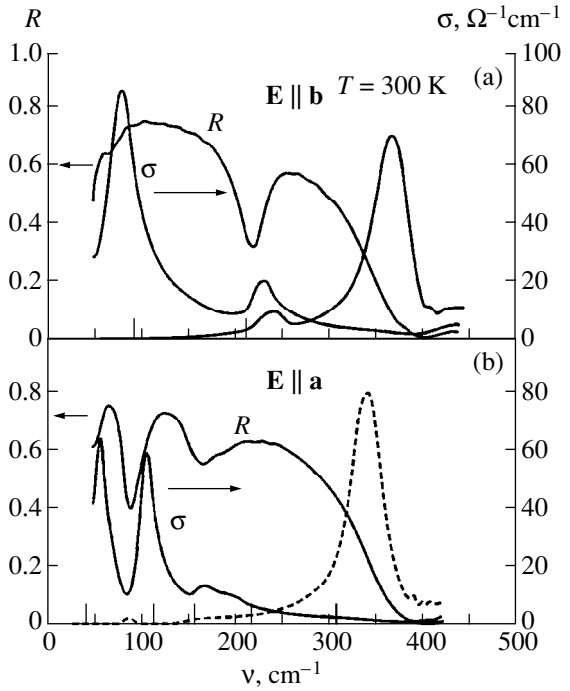

Fig. 2. Reflectivity (R), optical conductivity (σ), and Im($-1/\varepsilon$) (dashed line, arbitrary units) spectra of the orthorhombic PbF_2 single crystal at T = 300 K for (a) **E** ∥ **b** and (b) **E** ∥ **a** polarizations. Vertical dashes indicate the calculated TO frequencies.

the mathematical processing of the spectra with this method requires the integration with respect to the energy, generally speaking, in the interval from zero to infinity, the spectra were measured at frequencies up to 6000 cm^{-1} and, at higher energies, were fitted within the one-oscillator approximation. An approximation characteristic of dielectric crystals was applied at $\nu <$ 50 cm^{-1}. As can be seen from Fig. 1, the dependence $\sigma(\nu)$ for the PbF_2 cubic modification is characterized by a maximum at the frequency ν_{TO} = 103 cm^{-1}, which corresponds to the TO phonon. In the case of the orthorhombic crystals (Fig. 2), the $\sigma(\nu)$ curves show two maxima at the ν_{TO} frequencies for the **E** ∥ **b** polarization. For the **E** ∥ **a** polarization, the dependence $\sigma(\nu)$ exhibits three clear-cut maxima at ν_{TO} = 59, 107, and 168 cm^{-1} and a weak maximum at ν_{TO} = 198 cm^{-1}. The ν_{TO} and ν_{LO} frequencies obtained for the cubic and orthorhombic modifications of PbF_2 single crystals are summarized in Table 1.

The angular frequencies of the TO and LO modes ω_{TO} and ω_{LO} make it possible to calculate the effective dynamic charge Z_e of vibrating ions and to evaluate the degree of ionicity of interatomic coupling. According to Denham *et al.* [2], the charge of the fluorine ion in a cubic crystal is defined by the relationship

$$Z_e = [(\omega_{LO}^2 - \omega_{TO}^2)m\pi r_0^3]^{1/2}, \quad (1)$$

where $m = M_{Pb}M_F/(M_{Pb} + 2M_F)$ is the reduced mass of ions; M_{Pb} is the mass of the metal ion; M_F is the mass of the fluorine ion; $r_0 = a/2$, where a is the unit cell parameter; and ω_{TO} and ω_{LO} are the angular frequencies of the TO and LO modes, respectively.

Taking into account that $M_{Pb} \gg M_F$, the above formula gives the effective charge of fluorine ions. From formula (1), it follows that Z_e = 0.97 for the PbF_2 cubic phase at T = 300 K. This is in agreement with the data reported by Denham *et al.* [2], who studied PbF_2 thin films at T = 300 and 100 K and obtained the effective charges equal to 0.93 and 0.94, respectively. Axe [3] obtained an effective charge of 0.91 at T = 295 K.

Since the PbF_2 orthorhombic phase is characterized by three types of atoms (Pb, F1, and F2), the equation for the effective charges takes the following form [6]:

$$\sum_j (\omega_{jLO}^2 - \omega_{jTO}^2)_\alpha = \frac{4e^2}{\varepsilon_v}\left(\frac{Z_{Pb}^2}{m_{Pb}} + \frac{Z_{F1}^2}{m_{F1}} + \frac{Z_{F2}^2}{m_{F2}}\right), \quad (2)$$

$$Z_{Pb} + Z_{F1} + Z_{F2} = 0, \quad (3)$$

where α stands for the polarization; Z and m are the charges and masses of ions, respectively (subscripts indicate the ion type); V is the unit cell volume; ω_{TO} and ω_{LO} are the angular frequencies of the TO and LO modes, respectively; and ε_v is the electric permittivity of vacuum.

For anisotropic crystals, the measurements of the IR spectra in the polarized light provide information on the ion charges and, in some cases, enable one to determine the difference in charges of the symmetrically inequivalent ions of the same type. An example is the spectrum of La_2CuO_4, in which the anisotropy of the dynamic charge of oxygen was found experimentally [7, 8]. The possibility of revealing the charge anisotropy in

La_2CuO_4 stems from the fact that, for one polarization in all the modes, the energy is predominantly contributed by the O2 oxygen, whereas, for another polarization, the dominant contribution is provided by the O1 oxygen. The difference in charges of the O1 and O2 oxygens, which we experimentally observed in La_2CuO_4 in the earlier work [7], agrees with the results of calculations of the energy band structure in the strong coupling approximation, according to which the charges of the O2 and O1 oxygens are equal to $-1e$ and $-1.5e$, respectively [9]. This differences is associated with the short Cu–O2 distance (1.9 Å), which brings about a strong hybridization of the Cu and O2 electronic states. The hybridization of the Cu and O1 electronic state is considerably weaker because the Cu–O1 distance is equal to 2.43 Å.

The calculation of the effective fluorine charges in the PbF_2 orthorhombic phase for two polarizations gave close values: 0.92 for **E || a** and 0.94 for **E || b**. This can be explained as follows. Analysis of the eigenvectors of normal modes demonstrates that, in the crystal under consideration, both fluorine ions participate in the modes of both polarizations. The absence of dominant contribution from fluorine of one type in any polarization (see Fig. 4) leads to close effective charges in two polarization even at appreciably different charges of F1 and F2 ions. The difference between the effective charges in PbF_2 should be less than that in La_2CuO_4, because the Pb–F1 and Pb–F2 distances only slightly differ.

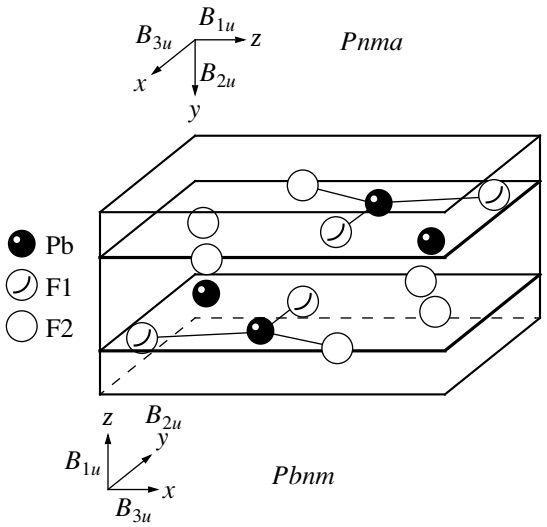

Fig. 3. The unit cell structure of the orthorhombic PbF_2 phase. Two orientations of the coordinate systems *Pnma* and *Pbnm* and the directions of the electric dipole moment vectors are indicated.

2. THEORETICAL CALCULATIONS OF NORMAL MODES IN PbF_2 ORTHORHOMBIC PHASE

2.1. Group-Theoretic Analysis of Normal Modes in the Pmna Orthorhombic Phase

Figure 3 demonstrates the crystal lattice of the PbF_2 orthorhombic phase. First and foremost, we note that, as follows from the lattice symmetry, all the fluorine ions in the cubic phase are equivalent. The X-ray diffraction analysis [10] revealed that the unit cell of the orthorhombic phase contains twelve ions: four lead ions and eight fluorine ions of two types F1 and F2. Four F1 ions (and, analogously, four F2 ions) can be transformed into each other by the symmetry operations, and, therefore, these atoms are symmetrically equivalent. However, there is no symmetry operation that can transform the F1 atom to the F2 atom. This stems from the fact that, although these atoms have the identical local symmetry C_s, the sets of their distances to the nearest lead ions are different: the F1–Pb distances are equal to 2.48, 2.51, and 2.50 Å, and the F2–Pb distances are 2.57, 2.81, and 2.84 Å. In general, the

Table 1. Frequencies of dipole-active optical phonons in PbF_2 single crystals

Cubic phase		Symmetry type	Orthorhombic phase			
ν_{TO}, cm^{-1}	ν_{LO}, cm^{-1}		ν_{TO}, cm^{-1}		ν_{LO}, cm^{-1}	
			observed	calculated	observed	calculated
103(105)	347(344)	F_{1u}				
168(176)		B_{3u}	59	40	87	124
200(218)			107	114	164	176
250(265)			168	156	196	248
(307)			198	218	343	260
				307		309
		B_{2u}	83	92	217	240
			232	214	358	273

Note: Parenthetic frequencies are obtained at $T = 5$ K.

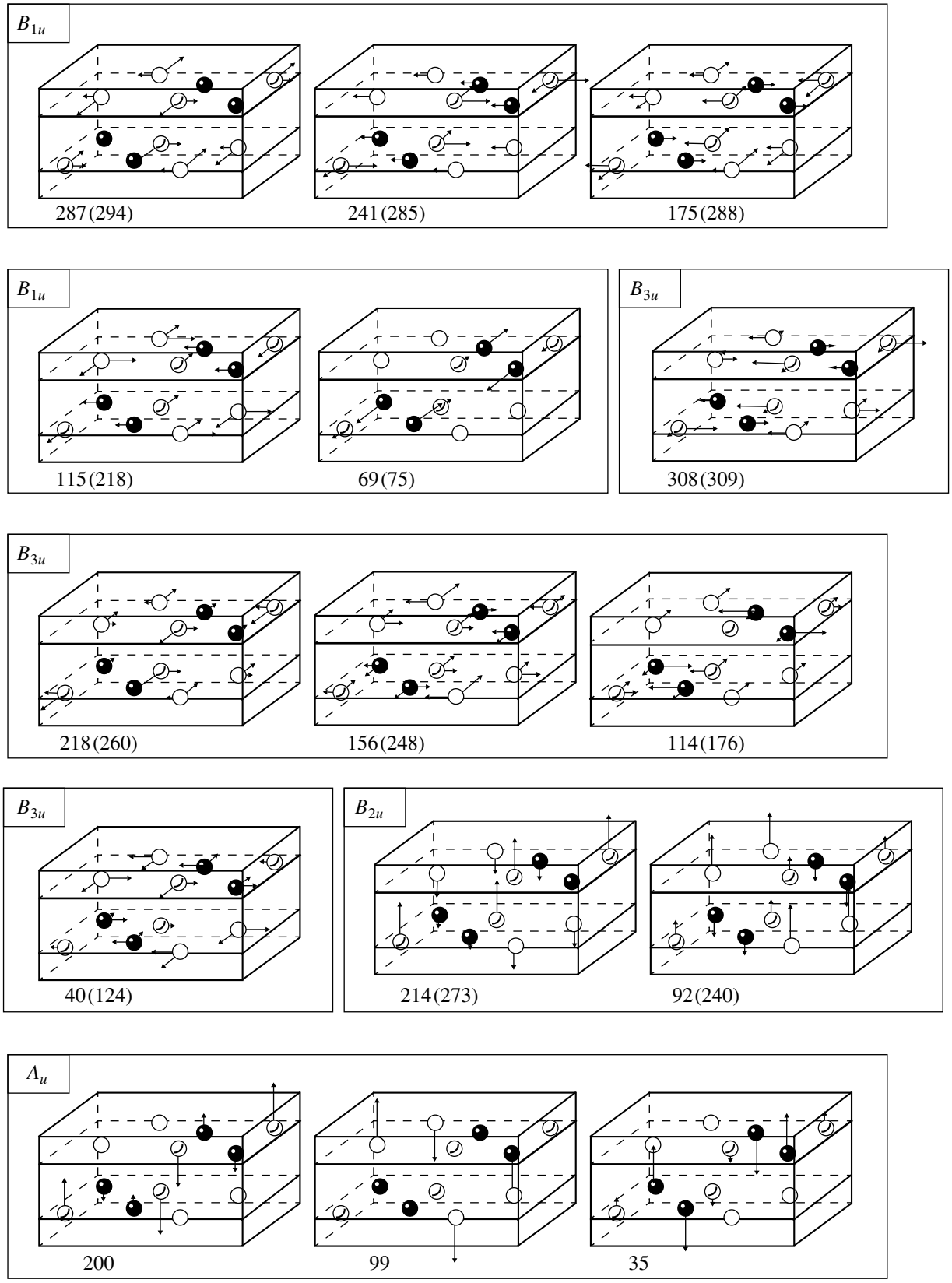

Fig. 4. Normal frequencies and normal vectors of the B_{1u}, B_{3u}, and B_{2u} modes and the silent A_u modes in the orthorhombic phase with the *Pnma* symmetry. The calculated frequencies of the LO phonons are given in parentheses.

symmetrically inequivalent F1 and F2 ions should possess different charges and different electric field gradients induced at a particular ion by the other ions in a crystal.

The symmetrically equivalent ions (for example, four F1 ions) should have the displacement vectors identical in magnitude for each vibrational mode, but the directions of the vectors can be different. The symmetrically inequivalent F1 and F2 ions can exhibit different magnitudes of the displacement vectors for each mode, and, hence, the PbF_2 orthorhombic phase can possess the vibrational modes in which the F1 ions execute vibrations, while the F2 ions remain virtually immobile, and vice versa. Examples of these modes are the B_{3g} modes with the calculated frequencies of 224 and 116 cm^{-1}, as illustrated in Fig. 5.

In the group-theoretic analysis of the phonon spectra of the cubic phase, the choice of the coordinate axes is of no consequence. However, in the case of the orthorhombic phase, the coordinate system and the axis orientations with respect to the symmetry elements should be chosen more carefully. In the PbF_2 orthorhombic phase, the symmetry plane determining the local symmetry of all the ions is normal to the direction of the smallest unit cell parameter. When the orientations of the axes correspond to the *International Tables for Crystallography* [11] (the standard coordinate system), the space group is *Pnma* (a = 6.42 Å, b = 3.89 Å, c = 7.63 Å). Another choice of the axis orientation leads to the space group *Pmnb* (a = 3.89 Å, b = 6.42 Å, c = 7.63 Å) or the space group *Pbnm* (a = 7.63, b = 6.42, c = 3.89 Å). It should be mentioned that Wyckoff [10] considered the PbF_2 orthorhombic phase in the *Pbnm* orientation of coordinate axes, which is not standard coordinate system.

In the space group *Pnma*, all the atoms have the local symmetry C_s. This point group involves two symmetry elements: the unit element E and the mirror plane m. For the *Pnma* orientation of the coordinate system, the m plane is the σ_y plane, and the local group is C_s^{xz}. In the case of the *Pbnm* and *Pmnb* orientations, the m planes are represented by the σ_z and σ_x planes, and the local groups are C_s^{xy} and C_s^{yz}, respectively. The C_s group has two irreducible representations: A' and A'' with group characters 1 and –1 relative to m. Two displacement components lying in the mirror plane are transformed through the irreducible representation A': these are x and z, x and y, and y and z components, respectively, in the *Pnma*, *Pbnm*, and *Pmnb* orientations of axes. The displacement component normal to the mirror plane is transformed through the irreducible representation A'': these are the y, z, and x components in the *Pnma*, *Pbnm*, and *Pmnb* orientations, respectively. As a result, for different axis orientations, the irreducible representations of the positional symmetry group induce the following

Table 2. Model parameters (A_{ij} and b_{ij} are the constants of the Born–Mayer potential, L_{ij} and T_{ij} are the longitudinal and tangential force constants for ith and jth ions, R is the bond length, and Z is the ion charge)

Bond	A_{ij}, eV	b_{ij}, Å	L_{ij}, N/m	T_{ij}, N/m	R, Å
Pb–F1	3300	3.86	53.36	–3.5	2.48
Pb–F1			52.66	–3.2	2.50
Pb–F1			52.9	–3.38	2.49
Pb–F2	3300	3.78	40.9	–2.4	2.57
Pb–F2			16.19	–1.06	2.81
Pb–F2			14.53	–0.94	2.84
F1–F1	3300	4.5	6.3	–0.5	2.97
F1–F2			11.16	–1.0	2.88
F1–F2			10.38	–0.93	2.90
F1–F2			4.7	–0.39	3.10
F1–F2			1.87	–0.14	3.35
Atom type	Pb	F1	F2		
$Z[e]$	1.77	–0.83	–0.94		

irreducible representations of the corresponding space groups at the Γ point:

$$Pnma:\ 2A' \Rightarrow 2A_g, 2B_{2g}, 2B_{1u}, 2B_{3u},$$
$$A'' \Rightarrow A_u, B_{1g}, B_{3g}, B_{2u};$$

$$Pbnm:\ 2A' \Rightarrow 2A_g, 2B_{1g}, 2B_{2u}, 2B_{3u},$$
$$A'' \Rightarrow A_u, B_{1g}, B_{3g}, B_{1u};$$

$$Pmnb:\ 2A' \Rightarrow 2A_g, 2B_{3g}, 2B_{1u}, 2B_{2u},$$
$$A'' \Rightarrow A_u, B_{1g}, B_{2g}, B_{3u}.$$

Therefore, different axis orientations of the orthorhombic crystal are characterized by different decompositions of the modes at the Γ point, that is,

$$Pnma:\ 6A_g + 3B_{1g} + 6B_{2g} + 3B_{3g}$$
$$+ 3A_u + 6B_{1u} + 3B_{2u} + 6B_{3u},$$

$$Pbnm:\ 6A_g + 6B_{1g} + 3B_{2g} + 3B_{3g}$$
$$+ 3A_u + 3B_{1u} + 6B_{2u} + 6B_{3u},$$

$$Pmnb:\ 6A_g + 3B_{1g} + 3B_{2g} + 6B_{3g}$$
$$+ 3A_u + 6B_{1u} + 6B_{2u} + 3B_{3u}.$$

By invoking the data obtained by Rousseau *et al.* [12], some authors have not quite correctly determined the decomposition of the modes into irreducible representations. We would like to draw attention to the fact that, in [12], all the space groups are considered only in the coordinate systems available in the *International Tables for Crystallography* [11]. Therefore, the data

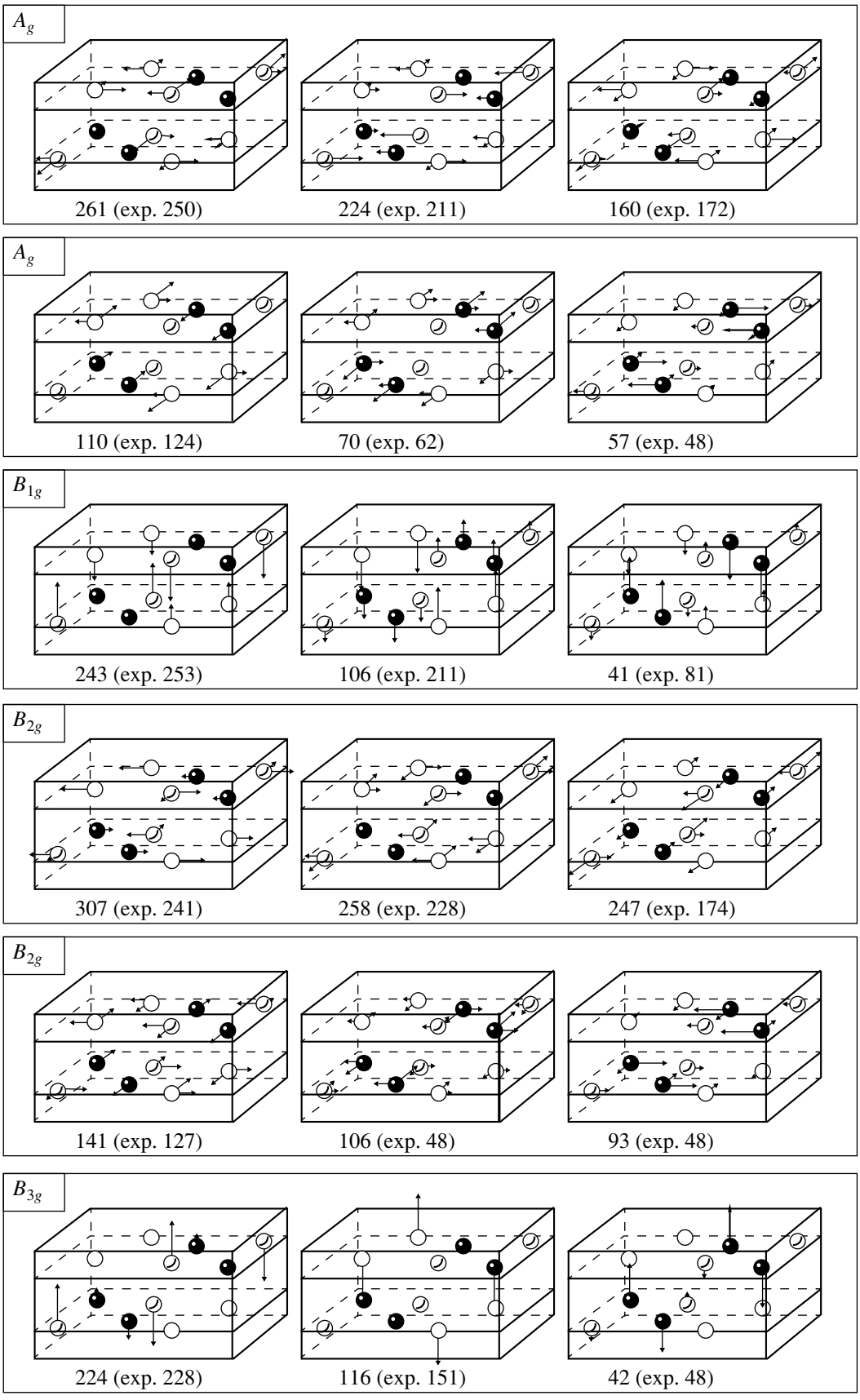

Fig. 5. Normal frequencies and normal vectors of the A_g, B_{2g}, B_{1g}, and B_{3g} modes in the orthorhombic phase with the *Pnma* symmetry. The parenthetic experimental frequencies are taken from [14].

reported in [12] are inapplicable in the case of any other axis orientation in orthorhombic PbF_2.

The choice of the coordinate system is important for both the decomposition of the modes into irreducible representations and the derivation of selection rules. The directions of the electric dipole moment vectors for two axis orientations *Pnma* and *Pbnm* are shown in Fig. 3.

The group-theoretic analysis of the $Fm\bar{3}m$ cubic phase indicates that PbF_2 exhibits one triply degenerate mode of F_{1u} symmetry that manifests itself in the IR spectrum. This is confirmed by the experimental reflectivity spectrum (Fig. 1). The phonon frequencies ν_{TO} = 103 cm^{-1} and ν_{LO} = 347 cm^{-1} are in good agreement with the frequencies obtained by Denham *et al.* [2] from the reflectivity spectra of thin films (ν_{TO} = 106 cm^{-1} and ν_{LO} = 338 cm^{-1}) and also with the frequencies determined by Axe *et al.* [3] from the reflectivity spectra of PbF_2 single crystals (ν_{TO} = 102 cm^{-1} and ν_{LO} = 337 cm^{-1}).

2.2. Model

The calculations were carried out within the model of rigid ions with effective charges. The interionic interaction between the *k*th and *k*'th atoms was described by the potential $V_{kk'}(r) = V^C_{kk'}(r) + V^{BM}_{kk'}(r)$, where $V^C_{kk'}(r) = Z_kZ_{k'}/(4\pi\varepsilon_0 r)$ is the Coulomb long-range potential, and $V^{BM}_{kk'}(r) = a_{kk'}\exp(-b_{kk'}r)$ is the Born–Mayer short-range potential. Since the unit cell parameters measured are almost coincident with those reported by Wyckoff [10], the positional parameters of the lattice virtually coincide with the parameters given in [10]; and, hence, the positional parameters of ions in the unit cell were taken from [10]. It should be remarked that both the unit cell parameters and the positional parameters slightly differ from those obtained by Boldrini and Loopstra [13].

In calculations within the rigid-ion approximation, it is important to know the effective ion charges Z_k, which can be used as the initial parameters in order to determine the Coulomb part of the dynamic matrix. The effective charges e^* used in our calculations were equal to 0.75 and 0.85 for the F1 and F2 ions, respectively. The mean fluorine charge (0.92–0.94), which was obtained in the experiment, somewhat exceeded the model mean value (0.8). The Coulomb part of the dynamic matrix was calculated by the Ewald method. For crystals with the low local symmetry, it is necessary to take into account a rather large number of coordination spheres. The control was exerted by the calculation of the electric field gradient produced at a particular ion site by the other ions in the crystal. The electric field gradient is described by the tensor of second rank, which should meet the following three conditions: (i) the tensor components should remain constant (to within a specified accuracy) with an increase in the number of coordination spheres; (ii) the spur of the tensor should be equal to zero, which implies the fulfillment of the electronegativity condition $\mathrm{div}\mathbf{E} = 0$; and (iii) the electric field gradient of each ion should possess the symmetry of local environment of this ion. The maximum number of coordination spheres *NMAX* was equal to 100, and the maximum distance of summation *DMAX* in the real space was 17.3 Å.

Table 2 lists the model parameters, which correspond to the best agreement between the calculated and experimental frequencies.

2.3. Infrared-Active Modes

The PbF_2 orthorhombic phase exhibits twelve dipole-active modes, including three silent A_u modes (Fig. 4). Let us consider the B_{2u} modes. For the *Pnma* axis orientation, there are two dipole-active B_{2u} modes whose symmetry admits the sole component u_y of ionic displacements (Fig. 4). One mode (with a calculated frequency of 214 cm^{-1}) is predominantly associated with the fluorine vibrations. Note that the vibration amplitude of the F1 ions is larger than that of the F2 ions. In the mode at 92 cm^{-1}, all the fluorine ions have the same direction of displacement vectors. The net dipole moment arising upon excitation of this mode is larger than that of the mode at 214 cm^{-1}, which involves the displacements of fluorine ions in the opposite directions. This is in agreement with the experimental data (Fig. 2a). The TO frequencies of these modes also reasonably agree with the frequencies observed experimentally. The TO–LO separation of these modes is very large: 134 cm^{-1} for the mode at 83 cm^{-1} and 125 cm^{-1} for the mode at 232 cm^{-1}. The calculated values are equal to 140 cm^{-1} for the mode at 92 cm^{-1} and 70 cm^{-1} for the mode at 215 cm^{-1}.

Moreover, the five B_{1u} and five B_{3u} modes should be observed. For these modes, the u_y displacement component is symmetry-forbidden ($u_y \equiv 0$), and, hence, the ionic vibrations in these modes can occur only in the symmetry plane. In our experiment, we measured only the B_{3u} modes active for the polarization $\mathbf{E} \parallel \mathbf{a}$ (a = 6.42 Å), $\mathbf{q} \parallel \mathbf{c}$ (c = 7.63 Å). The calculated frequencies of the four TO modes are in satisfactory agreement with the experimental data (see Table 1). The fifth modes (the calculated frequency is equal to 307 cm^{-1}) was not observed in our experiment.

In any orthorhombic crystal, all the irreducible representations are unidimensional, and, therefore, the vector of the electric dipole moment possesses one component in each dipole-active representation. This means that, for any dipole-active mode, all the symmetrically equivalent ions, for example, four F1 ions, should have identical directions of the displacement vectors for only one component (z for B_{1u}, y for B_{2u}, and x for B_{3u} at the *Pnma* orientation). The other displace-

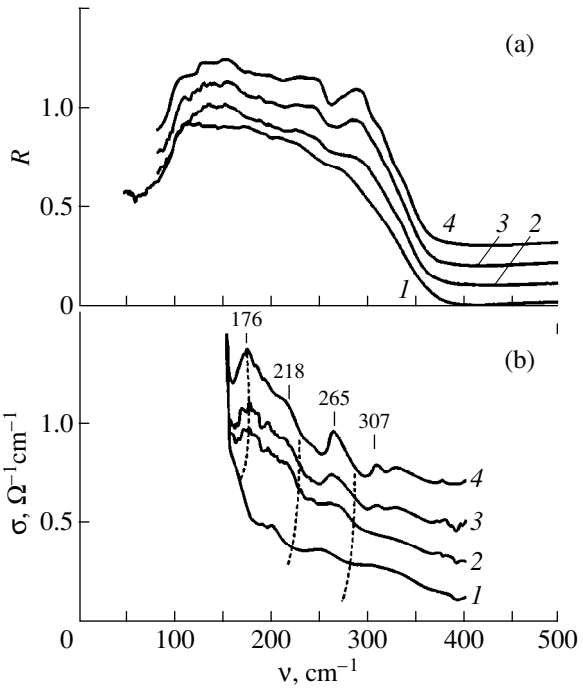

Fig. 6. Temperature evolution of (a) the reflectivity (R) and (b) optical conductivity (σ) spectra for the mechanically polished surface of the cubic PbF_2 single crystal. T, K: (*1*) 300, (*2*) 200, (*3*) 100, and (*4*) 5. Reflectivity spectra are shifted along the y-axis by the value $y = R - 0.1(n - 1)$, where n is the number of spectrum (n = 1–4).

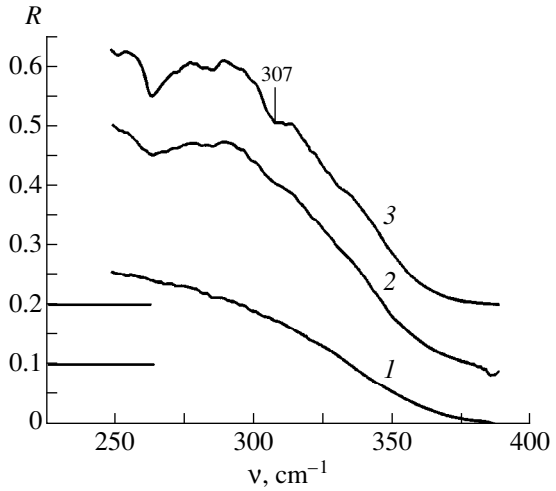

Fig. 7. Temperature evolution of the reflectivity spectra taken from as-prepared cleavage surface of the cubic PbF_2 single crystal. T, K: (*1*) 300, (*2*) 80, and (*3*) 5.

ment vector components of fluorine ions should have signs such that the corresponding component of the net dipole moment would be identically equal to zero. The components of the net dipole moment of some dipole-active modes can be too small to be represented in the figure on the chosen scale. The LO–TO separation of these modes is small. In particular, this is true for the B_{3u} mode at 307 cm^{-1} (see Fig. 4: the x component of the ionic displacement is small), for which the calculated LO–TO separation is equal to 2 cm^{-1}. Therefore, the oscillator strength of this mode is low, and the mode is difficult to observe in the experiment.

2.4. Raman-Active Modes

Figure 5 shows the Raman-active modes in PbF_2 for the *Pnma* orientation of the coordinate axes. The parenthetic experimental frequencies were taken from Kessler *et al.* [14]. These authors did not indicate the orientation of coordinate axes [14], but, reasoning from the number of the B_{1g} modes, it can be assumed that they dealt with the *Pbnm* orientation; i.e., the direction of the parameter c = 3.89 Å is chosen as the z-axis.

For the B_{1g} and B_{3g} modes, only the u_y component of the displacement of all the ions is symmetry-allowed, and $u_x \equiv 0$ and $u_z \equiv 0$. In this case, only three modes with the symmetry described by the B_{1g} and B_{3g} irreducible representations are possible. Note that the displacements of symmetrically equivalent ions (for example, F1) should be equal in magnitude, but can differ from the displacements of the F2 ions ($|u_y^{F1}| \neq |u_y^{F2}|$). Consequently, the situation can occur when fluorine ions of one type are displaced, while the ions of another type remain virtually immobile (Fig. 5, the B_{3g} modes at 233 and 119 cm^{-1}). A similar situation is impossible when all the fluorine atoms are symmetrically equivalent, as, for example, is the case of the cubic phase.

The calculated frequencies of the A_g modes coincide well with the experimental values. For the B_{1g}, B_{2g}, and B_{3g} modes, there are appreciable discrepancies between the calculated and experimental values of some frequencies. In particular, Kessler *et al.* [14] assigned the band at 48 cm^{-1} to all the Raman-active representations. In the case of the orthorhombic crystal, such an accidental degeneracy is unlikely. Analysis of the eigenvectors of the modes permits us to assume that, among the B_{2g} modes, there are no modes with a frequency of 48 cm^{-1}, but there is the mode at 81 cm^{-1}.

3. TEMPERATURE EVOLUTION OF THE REFLECTIVITY SPECTRA OF THE PbF_2 CUBIC PHASE

Figure 6a illustrates the evolution of the reflectivity spectra of optical phonons in the PbF_2 cubic phase in the temperature range 5–300 K. A decrease in the temperature brings about the transformation of the spectrum. This manifests itself in the appearance of relatively weak (but clearly defined at 5 K) minima at 176, 218, 265, and 307 cm^{-1} on the background of a high

reflectivity of the cubic phase. These minima are matched by the bands with maxima at the aforementioned frequencies in the spectrum of optical conductivity (Fig. 6b). The intensities of the additional bands are not high as compared to the intensity of the main maximum at 105 cm^{-1} (σ_{max} = 300 Ω^{-1} cm^{-1}) in the spectrum of optical conductivity of the cubic crystal. As the temperature increases up to room temperature, the first three additional bands become smoothed at 168, 200, and 250 cm^{-1}, and the relatively weak band at 307 cm^{-1} is not observed at $T > 100$ K. Analysis of the spectra showed that the additional bands become more pronounced with a decrease in the temperature due to the decrease in their halfwidths. The spectral location of these bands is close to the location of the B_{3u} modes at 168 and 198 cm^{-1} and the B_{2u} mode at 232 cm^{-1} for the orthorhombic phase. This suggests that the PbF_2 cubic phase contains inclusions of the orthorhombic phase.

It is common knowledge that, at room temperature, the thermodynamically equilibrium phase of lead difluoride is the orthorhombic modification. Upon heating, the orthorhombic phase transforms into the cubic modification (according to different authors, at temperatures from 200 to 450°C [15]; specifically at 447°C from the data reported by Wyckoff [10]). In the case of bulk single crystals, a decrease in the temperature down to room temperature at atmospheric pressure does not lead to the reverse transition from the cubic phase to the orthorhombic modification. The cubic PbF_2 single crystals grown by the Czochralski or Verneuil method also do not transform into the orthorhombic modification upon cooling. It is agreed that the main hindrance to the transformation from the cubic phase to the orthorhombic modification is a considerable decrease in the volume (~10%) upon phase transition. The thermogravimetric measurements revealed that the orthorhombic single crystals used in the present work exhibit transition to the cubic phase at 310°C and do not undergo transformation into the orthorhombic modification with a subsequent decrease in the temperature.

Samara [17] showed that the phase transition from the cubic modification to the orthorhombic modification can be initiated, for example, at room temperature, under the external pressure. In particular, the mechanical treatment leads to the appearance of the orthorhombic phase on the surface of cubic PbF_2 [18–20]. Alov and Rybchenko [18] experimentally demonstrated that chemical polishing of the surface does not ensure the complete removal of the orthorhombic phase from the surface layer. Based on the X-ray diffraction experiments, Shmyt'ko *et al.* [20] also made the inference that a thin layer of the orthorhombic phase is always formed on the free surface of cubic PbF_2 single crystals. According to [18], the surface free from the orthorhombic phase impurity can be observed on the cleavage surface of cubic PbF_2 single crystals.

From the foregoing, it is seen that the above assumption about the presence of the orthorhombic phase in the cubic PbF_2 single crystals is in agreement, in part, with the conclusions drawn in [18, 20]. The main difference resides in the fact that the spectrum measured in our experiments for the cleavage surface of the cubic single-crystal modification also contains additional bands (Fig. 7) similar to those observed in the spectrum of the orthorhombic phase. Furthermore, the band at 307 cm^{-1} is more pronounced in the spectrum of the cleavage surface, because, in this case, its width is less. It is worth noting that the spectral location of the band corresponds to the calculated value for the mode that is not observed in the room-temperature spectrum of the orthorhombic crystal.

Thus, the spectrum of dipole-active optical phonons is measured for the PbF_2 orthorhombic phase. With due regard for the data on the Raman-active modes obtained in [14], the theoretical calculation of the normal frequencies is performed in the rigid-ion model with effective charges. The model parameters that provide a reasonable agreement between the calculated and experimental frequencies are determined.

A number of excess vibrational modes are revealed in bulk single crystals of the PbF_2 cubic phase. It is shown that their presence in the spectrum of the crystal is caused by inclusions of the PbF_2 orthorhombic phase at the surface and in the bulk of the crystal.

ACKNOWLEDGMENTS

We would like to thank S.I. Rybchenko and D.L. Alov for helpful discussions.

REFERENCES

1. *Heavy Scintillators for Scientific and Industrial Applications: Proceedings of the "Crystal 2000" International Workshop* (Frontiers, France, 1992).
2. P. Denham, G. R. Field, and P. R. R. Morse, Proc. R. Soc. London **317**, 55 (1970).
3. J. D. Axe, J. W. Gagllianelo, and J. E. Scardefield, Phys. Rev. **139**, A1211 (1965); J. D. Axe, Phys. Rev. **139**, A1215 (1965).
4. N. Stubicar, M. Scrbak, and M. Stubicar, J. Cryst. Growth **100**, 261 (1990).
5. A. B. Kulakov, A. A. Zhokhov, G. A. Emel'chenko, *et al.*, J. Cryst. Growth **151**, 107 (1995).
6. F. Gervais, Solid State Commun. **18**, 191 (1976).
7. A. V. Bazhenov, K. B. Rezchikov, and I. S. Smirnova, Physica C (Amsterdam) **233**, 9 (1996).
8. S. Tajima, T. Ido, S. Ishibashi, *et al.*, Phys. Rev. B: Condens. Matter **43**, 10496 (1991).
9. S. V. Meshkov, S. N. Molotkov, S. S. Nazin, *et al.*, Physica C (Amsterdam) **161**, 497 (1989).
10. R. W. G. Wyckoff, *Crystal Structures*, 2nd ed. (Wiley–Interscience, New York, 1963), Vol. 1, p. 300.

11. *International Tables for Crystallography: Space-Group Symmetry*, 3rd ed., Ed. by T. Hahn (Kluwer Academic, Dordrecht, 1989), Vol. A.
12. D. L. Rousseau, R. P. Bauman, and S. P. S. Porto, J. Raman. Spectrosc. **10**, 253 (1981).
13. P. Boldrini and B. O. Loopstra, Acta Crytstallogr. **22**, 744 (1967).
14. J. R. Kessler, E. Monberg, and M. Nicol, J. Chem. Phys. **60**, 5057 (1974).
15. *Gmelins Handbuch der anorganischen Chemie* (Chemie, Weinheim, 1969), Vol. 47, Part C, p. 273.
16. *Chemical Encyclopedia* (Bol'shaya Rossiĭskaya Éntsiklopediya, Moscow, 1995), Vol. 4.
17. G. A. Samara, Phys. Rev. B: Solid State **13**, 4529 (1976).
18. D. L. Alov and S. I. Rybchenko, J. Phys.: Condens. Matter **7**, 1475 (1995).
19. E. B. Borisenko, N. V. Klassen, and I. B. Savchenko, Fiz. Tverd. Tela (St. Petersburg) **39**, 640 (1997).
20. I. M. Shmyt'ko, I. B. Savchenko, N. V. Klassen, *et al.*, Fiz. Tverd. Tela (St. Petersburg) **38**, 1240 (1996).

Translated by O. Borovik-Romanova

Physics of the Solid State, Vol. 42, No. 1, 2000, pp. 51–54. Translated from Fizika Tverdogo Tela, Vol. 42, No. 1, 2000, pp. 49–52.

SEMICONDUCTORS AND DIELECTRICS

Hyperfine and Quadrupole Interactions of Trigonal $^{157}Gd^{3+}$ Centers in SrF_2 and BaF_2. Analysis of Distortions in the Nearest Atomic Environment

A. D. Gorlov and A. P. Potapov

Research Institute of Physics and Applied Mathematics, Ural State University, Ekaterinburg, 620083 Russia
e-mail: anatoliy.gorlov@usu.ru

Received May 7, 1999

Abstract—Trigonal $^{157}Gd^{3+}$ impurity centers in SrF_2 and BaF_2 were experimentally studied by EPR and double electron-nuclear resonance (DENR) techniques. Parameters of the hyperfine and quadrupole interactions between these centers were determined. Possible distortions of the nearest atomic environment of the impurity centers are estimated within the framework of a superposition model using the EPR and DENR data for the centers of cubic and trigonal symmetry in the crystals studied. *© 2000 MAIK "Nauka/Interperiodica".*

Fluorine-compensated trigonal Gd^{3+} centers appear in SrF_2 and BaF_2 crystals grown in a fluorine-containing atmosphere. The excess positive charge of these impurity centers is compensated by an F^- ion localized in the lattice site adjacent to Gd^{3+} along the C_3 crystal axis [1]. This additional anion may lead to displacements of the eight nearest-neighbor F^- ions occupying cube vertices in the undistorted structure. These displacements cannot be determined using only data obtained by the EPR method alone. Data on the DENR on ligands are usually also insufficient to determine the coordinates of fluorine atoms, because the hyperfine interactions of ligands in the nearest-neighbor positions to the impurity center are not of a purely dipole-dipole nature. Below we will demonstrate that a combined use of the EPR, ligand DENR, and $^{157}Gd^{3+}$ DENR data elucidates the character of distortions in the crystal lattice in the environment of the impurity center and the compensator ion (F_k). The purpose of this work was to analyze these distortions within the framework of a superposition model for the spin Hamiltonian parameters [2, 3], using comparative data on these parameters for the cubic and trigonal $^{157}Gd^{3+}$ centers in SrF_2 and BaF_2 crystals.

1. EPR AND DENR MEASUREMENTS

Experiments were conducted on the samples of SrF_2 and BaF_2 single crystals with a $^{157}Gd_2O_3$ admixture (0.01 wt % in the initial charge), which were grown by the Czochralski method in an atmosphere containing excess fluorine. The measurements were performed using 3-cm-band superheterodyne EPR spectrometers at a temperature of $T = 1.8$ K. Both SrF_2 and BaF_2 samples exhibited all the known EPR spectra with local-fluorine and nonlocal compensation of the excess positive charge on the impurity atoms. When the external magnetic field **H** was oriented along the principal symmetry axes of the impurity centers, the EPR spectra exhibited a complicated structure determined by the combined effect of the intrinsic hyperfine coupling (HFC) and the ligand hyperfine coupling (LHFC) components. For the other (intermediate) orientations of **H**, the structure of the SHF absorption signals from all non-cubic centers was also significantly affected by the quadrupole coupling (QC).

The EPR spectra of the trigonal centers were described using a standard spin Hamiltonian [4] in the coordinate system *XYZ* with the axes parallel to the crystallographic directions $[\bar{1}\bar{1}2]$, $[1\bar{1}0]$, and [111], respectively. The parameters of the spin Hamiltonian are presented in Table 1. Our results for $BaF_3 : Gd^{3+}$ coincide, to within the margin of experimental error, with the data reported in [5].

The experimental investigations of hyperfine and quadrupole interactions were performed by the stationary and nutation DENR techniques [6]. The DENR spectra were analyzed using a spin Hamiltonian including a part describing the EPR spectrum and an additional term H' responsible for the HFC and QC of $^{157}Gd^{3+}$ ($S = 7/2$, $I = 3/2$) with the C_{3v} symmetry (we use the conventional notation according to [4]):

$$\begin{aligned} H' &= A_z S_z I_z + A_{xy}(S_x I_x + S_y I_y) - g_n \beta_n (\mathbf{HI}) \\ &+ 1/3 P_2^0 O_2^0(I) + 1/252[(B_1 + B_2 + B_4)(O_2^0(S)O_2^0(I)) \\ &+ (3B_1 - 3B_2 + 0.5B_4)(O_2^2(S)O_2^2(I) + \Omega_2^2(S)\Omega_2^2(I)) \\ &+ (12B_1 + 6B_2 - 8B_4)(O_2^1(S)O_2^1(I) + \Omega_2^1(S)\Omega_2^1(I))] \\ &+ A_1 O_3^0(S) O_1^0(I). \end{aligned} \quad (1)$$

1063-7834/00/4201-0051$20.00 © 2000 MAIK "Nauka/Interperiodica"

Table 1. Spin Hamiltonian parameters (MHz) describing EPR spectra of Gd^{3+} impurity centers in SrF_2 and BaF_2 at $T = 1.8$ K

Crystal	g_{xy}	g_z	b_2^0	b_4^0	b_4^3	b_6^0	b_6^3	b_6^6
SrF_2 (*tr*)	1.9902 (16)	1.9924 (15)	−461.1 (2.5)	86.5 (1.0)	–2448 (16)	−0.8 (1.0)	−0.7 (1.8)	–25.2 (25.0)
SrF_2 (*cub*)	1.9916 (7)	1.9916 (7)	0	84.3 (4)	–2384.4 (4)	−0.5 (5)	−6.6 (6.6)	–5 (5)
BaF_2 (*tr*)	1.9921 (15)	1.9921 (15)	−460.8 (2.6)	77.6 (1.0)	–2188 (17)	−0.8 (1.0)	–3.6 (4.0)	−6.0 (5.9)
BaF_2 (*cub*) [6]	1.9916 (5)	1.9916 (5)	0	75.5 (1.5)	–2134.5 (5.0)	−0.8 (2)	−9.3 (1.5)	–7.2 (1.3)

In (1), only those terms were retained among the symmetry-allowed terms which were determined from the experimental data. The corresponding spin Hamiltonian parameters are listed in Table 2.

The parameters presented in Tables 1 and 2 were calculated by the numerical minimization based on the total energy matrix and the set of the resonance fields of EPR transitions and DENR frequencies.

2. SUPERPOSITION ANALYSIS OF THE SPIN HAMILTONIAN PARAMETERS AND ESTIMATION OF LOCAL DISTORTIONS

An analysis of the data presented in Table 2 shows that the HFC constants for the trigonal centers in SrF_2 and BaF_2 are virtually isotropic, their values being equal (to within the experimental error) to those for the cubic centers [7]. Moreover, the b_4^0, b_4^3, and b_6^0 values are close for the impurity centers of two types both in SrF_2 and BaF_2 crystals, which was already noted in [5, 8] (see Table 1 for these parameters presented in the trigonal system of coordinates). As is known, the spin Hamiltonian parameters are significantly affected by coordinates of the nearest-neighbor ligands and depend both on the electrostatic interaction and on the overlap integral and covalency of the $Gd^{3+}F_8^-$ complex [2–4, 8]. In turn, the HFC component also depends on the distances R_i between the impurity center and the nearest-neighbor ligands and on the degree of ionicity in this complex [4] (see Table 3 in [7]). Taking into account these considerations and the above data, we infer that no significant changes in coordinates of the eight nearest-neighbor F^- ions takes place upon going from cubic to trigonal Gd^{3+} centers with fluorine compensation in the crystals studied.

Indeed, the ligand DENR data for a trigonal $BaF_2 : Gd^{3+}$ center (complete data will be reported in a separate communication) showed that noticeable F^{19} displacements are observed only in the vicinity of F_k. The environment of the impurity center can be conventionally divided into two regions by a plane, containing this center, perpendicular to its symmetry axis. In the first region (not containing F_k), the positions of anions are the same as for F^{19} nuclei in the second and more distant coordination shells of the cubic impurity center. The LHFC for these shells (as well as for F_k) has a purely magnetic-dipole character and the corresponding nuclear coordinates are readily determined. For the fluorine ions closest to Gd^{3+}, where the LHFC also significantly depends both on R_i and on the chemical bonds, only the angular coordinates can be directly and unambiguously determined. For the fluorine ions forming a triangle, these angles are virtually the same as in the cubic center (where $\theta = 109.47°$, $\varphi = 0° \pm 120°$), while the experimental data for the trigonal center give $\theta_1 = 109.59(11)°$ and $\varphi_1 = \varphi$. In our opinion, the R_1 values in the triangle structure must also be close to those in the cubic center (where $R = 2.431$ Å [7]), because noticeable displacements of the ligands in the nearest vicinity of the impurity center are usually accompanied by significant shifts of the nuclei in the second coordination shell [7]. A similar situation is observed for the fluorine ion situated on the C_3 axis.

The second region (containing F_k) includes, besides F^{19} nuclei of the second and other coordination shells, four remaining F^- nearest neighbors of the impurity center. Three of these fluorine ions also make a regular triangle with the angular coordinates $\theta_2 = 71.02(8)°$ and $\varphi_2 = \varphi$ (in the cube, $\theta = 70.53°$; $\varphi = 60°$, 180°, 300°), and one ion is situated on the C_3 axis. In this case, the distances are obviously different from those in the cubic case, because of the repulsion between compensator ion and the likely charged particles. A distance from the impurity center to the compensator ion determined from the ligand DENR data is $R_k = 5.178(9)$ Å.

In order to estimate displacements of the nearest-neighbor ligands in the second region, we have used a superposition model [2, 3] according to which the spin Hamiltonian parameters are represented in the form $b_n^m = \sum b_n(R_i)k_n^m(\theta_i, \varphi_i)$, where $b_n(R_i)$ is the "intrinsic" parameter corresponding to the *i*th nearest-neighbor ligand with the spherical coordinates R_i, θ_i, φ_i, and

Table 2. HFC and QC parameters (MHz) of $^{157}Gd^{3+}$ impurity centers in SrF_2 and BaF_2

Crystal	A_{xy}	A_z	A_1, 10^4	P_2^0	B_1, 10^{-2}	B_2, 10^{-2}	B_4, 10^{-2}
SrF_2 (*tr*)	16.767 (3)	16.759 (2)	4 (2)	–33.434 (5)	–70 (5)	6 (6)	–15 (5)
SrF_2 (*cub*) [8]	16.7534 (10)	16.7534 (10)	–3.4 (9)	0	–76 (8)	0	0
BaF_2 (*tr*)	16.640 (7)	16.646 (3)	4 (2)	–29.932 (10)	–85 (5)	–4 (5)	0
BaF_2 (*cub*) [8]	16.6398 (15)	16.6398 (15)	–3 (1)	0	–75 (10)	0	0

$k_n^m(\theta_i, \varphi_i)$ is the angular structural factor of this ligand [2].

We have analyzed these factors in the coordinate system of the trigonal impurity center. It was found that the main contributions to b_4^0 are due to the fluorine ions situated on the C_3 axis ($\theta = 0°$, 180°), while the main contribution to b_4^3 is that from fluorine ions with $\theta \neq 0°$, 180°. Thus, we can subdivide eight F^- nearest neighbors of the impurity center with respect to their contribution to the spin Hamiltonian parameters. Taking into account the fact that coordinates of the four closest ligands in the first region are the same for the trigonal and cubic centers, we can determine contributions for one of the F^- nearest neighbors from the second coordination shell and compare these values with those for the cubic center. For fluorines forming a triangle, the values are as follows [2]:

$$b_4(tr) = [b_4^3(tr) - b_4(cub)K_4^3(\theta_1, \varphi_1)]/K_4^3(\theta_2, \varphi_2), \quad (2)$$

where $b_4(cub) = b_4^0(cub)/K_4^0(\theta, \varphi) = b_4^3(cub)/K_4^3(\theta, \varphi)$ and $K_4^3(\theta_i, \varphi_i) = \sum_1^3 k_4^3(\theta_i, \varphi_i)$. because all fluorines in the triangle are equivalent.

For the cubic impurity centers in BaF_2 and SrF_2, we have $b_4(cub) = 36.4(2)$ and 40.6(1) MHz, while the corresponding values for the trigonal centers are $b_4(tr) = 38.4(8)$ and $\geq 41.7(1.2)$ MHz, respectively. The $b_4(tr)$ values for SrF_2 were calculated using $k_4^3(cub)$because no ligand DENR data for this crystal are available. Since the θ_2 value is greater than the corresponding angle in the cubic impurity center, it follows that $K_4^3(cub) \geq K_4^3(tr)$ and the thus obtained $b_4(tr)$ value for SrF_2 gives a lower estimate.

The condition $b_4(tr) \geq b_4(cub)$ shows evidence of a displacement of ligands close to the compensator ion and impurity center. The directions and magnitudes of these shifts can be determined using the function $b_4(R)$ for the cubic Gd^{3+} centers in CaF_2, SrF_3, and BaF_2. Taking the R_i values and the function from [7], we obtain

$$b_4(R) = b_4(R_0)(R_0/R)^n, \quad (3)$$

where $R_0 = 2.37$ Å [3], $b_4(R_0) = 40.9(3)$ MHz, and $n = 4.72(6)$.

The value of b_4 is independent of the local symmetry of impurity centers [2]. Therefore, we can estimate the R_i values by equation (3), using the experimentally determined $b_4(R)$ value corresponding to the *i*th ligand. For a trigonal impurity center in BaF_2, where the $k_n^m(\theta, \varphi)$ values for all ligands are known, we obtain $R_2 = 2.401(12)$ Å for F^- in the triangle close to F_k (provided that the R_i values of nuclei distant from F_k are the same as those in the cubic impurity center).

In order to estimate a distance from the impurity center to F^- situated on the C_3 axis, we have used the experimental value of b_2^0 that depends both on R_k and on the R_i values of all ligands. Taking the "intrinsic" parameters and the expression for b_2^0 from [3], we obtained $R_3 = 2.385(14)$ Å. Note that the R_3 value cannot be determined using the $b_4^0(tr)$ value containing an unknown contribution due to the compensator ion. The errors of the R_2 and R_3 values were calculated from errors of the experimental determination of the spin Hamiltonian parameters and the angular coordinates of ligands.

It was difficult to analogously calculate the trigonal impurity center in SrF_2, since no experimental data are available on the angular structural factors of the ligands adjacent to the impurity center. However, taking into account that the SrF_2 lattice is more "rigid," we may expect that the angular and radial distortions in this structure are smaller than in BaF_2. Assuming that the character of distortions in the two crystals is the same, we can take the R_1, θ_1, φ_1 values equal to those for the cubic impurity center in SrF_2 ($R_1 = 2.372$ Å [7]). In

order to estimate the R_2 value, we may use the fact that F^- ions forming a triangle in the second region are characterized by $70.53° < \theta_2 < 71.02°$, that is, by the angular coordinates intermediate between those for the cubic center and the trigonal center in BaF_2. In this approximation, we have $2.340 < R_2 < 2.346$ Å. All the subsequent estimates for the distances in SrF_2 are obtained for $R_2 = 2.343$ Å.

The value of R_3 can be estimated using the following considerations. By analogy with the trigonal impurity center in BaF_2, where the compensator ion is shifted by 0.03 Å toward Gd^{3+} relative to the midpoint between F^- ions on the C_3 axis of the first and fourth shells in the cubic impurity center, we assume that $R_k < R = 4.935$ Å (the distance to an analogous point in SrF_2). For $R_k = R$, the experimental b_2^0 yields $R_3 = 2.326$ Å. A decrease in the R_k by 0.03 Å (corresponding to the F_k shift in BaF_2) leads to $R_3 = 2.325$ Å, that is, has a little effect upon this distance. Errors in the R_2 ad R_3 values for SrF_2 calculated within the framework of the model described above are not less that 5% due to uncertainty in the "intrinsic" parameters [3], the errors of θ and R_k values, and the experimental scatter of b_n^m.

In order to verify the estimates obtained for distortions of the atomic environment of the impurity centers, let us calculate the average contributions to b_4^0 related to the nearest-neighbor ligands. Using equation (3) and the corresponding k_n^m and R_i values, we obtain $b_4^0(tr) = 80.2$ and 89.5 MHz for BaF_2 and SrF_2, respectively. These values are greater that the experimental distances, which is quite natural since the contribution of F_k (according to the LHFC data, acting as a point charge on the impurity center) in this case must be negative [4].

An additional evidence for validity of the R_i estimates obtained above is provided by calculation of the P_2^0 values for the centers studied, performed within the same superposition model [3]. Taking the "intrinsic" parameters $P_{2p} = -120 \times 10^{-4}$ cm^{-1} and $P_{2s} = 60 \times 10^{-4}$ cm^{-1}, we obtain (for $R_k = 4.915$ Å) the values $P_2^0 = -29$ and -31 MHz for BaF_2 and SrF_2, respectively, which are close to the experimental data. Note that P_{2p} ad P_{2s} differ from the values reported in [3], where these quantities were determined from a system of equations containing phenomenological parameters K_n^m. These K_n^m values were estimated using the crystal field parameters A_2^0 for the rare- earth ions other than Gd^{3+}, which may well account for the observed difference. Attempts at more accurately estimating the R_k and P_2^0 values are senseless because of the uncertainty in R_i and the "intrinsic" parameters

In summarizing the above considerations, we may ascertain that analysis of the combined EPR and DENR data within the framework of the superposition model allows a pattern of local distortions in the nearest-neighbor environment to be studied for the fluorine-compensated trigonal Gd^{3+} impurity centers in crystal structures of the fluorite type. According to this pattern, the Gd^{3+} ion is localized at the same site as in the cubic center; four nearest-neighbor F^- ions on the compensator ion side repulse from this ion so that the distances between these fluorines and the impurity centers tend to decrease; the other four F^- ions occupy the same positions as in the cubic center. Note that this model of distortions differs from that proposed by Newman [8], but is rather close to the data reported in [9] for the ligand DENR of trigonal Yb^{3+} impurity centers in the same crystals.

REFERENCES

1. U. Ranon and A. Yoniv, Phys. Lett. **9** (1), 17 (1964); J. Sierro, *ibid.* **4** (2), 178 (1963).
2. D. J. Newman and W. Urban, Adv. Phys. **24** (2), 793 (1973).
3. L. I. Levin and A. D. Gorlov, J. Phys.: Condens. Matter **4** (2), 1981 (1992).
4. S. A. Al'tshuller and B. M. Kozyrev, *Electron Paramagnetic Resonance* (Nauka, Moscow, 1972).
5. L. A. Boatner, R. W. Reynolds, and M. M. Abraham, J. Chem. Phys. **57** (5), 1248 (1970).
6. A. D. Gorlov, A. P. Potapov, and Yu. A. Sherstkov, Fiz. Tverd. Tela **27** (9), 2861 (1985).
7. V. A. Chernyshev, A. D. Gorlov, A. A. Mekhonoshin, *et al*., Appl. Magn. Reson. **14** (1), 37 (1998); A. D. Gorlov, V. B. Gusev, A. Yu. Zakharov, *et al*., Fiz. Tverd. Tela **40** (12), 2172 (1998).
8. A. Edgar and D. J. Newman, J. Phys. C: Solid State Phys. **8** (23), 4023 (1975).
9. O. V. Nazarova and T. I. Sanadze, Soobshch. Akad. Nauk GSSR **87** (2), 329 (1977).

Translated by P. Pozdeev

Physics of the Solid State, Vol. 42, No. 1, 2000, pp. 55–58. Translated from Fizika Tverdogo Tela, Vol. 42, No. 1, 2000, pp. 53–56.

SEMICONDUCTORS AND DIELECTRICS

Acoustooptical and Elastic Properties of Laminated $KY(MoO_4)_2$ Crystals

L. A. Kulakova

Ioffe Physicotechnical Institute, Russian Academy of Sciences, St. Petersburg, 194021 Russia
e-mail: L.Kulakova@shuvpop.ioffe.rssi.ru

Received May 17, 1999

Abstract—Data on acoustic (absorption and velocity of sound), optical (refractive index and optical absorption coefficient), and photoelastic (coefficients of acoustooptical quality and photoelastic constants) properties of $KY(MoO_4)_2$ crystals are obtained. It is shown that, not only does the anisotropy of binding forces lead to a significant anisotropy of acoustic and photoelastic properties, but it also determines anomalously high elastic nonlinearity in the direction of the *Y*-axis perpendicular to cleavage planes. *© 2000 MAIK "Nauka/Interperiodica".*

INTRODUCTION

Laminated crystals possessing a clearly defined anisotropy of the mechanical strength are a convenient object for studying the influence of anisotropy of binding forces on physical properties of solids. It was shown in a number of papers [1] that this influence on thermal, optical, electric, and other properties is so strong that it becomes possible to speak of a two-dimensional structure of such crystals.

The influence of anisotropy of binding forces on the photoelastic effect was studied in detail using hexagonal layered GaSe crystals as an example [2]. The authors of [2] showed that lamination of the structure leads to the exciton wave function becoming two-dimensional. But data on features of photoelastic properties of other laminated crystals are rather incomplete.

Acoustic properties of various laminated crystals were studied earlier by the pulsed echo method [3]. Because of restrictions associated with the integral nature of this method, the results obtained require that they be refined by using the acoustooptical method, allowing local measurements to be carried out (this is particularly important for laminated crystals with defects being possibly present in their structure).

This work is devoted to the study of photoelastic and acoustic properties of laminated $KY(MoO_4)_2$ crystals. They possess the rhombohedral symmetry (D_{2h}), a perfect cleavage in the *XZ*-plane, and a less perfect cleavage in the *XY*-plane [4]. Those crystals possessing a high optical transparency in the visible spectral region are an excellent object for studying features of acoustic absorption in laminated crystals by the acoustooptical method. We obtained data on optical properties, acoustooptical efficiencies, and components of the photoelastic tensor of these crystals. Features of propagation of acoustic waves are studied. Absorption of longitudinal and transverse acoustic waves is measured by the acoustooptical method in the frequency region of 300–1600 MHz. Data on the velocity of various acoustic waves are obtained.

MEASUREMENT TECHNIQUE

We used single crystals grown at the Institute of Inorganic Chemistry, Siberian Division of the Russian Academy of Sciences. Optically uniform samples of dimensions of $4 \times 4 \times 10$ mm^3 were oriented along the crystallographic axes. The faces perpendicular to the layers were processed by fine polishing with subsequent optical polishing. The faces parallel to the layers were processed by separating the destroyed layer. Sound was excited by lithium niobate resonant piezoelectric transducers cemented to the corresponding face of the sample by Nonaq Stopcock cement. Both the fundamental frequency of the transducer (f = 30 MHz) and its higher harmonics were used.

The method of Bragg diffraction of light from an acoustic wave was used in acoustooptical measurements. The acoustooptical Q-factor M_2 was measured by the traditional Dixon method [5]. We used a He–Ne laser (λ = 0.63 μm) as a light source and GaP single crystals as a reference.

We determined the absolute values of refractive indices with an accuracy of ~10^{-2} from the measurements of the displacement of the laser beam due to refraction as it passed through a plane-parallel $KY(MoO_4)_2$ sample of the corresponding geometry. The angle of incidence was 45°.

The velocity of acoustic waves was calculated with an accuracy up to 10^{-3} from the data of measurements of the time interval between the neighboring echo pulses by the method of combining UHF filling of these pulses.

RESULTS AND DISCUSSION

It is known that the efficiency of the Bragg diffraction of light from ultrasonic waves is determined by the

1063-7834/00/4201-0055$20.00 © 2000 MAIK "Nauka/Interperiodica"

acoustooptical Q-factor M_2

$$I_1 = 1/2 I_0 M_2 P(\pi d/(\lambda \cos\theta_i))^2, \quad (1)$$

$$(M_2)_{ik} = n_i^6 p_{ik}^2/(\rho V_k^3), \quad (2)$$

where I_1 and I_0 are the intensities of diffracted and incident light, respectively; P is the intensity of sound; λ is the wavelength of light; d is the width of the acoustic beam; θ_i is the angle of incidence; n_i is the refractive index; p_{ik} is a component of the photoelastic tensor; ρ is the density of the crystal; V_k is the velocity of the acoustic wave; $i, k = 1–6$; i is the index of polarization of light and k is the index of deformation in the matrix representation. As M_2 includes anisotropy of both elastic and optical properties, anisotropy of this parameter reflects the influence of anisotropy of binding forces on the photoelastic effect most completely.

The results of the measurements of the parameter of the acoustooptical Q-factor presented in the table demonstrate that the greatest photoelastic effect induced by longitudinal deformation is observed in the direction $Y(M_2)_{22}$, i.e., transverse to the main cleavage planes as in GaSe crystals [2]. However, the highest acoustooptical efficiency $(M_2)_{66}$ is observed for the shear deformation (S_6) of layers with respect to one another. It should be noted that this result is unique in a certain respect, since materials where the efficiency of light diffraction from shear waves would be higher than that from longitudinal ones were unknown up to now. We failed to observe light diffraction from the corresponding acoustic waves (deformations S_4 and S_5) in the studies of the photoelastic effect in laminated GaSe crystals [2]. Due to a large difference ($n_0 - n_e \sim 0.3$) of the refractive indices in these crystals, diffraction is possible in the region of high acoustic frequencies ($f \sim 1.5$ GHz) and, hence, large (~70°) diffraction angles, which makes the observation of the effect very difficult.

The values of the parameters of the acoustooptical Q-factor $(M_2)_{ik}$, the components of the photoelastic tensor (p_{ik}), the refractive indices (n_i), the optical absorption coefficients β_i, and the velocities of sound (V_k); $\rho = 3.9$ g/cm^3 and $\lambda = 0.63$ μm

ik	M_{ik}, 10^{-18} s^3 g^{-1}	p_{ik}	n_i	β_i, cm^{-3}	V_k, 10^5 cm s^{-1}
11	0.5	0.092	1.8342	0.015	5.08
12	21	0.253			2.87
13	1.93	0.108			3.6
21	4.15	0.242			
22	28	0.267	1.7658	0.1	
33	3.86	0.21	1.7474	0.1	
44					1.86
55					2.47
66	36	0.12			1.5

The study of light diffraction from shear (S_6) waves in $KY(MoO_4)_2$ crystals is important, and not only from the standpoint of the detection of high acoustic efficiency. It also enabled us to determine (with a sufficiently high accuracy) the differences of the refractive indices $\Delta n_{12} = 0.0683$ ($\Delta n_{12} = n_x - n_y$), $\Delta n_{13} = 0.0867$ ($\Delta n_{13} = n_x - n_z$), and $\Delta n_{23} = 0.0184$ ($\Delta n_{23} = n_y - n_z$). To do this, we utilized our experimental data on the geometry of light diffraction from transverse sound S_6 (Fig. 1) and familiar [6] relations for the angle of incidence outside of the crystal θ_i and the diffraction (θ_d) and scattering (θ_s) angles under the conditions of anisotropic Bragg diffraction

$$\sin\theta_i = \lambda f[1 + n\Delta n V^2/(f^2\lambda^2)]/2V,$$

$$\sin\theta_d = \lambda f[1 - n\Delta n V^2/(f^2\lambda^2)]/2V,$$

$$\theta_s = \theta_i + \theta_d, \quad (3)$$

where $n = (n_i + n_d)/2$ and $\Delta n = n_i - n_d$.

In our measurements, we have $n_i = n_2$ and $n_d = F(n_1, n_3)$. For $\theta_i = 0$, we have $n_d = n_1$ and, as it follows from (3), $\Delta n = f_0^2/2nV^2$. By measuring f_0 and knowing n, we can calculate Δn_{21}. Δn_{23} can be calculated through the fitting of the calculated and the experimental data (Fig. 1) for $\theta_i \neq 0$.

The value $n = 1.8$ used in the calculations of Δn was obtained from the measurements of the displacement of the laser beam due to refraction (the angle of incidence was 45°) as it passed through a plane-parallel $KY(MoO_4)_2$ sample of the corresponding geometry. The final values of n_i are presented in the table.

Our data on the velocity of sound (see table) demonstrate that elastic properties clearly correlate with anisotropy of binding forces: the greater the binding forces, the higher the sound velocity.

With the values of acoustic and optical parameters determined in this work (see table) and the foregoing relation (2) for $(M_2)_{ik}$, we calculated the components p_{ik} of the photoelastic tensor. As seen from these data (see table), anisotropy of the photoelastic tensor, as well as elastic properties, are unambiguously related to anisotropy of binding forces. However, this relation is qualitatively of the opposite type: the weaker the binding force, the higher the p_{ik}, i.e., the variations of the polarizability of the crystal are larger due to deformations.

The results of the measurements of sound absorption in the crystals studied in the frequency interval of 300–1800 MHz are presented in Fig. 2. The frequency dependences for all the cases studied have a form close to quadratic, which is typical of the Akhiezer mechanism for lattice absorption in crystals. The relative values of the absorption coefficients for various types of waves directly correlate with the relative magnitudes of

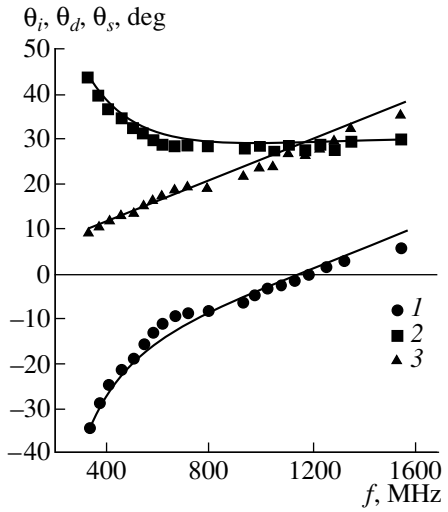

Fig. 1. The geometry of light diffraction from a shear acoustic wave (S_6): (*1*) θ_i, (*2*) θ_d, and (*3*) θ_s.

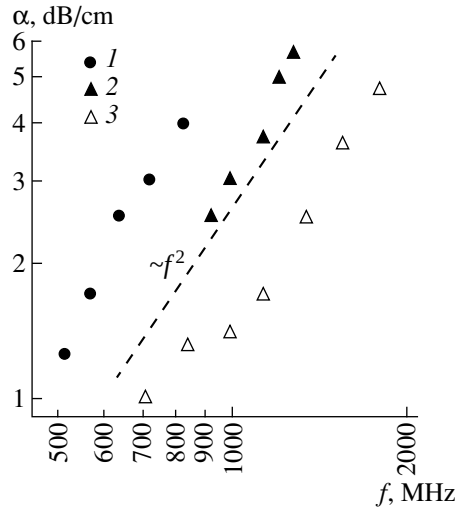

Fig. 2. The absorption coefficients of longitudinal (*1*) S_2 and (*3*) S_1 and transverse (*2*) S_6 acoustic waves as functions of the frequency.

the binding forces: the highest absorption is observed in the direction of the weakest bonds, the *Y*-direction. However, attention is attracted by a relatively small absorption for all types of waves. This is particularly surprising for both longitudinal and shear waves propagating in the direction of the *Y*-axis (perpendicular to the plane of main layers). A higher viscosity, and hence higher absorption of elastic waves could be expected in these crystals due to weak binding between the layers.

Of special note are the results of the study of the absorption of longitudinal sound (S_2) propagating transverse to the layers. The data on absorption for the wave presented in Fig. 2 were obtained under very low sound intensity conditions ($P < 0.1$ W/cm^2). As the intensity increases, absorption starts to grow and a sharp dependence of the absorption coefficient on the sound intensity is observed (Fig. 3), whereas higher harmonics appear and grow in the spectrum of the acoustic flux (Fig. 4). We follow the pattern of the spatial development of the spectrum of the acoustic flux for a lower frequency ($f = 334$ MHz), because it is possible to observe the development of a great number of harmonics with a decreasing frequency. For the levels of diffraction observed, nonlinear acoustooptical effects are possible in the first order. They can lead to the transfer of the intensity of diffracted light to higher orders. However, this should result in the inverse spatial effect, and the magnitude of absorption measured should decrease with the increasing intensity of sound. Therefore, it is clear that energy is transferred to higher harmonics due to elastic nonlinearity in the process of sound propagation when sound intensity is high.

To calculate the nonlinear coefficient Γ [7] ($u_2 = 8\Gamma u_1^2 \Delta x k_1^2$, where u_1 and u_2 are the amplitudes of the displacement of the corresponding component and k_1 is the wave number of the fundamental frequency), we measured the development of the second harmonic S_2 for a low level of the input signal (Fig. 4a). This made it possible to observe a region of linear growth of its amplitude. It is seen from this figure that in $KY(MoO_4)_2$ crystals in the linear region, the second-harmonic intensity increases by an order of magnitude at a distance less than 1 mm for a sound intensity $P \approx 4$ W/cm^2. The calculations using these data demonstrated that elastic nonlinearity is anomalously high in the *Y*-direction, $\Gamma \approx 40$. According to the data available [8], such a magnitude of the nonlinear coefficient was not observed in any familiar materials.

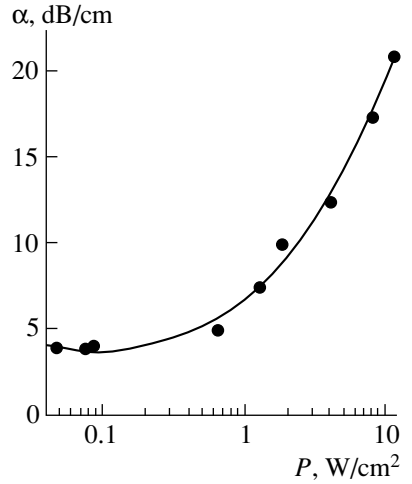

Fig. 3. The absorption coefficient of transverse waves (S_2, $f = 800$ MHz) as a function of the input intensity.

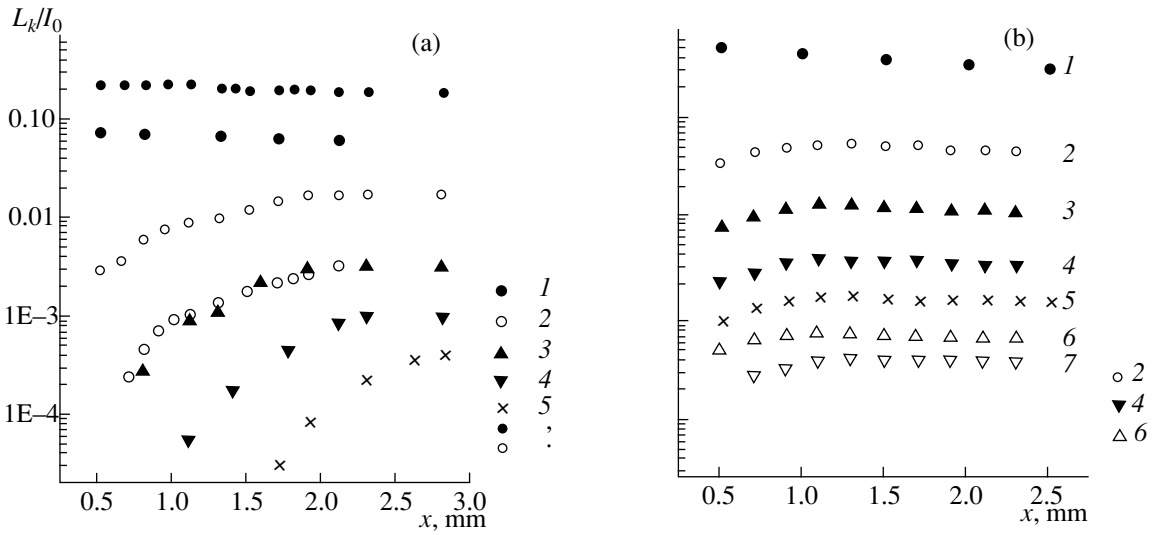

Fig. 4. The spatial development of the spectrum of the acoustic flux (along Y) for various intensities of the longitudinal acoustic wave at the entrance ($I_k/I_0 = 0.1$ corresponds to a sound intensity $P = 5.3$ W/cm^2); (*1–7*) are the numbers of the corresponding acoustic harmonics.

CONCLUSION

Thus, data on optical, photoelastic, and acoustic properties of $KY(MoO_4)_2$ crystals are obtained for the first time in this work. Their direct correlation with the anisotropy of binding forces is established. The values of the difference between the principal components of the refractive indices are calculated with a high degree of accuracy (10^{-4}) from the data on the geometry of anisotropic diffraction of transverse waves.

It is found that the propagation of transverse waves in the direction perpendicular to the plane of a layer is essentially nonlinear. The absorption coefficient of the corresponding longitudinal waves depends considerably on the sound intensity. The linear regime is realized only for intensities <0.1 W/cm^2. The value of the nonlinear coefficient is the highest ($\Gamma \approx 40$) of those in all familiar materials.

ACKNOWLEDGMENTS

The author is grateful to A.A. Pavlyuk for providing $KY(MoO_4)_2$ single crystals and Yu.V. Ilisavskiĭ for useful discussions.

The work was supported by the Russian Foundation for Basic Research, projects nos. 95-02-04093-a and 98-02-18305.

REFERENCES

1. G. L. Belen'kiĭ and V. B. Stopachinskiĭ, Usp. Fiz. Nauk **140**, 233 (1983).
2. N. S. Averkiev, Yu. V. Ilisavskiĭ, and L. A. Kulakova, Fiz. Tverd. Tela (St. Petersburg) **38**, 3556 (1996); *ibid.* **38**, 3570 (1996).
3. Yu. V. Ilisavskiĭ, V. L. Okulov, and S. V. Ordin, Pis'ma Zh. Tekh. Fiz. **12**, 377 (1986).
4. R. F. Klevtsov and S. V. Borisov, Dokl. Akad. Nauk SSSR **177**, 1333 (1967).
5. R.W. Dixon, IEEE J. Quantum Electron. **3**, 87 (1967).
6. A. M. D'yakonov, Yu. V. Ilisavskiĭ, and L. A. Kulakova, Fiz. Tverd. Tela (St. Petersburg) **14**, 95 (1972).
7. L. N. Zarembo and V. A. Krasil'nikov, Usp. Fiz. Nauk **102**, 549 (1970).
8. O. B. Gusev and V. V. Kludzin, *Acoustooptical Measurements* (LGU, Leningrad, 1987), p. 52.

Translated by A. Mozharovskii

Physics of the Solid State, Vol. 42, No. 1, 2000, pp. 59–64. Translated from Fizika Tverdogo Tela, Vol. 42, No. 1, 2000, pp. 57–61.

SEMICONDUCTORS AND DIELECTRICS

Molecular–Crystalline Approach to Evaluation of Correlation Corrections in the Theory of Chemical Bonding in Crystals: Electronic Structure of Ti_2O_3 Crystals

R. A. Évarestov and A. I. Panin

St. Petersburg State University, Universitetskaya nab. 7/9, St. Petersburg, 199034 Russia

Received May 31, 1999

Abstract—The problem of the partial inclusion of electron correlation effects has been considered in the framework of the unrestricted Hartree–Fock method. The calculation of the electronic structure of the $[Ti_2O_9]^{12-}$ cluster is performed. The results obtained demonstrate that, in some cases, a major part of static correlation effects can be taken into account in the unrestricted Hartree–Fock approximation. The influence of these effects on the local characteristics of crystals is analyzed. *© 2000 MAIK "Nauka/Interperiodica".*

The calculations of the electronic structure of crystals within the Hartree–Fock formalism at the LCAO level have been applied to the theory of chemical bonding in crystals only in recent years [1–3].

At the same time, the specific features of chemical bonding in molecules have already long been described by the so-called local characteristics of electronic structure (charges on atoms, orders of interatomic bonds, atomic covalences, and spin density in radicals), which are determined by the one-particle electron density matrix [4, 5].

However, even for molecular systems, these characteristics are usually considered either without regard for the electron correlation effects (in *ab initio* calculations) or with a partial implicit inclusion of these effects through the atomic parameters (in semiempirical calculations). To our knowledge, only a few attempts have been made to evaluate the influence of the electron correlation on the features of chemical bonding in molecules [6]. On the other hand, just the local characteristics of the electronic structure should be substantially affected by the correlation corrections owing to the short-range character of correlation interactions.

In modern techniques of computing the electronic structure of molecules, the electron correlation effects are included by using the post Hartree–Fock methods (configuration interaction method, coupled cluster method, etc.) with the aim of improving the quality of wavefunctions. In the case of crystals, the electron correlation effects, as a rule, are taken into account to evaluate the corrections to the total energy of a system and the binding energy, most frequently, in the framework of the density functional method [1].

In this work, we proposed the molecular–crystalline approach to the evaluation of correlation corrections in the investigations of the chemical bonding in crystals. Conceptually, the method is as follows. The local characteristics of a crystal are calculated within the band model by the Hartree–Fock method to choose the molecular cluster that adequately describes the local features of electronic structure. In the majority of cases, the number of atoms comprising this cluster is appreciably less than the number of atoms contained in the clusters simulating one-electron states in a crystal. At the next stage of the advanced approach, the chosen cluster is calculated in the framework of the multiconfigurational approximation with molecular programs providing the expansion of wavefunctions into determinants. Then, by applying the unrestricted Hartree–Fock (UHF) method to the calculations of the cluster and the crystal, one can obtain the one-determinant solutions, which correspond to the generalized valence bonds. Simple rearrangements of the multiconfigurational cluster function permit one to explicitly separate the obtained valence bonds in its expansion. If these valence bonds turn out to be dominant in the expansion, then, in order to construct the many-electron function of a crystal, it is sufficient to replace the cluster valence bonds by the crystal valence bonds. Thus constructed wavefunction explicitly includes the electron correlation effects. By convoluting the many-particle density matrix into two- and one-particle density matrices, it is possible to calculate the local characteristics of chemical bonding in a crystal by the known formulas.

The aim of the present work was to investigate the electron correlation effects in the Ti_2O_3 crystal within the molecular–crystalline approach. It is common knowledge that the electron correlation can play an important part in compounds of transition metals with unfilled *d* electronic shell. The density functional method, which has been widely employed for these crystals, often appears to be unsatisfactory because of incorrect description of the self-interaction.

1063-7834/00/4201-0059$20.00

In Section 1, the main local characteristics of the electronic structure of molecular systems are defined as applied to the many-determinant wavefunctions in the configuration interaction (CI) and multiconfigurational self-consistent field (MC SCF) methods.

In Section 2, the electronic structure of the crystal is calculated within the band and cluster models, and the results of calculations are compared to choose the $[Ti_2O_9]^{12-}$ cluster, which reproduces the features of the Ti–Ti and Ti–O bonds in the crystal.

In Section 3, the results of the UHF calculations of the crystal and the chosen cluster are analyzed. Moreover, consideration is given to the MC SCF calculations of the cluster, including the structure of the many-determinant wavefunction. It is demonstrated that the one-determinant approximation in these calculations adequately describes the influence of the electron correlation on the main characteristics of chemical bonds.

In conclusion, further possibilities of the proposed approach are discussed as applied to the theory of chemical bonding in crystals with ionic–covalent bonds.

1. LOCAL CHARACTERISTICS OF ELECTRONIC STRUCTURE IN POST-HF METHODS

Local characteristics (such as charges on atoms, bond orders, valences, and covalences) are very useful for the qualitative description of the electronic structure in molecular and crystalline systems. However, there are no rigorous quantum-mechanical definitions for these characteristics. Indeed, in attempting to separate an atomic subsystem or a molecular subsystem in systems with a strong coupling, we should refuse to describe this subsystem by using pure states, which leads to considerable conceptual and computational problems. For example, an atomic subsystem in a molecular system, as a rule, cannot be assigned a certain integral number of the electrons involved, which implies that this subsystem should be represented by an ensemble of states matched by different numbers of electrons.

However, there exists an approach that gets around the above difficulties. This approach rests on the analysis of reduced density matrices (as a rule, these are the first-order and second-order matrices) of a system as a whole, and the separation of a particular subsystem is generally based on some geometric criteria. This makes it possible to considerably simplify computations, but leads to some arbitrariness in the choice of the definitions for local characteristics of the electronic structure. This arbitrariness most clearly manifests itself in going beyond the scope of the Hartree–Fock approximation, as evidenced by a wide variety of definitions available in the literature for valences and bond orders in the case of post Hartree–Fock methods [4, 6].

The one-electron density operator associated with some multiconfigurational N-electron wavefunction Ψ can be written as

$$\hat{\rho}(\Psi) = \sum_{i=1}^{2n} \lambda_i |\psi_i\rangle\langle\psi_i|, \tag{1}$$

where ψ_i are the natural (molecular) spin orbitals, and λ_i are the natural orbital occupation numbers, which satisfy the following conditions:

$$\sum_{i=1}^{2n} \lambda_i = N, \tag{2}$$

$$0 \le \lambda_i \le 1$$

$$(i = 1, \ldots, 2n). \tag{3}$$

The density operator is the Hermitian positive semidefinite operator with a spur equal to the number of electrons. At the same time, in general, this operator does not possess any other specific properties such as, for example, idempontency. After the convolution over the spin variables, the density operator breaks down into two components whose matrix representation in the basis set of atomic orbitals (AOs) has the form

$$\hat{\rho}^{\sigma}(\Psi)\chi_{\mu} = \sum_{\nu=1}^{n} \chi_{\nu}(P^{\sigma}S)_{\nu\mu}, \tag{4}$$

where S is the AO overlap matrix, and the matrix elements of the P^{σ} matrix are related to the occupation numbers λ_i^{σ} and the coefficients φ_i^{σ} in the expansion of the spatial parts of natural spin orbitals in the AO basis set through the expressions

$$P_{\mu\nu}^{\sigma} = \sum_{i=1}^{n} C_{\mu i}^{\sigma}\lambda_i^{\sigma}(C_{i\nu}^{\sigma})^{+} \quad (\sigma = \alpha, \beta). \tag{5}$$

By assuming that the atomic basis set is well localized on atoms (or atomic fragments under consideration) and that it is orthonormal and also by using the expansion of the unit operator

$$\hat{I} = \sum_{A} \hat{\rho}_A \tag{6}$$

(where $\hat{\rho}_A$ is the orthogonal projector onto the AO space of the A atom), we can rewrite the condition for normalization of the σ-component of the density operator in the form

$$\mathrm{Sp}\hat{\rho}^{\sigma}(\Psi) = \sum_{A} \mathrm{Sp}\hat{\rho}^{\sigma}(\Psi)\hat{\rho}_A = N_{\sigma}, \tag{7}$$

where N_{σ} is the number of σ-electrons.[1] In this case, the quantity $\sum_{\sigma} \mathrm{Sp}\hat{\rho}^{\sigma}(\Psi)\hat{\rho}_A$ can be interpreted as the

occupation of the AO space of the A atom in a system under consideration or as the occupation of the A atom when the diffuse orbitals occurring in this space are occupied only slightly. Unfortunately, the atomic basis sets actually used in calculations are nonorthogonal, and attempts at their orthogonalization (by using, for example, the Löwdin scheme) result in an essential delocalization of AOs. Then, equality (7) holds true, but the interpretation of the $\sum_\sigma \mathrm{Sp}\hat{\rho}^\sigma(\Psi)\hat{\rho}_A$ quantities as occupations of atoms becomes very conventional. One of the most successful attempts to retain the localization of AOs without violation of equality (7) consists in going to the biorthogonal atomic basis set

$$\tilde{\chi} = \chi S^{-1}, \tag{8}$$

which obeys the relationships

$$\langle \chi_\mu | \tilde{\chi}_\mu \rangle = \delta_{\mu\nu}. \tag{9}$$

By introducing

$$\hat{\rho}_A = \sum_{\mu \in A} |\chi_\mu\rangle\langle\tilde{\chi}_\mu|, \tag{10}$$

we have the idempotent operators meeting equality (7). The nonorthogonality of the basis set manifests itself in non-Hermitian operators (9).

Going to the AO basis set in expression (1) and using definition (8), we obtain the occupation of the A atom

$$\begin{aligned} N_A &= N_A^\alpha + N_A^\beta \\ &= \sum_\sigma \mathrm{Sp}\hat{\rho}^\sigma(\Psi)\hat{\rho}_A = \sum_\sigma \sum_{\mu \in A} (P^\sigma S)_{\mu\mu}. \end{aligned} \tag{11}$$

In order to determine the two-center bond order, it is reasonable to attempt to obtain the expansion similar to (7), but for the squares of the density operator components. Unfortunately, in the general case, the spur of the density operator squared $\mathrm{Sp}(\hat{\rho}(\Psi))^2 = \sum_\sigma \mathrm{Sp}(\hat{\rho}^\sigma(\Psi))^2$ depends on both the AO basis set and the computational technique and can be treated as a certain characteristic of a system only with the very large basis sets and full configuration interaction. Furthermore, even in this limiting case, the physical meaning of the given characteristic is not quite clear. However, instead of the σ-components of the density operator, it is possible to consider their combinations

$$\hat{\rho}^{\alpha+\beta}(\Psi) = \hat{\rho}^\alpha(\Psi) + \hat{\rho}^\beta(\Psi) \tag{12}$$

and

$$\hat{\rho}^{\alpha-\beta}(\Psi) = \hat{\rho}^\alpha(\Psi) - \hat{\rho}^\beta(\Psi), \tag{13}$$

which are referred to as the total electron and spin density operators, respectively, and to examine the contributions to the squares of these operators. Both approaches are consistent with each other and with the standard analysis within the Hartree–Fock approximation for occupied shells when one uses the expansion of the doubled sum of the density operator σ-components squared

$$\begin{aligned} 2\sum_\sigma \mathrm{Sp}(\hat{\rho}^\sigma(\Psi))^2 &= 2\sum_\sigma \sum_{A,B} \mathrm{Sp}\hat{\rho}^\sigma(\Psi)\hat{\rho}_A\hat{\rho}^\sigma(\Psi)\hat{\rho}_B \\ &= 2\sum_\sigma \sum_{A,B} \sum_{\substack{\mu \in A \\ \nu \in B}} (P^\sigma S)_{\mu\nu}(P^\sigma S)_{\nu\mu}. \end{aligned} \tag{14}$$

The quantities

$$B_{AB} = 2\sum_\sigma \sum_{\substack{\mu \in A \\ \nu \in B}} (P^\sigma S)_{\mu\nu}(P^\sigma S)_{\nu\mu} \tag{15}$$

at $B \neq A$ can be interpreted as characteristics of the A–B bond orders, and their sum

$$C_A = \sum_{B \neq A} B_{AB} \tag{16}$$

can be treated as the covalence of the A atom. The one-center terms $F_A = B_{AA}$ in equation (14) are termed the free (nonrealized) valence of atoms.

2. BAND AND CLUSTER MODELS OF Ti_2O_3 CRYSTAL

The Ti_2O_3 crystal with a corundum structure (space group $R\bar{3}C$, rhombohedral crystal system) contain two Ti_2O_3 molecules in a unit cell. All four Ti atoms are arranged in pairs along the triad axis, and each pair consists of the nearest atoms (the bond length $R_{\mathrm{Ti–Ti}} = 2.58$ Å).

Catti *et al.* [7] calculated the electronic structure of the Ti_2O_3 crystal within the band model at the restricted Hartree–Fock (RHF) and unrestricted Hartree–Fock (UHF) levels with allowance made for the core electrons. It was demonstrated that the ground state of the crystal corresponds to an antiferromagnetic ordering of uncompensated spins of Ti atoms, and the Ti–O bond is essentially covalent. However, the features of chemical bonding in the Ti_2O_3 crystal were not analyzed in detail in [7], because the authors computed only the charges on atoms and Mulliken overlap populations, which provided only a qualitative description of the interatomic bonds. In order to consider in greater detail the chemi-

[1] In consideration of the states with the specified projection M_S of the total spin, the number of α- and β-electrons in the system is fixed, because $N = N_\alpha + N_\beta$ and $M_S = \frac{1}{2}(N_\alpha - N_\beta)$.

Table 1. Local characteristics of the electronic structure of the Ti_2O_3 crystal and the $[Ti_2O_9]^{12-}$ cluster

Parameter	Crystal				Cluster			
	with inclusion of core electrons		with core effective potential		with inclusion of core electrons		with core effective potential	
	RHF	UHF ($S_z = 0$)	RHF	UHF ($S_z = 0$)	RHF	UHF ($S_z = 0$)	RHF	UHF ($S_z = 0$)
Q_{Ti}	2.18	2.21	2.01	2.08	2.38	2.42	2.16	2.22
Q_{O1}	–1.46	–1.47	–1.34	–1.38	–1.72	–1.74	–1.65	–1.68
E_{O2}	–	–	–	–	–1.93	–1.94	–1.90	–1.90
$B_{Ti–Ti}$	0.925	0.04	0.87	0.05	0.95	0.04	0.88	0.03
$B_{Ti–O1}$	0.230	2.26	0.26	0.25	0.12	0.11	0.17	0.17
$B_{Ti–O2}$	0.221	2.20	0.26	0.24	0.24	0.21	0.30	0.27
C_{Ti}	2.42	1.50	2.56	1.64	2.04	1.06	2.32	1.37
C_{O1}	1.04	1.26	2.01	1.12	0.55	0.52	0.68	0.63
C_{O2}	–	–	–	–	0.17	0.16	0.22	0.21
V_{Ti}	3.71	3.08	3.67	3.05	3.61	3.01	3.61	3.01
V_{O1}	2.06	2.23	2.05	2.05	2.02	2.02	2.02	2.02
V_{O2}	–	–	–	–	2.02	2.02	2.01	2.01

cal bonding in this crystal with due regard for the electron correlation effects at the molecular–crystalline level, we used the pseudopotential approximation for the description of the core electrons.

Table 1 presents the results of our RHF and UHF calculations performed for the Ti_2O_3 crystal by using the Crystal-95 program [8] with inclusion of the core electrons and also in the pseudopotential approximation (for the Ti and O atoms, the pseudopotentials were taken from [9] and [10], respectively). A comparison with the results obtained in [11] with the use of the pseudopotential taken from [12] demonstrates that a specific set of pseudopotentials weakly affects the electron density distribution. Table 1 lists the charges on atoms Q_A, the interatomic bond orders B_{AB}, the covalences of atoms C_A (defined as the sums of the bond orders), and the total valences $V_A = (1/2)(C_A + \sqrt{4Q_A^2 + C_A^2})$. These quantities were calculated within the band model according to the formulas taken from [4]. Now, let us compare the corresponding values obtained with and without inclusion of the core electrons. It can be seen that the local characteristics of electronic structure of the crystal only slightly vary when the pseudopotential is introduced to describe the core electrons. Moreover, it turns out that the oxygen atoms of the two nearest spheres make the largest contribution to the covalent component for the titanium atoms. At the same time, as follows from Table 1, the Ti–Ti bond orders calculated at the RHF and UHF levels differ considerably. As shown below, this difference is associated with the inclusion of electron correlation effects in the UHF approximation.

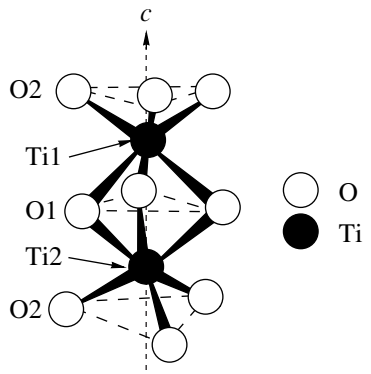

Geometric structure of the $[Ti_2O_9]^{12-}$ cluster.

On the basis of the performed calculations within the band model, we chose the $[Ti_2O_9]^{12-}$ cluster in which either of the two titanium atoms is surrounded by the atoms belonging to the three nearest spheres: one sphere of metal atoms and two spheres of oxygen atoms (see figure). The total number of electrons in the cluster is chosen reasoning from the ion model. In the cluster, the oxygen atoms (equivalent in the Ti_2O_3 crystal by virtue of the crystal symmetry) can be divided into two groups: the O1 atoms located between titanium atoms and the O2 boundary atoms (see figure).

It follows from Table 1 that all the main local characteristics of the electronic structure that are associated with the titanium atoms are sufficiently well reproduced by the chosen cluster both with explicit inclusion of the core electrons and in the pseudopotential approximation. Furthermore, the cluster also reproduces the appreciable difference in the Ti–Ti bond orders calculated with the UHF and RHF methods.

3. CORRELATION EFFECTS

So far, the molecular methods using multiconfigurational wavefunctions have not found application in the theory of crystal systems. It is believed that the direct use of these methods for calculating the electronic structure of crystals is impossible at all, and, hence, radically new approaches should be developed to evaluate the correlation effects. This raises the topical question as to whether the already existing and software-implemented methods, such as, for example, the UHF method, can account for the correlation effects in crystals. Generally, the answer to this question can be obtained only quantitatively by comparison of the UHF and MC SCF (or CI) functions [13] for any judiciously chosen cluster. To accomplish this, it is necessary to re-expand the UHF molecular orbitals (MOs) of the β-basis set into the MOs of the α-basis set

$$\varphi_i^{\beta} = \sum_j \varphi_j^{\alpha} T_{ji} \qquad (17)$$

and, after their substitution in the UHF determinant, to rewrite it in the form of multiconfigurational function constructed with the MO α-basis set. Then, one should obtain the projection of this expansion onto a pure spin state and compare the result with the function of the MC SCF method. If both functions involve the same dominant configurations, the UHF method accounts for a part of correlation effects.

Let us consider a rather usual case when the UHF and MC SCF functions are related by a simple transformation. Assume that the singlet nondegenerate state of a many-electron system (cluster) is described by the wavefunction

$$\Psi_{\text{MC SCF}} = C_1 \det|\ldots\varphi_h\alpha\varphi_h\beta| + C_2 \det|\ldots\varphi_l\alpha\varphi_l\beta|, \qquad (18)$$

which involves a double excitation from the Hartree–Fock reference state with a material weight. By using a nondegenerate transformation, we can pass on to the orbitals of the generalized valence bond method and rewrite function (18) as

$$\Psi_{\text{MC SCF}} \cong \Phi_{ab} + \Phi_{ba}. \qquad (19)$$

Here, Φ_{ab} and Φ_{ba} are the UHF determinants whose symmetric and antisymmetric combinations correspond to the singlet and the triplet states, respectively. Generally speaking, the nondiagonal matrix element $\langle\Phi_{ab}|\hat{H}|\Phi_{ba}\rangle$ differs from zero and serves as a measure of accounting for the correlation effects in the UHF approximation. Indeed, when this matrix element is small, the Φ_{ab} and Φ_{ba} UHF configurations virtually do not interact, and the UHF method makes allowance for a larger part of electron correlation effects.

Table 2. Energies and local characteristics of the electronic structure of the $[Ti_2O_9]^{12-}$ molecular cluster in the UHF and MC SCF approximations

Parameter	UHF		MC SCF	
	($S_z = 0$)	($S_z = 1$)	($S = 0$)	($S = 1$)
E (a. u.)	–137.874	–137.867	–137.913	–137.904
Q_{Ti}	2.22	2.28	2.11	2.12
Q_{O1}	–1.68	–1.68	–1.63	–1.64
E_{O2}	–1.90	–1.90	–1.89	–1.89
$B_{Ti–Ti}$	0.03	0.01	0.09	0.01
$B_{Ti–O1}$	0.17	0.17	0.19	0.20
$B_{Ti–O2}$	0.27	0.27	0.31	0.32
C_{Ti}	1.37	1.34	1.62	1.56
C_{O1}	0.63	0.62	0.70	0.71
C_{O2}	0.21	0.21	0.23	0.24
V_{Ti}	3.01	3.02	3.07	3.04
V_{O1}	2.02	2.02	2.02	2.03
V_{O2}	2.01	2.01	2.01	2.01

Table 2 lists the energies and local characteristics of the $[Ti_2O_9]^{12-}$ cluster, which were calculated by the UHF and MC SCF methods with the GAMESS computer program [14] for the lowest-lying singlet and triplet states. In the MC SCF method, the active space involved the five highest occupied and three lowest virtual MOs, which were obtained by the preliminary calculation of the singlet state of the cluster at the RHF level. In the chosen active space, we considered all the possible excitations from the occupied MOs to the vacant MOs. As a result, 1176 singlet and 1512 triplet many-electron basis functions were generated. It was found that the lowest-lying singlet state in the studied cluster is described by the two-term wavefunction

$$0.8[\varphi_h^2\varphi_l^0] - 0.6[\varphi_h^0\varphi_l^2], \qquad (20)$$

and the lowest-lying triplet state is determined by the one-determinant function.

Comparison between the total energies of the $[Ti_2O_9]^{12-}$ cluster indicates that the UHF calculations correctly describes the relative energies of the singlet and triplet states and, in particular, reproduces the small difference in these energies. Moreover, the difference between the RHF and MC SCF energies (correlation energy, 0.209 au) is satisfactorily simulated by the UHF method (0.170 au). This method also adequately reproduces the influence of the correlation effects on the Ti–Ti bond order. Actually, this bond order in the RHF

approximation is equal to 0.88 (Table 1), whereas its value in the UHF method is 0.03, which is in complete agreement with the data of the MC SCF method (0.09). At the same time, as can be seen from Table 2, the charges on atoms are weakly sensitive to the calculation technique.

ACKNOWLEDGMENTS

This work was supported by the Russian Foundation for Basic Research, project no. 99-03-33255.

REFERENCES

1. *Quantum-Chemical Ab-Initio Calculations of the Properties of Crystalline Materials: Lecture Notes in Chemistry*, Ed. by C. Pisani (Springer-Verlag, Heidelberg, 1996), Vol. 67.
2. I. V. Abarenkov, I. M. Antonova, V. G. Bar'yakhtar, V. L. Bulatov, and E. V. Zarochentsev, in *Electronic Structure of Perfect and Defect Crystals* (Naukova Dumka, Kiev, 1991).
3. V. A. Veryazov, A. V. Leko, and R. A. Évarestov, Fiz. Tverd. Tela (St. Petersburg) **41** (7), 1407 (1999).
4. I. Mayer, Int. Quantum Chem. **29**, 73 (1986).
5. S. G. Semenov, Vestn. Leningr. Univ., No. 16, 119 (1973).
6. R. C. Bochicchio, THEOCHEM **429**, 229 (1998).
7. M. Catti, G. Sandrone, and R. Dovesi, Phys. Rev. B: Condens. Matter **55**, 16122 (1997).
8. R. Dovesi, V. R. Saunders, C. Roetti, M. Causá, N. M. Harrison, R. Orlando, and E. Apra, *Crystal-95 Manual* (Torino, 1996).
9. P. J. Hay and W. R. Wadt, J. Chem. Phys. **82**, 270 (1985).
10. U. Wedig, M. Dolg, H. Stall, and H. Preuss, in *Quantum Chemistry: The Challenge of Transition Metals and Coordination Chemistry*, Ed. by A. Veillard (Reidel, Dordrecht, 1986).
11. R. A. Évarestov, A. V. Leko, and V. A. Veryazov, Phys. Status Solidi B **210**, R3 (1998).
12. B. Silvi, N. Fourati, R. Nada, *et al.*, J. Phys. Chem. Solids **52**, 1005 (1991).
13. B. O. Roos, in *Proceedings of European Summer School in Quantum Chemistry* (Lund, Sweden, 1991).
14. M. W. Schmidt, K. K. Baldridge, J. A. Boatz, *et al.*, J. Comput. Chem. **14**, 1347 (1993).

Translated by O. Borovik-Romanova

Physics of the Solid State, Vol. 42, No. 1, 2000, pp. 65–71. Translated from Fizika Tverdogo Tela, Vol. 42, No. 1, 2000, pp. 62–68.

SEMICONDUCTORS AND DIELECTRICS

Investigation of Amorphous States of SiO_2 by Raman Scattering Spectroscopy

V. K. Malinovsky*, V. N. Novikov*, N. V. Surovtsev*, and A. P. Shebanin**

** Institute of Automatics and Electrometry, Siberian Division, Russian Academy of Sciences, Universitetskiĭ pr. 1, Novosibirsk, 630090 Russia*

*** Institute of Geology and Geophysics, Siberian Division, Russian Academy of Sciences, pr. Nauki 3, Novosibirsk, 630090 Russia*

e-mail: malinovsky@iae.nsk.su

Received June 18, 1999

Abstract—The vitreous SiO_2 samples irradiated with fast neutrons at a dose of 5×10^{17}–2.2×10^{20} per cm^2 are investigated by the Raman scattering technique. It is demonstrated that the maximum of the low-frequency Raman spectrum (boson peak) shifts with an increase in the irradiation dose, and the medium-range order size decreases from 25 Å for the initial glass to 19 Å for the sample subjected to irradiation at a maximum dose. It is revealed that the fast relaxation intensity obtained from analysis of the low-frequency Raman spectra linearly correlates with the specific volume of the studied samples. *© 2000 MAIK "Nauka/Interperiodica".*

It is well known that vitreous SiO_2 undergoes a transition to an amorphous state under irradiation. This state is commonly referred to as the metamict phase. The metamict phase has attracted considerable attention of many scientists engaged on research into the fundamental properties of vitreous systems. It is established that the structure of glasses and liquids on the nanometer scale exhibit fragments similar to elements of the local structure of their crystal primogenitors. In the case of SiO_2, these elements are closed configurations of silicon–oxygen tetrahedra. An important problem of the solid state physics is to elucidate how the local structure changes its type under the action of external factors. Research in materials with identical chemical compositions and, correspondingly, the same short-range order, but differing in physical properties, has opened up fresh opportunities for critical verification of many theoretical and model approaches to the description of the amorphous state in solids.

The purpose of this work is to investigate the Raman scattering spectra of amorphous SiO_2 in vitreous and metamict phases. Particular attention is focused on the low-frequency Raman spectra, which, as shown below, provide important information regarding the dynamics of amorphous materials on the nanometer spatial scale.

The Raman scattering spectroscopy is an efficient method of investigating the structure and dynamics of materials. Traditionally, Raman light scattering is used to analyze the spectra of optical vibrations in crystal or their analogues—stretching vibrations in disordered condensed media. A characteristic feature of the low-frequency vibrational spectra of glasses and other amorphous materials is the occurrence of a broad vibrational mode with a maximum in the range 10–100 cm^{-1}, which was termed the boson peak. For amorphous materials, the appearance of the boson peak is associated with the excess density of quasi-local acoustic vibrations in the corresponding frequency range, which arises from the absence of the long-range order in these materials and the violation of translational symmetry.

The frequency at a maximum of the boson peak is correlated with the characteristic scale (size) in a material, on which it cannot be regarded as a homogeneous medium. The correlation radius of the physical parameters of a material on these scales is referred to as the medium-range order size. The numerical estimation of the characteristic medium-range order size from the experimental data gives values in the range 1–5 nm. A considerable body of currently available experimental data indicates that the medium-range order plays an important part in describing the behavior of amorphous materials.

1. EXPERIMENT AND BASIC RESULTS

The samples used in this work were prepared and studied earlier by other experimental techniques in [1, 2]. These samples are the KI silica glasses containing unintentional impurities (10^{-3}–10^{-1} wt %). The glasses were subjected to irradiation with fast neutrons. The irradiation doses are given in the table. A change in the amorphous state is accompanied by a change in the density of amorphous SiO_2. The densities of the samples used in the present work were measured in [2]. Their values are also listed in the table.

The Raman scattering spectra were recorded on a U1000 spectrometer using the 458-nm exciting line of an argon laser. All the spectra were measured in a 90° scattering geometry. The spectral resolution was equal

1063-7834/00/4201-0065$20.00

Characteristics of SiO_2 samples used in Raman scattering measurements and the found position of the boson peak

Sample	Dose, f.n./cm^2	Density, g/cm^3	Position of boson peak, cm^{-1}
KI0	–	2.206	51
KI1	5×10^{17}	2.226	53
KI2	5×10^{18}	2.265	63
KI3	2.2×10^{20}	2.265	70

to 2 cm^{-1}. The polarized spectra were measured in the frequency range 5–1500 cm^{-1}, and the depolarized spectra were taken in the range 5–500 cm^{-1}.

The polarized Raman spectrum of the sample irradiated at a maximum dose (KI3 sample, see table) is shown in Fig. 1 (curve *2*). It can be seen that the luminescence contribution completely predominates in the spectrum at frequencies above 900 cm^{-1}. Curve *3* represents the spectrum of the KI3 sample with the subtracted contribution of luminescence component. In order to perform the subtraction, the experimental spectrum at frequencies of 1300–1500 cm^{-1} was approximated by the Gaussian contour wing, and the contour obtained was subtracted from the experimental curve. An essential result of analyzing thus obtained spectrum is the inference that the luminescence contribution is negligibly small at frequencies below 500 cm^{-1} and cannot affect the shape of the low-frequency spectra. Curve *1* in Fig. 1 corresponds to the sample of the initial silica glass (KI0). For further analysis, we use the relative intensity of the Raman scattering spectra of irradiated and unirradiated samples. Such a normalization of the spectra can be achieved with the Raman scattering band at a frequency of ~810 cm^{-1}, which corresponds to the O–Si–O bending vibrations. It is evident that the number of these vibrations and their integral contribution to the inelastic light scattering should remain unchanged for both phases. Hence, the spectra were normalized to the integrated intensity of the band at ~810 cm^{-1} (Fig. 1).

Figure 2 displays the depolarized Raman spectra of the KI0 and KI3 samples at low frequencies. The depolarized spectra make it possible to avoid the contribution of the stretching vibrational modes observed in the polarized spectra at frequencies above 100 cm^{-1} (Fig. 1). As can be seen from Fig. 2, the spectrum of the sample irradiated at a maximum dose (curve *2*) is significantly shifted relative to the spectrum of the initial material (curve *1*) [3]. Maxima observed at ~50 and 70 cm^{-1} correspond to the boson peak. At frequencies below 100 cm^{-1}, the low-frequency polarized Raman spectra exhibit the same spectral shape as the spectra shown in Fig. 2, which agrees with the known result that the depolarization factor for the boson peak is frequency independent.

2. DISCUSSION

2.1. Stretching modes. As evident from Fig. 1, the transition to the metamict phase is accompanied with an increase in the intensity of the *D*1 and *D*2 lines, whose frequencies are 495 and 605 cm^{-1}, respectively. According to recent studies, these peaks correspond to the vibrations of four-membered and three-membered ring structures, respectively [4, 5]. It follows from the spectra that the number of rings involving three or four SiO_2 fragments increases under irradiation with fast neutrons. An increase in the number of three-mem-

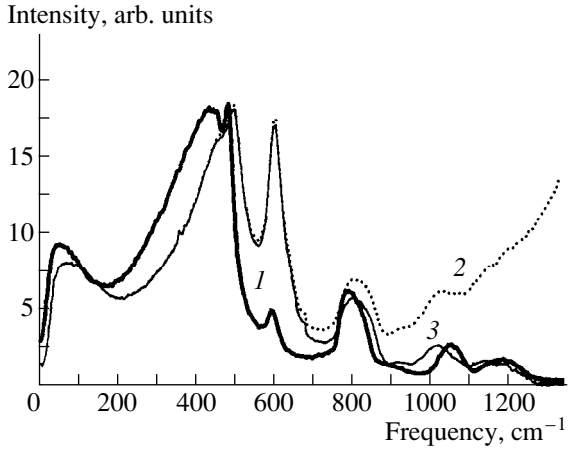

Fig. 1. Polarized spectra of (*1*) vitreous and (*2*) metamict SiO_2 samples. (*3*) Polarized spectrum of the metamict sample with the subtracted contribution of luminescence component.

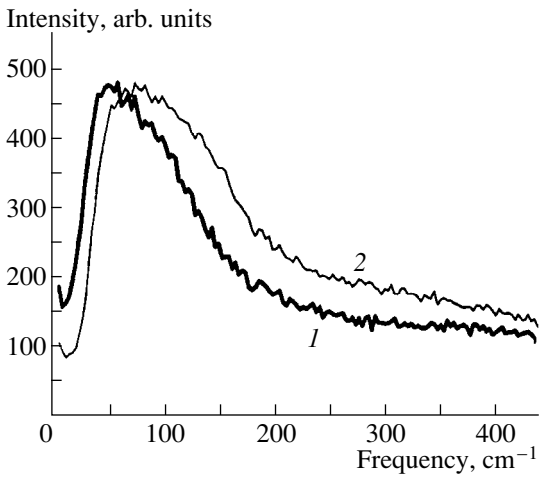

Fig. 2. Depolarized spectra of (*1*) vitreous and (*2*) metamict SiO_2 samples.

bered rings upon irradiation with fast neutrons was observed earlier in [6].

2.2. Boson peak. Earlier [7], we experimentally showed that glasses exhibit a universal shape of the low-frequency spectra; that is, the spectra of boson peak normalized to the frequency and intensity at a maximum of the spectrum coincides with each other. Pocsik and Koos [8] demonstrated that the boson peak at a maximum can be adequately described by the lognormal distribution function. On the other hand, as was shown in [9], the shape of the boson peak in low-frequency spectra of amorphous silicon differs from universal. It was concluded that the shape of the boson peak (different for glasses and nonvitreous amorphous materials) reflects the internal "structure" of an amorphous material. Strictly speaking, a metamict phase is not glass from the viewpoint of preparation technique—the latter materials are produced by cooling the melts [10]. Therefore, it would be expected that the spectral shape of the boson peak for a metamict phase differs from its universal shape for vitreous materials. To compare the boson peaks in their shapes, the low-frequency spectrum of the metamict phase was normalized to the frequency at a maximum of the boson peak for the unirradiated sample (Fig. 3). As is seen from Fig. 3, the shapes of the spectra for silica glass and the metamict phase are identical. For glasses subjected to irradiation at intermediate doses (KI1 and KI2 samples), the spectral shape of the boson peak also coincides with that of silica glass. Figure 3 demonstrates the reduced spectra, i.e., the spectra divided by $(n + 1)\omega$, where n is the Bose factor. We used such a normalization in order to compare the shape of the experimental spectrum with the spectral shape predicted from the lognormal distribution for this case. For comparison, the lognormal distribution with a maximum at a frequency of 51 cm^{-1} is shown in Fig. 3. From the similarity of the spectral shapes of boson peaks for irradiated and unirradiated SiO_2 samples, we can draw an important inference about the "glass-likeness" of the metamict phase on the nanometer scale.

The found positions of the boson peak for silica glass samples irradiated with fast neutrons are listed in the table. Noteworthy is a strong nonmonotonic dependence of the position of boson peak on the density of materials. This is an important point because the position of the boson peak is related to the medium-range order radius, which is proportional to the ratio of sound velocity to frequency of boson peak. In the simplest approximation, the medium-range order size R is defined by the expression [11]

$$R = S\frac{v}{\omega_0 c}. \quad (1)$$

Here, ω_0 is the frequency of boson peak (in cm^{-1}), c is the velocity of light, S is the factor of an order of unity (dependent on the cluster form: $S = 0.8$ for sphere),

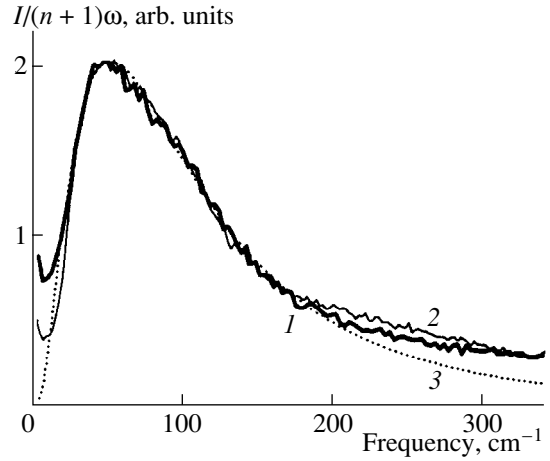

Fig. 3. Low-frequency Raman spectra (normalized to the maximum of the boson peak) for (*1*) vitreous and (*2*) metamict SiO_2 samples. (*3*) Lognormal distribution with a maximum at a frequency of 51 cm^{-1}.

and v is the Debye velocity determined by the relationship

$$\frac{3}{v^3} = \frac{1}{v_L^3} + \frac{2}{v_T^3}, \quad (2)$$

where v_L and v_T are the longitudinal and transverse velocities of light, respectively. The sound velocities for silica glass and the metamict phase can be taken, for example, from [12], in which the sound velocities were found from the experiments on the Mandel'shtam–Brillouin scattering: $v_L = 5.97$ km/s and $v_T = 3.78$ km/s for pure silica glass, and $v_L = 6.16$ km/s and $v_T = 3.89$ km/s for the metamict phase. The sound velocities measured for our sample (KI0) in the radio-frequency range and the results obtained in [12] coincide to within 1%. Thus, knowing the positions of boson peak and the sound velocities, one can estimate the characteristic medium-range order size by formula (1). For the KI0 and KI3 samples (irradiated at a maximum dose), the medium-range order size was evaluated with the sound velocities taken from [12], whereas, for the samples irradiated at an intermediate dose, the estimate was made by the linear approximation of sound velocities as a function of density. Since the sound velocity undergoes a very small relative change (<3.5%) upon metamictization as compared to the change in boson peak position (up to 37%), the accuracy of this approximation cannot substantially affect the drawn conclusions. For the KI0, KI1, KI2, and KI3 samples, the medium-range order sizes were estimated at 25, 24, 21, and 18 Å, respectively. Therefore, the medium-range order size considerably decreases in going from vitreous silicon dioxide to the metamict phase.

A nonmonotonic dependence of the position of the boson peak at a maximum on the density of materials is reflected in the nonmonotonic dependence of the

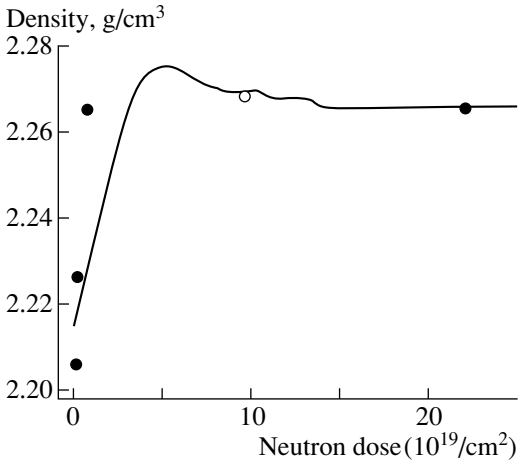

Fig. 4. Dependence of the sample density on the dose of irradiation with fast neutrons (circles); the solid line is taken from [13] for comparison.

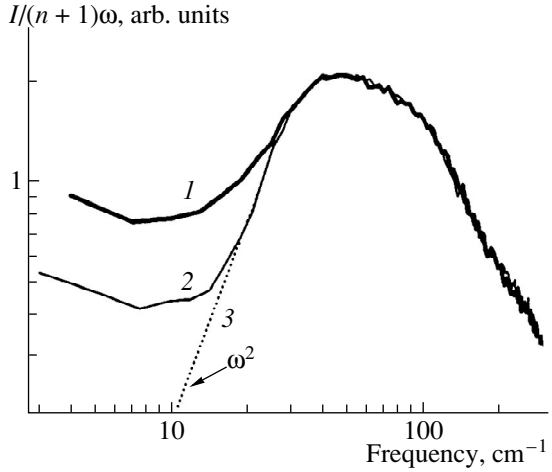

Fig. 5. Low-frequency Raman spectra (normalized to the maximum of the boson peak) for (*1*) vitreous and (*2*) metamict SiO_2 samples on the log–log scale. Dashed line *3* corresponds to the approximation by the quadratic power law at low frequencies.

medium-range order parameter *R*. For example, the positions of the boson peak and the relevant medium-range order sizes substantially differ for the KI2 and KI3 samples, whereas their densities are identical. An explanation for such a "paradox" is provided by the dependence of the density of silica glass (irradiated with fast neutrons) on the irradiation dose. Figure 4 demonstrates this dependence for samples used in our experiment (solid circles) and the data for the sample prepared in the same experiment, but not used in the present work (open circle). The solid line is taken from an analogues dependence reported in the review [13]. As can be seen from Fig. 4, the density of materials also exhibits nonmonotonic behavior with respect to the irradiation dose. Some deviation of the density data for our samples from the solid line in Fig. 4 can be caused by the difference in energies of neutrons used in two experiments. The metamict state itself, as is known (see, for example, [13]), does not depend on the neutron energy. It is evident that the states with the same density, but located on opposite sides of the maximum shown in Fig. 4 should be different because one of these states changes its structure upon further irradiation, while the structure of the other state remains unchanged. Thus, the difference in positions of the boson peak for the KI2 and KI3 samples indicates the physically different structure of these samples on the nanometer scale, even though their densities are identical.

It is worth noting that the positions of boson peak for the KI0 and KI1 samples are very close to each other, even though the densities of these samples differ significantly. Belitskiĭ *et al.* [2] examined the character of density relaxation in the KI1 sample and made the conclusion that the small irradiation dose initiated predominantly radiation-induced defects in this sample without transferring an appreciable part of the material to the metamict state. These authors assumed that the occurrence of the metamict state requires a certain critical concentration of defects [14]. The results of investigations into the low-frequency Raman scattering are also indirect evidence in support of this assumption.

2.3. Quasi-elastic light scattering. The term "quasi-elastic light scattering" is applied to the low-frequency part of Raman light scattering spectra for glasses (<20 cm^{-1}), which is characterized by an anomalous temperature dependence. The vibrational spectra of Raman light scattering follow the dependence $n(\omega) + 1$ for the Stokes component or $n(\omega)$ for the anti-Stokes component, whereas the quasi-elastic contribution increases with a rise in temperature considerably faster [15]. It is believed that the quasi-elastic light scattering is brought about by the relaxation motion in glasses whose rate increases with temperature (the so-called "fast" relaxation). At present, there has been no universally accepted theoretical description of the fast relaxation and its manifestation in the low-frequency Raman light scattering. The radiation-induced modification of vitreous SiO_2 provides an interesting opportunity to compare the characteristics of quasi-elastic light scattering in two different materials, but with the same chemical composition and at the same temperature, which can appreciably simplify theoretical interpretation.

Actually, a comparison of the intensities at low frequencies (<20 cm^{-1}) demonstrates a substantial difference in the samples irradiated with different doses (Figs. 2, 3). Figure 5 presents the reduced low-frequency spectra (shown in Fig. 3) for the unirradiated sample and the sample irradiated at a maximum dose on the log–log scale where the difference in the spectra at low frequencies is most clearly seen. The integral relaxation contribution to the low-frequency spectra

can be characterized by the δ quantity—the ratio of the integral relaxation contribution to integral vibrational contribution [16]. For the compete analysis of the relaxation contribution to the low-frequency spectra, it is necessary to investigate the Raman light scattering at very low temperatures (<10 K) and at very low frequencies (as small as 0.1 cm^{-1}) [17]. However, the amplitude of the relaxation spectrum can be evaluated from the intensity of the reduced spectrum at sufficiently low frequencies [18]. The relative change in the δ ratio for two glasses can be estimated by comparing the intensities at the same, sufficiently low frequency in the reduced spectra normalized to the position of the maximum and its value (as was done in Fig. 5). This estimation relies on the experimental fact that the width of the quasi-elastic scattering spectrum is proportional to the position of the maximum of the boson peak [19].

Our experimental data allow this estimation at frequencies of about 10 cm^{-1}, which can be considered as being sufficiently low (compared to the position of boson peak) and unaffected by the spurious contribution from the instrumental wing of the elastic line. For accurate estimation, it is necessary to subtract the vibrational contribution at the given frequencies. To accomplish this, the reduced spectrum was approximated by the power behavior ω^2. This corresponds to the approximation of decaying plane waves, which is assumed to be valid at frequencies considerably below the maximum of the boson peak [18]. Such a frequency dependence was observed earlier [20] for covalent glasses in the low-frequency region (<10 cm^{-1}) at rather low temperatures ($T \sim 10$ K) when the vibrational spectrum also dominates at low frequencies. In the case of the metamict phase, this dependence clearly manifests itself even at room temperature in the frequency range 20–30 cm^{-1} (Fig. 5). In order to estimate the vibrational contribution at a frequency of 10 cm^{-1}, we used the extrapolation of this dependence to lower frequencies as shown by line *3* in this figure.

The found quasi-elastic (or relaxation) contribution at a frequency of 10 cm^{-1}, which, as discussed above, is proportional to the integral contribution of the relaxation spectra, is depicted in Fig. 6 as a function of the specific density of samples. Interestingly, there is a clear correlation between the intensity of relaxation spectrum and the specific volume. This correlation naturally corresponds to the free volume theories. The theories relying on the free volume approach have long been in use to account for the viscosity properties of glass-forming materials above the glass transition temperature [21], whereas the currently available versions of this approach are efficient for descriptions of vitreous systems (see, for example, [22] and the references cited in this work). In [16], a similar correlation was revealed between the temperature dependence of the intensity of relaxation spectrum and the free volume, which was obtained by using the positron annihilation technique. The found correlation was illustrated by the

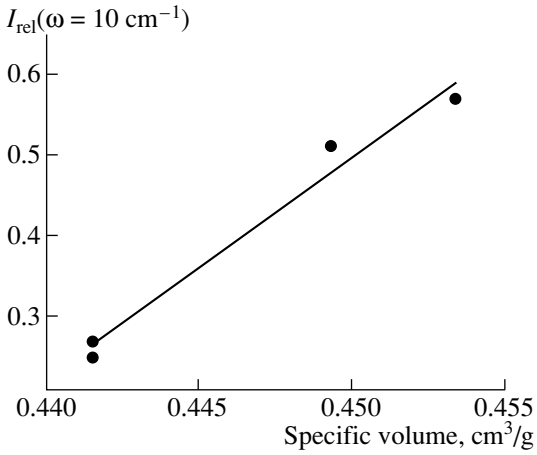

Fig. 6. Relaxation contribution to the low-frequency Raman spectrum at 10 cm^{-1} as a function of the specific density of samples. Solid line corresponds to a linear fitting.

example of four vitreous polymers [16]. This approach, as applied to polymers, is justified for reasons of a large difference between elastic constants for interchain interactions and those along polymeric chains. However, its extension to nonpolymeric glasses is not evident. The correlation revealed in the present work (Fig. 6) suggests that the given approach or its modification can also be efficient for covalent glasses. The found correlation is of particular value, because, as discussed above, the density is not a parameter characterizing the state of SiO_2; nonetheless, the specific volume is a good parameter describing fast relaxation intensity.

A linear fitting of the correlation between the intensity of the relaxation spectrum and the specific volume (shown by the solid line in Fig. 6) makes it possible to evaluate the density of vitreous (or metamict) SiO_2 in the absence of free volume. The line depicted in the figure gives the estimate $\rho = 2.31$ g/cm^3. In order to evaluate statistical and systematic errors, we performed similar calculations for a frequency of 16 cm^{-1}, which led to an estimate of the density of amorphous SiO_2 without free volume at $\rho = 2.29$ g/cm^3. It is of interest to compare this estimate with the model representations describing vitreous SiO_2 as consisting of the ordered domains separated by less ordered regions (the references to the models based on this approach are given in [13]). In these models, the domains are treated as having an ordering of the cristobalite or tridymite type, even if not completely crystalline. The densities of cristobalite and tridymite are equal to 2.32 and 2.26 g/cm^3, respectively. Therefore, our estimate of amorphous silicon dioxide without free volume (~2.30 g/cm^3) agrees well with the expected density of these clusters.

2.4. Low-temperature heat capacity. An important interesting point in the theory of low-frequency spectra of glasses is the calculation and explanation of the so-called coupling coefficient $C(\omega)$, which appears in the

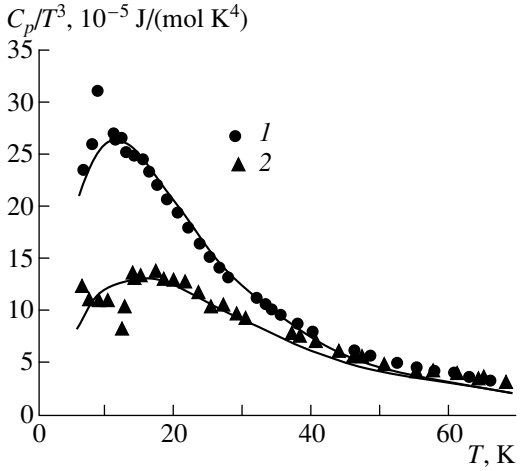

Fig. 7. Low-temperature heat capacity (divided by T^3) for (*1*) KI0 and (*2*) KI3 samples. Solid lines indicate the heat capacities calculated from the low-frequency Raman spectra.

Shuker–Gammon formula [23] relating the intensity of low-frequency Raman scattering $I(\omega)$ to the density of vibrational states $g(\omega)$

$$I(\omega) = C(\omega)g(\omega)\frac{n+1}{\omega}. \quad (3)$$

By now, it is established that $C(\omega)$ monotonically (linearly or almost linearly) increases with frequency of the low-frequency Raman scattering spectrum in the vicinity of the boson peak [24]. However, the theoretical justification of the $C(\omega)$ behavior remains the subject of discussions.

The behavior of $C(\omega)$ can be evaluated from measurements of the low-temperature heat capacity, which is related to the density of vibrational states by an integral expression. Assuming a certain dependence for $C(\omega)$, the density of vibrational states can be determined from experiments on the low-frequency Raman scattering, and then, the corresponding integral is compared with the experimental heat capacity. Earlier, this approach was used to reveal the frequency dependence of $C(\omega)$. It was found that the linear behavior of the coupling coefficient adequately describes the low-temperature heat capacity derived from the experimental Raman scattering spectra [20]. In these calculations, the magnitude of $C(\omega)$ remains as the fitting parameter. The investigation of glasses modified without changes in the chemical composition furnishes a unique opportunity to compare not only the frequency behavior in these glasses, but also the relative value of $C(\omega)$.

The heat capacities of the samples used in the present work—the unirradiated sample (KI0) and the sample irradiated at a maximum dose (KI3)—were measured in [1]. Figure 7 displays the low-temperature heat capacities divided by T^3 as is commonly accepted in the literature. It is clearly seen that the low-temperature heat capacities of irradiated and unirradiated samples differ in amplitude and position of the maximum. Every so often, the maximum in the low-temperature heat capacity of glasses is also referred to as the boson peak, because it reflects the spectral features of glasses near a maximum of the low-frequency Raman scattering spectrum. The heat capacity C_V is related to the density of vibrational states by the formula [25]

$$C_V = 3Nk_B\int_0^\infty g(\nu)(h\nu/k_BT)^2\frac{\exp(h\nu/k_BT)}{[\exp(h\nu/k_BT)-1]^2}d\nu. \quad (4)$$

Here, N is the number of atoms per gram (in our case, this quantity is proportional to the density), ν is the frequency in Hz, k_B is Boltzmann's constant, and h is Planck's constant. Assuming that the dependence $C(\omega) \propto \omega$ leads to the best result [20, 24], we introduce the constant A

$$C_V(\omega) = A\omega. \quad (5)$$

Then, formula (4) can be rewritten with the use of relationships (3) and (5) in the form

$$C_V = \rho B\int_0^\infty \frac{I(\omega)}{n+1}(\beta\omega/T)^2\frac{\exp(\beta\omega/T)}{[\exp(\beta\omega/T)-1]^2}d\omega. \quad (6)$$

Here, $\beta = 1.439$ K/cm^{-1}, ρ is the density of a sample, and B is a constant defined by the expression

$$B = \frac{3k_B}{AM}, \quad (7)$$

where M is the mean atomic weight. Integral (6) over the experimental dependence of $I(\omega)$ can be found by numerical integration. In the integration, we also used the approximation $I/((n+1)\omega) \propto \omega^2$ for low frequencies (Fig. 5) to avoid the errors introduced into the calculated heat capacity by relaxation contributions, which become frozen at these temperatures (~10–20 K). As was shown in [20], the contribution of the density of vibrational states to the low-temperature heat capacity at a frequency above 100 cm^{-1} is negligibly small. We restricted our integration to 150 cm^{-1}, at which the linear approximation for the coupling coefficient $C(\omega)$ is correct [24]. The fitting of the low-temperature heat capacity from the Raman scattering spectra of the unirradiated silica glass (KI0) was performed with the B constant as a free parameter. As can be seen, the numerical integral over the Raman scattering data (the solid line in Fig. 7) adequately describes the observed heat capacity. The calculation of the heat capacity from the low-frequency Raman spectrum (normalized to the intensity) of the irradiated sample (KI3), as already mentioned, was carried out using the same constant B as for the unirradiated sample. The heat capacity calculated for the irradiated sample KI3 also adequately describes the observed heat capacity. With allowance made for the fact that the Raman scat-

tering spectra were normalized to the intensity at 810 cm^{-1}, the equality of constants B implies the equality of constants A for irradiated and unirradiated samples in absolute units. Therefore, the $C(\omega)$ coefficients for vitreous and metamict phases are identical in their spectral dependence and absolute value. Note that the coupling coefficient is determined by the space integral of the vibration correlation function [23]. This suggests the equivalence of the vibration correlation function for vitreous and metamict phases at the same frequency. Hence, it follows that the metamict phase is "glasslike" on the nanometer scale.

Thus, the samples of amorphous SiO_2 in the vitreous state and in the phase state (metamict phase) obtained under irradiation with fast neutrons were studied by the Raman scattering spectroscopy. Analysis of the Raman scattering spectra led to the following inferences.

(1) The metamict phase exhibits a glasslike behavior of the low-frequency Raman scattering spectra (boson peak): their shape coincides with the spectral shape for vitreous SiO_2 and the universal spectral shape for glasses, and the coefficients of coupling between vibrations and light scattering are identical for these materials. Since the boson peak reflects the dynamic features of glasses on the nanometer scale, the conclusion can be drawn that the main nanometric fragments of SiO_2 glass are similar to those of its metamict phase.

(2) The characteristic medium-range order size estimated from the position of the boson peak decreases in the course of metamictization from 25 to 19 Å. In this case, the density is not a parameter characterizing the state of a material.

(3) The idea that the free volume of a vitreous material characterizes the intensity of fast relaxation is efficient in analyzing the properties of amorphous SiO_2. The density is the parameter characterizing the intensity of the relaxation spectrum with respect to the vibrational spectrum.

(4) The obtained estimate of amorphous SiO_2 without free volume provides support for the structural model that describes vitreous and metamict silicon dioxides as consisting of ordered clusters (an ordering of the cristobalite and tridymite type) separated by more disordered regions.

ACKNOWLEDGMENTS

This work was supported by the Interdisciplinary Science Fund at the Russian Foundation for Basic Research of the Siberian Division of the Russian Academy of Sciences (project no. 99-02-16697) and by the Young Investigator Grant from the Presidium of the Siberian Division of the Russian Academy of Sciences.

REFERENCES

1. G. A. Berezovskiĭ, O. D. Davronov, and L. M. Landa, Preprint No. 87-6, INKh SO AN SSSR (Inst. of Inorganic Chemistry, Siberian Division, Russian Academy of Sciences, 1987).
2. I. A. Belitskiĭ, O. D. Davronov, V. A. Drebushchak, and A. Z. Patashinskiĭ, Preprint No. 87-156, IYaF SO AN SSSR (Inst. of Nuclear Physics, Siberian Division, Russian Academy of Sciences, 1987).
3. O. D. Davronov, V. E. Istomin, A. P. Shebanin, and M. Ya. Shcherbakova, in *Proceedings of the Ninth Ampere Summer School, Novosibirsk, Russia, 1987*.
4. A. Pasquarello and R. Car, Phys. Rev. Lett. **80** (23), 5145 (1998).
5. T. Uchino, Y. Tokuda, and T. Yoko, Phys. Rev. B: Condens. Matter **58** (9), 5322 (1998).
6. J. B. Bates, J. Chem. Phys. **56**, 1910 (1972).
7. V. K. Malinovsky and A. P. Sokolov, Solid State Commun. **37** (9), 751 (1986).
8. I. Pocsik and M. Koos, in *Disordered Systems and New Materials* (WSP, Singapore, 1989), p. 539.
9. V. K. Malinovsky, V. N. Novikov, and A. P. Sokolov, J. Non-Cryst. Solids **90**, 485 (1987).
10. S. R. Elliott, *Physics of Amorphous Materials* (Longman Scientific & Technical, London, 1990).
11. E. Duval, A. Boukenter, and B. Champagnon, Phys. Rev. Lett. **56** (19), 2052 (1986).
12. F. Terki, C. Levelut, M. Boisser, *et al.*, Phys. Rev. B: Condens. Matter **53** (5), 2411 (1996).
13. L. Douillard and J. P. Duraund, J. Phys. III **6** (12), 1677 (1996).
14. A. Z. Patashinskiĭ, Preprint No. 87-82, IYaF SO AN SSSR (Inst. of Nuclear Physics, Siberian Division, Russian Academy of Sciences, 1987).
15. G. Winterling, Phys. Rev. B: Solid State **12** (6), 2432 (1975).
16. V. N. Novikov, A. P. Sokolov, B. Strube, *et al.*, J. Chem. Phys. **107** (4), 1057 (1997).
17. N. V. Surovtsev, J. A. Wiedersich, V. N. Novikov, *et al.*, Phys. Rev. B: Condens. Matter **58**, 14888 (1998).
18. J. Jäckle, in *Amorphous Solids: Low Temperature Properties*, Ed. by W. A. Phillips (Springer-Verlag, Berlin, 1981), p. 135.
19. V. N. Novikov, Phys. Rev. B: Condens. Matter **58** (10), 8367 (1998).
20. A. P. Sokolov, A. Kisliuk, D. Quitmann, *et al.*, Phys. Rev. B: Condens. Matter **48** (10), 7692 (1993).
21. M. H. Cohen and D. Turnbull, J. Chem. Phys. **31** (5), 1164 (1959).
22. D. S. Sanditov and S. Sh. Sangadiev, Fiz. Khim. Stekla **24** (4), 417 (1998) [Glass Phys. Chem. **24** (4), 285 (1998)].
23. R. Shuker and R. W. Gammon, Phys. Rev. Lett. **25** (4), 222 (1970).
24. A. P. Sokolov, U. Buchenau, W. Steffen, *et al.*, Phys. Rev. B: Condens. Matter **52** (14), R9815 (1995).
25. Ch. Kittel, *Introduction to Solid State Physics*, 5th ed., (Wiley & Sons, New York, 1976; Nauka, Moscow, 1978).

Translated by O. Borovik-Romanova

Physics of the Solid State, Vol. 42, No. 1, 2000, pp. 72–78. Translated from Fizika Tverdogo Tela, Vol. 42, No. 1, 2000, pp. 69–75.

DEFECTS, DISLOCATIONS AND PHYSICS OF STRENGTH

Acoustoplastic Effect and the Stress Superimposition Mechanism

G. A. Malygin

Ioffe Physicotechnical Institute, Russian Academy of Sciences, Politekhnicheskaya ul. 26, St. Petersburg, 194021 Russia

Received May 31, 1999

Abstract—The mechanism of the acoustoplastic effect is discussed which arises when an oscillatory stress of an acoustic frequency is superimposed during quasi-static deformation of a crystal. The kinetics of the acoustoplastic effect and its dependence on the amount of plastic deformation, amplitude of acoustic-frequency stresses, temperature, and strain rate are investigated in terms of the stress superimposition mechanism by a computer simulation method. *© 2000 MAIK "Nauka/Interperiodica".*

1. INTRODUCTION

The acoustoplastic (AP) effect is a decrease in the flow stress during deformation at a constant strain rate [1–12] or an increase in strain rate during plastic deformation under a constant stress [4, 13, 14], which is observed when an oscillatory stress of a sonic or an ultrasonic frequency is superimposed to the deforming crystal. Experimentally, this effect has been studied extensively and found practical use [15, 16]. However, its mechanism is still discussed [8–12, 17, 18]. The most popular is a theoretical model based on the stress superimposition mechanism [4, 5, 13, 19–22]. According to this model, when an oscillatory (acoustic) stress is superimposed to a deforming crystal under a quasi-static stress, the strain rate of thermally activated plastic deformation increases giving rise to relaxation of elastic stresses (in constant strain rate tests) or to an increased creep rate (under constant-stress conditions).

However, recent observations of the low sensitivity of the AP effect to temperature [8, 12] and strain rate [5, 7] have cast some doubt on the assumption of thermally activated dislocation motion through obstacles when oscillatory stresses are applied to a crystal. The suggestion has been made that, basically, the AP effect has an athermic nature and, under oscillatory stresses, dislocations surmount athermic obstacles and internal stress fields by interacting with each other [8–12]. Some doubts are also cast upon the stress superimposition mechanism itself [8–12, 17, 18].

In this paper, we perform computer simulation of the AP effect and show that under both quasi-static-deformation and creep conditions, the stress superimposition mechanism, in combination with dislocation overcoming short-range obstacles with the aid of thermal agitation, agrees best with the experiment. Nonetheless, some problems and contradictions associated with this mechanism remain to be resolved, which we will discuss in the Conclusion.

Our computer simulation of the AP effect is based on a known phenomenological model involving the stress superimposition mechanism and the assumption of the thermally activated plastic deformation [4, 5, 13, 19–22]. In this paper, the model is developed further and used for the first time to investigate the kinetics of the AP effect and the dependence of its magnitude on the amount of plastic deformation, temperature, and strain rate.

2. STRESS SUPERIMPOSITION MECHANISM

According to the stress superimposition mechanism, an oscillatory stress with amplitude τ_m and frequency ω causes a periodic variation in the effective stress

$$\tau^*_{\sim}(t) = \tau^* + \tau_m \cos\omega t, \tag{1}$$

which determines the rate of dislocation overcoming short-range obstacles with the aid of thermal agitation. In equation (1), τ^* is the effective stress in the absence of acoustic stresses,

$$\tau^* = \tau - \tau_f - \tau_\mu, \tag{2}$$

τ is the stress applied to the crystal, τ_f is the athermal component of friction stress due to the interaction of dislocations with impurity atoms and their clusters, $\tau_\mu = \tau_\mu(\varepsilon)$ is the strain hardening of the crystal due to the interaction between dislocations, and ε is the plastic strain.

The rate of plastic deformation is governed by the Arrhenius equation

$$\dot{\varepsilon} = \dot{\varepsilon}_v \exp\left[-\frac{H(\tau^*)}{kT}\right]. \tag{3}$$

Here, $H(\tau^*)$ is the activation energy; T is temperature; k is the Boltzmann constant; and $\dot{\varepsilon}_v$ is the preexponential factor (depending on the density of mobile dislocations), which will be assumed to be constant. When the crystal is loaded at a constant strain rate $\dot{\varepsilon}_0$ in a machine with effective modulus E, the anelastic relax-

1063-7834/00/4201-0072$20.00

ation rate of the stress applied to the crystal is given by the expression

$$\frac{d\tau}{Edt} = \dot{\varepsilon}_0 - \dot{\varepsilon}. \tag{4}$$

Solving the system of equations (1)–(4), we will find the AP effect and its dependence on the length of time for which the acoustic stress is applied, the amplitude and frequency of this stress, the test temperature, and also on the strain rate $\dot{\varepsilon}_0$ and the amount of deformation $\varepsilon = \dot{\varepsilon}_0 t$ controlled by the machine.

To solve these equations analytically, we linearize the activation energy in (3) as a function of the effective stress

$$H(\tau^*) = H_0 - V\tau^*, \tag{5}$$

where $V = -dH/d\tau$ is the activation volume. In this case, after substitution of (3) into (4), the variables τ and t can be separated [19–22] and we obtain the following expressions for the stress applied to the crystal: in the absence of the acoustic stress,

$$\tau(t) = E\dot{\varepsilon}_0 t - \frac{kT}{V}\ln[1 - q(t)],$$

$$q(t) = \frac{VE}{kT}\dot{\varepsilon}_0(0)\int_0^t \exp\left\{\frac{V}{kT}[E\dot{\varepsilon}_0 t - \tau_f - \tau_\mu(\varepsilon)]\right\}dt, \tag{6}$$

and in the presence of the acoustic stress,

$$\tau_\sim(t) = E\dot{\varepsilon}_0 t - \frac{kT}{V}\ln[1 - q_\sim(t)],$$

$$q_\sim(t) = \frac{VE}{kT}\dot{\varepsilon}_0(0) \times \int_{t_1}^t \exp\left\{\frac{V}{kT}[E\dot{\varepsilon}_0 t - \tau_f - \tau_\mu(\varepsilon) + \tau_m\cos\omega t]\right\}dt, \tag{7}$$

where $\dot{\varepsilon}(0) = \dot{\varepsilon}_\nu \exp(-H_0/kT)$, t_1 is the time at which the oscillatory stress is applied. The magnitude of the AP effect $\Delta\tau(t) = \tau_\sim(t) - \tau(t)$ is obtained to be

$$\Delta\tau(t) = \frac{kT}{V}\ln\frac{1 + q(t)}{1 + q_\sim(t)}. \tag{8}$$

Equation (6) gives the time dependence of the applied stress $\tau(t)$ and, therefore, the stress–strain (τ–ε) curve of the crystal in the linear approximation (5) in the absence of the oscillatory stress. Figure 1a shows this curve (curve *1*) in the (τ/E–t/t_0) or, equivalently, (τ/E–$\varepsilon/\varepsilon_0$) coordinates, where $t_0 = kT/VE\dot{\varepsilon}_0$. The parameters are taken to be $\varepsilon_0 = kT/VE = 10^{-4}$, $\tau_f/E = 2 \times 10^{-3}$, $\dot{\varepsilon}(0)/\dot{\varepsilon}_0 = 10^6$, $\tau_\mu(\varepsilon) = \chi\varepsilon^{1/2}$; and $\chi/E = 5 \times 10^{-2}$. Curve *2* in this figure is the time dependence of the plastic strain rate during deformation of the crystal,

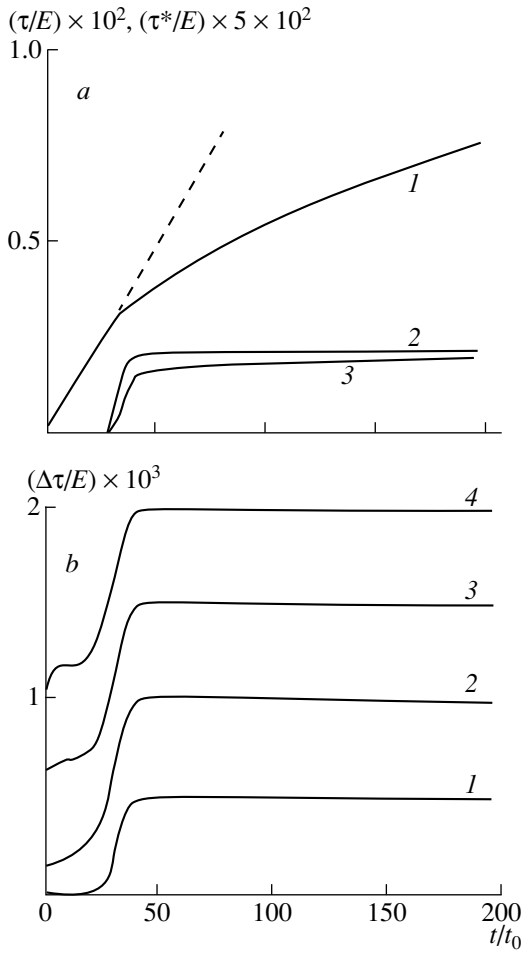

Fig. 1. (a) Stress–strain (time) curve (curve *1*), the time dependencies of the effective stress (curve *2*) and of the plastic strain rate (curve *3*); and (b) the AP effect as a function of the time for which the stresses were applied for the oscillatory-stress amplitude τ_m/E equal to 5×10^{-4} (curve *1*), 10^{-3} (*2*), 1.5×10^{-3} (*3*), and 2×10^{-3} (*4*).

$$\dot{\varepsilon}(t) = \frac{\dot{\varepsilon}(0)\exp\left[\frac{V}{kT}(E\dot{\varepsilon}_0 t - \tau_f - \tau_\mu(\dot{\varepsilon}_0 t))\right]}{1 + q(t)} = \dot{\varepsilon}(0)\exp\left[\frac{V}{kT}(\tau - \tau_f - \tau_\mu(\dot{\varepsilon}_0 t))\right]. \tag{9}$$

On the elastic portion of the $\tau(t)$ curve, the plastic strain rate is virtually zero, but near the yield point it rises steeply and rapidly approaches the strain rate $\dot{\varepsilon}_0$ controlled by the test machine. Curve *3* in Fig. 1a is the time (or strain) dependence of the effective stress

$$\tau^*(t) = \frac{H_0 - kT\ln(\dot{\varepsilon}_\nu/\dot{\varepsilon}(t))}{V} \tag{10}$$

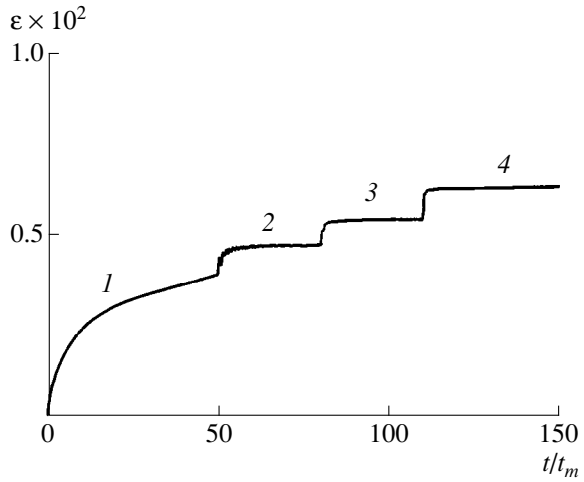

Fig. 2. Creep curves in the absence (portion *1*) and in the presence (portions *2*–*4*) of the superimposed oscillatory stress with amplitude τ_m/E equal to 2×10^{-4} (*2*), 3×10^{-4} (*3*), and 4×10^{-4} (*4*).

for $H_0/kT = 30$, $\dot{\varepsilon}_v = 10^7$ s^{-1}, and a fixed value of the activation volume. On the elastic portion of curve *3*, we have $\tau < \tau_f$ and, hence, the stress level is not high enough for dislocations to become mobile. This occurs at $\tau > \tau_f$, and mobile dislocations make plastic deformation possible. On further deformation, the effective stress becomes constant, its magnitude being determined by the controlled strain rate $\dot{\varepsilon}_0$.

It is obvious that, owing to the oscillatory stress in (7), the plastic strain rate becomes higher during positive half-cycles, which leads to relaxation of the applied stress determined by (8). As an illustration, Fig. 1b shows the time dependence of the magnitude of the AP effect $\Delta\tau = |\Delta\tau|$ calculated from (8) for the case where the acoustic stress is applied coincidentally with the beginning of the crystal deformation [$t_1 = 0$ in (7)]. In this figure, $\Delta\tau(t)/E$ is plotted against t/t_0 for four values of the amplitude of the oscillatory stress (curves *1* to *4*). It is seen that the AP effect is nonzero on the anelastic portion of the stress–strain curves if the amplitude of the oscillatory stress is so large that the effective stress is positive and can produce an increase in the plastic strain rate high enough for the relaxation of the applied stress to occur. When the plastic deformation occurs everywhere in the crystal, the magnitude of the AP effect increases sharply and rapidly approaches its steady-state value

$$\Delta\tau = \frac{kT}{V}\ln\frac{\dot{\varepsilon}_\omega}{\dot{\varepsilon}_0} = \frac{kT}{V}\ln I_0(V\tau_m/kT), \qquad (11a)$$

where

$$\dot{\varepsilon}_\omega = \dot{\varepsilon}_0\omega\int_0^{2\pi}\exp\left(\frac{V\tau_m}{kT}\cos\omega t\right)dt = \dot{\varepsilon}_0 I_0(V\tau_m/kT) \qquad (11b)$$

is the steady-state plastic strain rate in the presence of the oscillatory stress [3, 4] and $I_0(x)$ is the modified Bessel function of order zero. Experimental curves similar to those presented in Fig. 1b were observed in [7, 10].

Concluding the section, we consider the AP effect under low-temperature (logarithmic) creep conditions. In this case, the plastic strain rate (in the absence and in the presence of the oscillatory stress, respectively) is given by

$$\dot{\varepsilon} = \dot{\varepsilon}_v\exp\left[-\frac{H_0 - V(\tau - \tau_f - \tau_\mu(\varepsilon_0')) - \theta\varepsilon}{kT}\right], \qquad (12a)$$

$$\dot{\varepsilon}_\sim = \dot{\varepsilon}_v \qquad (12b)$$

$$\times\exp\left[-\frac{H_0 - V\tau - \tau_f - \tau_\mu(\varepsilon_1') - (\theta\varepsilon_\sim + \tau_m\cos(\omega t))}{kT}\right],$$

where $\theta = d\tau_\mu/d\varepsilon$ is the strain hardening coefficient, ε_0' is the strain jump at the instant the static stress is applied, and ε_1 is the strain at the moment the acoustic stress is applied. Integrating (12) gives the strain in the process of logarithmic creep

$$\varepsilon = \frac{kT}{V\theta}\ln(1 + t/t_m),$$
$$t_m^{-1} = \dot{\varepsilon}_v\exp\left[-\frac{H_0 - V(\tau - \tau_f - \tau_\mu(\varepsilon_1))}{kT}\right], \qquad (13a)$$

$$\varepsilon_\sim = \frac{kT}{V\theta}\ln[1 + q_\sim(t)],$$
$$q_\sim(t) = t_m^{-1}\int_{t_1}^{t}\exp\left(\frac{V\tau_m}{kT}\cos(\omega t)\right)dt. \qquad (13b)$$

Figure 2 shows the creep function given by (13a) (curve *1*) and by (13b) (curves *2* to *4*). In the latter case, the dimensionless amplitude of the oscillatory stress $V\tau_m/kT$ equals 2, 3, and 4, respectively. The magnitude of the AP effect under logarithmic creep conditions $\Delta\varepsilon = \varepsilon_\sim - \varepsilon$ is equal to

$$\Delta\varepsilon = \frac{kT}{V\theta}\ln\frac{1 + q_\sim(t)}{1 + t/t_m}. \qquad (14a)$$

Taking the time average of (12b) gives

$$\Delta\varepsilon = \frac{kT}{V\theta}\ln\frac{1 + (t/t_m)I_0(V\tau_m/kT)}{1 + t/t_m}$$
$$\approx \frac{kT}{V\theta}\ln I_0\left(\frac{V\tau_m}{kT}\right). \qquad (14b)$$

The dependencies similar to those presented in Fig. 2 were observed in [4, 13, 14]. It was found in [13] that when the time for which the oscillatory stress was

applied was longer than several seconds, the strain jump was described by (14b) for different values of the amplitude τ_m. From (14b) it follows that the magnitude of the AP effect equals $\Delta\varepsilon = \tau_m/\theta$ when the oscillatory stress is high enough ($\tau_m \gg kT/V$).

3. THE KINETICS OF THE ACOUSTOPLASTIC EFFECT

Figure 3 shows the time dependence of the applied stress during loading and unloading as calculated from (7) for the case where oscillatory stress pulses of short duration ($\Delta t = 3t_0$) are applied at some instants of time (labeled *1* to *6* in the figure) with amplitude $\tau_m/E = 10^{-3}$ and frequency $\omega = 2\pi t_0^{-1}$. It is seen that the AP effect takes place during both loading and unloading [8, 10]. During unloading, the calculated plastic strain rate and the effective stress decrease; hence, this process is opposite in direction to that taking place during loading (Fig. 1a). In [8, 10], the AP effect was observed to be of an opposite sign at the final stage of unloading, the reason for which is still unclear. In our computer simulation, the change in sign of the AP effect does not occur.

In order to elucidate during which half-cycles of the oscillatory stress the AP effect occurs, the oscillatory stress pulses are taken separately to consist of complete cycles (instant *2* in Fig. 3), of positive half-cycles only (instant *3*), and of negative half-cycles only (instant *4*). It is seen that the presence of positive half-cycles leads to an increase in the effective stress giving rise to relaxation of the applied stress (instants *2* and *3*). During negative half-cycles, the effective stress decreases thereby causing the applied stress to increase slightly (instant *4*) because the plastic strain rate becomes lower in comparison with the controlled strain rate $\dot{\varepsilon}_0$; hence, the AP effect disappears.

Calculations show that the occurrence of the AP effect is not due to the oscillatory character of additionally applied stresses, but depends crucially on whether they increase or decrease the effective stress. Instant *5* in Fig. 3 corresponds to the application to the crystal of a rectangular positive stress pulse of the same duration and amplitude as at instants *2* and *3*. It is seen that in the case of the positive pulse the AP effect is qualitatively the same, but the magnitude of the stress relaxation is somewhat larger.

Figure 4 shows the calculated time dependence of the AP effect for amounts of strain corresponding to the steady-state values of $\tau*$ and $\Delta\tau$ (see Figs. 1a and 1b, respectively) and for different values of the amplitude of the oscillatory stress. The curves are seen to consist of two different portions. On the initial portion, the relaxation of the applied stress is fast, while the other portion corresponds to noticeably slower stress relaxation. This character of the dependence of $\Delta\tau$ on the length of time during which the oscillatory stress is applied is explained by the fact that the plastic strain

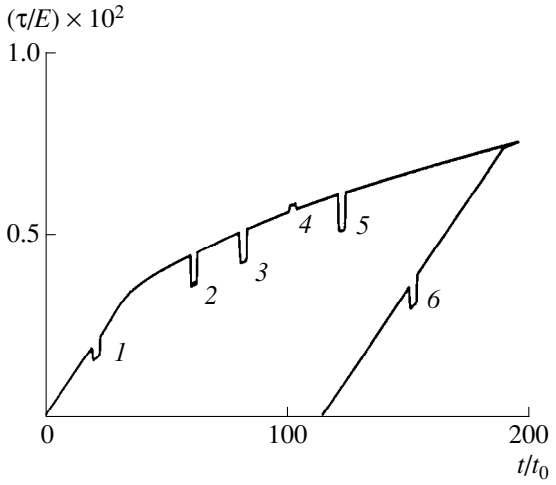

Fig. 3. Dependence of the AP effect on the sign of the oscillatory stress: portions *1*, *2*, and *6* correspond to complete cycles of the oscillatory stress; portions *3* and 5, to positive half-cycles only; and portion *4*, to negative half-cycles only.

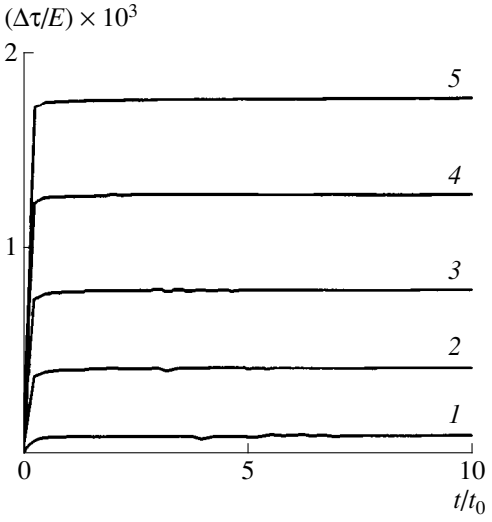

Fig. 4. Dependence of the AP effect on the time for which the acoustic stress is superimposed with amplitude τ_m/E equal to 2×10^{-4} (curve *1*), 6×10^{-4} (*2*), 10^{-3} (*3*), 1.5×10^{-3} (*4*), and 2×10^{-3} (*5*).

rate increases exponentially with the oscillatory-stress amplitude; hence, the rate of stress relaxation also increases and higher steady-state values of $\Delta\tau$ can be reached for the same time t_0.

According to [11], the existence of portions of AP-effect curves with fast stress relaxation is one of the reasons for the athermal nature of obstacles that dislocations overcome when acoustic stresses are applied to a crystal. The results presented in this paper show that this character of the kinetics of the AP effect is naturally explained in terms of the stress superimposition

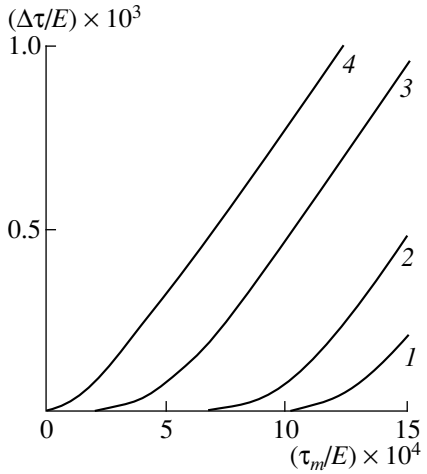

Fig. 5. AP effect as a function of the amplitude of the acoustic stress superimposed for the time $\Delta t = 5t_0$ at different moments during loading: $t/t_0 = 5$ (curve *1*), 15 (*2*), 25 (*3*), and 60 (*4*).

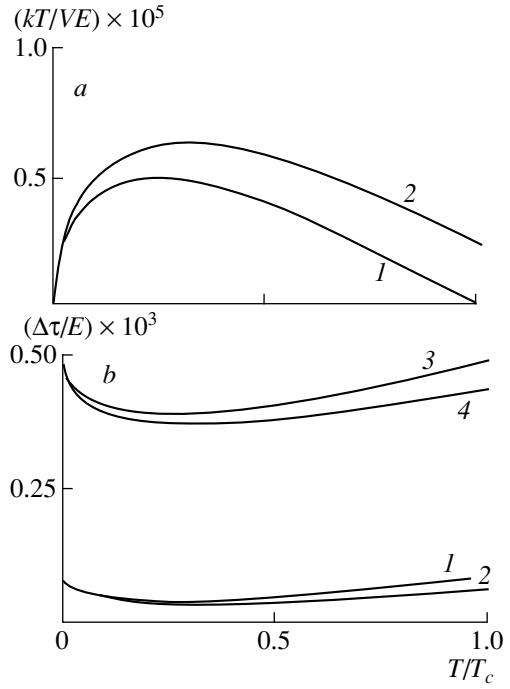

Fig. 6. (a) Temperature dependence of the parameter kT/V for two different magnitudes of the strain rate: $\dot{\varepsilon}_1$ (curve *1*) and $\dot{\varepsilon}_2 > \dot{\varepsilon}_1$ (curve *2*) and (b) temperature dependence of the AP effect for two different magnitudes of the oscillatory-stress amplitude, τ_{m1} (curves *1* and *2*) and $\tau_{m2} > \tau_{m1}$ (curves *3* and *4*), and for two different strain rates, $\dot{\varepsilon}_1$ (curves *1* and *3*) and $\dot{\varepsilon}_2 > \dot{\varepsilon}_1$ (curves *2* and *4*).

mechanism and thermally activated dislocation motion over barriers.

Figure 5 shows the dependence of the AP effect on the oscillatory-stress amplitude as calculated from (8) for different amounts of plastic strain, i.e., at different moments t during loading (see Fig. 1a). As in Fig. 1b, the magnitude of the AP effect increases with the amount of deformation. When $\Delta\tau(\tau_m)$ is plotted against $\ln I_0(V\tau_m/kT)$, it is seen that dependence (11a) takes place for all values of the oscillatory-stress amplitude only if the amount of deformation corresponds to a steady-state value of $\Delta\tau$ in Fig. 1b.

As for the dependence of the AP effect on the frequency of oscillatory stresses, it was found in [20] that the effect is independent of the frequency if $\omega \gg \omega_0$, where $\omega_0 = t_0^{-1}$ and $t_0 = kT/VE\dot{\varepsilon}_0$ is the stress relaxation time. At $\dot{\varepsilon}_0 = 10^{-6}$–$10^{-2}$ s^{-1} and $kT/VE \approx 10^{-4}$, we have $\omega_0 \approx 10^{-2}$–10^2 Hz. Therefore, one might expect the AP effect to be frequency independent in the range of sonic and ultrasonic frequencies.

4. THE TEMPERATURE AND RATE DEPENDENCES OF THE AP EFFECT

The fact that the AP effect depends only weakly on temperature and strain rate is one of the reasons for the athermal nature of obstacles that dislocations overcome when acoustic stresses are applied to a crystal. According to (11a), the steady-state AP effect depends on temperature and strain rate through the parameter $kT/V = \partial\tau^*/\partial\ln\dot{\varepsilon}$, which is the sensitivity coefficient of the flow stress to the strain rate. To calculate this dependence, information is needed about the activation energy for plastic deformation as a function of the effective stress.

Generally, $H(\tau^*)$ can be written in the form [23]

$$H(\tau^*) = H_c[1 - (\tau^*/\tau_c)^p]^q = kT\ln(\dot{\varepsilon}_v/\dot{\varepsilon}), \quad (15)$$

where H_c, τ_c, p, and q are parameters of an activation barrier ($0 < p < 1$ and $1 < q < 2$). At $p = 1/2$ and $q = 2$, which corresponds to the case where dislocations overcome barriers such as impurity atoms in a solid solution, we obtain

$$\frac{kT}{V(T,\dot{\varepsilon})} = \frac{kT_c}{V_c}\left(\frac{T}{T_c}\right)^{1/2}\left[1 - \left(\frac{T}{T_c}\right)^{1/2}\right],$$

$$T_c = \frac{H_c}{k\ln(\dot{\varepsilon}_v/\dot{\varepsilon})}, \quad (16)$$

where $V_c = H_c/4\tau_c$. At $H_c = 0.2$–0.6 eV and $\ln(\dot{\varepsilon}_v/\dot{\varepsilon}) = 23$, we have $T_c = 100$–300 K. The plot of the temperature dependence of the parameter kT/V is a parabola convex upwards, with its vertex being at the point $T_m = 0.25T_c$ (Fig. 6a, curve *1*, corresponding to $kT_c/V_cE = 10^{-3}$ and $\dot{\varepsilon} = 10^{-4}$ s^{-1}). The temperature T_c and the parameter kT/V increase with strain rate (see curve *2*, corresponding to $\dot{\varepsilon} = 10^{-2}$ s^{-2}).

Figure 6b shows the temperature dependence of the AP effect calculated from (11a) and (16) for $\tau_m/E = 1 \times 10^{-4}$ (curves *1* and *2*) and $\tau_m/E = 5 \times 10^{-4}$ (curves *3* and *4*) and for two values of the strain rate: $\dot{\varepsilon} = 10^{-4}\ s^{-1}$ (curves *1* and *3*) and $10^{-2}\ s^{-1}$ (curves *2* and *4*). It is seen that at $T > T_m$, the AP effect increases only slightly with temperature, which is in agreement with findings of [9, 12]. At $T < T_m$, in contrast, the AP effect decreases with increasing temperature. It is also seen that the AP effect decreases slightly with increasing strain rate. In [8], the reverse situation was observed for aluminum: the AP effect increased with the strain rate. As was pointed out in [7], this may be due to the fact that mobile dislocations are locked by atmospheres of impurity atoms (dynamical aging). It is known that in this case, as the strain rate is increased, the parameter kT/V becomes smaller [24] and, hence, the AP effect increases.

Let us consider the dependence of the AP effect on the concentration of impurity atoms c in a solid solution. In (16), we have $V_c^{-1} \sim \tau_c \sim c^{1/2}$ [25], and in the case of small oscillatory-stress amplitudes, using the approximation $\ln I_0(x) \sim x^2$ in (11a), we obtain

$$\Delta\tau \approx \frac{V}{4kT}\tau_m^2 \sim c^{-1/2}. \qquad (17)$$

Thus, at small amplitudes, the AP effect decreases as the concentration of impurity atoms increases. The dependence $\Delta\tau(\tau_m)$ becomes linear in the case of $\ln I_0(x) \sim x$ at a characteristic amplitude $\tau_{mc} \approx kT/V \sim c^{1/2}$, which increases with c. These results are in agreement with the findings of [11]. It was also found in [11] that at large amplitudes, $\Delta\tau(\tau_m)$ curves for crystals with different concentrations of impurity atoms approached each other and the reverse situation was observed: the AP effect was larger in a more concentrated alloy. However, this does not occur in our model.

Concluding this section, the following comment should be made. The AP effect was investigated theoretically in [5, 7, 22] and instead of the Arrhenius dependence of the plastic strain rate on temperature and stress (3), the power-law dependence was used,

$$\dot{\varepsilon} = A\left(\frac{\tau - \tau_O}{\tau_c}\right)^n, \qquad (18)$$

which is more consistent with the experiment, particularly in the case of alkali halide crystals for which $n = n(T)$. It was shown in [23] that the power-law dependence (18) follows from the Arrhenius equation (3) near the Orowan stress τ_O associated with a bowing of dislocations moving through a cluster of impurity atoms or a dispersion of particles; in that case, $n = H_c/kT$.

5. CONCLUSION

Thus, the experimental data on the acoustoplastic effect, which take place when oscillatory (acoustic) stresses are superimposed on a static stress applied to a crystal, are adequately described in terms of the stress superimposition mechanism combined with thermally activated plastic deformation. In particular, the character of the calculated dependencies of the AP effect on the oscillatory-stress amplitude under different loading conditions and the influence on it of different structure factors are consistent with the experiment. However, there are a number of facts and contradictions which call for further investigation in our model.

One of the questions is the association of the AP effect and the amplitude-dependent internal friction (ADIF), which were observed in the same experiment [8–12] and are due to the motion of the same dislocations. Although these two effects seem to be associated, it is clear that they have different physical natures. Indeed, in the case of the AP effect, a superimposed oscillatory stress causes relaxation of the applied stress because of an increase in the plastic strain rate, as demonstrated in this paper, whereas the ADIF is associated with energy dissipation due to the application of the acoustic stress and to the cyclic plastic deformation it causes in the crystal. In the latter case, therefore, the energetic aspect of the problem, rather than the force aspect, is of importance. Of course, the effects under question may be associated, but that association will be indirect in nature.

Another question arises when one considers the character of the motion of dislocations under the action of oscillatory stresses. The models proposed for the ADIF are based on the assumption of reciprocal motion of dislocations which leads to dissipation of the energy associated with oscillatory stresses. On the other hand, the stress superimposition mechanism of the AP effect assumes no reciprocating motion of dislocations; the decrease in the effective stress during negative half-cycles produces a decrease in the dislocation velocity and dislocations cease to move when the effective stress becomes either zero or negative [22].

These inconsistencies between the mechanisms of the AP effect and ADIF discussed in the literature [7, 8–12, 17, 18] show that further experimental and theoretical investigations of these effects should be conducted.

REFERENCES

1. F. Blaha and B. Langenecker, Naturwissenschaften **42** (20), 556 (1955).
2. O. Izumi, K. Oyama, and Y. Suzuki, Trans. Jpn. Inst. Met. **7** (3), 158 (1966).
3. G. S. Baker and S. H. Carpenter, J. Appl. Phys. **38**, 1586 (1967).
4. R. Friedrich, G. Kaiser, and W. Pechhold, Z. Metallkd. **60** (5), 390 (1969).

5. T. Endo, K. Suzuki, and M. Ishikawa, Trans. Jpn. Inst. Met. **20** (12), 706 (1979).
6. H. O. Kirchner, W. K. Kromp, F. B. Prinz, *et al.*, Mater. Sci. Eng. **68** (2), 197 (1985).
7. T. Ohgaku and N. Takeuchi, Phys. Status Solidi A **102** (1), 293 (1987).
8. K. V. Sapozhnikov and S. B. Kustov, Fiz. Tverd. Tela (St. Petersburg) **39**, 1794 (1997) [Phys. Solid State **39**, 1601 (1997)].
9. K. V. Sapozhnikov and S. B. Kustov, Fiz. Tverd. Tela (St. Petersburg) **38**, 127 (1996) [Phys. Solid State **38** (1996)].
10. K. V. Sapozhnikov and S. B. Kustov, J. de Physique IV **6** (12), C8-297 (1996).
11. K. V. Sapozhnikov, S. N. Golyandin, S. B. Kustov, *et al.*, Philos. Mag. A **77** (1), 151 (1997).
12. K. V. Sapozhnikov and S. B. Kustov, Philos. Mag. A **76** (6), 1153 (1997).
13. V. G. Badalyan, Fiz. Met. Metalloved. **50**, 612 (1980).
14. A. V. Kulemin and V. P. Chernov, Akust. Zh. **20** (3), 575 (1974).
15. D. C. Biddell and D. H. Sansome, Ultrasonics **12** (5), 195 (1974).
16. V. P. Severdenko, A. L. Skripchenko, and M. D. Tyavlovskiĭ, *Ultrasonics and Strength* (Nauka i Tekhnika, Minsk, 1979).
17. T. Ohgaku and N. Takeuchi, Phys. Status Solidi A **105** (1), 153 (1988).
18. A. B. Lebedev, Fiz. Tverd. Tela (Leningrad) **35**, 1141 (1993) [Phys. Solid State **35** (1993)].
19. A. V. Kozlov, N. S. Mordyuk, and S. I. Selitser, Fiz. Tverd. Tela (Leningrad) **28**, 1818 (1986) [Phys. Solid State **28**, 1008 (1986)].
20. A. V. Kozlov and S. I. Selitser, Mater. Sci. Eng. A **131** (1), 17 (1991).
21. A. V. Kozlov and S. I. Selitser, Mater. Sci. Eng. A **102** (1), 143 (1988).
22. M. Tanibayashi, Phys. Status Solidi A **128** (1), 83 (1991).
23. U. F. Kocks, A. S. Argon, and M. F. Ashby, *Thermodynamics and Kinetics of Slip* (Pergamon, Oxford, 1975).
24. G. A. Malygin, Phys. Status Solidi A **72** (2), 493 (1982).
25. P. Haazen, in *Dislocations in Solids*, Ed. by F. N. R. Nabarro (North-Holland, Amsterdam, 1979), Vol. 4, p. 157.

Translated by Yu. Epifanov

Physics of the Solid State, Vol. 42, No. 1, 2000, pp. 79–83. Translated from Fizika Tverdogo Tela, Vol. 42, No. 1, 2000, pp. 76–80.

MAGNETISM AND FERROELECTRICITY

Effect of Mn^{2+} Ions on the Magnetic Microstructure of Hexaferrites

Sh. Sh. Bashkirov, A. B. Liberman,† A. A. Valiullin, L. D. Zaripova, and S. V. Kokin

Kazan State University, Kazan, Tatarstan, 420008 Russia
e-mail: proton@tbit.ru

Received April 12, 1999

Abstract—Effect of Mn^{2+} ions on the magnetic microstructure of substituted hexaferrites $SrFe_{12-2x}Mn_xTi_xO_{19}$ was studied using the Mössbauer spectroscopy data. A new method is developed for estimating the hyperfine interaction parameters in substituted ferrites, and is based on a quasicontinuous description of their Mössbauer spectra. It is shown that a single substitution of manganese for iron in the second coordination shell of Fe^{3+} changes the local magnetic field strength at this ion by approximately 20 kOe, this value being independent of the concentration of substituted ions. © *2000 MAIK "Nauka/Interperiodica".*

The need for new magnetic materials explains the considerable interest of researchers in the study of hexagonal ferrites, the technological potential of which is still far from being exploited. Much attention is paid to the attempts at replacing a part of iron ions by cations of some other metals, which allows various types of magnetic ordering to be obtained within the framework of the same crystalline structure. The task of obtaining optimum magnetic and technological parameters and providing for their reproducibility requires most complete information to be obtained concerning the effect of such a substitution. Of special interest is the study of hexagonal ferrites of the *M*-type with correlated nonisomorphous substitution of Me^{2+}–Me^{4+} pairs for Fe^{3+} ions so as to obey the condition of electroneutrality [1]. Previously, we have studied the *M*-type hexaferrites by Mössbauer spectroscopy with the traditional discrete processing of the spectra [2, 3]. However, the ambiguity of results led us to the necessity of using other approaches to interpretation of the Mössbauer data. In this paper, we propose a more detailed analysis of the additional components observed in the Mössbauer spectra of substituted hexaferrites, which is based on the method of quasicontinuous description of the spectra.

1. INTERPRETATION OF THE MÖSSBAUER SPECTRA OF SUBSTITUTED HEXAFERRITES

We will consider the hexagonal ferrites of strontium having a magnetoplumbite structure (*M*-type) with correlated nonisomorphous substitution of Mn^{2+}–Ti^{4+} pairs for a part of Fe^{3+} ions. The samples have a general chemical formula of $SrFe_{12-x}Mn_x^{2+}Ti_x^{4+}O_{19}$ ($x \le 1.5$).

The crystal structure of compounds belonging to this class represents a closest package of oxygen ions with metal ions in the cavities. The hexaferrite structure is conveniently analyzed by conventionally dividing into blocks with hexagonal and spinel (cubic) structures.

The magnetic structure of the *M*-type hexaferrites is determined by the superexchange interaction through oxygen ions. In the absence of substitution, the magnetic structure is collinear and comprises five magnetic sublattices: octahedra 2*a*, 12*k*, $4f_2$; $4f_1$ tetrahedron, and 2*b* trigonal bipyramid [1]. The substitution of other magnetic or diamagnetic cations for a part of iron ions leads both to changes in the parameters of exchange interactions between the magnetic sublattices and to the appearance of new inequivalent positions of the iron ions.

The ^{57}Fe Mössbauer spectra were measured at room temperature in a constant-acceleration mode using an MS 1101E spectrometer equipped with a ^{57}Co source in the Cr matrix. The velocity scale of the spectrometer was calibrated with respect to metallic iron. Typical Mössbauer spectra of the samples studied are presented in the figure.

Preliminary mathematical processing of the Mössbauer spectra obtained was performed by the traditional optimization methods and the resulting model spectrum was assessed in terms of the Pearson criterion.

The Mössbauer parameters of the spectra of hexagonal ferrites obtained as a result of this traditional treatment are listed in Table 1.

The Mössbauer spectra of hexaferrites are usually described within the framework of discrete models based on a physically justified assignment of the individual resolved components to various inequivalent positions of the iron ions.

According to this approach, the Mössbauer spectra of substituted hexaferrites of the *M*-type studied in ear-

† Deceased.

1063-7834/00/4201-0079$20.00 © 2000 MAIK "Nauka/Interperiodica"

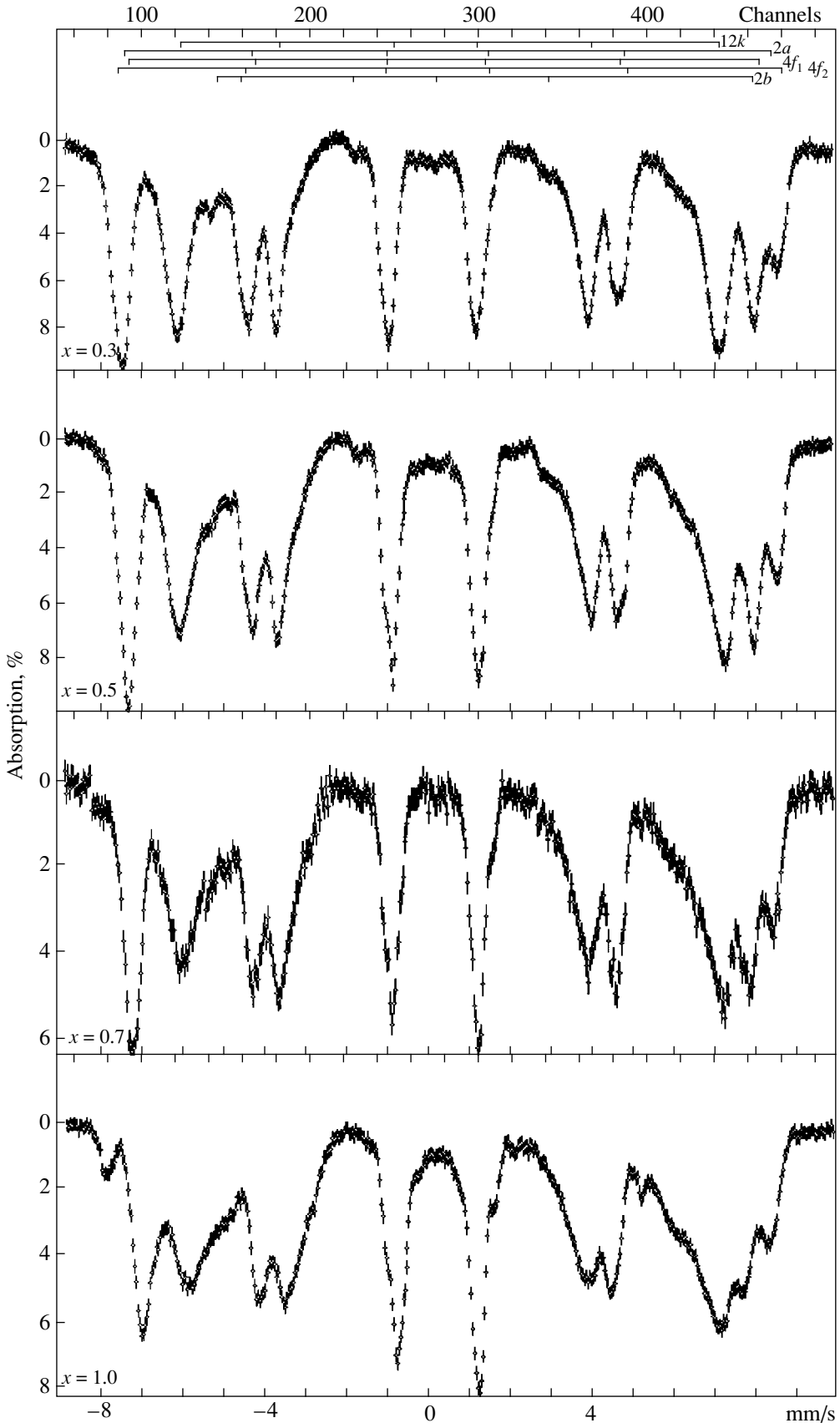

Typical Mössbauer spectra of $SrFe_{12-x}Mn_x^{2+}Ti_x^{4+}O_{19}$ hexaferrite samples.

Table 1. Parameters of discrete description of the Mössbauer spectra of $SrFe_{12-x}Mn_x^{2+}Ti_x^{4+}O_{19}$ samples

x	Sublattice	I_s, mm/s	Q_s, mm/s	H_{eff}, kOe	A, %	W, mm/s	S, %
0	12k	0.32	0.41	409.5	13.18	0.36	49.23
	2a	0.33	0.15	500.8	2.38	0.25	6.26
	4f_1	0.24	0.20	485.9	6.35	0.36	23.68
	4f_2	0.36	0.28	512.9	5.19	0.23	15.52
	2b	0.25	2.21	406.2	2.03	0.25	5.31
0.3	12k	0.32	0.37	408.4	9.10	0.70	59.74
	2a	0.31	0.25	489.3	2.27	0.33	6.95
	4f_1	0.25	0.17	476.7	5.58	0.32	16.69
	4f_2	0.34	0.33	502.8	4.48	0.30	12.35
	2b	0.25	2.16	404.5	1.47	0.31	4.27
0.5	12k	0.37	0.38	408.4	7.85	0.87	65.37
	2a	0.32	0.24	479.9	1.40	0.28	3.83
	4f_1	0.29	0.16	472.1	5.05	0.32	15.72
	4f_2	0.39	0.35	496.0	4.53	0.29	12.62
	2b	0.26	2.07	403.6	0.88	0.29	2.47
0.7	12k	0.37	0.38	403.8	4.89	1.06	69.01
	2a	0.35	0.45	477.8	1.15	0.29	4.53
	4f_1	0.29	0.10	469.4	3.53	0.33	15.51
	4f_2	0.38	0.39	492.7	2.45	0.29	9.41
	2b	0.2	1.95	381.7	0.76	0.15	1.54
1.0	12k	0.33	0.31	393.0	5.60	1.20	74.95
	2a	0.32	0.55	462.2	1.23	0.28	3.87
	4f_1	0.25	0.09	454.1	3.13	0.37	13.06
	4f_2	0.38	0.41	479.4	2.27	0.27	6.94
	2b	0.22	1.93	374.3	0.69	0.15	1.18

Note: I_x is the isomer shift relative to metallic iron; Q_s is the quadrupole splitting; H_{eff} is the effective magnetic field; A is the component intensity; W is the full linewidth at half height; S is the relative area %; The errors of determination (for $p = 0.95$) are 0.04 mm/s for I_s, Q_s, and W; 5 kOe for H_{eff}; 3% for S.

lier works were described using a discrete set of components corresponding to various crystallographically inequivalent positions of iron ions. Additional inequivalent iron ion positions, appearing due to the substitution of other metal ions for iron, were assigned to an additional strongly broadened spectral component [2]. In this work, we suggest a different approach to interpreting the additional components that appear in the Mössbauer spectra of substituted hexaferrites.

As is known, the electron configurations of the Mn^{2+} ions and Fe^{3+} ions are identical, but the integral of the superexchange interaction in the Mn–O–Fe chain is smaller than that in the Fe–O–Fe chain [4]. For this reason, the substitution of manganese for iron in a given sublattice not only leads to a decrease in the intensity of components corresponding to this sublattice, but gives rise to additional components with smaller values of the local magnetic field corresponding to the crystallographic positions of iron ions adjacent to the substitution sublattice. Unfortunately, the line broadening as a result of this substitution, as well as the small values of the changes in the local magnetic field in these sublattices, hinder unambiguous interpretation of the additional components within the framework of traditional methods.

In order to obtain additional information about the effect of substituted cations, it would be expedient to employ quasicontinuous methods, which are capable of providing a distribution of the probability density of a determining parameter. Using these methods, it is possible to resolve the components that remain unresolved in a discrete description. In this work, we have used one of the possible quasicontinuous methods, namely, the Hesse–Rübartsch regularization technique [5]. Using this method, we have estimated a change in the local magnetic field strength at the iron ion upon substituting

Table 2. Variation of the hyperfine magnetic field at the iron nucleus in hexaferrite upon single substitution of manganese for iron in the second coordination shell

x	H_{12k}, kOe	Δ_h, kOe
0.3	408	22
0.5	408	22
0.7	407	20
1.0	403	20

* The error of Δh determination (for $p = 0.95$) is 5 kOe.

manganese for iron in the nearest environment of the former iron ion. The calculation was performed using the following procedure.

First, the parameters of the Mössbauer spectra determined by the conventional methods were used in the Hesse–Rübartsch regularization procedure to restore the local magnetic field distribution with the other parameters fixed. This allowed us to make preliminary conclusions concerning the presence of additional components in the Mössbauer spectra measured upon substitution and to refine the values of local fields corresponding to the main spectral components.

Then, using a binomial distribution, assuming a statistical distribution of substituted cations in a given sublattice, and employing aprioric information on the substituent concentration, we calculated the probabilities of all components of the line of this sublattice. These probabilities were calculated using information about the possible distribution of iron ions and substituted cations in various sublattices and the number of the nearest neighbors in each particular sublattice:

$$P_j(m, x) = C_m^N x^m (1-x)^{N-m}, \tag{1}$$

where j is the index of the sublattice under consideration, N is the total number of positions belonging to the given substitution sublattice in the nearest environment of the initial sublattice, m is the number of substituted ions, and x is the relative concentration of ions in the substitution sublattice.

Since the Mössbauer intensity determined by the traditional method characterizes the whole set of sublattices having various degrees of substitution of the nearest-neighbor ions, the intensity of each sublattice, corresponding to the positions of iron ions with different numbers of substituted cations in the nearest environment, was normalized to this overall characteristic.

In the third stage, we employed the Hesse–Rübartsch regularization method [5] to restore the probability distribution density of the quantity Δh representing a change in the local magnetic field strength at the iron nucleus in the given sublattice upon replacement of a single iron ion in the second coordination shell of the nucleus under consideration. In our particular case, iron was replaced by manganese. Under these conditions, we have used the following matrix to describe the shape of the Mössbauer spectrum within the framework of the regularization procedure:

$$L_{l,n} = \sum_{i \neq j} \sum_{k=1}^{6} \frac{a_i \alpha_k}{1 + [(v_l - \delta_i - \beta_k e_i/2 - \gamma_k H_i)/(\Gamma_i/2)]^2} + \sum_{m=0}^{M} \sum_{k=1}^{6} \frac{a_j P_j(m, x) \alpha_k}{1 + [(v_l - \delta_j - \beta_k e_j/2 - \gamma_k (H_j - n\Delta h m))/(\Gamma_j/2)]}, \tag{2}$$

where Δh is a change in the local magnetic field strength to be determined; n is the index of discretization for the unknown value distribution; v_l is the Doppler velocity of the lth analyzer channel; $P_j(m, x)$ is the distribution function from equation (1); j is the sublattice number; M is the number of nearest neighbors in the second coordination shell of the iron ion under consideration; a_i, δ_i, e_i, H_i, and Γ_i are the reduced amplitude, isomer shift, quadrupole splitting, local field strength, and halfwidth of the ith spectral component, respectively; α_k, β_k, and γ_k are the Mössbauer coefficients of the kth line.

The value of the smoothness factor necessary for applying the regularization method was obtained from the model spectra of substituted hexaferrite. The same model spectra were used to assess the reliability of the calculated results.

2. ANALYSIS OF RESULTS

The Mössbauer spectra of the samples studied represent a superposition of several Zeeman sextets related to the magnetic ordering typical of the hexagonal ferrites. According to the model structure described by discrete methods, there are five magnetic sublattices corresponding to different inequivalent positions of iron ions. Changes in the local fields in these sublattices are observed already for $x = 0.3$, and further increase in the degree of substitution markedly alters the shape of the spectrum as well. A maximum change in the local magnetic field strength is observed for the $4f_1$ and $4f_2$ sublattices, while the fields in other sublattices vary to a lower extent. A characteristic feature of changes in the Mössbauer spectrum is the anomalous behavior of intensities and broadening of the lines of some sublattices. An example is offered by the $12k$ sublattice,

which can be described only by using an asymmetrically broadened line shape. This is evidence for the appearance of additional inequivalent positions of the iron ions upon the substitution of manganese for iron in the nearest cationic environment of the 12*k* sublattice.

Taking into account that Mn^{2+} ions possess a greater energy of affinity to the tetrahedral positions [4], we can suggest that manganese ions in the samples studied would also occupy the tetragonal $4f_1$ positions occurring in the spinel blocks. This assumption is confirmed by decrease in the local magnetic field strength and in the relative intensity of lines corresponding to this sublattice observed with increasing degree of substitution. An analysis of the crystalline structure shows that these positions occur in the nearest cationic environment of the 12*k* and 2*a* octahedra. A small intensity of the 2*a* component keeps us from making a reliable description of the effect of manganese ions on the local magnetic field in this sublattice. At the same time, application of the above method provides reliable data for the 12*k* sublattice.

The Δh values calculated using the procedure described above are presented in Table 2. As seen, this parameter remains virtually constant when the degree of substitution increases, which confirms the initial assumption concerning the distribution of cations in hexaferrites of the type studied. Moreover, the value is close to that reported previously for the spinel ferrites [4, 6]. This proximity is probably related to the fact that the 12*k* sublattice occurs in the spinel block of the hexaferrite structure studied.

Further development of the method described above would involve a more thorough description of effects caused by the Mn^{2+} substitution for iron ions, including changes in the 2*a* sublattice.

The above results allow us to ascertain that the hexagonal ferrites of the *M*-type studied, with a correlated nonisomorphous substitution of Mn^{2+}–Ti^{4+} pairs for Fe^{3+} ions, are characterized by the manganese ions occupying the tetrahedral $4f_1$ positions.

The observed position of maximum of the Δh distribution is independent of the concentration of substituted ions and is of the same order of magnitude as the value reported for the manganese- containing spinels [4, 6].

The proposed method may be also useful for the study of ferrites with different crystal structures, in which the iron ions are replaced by ions other than manganese.

REFERENCES

1. A. A. Belous, V. P. Ivanitskiĭ, B. A. Elshanskiĭ, *et al.*, Zh. Neorg. Khim. **43** (4), 588 (1998).
2. Sh. Sh. Bashkirov, A. B. Liberman, L.D. Zaripova, *et al.*, Fiz. Tverd. Tela **39** (4), 676 (1997).
3. Sh. Sh. Bashkirov, A. B. Liberman, and E. G. Groshev, Izv. Ross. Akad. Nauk, Ser. Fiz. **56** (7), 124 (1992).
4. Sh. Sh. Bashkirov, A. B. Liberman, and V. I. Sinyavskiĭ, *Magnetic Microstructure of Ferrites* (Kazan. Gos. Univ., Kazan, 1978).
5. J. Hesse and A. Rübartsch, J. Phys. E: Sci. Instrum. **7** (7), 526 (1974).
6. I. S. Lyubutin, *Physics and Chemistry of Ferrites* (Mosk. Gos. Univ., 1973).

Translated by P. Pozdeev

Physics of the Solid State, Vol. 42, No. 1, 2000, pp. 84–88. Translated from Fizika Tverdogo Tela, Vol. 42, No. 1, 2000, pp. 81–85.

MAGNETISM AND FERROELECTRICITY

Magnetic Ordering and Magnetoresistive Effect in $La_{1-x}Sr_x(Mn_{1-y}Me_y)O_3$ Perovskites (Me = Nb, Mg)

I. O. Troyanchuk, D. A. Efimov, D. D. Khalyavin, N. V. Pushkarev, and R. Shimchak

Institute of Solid-State and Semiconductor Physics, Belarussian Academy of Sciences, ul. P. Brovki 17, Minsk, 220072 Belarus

e-mail: troyan@ifttp.bas-net.by

Received April 13, 1999

Abstract—Perovskites of composition $La_{1-x}Sr_x(Mn_{1-x/2}Nb_{x/2})O_3$ and $La_{0.49}Sr_{0.51}(Mn_{1-y}Nb_y)O_3$ have been synthesized and investigated. The substitution of nonmagnetic niobium ions for manganese was shown to lead to a transition from the metallic into the insulating state due to a decrease in the number of dissimilar (different-valence) manganese atoms in the lattice. In spite of the high resistivity, the niobium-containing perovskites exhibit a large magnetoresistive effect and ferromagnetic ordering. Small additions of Nb^{5+} to $La_{0.49}Sr_{0.51}MnO_3$ stimulate the transition from the antiferromagnetic into the ferromagnetic state, whereas the substitution of Mg^{2+} for Mn stabilizes the antiferromagnetic state. It is supposed that the ferromagnetism in the insulating perovskites at hand is due to the positive superexchange of the Mn^{3+}–O–Mn^{3+} type, and the magnetoresistive effect owes to the intergranular transfer of spin-polarized charge carriers and the suppression of magnetic nonuniformities by an applied magnetic field near T_C. © *2000 MAIK "Nauka/Interperiodica".*

INTRODUCTION

The discovery of the effect of "giant magnetoresistance" (GMR) greatly stimulated the interest in the manganites with a perovskite structure. These compounds exhibit a very interesting interrelation between the magnetism, charge ordering, and electrical transport properties. The metal–insulator transition near the Curie temperature in $La_{1-x}Sr_x(Mn^{3+}_{1-x}Mn^{4+}_x)O_3$ have long been interpreted (starting from 1950) in terms of the "double exchange" model, in which the electrical conductivity and ferromagnetic ordering are closely related [1]. In recent years, attempts have been made to modify the theory of double exchange [2–4] with the purpose of accounting for a number of new facts. Nagaev [5, 6] emphasized the important role of magnetic impurities in the GMR effect. The efficiency of the double exchange is controlled by the relation between the amounts of Mn^{4+} and Mn^{3+} ions. In terms of the double exchange model, the system undergoes a transition into the antiferromagnetic insulating state as the concentration of Mn^{4+} ions decreases; this indeed is observed in the $La_{1-x}Sr_xMnO_3$ system as the amount of Sr decreases. Another way to decrease the concentration of higher-valence Mn ions is to substitute some other ions of higher valence for manganese ions, e.g., niobium ions. These ions in the lattice of perovskite-type manganites have the oxidation state Nb^{5+}, since the synthesis of Nb^{4+}-containing perovskites is carried out under strongly reducing conditions incompatible with the stability of $La_{1-x}Sr_xMnO_3$-type perovskites. The magnesium ions in oxides are always in the divalent state. Their introduction into the manganite lattice must therefore lead to an increase in the average oxidation state of Mn ions. In this work, we studied the effect of Nb^{5+} and Mg^{2+} ions on the magnetic and electrical properties of manganites.

1. EXPERIMENTAL

The samples for this investigation were obtained from starting materials (La_2O_3, $SrCO_3$, Mn_2O_3, MgO, and Nb_2O_5) of at least 99.99% purity. The initial components were mixed in proportions necessary to obtain the desired stoichiometry. The synthesis was carried out in air by heating the oxide mixtures for 2 h at 1550°C. The high temperature of synthesis was necessary to obtain a dense ceramics of good quality. The samples were cooled at a rate of 200 K/h. Some of the samples were annealed at 800°C in a vacuum of 10^{-5} atm in order to minimize the concentration of Mn^{4+} ions. X-ray diffraction revealed no traces of foreign phases. The lattice parameters of the phases that were synthesized are listed in the table. The unit-cell volume of niobium-containing perovskites is much higher than that of the $La_{1-x}Sr_xMnO_3$ compounds with the corresponding amount of strontium. This is because the ionic radius of Nb^{5+} is greater than that of Mn^{4+}.

The magnetic measurements were performed with a Foner vibrating-sample magnetometer in fields up to 15 kOe and with a SQUID magnetometer in fields up to 50 kOe. The electrical conductivity was measured by the four-probe method with indium electrodes deposited by the ultrasonic technique.

1063-7834/00/4201-0084$20.00

Lattice parameters

Composition	Lattice type	*a*	*c*	α	*V*
$La_{0.49}Sr_{0.51}MnO_3$	Tetragonal	3.848	3.878		57.789
$La_{0.49}Sr_{0.51}Mn_{0.92}Mg_{0.05}O_3$	Tetragonal	3.843	3.879		57.282
$La_{0.49}Sr_{0.51}Mn_{0.975}Nb_{0.025}O_3$	Tetragonal	3.863	3.877		57.820
$La_{0.49}Sr_{0.51}Mn_{0.95}Nb_{0.05}O_3$	Cubic	3.877			58.309
$La_{0.49}Sr_{0.51}Mn_{0.85}Nb_{0.15}O_3$	Cubic	3.911			59.808
$La_{0.49}Sr_{0.51}Mn_{0.75}Nb_{0.25}O_3$	Cubic	3.939			61.101
$La_{0.8}Sr_{0.2}Mn_{0.9}Nb_{0.1}O_3$	Rhombohedral	3.890		90.404	58.837
$La_{0.8}Sr_{0.2}Mn_{0.9}Nb_{0.1}O_3^*$	Cubic	3.927			60.555
$La_{0.7}Sr_{0.3}Mn_{0.85}Mn_{0.15}O_3$	Rhombohedral	3.923		90.257	60.376
$La_{0.6}Sr_{0.4}Mn_{0.8}Nb_{0.2}O_3$	Cubic	3.929			60.655
$La_{0.6}Sr_{0.4}Mn_{0.8}Nb_{0.2}O_3^*$	Cubic	3.949			61.582

* Reduced.

2. RESULTS AND DISCUSSION

The results of the measurements of field dependences of the magnetization of $La_{1-x}Sr_x(Mn_{1-x/2}Nb_{x/2})O_3$ samples at $T = 12$ K are given in Fig. 1. The samples with $x \le 0.2$ are at this temperature in the ferromagnetic state, since the magnetic moment of Mn^{3+} ions in the perovskites is about 3.5 μB, while niobium ions do not contribute to the magnetization. The Curie temperatures vary between 110 and 190 K, depending on the niobium concentration and the synthesis conditions (Fig. 2). The diamagnetic Nb^{5+} ions do not participate directly in exchange interactions; this leads to a decrease in the Curie temperature as compared to the initial $La_{1-x}Sr_xMnO_3$ perovskites. All the samples, both vacuum-annealed and prepared in air, have relatively close magnetic properties. Vacuum annealing decreases oxygen content in the samples; this is accompanied by the transition of Mn^{4+} into Mn^{3+} or Mn^{3+} into Mn^{2+} ions. A small amount of Mn^{4+} ions may be present in the samples prepared in air because of the inclination of the manganites to deviations from stoichiometry in the cation sublattice, which manifests itself, e.g., in the formation of equivalent amounts of manganese and lanthanum vacancies [7]. Unlike $La_{0.7}Sr_{0.3}(Mn_{0.85}Nb_{0.15})O_3$, the 15% substitution of magnesium ions for manganese ions destroys the long-range magnetic order, which is seen from the $M(H)$ dependence at 4.2 K (Fig. 1, curve *4*).

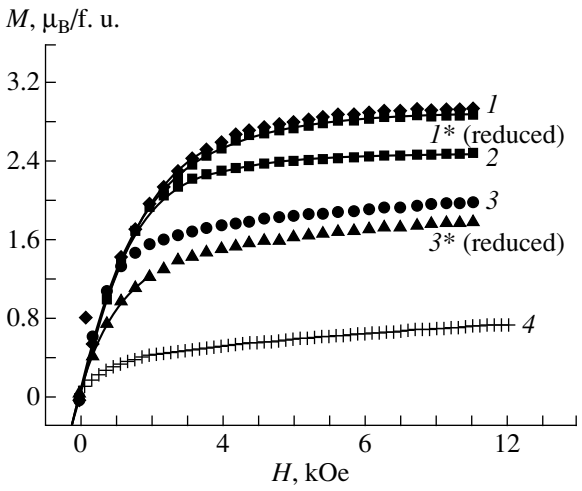

Fig. 1. Magnetization at $T = 12$ K as a function of magnetic field in $La_{1-x}Sr_x(Mn_{1-x/2}Nb_{x/2})O_3$ compounds: (*1*, *1**) $x =$ 0.2; (*2*) 0.3; (*3*, *3**) 0.4; and (*4*) $La_{0.7}Sr_{0.3}(Mn_{0.85}Mg_{0.15})O_3$ at 4.2 K.

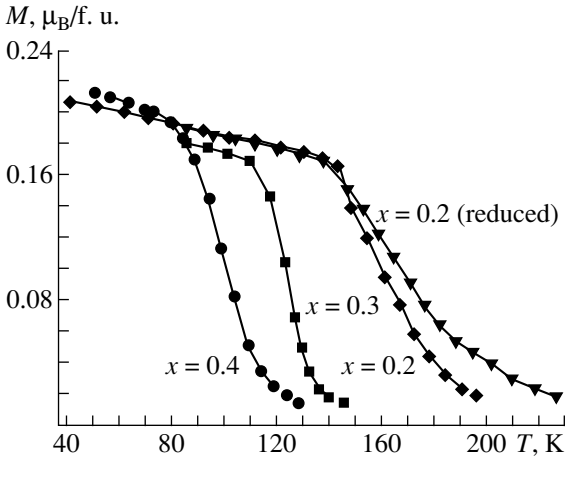

Fig. 2. Magnetization as a function of temperature for $La_{1-x}Sr_x(Mn_{1-x/2}Nb_{x/2})O_3$ in a field of 100 Oe. The measurements were performed after cooling in a field of 100 Oe.

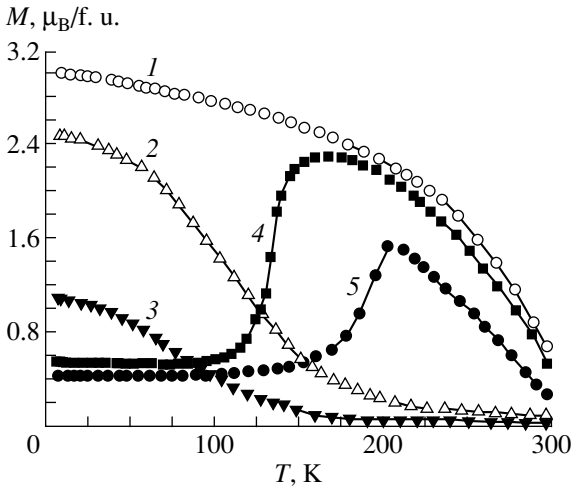

Fig. 3. Magnetization of $La_{0.49}Sr_{0.51}(Mn_{1-y}Me_y)O_3$ (Me = Nb, Mg) in a field of 12 kOe as a function of temperature: (*1*) *M* = Nb, *y* = 0.05; (*2*) Nb, *y* = 0.15; (*3*) Nb, *y* = 0.25; (*4*) *y* = 0; and (*5*) Me = Mg, *y* = 0.05.

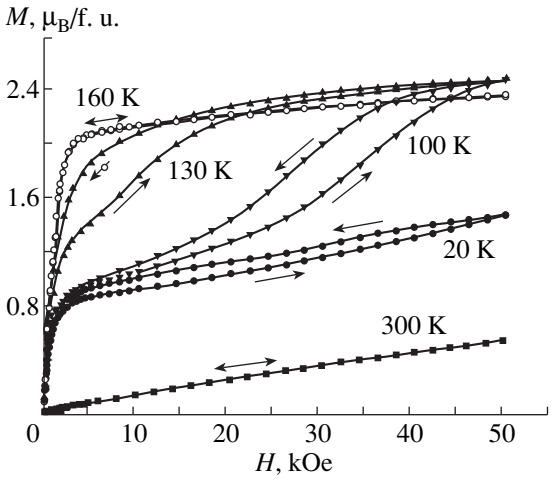

Fig. 4. Magnetization of a $La_{0.49}Sr_{0.51}MnO_3$ sample as a function of magnetic field at various temperatures.

Figure 3 displays the magnetization of $La_{0.49}Sr_{0.51}(Mn_{1-y}Me_y)O_3$ samples as a function of temperature.

$La_{0.49}Sr_{0.51}MnO_3$ exhibits a magnetization jump near 150 K, which is related to its transition from the antiferromagnetic into ferromagnetic state. At temperatures below 150 K, this compound, as is seen from Fig. 4, exhibits metamagnetic behavior.

The spontaneous magnetization below 150 K appears to be due to the presence of a magnetic phase that does not go over into the antiferromagnetic state due to the enhanced local concentration of lanthanum ions. The substitution of niobium for manganese ions fully suppresses the antiferromagnetic state and stabilizes the ferromagnetic state. As the concentration of niobium ions increases, the Curie temperature decreases gradually. Near a niobium concentration of 20%, the system changes into a cluster state of the spin-glass type, which follows from the results of magnetization measurements in small magnetic fields. In the Mg^{2+}-doped compound, on the contrary, the antiferromagnetic state is stabilized, since magnesium increases the antiferromagnetic–ferromagnetic transition temperature.

Figure 5 shows the results of measurements of electrical conductivity. All $La_{1-x}Sr_x(Mn_{1-x/2}Nb_{x/2})O_3$ compounds exhibit conductivity behavior characteristic of semiconductors. In the temperature range close to 100 K, the resistivity varies from 10^3 to 10^6 Ω cm, depending on the sample. These values are higher by 6–9 orders of magnitude than those characteristic of the corresponding $La_{1-x}Sr_xMnO_3$ samples. Vacuum annealing of the samples increases their resistivity.

As a rule, the transition into a magnetically ordered state in niobium-substituted manganites is not accompanied by the appearance of any sharp anomalies in the ρ(*T*) dependences. The resistivity continues to grow in the ferromagnetic region. Such behavior was previously observed for ferromagnetic samples of $R_{0.8}Ca_{0.2}(Mn^{3+}_{0.8}Mn^{4+}_{0.2})O_3$ (*R* = Pr, Nd) with Curie temperatures of 110–130 K [8].

Figure 6 displays the temperature dependences of the magnetoresistivity $MR = \{[\rho(H = 0) - \rho(H = 9\text{ kOe}/\rho(H = 0)\} \times 100\%$ measured in a relatively small magnetic field of 9 kOe. Upon the transition into the ferromagnetic state, all the samples exhibit a magnetoresistivity jump. With decreasing temperatures, the magnetoresistivity, as a rule, increases gradually, reaching 25%. The niobium-free manganite $La_{0.7}Sr_{0.3}MnO_3$ exhibits a maximum MR (10%) near T_C; then, the MR increases with the falling temperature, reaching 15% at 77 K. The MR of niobium-containing samples only slightly depends on the direction of the magnetic field with respect to the current direction. The MR gradually rises, almost linearly, with increasing magnetic field.

When studying the $La(Mn_{1-x}Ga_x)O_3$ system, in which no different-valence Mn ions are present, it was revealed that as the gallium ions substituted for manganese, the antiferromagnetic state changed into the ferromagnetic state [9]. In order to explain this phenomenon, Goodenough [9] supposed that the sign of exchange interactions between the ions of trivalent manganese is determined by the type of the Jahn–Teller effect. In the case of static Jahn–Teller distortions, the exchange interaction is negative, whereas in the case of dynamic Jahn–Teller effect, the exchange Mn^{3+}–O–Mn^{3+} interaction is positive. Upon the dilution of the system by adding gallium ions, the cooperative orbital ordering becomes destroyed, which changes the sign of exchange interactions. A similar situation appears to take place in the compounds that were studied in this work, in which

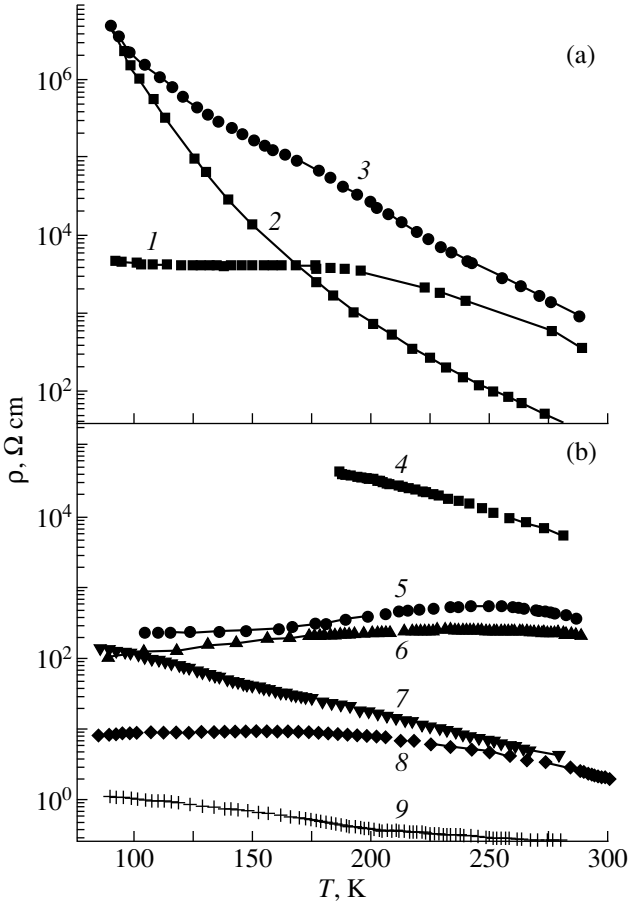

Fig. 5. Temperature dependence of the electrical conductivity of (a) $La_{1-x}Sr_x(Mn_{1-x/2}Nb_{x/2})O_3$ and (b) $La_{0.49}Sr_{0.51}(Mn_{1-y}Me_y)O_3$: (*1*) $x = 0.2$ (reduced); (*2*) $x = 0.4$ (reduced); (*3*) $x = 0.3$; (*4*) $y = 0.15$, Me = Nb; (*5*) $y = 0.1$, Nb; (*6*) $y = 0.05$, Nb; (*7*) $y = 0$; (*8*) $y = 0.025$, Nb; and (*9*) $y = 0.05$, Me = Mg.

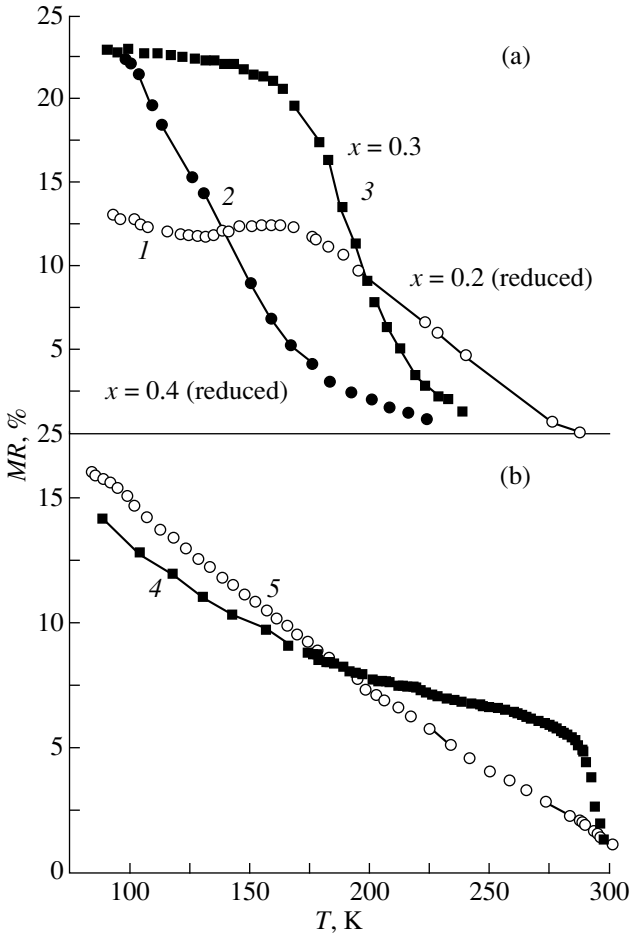

Fig. 6. Magnetoresistance as a function of temperature for (a) $La_{1-x}Sr_x(Mn_{1-x/2}Nb_{x/2})O_3$ and (b) $La_{0.49}Sr_{0.51}(Mn_{1-y}Nb_y)O_3$: (*1*) $x = 0.2$ (reduced); (*2*) $x = 0.4$ (reduced); (*3*) $x = 0.3$; (*4*) $y = 0.05$, Nb; and (*5*) $y = 0.025$, Nb.

Nb^{5+} ions are present instead of the Mn^{4+} ones. Therefore, many niobium-containing perovskites exhibit ferromagnetic properties, in spite of the absence or a very small concentration of Mn^{4+} ions, as compared to the $La_{1-x}Sr_xMnO_3$ system. The strength of the Mn^{3+}–O–Mn^{3+} ferromagnetic interaction appears to be comparable to that of the Mn^{3+}–O–Mn^{4+} ferromagnetic interaction, since the niobium-containing manganites are dilute. In the case of the Mn^{3+}-based niobium-free compounds, we may expect that the Curie temperature of the orbitally disordered phase will be close to room temperature. With the Mn^{3+}/Mn^{4+} cation ratio less than unity, the antiferromagnetic exchange interactions predominate over the ferromagnetic ones, which manifests itself in the antiferromagnetic behavior observed in $La_{0.49}Sr_{0.51}MnO_3$ and $La_{0.49}Sr_{0.51}(Mn_{0.95}Mg_{0.05})O_3$ at low temperatures.

There are works at present in which the charge carriers in manganites are assumed to be *p* holes in a wide valence band formed mainly by oxygen orbitals [10, 11]. Upon the transition from the ferromagnetic into the paramagnetic state, the density of charge carriers in the wide *p* band collapses, which may be the cause for the metal–insulator transition and the large magnetoresistance. We established that the decrease in the concentration of different-valence manganese leads to a sharp increase in the resistivity—by many orders of magnitude as compared to the stoichiometric $La_{0.7}Sr_{0.3}MnO_3$. The temperature dependence of the conductivity of ferromagnetic $La_{0.7}Sr_{0.15}(Mn_{0.85}Nb_{0.15})O_3$ only slightly differs from that of the antiferromagnetic $LaMnO_3$, which also contains only small concentration of Mn^{3+}–Mn^{4+} pairs. Therefore, formally, the electrical conductivity is determined by the concentration of these pairs. In order for the metal–insulator transition to occur near T_C, a sufficiently large concentration of Mn^{4+} ions and a proper width of the 3*d* band are necessary. The latter width is controlled by the ratio of the ionic radii of the A and *B* cations in the structure of ABO_3 perovskites.

This width should not be too large, since the $La_{1-x}Sr_xMnO_3$ perovskites at $x > 0.54$ are metals in a wide temperature range, notwithstanding that their ground state is antiferromagnetic [12], whereas $Pr_{0.8}Ca_{0.2}MnO_3$ is an insulator, notwithstanding that its ground state is ferromagnetic [8]. The ferromagnetic insulators based on the lanthanum manganite usually exhibit a very high magnetoresistance (20–30% in fields to 10 kOe), whereas $La_{1-x}Sr_xMnO_3$ with a high Sr concentration ($x \cong 0.5$) has a low MR. The applied magnetic field appears to only slightly affect the processes of electronic transport in the manganites with their wide 3*d* band.

CONCLUSION

It follows from the results of this work that the presence of different-valence manganese ions is by no means required to obtain the GMR effect and ferromagnetic ordering in manganites. A large magnetoresistive effect was revealed in pyrochlores such as $Tl_2Mn_2O_7$ [13], which also contain no different-valence manganese ions. In this compound, the MR effect is ascribed to charge-carrier scattering by critical fluctuations [14]. The largest effect in strong fields apparently must be observed in samples with weakened exchange interactions and high resistivity near T_C. In this case, the magnetoresistive effect is not saturated in strong fields and is determined by to what degree the applied field is capable of maintaining the magnetic order. It follows from neutron diffraction data [15] that cluster magnetic states exist in manganites in a wide temperature range near T_C.

ACKNOWLEDGMENT

This work was supported by the Belarussian Foundation for Basic Research, grant no. Φ.98-057.

REFERENCES

1. C. Zener, Phys. Rev. **82**, 403 (1951).
2. A. J. Millis, P. B. Littlewood, and B. I. Shraiman, Phys. Rev. Lett. **74**, 5144 (1995).
3. N. Furukawa, J. Phys. Soc. Jpn. **63**, 3214 (1994).
4. D. I. Golosov, M. R. Norman, and K. Levin, Phys. Rev. B: Condens. Matter **58**, 8617 (1998).
5. E. L. Nagaev, Phys. Rev. B: Condens. Matter **54**, 16 608 (1996).
6. E. L. Nagaev, Phys. Rev. Lett. A **215**, 321 (1996).
7. J. A. M. van Roosmalen, E. H. P. Cordfunke, R. B. Helmholdt, *et al.*, J. Solid State Chem. **110**, 100 (1994).
8. I. O. Troyanchuk, D. A. Efimov, N. V. Samsonenko, *et al.*, J. Phys.: Condens. Matter **10**, 7957 (1998).
9. J. B. Goodenough, A. Wold, R. J. Arnott, *et al.*, Phys. Rev. **124** (2), 373 (1961).
10. H. L. Ju, H.-C. Sohn, and Kannan M. Krishnan, Phys. Rev. Lett. **79** (17), 3230 (1997).
11. P. Calvani, G. de Marzi. P. Dore, *et al.*, Phys. Rev. Lett. **81** (20), 4505 (1998).
12. Y. Moritomo, T. Akimoto, A. Nakamura, *et al.*, Phys. Rev. B: Condens. Matter **58**, 5544 (1998).
13. Y. Shimikawa, *et al.*, Nature **379**, 53 (1996).
14. P. Majumdar and P. Littlewood, Phys. Rev. Lett. **81** (6), 1314 (1998).
15. J. W. Lynn, R. W. Erwin, J. A. Borchers, *et al.*, Phys. Rev. Lett. **76**, 4046 (1996).

Translated by S. Gorin

Physics of the Solid State, Vol. 42, No. 1, 2000, pp. 89–95. Translated from Fizika Tverdogo Tela, Vol. 42, No. 1, 2000, pp. 86–92.

MAGNETISM AND FERROELECTRICITY

Local Magnetic Moments and Hyperfine Magnetic Fields in Fe–*M* (*M* = Si, Sn) Alloys at Small Metalloid Concentrations

A. K. Arzhnikov*, L. V. Dobysheva*, and F. Brauers**

** Physicotechnical Institute, Ural Division, Russian Academy of Sciences, Izhevsk, 426001 Russia*
*** Universite de Liège, Liège, 4000 Belgium*
e-mail: arg@otf.fti.udmurtia.su

Received February 1, 1999; in final form, May 13, 1999

Abstract—The main tendencies in the formation of local magnetic moments and hyperfine magnetic fields at Fe nuclei in Fe–Sn and Fe–Si alloys at low metalloid concentrations are analyzed on the basis of "first-principles" calculations. The results of calculations are compared with experimental data. The main differences between these alloys were proved to be due to the differences in their lattice parameters. It is shown that a significant contribution to the formation of the hyperfine field comes from the orbital magnetic moment and the Ruderman–Kittel–Kasuya–Yosida polarization, which depend on the impurity concentration and the distance to an impurity atom in the crystal lattice. © *2000 MAIK "Nauka/Interperiodica".*

INTRODUCTION

At present, numerous experimental data are available on the disordered binary alloys of iron with *sp* elements such as Si, Sn, Al, etc. [1–10]. The wide concentration range of existence of the atomically disordered state in these alloys makes them good model objects for studying fundamental mechanisms that are responsible for the formation of their magnetic properties. Some common features observed in the magnetic behavior of these alloy with various metalloids depending on the concentration of a metalloid made it possible to separate a limited number of factors that determine these features. Using this fact, the authors of [6, 11, 12] obtained, based on model Hamiltonians, a qualitative and, in some cases, even satisfactory quantitative description of the formation of local magnetic moments, total magnetic moments, and Curie temperatures as functions of the metalloid concentration and temperature. However, already in those works, the authors indicated the necessity of using *ab initio* microscopic calculations for the substantiation of the models and the description of some differences in the behavior of the magnetic characteristics of these alloys.

In this work, we focused our attention of low-concentration dependences of the local magnetic moments and hyperfine magnetic fields (HFFs) at Fe nuclei for the most typical representatives of the metal–metalloid alloys—$Fe_{1-x}Si_x$ and $Fe_{1-x}Sn_x$. Figures 1–3 show experimental data that demonstrate differences in the lattice parameters of the bcc structure (the bcc structure in these alloys is retained up to impurity concentrations of 30 at. % [1, 5]), the average magnetic moments, and the hyperfine magnetic fields (H_0, the HFF at an iron nucleus whose nearest neighborhood contains no metalloid atoms; and H_1, the HFF at an iron atom whose nearest neighborhood contains a single metalloid atom). Linearly approximating the concentration dependences of H_0 and M, we obtain $\Delta H_0/\Delta M \approx -120$ kG/μ_B. This value is close to the coefficient of the Fermi-contact contribution to the HFF at Fe nuclei; therefore, it is natural to suppose that the changes in H_0 are mainly related to an increase in the local magnetic moments. Note that this is by no means a trivial fact, as it may seem at first glance. Indeed, a significant contribution to HFF comes from the orbital magnetic moment and the Ruderman–Kittel–Kasuya–Iosida (RKKY) polarization. However, the coefficient of the orbital contribution to the HFF at Fe has a large positive value (≈313 kG/μ_B [13]), whereas the oscillating coefficient of the RKKY polarization due

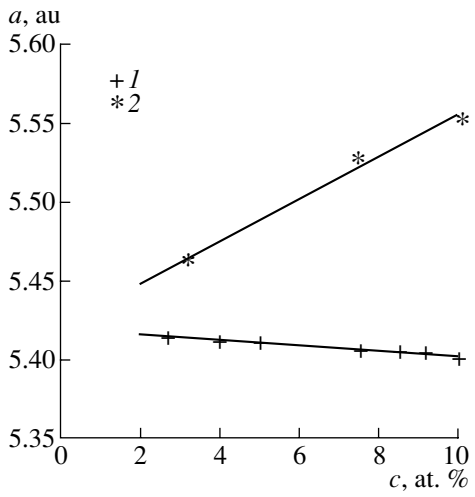

Fig. 1. Concentration dependence of the lattice parameter of bcc disordered alloys: (*1*) Fe–Si [3–5] and (*2*) Fe–Sn [6].

1063-7834/00/4201-0089$20.00 © 2000 MAIK "Nauka/Interperiodica"

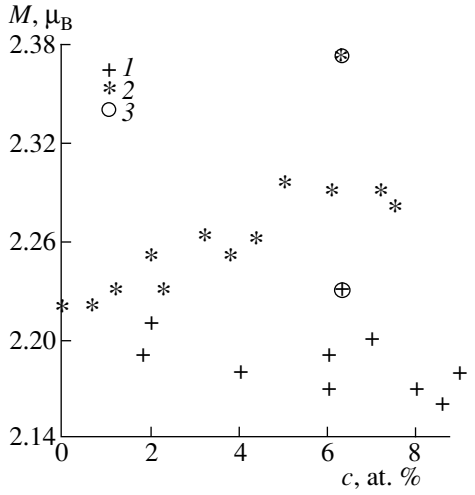

Fig. 2. Concentration dependence of the average magnetic moment per Fe atom in disordered alloys: (*1*) Fe–Si [7–9] and (*2*) Fe–Sn [6, 7]; (*3*) calculated in this work.

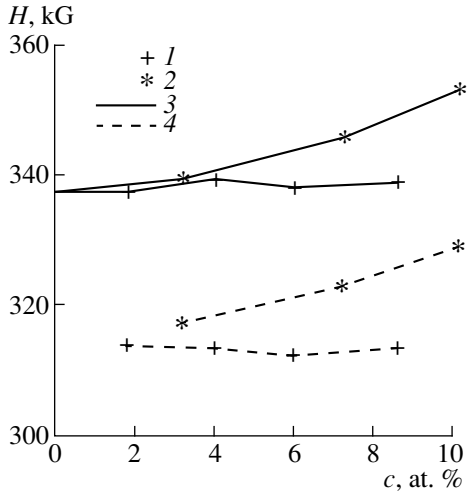

Fig. 3. Concentration dependence of hyperfine magnetic fields H_0 and H_1 at Fe nuclei in disordered alloys: (*1*) Fe–Si [9] and (*2*) Fe–Sn [10]; (*3*) H_0 (no nonmagnetic impurities in the nearest neighborhood of Fe atoms) and (*4*) H_1 (one nonmagnetic atom in the nearest neighborhood of Fe atoms).

to distant atoms does not exceed 8 kG/μ_B in the absolute magnitude, as is shown below.

In order to study the spatial distribution of the magnetic moment and its interrelation with the HFF at Fe nuclei, we performed "first-principles" calculations for ordered substitutional alloys $Fe_{15}Sn$ and $Fe_{15}Si$, whose lattices are formed as a result of substitution of one Sn atom for a Fe atom per extended cell of the bcc structure containing 16 atoms. In such a unit cell, Fe atoms have four nonequivalent positions located at different distances from the metalloid atom (see Fig. 4). The self-consistent band-structure calculations were performed by the full-potential linearized augmented plane wave (FLAPW) method using the WIEN97 program [14, 15]. The exchange–correlation contribution was described in terms of the generalized gradient approximation (GGA) [16]. The results obtained are given in Tables 1–3.

1. LATTICE

Based on experimental data, we may assume that at low solute concentrations, the disordered alloys are substitutional solid solutions with a bcc structure. In calculations, we used the experimental values of the lattice parameters corresponding to an impurity concentration of 6.25 at. % (Fig. 1) extrapolated to the absolute zero (a = 10.9924 au for $Fe_{15}Sn$ and a = 10.7926 au for $Fe_{15}Si$). To illustrate the effect of the magnitude of the lattice parameter on the numerical results, we also performed calculations for $Fe_{15}Sn$ with a = 10.8114 au, which corresponds to the experimentally measured lattice parameter of pure Fe, and for a partially relaxed lattice with a = 10.9924 au (the relaxation was realized by shifting Fe atoms nearest to the Sn atom by a distance δr = 0.038 au along the large diagonal of the cube). Note that the total energy of the relaxed lattice (E = –50542.2470 Ry) is slightly lower than the corresponding energy of the unrelaxed lattice (E = –50542.2329 Ry). This indicates that, in reality, a somewhat distorted bcc structure should be formed. However, the results obtained for the magnetic moments and hyperfine fields (Table 1) only slightly differ for the cases with and without relaxation; for this reason, we have not considered relaxation effects in this work. In what follows, the comparison and the discussion of the results of calculations will be carried out for $Fe_{15}Sn$ with a = 10.9924 au and $Fe_{15}Si$ with a = 10.7926 au without indicating their lattice parameters except for specified cases.

2. AVERAGE AND LOCAL MAGNETIC MOMENTS

The experimentally measured magnetizations (Fig. 2) yield the average magnetic moment per Fe atom M_{tot}. In calculations, this value corresponds to the magnetic moment of the unit cell divided by the number of magnetic atoms in the cell. Under the local magnetic moment M_d, we mean the total spin density of d-like electrons inside a muffin-tin sphere.

The measured average magnetic moments per magnetic atom (M_{tot} = 2.380 μ_B for $Fe_{15}Sn$ and 2.228 μ_B for $Fe_{15}Si$) exceed the experimental values obtained for the corresponding disordered alloys. However, their difference ΔM = 0.146 μ_B coincides within the experimental error with the experimentally observed value (Fig. 2). Taking into account that the disordering leads to a 1.5–2% decrease in the values of the magnetic moment at the solute concentration of 6.25 at. % in comparison with the initial value [6], we may speak of the applica-

Table 1. Calculated values of the hyperfine fields and magnetic moments in $Fe_{15}Sn$

Quantity	Unit cell parameter, au	Type of nonequivalent Fe positions relative to Sn atom				M_{tot}, μ_B
		I	II	III	IV	
H_{cor}, kG	10.8114[1]	–281.9	–291.7	–304.4	–316.3	
	10.9924[2]	–295.5	–304.0	–317.9	–317.7	
	10.9924[3]	–299.4	–308.3	–321.7	–317.5	
H_{val}, kG	10.8114[1]	–17.4	–24.6	17.4	–7.1	
	10.9924[2]	–18.4	–32.2	11.7	–14.2	
	10.9924[3]	–22.5	–35.3	8.0	–17.8	
H_{tot}, kG	10.8114[1]	–299.3	–316.3	–287.0	–323.3	
	10.9924[2]	–313.8	–336.2	–306.2	–331.9	
	10.9924[3]	–321.9	–343.6	–313.1	–335.3	
M_d, μ_B	10.8114[1]	2.303	2.371	2.472	2.552	2.269
	10.9924[2]	2.418	2.489	2.624	2.614	2.374
	10.9924[3]	2.433	2.503	2.606	2.565	2.377

[1] Unit cell parameter (au) corresponding to the doubled lattice parameter of pure iron.

[2] Unit cell parameter corresponding to the doubled lattice parameter of disordered alloy $Fe_{1-x}Sn_x$ ($x = 0.0625$).

[3] Fe atoms that are nearest neighbors of Sn atoms are shifted by $\delta r = 0.038$ au along the large diagonal of the unit cell cube (partially relaxed lattice).

Table 2. Calculated values of the hyperfine fields and magnetic moments in $Fe_{15}Si$. Unit cell parameter (au) corresponds to the doubled lattice parameter of the disordered alloy $Fe_{1-x}Si_x$ ($x = 0.0625$)

Quantity	Unit cell parameter, au	Type of nonequivalent Fe positions relative to Si atom				M_{tot}, μ_B
		I	II	III	IV	
H_{cor}, kG	10.7926	–277.8	–290.7	–297.1	–311.7	
H_{val}, kG	10.7926	–27.8	–20.0	4.1	–11.5	
H_{tot}, kG	10.7926	–305.5	–310.7	–293.0	–323.2	
M_d, μ_B	10.7926	2.264	2.360	2.418	2.518	2.228

bility of our calculations for the analysis of differences in the formation of magnetic moments in alloys with impurities such as Sn and Si.

The values of the local magnetic moment at an Fe atom depending on the distance to the metalloid atom in ordered $Fe_{15}M$ alloys (M = Sn, Si) are shown in Fig. 5. As was supposed previously [11], the local magnetic moments are determined by at least two opposite factors. The first is connected with the effective overlap of *d*-like wave functions, which decreases with increasing number of impurity atoms or with increasing spacing between the atoms. The second factor is related to flattening of the *d* band by increasing the degree of *s*–*d* hybridization at an Fe site due to a distortion of the potential by an impurity atom. The locality of the *s*–*d* hybridization leads to a strong dependence of this effect on the interatomic spacings. Figure 6 demonstrates the different influence of these factors on the width of the *d*-state distribution for the Fe atoms located in nonequivalent positions I and IV. The narrowing of this distribution for an Fe atom of type IV leads to an increase in the magnetic moment compared with an atom in position I. The different values of the local magnetic moments in the equivalent positions in the alloys with Sn and Si are only related to the differences in atomic spacings in these alloys. To prove this, we performed calculations for the $Fe_{15}Sn$ alloy with lattice parameter

Table 3. Calculated magnetic moments in pure iron

a, au	10.7926[1]	10.8114[2]	10.9924[3]
M_d, μ_B	2.321	2.327	2.439
M_{tot}, μ_B	2.214	2.219	2.319

[1] Unit cell parameter corresponds to the doubled lattice parameter of the disordered alloy $Fe_{1-x}Si_x$ ($x = 0.0625$).

[2] Unit cell parameter corresponds to the doubled lattice parameter of pure iron.

[3] Unit cell parameter corresponds to the doubled lattice parameter of the disordered alloy $Fe_{1-x}Sn_x$ ($x = 0.0625$).

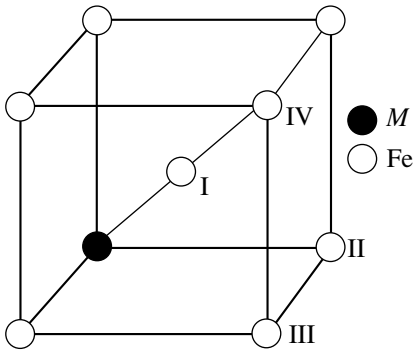

Fig. 4. Nonequivalent positions of Fe atoms in the unit cell of an ordered alloy $Fe_{15}M$ (M = Si, Sn).

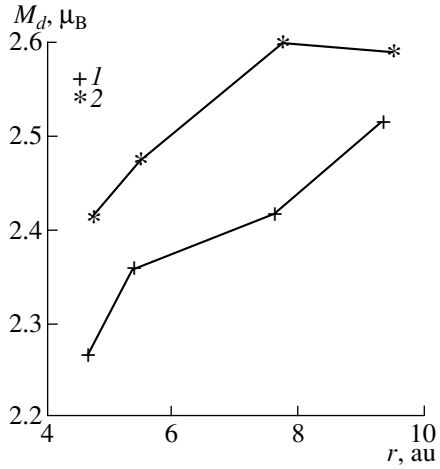

Fig. 5. Local magnetic moments at Fe nuclei in four nonequivalent positions: (*1*) $Fe_{15}Si$ and (*2*) $Fe_{15}Sn$.

a = 10.8114 au (Table 1) and for the bcc Fe with lattice parameters $2a$ = 10.7926, 10.8114, and 10.9924 au (Table 3). (Here, $2a$ = 10.8114 is the experimentally observed value of the lattice parameter of Fe.) It is seen from the results obtained that the values of the local magnetic moments in the alloys with Sn and Si are close to one another (Tables 1 and 2) if their lattice parameters are close, and that the magnetic moment increases with increasing lattice parameter (Table 3).

3. HYPERFINE MAGNETIC FIELDS AT IRON NUCLEI

In hyperfine interactions between the nuclear magnetic moment and the electron subsystem, we only take into account the Fermi contact contribution. The other contributions to the HFF or related measurements are usually assumed to be small in virtue of the cubic symmetry of the crystal lattice. These additional contributions may, however, be significant; we will discuss one case below for illustration. The calculations of the Fermi contact contribution to the HFF were carried out using the standard procedure of integrating the electron spin density with allowance for relativistic effects [17]. This contribution is determined by two terms: H_{cor}, the polarization of electrons of the inner shells ("core electrons"); and H_{val}, the polarization of valence electrons. The mechanisms of polarization of these groups of electrons are somewhat different.

When analyzing the HFFs, we should primarily note two circumstances. First, the polarization of core electrons satisfies (to a great degree of accuracy) the relationship $H_{cor} = \gamma M_d$, where M_d is the spin polarization of d electrons in the muffin-tin sphere, and $\gamma = -123$ kG/μ_B.

Second, the dependence of H_{val} on the distance to an impurity atom is of oscillation character (Fig. 7) and resembles the RKKY polarization. From the simple relationships for free electrons between K_F and the number of s electrons per unit cell ($N_s \approx 11$–15), we can easily estimate the period of the RKKY polarization oscillations [18]:

$$T = a\sqrt{\frac{\pi}{3N_s}} \approx 4.3\text{–}4.8 \text{ au}. \qquad (1)$$

This magnitude corresponds to the period of oscillations in Fig. 7, which confirms the origin of periodic changes in H_{val}. In the simple model of the polarization of free electrons by a localized magnetic moment, the expression for the spin density has the form $\cos(2K_Fr)/(K_Fr)^3$ [18]. Using this relation, we write the contribution of valence electrons to the HFF at a site r_i in the form

$$H_{val}(r_i) = A + B\sum_{j\in Fe,\, j\neq i}^{r_{i-j}=r^{max}} \frac{\sin\left[2\pi\left(\frac{r_{i-j}}{T}+\phi\right)\right]}{r_{i-j}^3}. \qquad (2)$$

Given four values of $H_{val}(r_i)$ for the four nonequivalent positions of Fe atoms in the lattice of $Fe_{15}Sn$ and H_{val} for pure iron, we solved the set of equations (2) by the least-squares method (the summation was restricted to the atoms that were located inside a sphere of radius $r^{max} \approx 70$ au) to obtain $A = -121.24$ kG, $B = 917$ kG au^3, $T = 4.850$ au, and $\phi = 0.128$. The graph of the RKKY polarization by a single Fe atom, corresponding to the second term in (2), is given in Fig. 8. Using this solution and expression (2), we calculated the values of H_{val} for the $Fe_{15}Si$ system and obtained a significant discrepancy with the results of first-principles calculations (Table 2). This indicates the unsubstantiated arbitrariness of the choice of the simple functional dependence of the form $\cos(2K_Fr)/r^3$, which does not take into account the spatial distribution of the s–d exchange interaction and the nonuniformity of the s-electron density distribution. However, for the estimation of the polarization of valence electrons by Fe atoms randomly located in the lattice, i.e., for the estimation of average quantities, expression (2) appears to be quite accept-

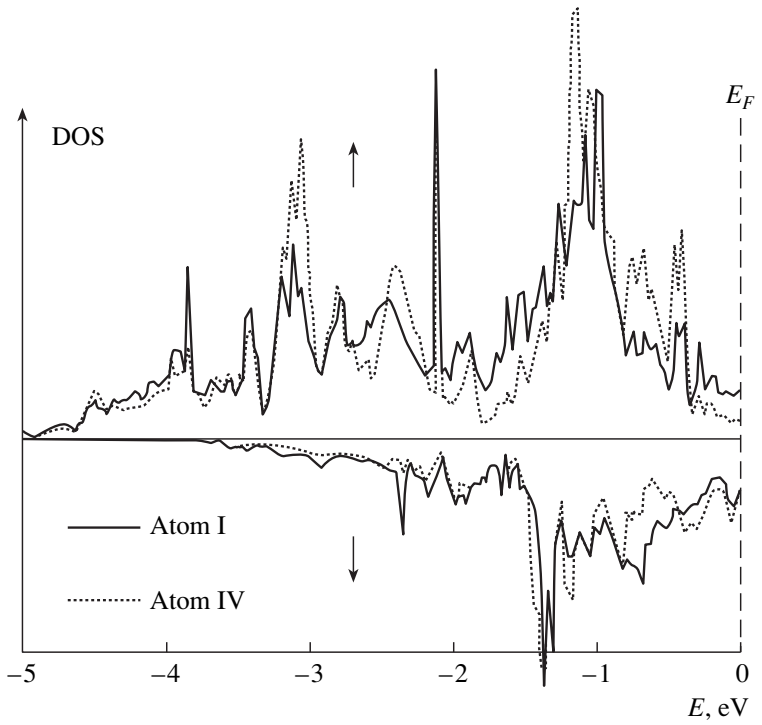

Fig. 6. Spin-polarized density of states of *d* electrons at Fe atoms. The upper part of the figure, electrons with spins up, the lower part, for electrons with spins down.

able, since it satisfactorily reflects the main features of the RKKY polarization: its period, amplitude, and phase. Figure 9 displays the average contributions H_{val} to the HFF caused by the RKKY polarization. The averaging was performed over the Fe atoms randomly located inside a sphere of radius $r^{max} \approx 70$ au. To allow for the attenuation, the contribution of the RKKY polarization was multiplied by $\exp(-r_{i-j}/l_0)$ [19]. The quantity l_0—the electron free path—corresponded to the average spacing of impurity atoms and changed from ≈220 to ≈20 au with changing the metalloid concentration from 0 to 6.25 at. %.

Using the model assumptions, let us estimate the possible contribution of the averaged RKKY polarization from the experiment. To this end, we assume that in the disordered FeSn alloys at hand, the changes in the magnetic moment are described by a step function of the type

$$M = \begin{cases} M_1 = M_{Fe}, & \text{if an atom is a nearest neighbor} \\ & \text{of an impurity atom;} \\ M_0 = \text{const}, & \text{otherwise.} \end{cases} \quad (3)$$

This functional dependence agrees with our values of the calculated magnetic moment (Fig. 5). From (3) and the experimental data given in Fig. 2, we calculate the changes (depending on the concentration) in the magnetic moment $\Delta M_0(c)$ at a Fe atom whose nearest neighborhood contains no metalloid atoms ($\Delta M_0(c = 3$ at. %) = 0.05 μ_B, $\Delta M_0(c = 6.25$ at. %) = 0.17 μ_B). Using a value of –151.8 kG/μ_B for the coefficient α that relates the experimental values of the magnetic moment and the HFF in pure iron ($H = \alpha M$), we obtain $\Delta H_0(c = 3$ at. %) = –8.1 kG and $\Delta H_0(c = 6.25$ at. %) = –22.8 kG. Both these values noticeably exceed the experimentally observed changes in H_0 (Fig. 3). Based on the fact that our calculations yield an almost ideal linear dependence

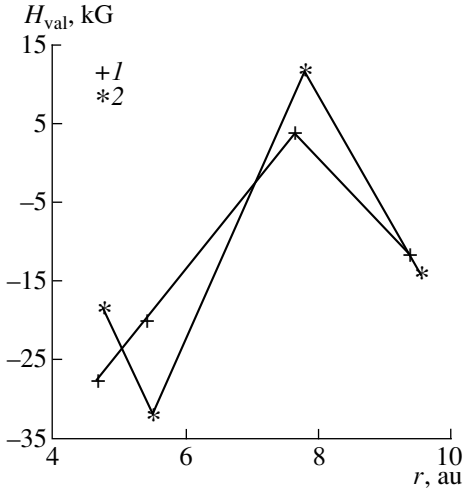

Fig. 7. Contribution of the polarization of valence electrons to the hyperfine magnetic fields at Fe nuclei in four nonequivalent positions: (*1*) $Fe_{15}Si$ and (*2*) $Fe_{15}Sn$.

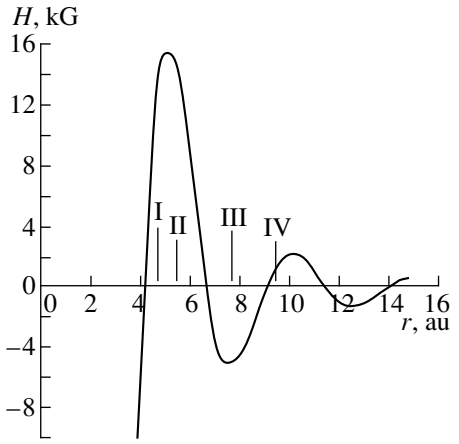

Fig. 8. RKKY polarization by one Fe atom. I–IV are the nonequivalent positions of Fe atoms relative to Sn atoms.

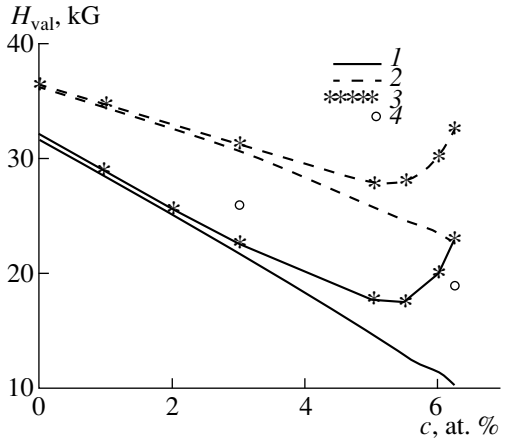

Fig. 9. Concentrational dependence of the averaged valence-electron to the HFF in a disordered FeSn alloy: (*1*) the field H_0, (*2*) the field H_1, (*3*) with damping included, and (*4*) this contribution to H_0 as evaluated from experimental data.

of the polarization of core electrons upon the local magnetic moment, we can state that the difference between the calculated and experimentally measured changes of ΔH_0 is equal to the averaged contribution of the RKKY polarization. This yields $\Delta H_{0\,\mathrm{exp}}^{\mathrm{val}}(c = 3$ at. %) = 6.1 kG and $\Delta H_{0\,\mathrm{exp}}^{\mathrm{val}}(c = 6.25$ at. %) = 13.8 kG, which satisfactorily agrees with the concentration dependence of $\Delta H_{0\,\mathrm{calc}}^{\mathrm{val}}$ obtained upon averaging using (2) (Fig. 9).

The behavior of mean-square fluctuations also is consistent with the experimentally observed broadening of the distribution of HFFs at Fe nuclei depending on the concentration, which suggests that the fluctuations of the RKKY polarization give one of the major contributions to the broadening of the HFF distribution.

After averaging the contributions of core electrons to the HFF (Table 1), we obtain, taking into account the changes in the average value of valence-electron contribution (Fig. 8), the following figures:

$$\frac{\overline{H}_0^{(\mathrm{Fe_{15}Sn})}}{H^{(\mathrm{Fe})}} = 1.041, \quad \frac{\overline{H}_1^{(\mathrm{Fe_{15}Sn})}}{H^{(\mathrm{Fe})}} = 1.019.$$

Similar to the case of the magnetic moment, the value of $\overline{H}_0^{(\mathrm{Fe_{15}Sn})}$ is somewhat greater than the experimental values. Since the increase in $\overline{H}_0^{(\mathrm{Fe_{15}Sn})}$ is mainly related to the increase in the local magnetic moment, the discrepancy with the experiment can be explained by the effect of disordering (a 1.5–2% decrease of the magnetic moment due to disordering will square the experimental results with theoretical data).

The case of the field $\overline{H}_1$ is different. Its relative value differs strongly from the experimental one (Fig. 3). In the framework of our calculations, this difference can only be explained by an additional contribution related to the orbital magnetic moment. Up to here, we have not discussed this contribution to the magnetization and the HFF. In pure iron, this quantity caused by the distortion of the cubic symmetry of the Hamiltonian due to relativistic corrections, is $\approx 0.08\ \mu_B$. At the same time, the incorporation of a metalloid atom breaks the cubic symmetry of the crystalline potential, which should lead to an additional "defreezing" of the orbital magnetic moment, and the increase in the crystalline potential should decrease the absolute value of the HFF at the nuclei. Note that a decrease in the absolute value of the HFF by 20 kG may be caused by an insignificant increase in the orbital magnetic moment (by about 0.06 μ_B) [20]. The maximum change in the crystalline potential occurs near a metalloid atom, i.e., in the first coordination shell, where the main changes related to the contribution from the orbital magnetic moment occur. This is confirmed by the almost the same difference $H_0 - H_1 \approx 20$ kG for both $Fe_{100-c}Sn_c$ and $Fe_{100-c}Si_c$.

ACKNOWLEDGMENTS

The authors are grateful to the International Center of Theoretical Physics (Triest, Italy) for the opportunity of participating in the seminar *The Physics of the Electronic Behavior in the Core Region: All-Electron LAPW Electronic Structure Calculations* held on June 22–July 4, 1998. This work was supported by the Russian Foundation for Basic Research, project no. 97-02-16270.

REFERENCES

1. E. P. Yelsukov, E. V. Voronina, and V. A. Barinov, J. Magn. Magn. Mater. **115**, 271 (1992).
2. A. Taylor and R. M. Jones, J. Phys. Chem. Solids **6**, 16 (1958).

3. M. C. M. Farquhar, H. Lipson, and A. R. Weil, J. Iron Steel Inst. **152**, 457 (1945).
4. F. Richter and W. Pepperhoff, Arch. Eisenhüttenw. **45**, 107 (1974).
5. E. P. Elsukov, V. A. Barinov, and G. N. Konygin, Fiz. Met. Metalloved. **62**, 719 (1986).
6. A. K. Arzhnikov, L. V. Dobysheva, E. P. Elsukov, *et al.*, Zh. Eksper. Teor. Fiz. **110**, 1127 (1996).
7. M. Fallot, Ann. Phys. **6**, 305 (1936).
8. D. Parsons, W. Sucksmith, and J. E. Thompson, Philos. Mag. **3**, 1174 (1958).
9. E. P. Elsukov, G. N. Konygin, V. A. Barinov, *et al.*, J. Phys.: Condens Matter **4**, 7597 (1992).
10. E. P. Elsukov, E. V. Voronina, F. M. Fomin, *et al.*, Fiz. Met. Metalloved. **85**, 89 (1998) [Phys. Met. Metallogr. **85** (3), 307 (1998)].
11. A. K. Arzhnikov and L. V. Dobysheva, J. Magn. Magn. Mater. **117**, 87 (1992).
12. A. K. Arzhnikov and L. V. Dobysheva, Phys. Lett. A **195** (2), 176 (1994).
13. H. Ebert and H. Akai, Hyperfine Interact. **78**, 361 (1993).
14. P. Blaha, K. Schwarz, and J. Luitz, *WIEN97* (Vienna Univ. of Technology, 1997).
15. P. Blaha, K. Schwarz, P. Sorantin, *et al.*, Comput. Phys. Commun. **59**, 399 (1990).
16. J. P. Perdew, S. Burke, and M. Ernzerhof, Phys. Rev. Lett. **77**, 3865 (1996).
17. H. Akai, M. Akai, S. Blügel, *et al.*, Prog. Theor. Phys. Suppl. **101**, 11 (1990).
18. N. W. Ashcroft and N. D. Mermin, *Solid State Physics* (Holt, Rinehart, and Winston, New York, 1976; Mir, Moscow, 1979), Vol. 2.
19. *Hyperfine Interactions*, Ed. by A. Freeman and R. Frankel (New York, 1967; Mir, Moscow, 1970).
20. M. Battocletti, H. Ebert, and H. Akai, Phys. Rev. B: Condens. Matter **53** (15), 9776 (1996).

Translated by S. Gorin

Physics of the Solid State, Vol. 42, No. 1, 2000, pp. 96–102. Translated from Fizika Tverdogo Tela, Vol. 42, No. 1, 2000, pp. 93–99.

MAGNETISM AND FERROELECTRICITY

Antiferromagnetic Resonance in CuB_2O_4 Single Crystal

A. I. Pankrats, G. A. Petrakovskiĭ, and N. V. Volkov

Kirenskii Institute of Physics, Siberian Division, Russian Academy of Sciences, Akademgorodok, Krasnoyarsk, 660036 Russia
e-mail: pank@cc.krascience.rssi.ru

Received May 18, 1999

Abstract—The frequency–field, temperature, and angular dependences of the antiferromagnetic resonance parameters for the tetragonal CuB_2O_4 single crystal are studied in the frequency range 2.6–80 GHz and at temperatures of 4.2–30 K. The results obtained confirm the fact that, in the high-temperature state in the range 10–21 K, this compound is an easy-plane weak ferromagnet. The temperature dependence of the Dzyaloshinski field is determined. An abrupt change observed in the frequency–field dependence of the magnetic resonance at $T = 4.2$ K and $\mathbf{H} \perp C_4$ indicates the transition to the weak ferromagnetic state induced by the external field $H_\perp$. The phase diagram for CuB_2O_4 is constructed on the $H_\perp$–T coordinates. It is demonstrated that, in the low-temperature state, the magnetic moments of copper ions remain in the basal plane, but the weak ferromagnetism is absent. © *2000 MAIK "Nauka/Interperiodica".*

The discovery of the high-temperature superconductivity gave impetus to active research in copper oxide compounds. These materials possess a broad spectrum of magnetic structures from usual three-dimensional antiferromagnets (Bi_2CuO_4 [1]) to quasi-low-dimensional magnets with a spin-Peierls state ($CuGeO_3$ [2]) and a ladder structure ($KCuCl_3$ and $LiCu_2O_2$ [3, 4]).

Tetragonal CuB_2O_4 single crystals with the space group D_{2d}^{12} have been grown in recent experiments [5]. Preliminary studies [5–7] showed that, at temperatures below $T_N = 21$ K, this crystal is an easy-plane weak ferromagnet. According to the data on static magnetic measurements and heat capacity, the magnetic phase transition is observed at $T \approx 10$ K. It was assumed that this transition is the Morine transition from the weak ferromagnetic state to the collinear state with the easy anisotropy axis parallel to the C_4 axis [6, 7].

The aim of the present work was to investigate the frequency–field and temperature dependences of the magnetic resonance absorption in the CuB_2O_4 crystal in order to obtain additional information regarding the magnetic structure of this crystal, specifically in the low-temperature state.

EXPERIMENTAL

Samples of CuB_2O_4 were grown by the spontaneous crystallization technique [5].

The magnetic resonance measurements in the frequency range 28–80 GHz were carried out with a pulsed-magnetic-field spectrometer, in which the sample was placed in a plunged waveguide unit. In the frequency range 2.5–10 GHz, the measurements were performed on a magnetic resonance spectrometer with a stationary magnetic field: at a frequency of 2.5–6 GHz, the sample was mounted in a plunged coaxial unit, and, at 8–10 GHz, it was placed in a plunged waveguide or a resonant cavity.

RESULTS

Figures 1 and 2 depict the frequency–field dependences of the antiferromagnetic resonance in CuB_2O_4 at $T = 4.2$ K for two orientations of magnetic field with respect to the C_4 axis of the crystal: $\mathbf{H} \parallel C_4$ and $\mathbf{H} \perp C_4$. At $\mathbf{H} \parallel C_4$, the frequency–field dependence of the antiferromagnetic resonance is almost linear and tends to $\omega_c \approx 1.5$ GHz at $H \longrightarrow 0$. At $\mathbf{H} \perp C_4$, the frequency–field dependence also exhibits a small gap at $\omega_c = 2.4$ GHz (Fig. 2, inset 1). Moreover, an increase in the field leads to an abrupt change in the magnetic resonance frequency at $H \approx 12$ kOe. This portion of the frequency–field dependence of the antiferromagnetic resonance is displayed in inset 2 (Fig. 2).

The temperature dependences of the resonance parameters were measured at several frequencies for orientations of the external magnetic field along the C_4 axis and in the basal plane. Figure 3 shows the temperature dependences of the resonance field and the absorption linewidth at two frequencies and $\mathbf{H} \parallel C_4$. At both frequencies, the resonance field drastically decrease at $T \approx 8.5$ K, which is accompanied by a strong broadening of the absorption line. Upon further heating of the sample, the resonance field smoothly increases up to the value characteristic of the paramagnetic state at $T > 20$ K [6].

Figure 4 demonstrates typical temperature dependences of the resonance field measured at three different frequencies for the orientation $\mathbf{H} \perp C_4$. At frequencies of 10.6 and 28.65 GHz, the resonance field under-

goes a sharp change in the low-temperature range. The temperature that corresponds to this change in the resonance field decreases with an increase in the frequency. At a frequency of 56.59 GHz, the low-temperature anomaly of the resonance field is not observed down to $T = 4.2$ K. Upon heating, as the sample temperature approaches $T_N = 20$ K, the resonance field increases up to the value characteristic of the paramagnetic state. Moreover, the temperature range, in which the resonance field undergoes the above change, becomes narrower with a decrease in the frequency.

The temperature dependences of the linewidth at different frequencies for the orientation $\mathbf{H} \perp C_4$ are also shown in Fig. 4. It worth nothing that, at a frequency of 56.59 GHz, the linewidth, like the resonance field, does not exhibit anomalous behavior in the low-temperature range, whereas a pronounced broadening of the absorption line is observed at frequencies below ~45 GHz. As regards the broadening of the absorption line in the vicinity of T_N, the temperature range, in which this broadening takes place, becomes broader with an increase in the frequency of the experiment.

The angular dependences of the resonance field and the absorption linewidth for the magnetic field measured in the basal plane of the crystal for two frequencies at $T = 4.2$ K are displayed in Fig. 5.

DISCUSSION

In [6, 7], it was assumed that the tetragonal CuB_2O_4 crystal in the temperature range 10–21 K is an easy-plane weak ferromagnet with the spontaneous magnetic moment lying in the basal plane of the crystal. The energy density of this magnet can be written in the form [8]

$$F = J\mathbf{M}_1\mathbf{M}_2 - \mathbf{D}[\mathbf{M}_1 \times \mathbf{M}_2] - \mathbf{H}(\mathbf{M}_1 + \mathbf{M}_2) - K_1/2(\cos^2\beta_1 + \cos^2\beta_2) - K_2/2(\cos^4\beta_1 + \cos^4\beta_2). \quad (1)$$

Here, J is the exchange interaction constant; $\mathbf{M}_i$ are the magnetic moments of the sublattices; $\mathbf{D}$ is the Dzyaloshinski vector directed, in our case, along the $\mathbf{z} \parallel C_4$; K_1 and K_2 are the first-order and second-order constants of uniaxial anisotropy, respectively; and β_i are the angles between the magnetic moments of the sublattices and the principal crystal axis. The effective exchange field, Dzyaloshinski interaction, and uniaxial anisotropy field that correspond to relationship (1) are defined as follows:

$$H_E = JM_0, \quad H_D = DM_0, \quad H_{k1} = K_1/M_0,$$
$$H_{k2} = K_2/M_0,$$
$$M_0 = |\mathbf{M}_1| = |\mathbf{M}_2|.$$

If the transition observed in CuB_2O_4 at $T = 10$ K in weak fields is a spin-reorientation transition to the collinear antiferromagnetic state, it is caused by the change in sign of the effective uniaxial anisotropy field $H_a = H_{k1} + H_{k2}$. A similar transition referred to as the Morine transition is observed in hematite α-Fe_2O_3 at $T_M = 262$ K [8]. Below this temperature, the hematite transforms into the collinear antiferromagnetic state with the magnetic moments oriented along the principal crystal axis.

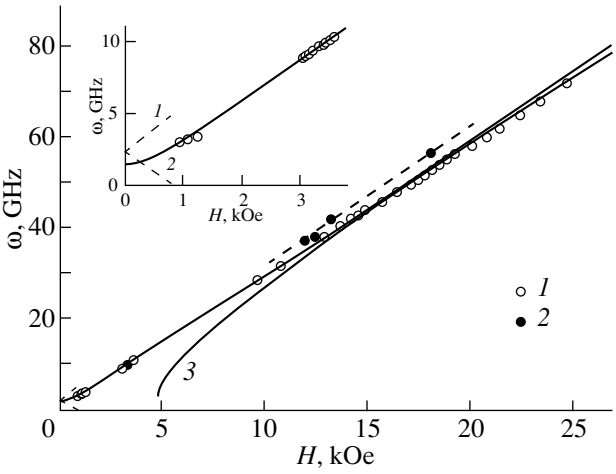

Fig. 1. Frequency–field dependences of the antiferromagnetic resonance in CuB_2O_4 for $\mathbf{H} \parallel C_4$ at $T = (1)$ 4.2 and (2) 13 K. The solid line corresponds to the results of calculations by formula (11). Dashed lines *1*, *2*, and *3* represent the data calculated by formulas (9) and (10) for ω_{21}, ω_{11}, and ω_{12}, respectively.

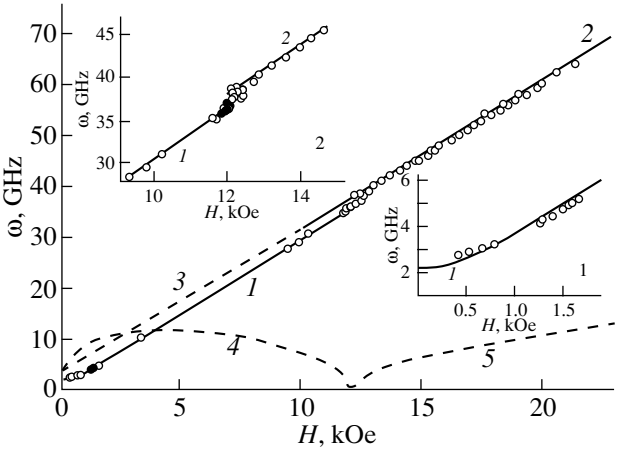

Fig. 2. Frequency–field dependences of the antiferromagnetic resonance in CuB_2O_4 for $\mathbf{H} \perp C_4$ at $T = 4.2$ K. Solid lines *1* and *2* correspond to the results of calculations for ω_{22} by formulas (7) and (5), respectively. Dashed lines *3*, *4*, and *5* represent the data calculated by formulas (4) and (5) for ω_{21}, ω_{11}, and ω_{12}, respectively.

Although the weak ferromagnetism is absent in the low-temperature collinear state, the Dzyaloshinski interaction affects the behavior of the antiferromagnet in the magnetic field [8–10]. Specifically, upon magne-

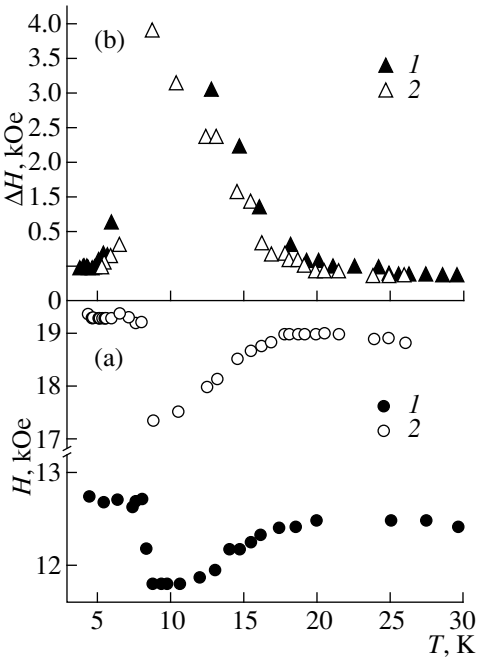

Fig. 3. Temperature dependences of (a) the resonance field and (b) the absorption linewidth for $\mathbf{H} \parallel C_4$. Frequency, GHz: (*1*) 37.76 and (*2*) 56.00.

tization along the principal crystal axis, the transition to the spin-flop state occurs in the critical field

$$H_c^2 = 2H_E(H_{k1} + H_{k2}) - H_D^2. \quad (2)$$

Upon magnetization in the basal plane of the crystal, the Dzyaloshinski interaction leads not only to the alignment of magnetic moments with the magnetic field, but also to the rotation of the antiferromagnetic vector $\mathbf{l} = (\mathbf{M}_1 - \mathbf{M}_2)/2M_0$ away from the principal crystal axis toward the basal plane. The angle θ between the C_4 axis and vector $\mathbf{l}$ increases with an increase in the magnetic field and reaches $\pi/2$ at the critical field $H_{c\perp}$

$$H_{c\perp} = (2H_E H_{k1} - H_D^2)/H_D. \quad (3)$$

In this case, depending on the ratio between the values of H_E, H_{k1}, H_{k2}, and H_D, the transition to the magnetic-field-induced weak ferromagnetic state at $H = H_{c\perp}$ can be eithera first-order or second-order phase transition.

As follows from the investigation on the temperature–field dependences of the magnetization for CuB_2O_4 [11], the critical field $H_{c\perp}$ depends on the temperature and reaches 12 kOe at $T = 4.2$ K. Upon magnetization along the C_4 axis at $T = 4.2$ K, the field dependence of the magnetization shows a weakly pronounced anomaly in the field $H = 2$ kOe, which can be taken as the critical field $H_{c\parallel}$. Using these values of the critical fields and the value of $H_D = 1.9$ kOe obtained in [6] for $T = 10$ K and also ignoring the temperature dependence of H_D below 10 K, at $T = 4.2$ K, we can calculate the parameters $2H_E H_{k1} = 26.41$ kOe^2 and $2H_E H_{k2} = -18.8$ kOe^2.

The resonance properties of an easy-axis antiferromagnet with the Dzyaloshinski interaction were discussed in detail in [8–10] on the condition that $H_a \ll H_D \ll H_E$, which holds true for CuB_2O_4. Let us use the results of these calculations to analyze the experimental data on the magnetic resonance in CuB_2O_4.

First and foremost, we consider the frequency–field dependences of the antiferromagnetic resonance measured at $T = 4.2$ K. It should be mentioned that the frequency jump at $\mathbf{H} \perp C_4$ occurs in the field coinciding with $H_{c\perp}$. For $\mathbf{H} \perp C_4$, the resonance frequencies at $H < H_{c\perp}$ (state 1) take the form

$$(\omega_{11}/\gamma)^2 = ((\omega_c/\gamma)^2 - 12H_E H_{k2}\sin^2\theta)\cos^2\theta,$$

$$(\omega_{21}/\gamma)^2 = (\omega_c/\gamma)^2 - 4H_E H_{k2}\sin^2\theta + H^2,$$

$$\sin\theta = HH_D/(2H_E(H_{k1} + 2H_{k2}\cos^2\theta) - H_D^2), \quad (4)$$

where $(\omega_c/\gamma)^2 = 2H_E(H_{k1} + 2H_{k2}) - H_D^2 = H_{c\parallel}^2 + 2H_E H_{k2}$ is the energy gap in the spectrum. In ω_{ij}, the subscript i is the number of vibrational mode, and the subscript j is the number of state.

In the field range $H > H_{c\perp}$ (state 2), the resonance frequencies are given by

$$(\omega_{12}/\gamma)^2 = HH_D - (2H_E H_{k1} - H_D^2) = H_D(H - H_E), \quad (5)$$

$$(\omega_{22}/\gamma)^2 = H(H + H_D).$$

The experimental data for $H > H_{c\perp}$ are adequately described by formula (5) for the high-frequency vibrational mode ω_{22}. The solid line in Fig. 2 represents the theoretical dependence at $H_D = 1.91$ kOe. At the same time, the resonance lines that correspond to the low-frequency vibrational mode ω_{12} (shown by the dashed line in Fig. 2) are not observed at the fields up to 80 kOe.

In the field range $H < H_{c\perp}$ (state 1), the experimental data coincide with none of the modes, which are described by expressions (4) and calculated with the above parameters $2H_E H_{k1}$ and $2H_E H_{k2}$. Furthermore, the ω_{11} and ω_{12} frequencies have real values beginning with the fields $H \approx 1$ kOe, whereas the energy gap ω_c and the frequencies of both vibrational modes in the fields $H < 1$ kOe are imaginary, which indicates that the ground state is chosen incorrectly.

Such a disagreement between the calculated and experimental data for the fields $H < H_{c\perp}$ and also the imaginary resonance frequencies could be explained by the fact that an incorrect experimental value of $H_{c\parallel}$ was used to determine the $2H_E H_{k2}$ parameter.

Hence, it is reasonable to describe the experimental data on the antiferromagnetic resonance by using for-

mulas (4) under the assumption that the $H_{c\perp}$ value and, therefore, the parameter $2H_EH_{k1}$ = 26.41 kOe^2 are uniquely determined from the experiment, and the $2H_EH_{k2}$ parameter can be obtained from the experimental energy gap ω_c = 2.4 GHz. This approach leads to $2H_EH_{k2}$ = –11.07 kOe^2. In this case, the theoretical frequency–field dependences (4) for ω_{11} and ω_{21} (shown by dashed lines in Fig. 2) are real over the entire range of fields from 0 to $H_{c\perp}$, but none of these curves coincides with the experimental frequency–field dependence.

Note that, at these values of $2H_EH_{k1}$ and $2H_EH_{k2}$, the calculated critical field $H_{c\|}$ is equal to 3.4 kOe; however, at this field, no specific features are observed in the experimental field dependence of the magnetization [11].

Another aspect is noteworthy. In [10], it was shown that, as the field increases from 0 to $H = H_{c\perp}$, the θ angle either continuously increases from 0 to $\pi/2$ (the second-order transition) or, first, continuously increases from 0 to $\theta_1 < \pi/2$ and, then, at the field $H = H_{c\perp}$, undergoes an abrupt change to $\theta = \pi/2$ (the first-order transition). The relationship for the ω_{21} frequency in the vicinity of $H = H_{c\perp}$ can be rewritten as follows:

$$(\omega_{21}/\gamma)^2 = H(H + H_D/\sin\theta). \qquad (6)$$

Consequently, upon transition from the collinear state to the weak ferromagnetic state, the change $\omega_{21} \longrightarrow \omega_{22}$ proceeds continuously for the second-order transition and in a stepwise fashion for the first-order transition, so that $\Delta\omega = \omega_{22} - \omega_{21} < 0$.

However, as is seen from Fig. 2, in our case, $\Delta\omega > 0$. Moreover, the experimental frequency–field dependence at T = 4.2 K in the field range from 0 to $H_{c\perp}$ is well described by the law

$$(\omega/\gamma_\perp)^2 = H^2(1 + |H_a|/2H_E) + H_\Delta^2 \qquad (7)$$

with $|H_a|/2H_E$ = 0.031 ± 0.005 and H_Δ^2 = (0.526 ± 0.004) kOe^2 (solid line in Fig. 2). Here, H_a is the effective field of anisotropy with respect to the C_4 axis, and H_Δ^2 is the isotropic energy gap, which can arise from magnetoelastic [12] or other interactions. The gyromagnetic ratio $\gamma_\perp$ = 2.983 MHz/Oe corresponds to the value $g_\perp$ = 2.133 obtained from the ESR experiment at room temperature [6]. Dependence (7) is characteristic of easy-plane antiferromagnets without weak ferromagnetism (see, for example, [13, 14]).

Therefore, the above findings put in doubt the fact that, as the temperature decreases, the weak ferromagnet CuB_2O_4 at T = 10 K transforms into the collinear state with the easy anisotropy axis aligned parallel to the C_4 axis.

It can be assumed that, in CuB_2O_4, the magnetic moments at T < 10 K also remain in the basal plane; however, the magnetic structure in this state allows no macroscopic spontaneous magnetic moment. Possible variants of this magnetic structure will be considered below.

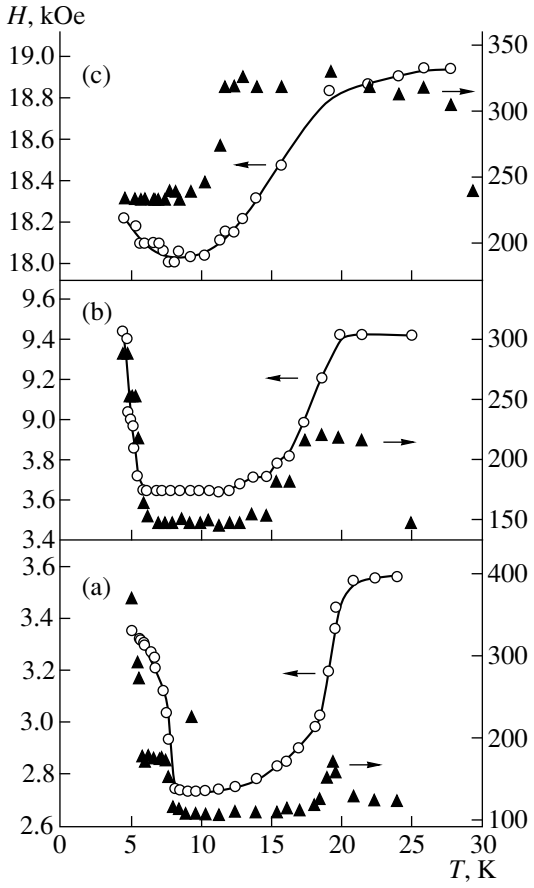

Fig. 4. Temperature dependences of the resonance field and the absorption linewidth for $\mathbf{H} \perp C_4$. Frequency, GHz: (a) 10.6, (b) 28.655, and (c) 56.59.

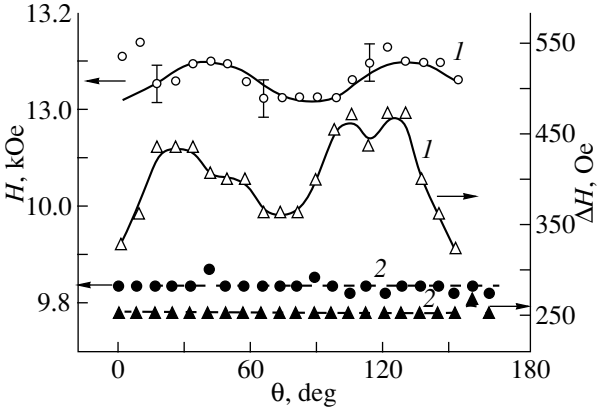

Fig. 5. Angular dependences of the resonance field and the absorption linewidth for $\mathbf{H} \perp C_4$. Frequency, GHz: (*1*) 41.51 and (*2*) 29.008.

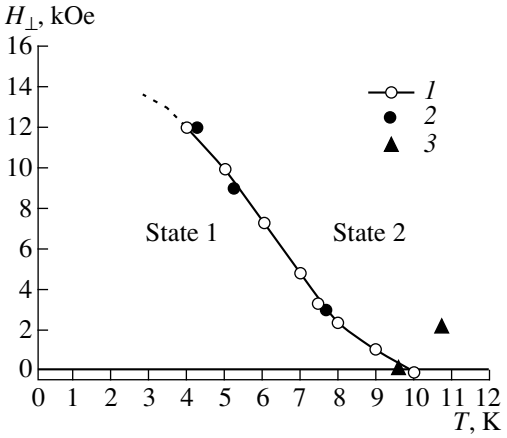

Fig. 6. The $H_\perp$–T phase diagram for CuB_2O_4 according to the data on (*1*) static magnetic measurements, (*2*) magnetic resonance, and (*3*) heat capacity.

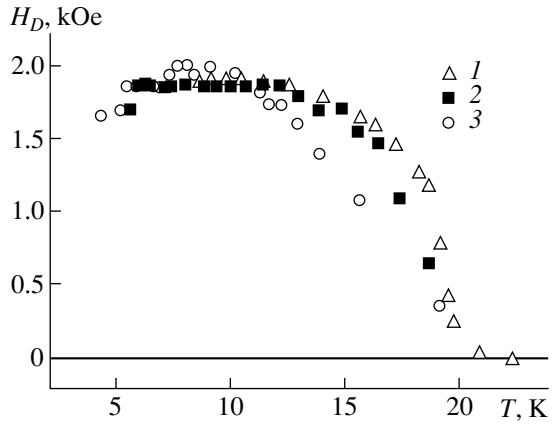

Fig. 7. Temperature dependences of the Dzyaloshinski field. Frequency, GHz: (*1*) 10.6, (*2*) 28.655, and (*3*) 56.59.

Sharply defined anomalies in the temperature dependences of the resonance parameters for CuB_2O_4 at $T < 10$ K (Fig. 4) are observed at some frequencies in the basal-plane fields. They are associated with the transition from the low-temperature state 1 to the weak ferromagnetic state 2 in the field $H_{c\perp}$. It is seen from Fig. 4 that the transition temperature depends on the frequency of the measurement, which suggests the temperature dependence of the critical field $H_{c\perp}$. Figure 6 demonstrates the $H_\perp$–T phase diagram constructed from the data on static magnetic measurements [11], heat capacity [7], and magnetic resonance. From the phase diagram, it is evident that the absence of low-temperature anomaly at a frequency of 56.09 GHz (Fig. 4c) is explained by the fact that, in the resonance field for this frequency (~18 kOe), the CuB_2O_4 crystal already at $T = 4.2$ K is in the magnetic-field-induced weak ferromagnetic state.

With equation (5) for ω_{22} and the temperature dependence of the resonance field for the weak ferromagnetic state, we calculated the temperature dependences of the Dzyaloshinski field $H_D(T)$ (Fig. 7). It is seen that thus obtained values of H_D are independent of the frequency of the measurement at temperatures below ~12 K. Above this temperature, as the temperature approaches T_N, the higher the frequency of a measurement, the steeper the dependence $H_D(T)$ declines to zero. This is likely due to the fact that the resonance fields corresponding to high frequencies of the measurement become comparable to the exchange field, which is anomalously weak in the CuB_2O_4 crystal [11]. As a result, the canting angle of magnetic sublattices φ in the external field cannot be treated as small, and, instead of equation (5), ω_{22} should be calculated by the formula [15]

$$(\omega_{22}/\gamma)^2 = H(H + |H_a|\sin\varphi + H_D\cos\varphi). \qquad (8)$$

It is clear that the role of this factor increases with a decrease in the H_E field as the temperature approaches T_N. Assuming that measurements at a frequency of 10.6 GHz give the $H_D(T)$ dependence, which is the closest to actual, and ignoring the contribution of H_a ($|H_a| \ll H_D, H$), we obtain that, in the resonance field $H \approx 18$ kOe corresponding to a frequency of 56.09 GHz, the canting angle of sublattices φ is equal to approximately 50° at $T = 15$ K.

The broadening of the absorption line in the vicinity of T_N at a frequency of 10.6 GHz is typical of the fluctuation broadening. Usually, an increase in the frequency of the measurement leads to a narrowing of the peak in the temperature dependence of the linewidth and a decrease in its height, because the strong field more efficiently suppresses fluctuations disturbing the magnetic ordering (see, for example, [16]). However, the reverse situation is observed for the CuB_2O_4 crystal: the peak in the temperature dependence of the linewidth is substantially broadened with an increase in the frequency. Moreover, at the same frequency, as the temperature approaches T_N, a clear correlation is observed between sharp broadening of the absorption line and the deviation from the true temperature dependence of the Dzyaloshinski field. Therefore, it is quite possible that such an unusual behavior of the linewidth is caused by the "collapse" of sublattices.

Let us now analyze the data on the magnetic resonance for the orientation $\mathbf{H} \parallel C_4$. In the case of a collinear antiferromagnet with the easy anisotropy axis aligned parallel to C_4, the frequency–field dependences have the form

$$\omega_{11,21}/\gamma = \omega_c/\gamma \pm H, \quad H < H_{c\parallel} \qquad (9)$$

$$(\omega_{12}/\gamma)^2 = H^2 - (2H_E H_{k1} - H_D^2), \quad H > H_{c\parallel} \qquad (10)$$

$$\omega_{22} = 0,$$

where ω_c/γ is the energy gap in the spectrum in the same form as in formula (4). The frequency–field dependences were calculated with the same values of $2H_EH_{k1}$ and $2H_EH_{k2}$ as in the case when $\mathbf{H} \perp C_4$. The calculated dependences of ω_{11}, ω_{21}, and ω_{12} (see Fig. 1 and inset) disagree with the experimental data. Furthermore, it follows from the calculations that, at the values used for $2H_EH_{k1}$ and $2H_EH_{k2}$, the resonance absorption should be absent at all in the field range from approximately 0.8 to 4.8 kOe; nonetheless, this absorption is observed experimentally.

Furthermore, the experimental frequency–field dependence of the antiferromagnetic resonance at T = 4.2 K for $\mathbf{H} \parallel C_4$ is smooth over the entire field range from 0.8 to 25 kOe and does not exhibit features accompanying the spin-reorientation transition from the easy-axis state to the spin-flop state. The absence of this transition at T = 4.2 K is also evidenced by anomalies in the temperature dependences of the resonance field and the linewidth (Fig. 3). Obviously, it is this abrupt change in the resonance field and this broadening of the absorption linewidth that are connected with the transition from the low-temperature state to the easy-plane weak ferromagnetic phase. Within the limits of experimental error, the temperature of the anomalies coincides with the transition temperature found from the heat capacity data [7] and does not depend on the external field, as would be the case of the transition from the easy-axis state to the easy-plane state.

At T = 4.2 K, the frequency–field dependence for $\mathbf{H} \parallel C_4$ is well represented by the relationship

$$(\omega/\gamma_\parallel)^2 = H^2 + H_\Delta^2 \qquad (11)$$

with $\gamma_\parallel = 2.92 \pm 0.01$ and $H_\Delta^2 = 0.26 \pm 0.03$ kOe^2 (solid line in Fig. 1). This dependence is characteristic of easy-plane antiferromagnets; in this case, the energy gap $H_\Delta^2 = 2H_EH_{k1} + H_D^2$. Certainly, a small value of the gap is surprising. However, the frequency–field dependence similar in character to relation (11) with the same value of H_Δ^2 is retained upon transition to the weak ferromagnetic state. An abrupt change in the resonance field upon this transition can be formally described by the variation in the g value from $g_\parallel = 2.087$ at T = 4.2 K to $g_\parallel = 2.210$ at T = 13 K. The reason for this behavior of the g value upon transition remains unclear.

Therefore, the resonance data for $\mathbf{H} \parallel C_4$ also indicate that CuB_2O_4 in the low-temperature phase is not collinear antiferromagnet with the easy anisotropy axis aligned parallel to the C_4 axis.

As regards the hypothetical magnetic structures, which could be realized in the low-temperature phase of CuB_2O_4, a possible cause of the absence of weak ferromagnetic moment in the low-temperature state resides in the fact that the adjacent, local weak ferromagnetic moments in this state are ordered antiferromagnetically. In particular, a similar structure is observed in the Y_2CuO_4 compound [17] and in the $YFe_{1-x}Cr_xO_3$ system [18]. These magnetic structures can be regarded as slightly noncollinear four-sublattice structures, which were investigated, for example, in [19]. Note that the external field applied across the basal plane of the Y_2CuO_4 crystal, as for the CuB_2O_4 crystal, induces the transition to the weak ferromagnetic state.

The absence of weak ferromagnetic moment in the low-temperature state of CuB_2O_4 can also be associated with a helical magnetic structure. A similar pattern is observed for the hexagonal $NiBr_2$ crystal [20]. In this crystal, the collinear magnetic ordering with the easy anisotropy plane perpendicular to the hexagonal axis is achieved at T_N = 52 K, and, with a further decrease in the temperature below T = 22.8 K, $NiBr_2$ transforms into the helical incommensurable phase. At temperatures below 22.8 K, the external magnetic field applied across the basal plane destroys the helical structure and transforms this crystal to the easy-plane collinear state.

The occurrence of the helical magnetic structure in the low-temperature state of CuB_2O_4 can be supported by the presence and absence of the angular dependence of the resonance parameters in the basal plane at fields above and below $H_{c\perp}$, respectively. In the absence of external magnetic field, the local antiferromagnetic vectors in the helical structure are uniformly distributed over all directions in the basal plane. Under the external magnetic field, the helicoid is distorted and transformed into a fanlike structure, in which the antiferromagnetic vectors are distributed within the sector of angular size α. If the α value is comparable to the period of tetragonal angular dependence ($\pi/2$), the averaging over all the local positions results in the absence of the angular dependence of the resonance parameters in the basal plane.

For the refinement of the magnetic structure of CuB_2O_4, it is necessary to perform the neutron diffraction analysis of this crystal.

Thus, in the present work, we studied the frequency–field and temperature dependences of the resonance absorption in the tetragonal CuB_2O_4 single crystal.

At T = 4.2 K, the frequency–field dependence at $\mathbf{H} \perp C_4$ exhibits an abrupt change in the field $H \approx$ 12 kOe, which is connected with the transition from the low-temperature state to the weak ferromagnetic state. It is found that the temperature of this transition depends on the magnetic field $H_\perp$ applied across the basal plane of the crystal and is independent of the field along the C_4 axis.

The phase diagram for the CuB_2O_4 crystal is constructed on the $H_\perp$–T coordinates.

In the weak ferromagnetic state, the frequency–field dependence at $\mathbf{H} \perp C_4$ is typical of easy-plane antifer-

romagnets with the Dzyaloshinski interaction. The temperature dependence of the Dzyaloshinski field is determined from the experimental data at temperatures of 4.2–20 K.

An analysis of the frequency–field dependences at $T = 4.2$ K demonstrates that CuB_2O_4 in the low-temperature phase is not a collinear antiferromagnet with the easy anisotropy axis aligned parallel to the C_4 axis. It is assumed that, upon transition to the low-temperature state, the magnetic moments remain in the basal plane of the crystal, but the resulting magnetic structure allows no weak ferromagnetic moment.

ACKNOWLEDGMENTS

We would like to thank K.A. Sablina for the growth of high-quality CuB_2O_4 single-crystals and A.M. Vorotynov for fruitful discussions.

This work was supported by the Krasnoyarsk Regional Scientific Foundation, project no. 8F0156.

REFERENCES

1. G. A. Petrakovskiĭ, K. A. Sablina, A. I. Pankrats, *et al.*, J. Magn. Magn. Mater. **140–144**, 1991 (1995).
2. G. A. Petrakovskiĭ, Izv. Vyssh. Uchebn. Zaved., Fiz. (1), 91 (1998).
3. H. Tanaka, K. Takatsu, W. Shiramura, *et al.*, J. Phys. Soc. Jpn. **65** (7), 1945 (1996).
4. A. M. Vorotynov, A. I. Pankrats, G. A. Petrakovskiĭ, *et al.*, Zh. Éksp. Teor. Fiz. **113** (5), 1866 (1998).
5. G. A. Petrakovskiĭ, K. A. Sablina, D. A. Velikanov, *et al.*, Kristallografiya, 1999 (in press).
6. G. A. Petrakovskiĭ, K. A. Sablina, D. A. Velikanov, *et al.*, Fiz. Tverd. Tela (St. Petersburg) **41** (7–8) (1999).
7. G. Petrakovskiĭ, D. Velikanov, A. Vorotinov, *et al.*, J. Magn. Magn. Mater., 1999 (in press).
8. I. S. Jacobs, R. A. Beyerlein, S. Foner, *et al.*, Int. J. Magn. **1** (1), 193 (1971).
9. V. I. Ozhegin and V. G. Shapiro, Zh. Éksp. Teor. Fiz. **54** (1), 96 (1968).
10. V. I. Ozhegin and V. G. Shapiro, Zh. Éksp. Teor. Fiz. **55** (5), 1737 (1968).
11. G. A. Petrakovskiĭ, A. D. Balaev, and A. M. Vorotynov, Fiz. Tverd. Tela (St. Petersburg, 1999) (in press).
12. A. S. Borovik-Romanov and E. G. Rudashevsky, Zh. Eksp. Teor. Fiz. **47** (6), 2095 (1964).
13. A. I. Pankrats, D. Yu. Sobyanin, A. M. Vorotinov, *et al.*, Solid State Commun. **109** (4), 263 (1999).
14. L. P. Regnault, J. Rossat-Mignod, A. Adam, *et al.*, J. Phys. (Paris) **43** (8), 1283 (1982).
15. A. G. Gurevich, *Magnetic Resonance in Ferrites and Antiferromagnets* (Nauka, Moscow, 1973).
16. E. G. Rudashevsky, V. N. Seleznyov, and L. V. Velikov, Solid State Phys. **11** (8), 959 (1972).
17. A. Rouco, X. Obradors, M. Tovar, *et al.*, Phys. Rev. B: Condens. Matter **50** (14), 9924 (1994).
18. A. M. Kadomtseva, A. S. Moskvin, I. G. Bostrem, *et al.*, Fiz. Tverd. Tela (Leningrad) **19** (6), 2286 (1977).
19. E. A. Turov, *Physical Properties of Magnetically Ordered Crystals* (Akad. Nauk SSSR, Moscow, 1963).
20. A. Adam, D. Billerey, C. Terrier, *et al.*, Phys. Lett. A **79** (4), 353 (1980).

Translated by O. Borovik-Romanova